THE AERODYNAMIC PERFORMANCE OF AN ANNULAR S-SHAPED DUCT

by

D.W.Bailey

Submitted for the degree of Doctor of Philosophy

Department of Aeronautical and Automotive Engineering and Transport Studies

Loughborough University

August 1997

Dedication

To Mum and Dad

Abstract

An experimental investigation has been carried out to determine the aerodynamic performance of an annular S-shaped duct representative of that used to connect the compressor spools of aircraft gas turbine engines. Measurements of both the mean flow and turbulent structure have been obtained using both 5 hole pressure probes and a 3 component Laser Doppler Anemometry (LDA) system. The measurements indicate that development of the flow within the duct is complex and significantly influenced by the combined effects of streamwise pressure gradients and flow curvature.

For inlet conditions in which boundary layers are developed along an upstream entry length the static pressure, shear stress and velocity distributions are presented. The data shows that as a result of flow curvature significant streamwise pressure gradients exist within the duct, with this curvature also affecting the generation and suppression of turbulence. The stagnation pressure loss within the duct is also assessed and is consistent with the measured distributions of shear stress. More engine representative conditions are provided by locating a single stage compressor at inlet to the duct. Relative to the naturally developed inlet conditions the flow within the duct is less likely to separate, but mixing out of the compressor blade wakes increases the measured duct loss. With both types of inlet conditions the effect of a radial strut, such as that used for carrying loads and engine services, is also described both in terms of the static pressure distribution along the strut and its contribution to overall loss.

The effects of inlet swirl on the flow field that develops within an annular S-shaped duct have also been investigated. By removing the outlet guide vanes from an upstream single stage compressor swirl angles in excess of 30° were generated. Results show that within the S-shaped duct tangential momentum is conserved, leading to increasing swirl velocities through the duct as its radius decreases. Furthermore, this component influences the streamwise velocity as pressure gradients are established to ensure the mean flow follows the duct curvature. Consequently in the critical region adjacent to the inner casing, where separation is most likely to occur, higher streamwise velocities are observed. Within the duct substantial changes also occur to the turbulence field which results in an increased stagnation pressure loss between duct inlet and exit. Data is also presented showing the increasing swirl angles through the duct which has consequences both for the design of the downstream compressor spool and of any radial struts which may be located within the duct.

Acknowledgements

This work was carried out in, and financially supported by, the Department of Aeronautical and Automotive Engineering and Transport Studies, Loughborough University, and the author is grateful for the opportunity to carry out this research.

The research was supervised by Dr.J.F.Carrotte whose guidance and contribution to the work is gratefully appreciated. In particular, the author is indebted for the guidance and assistance he has received in the acquisition of LDA measurements. Dr.J.F.Carrotte's approachability and enthusiasm have been important factors in the completion of this work, while his professionalism and sense of humour have made the work both rewarding and enjoyable.

As overall director of research, Professor J.J.McGuirk has provided valuable advice throughout and has encouraged the publication of results. A special acknowledgement is given to Professor S.J.Stevens, whose encouragement and guidance has been invaluable.

The author would also like to express his appreciation to the other members of the research group, including Mr.A.P.Wray, Dr.P.A.Denman, for the help and advice they have given during the course of this work. In particular, Mr.A.P.Wray's 5 hole probe analysis techniques and Dr.P.A.Denmans help with hot wire anemometry measurements are gratefully acknowledged. A special acknowledgement is given to Mr.K.M.Britchford whose original work has provided a basis for comparison and, whose encouragement of this later study is gratefully appreciated.

The author would like to express his appreciation to Messrs. R.Marson, D.Glover, L.Monk and B.Niven for their technical assistance in the modification of the test facility and instrumentation hardware. In addition, the author would like to thank his office colleagues Mr.A.Barker, Mr.N.Eccles, Mr.A.Little and Mr.A.Spencer for their assistance and cooperation and, as for all of the aforementioned, with whom it has been a pleasure to work.

Finally, to both family and friends who have patiently endured my company (or the lack of it!) during the writing of this thesis - Cheers, I think it's my round.

They think it's all over, ...It is now.

List of Contents

List of Figures

List of Tables

NOMENCLATURE

In order not to depart from the conventions normally employed in the published work, it was found necessary to use the same symbol to denote several different quantities.

A	area
A_1	annulus area at inlet to S-shaped duct
A_2	annulus area at exit from S-shaped duct
a_{ij}	direction cosine
BW	band width
b	wake width
$b_{1/2}$	semi-wake width
C_a	LDA calibration factor
C_D	drag coefficient
C_f	skin friction coefficient
C_p	static pressure coefficient
C_μ	constant in eddy viscosity
c	true chord
D	inlet dynamic head
D	diameter
D	drag force
D/Dt	substantial derivative
DF	diffusion factor
D_p	dynamic pressure parameter
d	diameter
F	empirical curvature correction factor
f_D	Doppler frequency
f_n	frequency resolution
f_s	sampling frequency
H	boundary layer shape parameter ($=\delta^*/\theta$)
H	annulus height at inlet of S-shaped duct
h	annulus height

Nomenclature

h	ratio of local (R+n) to reference (R) radius of curvature (=1+n/R)
h_1,h_2,h_3	metric coefficients
2I	integral time scale
K	tangential blockage
K_n	fractional part of dynamic head which is sensed by hole n
k	turbulent kinetic energy (=½(u'2+v'2+w'2))
L	S-shaped duct axial length
L_c	length scale (proportional to the eddy size)
L_{ps}	pressure surface semi-wake width
L_{ss}	suction surface semi-wake width
l	mixing length
M	Mach number
M_x	axial momentum
M_θ	tangential momentum
m	mass flow
$mT^{1/2}/Ap$	non-dimensional mass flow coefficient
N	number of signal samples
N	number of samples in the statistical population
N	compressor speed (rpm)
$N/T^{1/2}$	non-dimensional compressor speed
N_0	particle arrival rate
N_2	validation rate
n	cross-stream co-ordinate normal to the s direction (see Fig.3)
P_i	pressure sensed by one of the side holes (2 or 4)
P_{ij}	generation term
P_n	pressure senced by hole n
P_t,p	stagnation pressure, static pressure
PPS	pseudo pitch angle
q	dynamic pressure
R	geometrical radius of curvature

Re	Reynolds number
Re_θ	Reynolds number based on momentum thickness
Ri	Richardson number
RI	record interval
r	radius
SNR	signal to noise ratio
S_p	stagnation pressure parameter
s	streamwise co-ordinate
s	blade pitch
T	temperature
Tu	turbulence intensity (u/U)
T_λ	Taylor microscale
t	blade thickness
U	mean velocity component in streamwise direction
U	blade speed
U_{BSA}	measured non-orthogonal velocity component
U_c	wake center line streamwise velocity
U_{edge}	streamwise velocity at edge of wake
U_{mean}	overall area weighted spatial mean streamwise velocity
$U_p(r)$	inviscid potential streamwise velocity at radius r
U_{pw}	inviscid potential streamwise velocity at the wall
U_τ	friction velocity
U^+	dimensionless velocity
u'	fluctuating velocity component in streamwise direction
$\overline{u_i'u_j'}$	Reynolds shear stress component ($\overline{u'v'}$, $\overline{v'w'}$, $\overline{u'w'}$)
$\overline{u_i'u_i'}$	Reynolds normal stress component ($\overline{u'u'}$, $\overline{v'v'}$, $\overline{w'w'}$)
$\overline{u'v'}$	primary Reynolds shear stress component
V	mean velocity component in normal direction
V_a	axial velocity
V_c	velocity scale (proportional to the turbulence intensity)
v'	fluctuating velocity component in normal direction
W	mean velocity component in tangential direction
w'	fluctuating velocity component in tangential direction

X	pitch pressure parameter
x	axial distance
x,y,z	Cartesian coordinates
Y	yaw pressure parameter
YTR	true yaw angle
y	normal distance from wall
y^+	dimensionless distance from wall
Z	confidence interval

GREEK

α	kinetic energy flux coefficient
α	angle between 1D probe and traverse plane
β	angle between 2D probe and traverse plane
β	empircal curvature coefficient
ΔC_p	pressure difference between casings
Δp	peak static pressure rise
Δt_i	transit time of the ith particle
ΔV_θ	change in swirl velocity across the blade row
δ	boundary layer thickness
δ^*	displacement thickness
δ_{ij}	Kronecker delta
ε	dissipation rate of turbulent kinetic energy
ε_μ	error associated with the true mean (μ)
Φ	scalar
ϕ	coordinate in circumferential direction
ϕ	flow coefficient (=Va/U)
γ_g,γ_b	angle of 2D beams from the axial-radial plane
γ	confidence level
Λ	streamwise velocity defect in the wake
λ	laser light wavelength
λ	stagnation pressure loss coefficient
μ	true mean
μ	absolute viscosity
μ_t	eddy viscosity
υ	kinematic viscosity
ψ	blade loading coefficient

θ	laser beam intersection angle, or angular separation
θ	momentum thickness
ρ	density
Ω_s	streamwise vorticity
σ	signal variance
σ	solidity (=c/s)
τ_{ij}	total shear stress
τ_w	wall shear stress

SUPERSCRIPTS

-	time average
-	area weighted spatial mean value
~	mass weighted spatial mean value
aw	area weighted spatial mean value
mw	mass weighted spatial mean value

SUBSCRIPTS

i,j	tensor notations
i	inner casing
o	outer casing
p	potential velocity
pw	potential velocity at wall
w	wall value
1,2....	traverse plane location (see Fig.2.23)

Chapter 1 Introduction

1.1 Application of Annular S-Shaped Ducts Within Gas Turbine Engines

Since the running of the first experimental prototype in 1937, the gas turbine jet engine has become widely used in aircraft propulsion due to its ability to produce large amounts of power, at low weight, relative to other power-plants. The gas turbine engine basically consists of a compressor, which supplies air to a combustion chamber where fuel is injected and combustion takes place, so adding thermal energy to the flow which is then expanded through a turbine. The resulting high pressure and temperature gas is then expanded through a nozzle to produce a high velocity jet.

In the continuing quest for increased power-plant performance considerable attention has, and is, being focused on ways of improving component efficiency. In the case of the compressor, for example, flow stability dictates that compression be divided between 2 or 3 compressor spools. Furthermore, efficiency considerations dictate that the mean diameter of each spool must reduce as the air density increases through the compression system. Thus, the annular duct (Fig.1.1.a) connecting the low and high pressure spools takes the form of an S-shape. In a similar way, annular S-shaped ducts (Fig.1.1.b) are also used to provide continuity between the flow passages of the high pressure (HP) and low pressure (LP) turbines. However, in contrast with the compression system, the mean diameter of each turbine spool increases through the engine offering the potential advantage of reducing the flow coefficient (V_a/U) in the following stages and leading to an increased efficiency. In industrial and marine engines, annular S-shaped ducts (Fig.1.1.c) are used to match the gas generator, which is typically a high speed core at a small diameter, with the power turbine which has a lower speed and operates at a larger diameter. It can therefore be seen that annular S-shaped ducts are present in many gas turbine engines connecting the flow passages of both low and high pressure turbine and compressor spools.

Whilst further development of the gas turbine engine implies a need for continuing improvement in overall cycle and individual component efficiencies, inter-component ducting must no longer be considered to merely perform the service function of transporting fluid from one component to the next. This ducting must be seen as an important engine part, its operation having a significant bearing on engine

performance. To optimise the geometry of such ducts though, manufacturers must investigate in greater detail the aerodynamic process taking place, both by measurements and through the development and utilisation of calibrated numerical flow prediction techniques. As an aid to the development of such an understanding, this work details an experimental investigation to determine the aerodynamic performance of an annular S-shaped duct representative of that used to connect the compressor spools of aircraft gas turbine engines.

Within an S-shaped duct, flow separation must be avoided if the performance of the downstream compressor spool is not to be adversely affected. Furthermore, the provision of a suitable and known flow distribution at duct exit, to which a downstream spool can be designed, must also be achieved whilst stagnation pressure loss within the duct should be minimised. As well as satisfying these objectives though, several other conflicting requirements should also be considered. For example, in aircraft applications it may be desirable for the axial length of the duct to be minimised in order to reduce the weight penalties associated with engine length. For example, the compressor interconnecting duct of the twin-spool Pratt and Whitney PW4000 (Fig.1.1.a) represents approximately 6.5% of the overall engine length. The three-spool Rolls Royce RB211 and Trent engines both use interconnecting ducts between the intermediate (IP) and high (HP) pressure compressors, with these ducts representing approximately 4.8% and 4.1% of engine length respectively. In addition, the duct passage may be further complicated by the presence of radial struts, such as those within the Rolls Royce Trent engine (Fig.1.2) which carry loads and engine services, or by the flow characteristics of the turbomachinery environment.

The flow at inlet to the compressor interconnecting duct tends to be complex, possessing rotor and stator wake components as well as radial profiles of total pressure, axial and swirl velocity. If the flow at entry to the duct is swirling then the boundary layers will be further modified. In a gas turbine engine potential benefits could arise, in terms of a reduction in the overall length of the compression system or in terms of overall performance, if swirling flow were allowed to pass between the upstream and downstream compressor spools linked by the duct. However, improvements in compressor performance brought about by allowing some degree of residual swirl to pass down the duct can have serious implications on the design of both the duct and the radial struts often found within such ducts. To optimise the design of an interconnecting passage to fulfil these conflicting requirements is

therefore difficult to achieve in practice, and is made more difficult by the complex flow field that develops within the duct.

As the flow follows a curved path within the annular S-shaped duct a modification to the static pressure field occurs (Fig.1.3). Thus, across the first bend a pressure gradient is present, with the pressure close to the outer casing being higher than that adjacent to the inner. However, this situation is reversed within the second bend as the flow is returned to the axial direction. Consequently streamwise pressure gradients arise which have a significant influence on boundary layer development along each casing. In addition, streamline curvature can have a direct effect on the turbulence structure due to the imbalance that can arise between the centripetal acceleration of a turbulent fluid element and its surrounding pressure field. It is therefore necessary to have a thorough and detailed knowledge of the flow physics before an improved duct design method can be formulated and applied to a variety of applications.

The evolution of the design process, through advances in computer performance, has led to ever more complex aerodynamic predictions replacing the geometrical methods used in the past. In recent years axisymmetric throughflow methods incorporating the streamline curvature type of calculation for the inviscid core flow, coupled with predictions of the boundary layer development, have replaced potential flow analysis. These methods assume that, at any point along the duct, the throughflow may be considered to consist of an inviscid core upon which a boundary layer profile may be superimposed. In calculation of this boundary layer profile, the free stream pressure gradient is assumed to be that existing at the edge of this inviscid core even though the streamwise pressure gradient at the wall is likely to be significantly greater. Once the distribution of boundary layer thickness is known the edge of the inviscid core may be redefined and the entire calculation repeated. The solution proceeds in an iterative manner until convergence is obtained. The design criterion has also changed with the ability to more accurately predict boundary layer development. Previously, the effects of diffusion rate upon boundary layer growth and separation in ducts were assessed using a loading factor ($\Delta p/D$). It was found that a limiting value of the ratio of the peak static pressure rise (Δp) to the inlet dynamic head (D) existed, beyond which separation was imminent and duct performance deteriorated rapidly. However, the ability to predict boundary layer development has led to the 'loading factor' being replaced by the 'shape factor' (H) as the guide to imminent separation within the duct.

While this form of analysis is relatively simple and not particularly time consuming, compared to more complex turbulence modelling, it has long been thought to give adequately accurate answers for conservatively designed geometries. However, if the design of a wide variety of annular S-shaped ducts is to be optimised, it is probable that such a method will not give adequate results in more highly loaded ducts since, for example, the throughflow method is unable to resolve the already noted effects of streamline curvature on the turbulence field or the variation of the streamwise pressure gradient across the boundary layer.

The current 'state of the art' design methodology is based on the prediction of the flow using turbulence modelling. However, the ability of even the most complex models to resolve the effects of streamline curvature on the turbulence field is questionable, while the predictions of boundary layers subjected to strong pressure gradients remain largely unvalidated due to the lack of good quality experimental data free from 3 dimensional effects. Furthermore, while computing power is now sufficient for the three dimensional flow field that exists within the S-shaped duct of a modern gas turbine engine to be calculated, detailed measurements of both the mean and fluctuating flow fields are required both to validate and define the boundary conditions to such calculations.

The effects of both streamwise pressure gradients and curvature on this complex flow field must therefore be understood before a new design methodology can be introduced. Furthermore, any new design process should be based on inlet conditions representative of those that exist within a modern gas turbine. The prediction of strut loss and the effect of struts on the basic flow field within the duct should also be an important part of the design process if overall performance is to be optimised. Thus, there is a requirement for more detailed information before the gas turbine engineer can confidently specify annular S-shaped duct geometries, for various applications, which achieve the desired flow field whilst optimising many of the other conflicting requirements.

1.1.1 Annular S-Shaped Duct Geometry

An annular S-shaped duct may have a wide variety of cross sections and wall shapes. For engineering purposes though, where the S-shaped duct geometries are used to connect the flow passages of turbomachinery components, ease of design and manufacture dictate that simple geometries are used where possible.

The duct geometry is initially defined by the position and passage height of the exit annulus relative to the inlet annulus, and therefore determines to a large extent the severity of the design. However it does not determine absolutely the performance of the duct which is governed by the wall profiles. For example, the duct centreline curvature determines how rapidly the flow is turned and at what stage the turning is done. The first turn away from the engine axis is normally constrained to have a smaller radius of curvature than the second turn back to the engine axis. This has two potential benefits; firstly exit profile distortion is reduced by reducing the radial pressure gradients in the latter part of the duct and, secondly, there is less local diffusion required in the latter part of the duct thus reducing boundary layer growth and the likelihood of flow separation.

Having defined the inlet/exit geometry and the centreline curvature, the next design constraint is made on the variation of geometric duct area with axial distance. The cross sectional area determines the overall amount and rate of diffusion within the duct. If the duct is required to diffuse the flow, then it is thought that rapid diffusion in the early stages of the duct reduces the overall stagnation pressure loss and the likelihood of flow separation, by allowing the diffusion to occur before the casing boundary layers have thickened. The wall profiles are then smoothed to avoid discontinuities and high local curvatures in regions of adverse pressure gradient. The inner wall profile is typically defined by a trigonometric function of the form;

$$r_i = H\cos\frac{\pi x}{L} - h\sin^2\frac{\pi x}{L} \qquad \text{(Eqn 1.1)}$$

with the outer wall then being fitted to give a linear variation of cross sectional area with axial distance.

The geometry of an annular S-shaped duct can be uniquely defined by a series of four non-dimensional parameters (Fig.1.4),

1. the area ratio (A_2/A_1)
2. length to inlet annulus height ratio (L/H)
3. the inlet hub to tip radius ratio (r_{1h}/r_{1t})
4. exit to inlet mean radius ratio (r_{2m}/r_{1m})

Treating duct geometries in terms of these non-dimensional parameters allows

the duct to be classified in a way similar to that, for example, of straight walled diffusers. It is therefore likely that a static pressure recovery map similar to that which exists for straight walled annular diffusers (Fig.1.5) also exists for S-shaped ducts with a common design philosophy. However, there is insufficient published work to generate such a map at the present time.

1.2 General Review of Relevant Work

Although there is very little published data available specifically on annular S-shaped ducts, a wide range of studies has been performed on flows subjected to curvature and/or pressure gradients. Furthermore, a large amount of data is available on the effects of inlet conditions, for example, on the flow within straight walled diffusers. This Chapter contains a review of what is thought to be the most relevant previous work to the study of the flow within an annular S-shaped duct.

1.2.1 Effect of Wall Curvature

As already discussed (Section 1.1), streamwise curvature of the flow within an annular S-shaped duct gives rise to two effects:

1. An adjustment of the radial pressure distributions to provide the forces necessary to turn the flow and thereby produce streamwise pressure gradients.

2. A direct effect on the turbulent flow field due to the imbalance that can arise between the centripetal acceleration of a turbulent fluid element and its surrounding pressure field.

These effects can therefore have a significant role in the development of the wall boundary layers, though the fact that they occur simultaneously within an S-shaped duct presents a further complication. Although a large number of relevant studies have been made, the vast majority of investigations have considered these effects in isolation.

1.2.1.1 Pressure Gradient Effects

The behaviour of a turbulent boundary layer in the presence of a positive (adverse) or negative (favourable) pressure gradient was initially studied by Nikuradse (1929). The author carried out a number of experiments on two-dimensional flows in

convergent and divergent flat walled channels with the semi-angle of the channels ranging from -8 degrees (convergent) to +4 degrees (divergent). Nikuradse found that the boundary layer in a favourable pressure gradient is much thinner than that within a zero pressure gradient (Fig.1.6.a), while in contrast the boundary layer within an adverse pressure gradient becomes much thicker. Furthermore, the author observed that at larger semi-angles and therefore stronger adverse pressure gradients, the turbulent boundary layer undergoes a fundamental change. The mean velocity profiles cease to be symmetrical and the flow becomes unstable. In such a situation the flow separates from one of the walls while the flow remains attached, largely due to minor surface disturbances, at the opposite wall (Fig.1.6.b). Nikuradse observed significant regions of flow reversal, the width of which tended to grow as the adverse pressure gradient becomes more severe. These experiments demonstrate the direct effect the applied pressure gradient has on the shape of the mean velocity profile.

A thorough experimental investigation of the effects of streamwise pressure gradients on the development of a turbulent boundary layer, including measurements of both the mean and fluctuating velocity components, was performed by Schubauer and Klebanoff (1951). This investigation consisted of measurements of the mean flow, three components of turbulence intensity and the primary shearing stress. The authors confirm Nikuradse's observation that upon entering a pressure gradient, a change in the boundary layer's mean velocity profile occurs. Furthermore, the pressure gradient was shown to have a greater effect on the momentum of the slower moving near wall fluid, compared to the relatively higher velocity fluid in the outer regions of the boundary layer.

As a result of these changes to the mean velocity profile, due to the pressure forces, the Reynolds stresses and their distribution within the boundary layer are also subsequently modified since the production of turbulence is a function of the velocity gradient ($\partial U/\partial n$). Hence, the mean velocity profile is then further altered due to these modified stresses acting on it. For example, Schubauer and Klebanoff (1951) showed how the shearing stress always acts in such a direction that fluid layers at larger distances from the surface "pull" on layers closer to it. When the pressure gradient is either constant or falling, all pull is ultimately exerted on the surface, and therefore the shear stress would be expected to be a maximum there. However, in an adverse pressure gradient, part of the pull must be exerted on the fluid near the surface that has insufficient energy of its own to advance against the regions of increasing pressure.

This means that the shear stress must have a maximum away from the surface (Fig.1.7) in regions of adverse pressure gradient, and the region between the casing and the maximum must be receiving energy from the region beyond the maximum. Thus, the fall in the shear stress towards the surface produces a positive gradient of shear stress, which leads to a diffusion of momentum towards the wall and allows the near wall fluid to advance against the increasing pressure. In contrast, when a favourable pressure gradient is applied the relative increase of momentum in the near wall region increases the wall shear stress, while the level of shear stress across the outer region of the boundary layer tends to reduce.

Of course the most critical condition, flow separation, occurs within an adverse pressure gradient when the flow next to the surface no longer continues to advance downstream. This is a result of the flow having insufficient energy to advance further into a region of increasing pressure. As a general rule, previous work has shown that the shape factor (H) can be used as guide to the imminence of separation. For example Schubauer and Klebanoff (1951) indicate that a shape factor (H) greater than 2.0 can be expected in regions close to separation, while a shape factor of 2.7 was found at the separation point. This result was in good agreement with a shape factor of 2.6 at the separation point given by Von Doenhoff et al. (1943), and the value of 2.5 obtained by Clauser (1953).

However, the above conclusions were obtained from boundary layers subjected to pressure gradients of constant sign and with no variation in pressure across the boundary layer ($\partial p/\partial n=0$). It can be seen that within the S-shaped duct complex distributions of shear stress develop, adjacent to each casing, as each boundary layer responds to the varying pressure gradients in both the streamwise ($\partial p/\partial s$) and radial ($\partial p/\partial n$) directions.

1.2.1.2 Streamline Curvature Effects

The effects of curvature on turbulent boundary layers have been under both experimental and theoretical investigation for some time. This is because of the many engineering applications where turbulent boundary layers pass over longitudinally curved surfaces including, for example, turbomachinery blade passages, aircraft wings and ducting. Boundary layers of this type have traditionally been calculated by ignoring wall curvature and using turbulence models appropriate to flat plate boundary layers. However, Bradshaw (1969) suggests that the behaviour of the turbulent

boundary layer is very sensitive to streamline curvature. The author showed that even a very mild wall curvature (corresponding to $\delta/R = 1/300$, where δ is the boundary layer thickness and R is the wall radius of curvature taken to be positive for convex curvature and negative for concave curvature) can cause a significant effect on the structure of the turbulence in the boundary layer.

Bradshaw (1973) provided a comprehensive review of the early work on streamline curvature effects and highlighted their importance. For example, Wilcken (1930) observed boundary layers that grew much faster on concave surfaces than on flat surfaces while, conversely, boundary layers were observed to grow slower over convex surfaces. Wall shear stresses were also greatly affected, increasing on a concave wall and decreasing on a convex wall, this being confirmed by the subsequent work of Eskinazi and Yeh (1956). An early experimental study of the effect of curvature on turbulence (Wattendorf, 1935) revealed changes in mean-flow properties much larger than had previously been predicted by mixing-length arguments. Wattendorf (1935) was able to relate these changes in the mean-flow properties to the imbalance that exists between the centripetal acceleration of a turbulent fluid element and its surrounding pressure field.

Bradshaw (1973) presented the traditional qualitative explanation, first given by Von Karman (1934) of the effect of streamline curvature on a fluid flow based on the motion of a disturbed element of fluid. This argument can be expressed in terms of a fluid element (Fig.1.8) moving with mean velocity (U_1) in a circular path of radius (r_1), with the centripetal force being balanced by a pressure gradient to maintain the trajectory.

$$\frac{\partial p}{\partial n} = \frac{\rho U_1^2}{r_1} \qquad \text{(Eqn 1.2)}$$

If the element of fluid is then displaced, by some externally applied force to a new radius (r_2), then its new velocity (U') can be calculated by assuming constant angular momentum (i.e. U.r = const.),

$$U' = \frac{U_1 r_1}{r_2} \qquad \text{(Eqn 1.3)}$$

However, this may result in a discrepancy between the centripetal force on the element and the pressure gradient which is required to maintain the trajectory of the mean flow with velocity U_2 at radius r_2 i.e.

$$\frac{\rho U_1^2 r_1^2}{r_2^3} \neq \frac{\rho U_2^2}{r_2} \qquad \text{(Eqn 1.4)}$$

Thus, it can be shown that if the angular momentum of the mean flow increases with radius, i.e. $(U_2r_2) > (U_1r_1)$, then the displaced element will be forced back towards its original position. Conversely, if the angular momentum of the mean flow decreases with radius, i.e. $(U_2r_2) < (U_1r_1)$, then the radial pressure gradient which keeps the mean flow in its circular path will be too small to keep the displaced element of fluid in equilibrium and it will move even further away from its original trajectory. Thus, the turbulent shear stress and intensity are reduced by curvature when the angular momentum of the flow increases in the direction of the radius of curvature, as in the case of a turbulent boundary layer passing over a convex surface. In contrast, for flow over concave surfaces, an increase in the turbulent shear stress and intensity occurs since the angular momentum decreases with radius. The experimental results reviewed thoroughly by Bradshaw (1973) consistently demonstrate an enhancement of turbulence mixing in shear layers passing over concave surfaces, with turbulence mixing being suppressed over convex surfaces.

Gillis & Johnston (1983) and Barlow & Johnston (1988) suggest that the ratio of boundary layer thickness (δ) to wall radius of curvature (R) should be the widely accepted parameter describing the magnitude of the curvature effects on the outer layer of the flow. They suggested an order of magnitude relation, where $\delta/R = 0.01$ was considered to be relatively mild curvature, whereas $\delta/R = 0.1$ was considered to be relatively strong curvature. Hoffmann and Bradshaw (1978) observed small changes in the turbulence quantities for both mild concave and convex curvature. They observed increases in the turbulence intensities of 10-20% over a concave wall and reductions of the same order over a convex wall. Furthermore, the turbulent shear stresses over a concave wall increased by approximately 10%, relative to the values found within the flat plate boundary layer, with a corresponding decrease of 10% over a convex wall. In strongly curved boundary layers, the curvature effect on the turbulence intensities has been shown to be very large. So and Mellor (1975) observed intensities and shear

stresses of twice the flat plate values in a concave boundary layer. In a strongly curved convex boundary layer, So and Mellor (1973) and Gillis and Johnston (1983) observed that the turbulent stresses fell to zero in the outer regions of the boundary layer. Furthermore, Baskaran et. al. (1991) showed (Fig.1.9) why the generation of primary shear stress ($\overline{u'v'}$), due to curvature ($u'^2(\partial V/\partial s - U/R)$), is most substantial in the outer layer, since this is where the streamwise velocity component (U) is greatest. Similarly, Bradshaw (1973) argued that curvature should have a larger effect on the outer layer than on the near wall region, because the strain-rate ratio $(U/R)/(\partial U/\partial y)$ diminishes approaching the wall. Further evidence of streamline curvature affecting different parts of the boundary layer has been seen in the mean velocity profiles. So and Mellor (1973, 1975) and Ellis and Joubert (1974) have shown that the mean velocity profile obeys the "law of the wall" in the near wall region for both concave and convex curved boundary layer flows. However, this near wall similarity was shown to extend no further than $y^+ = 50$, a result later confirmed by the work of Barlow and Johnston (1988) on the turbulent boundary layer on a concave surface. At larger distances from the wall, the mean velocity (Fig.1.10) either exceeds (convex) or lies below (concave) that of a flat wall profile when plotted in "law of the wall" coordinates. It should be noted that this work was performed using wall contouring in order to minimise streamwise pressure gradients which also effect the velocity profile. For example, an adverse pressure gradient leads to an upwards deviation from the log-law line. Thus, Moser and Moin (1987) postulated that, in the absence of streamwise pressure gradients, the point where the mean velocity profile deviates from the "law of the wall", and the magnitude of the deviation, must be dependent on the curvature parameter (δ/R). Shivaprasad and Ramaprian (1978) proposed that the effect of wall curvature is a nonlinear function of δ/R, being very strong at small values of δ/R, but increasing less proportionately as δ/R increases.

The difference in the rate of response of the turbulence to the onset of curvature has been noted in previous studies. Bandyopadhyay & Ahmed (1993) confirmed the early submissions of Ramaprian & Shivaprasad (1977), Prabhu, Narasimha & Rao (1983) and Muck, Hoffman & Bradshaw (1985) that a turbulent boundary layer is slower to respond to concave curvature than to convex. They showed that when the preceeding section is flat, the onset of concave curvature produces a change in wall shear stress after a delay of over 4 boundary layer thicknesses, while in contrast the lag was less than 3 boundary layer thicknesses for convex curvature. In experiments on the

response of a boundary layer to a sudden change from flat wall to convex curvature, Gillis and Johnston (1983) showed how curvature effects were clearly apparent one or two boundary layer thicknesses downstream of the start of curvature.

Several of the investigations already discussed (So and Mellor 1975, Barlow and Johnston 1988,) have reported large spanwise variations in boundary layers on concave surfaces that were quite persistent in the streamwise direction. These studies have shown that while mild convex curvature will attenuate the pre-existing turbulence, concave curvature leads to a significant change of the turbulence structure, induced directly by the curvature and indirectly by the formation of longitudinal vortices. These spanwise vortices are believed to be caused by large-scale roll cells produced by the same type of instability that leads to the formation of the Taylor-Gortler vortices (Fig.1.11) in a laminar boundary layer on a concave surface. Tani (1962) proposed that a turbulent version of the laminar Taylor-Gortler vortices exists after observing stationary spanwise variations in mean velocity in a boundary layer with concave curvature. These longitudinal vortices were found to give rise to spanwise variations in boundary layer thickness and skin friction. Many investigators have since made similar discoveries (So and Mellor 1975, Meroney and Bradshaw 1975), and have observed repeatable stationary patterns of spanwise variation. However, while some work has shown clear spanwise variations and attributed these to streamwise vortices, others (Jeans and Johnston 1982, Barlow and Johnston 1985) have found no evidence of such structures in time-averaged measurements. Meroney and Bradshaw (1975) attributed the repeatability of a stationary pattern of spanwise variation to upstream disturbances which serve to lock the longitudinal vortices to a particular position. Barlow and Johnston were able to make the roll cell pattern stationary by placing vortex generators upstream of the curved section, with these patterns extending the entire length of the duct. However, if the flow is relatively free of upstream disturbances, then Barlow and Johnston (1988) have shown that destabilising curvature leads to the formation of large scale structures which wander, merge separate, appear and disappear with no fixed spatial location. These large scale structures were shown not to produce significant spanwise variations in the mean properties of the boundary layer, and should not be described as longitudinal vortices as they are typically only 3 to 5 times the boundary layer thickness in length.

Axisymmetric swirling flows are closely related geometrically to flows over curved surfaces. The presence of swirl in a straight-walled annular passage introduces

an additional radial pressure gradient required to balance the centripetal acceleration acting on the mean flow. As a result, curvature effects are then introduced with the production of turbulent mixing being suppressed near the inner wall (convex curvature) and enhanced near the outer wall (concave curvature). These differences in turbulent energy production imply variation in the growth of the boundary layers and their ability to sustain streamwise pressure gradients without separation. Schlichting (1968), in a review of the work of Himmelskamp (1945), explained how separation can be delayed by the appearance of an additional acceleration created by a Coriolis force which acts in the flow direction and has the same effect as a favourable pressure gradient.

1.2.2 Effect of Inlet Conditions

All of the investigations discussed so far have been carried out under naturally developed inlet conditions, with velocity profiles generated by a carefully controlled growth of the boundary layers along an entry length, enabling the investigators to obtain a better understanding of the effects by using such well defined inlet conditions. However, the performance of an annular S-shaped duct is likely to be further influenced by inlet flow conditions such as;

1. Effect of the mean velocity profile and flow mixing.

2. Effect of Reynolds number and Mach number

3. Effect of flow non-uniformities due to blading.

4. Effect of swirling flows.

the impact of which, on the performance of an annular S-shaped duct, will be due to the effects on the boundary layer development within the duct.

Although little data directly pertinent to the flow in annular S-shaped ducts can be found, a number of studies offer indications as to the effects of inlet conditions on boundary layer development and it should be noted that this is the only published work available. The vast majority of these studies have been performed on two dimensional, conical and annular diffusers, and though most of the references in this section do not offer directly comparable data, work thought to provide meaningful background information is included for completeness. The objective of this review is therefore to offer some indication of the likely effect of inlet conditions on boundary layer

development and therefore the performance of an annular S-shaped duct.

1.2.2.1 Effect of the Mean Velocity Profile and Flow Mixing.

Sovran and Klomp (1967) presented a correlation method to determine the influence of inlet velocity profiles on diffuser performance. The non-uniformity of the inlet profile was defined in terms of the ratio of inlet boundary layer blockage to the inlet cross sectional area. Their method assumed negligible loss and low turbulence in the core flow. The correlation (Fig.1.12) shows a decrease in diffuser pressure recovery coefficient with the thickening of the inlet boundary layers. Later work though, by Stevens and Markland (1968) on an annular diffuser, indicated that thickening of the inlet boundary layer leads to a reduction in diffuser performance. However, Stevens, Williams and Nayak (1978) investigated the effect of both inlet blockage and turbulence on the performance of two straight core annular diffusers, finding that an increase in pressure recovery coefficient is obtained as fully developed flow conditions are approached. This work appears to contradict the earlier correlation, but the benefit is attributed to the increased turbulent mixing with the increase of blockage at diffuser inlet. The work of Williams and Stevens (1971) and Stevens and Fry (1973) considered the performance of annular diffusers with detailed hot wire measurements at the inlet to determine the actual turbulence intensity distribution. The shear stress ($\overline{u'v'}$) distribution showed that substantial improvements in radial momentum transport were achieved by turbulence producing grids and wall spoilers.

Klein's review (1981) reported that the effects of initial turbulence and boundary layer shape factor are interconnected because profile distortion depends on both. Furthermore, diffuser performance is improved with the growth rate of the boundary layer's shape factor (H) being retarded as the inlet turbulence increases. Conversely, large values of the boundary layer shape factor (H) reduce the diffuser pressure recovery. Klein concludes that the inlet velocity profiles and turbulence have a significant effect on diffuser performance. For boundary layers generated carefully along an inlet section, the diffuser performance decreases as the inlet blockage is increased. However, an improvement in diffuser performance can be obtained with much thicker inlet boundary layers when combined with increased turbulent mixing. The effect of increased inlet turbulence is to reduce the boundary layer growth leading to an improvement in the pressure recovery coefficient, though an increase of inlet turbulence leads to an increase in total pressure loss.

In the only study that can be found, free stream turbulence intensity effects on a convex curved turbulent boundary layer have been investigated by You et. al. (1989). In their experiments, a fully turbulent boundary layer was grown on a flat plate and then introduced to a convex wall with constant radius of curvature ($\delta/R = 0.03$). Experiments were conducted with free stream turbulence intensities ($Tu=u'/U_{pw}$) of 1.85% and 0.65%, while turbulence levels exceeded 10% and 5% respectively in the near wall regions. Measurements were obtained in a zero streamwise pressure gradient and with similar flow conditions upon entry to the curved surface, thus separating the free stream turbulence effects from other effects. The authors found similar turbulence intensity profiles near the end of the curved surface for the two cases, even though the turbulence intensity profiles differed at entry. The authors therefore concluded that the effect of streamline curvature, of reducing turbulence levels, is dominating over free-stream turbulence intensity. Furthermore, though the higher turbulence case has an approximately 5% higher skin friction coefficient (C_f) upstream of the curve, this difference has diminished by the end of the curvature. However, no reference is made to the effects of free stream turbulence on a concave surface and it should be noted that these turbulence levels are significantly lower than those that might be expected in turbomachinery.

1.2.2.2 Effect of Reynolds Number and Mach Number

Williams (1972) discussed how an initial increase in inlet Reynolds number for a given profile generation length, causes changes in the velocity profile and turbulence structure, which is likely to affect diffuser performance. However, it is generally accepted (Klein, 1981) that the Reynolds number does not affect diffuser performance if the Reynolds number is large enough for transition phenomena to be absent. Furthermore, a high free stream turbulence level and boundary layer tripping devices will further inhibit it.

In tests on a diffusing interstage duct between a gas generator turbine and a power turbine, Japikse and Pampreen (1979) showed (Fig.1.13) that the compressibility effects of Mach numbers up to 0.7 have little effect on the diffuser pressure recovery.

1.2.2.3 Effect of Flow Non-Uniformities due to Blading.

Many of the experiments so far discussed have been conducted with inlet

conditions which are generally considered to be naturally developed, though a modified turbulence structure may be present. However, it is also important to consider the effects of more engine representative inlet conditions. In this section the non-uniformity of the inlet profile is taken to have been generated by flow spoilers, guide vanes or a complete compressor/turbine stage.

Wolf and Johnston (1966) tested symmetrical two dimensional diffusers for wake, jet, shear step and uniform shear flow inlet conditions. For the latter three profiles, with low velocity near the wall, a general deterioration in performance and flow stability was observed. However, with wake flow at inlet the performance increased above that obtained with naturally developed flow, although there was some uncertainty as to the origins of the performance gain. Senoo et. al. (1981) investigated the effects of upstream struts on an annular diffuser for inlet conditions with and without swirl. In the case with no swirl present, they found that the pressure recovery in the annular diffuser may sometimes be improved by the residual weak swirl left behind the struts.

Though little data was made available, Burrill and Barnes (1971) suggested that the performance of a duct behind a single stage compressor was dependent on the operating conditions of the outlet guide vanes, since it is the deflection which determines the magnitude of the secondary flows induced through the blade channel. The level of secondary flows in the channel implies a level of mixing between low momentum boundary layer fluid and the high momentum mainstream flow. Similarly, proximity of the OGV row to stall implies the character of the wake profiles and hence the level of mixing between wake fluid and the core flow. However insufficient measurements were available to form strong conclusions based on physical evidence.

In a study of the performance of outwardly curved annular diffusers, Stevens and Wray (1985) show how the presence of blade wakes generated by a single stage axial flow compressor can help to lessen the risk of separation by re-energising the wall boundary layers. They have shown that although a greater level of mixing associated with the blade wakes results in higher total pressure losses, a significant reduction in the distortion of the exit velocity profile takes place. Pfeil and Gong (1987) observed that the development of the turbulent boundary layers in a straight cored annular diffuser behind a single compressor stage were greatly influenced by the presence of wakes. The data presented from radial traverses both mid-way between, and within, the stator wakes were in distinct contrast. Outside of the influence of the stator wake,

the flow was essentially two dimensional, while a strongly three dimensional flow was observed within the stator wake. The turbulence structure was also observed to be significantly different for the two cases, though unfortunately there was insufficient data to form any sound conclusions on the extent of the wakes influence. The authors concluded that the design of such diffusers using two dimensional methods was questionable with the presence of upstream blade wakes.

1.2.2.4 Effect of Swirling Flows.

Bradshaw (1973) establishes a clear definition of a swirling flow in a review of the effects of streamline curvature on turbulent flow. In all cases, the mean velocity component (W) in the circumferential direction (θ) is assumed to be of the same order as the mean velocity component (U) in the streamwise direction (s). Bradshaw recommends that if it is much smaller, then the flow is better regarded as slightly three dimensional. In effect, swirling flows can be regarded as simple shear layers perturbed by an extra rate of strain (W/r) analogous to the extra rate of strain (-U/R) that appears in two dimensional curved flows. Bradshaw concludes that although some practical results and data correlations have been obtained, the subject is confusing, and that our basic knowledge is accordingly confused.

The majority of the data thought to be applicable to annular S-shaped duct studies has taken place only on annular diffusers in the absence of longitudinal surface curvature. Schwartz (1949), measured the effect of swirl on annular diffuser performance in tests on a geometry comprising of a cylindrical outer wall and a converging inner wall. It was found that maximum efficiency was achieved when the inlet swirl angle was equal to the expansion angle of the inner wall. Furthermore, it was noted that the swirl angles increased at the exit of the diffuser owing to the conservation of angular momentum (W.r = constant). Thus, as the radius of the inner wall decreased, the swirl angles in this region increased. Lohmann et. al. (1979) measured the effect of swirl on straight-wall annular diffusers. They concluded that increases in the inlet swirl angle lead to an increased distortion of the meridional velocity profile at diffuser exit, though the tangential component of the flow is relatively independent of the meridional flow in that angular momentum is essentially conserved. This effect has been seen in the work of Carrotte et. al. (1994) in work on annular combustor dump diffusers where the presence of tangential momentum at entrance to the diffuser system leads to significant changes in the swirl angles further

downstream. This is due to the change in radius, relative to the engine centreline that is undertaken by the flow within the diffuser system and the reduction in axial velocity. This provides some indication of the likely effects on swirl angle of the relatively large change in radius present within an annular S-shaped duct if tangential momentum is conserved.

Yeh (1958) conducted experiments with and without swirl on two concentric cylindrical walls to measure axial and tangential velocity profiles as well as turbulence intensities. It was found that for the case without inlet swirl, the two concentric walls behaved like flat plates with no pressure gradient. However, for the case with 25 degrees of inlet swirl, similar effects are seen over the two concentric walls as are seen over curved surfaces. Yeh observed that the boundary layer grew faster, and higher turbulence intensities were present, over the "concave" outer wall. Furthermore, the wall shear stress remained constant or even increased. In similar work Scott and Rask (1973) have shown how boundary layer development within an annular passage of constant radius is influenced by curvature effects introduced by a swirling flow.

A comprehensive experimental study of the effects of swirl on an equiangular straight walled annular diffuser was performed by Srinath (1968). It was found that overall pressure recovery increased with swirl angles up to a maximum of approximately 15 degrees. Furthermore, Srinath found that regions of flow separation could be removed with the introduction of swirl. Hoadley (1970) reported work from tests on straight core annular diffusers which showed an outer casing stall for zero inlet swirl which was removed with the introduction of inlet swirl. However, at high swirl angles the separation moved from the outer wall to the hub. Kumar and Kumar (1980) reported an experimental investigation of subsonic swirling flows through annular diffusers having both hub and casing divergence. The report concludes that the presence of inlet swirl was found to increase pressure recovery. It was found that the introduction of swirl substantially reduced the likelihood of separation at the casing and to shift the stall from the casing to the hub for stalled diffusers, due to the readjustment of the axial velocity profile when swirl was introduced. An investigation into the design and performance of annular diffusers by Kersh (1983) showed how separation could be delayed with the introduction of up to 30 degrees of inlet swirl, although the total pressure loss was shown to increase by over 50%.

Japikse and Pampreen (1979) reported a series of experimental test and computational analyses for two automotive gas turbine diffusers. The diffusers

included a turbine interstage diffuser and a turbine exhaust diffuser (Fig.1.14.a). In the case of the interstage diffuser they found that the good pressure recovery obtained for zero inlet swirl degraded at high swirl angles, while the exhaust diffuser showed little sensitivity to inlet swirl angle. Of particular interest, they note substantial differences in measured recovery between model and engine tests for the interstage diffuser. In the case of the model test the inlet swirl was generated by a row of stator vanes (Fig.1.14.b), while inlet conditions for the engine test were provided by a two-stage turbine (Fig.1.14.a). The higher recovery levels of the engine test indicating that the upstream effects of a rotor play an important role in subsequent flow development. In a later study Japikse (1984) argues that the method of swirl generation can yield different results in the performance of an annular diffuser. Japikse points out that most investigators who have studied the performance of annular diffusers under the influence of swirling flow have chosen to generate their swirl in a radial inflow plane in order to take advantage of the simple cascade design geometry. However, several investigations have been performed using axial cascades which offer the advantage that they more closely simulate the turbomachinery environment. It should be noted though, that these cascades are often of the variable geometry type, of simple flat plate design, and will tend to introduce hub and tip leakage. Japikse further notes that though inlet swirl is the essential subject of these investigations, important changes to the inlet turbulence intensity, velocity, pressure gradients, vorticity and inlet aerodynamic blockage are likely to be indirect variables.

It is likely that further understanding of the effects of inlet conditions on flow development within an annular S-shaped duct can be obtained by comparing experimental data with theoretical predictions.

1.3 Review of Predictive Methods.

Practically all turbulent shear flows, whether in turbomachinery or any other branch of engineering, are almost invariably subjected to complex strain features arising from the effects of curvature, swirl, pressure gradients, separation, impingement and body forces. The turbulence structure in such flows is known to be sensitive to all of these features and therefore if accurate predictions of these flows are to be made, the turbulence must be realistically modelled.

The starting point for the mathematical modelling of turbulence are the mean flow transport equations, or the Navier Stokes equations, which define the

instantaneous motion in a turbulent flow. Though solving these equations is mathematically possible (Direct Numerical Simulation), it is unlikely to be used to model any significant engineering flows at the present time and for the foreseeable future since the process is exceedingly expensive both in computer storage and processor time. There has therefore been a need to adopt a statistical approach for most engineering calculations.

Reynolds suggested the velocity be composed into a time average motion and a turbulent fluctuation from the mean, and time averaged the equations to form the Reynolds averaged Navier-Stokes equations (RANS). However, averaging leads to a loss of information, and introduces an additional group of terms in the mean momentum equation, namely the Reynolds stresses.

$$\frac{\partial}{\partial x_j}(\rho U_i U_j) = -\frac{\partial P}{\partial x_i} + \frac{\partial}{\partial x_j}\left[\mu\left(\frac{\partial U_i}{\partial x_j} + \frac{\partial U_j}{\partial x_i}\right) - \overline{\rho u_i u_j}\right] \qquad \text{(Eqn 1.5)}$$

Reynolds stresses

The task of turbulence modelling is therefore to produce equations to approximate the Reynolds stresses ($\overline{u}_i\overline{u}_j$), which arise in the momentum equations as a consequence of averaging the convection terms. Transport equations for the Reynolds stresses themselves can be obtained by manipulating the Navier-Stokes equations however, the Reynolds stresses are often related to other turbulence parameters which can be determined more simply than solving the differential equations. Most turbulence models use the parameters velocity scale (V_c, proportional to the turbulence intensity) and length scale (L_c, proportional to the eddy size) which characterise the motion of the large energy containing turbulence elements.

Turbulence models can be classified according to the number of transport differential equations which are solved for the turbulence parameters, velocity scale and length scale. The mixing length model proposed by Prandtl (1925) and Taylor (1915) has, for a long time, been one of the most popular models. It is sometimes referred to as a zero-equation model because it does not involve any transport (differential) equations. Simple models such as the mixing length model are based on the local equilibrium assumption, which implies that in simple shear flows the rate of dissipation (ε) is equal to the production of turbulent kinetic energy.

As already noted, Bradshaw (1973) published a comprehensive review of the literature on the effects of streamline curvature, and made it clear in this document that the effects of extra strain rates are large, being an order of magnitude greater than would be predicted by straightforward extensions of calculation methods for simple shear layers. Bradshaw recommended that mixing length models require drastic empirical modifications in order to reproduce the characteristics of curved shear layer flows. In most cases, the mixing length is multiplied by an empirical curvature correction, $F = 1 - \beta R_i$, where the sign of the Richardson number (Ri, a curvature parameter characterising the ratio of the extra rate of strain produced by curvature to the inherent shear strain) either gives a reduction or increase in length scale. Qualitatively, the effects observed are that convex curvature ($Ri > 0$) reduces turbulent energy and stress relative to levels in an otherwise equivalent but normal state of flow ($Ri = 0$) while concave curvature ($Ri < 0$) has the opposite effect. According to Bradshaw, the constant varies in the range $6 < \beta < 14$ for wall flows, and numerous studies of empirical modifications of the mixing length (Cebeci et. al. 1979, Johnston and Eide 1976) have failed to produce a universal value for the empirical curvature coefficient β. However, Johnston and Eide demonstrated the significant improvement which can be achieved with such a simple form of modification. The authors successfully calculated a number of flows with both curvature and rotation in practical turbomachinery flows. However, they declined to attempt flows with a strong destabilising effect due to concave curvature, arguing that they did not believe that a simple mixing length correction factor would, or should give realistic property variations due to complex changes of flow structure, even on the average. Furthermore, the authors were concerned at the suitability of applying a model based on the assumption of local equilibrium to a case where transport effects might be expected to be far from negligible.

The methods discussed so far are extensions of mixing length models that do not involve transport equations for the calculation of the turbulence parameters (velocity scale and length scale). However, these methods have been shown to lack generality in terms of the difficulty in prescribing an appropriate length scale distribution in complex flows. Greater generality can therefore only be achieved through models in which the turbulent velocity and the turbulent length scale are determined from the solution of additional transport equations.

The eddy viscosity hypothesis is an important element of most two-equation

turbulence models. Analogous to molecular transport, the Reynolds stresses are set proportional to the mean rates of strain;

$$-\rho\overline{u_i u_j} = \mu_t\left(\frac{\partial U_i}{\partial x_j}+\frac{\partial U_j}{\partial x_i}\right)-\frac{2}{3}\rho k\delta_{ij} \qquad \text{(Eqn 1.6)}$$

where; μ_t is the eddy (or effective) viscosity and by dimensional analysis can be shown to be proportional to $\rho V_c L_c$, k is the turbulent kinetic energy $0.5(\overline{u_1'}^2+\overline{u_2'}^2+\overline{u_3'}^2)$ and the term on the r.h.s. of the equation satisfies consistency with the definition of turbulent kinetic energy. Thus, in order to calculate the eddy viscosity, it is first necessary to calculate the turbulence velocity (V_c) and length (L_c) scales.

The most popular and widely tested two-equation turbulence model is the k-ε model (Jones and Launder, 1973) which uses the turbulent kinetic energy (k) and its dissipation rate (ε) as velocity and length scale variables respectively. While, in principle, any equation containing the characteristic velocity and length scales can be used, the modelled turbulent kinetic energy equation has been used most often as it contains very little empiricism. The k-ε model uses the eddy-viscosity hypothesis to relate the Reynolds stresses $\rho u_i u_j$ to the mean deformation rates through the relations $\mu_t \propto \rho V_c L_c$, $V_c = k^{1/2}$ and $L_c = k^{3/2}/\varepsilon$ leading to the following formula for the eddy-viscosity;

$$\mu_t \propto \rho\frac{k^2}{\varepsilon} = \rho c_\mu \frac{k^2}{\varepsilon} \qquad \text{(Eqn 1.7)}$$

where c_μ is a constant in many high turbulence Reynolds number flows and can be obtained form experimental data.

The k-ε model of Launder and Spalding (1974) emerged as a standard because of its relative simplicity and its success in predicting a wide variety of flows. However, some authors have reported serious deficiencies in the k-ε model for flows with strong streamline curvature and/or adverse pressure gradients. Rodi and Scheuerer (1983) tested three variations of the k-ε model in calculations of curved shear layers. They showed that none of the modifications to the k-ε model were fully satisfactory with respect to simulating all the details of the effects of curvature, with the main problems being encountered in the region of recovery from curvature. In a later study Rodi and

Scheuerer (1986) found that for flows in a strong adverse pressure gradient, the predicted dissipation is too small with the result that turbulent stresses are too large. In addition, the k-ε model consistently over estimates the value of the skin friction coefficient with the result that the calculated flow tends to remain attached where experiments indicate separation. The inability of the k-ε model to predict flows in adverse pressure gradients was also shown at the 1980-81 AFOSR-HTTM-Stanford Conference on Complex Turbulent Flows reviewed by Kline et. al. (1981). Furthermore, Wilcox (1993) argued that the k-ε model is only capable of providing satisfactory predictions for constant pressure and favourable pressure gradient shear layers, as inaccuracy in the modelling of the near wall regions dominates the solution in adverse pressure gradients. The prediction of swirling flows has also provided difficult problems for turbulence modellers, with the interaction between curvature and turbulence being particularly pronounced. Bradshaw (1973) recognised that though mixing-length and eddy viscosity type models may be adequate for some mildly-curved flows, they are unlikely to attain the standards of accuracy required for turbomachinery flows.

The use of nonlinear eddy-viscosity represents the current state-of-the-art in two equation modelling. Craft et. al. (1996) have developed a cubic eddy-viscosity model which performs much better than a conventional eddy-viscosity scheme in capturing the effects of streamline curvature over a range of flows. In order to assess the models prediction of streamline curvature effects, calculations of Ellis and Joubert's (1974) experiment on a fully developed curved channel flow were performed. The curvature leads to increased mixing near the concave surface and damping of the turbulence near the convex wall, with the shear stress on the convex wall being approximately 40% of that on the concave wall. This adjustment of the turbulence levels in the respective boundary layers results in an adjustment of the mean velocity profile which skews towards the concave surface (Fig.1.15). Craft et. al. (1996) have shown that the non-linear eddy-viscosity model is better able to predict the effects of streamline curvature than the standard model of Launder and Sharma (1974). The non-linear model predicts a shear stress ratio on the two walls of approximately 60% compared with nearly 90% in the case of the standard model. This is further reflected in the mean velocity profile, which the non-linear model predicts to have the correct asymmetry. However, the results are still quantitatively in error and, significantly, have been performed in the absence of streamwise pressure gradients.

Two-equation models originate from efforts to compute relatively simple flows. They work well in circumstances in which the flow is dominated by one shear stress and in which normal stresses and strains are of secondary importance. However, turbulence models based on the eddy-viscosity hypothesis treat the turbulent field as being isotropic ($\overline{u}^{,2}=\overline{v}^{,2}=\overline{w}^{,2}=2/3k$). Leschziner and Rodi (1981) found that the measured anisotropy of the normal stresses mean that the magnitude of the shear stresses may not be well predicted by the k-ε model. Furthermore, it is an inescapable fact that the Reynolds stresses are generated, transported and dissipated at different rates. There has therefore been a requirement for more advanced models which proceed via the exact equations describing the evolution of the Reynolds stresses.

The exact Reynolds stress transport equations (see Versteeg and Malalasekera 1995 for example), obviously contain many more unknowns than there are equations. A turbulence model is therefore required to represent these unknowns in terms of the Reynolds stresses themselves, the mean velocity gradient and any other quantities for which transport equations or algebraic formulae are available. Launder (1988) showed that the main reason for expecting that a second-moment closure model should achieve substantially greater predictive power than an eddy viscosity model is that the generation term may be handled without approximation, thus;

$$P_{ij} = -\left(\overline{u_i u}_k \frac{\partial U_j}{\partial x_k} + \overline{u_j u}_k \frac{\partial U_i}{\partial x_k}\right) \qquad \text{(Eqn 1.8)}$$

reveals exactly how the components of the strain field interact with the Reynolds stress field to affect the generation of Reynolds stress. All other terms contain higher order correlations, or correlations of gradients of fluctuations, and must therefore be approximated, to obtain closure of the Reynolds stress transport equation. However, as Leschziner (1994) points out, second-moment closure is not a single model but a framework within which a hierarchy of models are contained with considerable differences in complexity.

The variety and complexity of these models is rooted principally in the modelling of the redistribution of the Reynolds stresses by velocity and pressure fluctuations, termed the pressure-strain interaction. It is this term which is responsible for directing turbulence towards isotropy through the transfer of energy from high normal stresses to low normal stresses. Thus, though the second moment closure is

complex (indeed a full explanation of the complexity and variety of the models is thought beyond the scope of this work), these models are thought to represent a considerable advance on the mixing length and eddy viscosity formulations discussed earlier.

Bradshaw (1972) held the view that the most promising class of turbulence models for making numerical calculations of complex flows is that based on the solution of approximated equations for the Reynolds stresses (u_iu_j). The first model of this kind was proposed by Rotta (1951) and a few predictions of this type were obtained by Daly and Harlow (1970) and Reynolds (1970). However, the range of flows considered was too narrow to enable conclusions to be drawn on the general applicability of the models. Furthermore, their validity was limited to high Reynolds number regions, relying on the "universal" law to specify the boundary conditions at the wall. Since, there are many flows where the "universal" law is not valid, several workers (Launder et. al., 1975, Hanjalic and Launder, 1976) made attempts to extend the applicability right up to the wall.

Irwin and Smith (1975) used the model of Launder et. al. (1975) to calculate the development of a number of flows with streamline curvature. Their results demonstrated the ability of the model to predict the main features of curved flow, showing that the curvature terms in the Reynolds stress equations, though small, have an unexpectedly large effect. Furthermore, calculations based on the experiments of Meroney and Bradshaw (1975) on both convex and concave curved boundary layers showed how well the model predicted the development of shape parameter (H) and skin friction coefficient (C_f). In a later study Gibson et. al. (1981) performed a number of calculations of turbulent boundary layers over curved surfaces including Meroney and Bradshaw's (1975) experiment. This model reproduced quite closely the influence of the streamwise pressure gradient at the start of curvature and the downstream effects of curvature, with the results being comparable to those of Irwin and Smith (1975). However, as the authors indicate, the scope of Irwin and Smith's work was restricted by the limited amount of experimental data, and the authors therefore concentrated on more recent studies. Calculations were performed on a broad range of surface curvature using the experimental data of So and Mellor (1973), Smits et. al. (1979) and Gillis and Johnston (1979). The results demonstrated the ability of the second moment closure model to predict the main features of boundary layer flow over a convex surface, i.e. a reduction in growth rate, and the suppression of turbulence intensity and

shear stress in the outer part of the layer.

Shima (1993) provides a comprehensive assessment of the performance of a second moment closure, considering the effects of pressure gradient, free stream turbulence, streamline curvature and spanwise rotation. The model (Launder and Shima, 1989) has been applied to boundary layers in zero, favourable and adverse pressure gradients, with the results generally being in close agreement with experimental data. Of particular significance is the models ability to predict reasonable levels of shear stress for turbulent boundary layers subjected to strong adverse pressure gradients.

Previous works by Gibson and Younis (1986), Hogg and Leschziner (1989) and Jones and Pascau (1989) have established that the second moment closure model is better than the k-ε model at reproducing the main features of swirling flows. Gibson and Younis found the second moment closure model to be comparable with the experimental data for weakly swirling flows, while Hogg and Leschziner and Jones and Pascau concluded that the second moment closure has the proper mechanism to account for strong swirl effects. However, due to both the increased complexity required to model such a flow (since a 2D model will not predict axisymmetric flows without some modification) and to the lack of quality experimental data, the little work that exists has focused on swirling jet flows and is not pertinent to this investigation.

In one of the few studies incorporating both streamline curvature and pressure gradient effects, Jones and Manners (1989) performed calculations using both a k-ε and a second moment closure model on an S-shaped annular diffuser (Fig.1.16). Comprehensive mean velocity and shear stress measurements obtained for this case were presented by Stevens and Ecclestone (1969) and Stevens and Fry (1973). Mean velocity and shear stress profiles throughout the duct indicated a much better level of agreement, between prediction and experiment, for the second moment closure model. For example, at inlet to the first bend, the k-ε model over predicts the velocity near the outer wall, while the velocity near the inner wall is underpredicted. The authors argue that the effect of the bend should be to suppress the turbulence and shear stress near the outer wall while in contrast, the turbulence and shear stress increases near the inner wall. However, the k-ε model fails to reproduce this effect (Fig.1.17), incorrectly predicting the location of zero shear stress. In contrast, the radial distribution of shear stress is well predicted by the second moment closure model (Fig.1.17), resulting in a mean velocity profile comparable with the experimental data. However, of most

significance to the gas turbine engineer, the authors found that the k-ε model was unable to reproduce the recovery of the velocity profile from the adverse pressure gradient of the diffusing section resulting in a predicted velocity distribution with an opposite skew to the measured profile at diffuser exit (Fig.1.18). In contrast, the second moment closure model was able to more accurately reproduce the effects of streamline curvature, with the mean velocity profile at exit from the diffuser being in good qualitative agreement with the measurements. Thus, though the two-equation model predicted a profile slightly biased towards the inner wall, the second moment closure correctly predicts the velocity profile to be strongly skewed towards the outer wall. It is not surprising that the authors therefore conclude that the second moment transport equation turbulence models offer the only practical means of successfully computing flows of this type.

Leschziner (1994) points out that the standard k-ε model of Jones and Launder (1972) is still the most widely used turbulence model in industrial CFD. This result therefore has serious implications for the gas turbine engineer, since not only was the prediction quantitatively in error but also qualitatively, which may lead to the design of downstream components based on a profile completely opposite to that which really exists. Indeed a recent brief report (Bradshaw et. al., 1996) on the collaborative testing of over 100 turbulence modellers indicates that though eddy viscosity models have been successful enough to be used widely in industry, many real life engineering flows change rapidly in the streamwise direction. In such "non-equilibrium" flows eddy viscosity models can give misleading results as the turbulent stresses change much less rapidly than the mean flow field, while models based directly on the Reynolds stress transport equations perform much better. Furthermore, the publishing of detailed measurements, such as those contained in this thesis, may help gain the further understanding required to achieve good engineering accuracy.

1.4 Review of Work Specific to this Investigation

Within an annular S-shaped duct the pressure gradient and curvature vary continuously along the duct. Although it has already been shown that such effects have mostly been considered in isolation, there are a few examples where the combined effects have been investigated. Baskaran et. al. (1987) observed the effects of streamline curvature and streamwise pressure gradient on the turbulent boundary layer over a curved hill. It was noted that at the transition from concave to convex curvature,

in a region of strong favourable pressure gradient, an "internal layer" was formed. The behaviour of the "internal layer" was identical to that of a newly formed boundary layer, and was predominantly acted on by pressure gradient effects, whereas in the flow above the "inner layer" curvature effects dominated. A further study of the combined effects of pressure gradients and streamline curvature was performed by Bandyopadhyay and Ahmed (1993) for an S-shaped duct with rectangular cross-section. Although the flow was dominated by secondary end-wall effects, they also confirmed the formation of an "internal layer" at the point of curvature transition.

A review of published work on annular S-shaped ducts reveals only a few examples, the most relevant being tests on curved annular diffusers. Stevens and Ecclestone (1969) presented a detailed investigation of the flow through an annular diffuser similar in geometry to that proposed for the outer annulus of a combustion chamber (Fig.1.16), subsequently predicted by Jones and Manners (1989). Tests were carried out with a fully developed inlet flow at a Mach number of 0.12 and a Reynolds number of 1.4×10^5. The overall total pressure loss of the system, including inlet and outlet bends, was 21% of the mean inlet dynamic head, with almost all (82%) of this loss occurring within the diffusing section between each bend. They concluded that whilst the inlet bend has a relatively low loss coefficient it presents the diffuser with a distorted inlet velocity profile which is then accentuated by the adverse pressure gradient within the diffuser. The subsequent work of Stevens and Fry (1973) on the same geometry included turbulent shear stress data, analysis of which confirmed that the influence of the pressure forces in this diffusing region were dominant. Therefore the growth in the shape factor is attributed to initial flow distortion, caused by curvature of the flow in the inlet bend, which is then accentuated by the severe downstream adverse pressure gradients. Similar conclusions have been drawn by Stevens and Williams (1980) in studies on the performance of straight-core annular diffusers.

Further relevant work includes Thayers (1971) investigation of a curved wall infrared-suppressing exhaust diffuser. Two general types of curved-wall diffuser were evaluated: a) a single-curved diffuser with inner and outer walls that initially diverge from the engine centreline, and b) a double-curved diffuser, where both walls initially converge towards the centreline and then diverge. Tests were conducted with ambient air at diffuser inlet Mach numbers between 0.25 and 0.45 and inlet swirl angles between 0 and 32 degrees. Data showed that diffuser performance increased slightly

with swirl angle up to 20 degrees, but that the static pressure recovery dropped by 15% between 20 and 32 degrees of inlet swirl. The author has also produced one of only two relevant studies of the effect of struts within an annular curved diffuser. Six struts with elliptic cross section and zero camber were located within the duct such that the strut trailing edge was slightly upstream of the duct exit. Furthermore, the walls were contoured in order to take into account effects due to the aerodynamic blockage presented by the struts. Thayer found that when six struts were installed, increasing the inlet swirl angle to 20 degrees resulted in a reduction in static pressure recovery of up to 20%, while drastic losses occurred at swirl angles of 32 degrees. This was almost certainly due to high incidence onto the struts which will produce large wakes downstream. In addition, Thayer recorded the wall static pressure distribution adjacent to a strut and midway between struts for swirl angles of 0, 20 and 32 degrees. For the zero inlet swirl angle, the different shapes of the inner and outer wall pressure distributions indicated that large radial pressure gradients exist at some locations (Fig.1.19.a), with slight differences being seen between measurements adjacent to the strut compared with those taken mid-way between struts (Fig.1.19.b). Thayer observed much larger discrepancies as the inlet swirl angle was increased (Fig.1.19.c). However, only mean flow measurements have been obtained, using rakes and single radial traverses, and therefore detailed information on flow development is lacking. Burrill and Barnes (1971), whose work on the influence of inlet conditions has been reviewed earlier, have also produced work on an inter-compressor duct containing struts, but again there is insufficient data to draw any conclusions on flow development.

S-shaped ducts are commonly used between turbine stages of modern gas turbine engines. Dominy and Kirkham (1996) have produced a detailed investigation on the influence of blade wakes on the performance of interturbine diffusers. The experimental facility consisted of a diffusing annular S-shaped duct (Fig.1.20) with the following geometrical parameters:

1. area ratio (A_2/A_1) = 1.5
2. length to inlet annulus height ratio (L/H) = 5.0
3. the inlet hub to tip radius ratio (r_{1h}/r_{1t}) = 0.7
4. exit to inlet mean radius ratio (r_{2m}/r_{1m}) = 1.74

Inlet conditions were developed along a parallel section which contains a row of 34 fixed swirl vanes. A turbulence grid was fitted over the inlet contraction, producing a mean turbulence level of 4% at the inlet plane. The operating Reynolds number at

inlet to the duct was 3.9×10^5 based upon the inlet passage height. Test were carried out both with and without the flat plate swirl vanes which generate wakes comparable both in area and intensity to those of HP and IP turbine blades.

For the case with naturally developed inlet conditions, i.e with neither swirl nor wakes present, the static pressure distribution (Fig.1.21) along the inner and outer walls reflects both the wall curvature and the rapidly increasing duct cross sectional area. Regions of both favourable and adverse pressure gradient are apparent, with a long adverse pressure gradient beginning at the convex casing bend immediately downstream from the point of minimum static pressure. The development of the casing boundary layers is presented in terms of the boundary layer parameters (Fig.1.22). Dominy and Kirkham have shown that the peak shape factor occurs along the outer casing surface, peaking to a value of approximately 2.5 at 30% of the ducts axial length. However, the growth of the outer casing boundary layer in the rapidly diffusing flow after the first bend does not reveal a sufficiently rapid fall in shear stress to cause separation. Dominy and Kirkham conclude that this case represents a severe but stable datum against which the effect of wakes can be evaluated.

For the case with the flat plate swirl vanes, which can provide swirl of up to 40 degrees but in this case used to provide a nominally zero inlet swirl, Dominy and Kirkham have provided detailed area traversing of the flow field at 4 stations. At inlet to the diffuser, the vane wakes that have been generated some 2.5 axial chord upstream can be seen to be essentially two dimensional with only minor interactions between the wake and the wall boundary layers.

The effect of the strong pressure gradients, that occur within the S-shaped duct, on the wake and casing boundary layers has also been investigated. In the first bend, a radial pressure gradient is established which acts to turn the flow away from the rig centre line. As initially indicated by Britchford et. al. (1993) (reviewed later in Section 1.5) Dominy and Kirkham have confirmed that this cross-passage pressure gradient leads to a radial velocity component within the wake which is greatest towards the inner casing (Fig.1.23). Total pressure contours indicate some mixing out of the wake, though the authors indicate the wakes remain essentially two dimensional and appear to influence the wall boundary layers only in the immediate vicinity of the wake-boundary layer confluent region. At a traverse plane prior to the second bend, the effect of the strong adverse pressure gradient can be seen on the outer casing boundary layer. Dominy and Kirkham suggest that this is further exaggerated by the radial

movement of high loss wake fluid into the boundary layer, coupled with additional vorticity either side of the wake. The final traverse plane is located downstream of the second bend of the S-shaped duct, where the flow has been returned to the axial direction. As the flow is turned back towards the axial direction, the radial pressure gradient reverses, though its influence on the three dimensional flow characteristics that have developed upstream is thought to be negligible. Strong secondary flows are evident either side of the wake at both the inner and outer walls. These secondary flows lead to total pressure distortions and significant (±4°) local pitch and swirl angles over much of the passage. However, the authors have shown that despite the growth of the wake induced secondary flows within the duct, their influence on the performance of the S-shaped duct is remarkably slight. They reported no significant change in the wall static pressure distribution or the overall pressure recovery coefficient. However, it should be noted that in a more highly loaded duct, such wake induced secondary flows could help to avoid flow separation, with their influence on performance being of much more significance. Dominy and Kirkham imply that the three dimensional flows that are observed result primarily in a redistribution of the inlet loss and are not a creation of additional loss. Although the authors do not present any data pertaining to the actual stagnation pressure loss through the duct, from an analysis of the data presented, a loss coefficient based on the inviscid core stagnation pressure can be estimated. The loss coefficient is estimated to be of the order 0.065, this being the increase in loss relative to the stagnation pressure loss measured at the inlet plane and therefore represents the loss generated within the duct itself.

Dominy and Kirkham have provided important evidence of the influence of simple wakes on the flow within an annular S-shaped duct. They have shown how the flow downstream of the S-shaped duct presented to the turbine stage is significantly effected by casing boundary layers that have been affected by both the strong radial pressure gradients but also by radial wake flow and strong secondary flows. The authors note that the wake influences reported are of the simplest two dimensional case and the presence of more realistic wakes and swirl may contribute significantly to the development of the flow through an annular S-shaped duct. However, the authors provide no information of the turbulence structure of the flow, which is likely to be as important as the mean flow field in determining the development of the flow.

1.5 A Review of the Loughborough University Programme.

This section covers exclusively the annular S-shaped duct studies that have taken place in the Air Flow Laboratory at Loughborough University of Technology (LUT). The Air Flow Laboratory is particularly well equipped for this type of work having carried out experimental work on fully annular combustor diffusers and compressor OGV's for over 30 years, much of which is reviewed by Carrotte et. al. (1995). In recent years, the experimental group has been complemented with a theoretical group, experienced in advanced turbulence modelling. The study of advanced S-shaped duct concepts was first started at LUT in 1989 as part of a long term investigation. Britchford (1997) completed the first phase of the work, while this investigation forms the second phase of the programme.

The early work of Britchford et. al. (1993) focused on the development of the mean flow field within the S-shaped duct. Measurements were obtained both for inlet conditions in which boundary layers were developed along an upstream entry length (termed the "clean" inlet condition) and for more representative conditions provided by a single stage compressor. Britchford et. al. indicate that with a compressor stage at inlet the tendency for the flow along the inner wall to separate was reduced. The authors have shown that for the "clean" inlet condition, the peak value of shape factor (H) was 1.65. However, with the complete compressor stage at inlet to the duct, the peak shape factor reduced to 1.47. The authors have attributed this beneficial effect, in part, to the re-energising of the inner wall boundary layer by wake fluid which is driven towards the inner casing by the radial pressure gradient. The authors explain that though this fluid has a total pressure deficit, compared with the core flow between wakes, it is less than the deficit resident in the inner wall boundary layer. The consequence of this effect is that the inner wall boundary layer is more able to resist the effects of the adverse pressure gradient.

Carrotte et. al. (1993) developed techniques for making 3D coincident LDA measurements within an annular S-shaped duct. For inlet conditions in which boundary layers were developed along the upstream entry length, detailed measurements were made at a single traverse station located approximately one hydraulic diameter upstream of the S-shaped duct. The measurements therefore relate to flow which has developed within an annular passage but which has not been subjected to the effects of streamline curvature. Measurements were obtained within the transition region between the laminar sublayer ($y^+ \cong 10$) and the outer regions of

each of the casing boundary layers ($y^+ \cong 70$). From this data, Carrotte et. al. have determined the mean velocity profiles and all 6 Reynolds stresses, and calculated velocity skew, flatness and the triple correlations of the fluctuating velocities. The authors have compared the data with the widely published work relating to two dimensional turbulent boundary layers developed on flat surfaces. For example, the radial distribution of shear stress ($\overline{u'v'}$) within each boundary layer compares favourably with the data of Klebanoff (1955) and Schubauer and Klebanoff (1951). In addition, the distribution of the three components of turbulence intensity indicate similar trends as those obtained by Schubauer and Klebanoff (1951). The authors note that some discrepancies are apparent, particularly in the radial component (v'), which is suppressed significantly less by the casing. Some of this variation was thought to be due to differences in the way that each of the boundary layers was developed. Measurements such as these though are becoming increasingly important for the development of turbulence models. The anisotropy displayed in the data is of crucial importance to the correct representation of the Reynolds stresses as discussed earlier (Section 1.3.3).

Britchford et. al. (1994) used the techniques developed by Carrotte et. al. (1993) to measure the turbulent structure within the annular S-shaped duct for the "clean" inlet condition. This inlet condition has been used, in the first phase of the work, to gain a better understanding of the effects of streamline curvature on the flow within an annular S-shaped duct. Measurements have been obtained using a 3 component LDA system, providing information on mean velocity, all six Reynolds stresses and higher order correlations. For example, the authors present the development of the Reynolds shear stress ($\overline{u'v'}$) at 11 streamwise stations, with the remaining Reynolds stress distributions being the subject of a future publication (Britchford, 1997). In addition, CFD predictions of the flow using both the k-ε and second moment closure models of Jones and Manners (1989) have been carried out and compared with the experimental data. The authors have found that curvature effects are not described properly by the two-equation model, while such effects are better represented by the second moment closure model. The more accurate modelling of the Reynolds shear stress distribution results in a better prediction of the mean velocity profile. Thus, at the critical point along the inner wall, towards the end of the region of strong adverse pressure gradient, where the flow is most likely to separate, the second moment closure model predicts a shape factor (H) significantly closer to the measured value.

1.6 Objectives and Scope of the Present Investigation.

A survey of the published literature on annular S-shaped ducts shows that, while such ducts are important in turbomachinery applications, little work has been done in this field. This is thought due to both the difficulty of building a suitable test facility and to the long time scale required for an investigation into such a complex flow field. Thus, in view of the practical importance of the annular S-shaped duct and the lack of data available to the gas turbine engineer, such a duct was chosen as the subject of this investigation. Furthermore, while the majority of the previous work has been performed on ducts connecting turbine stages, this investigation focuses on an annular S-shaped duct representative of that used to connect the compressor spools of multi-spool gas turbine engines.

This thesis forms the second phase of a continuing investigation within the Air Flow Laboratory at Loughborough University of Technology. The scope of this second phase of the investigation is to provide the gas turbine engineer with information pertinent to the design of compressor inter-connecting ducts. The main objectives of this investigation being;

- To evaluate the overall performance of the annular S-shaped duct, both in terms of boundary layer development and stagnation pressure loss, over a range of inlet conditions.

- To indicate the flow mechanisms that contribute to the generation of stagnation pressure loss within the duct.

- To assess the effect on performance of a radial strut, such as that used for carrying loads and engine services, both in terms of the static pressure distribution around the strut and its contribution to overall loss.

- To identify the important flow mechanisms that are introduced when more representative inlet conditions are generated using a single stage axial compressor.

- To investigate the effects of inlet swirl on the flow field that develops within an annular S-shaped duct and to assess the consequences both for the design of the downstream compressor spool and of any radial struts which may be located within the duct.

- To provide detailed data which can validate and assist in the development

of prediction methods.

This thesis includes comprehensive measurements of the mean flow and turbulence structure within an annular S-shaped duct, some of the results having already been presented. Bailey et. al. (1995) have presented results on the performance of an annular S-shaped duct both for "clean" and compressor generated inlet conditions, with the effect of a single radial strut on the flow also being assessed. Furthermore, Bailey and Carrotte (1996) have presented results on the influence of inlet swirl on the flow within an annular S-shaped duct. Thus, significant steps forward have been made in the investigation of advanced S-shaped duct concepts. The long term objective of this investigation being the formulation of new methods for the optimum design of S-shaped ducts for a variety of engine configurations and operating conditions.

Chapter 2 Experimental Facility and Test Procedures

2.0 Experimental Facility and Test Procedures

Compressor inter-connecting ducts typically exist in harsh environments, with gas at elevated temperatures and pressures being supplied by complex rotating machinery. However, while it is desirable for a test facility to replicate the operating conditions that exist within modern gas turbines, such a facility is impractical both in terms of manufacture and operating costs. It should be noted that even gas turbine engine manufacturers are unable to obtain detailed measurements at design conditions due to the enormous expense of engine testing. Thus, in order to perform a detailed investigation of the flow within a compressor-interconnecting duct a test facility specifically for this purpose must be designed. The facility must simulate the main aerodynamic features associated with the S-shaped ducts, as typically found within modern gas turbine engines, whilst being practical to manufacture and operate.

Much of the work reviewed earlier (Chapter 1) has been carried out using 2D rigs, the simplest form of which has a rectangular cross section and offers the advantages of being inexpensive and relatively easy to modify. However, Wray et. al. (1993) indicate that such test facilities are aerodynamically compromised in two fundamental ways;

1. They cannot accurately model the effects of large changes in radius.
2. The build up of boundary layers on the end walls causes a significant migration of fluid towards the centre of the test section, so producing an effective reduction in area along the length of the facility.

Wray et. al. indicate that such effects are significant even in high aspect ratio test facilities. Measurements made by Carrotte et. al. (1992) in a high aspect ratio combustor diffuser facility (Width/Height=12) revealed an increase in mass flow, for the central sector region, of 10% between inlet and exit. Furthermore, although the use of more complex segmentally shaped rigs allows the effects of radius changes to be represented, the growth of end wall boundary layers is still a problem. Klein (1995) further suggests that the stagnation pressure losses derived from combustor diffuser tests on plane and sector models are inaccurate. Klein indicates that the flow in a fully annular test facility diffuses in both the streamwise and circumferential directions, thus creating more mixing and therefore higher losses, while the flow in sector facilities is only able to diffuse in the streamwise direction. Hence, to avoid these effects it is

therefore thought essential that the aerodynamic performance of an S-shaped duct be investigated in a fully annular test facility. Such a test facility though also lends itself to the generation of engine representative inlet conditions.

Previous work by Stevens et. al. (1984), Stevens and Wray (1985) and Carrotte et. al. (1994) has shown how the flow in combustor pre-diffusers is modified by the mixing of OGV wakes. This work includes the significant effects of OGV wake mixing on the boundary layers within combustor pre-diffusers, and such effects may therefore be important within S-shaped ducts. In previous S-shaped duct studies (e.g. Dominy and Kirkham, 1996), OGV wakes have been generated using a single row of flat plate vanes. However, the absence of secondary flow and tip leakage effects from an upstream rotor, means that the resulting wake structure is essentially two dimensional and not engine representative. Furthermore, the turbulence levels tend to be low compared to those that typically exist within a modern gas turbine. Thus, while the ideal method of generating inlet conditions would be to use a multi-stage compressor upstream of the working section, in this investigation a single-stage compressor has been used which provides a compromise between capturing the main aerodynamic features and operating cost. Furthermore, the single stage compressor can be easily removed, so that well defined inlet conditions, in which boundary layers are grown along the upstream entry length, can be generated.

The size of the test facility is restricted by the infrastructure of the laboratory in which it is located. The test facility is designed to fit into an existing stand within the lab, and to use the inlet and exhaust ducting already in place. The facility has therefore been made as large as practicable relative to these restrictions. Furthermore, while the operating conditions of the test facility are compromised, due to the practical limitations of running a facility at high speeds, it is thought the main aerodynamic features are retained. For example, the test facility is designed to operate such that the Reynolds number on each OGV blade is above its critical range, whilst the boundary layers at entry to the working section are turbulent. Within a gas turbine engine it is thought that low Reynolds number effects are not likely to be appreciable, with compressibility effects also being relatively small.

2.1 Description of the Test Facility

The general layout of the fully annular S-shaped duct test facility is shown in Fig.2.1. The choice of a vertical rig layout reduces the number of inlet support struts

needed, ensuring that the associated strut interference effects are minimised. Furthermore, while horizontal test facilities can become asymmetric due to deflection of the casings under their own weight, the choice of a vertical facility reduces such asymmetry. For ease of construction, the inner and outer tubes were manufactured in sections using a flange and spigot assembly to ensure concentricity. Since the flow is at ambient temperature, the majority of the inner and outer casings have been fabricated from acrylic, the remainder being hardwood. Acrylic has the advantages of being easy to form and machine, while the use of a transparent material helps the setting up of instrumentation and facilitates flow visualisation.

Air is drawn from outside the laboratory, to pass through an air filter and into a large inlet plenum. Having settled in this large plenum, the clean air is drawn through a scroll intake containing a honeycomb flow straightener. The air is accelerated in a contraction (incorporating aerodynamic struts which support the inner casing) formed by a centre bullet, the exit of which matches the annulus dimensions at inlet to the S-shaped duct. The flow adjacent to the inner and outer casings is artificially tripped in order to ensure stable transition to turbulent flow before entering the inlet section of passage height 0.071m and 7 hydraulic diameters long. Boundary layers are allowed to grow along the inlet length, and either provide axisymmetric inlet conditions to the working section or provide a velocity profile thought representative for inlet to the single stage axial flow compressor.

The most engine representative inlet conditions are provided by a single stage axial flow compressor (Fig.2.2) situated directly upstream of the S-shaped duct. The compressor rotor, comprising 43 blades, is driven by a DC motor sited beneath the test rig, regulated using a thyristor type controller which allows any speed in the range 0-3000 rpm to be maintained within a tolerance of 3rpm. The ambient air temperature and modest shaft speeds enable the compressor blades (rotor and OGV) to be manufactured relatively quickly and cheaply from Acrylonitrile-Butadiene-Styrene (ABS-101).

The compressor was designed to operate, at mid-height (Fig.2.3), with a blade loading coefficient (ψ) of 0.285 and a flow coefficient ($\phi=V_a/U$) of 0.56. The fully shrouded outlet guide vanes (OGV's), are designed to remove 30 degrees of rotor exit swirl and operate at a Reynolds number, based on OGV blade chord, of order 2.0×10^5. Although this value is not engine representative it is above the blading critical value, and previous work reported by Stevens and Young (1987) has indicated good

agreement between test data and previously published work at this and higher Reynolds numbers. The outlet guide vanes are housed in a ring with the stator row containing 62 blades of chord 0.051m, although for certain tests the outlet guide vanes can be removed. In such tests, the rotor was operated with a flow coefficient of 0.50, providing swirl angles in excess of 30 degrees at entry to the working section.

After passing through the working section the flow enters a parallel settling length, of 3.1 hydraulic diameters, and is discharged into the lower plenum chamber. The air then passes into the exhaust duct through a motorised throttle, which is used to maintain the compressor on its chosen operating point, prior to being expelled to atmosphere.

As already mentioned in Chapter 1, the annular S-shaped duct can be defined (Fig2.4) from four geometric parameters which have the following values;

1. area ratio (A_2/A_1) = 1.0
2. length to inlet annulus height ratio (L/H) = 3.4
3. the inlet hub to tip radius ratio (r_{1h}/r_{1t}) = 0.8
4. exit to inlet mean radius ratio (r_{2m}/r_{1m}) = 0.8

This combination of axial length and reduction in mean radius were chosen to give a conservative design to ensure well behaved flow. However, it should be noted that aerodynamic loading of the duct is still (thought to be) significantly higher than that associated with existing engine design practice. Within both bends of the S-shaped duct, the ratio of boundary layer thickness (δ) to wall radius of curvature (R) is of order 0.1. As suggested by Gillis & Johnston (1983) and Barlow & Johnston (1988) this indicates that relatively strong curvature effects are present within the duct.

2.2 Description of the Radial Strut

For certain tests a radial strut was located within the S-shaped duct (Fig.2.5). A single strut only was used since the significant aerodynamic blockage associated with a number of struts would require extensive modification to the facility. The use of a single strut in an unmodified test facility allows a direct comparison of the results with previous work. In addition, since existing gas turbine engines tend to have very few struts, typically of order 10 within the compressor inter-connecting duct, it is thought that the interaction between struts is relatively unimportant.

The uncambered strut was designed with a 12% thickness to chord ratio (c=190.94mm), thought to be representative of the load bearing struts found within modern gas turbine engines. A NACA65T profile was used to define the strut on the surface of revolution which bisects the annulus into equal areas. This thickness distribution (Fig.2.6) was then extrapolated, along radial lines, to define the distribution along each casing. A NACA '6' series profile has been chosen in this investigation since this low-drag family of airfoils have been the subject of extensive research and are therefore well understood. The NACA '6' series was designed (Abott and Von Doenhoff, 1949) to give a virtually constant loading (Fig.2.7) between suction and pressure surfaces from leading edge to trailing edge combined with a virtually constant surface static pressure over approximately 50% of the chord.

The strut within the S-shaped duct was manufactured from hard wood (Jelotong), using a number of profile templates. These templates were derived from the NACA65T profile which incorporates a finite thickness trailing edge, in contrast with the original NACA65 profile which has zero thickness at the trailing edge of the blade. This design (65T) was thought to be more representative of the struts typically found within modern gas turbine engines, while the finite thickness trailing edge is considerably easier to manufacture. After manufacture, the strut was then coated in an aluminium lacquer to give a high standard of surface finish and prevent the strut from absorbing any moisture in the air flow.

The leading edge of the strut (Fig.2.5) is located approximately 0.16 strut chord lengths downstream of the inlet to the S-shaped duct, while the trailing edge of the strut was positioned at the location where the pressure gradients within the duct were changing sign. Thus, immediately downstream of the strut in the critical inner wall region, the strut wake is subjected to a favourable pressure gradient, which is also accompanied by enhanced levels of shear stress due to curvature.

2.3 Instrumentation

While the test facility has been designed to capture the main aerodynamic features, provision must also be made to allow the measurement of such features. The instrumentation on the test facility is designed to provide detailed measurements of the mean flow, using mainly 5-hole pressure probes, and the turbulence structure within the S-shaped duct, which has been obtained using a colour separated 3 component LDA system.

2.3.1 Measurement of the Mean Flow Field

Pressure measurements were made using sub-miniature five hole pressure probes which provide information on total and static pressures and the velocity vector. The probe (Fig.2.8) consists of a cluster of five tubes (0.25mm inside diameter) giving an overall diameter of approximately 1.75mm. The five tubes are aligned such that one hole lies in the plane normal to the tip axis and four side holes lie in chamfered faces around the central hole.

The probes were used in a non-nulled mode as opposed to the more conventional method of manoeuvring the probe in both pitch and yaw directions until the pressures on the two opposing pairs of side tubes are in balance. At this point, the pitch and yaw angles are noted, while the central tube registers the local stagnation pressure. The dynamic pressure can then be shown to be a function of the difference between the pressures registered by the central hole and the four side holes. However, it has not been possible to implement this more conventional method of using the 5 hole probe since access into the test facility is limited, with rotation of the probe in the pitch direction being difficult to achieve. The probes in this investigation were therefore used in a non-nulled mode, as outlined by Wray (1986), to which further reference should be made since it is from this work that the present method has been adopted. However, a brief summary of the technique is presented in Chapter 3, based on the assumption that when a five hole probe is pointed into the flow the pressure registered by any tube is the sum of the local static pressure and some fraction of the dynamic pressure. The geometry of the probe tip limits the use of the probe to flows in which the local vector is within approximately ± 36 degrees in pitch and yaw. However, for more extreme yaw angles the probe can be rotated towards the velocity vector (Fig.2.9) so that large angles, relative to the rig axial direction, can be accommodated.

Prior to being used on the test facility, each probe is calibrated by being placed in the discharge from a calibrated convergent nozzle (Fig.2.10) which provides flow of known dynamic pressure. The probe is mounted in twin axis gimbals (Fig.2.10) which can be moved automatically to provide various combinations of pitch and yaw angle. The theory and procedures of Bryer and Pankhurst (1971) are then used to calculate pitch (X) and yaw (Y) parameters along with stagnation (S_p) and dynamic (D_p) pressure parameters. For each point in the calibration, these four non-dimensional parameters can be calculated from the five recorded pressures and stored in a look-up-table in the form of a two dimensional array.

Having obtained measurements in the test facility, the pitch (X) and yaw (Y) parameters are calculated from the pressures sensed by the five tubes. The corresponding pitch and yaw angles, stagnation (S_p) and dynamic (D_p) pressure parameters are then obtained with reference to the look-up table, from which values of the stagnation, static and dynamic pressures can be calculated in addition to the three velocity components. These calculations are performed off-line using a suite of software which also compensates for variations in rig operating conditions and for the finite size of the probe, discussed in more detail in Chapter 3. The four non-dimensional parameters are independent of flow velocity, hence a single calibration can be used for any real flow. However, since the velocity data is derived from the dynamic head ($\frac{1}{2}\rho U^2$), the use of the five hole probe is limited to a flow field where the density (ρ) is known and is incompressible ($M<0.3$).

In addition to the pressure instrumentation directly used in measuring the behaviour of the flow within the S-shaped duct, further pressure data can be obtained. Static pressure tappings of diameter 0.75 mm are positioned at various stations along the walls of the test facility. Experience has shown that static pressure readings may be seriously affected by the presence of an upstream tapping. Consequently, due to the high concentration of tappings along the inner and outer casings of the S-shaped duct, the tappings were positioned along a helical path (Fig.2.11). In addition, surface static pressure data can also be obtained on the strut. Static pressure tappings have been placed on both sides of the struts surface, along streamlines corresponding to 10%, 50% and 90% strut height.

All pressures are measured using Furness pressure transducers which produce an analogue output voltage proportional to the pressure measured. Transducers used include those with input ranges of ±500 mm H_2O, ±100 mm H_2O and ±25 mm H_2O which produce a linear D.C. output voltage of ±1.0 volt. The time response of the system is determined by the length and bore of the pressure tubes and upon the flow gradients. Furthermore, after movement of the instrumentation an experimentally determined settling time of 11.5 seconds is adopted prior to the pressures being recorded. The pressure transducer output signal is supplied to a 12 bit resolution analogue to digital (ADC) converter taking 250 samples at intervals of 20 milliseconds, thus giving a time averaged measurement over 5.0 seconds.

2.3.2 Measurement of the Turbulence Structure

Turbulence measurements were obtained using a laser doppler anemometry (LDA) system. Such a system comprises of a laser, transmitting optics, photodetectors and signal processing equipment. To measure a 1D flow, for example, the laser and associated optical system generates 2 beams which are focused to a point in space (Fig.2.12). Within this region one may think of a fringe pattern being generated and so small seeding particles in the fluid, which move across the fringe pattern, will scatter light which can be converted to an electronic signal using photodetectors. As each particle passes through the fringes, the intensity of the scattered light rises and falls at a rate directly proportional to the particles speed. In reality however, the particle moves across the measurement volume with a finite velocity and scatters light with a different frequency from that of the transmitted laser light. This phenomena is known as the Doppler effect, with the result that a frequency-modulated signal is registered by the detector and is known as a Doppler "burst". The Doppler frequency (f_D) of the signal is determined by the fringe spacing, which can be calculated, and the particles speed. Hence the speed of the particles, assumed to be identical to that of the flow, can be derived by suitable processing of the signal to determine the frequency content. It can be shown that the velocity (U) of the flow and the Doppler frequency (f_D) are related by;

$$U = f_D \frac{(\lambda/2)}{\sin(\theta/2)} \qquad \text{(Eqn.3.1)}$$

where λ is the laser wavelength and θ is the angle at which the laser beams intersect (Fig.2.12). The flow velocity component measured is that perpendicular to the line that halves the angle between the two laser beams. Thus, in 3 dimensional flows, three pairs of laser beams are required to measure the three components of velocity. The "measurement volume" thus being formed by the intersection, at the same spatial location, of all six beams. Furthermore, by separating each pair of beams into light of different wavelengths (and hence colour), the receiving optics is able to distinguish between the scattered signals from each beam pair. It is also desirable to try and ensure that each of the channels registers a signal from the same particle crossing the fringes. Thus, the system used in this investigation is able to measure the time of a particles arrival and the amount of time that a particle spends within the measurement volume (the residence time). Hence, if required, signals may only be recorded when all three

channels register a particle within the control volume. Such measurements are often termed "coincident" and, in air, assumes the data for all channels is associated with the same particle.

It should also be noted that unlike hot-wire anemometry, for example, laser doppler anemometry is a non-intrusive technique, thus avoiding flow disruption by the measurement system itself. Furthermore, laser doppler anemometry offers the potential benefit of high spatial resolution since the laser beams can be focused into a very small measurement volume. In this investigation the turbulent measurements were obtained using a 3D LDA system. It is thought beyond the scope of this thesis to provide a detailed description of the laser, optics and signal processing methods that were used. Rather, an outline of the fundamental principles necessary for the successful use of the LDA system are presented.

2.3.2.1 Transmitting and Receiving Optics

Measurements have been made using a Dantec colour separated 3 channel LDA system (Fig.2.13). Light from a 5 watt Argon Ion laser is separated into the green (514nm), blue (488nm) and violet (476.5nm) wavelengths within the transmitter box. Each channel incorporates a 40Mhz frequency shift to eliminate fringe bias and remove directional ambiguity, a more detailed discussion of which is conducted in Chapter 3. The transmitting optics consist of a 1D probe (Violet) and a 2D probe (green-blue) linked to the transmitting box via fibre optic cables. The probe heads also contain the receiving optics and a multi-mode fibre for signal transmission to the photomultipliers. Cross coupled detection was used in all of the measurements recorded, with the 1D probe head (violet) being used to detect signals from the 2D probe head (green-blue) and vice-versa. Beam expanders were also used (Fig.2.14) resulting in each channel having a beam separation of 16mm at exit from the expander, a receiving optics aperture of diameter 22mm and a focal length of 120mm. The included angle between the 1D and 2D probe heads is limited by the size of the access windows and the traverse distance. With a nominal included angle of 42.5 degrees between probe heads this gives an effective measurement volume (Fig.2.14) of approximately $0.1 \times 0.1 \times 0.3$mm.

2.3.2.2 Laser Beam Alignment

Swales et. al. (1993) have shown that in order to achieve high data rates and high data validity, all six laser beams must be correctly aligned. Poor alignment of the laser

beams causes a distortion of the interference pattern at their intersection, resulting in non-parallel fringes. As a consequence, the velocity recorded depends on the path of the seeding particle through the measuring volume. Optical access to the test facility is provided by windows formed from perspex, the geometry of which matches the outer casing profile of the S-shaped duct, and therefore contain complex double curvature. In order to reduce the amount of refraction of the laser beams, the window thickness is limited to 1mm. The 1D and 2D probes are rigidly mounted on a plate which attaches with the window, onto the side of the test facility (Fig.2.15). This plate maintains the probes in their relative position, and can be moved radially using a stepper motor. In order to align the beams, the plate and window are removed from the test facility and attached to the alignment beam (Fig.2.16). This beam is manufactured from extruded 'L' section steel and is designed to hold the optics, without deflecting, in the vertical plane. All six beams are then projected through the window and aligned to pass concurrently through a 50 micron diameter pin hole. As the aperture (0.05mm) is much smaller than the beam diameter (0.3mm) it is possible to detect the Gaussian nature of the light intensity. The beams were therefore thought to be aligned when the images of all six beams, after they had passed through the pin hole and viewed on a screen, were of maximum intensity. The main disadvantage of this technique though is that its accuracy is limited by the ability of the human eye to resolve the lights intensity, and is therefore dependent on qualitative interpretation of the images. A quantitative method was developed by mounting a light dependent resistor immediately behind the pin hole, with beams being adjusted until a minimum reading, corresponding to maximum light intensity, is obtained on a digital volt meter. In addition, the pin hole was also used to trace the path of each beam which allowed beam alignment, relative to the axial direction, to be determined to within ±0.2 degrees. These angles are required in order to translate the measured velocity components into the three orthogonal velocity components, streamwise (U), radial (V) and tangential (W), using an optical transformation matrix.

2.3.2.3 Seeding

Seeding of the flow is provided by a TSI six-jet atomiser using a relatively low viscosity oil. The particles produced by the atomiser were measured by the Department of Mechanical Engineering at Loughborough University. From a sample of approximately 270,000 particles, the mean size was found to be approximately 1.07 μm (Fig.2.17). Ahmed et. al. (1991) indicate that particles of such small size are

necessary, to ensure they accurately follow the air path which, in the case of swirling flows, also includes the possible effects on the particles associated with centripetal forces. The particles are dispersed into the test facility by a radial pipe with a multitude of small holes, placed (Fig.2.18) across the scroll intake within the inlet plenum. The height of the pipe above the scroll intake is kept at a maximum, in order to reduce any asymmetry of the flow that might arise. Furthermore, while this method allows the seed to be localised, resulting in more efficient use of the seed, it is estimated that a 30 degree sector of the annulus is seeded. However, the use of oil as a seed does have the disadvantage of contaminating the optical access windows resulting, with time, in reduced data rates. Thus, during the course of a traverse, the windows have to be cleaned at regular intervals.

At the start of each test, both the signal processors and the seed pipe location are adjusted to achieve as high a validated data rate as possible, typically 1KHz on each channel, with the measurement volume in the middle of the annulus. However, close to each of the casing surfaces, it is difficult to avoid the detrimental effect, on signal to noise ratio, caused by the scattering of light by reflection from the casing surfaces. Thus, much lower data rates, typically 50Hz, are obtained in the near wall regions. Furthermore, data validation rates vary from about 60% to 20%, depending on the location of the measurement volume.

2.3.2.4 Signal Processing

In this investigation processors which operate in the frequency domain, using a Fast Fourier Transform (FFT), have been used in preference to time domain processors such as "counters". The Dantec 57N10 Burst Spectrum Analyser (BSA) processes the Doppler "bursts" in the frequency domain and so the analysis uses most of the information within the Doppler signal. In contrast, processors such as counters use only the information associated with the signals zero-crossing points (Fig.2.19). Hence, the processors used in this investigation are capable of operating at much lower signal to noise ratios, relative to other systems, with little detriment to the calculated Doppler frequency (Fig.2.20). This is thought important in this investigation due to the harsh measuring environment with, for example, high turbulence levels and reflections from nearby casing surfaces. While a full explanation of the Burst Spectrum Analyser is thought beyond the scope of this investigation, information thought pertinent is presented and, for a more detailed explanation the reader should consult Dantec Elektronik(1991).

As the name implies, the Burst Spectrum Analyser, performs a spectrum analysis of the Doppler "burst" time signal (Fig.2.21.a), from which the fundamental Doppler frequency can be extracted. The BSA achieves this by taking a number of samples (N) of the input time signal (Fig.2.21.b). The frequency spectrum of the sampled time signal is then calculated using the Fourier Transform (Fig.2.21.c) of the time signal, where the distance between the frequency samples (the frequency resolution, f_n) is equal to the sampling frequency (f_S) divided by the number of samples (N). The sampling frequency must satisfy the Nyquist criterion in order to avoid frequency distortions, and must therefore be at least twice the upper frequency of the signal being measured.

The BSA actually operates with a sampling frequency of 1.5 times the selected signal bandwidth (BW), with the maximum sampling frequency being 48MHz. However, this, together with the number of samples recorded of a Doppler burst (N) could lead to a poor resolution of the frequency spectrum and hence the measured velocity. A technique whereby the frequency spectrum is shifted downwards to zero frequency is therefore used before sampling.

The power spectrum is calculated from the down-shifted version of the frequency spectrum. The BSA uses a maximum of 64 samples of the input signal to calculate the power spectrum and interprets the location of the spectrums maximum power as the Doppler frequency (f_D). The position of the maximum of the spectrum is found by fitting a curve through the frequency samples using an interpolation technique, both of which improve the resolution of the spectrum around the maximum. A zero-filling technique, whereby N zeroes are added to the N signal samples, results in the FFT being calculated from 2N samples. This technique doubles the number of frequency samples and therefore improves the frequency resolution ($f_n=f_S/2N$) by a factor of 2 but without affecting the spectrum, or adding any information to the signal. To validate the spectrum, the BSA compares the absolute level of the maximum with the two largest local maxima. The burst is only validated if the ratio between them is greater than 4, with this empirical factor being a compromise between the quality and rate of data acquired.

As already shown, the frequency resolution (f_n) is dependent on both the number of samples (N) and the sampling frequency ($f_S=1.5\times BW$), the inverse of which is known as the "record interval" ($RI=f_n^{-1}$). The record interval (RI) is therefore a measure of the time period over which a Doppler burst is sampled and, for

"coincident" measurements, should be selected by the user to reflect the time taken for the particles to cross the control volume (the residence time). In the case of a three channel system the record intervals on all three channels must be identical in order to ensure the data is "coincident", with data only collected when simultaneous bursts are registered by all three channels. However, fixing the record interval of all three channels can lead to either reductions in the signal-to-noise ratio (SNR) or, in certain circumstances, losing part of the signal. In regions of relatively high turbulence, close to casing surfaces for example, it is often necessary to increase the bandwidth in an attempt to fully encapsulate the signal. Furthermore, while one of the velocity components may be relatively large (e.g. the streamwise velocity), the other components of velocity can be an order of magnitude smaller. As a result the processor settings and signal to noise ratio is influenced, to a limited extent, by the velocity signals being measured on the other channels. With this in mind, the beams in this investigation have (where possible) been approximately arranged within the test facility, so that all three of the measured velocity components are of a similar magnitude.

In this investigation, all measurements were obtained with coincidence filtering i.e. data were only recorded when bursts were simultaneously registered by all three BSA's. Off-line software coincidence filtering was also performed in which a data point was only accepted as coincident if the arrival time registered by each channel was within the time estimated for the particle to pass through the measurement volume. A nominal 20,000 bursts were collected at each point, however the internal validation process and coincidence filtering meant that the number of actual coincidence bursts analysed was significantly less. Within the core flow, typically 15,000 samples were obtained, whilst towards each casing the number of samples fell due to the reduction in signal to noise ratio (SNR). At the closest points, typically 0.8% and 99.2% passage height, the number of coincident bursts analysed was 8000 and 5000 respectively.

2.4 Rig Traversing

The instrumentation used to investigate the flow within the annular S-shaped duct is mounted within a traversing mechanism attached to the outer casing of the test facility. For example, the traverse mechanism used to move the 5 hole probe is presented in Fig.2.22. This moves the probe in the direction of its stem axis, allowing the instrumentation to be typically positioned at 23 radial locations. The positional

accuracy of the radial traverse can be estimated from tests in which the traverse was moved from a datum position, back and forth, a distance of 70mm over 500 times. The final location of the probe measured to be within 0.1mm of the datum. In order to provide circumferential movement, the OGV blade row is mounted in a cassette which can be rotated using a drive shaft and stepper motor assembly. Thus, in the case where a complete compressor stage is located immediately upstream of the working section, the outlet guide vanes can be traversed relative to the probe whose circumferential location is fixed. Such a system avoids the need for numerous circumferential locations. Furthermore, although the outer wall is mounted on a fixed pedestal, the inner casing are mounted on two sets of bearings and can be rotated. Thus in the case where a single radial strut is located within the S-shaped duct, the inner wall can be rotated in order to provide circumferential movement relative to the probe. The positional accuracy of a typical circumferential traverse over one blade space (0.1013 rads), is estimated to be within 0.001 radians of the required value.

2.4.1 Single Radial Traverses

Measurements can be been performed at up to 11 traverse stations within the S-shaped duct and surrounding passages (Fig.2.23). For the cases where the inlet conditions were assumed to be axisymmetric, both pressure and LDA measurements were made at a single circumferential location at all 11 traverse stations. At each of the traverse stations, the radial location of either the tip of the 5 hole probe, or the focal point of the laser beams, is defined by first locating the inner and outer casings. In the case of the five hole probe, the probe is manoeuvred into positions adjacent to each wall which defines the overall length of the traverse. For the LDA system, the laser beams are traversed until they focus on the wall surfaces. This is indicated by the magnitude of reflected light which is monitored by a light dependent resistor. It is estimated that the accuracy of the radial positioning using these methods is approximately ±0.1mm. Having determined the radial location of the inner and outer walls respectively, the measurement probe can then be traversed across the annulus. Data is recorded at nominally 23 radial locations, spaced to provide more definition in the regions where the gradients of the flow properties are likely to be greatest, such as within the wall boundary layers. Measurements performed using a 5 hole probe have been recorded at distances within 1.5mm of the walls while, due to the non-intrusive nature of the LDA system, data has been recorded to within 0.4mm of the casing surfaces.

2.4.2 Area Traverses

For inlet conditions generated by a single stage compressor, area traversing is achieved by indexing of the OGV ring, to provide the required circumferential movement, together with radial movement of the probe. Using these techniques data were recorded at typically 23 radial locations, repeated at 21 circumferential positions, corresponding to either one or two OGV blade spaces (Fig.2.24). Thus, a typical area traverse comprised 483 data points, with data recorded at this number of points being thought to give good resolution of the flow features. Area traversing has been performed at all 11 traverse stations using the 5 hole probe, while only 4 planes were traversed using the LDA system due to time considerations.

2.5 Test Procedures and Data Acquisition

Operation of the test facility, positioning of the instrumentation, and digitising of all pressure transducer signals were controlled (Fig.2.25) by a personal computer (PC). The computer executes the data acquisition software enabling it to communicate, through a ribbon cable and a CIL Alpha-03 controller card, with a range of CIL Microsystems control modules. The controller card transmits commands and receives both analogue and digitised data from a number of other control cards. For example, pressure readings are obtained from the transducers via an 8-channel analogue input module (A-Block), while the traverse gear is driven by a stepper-motor which is controlled by a single channel module (S-Block).

The temperature of the flow passing through the test facility is measured by a type K Chromel/Alumel thermocouple, located in the inlet plenum chamber, connected to a control unit which provides a reference cold junction and a linear ±10 mV signal for a 0C to 200C temperature range. A typical resolution of 0.12 deg C is quoted by the manufacturers along with a response time of order 0.5 seconds. The air temperature is monitored by the personal computer using a 6-channel K-Block.

For tests conducted using the LDA system, a second PC is required to operate the LDA equipment (Fig.2.26). This dedicated PC is fitted with a 400 mega-byte hard disc, to store the large amounts of data obtained using the LDA system. This PC runs the data acquisition software (discussed in more detail in Chapter 3) which is used to remotely control the settings of the Burst Spectrum Analysers, as well as to receive and store "frequency burst" information in real time.

Prior to each test, before any measurements are recorded, the 5 hole probe and all

of the piping are checked for leaks and blockages. The transducers are then adjusted to give a zero pressure difference across the diaphragm, while the voltage from the thermocouple is checked. The inlet plenum is examined for foreign bodies and the plenum filter is secured. When commencing a test, the rig is started up and allowed to run for some 20 minutes, in order to allow the rig casings to reach a stable temperature. Furthermore, this also allows the pressure transducers and thermocouple to warm up and stabilise.

All measurements of the flow were made at known operating conditions. With the complete compressor stage present, the rotor is operated at a design non-dimensional speed ($N/\sqrt{T}$) of 160.7 and with a non-dimensional mass flow coefficient ($m\sqrt{T}/Ap$) of 0.0102 (Fig.2.27). With the OGV row removed, the rotor is operated at a design non-dimensional speed ($N/\sqrt{T}$) of 128.6 and with a non-dimensional mass flow coefficient ($m\sqrt{T}/Ap$) of 0.0755. The operating conditions are assessed at each point in a traverse and must be met, within a tolerance of typically 0.2%, before data is recorded.

All pressure measurements are referenced to a wall static pressure measured at the inlet plane and corrected for day to day variations in atmospheric temperature and pressure. When operating with a constant inlet plane Mach number this pressure correction takes the form;

$$(P - p_{ref})_{std} = (P - p_{ref})_{meas} \times \frac{p_{std}}{p_{meas}}$$

where the subscripts refer to the measured value and the value that would be obtained on a standard day with atmospheric conditions defined as;

$P = 101325\ N/m^2$

$T = 288.15\ K$

The experimental data, along with the operating conditions and positional information, is time-stamped and written to the hard disk after each point in the traverse. After the test has finished, the operational drift of each pressure transducer is recorded, with drifts in excess of ±1.0mV of the starting value, on the $100mmH_2O$ transducers for example, indicating a problem with the transducer. The data can then be processed and analysed using a suite of computer programs.

Chapter 3 Data Reduction and Analytical Procedures

3.0 Data Reduction and Analytical Procedures

3.1 Five Hole Probe Data Reduction Method s

3.1.1 Derivation of Flow Properties

Pressure measurements were made using sub-miniature five hole pressure probes (Fig.3.1) which consist of a cluster of five tubes, aligned such that one hole (designated hole 5) lies in the plane normal to the tip axis and the four side holes (1,2,3 and 4) lie in chamfered faces in the directions North, East, South and West around the central hole respectively. Such pressure probes, when suitable procedures are applied, are capable of providing information on stagnation (P_t), static (p_s) and dynamic (q) pressures as well as the three velocity components (U, V, W). In this investigation the procedure for deriving the flow properties, illustrated in Fig.3.2, is based on a suite of computer programs capable of processing large amounts of data relatively quickly. In order to derive the flow properties, the computer software requires information both from the experiment and the calibration. As explained earlier (Chapter 2), prior to the probe being used on the test facility it was necessary to calibrate the probe at a range of known pitch and yaw angles. At each point in the calibration, the pitch (PPS) and yaw (YTR) angles are recorded along with four pressure parameters (X, Y, D_p, S_p) and stored in the form of a look-up table. Having obtained measurements in the test facility, the pitch (X) and yaw (Y) parameters are calculated from the pressures sensed by the five tubes. The corresponding pitch and yaw angles, stagnation (S_p) and dynamic (D_p) pressure parameters are then obtained with reference to the look-up table, from which values of the stagnation (Pt), static (p_s) and dynamic (q) pressures can be calculated in addition to the three velocity components (U, V, W).

The first step in the procedure (Fig.3.2) is to convert the voltages, recorded during experimental work by the transducers connected to each of the five tubes, into pressures. However, due to the finite size of the probe, the five recorded pressures are obtained at five different spatial locations. Consequently, when the probe is positioned at a particular point in the flow field, only tube 5 is at the correct location. Thus, in regions where pressure gradients are severe, large discrepancies can arise between the pressure recorded by each side tube and the value which would have been recorded if cited at the nominal probe position. In this investigation the pressures which would have been recorded by tubes 1 through 4 at the position of tube 5 is estimated by

interpolating between the experimental data. This is performed using a natural cubic interpolatory spline (Wray, 1986) which can be considered to be a continuous function of pressure with probe position.

Having obtained the five pressures at the correct spatial location, the next step in the procedure (Fig.3.2) is to calculate the pitch and yaw pressure parameters (X,Y). The probes were used in a non-nulled mode as opposed to the more conventional method of manoeuvring the probe in both pitch and yaw directions until the pressures on the two opposing pairs of side tubes are in balance. At this point, the central tube registers the local stagnation pressure while the dynamic pressure can be shown to be a function of the difference between the pressures registered by the central hole and the four side holes. However, it has not been possible to implement this more conventional method of using the 5 hole probe since access into the test facility is limited, with rotation of the probe in the pitch direction being difficult to achieve. The probes in this investigation were therefore used in a non-nulled mode, as outlined by Wray (1986), based on the assumption that when a five hole probe is pointed into the flow the pressure registered by any tube (p_n) is the sum of the local static pressure (p_s) and some fraction (K_n) of the dynamic pressure ($q=\frac{1}{2}\rho U^2$);

$$p_n = p_s + K_n q \qquad \text{(Eqn.3.1)}$$

The coefficient K_n has a value which depends only upon the flow direction relative to tube n since Mach number and Reynolds number effects can reasonably be considered to be negligible. Thus, the differences in pressure between the North and South tubes (p_1-p_3) and the East and West tubes (p_2-p_4) can be assumed to be representative of the flows pitch and yaw angles. The pitch (X) and yaw (Y) pressure parameters (which are independent of flow velocity) can be obtained by non-dimensionalising the two pressure differences with respect to some function of the dynamic pressure. For any given flow direction, the difference between the pressure sensed by the centre hole (p_5) and one of the surrounding holes (p_i) must be a function of the dynamic pressure (q). Using Eqn.3.1 this pressure difference can be shown to be;

$$(p_5 - p_i) = q\,(K_5 - K_i) \qquad \text{(Eqn.3.2)}$$

and is used in the definition of the pitch and yaw pressure parameters (X,Y);

$$X = \frac{p_1 - p_3}{p_5 - p_i} = \frac{K_1 - K_3}{K_5 - K_i} \qquad \text{(Eqn.3.3)}$$

$$Y = \frac{p_2 - p_4}{p_5 - p_i} = \frac{K_2 - K_4}{K_5 - K_i} \qquad \text{(Eqn.3.4)}$$

The particular hole denoted by the subscript (i) can legitimately be taken as any of the holes 1 through 4, irrespective of flow direction, provided that both the calibration and experimental techniques are consistent. In this investigation the choice of p_i is taken from either hole 2 or hole 4, depending on which gives the largest value of (p_5-p_i), in order to obtain a sensible range of X and Y values.

The pitch (X) and yaw (Y) pressure parameters are then used to obtain the values of the dynamic (D_p) and stagnation (S_p) pressure parameters, in addition to the pitch (PPS) and yaw (YTR) angles, from the calibration data (Fig.3.2). The full calibration can be considered to be four separate surfaces with the pitch (X) and yaw (Y) pressure parameters representing the x,y co-ordinates, while PPS,YTR, D_p and S_p are in the z direction (Fig.3.3). The value of each parameter in the z direction at a given experimental point can be found by operating on each surface in turn. For each (X,Y) co-ordinate pair, the closest 25 points from the calibration file are selected, forming four parameter arrays. A least squares technique is used to approximate the localised area of the calibration data to a bi-quadratic surface, from which the values of the four parameters (PPS, YTR, D_p and S_p) corresponding to the (X,Y) coordinate pair can be interpolated.

The dynamic pressure parameter D_p is defined as (K_5-K_i), thus producing a further pressure parameter, like X and Y, which is a function of flow direction only. The dynamic pressure (q) can then be readily found (using Eqn.3.2) from;

$$q = \frac{(p_5 - p_i)}{D_p} \qquad \text{(Eqn.3.5)}$$

A further pressure parameter (S_p) is determined by considering incompressible flow along a streamline, such that;

$$P_t = p_s + q \qquad \text{(Eqn.3.6)}$$

where the static pressure (p_s) can be shown, using Eqn.3.1, to be;

$$p_s = p_5 - K_5 q \qquad \text{(Eqn.3.7)}$$

and by substituting Eqn.3.7 in Eqn.3.6 and non-dimensionalising with respect to (p_5-p_i), then;

$$\frac{P_t - p_5}{p_5 - p_i} = \frac{q(1 - K_5)}{p_5 - p_i} = \frac{1 - K_5}{K_5 - K_i} \qquad \text{(Eqn.3.8)}$$

where the stagnation pressure parameter (S_p) is defined as the dimensionless group;

$$S_p = \frac{1 - K_5}{K_5 - K_i} \qquad \text{(Eqn.3.9)}$$

such that the stagnation pressure can be obtained from the following expression;

$$P_t = p_5 + S_p (p_5 - p_i) \qquad \text{(Eqn.3.10)}$$

Thus, values of the dynamic (D_p) and stagnation (S_p) pressure parameters, together with the tube pressures (p_5, p_i), can be used to calculate the stagnation pressure (P_t), dynamic head (q) and static pressure (p_s) for each data point. Furthermore, the three components of velocity (U, V, W) can be calculated for each data point using the pitch and yaw angles in conjunction with the dynamic pressure.

3.1.2 Estimate of Experimental Errors

Miniature 5 hole pressure probes have been used to assess the development of the mean flow field within an annular S-shaped duct. However, a detailed assessment of the performance limits of such a probe is though to be beyond the scope of this work, and could indeed form the basis of a separate and lengthy research programme. The work of others has therefore been used to assess the accuracy of the 5 hole probe,

and where possible, suggested experimental techniques have been used to minimise errors.

The 5 hole probes used in this investigation are calibrated for a range of flow angles up to ±36° in both pitch and yaw as outlined in Chapter 2. The accuracy of this calibration technique has been assessed by Wray (1997), who indicated negligible errors in terms of both the flow angles and velocities measured. However, when used for measuring flow in the near wall regions of the duct, errors are introduced due to the proximity of the casing surface. Wall proximity effects have been investigated by Tamigniaux and Oates (1986) who found that with probes of a conical geometry a maximum error of 2° can occur, while Sitaram et. al. (1981) expressed the error in terms of a 1% variation in velocity. These errors are, however, restricted to within a single probe diameter (1.75mm) of the casing surface, and as such the vast majority of measurements incur negligible wall proximity errors. The effect of turbulence on 5 hole probe measurements was also assessed by Sitaram, who indicated likely errors of approximately 0.3% for turbulence intensities of 10%. Similar levels of turbulence have been recorded within the S-shaped duct, particularly with inlet conditions provided by a single stage compressor. Sitaram also suggests a spatial error is introduced when measurements are made in highly sheared flows due to the finite distance between the 5 holes on the probe tip. However, as explained earlier, in this investigation the spatial error associated with the finite size of the probe has been limited by both radial and circumferential interpolation of the side pressures onto the central measurement hole. Spatial errors can be further minimised by recording more data points in regions where large changes in the mean flow field occur, such as within the casing boundary layer.

The physical size of the probe also effects the accuracy of the measurements due to the obstruction the probe presents to the fluid. However, it is thought this effect is relatively small since for this investigation the probe diameter represents less than 2.5% of the inlet annulus height and corresponds to less than 0.002% of the inlet annulus area.

The pressures sensed by the 5 hole probe are converted into voltages by the transducers. Thus, as discussed earlier in Chapter 2, a significant error can be introduced by any drifting of the transducers. After each test, the magnitude of the transducer drift, is a function of the measured velocity. The magnitude of the error can be estimated by changing a raw data file to simulate such an effect. For example,

Carrotte (1990) has shown that by simulating a drift of 1mV on a transducer with a range of ±100mm H_2O an error of 0.2% is introduced when measuring a flow with velocity 30m/s. However, at a velocity of 15m/s the error is approximately 0.7%. Furthermore, changes in flow angles of approximately 0.05° and 0.2° occur for the higher and lower velocities respectively. Thus, in this investigation, transducer drifts have been monitored closely, with measurements being rejected if the transducers should drift by more than ±1mV.

Although it is difficult to estimate the overall magnitude of the errors associated with the measured mean flow field, repeating the test results eliminates errors due to transducer drifts and increases confidence in the averaged measurements of time dependent flow features such as secondary flows and tip vortices. For the clean inlet condition the spatially averaged total and static pressure at a traverse plane were repeatable to within 0.5mm H_2O, with discrepancies in mass-flow between planes of less than 2.5%. Based on these values and the repeatability of test data it was estimated the stagnation pressure loss coefficients were repeatable to within ±0.005. With the compressor at inlet this increased to ±0.0075 as the compressor operating point could only be maintained to within a finite resolution. However, it should be noted that although the overall loss levels at a plane can vary, the non-dimensional radial distributions of pressure were, within experimental error, the same.

3.2 Laser Doppler Anemometry Data Reduction Methods

3.2.1 Derivation of Flow Properties

For measurements obtained using a 3D LDA system, the flow properties have been derived using a dedicated software package (Burstware Version 3.0, 1991) and for a more detailed explanation of the software the reader should consult the proprietors. The software package enables the user to build a procedure for obtaining the flow properties using a number of independent data processing algorithms. The user is able to specify the type of processing to be performed along with the specific algorithms and weighting factors to be used. The procedure used in this investigation for obtaining the flow properties is illustrated in Fig.3.4 and should only be considered as one method of obtaining the flow properties.

The first step in the procedure (Fig.3.4) is to read in the experimental data, which consists of the Doppler frequencies (f_D), the arrival times and the transit times

recorded by each of the burst spectrum analysers at each measurement location. In this investigation, the arrival time is taken to be the time at which each of the processors first registers the presence of a particle within the measurement volume, while the transit (or residence) time reflects the time taken by the particle to move across the measurement volume. The experimental data is stored in the form of digital binary output, with a separate file for each of the processors at each of the traverse positions. The Doppler frequencies (f_D) are then converted into velocities (V) using the calibration factor (C) such that;

$$V = f_D \times C \qquad \text{(Eqn.3.11)}$$

where the calibration factor C is a function of the wavelength (λ) and the angular separation (θ) between the two beams. Burstware converts the raw data from the integer numbers associated with the digital binary output into floating point numbers which are stored in "converted" data files.

The next routine in the procedure (Fig.3.4) performs software coincidence filtering of the converted data. This algorithm is used, in addition to the hardware filtering (discussed earlier in Chapter 2), in order to ensure that the 3 velocity components recorded for each data point are associated with the same particle passing through the control volume. Thus, each data point is only accepted as coincident if the arrival time registered by each of the three processors is within the time estimated for the particle to pass through the control volume. This time is termed the "coincidence window", and if too small a value is selected the number of coincident bursts will be low. In this investigation a "coincidence window" of two-thirds of the transit time of the fastest particles has been used (Dantec, 1991) in an attempt to ensure the data is coincident. A single "sorted" data file is created at each measurement location, as a result of coincidence filtering, corresponding to the three "converted" files associated with each processor.

Having filtered the data, the next routine in the procedure transforms the measured non-orthogonal velocities (U_{BSA1},U_{BSA2},U_{BSA3},) into the three mutually orthogonal components (U, V, W) aligned with the rig axis. This is performed using a matrix, often termed the "optical transformation matrix", comprised of coefficients (direction cosines, a_{ij}) which can be derived from knowledge of the laser beam

alignment;,

$$\begin{bmatrix} U \\ V \\ W \end{bmatrix} = \begin{bmatrix} a_{11} & a_{12} & a_{13} \\ a_{21} & a_{22} & a_{23} \\ a_{31} & a_{32} & a_{33} \end{bmatrix} \begin{bmatrix} U_{BSA1} \\ U_{BSA2} \\ U_{BSA3} \end{bmatrix} \qquad \text{(Eqn.3.12)}$$

For example, if the 1D and 2D probes are placed at angles of α and β to the traverse plane (Fig.3.5), with the violet (1D) beams constrained to lie in the axial-radial plane while the green and blue (2D) beams are rotated about the 2D probe axis by angles γ_g and γ_b respectively, then the coefficients can be shown (Appendix 1) to be;

$$a_{11} = -\frac{\sin(\alpha)\sin(\gamma_b)}{\sin(\alpha-\beta)\sin(\gamma_g-\gamma_b)} \qquad \text{(Eqn.3.13)}$$

$$a_{12} = \frac{\sin(\alpha)\sin(\gamma_g)}{\sin(\alpha-\beta)\sin(\gamma_g-\gamma_b)} \qquad \text{(Eqn.3.14)}$$

$$a_{13} = -\frac{\sin(\beta)}{\sin(\alpha-\beta)} \qquad \text{(Eqn.3.15)}$$

$$a_{21} = \frac{\cos(\alpha)\sin(\gamma_b)}{\sin(\alpha-\beta)\sin(\gamma_g-\gamma_b)} \qquad \text{(Eqn.3.16)}$$

$$a_{22} = -\frac{\cos(\alpha)\sin(\gamma_g)}{\sin(\alpha-\beta)\sin(\gamma_g-\gamma_b)} \qquad \text{(Eqn.3.17)}$$

$$a_{23} = \frac{\cos(\beta)}{\sin(\alpha-\beta)} \qquad \text{(Eqn.3.18)}$$

$$a_{31} = \frac{\cos(\gamma_b)}{\sin(\gamma_g-\gamma_b)} \qquad \text{(Eqn.3.19)}$$

$$a_{32} = -\frac{\cos(\gamma_g)}{\sin(\gamma_g-\gamma_b)} \qquad \text{(Eqn.3.20)}$$

$$a_{33} = 0 \qquad \text{(Eqn.3.21)}$$

The transformed velocity components (U, V, W) are output in a single "moments" file for each traverse location prior to statistical processing. The statistical

processing is performed on each of the moments files, producing a single "list" file which provides details of the flow properties (U, V, W, u_{rms}, v_{rms}, w_{rms}, $\overline{u'v'}$, $\overline{v'w'}$, $\overline{u'w'}$) at each of the traverse locations. For example, the mean streamwise velocity has been averaged such that;

$$\overline{U} = \frac{\sum U_i}{N} \qquad \text{(Eqn.3.22)}$$

where U_i is the streamwise velocity of the i^{th} particle in the sample population (N). The r.m.s of the streamwise velocity (u_{rms}) has been calculated from the variance of the sample population (N) so that;

$$u_{rms} = \sqrt{\left(\sum_i (U_i - \overline{U})^2\right)/N} \qquad \text{(Eqn.3.23)}$$

Furthermore, since 3D coincident data has been obtained, the three cross moments ($\overline{u'v'}$, $\overline{v'w'}$,$\overline{u'w'}$) can be determined. For example, the $\overline{u'v'}$ component has been calculated using;

$$\overline{u'v'} = \frac{\sum (U_i - \overline{U})\ (V_i - \overline{V})}{N} \qquad \text{(Eqn.3.24)}$$

The statistical processing algorithms also incorporate user defined weighting factors which can be used to compensate for the effects of statistical bias which is discussed in more detail in the next section. Burstware allows the user to apply a variety of weightings to the data in order to minimise the effects of statistical bias. For example, the mean streamwise velocity can be averaged using residence time weighting such that;

$$\overline{U} = \frac{\sum U_i \Delta t_i}{\sum \Delta t_i} \qquad \text{(Eqn.3.25)}$$

where Δt_i is the transit (or residence) time of the i^{th} particle. An estimate of the error associated with the effects of statistical bias is presented in the next section, which includes an assessment of both the statistical and systematic errors associated with the

LDA measurements obtained in this investigation.

3.2.2 Estimate of Experimental Errors

The errors associated with LDA measurements can be separated into two areas. The first area covers the statistical errors which occur due to the flow quantities being estimated from a finite number of samples of the velocity signal while the second area includes the systematic errors associated with the instrumentation.

3.2.2.1 LDA Statistical Errors

Hinze (1959) describes turbulence as an "irregular condition of flow in which the various quantities show a random variation with time and space coordinates, so that statistically distinct average values can be discerned". Thus, turbulence may be considered to be a highly chaotic and yet organised collection of eddies, which can be described statistically in terms of time-averaged correlations and properties. Thus, these average values can be determined experimentally by sampling the velocity signal.

Conventional statistical techniques can be used to estimate the errors associated with the flow quantities obtained by sampling of the velocity signal (Kreysig, 1988). For example, if it is assumed that the velocity signal is normally distributed about the mean value then the number of statistically independent samples (N) required to calculate the true mean (μ) within specified limits ($\pm\varepsilon$) can be found from

$$N = \left(\frac{z\sigma}{\varepsilon_{\mu}}\right)^2 \qquad \text{(Eqn.3.26)}$$

This is for a signal of known variance (σ^2) and where z is a measure of the confidence that the calculated mean lies within $\pm\varepsilon$ of the true mean value. Values of z can be obtained for confidence levels in the range from 0.1 to 99.9%, with a value of 2.576 reflecting a 99% confidence level. Thus, if the streamwise velocity (U) is assumed to be normally distributed with a variance (σ^2) comparable with the flows normal stress ($\overline{u'^2}$), then the number of samples required to obtain a specified accuracy can be calculated. For example, at inlet to the duct, and with inlet conditions provided by a rotor, the turbulent fluctuations at mid-passage height are relatively small (u' = 1.45m/s) and with 99% confidence in the calculated mean velocity being within

±0.1m/s of the true mean value, the number of samples is given by;

$$N = \left(\frac{2576 \times 1.45}{0.1}\right)^2 = 1395.17$$

In contrast, in the near wall regions (at 0.8% and 99.2% passage height) where turbulence intensities are much higher, approximately 8,000 and 16,000 statistically independent samples respectively are required.

It is important to note that the accuracy of the average values obtained during experimental work are dependent on both the number of samples and the frequency at which samples are taken. For example, a single eddy sampled so quickly that a number of measurements are obtained contributes no more to the accuracy of the average than if a single sample is taken since all of the data taken within a single eddy will be correlated. Thus, in order to obtain statistically independent samples the velocity signal must be sampled at time intervals greater than the time taken for a single eddy to move across the control volume. This is difficult to achieve in practice since the flow can be assumed to be characterized by a broad spectrum of time and length scales. However, the integral time scale (2I) of the flow can be estimated either from an autocorrelation of the velocity signal (Fig.3.6), or by relating the integral time scale to a suitable length scale and the local mean velocity (U). For example, assuming the large energy containing eddies possess a length scale of the same order as the boundary layer height (δ), then at duct inlet the integral time scale (2I) is approximately 0.00036 seconds. Frequency bursts recorded at intervals less than the integral time scale can be presumed not to be statistically independent and therefore do not contribute to an improvement of the accuracy of the measurement.

In this investigation, some 16,000 coincident samples were obtained at mid passage height over a period of approximately 35 seconds, giving a mean sampling frequency of approximately 457Hz. Comparison of this data rate (one sample per 0.00219 seconds) with the estimated integral time scale of the flow (0.00036 seconds) indicates that data is acquired, on average, at a rate of one sample in every six time scales. It is therefore thought reasonable, whilst acknowledging that a turbulent flow comprises eddies covering a wide spectrum of sizes and the use of a single length scale can only be regarded as a crude approximation, to assume that the data obtained in this investigation is statistically independent. Furthermore, in assuming the data to be

statistically independent, it is possible to estimate the statistical error (using Eqn.3.26) associated with the calculated mean velocity for each of the sample size's obtained. For example, with a population of 16,000 statistically independent samples at mid-passage height, the error associated with the calculated mean velocity is;

$$\varepsilon_U = \frac{zu'}{\sqrt{N}} = \frac{2.576 \times 1.45}{\sqrt{16000}} = 0.0295\,(m/s)$$

and so there is 99% confidence that the calculated mean velocity lies within ±0.03m/s of its true value. However, in the near wall regions less samples have been acquired, due to the relatively poor signal to noise ratio, and turbulence intensities are high. Thus, for example, at 0.8% and 99.2% passage height, approximately 9000 and 5000 samples respectively were obtained. It is estimated that the calculated local mean velocity at these locations lies within ±0.1m/s and ±0.17m/s for each of the examples. For measurements obtained with the "clean" inlet condition, Carrotte et. al. (1993) have estimated that the error associated with the calculated mean velocity at the centre of the passage is negligible, while in the near wall region (1mm from the casing), the calculated mean velocity lies within ±0.11m/s.

The statistical error associated with the calculated value of the flows normal stresses ($\overline{u'u'}$, $\overline{v'v'}$, $\overline{w'w'}$) can be derived from the determination of a confidence interval for the variance (σ^2) of a normal distribution. Thus, if the normal stresses ($\overline{u'u'}$, $\overline{v'v'}$, $\overline{w'w'}$) are considered to represent the variance (σ^2) of the velocity signal, the bounds of the error associated with the calculated normal stress can be determined. The method presumes a confidence level (γ), and solutions of the equations;

$$F(c_1) = \frac{1}{2}(1-\gamma) \qquad F(c_2) = \frac{1}{2}(1+\gamma) \qquad \text{(Eqn.3.27)}$$

can be found from tables (Kreysig,1988) of the chi-square distribution. Having derived the values of the constants (c_1, c_2), the bounds of the calculated normal stress can be computed from;

$$k_1 = \frac{(N-1)\,\overline{u_i u_i}}{c_1} \qquad k_2 = \frac{(N-1)\,\overline{u_i u_i}}{c_2} \qquad \text{(Eqn.3.28)}$$

where there is a confidence level of γ that the calculated normal stress lies within $k_1 < uu < k_2$. For example, at mid-passage height with 16000 samples, and with a 99% confidence level, it has been estimated that the calculated normal stresses will lie within ±3% of their true values. Furthermore, in the near wall regions, where turbulence levels are higher, and less samples have been obtained, it is estimated that the calculated normal stresses will be within ±5% of their true values. For measurements obtained using "clean" inlet conditions Carrotte et. al. (1993) have estimated that in the near wall region, the measured normal stresses will lie within ±8% of their true values, with the significantly higher error being associated with far fewer samples being obtained in their experiments. In addition, Carrotte and Britchford (1994) have shown that though the statistical errors are significant, the systematic errors associated with the instrumentation can be of greater significance.

3.2.2.2 LDA Systematic Errors

The systematic errors that contribute to the experimental accuracy of the LDA measurements in this investigation have been identified as effects due to statistical bias, laser beam alignment and processor resolution. Furthermore, such systematic errors are a function of the turbulence intensity and the signal to noise ratio of the velocity signal which varies with each measurement. It is therefore difficult to make an error estimate for an individual measurement, though methods used to reduce such errors and the likely range of the errors are assessed.

3.2.2.2.1 Statistical Bias

Though the title "Statistical Bias" might imply that the associated errors are statistical in nature, the effect is systematic. Indeed, while statistical errors associated with sampling of the velocity signal may be zero, bias errors still remain and stem from a number of sources. In this investigation, the laser doppler anemometry system has been used to perform measurements in which air is the fluid media. Measurements have typically been obtained such that only one particle is present in the sensing volume at any instant, with this mode of operation often referred to as individual realization (IR). For applications where high seeding concentrations are easily obtained, such as where water is the fluid media, the mode of operation is referred to as continuous wave (CW). In the IR mode, the sampling of data is dependent on the occurrences of particles crossing the measurement volume, and is therefore statistical in nature. However, in the early applications of LDA it was thought that sampling of

the velocity signal in IR mode was random, with statistical averaging of the mean and fluctuating velocities performed assuming the sampling was unbiased. McLaughlin and Teiderman (1973), in an analytical study, pointed out that sampling was not totally random in turbulent flows, with the probability of sampling high velocity particles being greater than sampling relatively low velocity particles. Thus, for a volume of flow that is uniformly seeded more particles will pass through the control volume when velocities are high relative to when velocities are low. Subsequently, the arithmetic mean calculated from measurements over a given time is higher than the true mean velocity. However, it should be noted that after the original suggestions of McLaughlin and Teiderman, subsequent attempts by a number of investigators (e.g. Giel and Barnett (1979) to experimentally verify the theory have produced conflicting results as to the magnitude and even the existence of this bias effect. Thus, in order to obtain some consensus, a special panel produced a report (Edwards, 1987) detailing what was known about statistical bias in laser anemometry and made recommendations for future work. Edwards makes suggestions as to the need and type of processing methods for the elimination of statistical bias based on the rate at which data is obtained. The panel suggest that imprecise terminology, especially in terms of "data rates" has led to some confusion, and therefore provide the following definitions;

1.) Particle arrival rate (N_0) - The rate that measurable particles pass through the measurement volume and reflects the number of particles that could be measured by an ideal laser anemometer.

2) Validation rate (N_2) - The rate that a burst processor measures particles, and therefore depends on the processor settings.

In this investigation, as noted earlier, some 16,000 samples were obtained in approximately 35 seconds at duct mid-height downstream of the rotor, giving an estimated validation rate of 457 samples per second. However, Edwards contends that the data rate has no meaning unless it is compared to one of the flows relevant time scales, and further suggests that this should be the Taylor microscale (T_λ). In doing so, Edwards has formulated a definition of the magnitude of the data density (N_2T_λ) such that;

1) High data density	$N_2T_\lambda > 5.0$
2) Intermediate data density	$0.05 < N_2T_\lambda < 5$

3) Low data density $N_2T_\lambda < 0.05$

Since it was not possible to obtain data at a sufficiently high rate to define an autocorrelation function, the data density for this investigation has been estimated using the integral time scale. Using such a definition, the data density for measurements obtained downstream of a rotor is estimated to be 0.2 which therefore indicates an intermediate data density. Edwards further suggests that whether velocity bias is of concern or not can be based on the method of McLaughlin and Teiderman (1973). This indicates that the bias magnitude is a function of the square of the turbulence intensity such that;

$$\overline{U}_{meas} \approx \overline{U}_{true}\left(1 + \frac{\sigma_U^2}{\overline{U}_{true}^2}\right) \qquad \text{(Eqn.3.29)}$$

where $\overline{U}_{meas}$ represents the measured mean velocity, $\overline{U}_{true}$ represents the true mean velocity and $\sigma_U{}^2$ is the flow variance. Thus, in this investigation the bias should be negligible within the central core of the flow where turbulence intensities are, typically, 0.7% and 3.9% for the "clean" and rotor inlet conditions respectively. However, in the near wall regions, turbulence intensities typically of the order of 10% would indicate errors in the calculated local mean velocity of the order 1%. As suggested by Edwards though, "residence time weighting" can be used to correct for such velocity bias at intermediate data rates. Here, the amount of time that a particle spends in the measurement volume (known as the residence or transit time) is measured in addition to the particles velocity. The weighted mean flow quantities can then be calculated based on the measured transit time, with the weighted mean velocity (as already shown in Chapter 2) calculated using Eqn.3.25. Buchave (1979) concludes that such a method provides the correct statistical results in uniformly seeded flows, since it is equivalent to a time averaging of the data. In this investigation, a sample traverse (x/L=0.0, swirl case) was used to estimate the magnitude of the effect of velocity bias by weighting each burst according to its transit time through the measurement volume. Comparison of the residence time weighted data with the unweighted data (Fig.3.7) indicates that over the majority of the passage height velocity bias is negligible, while in the near wall regions the effect on the local velocity is of the same order as that predicted using the method of McLaughlin and Teiderman. It can be seen though that generally the applied correction is relatively small.

A further source of statistical bias is the tendency of processors to have a measurement efficiency dependent on the speed of the measured particle. Edwards argued that the slower moving particles produce signals of higher amplitude than faster moving particles, as a result of the frequency response characteristics of the processor, and therefore have a higher probability of being validated. Furthermore, a particle with a velocity that generates a frequency outside of the operating range of the processor can be missed. Edwards makes no specific recommendation for dealing with such bias, except to ensure that the operating range of each processor encompasses the expected velocity signal. Edwards suggests that "All velocities in the flow must be measurable since no correction scheme can reasonably correct for missing velocities". In this investigation, serious thought has been given to the filter settings of the processors, with adjustments made at each data point in order to minimise such effects.

Angle (or fringe) biasing occurs due to fluctuations of the flows direction with time. Consequently, a greater number of measurements are obtained when the flow is normal to the fringes than when the flow fluctuates away from the normal. In the extreme, a particle passing across the control volume in a direction parallel to the fringes will not register a signal. In this investigation, a Bragg-Cell has been used to move the fringes within the measurement volume, reducing the effects of angle bias. A further statistical bias occurs due to any gradient of the mean velocity across the finite size of the measurement volume. As discussed earlier, the arrival rate of the measurable particles is not statistically independent of velocity and thus the arithmetic average of the measurements is not the same as the true average in the measurement volume. Durst et. al. (1995) present a method of correcting effects due to the finite measuring volume. Durst et. al. showed that the correction for mean velocity depends on the second derivative of the variation of mean velocity with distance from the wall, while for turbulence intensity the correction is dependent on the gradient of the mean velocity. However, the authors have shown that the corrections were significant only for the axial component of velocity in the region of the viscous sublayer, where velocity gradients can be expected to be high. Thus, measurements in this investigation have not been corrected for the influence of the finite size of the measuring control volume.

3.2.2.2.2 Laser Beam Alignment

The LDA system allows 3 velocity components (U_{BSA1},U_{BSA2},U_{BSA3},) to be measured simultaneously, from which the orthogonal components (U,V,W) that are

aligned with the test rig axis can be derived. What must be established is the errors associated with the transformation process and how they can be minimised.

In most practical test facilities access into the measurement region is restricted. Within an annular facility, for example, access is often through the outer casing and to minimise refractive effects the 1D and 2D probes lie in the radial plane. Such a configuration therefore could allow the streamwise (U) and circumferential (W) velocity components to be measured directly, but a large error can be associated with the radial (V) component which is derived by resolving two or more velocity components. Further reasons also exist as to why this configuration is not suitable. Britchford and Carrotte (1994) describe the errors that can occur, due to transformation, and indicate how they may be minimised by suitable alignment of the beams. Where practical, based on this conclusion, the following guidelines have been used;

1. The included angle between the 1D and 2D probes should be as large as is practical so as to minimise the error associated with the measured radial component. In addition, in order to minimise shear stress errors, the angle between the 1D probe (α) and the traverse plane should be similar, where practical, to that of the 2D probe (β).

2. Even though measurements can be obtained using off-axis detection, where the receiving optics of the 1D probe are used to detect signals from the blue-green velocity components and vice-versa, the 1D and 2D probes should not be positioned such that the laser beams are normal to the casing surfaces in order to reduce the effects of reflected light.

3. All 3 components (U_{BSA1},U_{BSA2},U_{BSA3}) should be positioned such that the mean velocity magnitude is similar on all processors. This is because in 3D work the processors must operate with the same record interval which therefore influences the record length and bandwidth on all 3 channels. Thus, in an orthogonal system for example, measurement of the large streamwise (U) component directly dictates the bandwidth and record interval of the relatively small radial and circumferential components. This may lead to a poor resolution of these components.

For all configurations it can be seen that a transformation matrix (discussed earlier in section 3.2.1) is required to convert the measured velocities (U_{BSA1},U_{BSA2},U_{BSA3},) into the three mutually orthogonal components (U, V, W) aligned with the rig axis. The transformation matrix comprises 9 coefficients, the values of which depend on the alignment of the laser beams within the facility. Errors in the transformed velocity components are therefore determined by the finite magnitude within which the laser beam alignment can be resolved.

In tests conducted downstream of a rotor providing in excess of 30 degrees of swirl to the S-shaped duct, the 1D and 2D probes were placed at angles of α=-49.5° and β=-11.3° to the traverse plane, with the violet (1D) beams constrained to lie in the axial-radial plane while the green and blue beams were rotated about the 2D probe axis to angles of γ_g=45.0° and γ_b=-45.0° (Fig.3.5). The transformed velocity components (U,V,W) aligned with the rig axis were obtained by operating on the measured velocity components (U_{BSA1},U_{BSA2},U_{BSA3},) and the optical transformation matrix (calculated using equations 3.13 through 3.21) such that;

$$\begin{bmatrix} U \\ V \\ W \end{bmatrix} = \begin{bmatrix} 0.8239 & 0.8365 & -0.2538 \\ 0.7549 & 0.7665 & -1.5889 \\ 0.7198 & -0.7094 & 0.0 \end{bmatrix} \begin{bmatrix} U_{BSA1} \\ U_{BSA2} \\ U_{BSA3} \end{bmatrix}$$

For example, at 50% duct height, the non-orthogonal velocity components, U_{BSA1}, U_{BSA2}, and U_{BSA3} were 45.04, 12.26 and 28.60m/s respectively. The streamwise (U), radial (V) and circumferential (W) can therefore be shown to be 40.10, -2.05 and 23.72m/s respectively. However, while the beams can be defined very accurately on the alignment beam when setting up coincidence with a 50μm diameter pin hole, the process of attaching the probes and traverse mechanism to the test facility is thought to introduce errors in the measured angles (α, β, γ_g and γ_b) of up to 0.5 degrees. The effect of any such misalignment of the laser beams on the transformed velocity components can, however, be estimated by re-calculating the affected coefficients in the optical transformation matrix. Hence, for the previous example, a variation of +0.5° on the angle between the 1D probe and the traverse plane (α=-47.5°) would adjust the optical transformation matrix such that the derived streamwise (U), radial (V) and circumferential (W) components of velocity are 40.08, -2.39 and 23.72m/s

respectively. The magnitude of the errors on the transformed velocity components due to a half degree variation in the alignment of the 1D probe are therefore 0.02 and 0.34m/s on the streamwise and radial velocities respectively, while the circumferential component is unaffected.

While similar errors occur due to variation of the angle between the 2D probe and the traverse plane (β) on the streamwise and circumferential velocity components, larger errors can occur with variation of the angles γ_g and γ_b due to misalignment of the 2D probe. For example, a half degree variation such that γ_g=44.5° and γ_b=–45.5° leads to an adjustment of the optical transformation matrix such that the streamwise (U), radial (V) and circumferential (W) velocity components are calculated to be 40.35, -1.82 and 23.38m/s respectively. The magnitude of the associated errors are therefore 0.25, 0.23 and 0.34m/s respectively. Thus, errors in the derived orthogonal mean velocities are determined by the accuracy to which the laser beam alignment can be obtained.

3.2.2.2.3 Processor Resolution

Further errors arise due to the finite resolution to which each velocity sample can be determined, and Carrotte and Britchford (1994) have presented a detailed analysis of the effect of processor resolution. The authors have shown that the accuracy to which a burst can be resolved is a function of the record interval (RI), this being the time period over which the burst is sampled. Thus, the processor resolution can be shown to be;

$$Resolution = \frac{C_a}{16RI} \qquad \text{(Eqn.3.30)}$$

where C_a is the calibration factor and is determined by the light wavelength and the angle between the beams forming the control volume. In this investigation, measurements were obtained using processors with a calibration factor of the order 3.0m/s/MHz. Furthermore, for this calibration factor, the relationship between processor resolution and record interval (Fig.3.8) indicates that at a typical record interval of 1.333μs, the processor resolution is approximately ±0.14 m/s. However it should be noted that the processor resolution is also dependent on the signal to noise ratio, with processor resolution becoming significantly poorer in regions where the noise content increases. Thus, while a processor resolution of ±0.14m/s is thought to

be representative of the green component (BSA1), which possesses significantly more light power, the blue and violet components are thought to be poorer. Carrotte and Britchford suggest that the resolutions of the blue (BSA2) and violet (BSA3) components are approximately ±0.21m/s and ±0.28m/s respectively.

3.2.3 Overall Estimate of LDA Errors

The statistical and systematic errors thought to contribute to the experimental accuracy of the LDA measurements have been identified and, the methods used to reduce such errors in this investigation have been discussed. Furthermore, since the errors have been shown to be a function of the turbulence intensity and the signal to noise ratio of the velocity signal which varies with each measurement, it is difficult to make an error estimate for an individual measurement. However, it is not thought unreasonable to estimate that overall the mean velocity components have been measured within ±0.5m/s of their true values, while the turbulent stresses are within ±5%. In addition, such an estimate is significantly in good agreement with the discrepancies in mass-flow observed between planes of less than 2.0%

It should be noted that, in this investigation, measurements have been obtained using both laser doppler anemometry and a 5 hole probe. Thus, two separate instruments have been used to obtain measurements, with the mean flow field measurements being in good agreement.

3.3 Analytical Procedures

3.3.1 Definition of Mean Flow Properties

Mean velocity information is provided both by the 5 hole probe and LDA measurement system with this data generally being in good agreement. At each traverse location the 5 hole probes also allow the stagnation and static pressures to be obtained which is complemented by the turbulent stresses measured using the LDA system.

In this investigation, the overall mean streamwise velocity (U_{Mean}) at a traverse plane has been calculated using an area weighted method such that;

$$U_{Mean} = \frac{1}{A}\int U dA \qquad \text{(Eqn.3.31)}$$

with the mass flow through a traverse being subsequently defined as;

$$m = \int \rho U dA = \rho U_{Mean} A \qquad \text{(Eqn.3.32)}$$

The spatially averaged values of stagnation pressure and static pressure have been calculated by mass weighting the individual values such that;

$$\tilde{P} = \frac{1}{m} \int P dm \qquad \text{(Eqn.3.33)}$$

$$\tilde{p} = \frac{1}{m} \int p dm \qquad \text{(Eqn.3.34)}$$

The difference between these mass weighted stagnation and static pressure values at a given plane were then used to obtain the mass weighted dynamic head,;

$$\tilde{P} = \tilde{p} + \alpha \frac{1}{2} \rho U^2_{Mean} \qquad \text{(Eqn.3.35)}$$

Furthermore, based on the equations presented by Dring (1992), the tangential momentum of the flow at each traverse plane has been defined per unit mass flow as;,

$$\frac{M_\theta}{m} = \frac{1}{m} \int \rho \bar{U} \tilde{W} r dA \qquad \text{(Eqn.3.36)}$$

while the axial momentum (per unit mass flow) can only legitimately be calculated within the parallel lengths at inlet to and exit from the S-shaped duct using;

$$\frac{M_x}{m} = \frac{1}{m} \int (\bar{p} + \rho \bar{U} \tilde{U}) \, dA \qquad \text{(Eqn.3.37)}$$

It should however be noted that all these averaged quantities are derived by numerical integration of the data. A linear extrapolation of the static pressure data to the casing surfaces was performed while the velocity at these locations was set to zero. A cubic interpolatory spline was then fitted to the data using a method outlined by Wray (1986) in order to obtain the equally spaced data required for numerical integration using the trapezium rule.

Radial distributions of the pitch averaged quantities have been derived from averaging of the data in the circumferential direction only, with area weighting used for the velocity distributions while mass-weighted averaging is used for most other parameters. All flow angles are, however, derived from the mass weighted tangential (W) and area weighted streamwise (U) velocity components as outlined by Dring and Spear (1992). This information is presented either in the form of the flow vector at each data point or, for example, in terms of the radial distribution of swirl angle.

3.3.2 Integral Boundary Layer Parameters

Some care must be taken in defining the integral boundary layer parameters for a curved flowfield. It is inappropriate to define a boundary layer thickness as 99% of the edge velocity since a region of potential core exists across the duct. So (1975) and Meroney and Bradshaw (1975) suggest that instead, all velocities in the boundary layer should be compared with the potential velocity which would exist for an inviscid fluid (Fig.3.9). Therefore, the displacement thickness (δ*) of each casing boundary layer is defined as;

$$\delta^{*} = \frac{1}{U_{pw_0}} \int_{0}^{\delta} (U_p(r) - U(r)) \frac{r}{r_{i/o}} dr \qquad \text{(Eqn.3.38)}$$

where $U_p(r)$ is the inviscid potential velocity of the curved flow at radius r, U_{pw} is the potential velocity that would exist at the wall for an inviscid flow, and $r_{i/o}$ is the radius of the inner wall or outer wall respectively. Furthermore, to be consistent, the

momentum thickness (θ) and shape parameter (H) are defined as;

$$\theta = \frac{1}{U_{pw0}^2} \int^{\delta} U(r)\,(U_p(r) - U(r))\,\frac{r}{r_{i/o}}\,dr \qquad \text{(Eqn.3.39)}$$

$$H = \frac{\delta^*}{\theta} \qquad \text{(Eqn.3.40)}$$

These integral parameters were calculated directly from the experimental data for axisymmetric inlet conditions, whilst with the compressor present, the data was first pitch averaged. In both cases, the data was extrapolated to the casing using the law of the wall.

$$\frac{U}{U_\tau} = 2.44 ln\left(\frac{U_\tau y}{\nu}\right) + 5.0 \qquad \text{(Eqn.3.41)}$$

where the friction velocity (U_τ) is calculated at each position (y) from the experimental data within the boundary layer using a Newton Raphson iterative method. This method produces a distribution of the friction (U_τ) velocity which tends towards a constant value at small distances from the casing surface where the law of the wall is applicable, and from which extrapolated data can be defined. The velocity profile, comprising both experimental and extrapolated data, is then splined and a least squares straight line fit is performed on the core of the flow in order to develop a potential velocity (U_p) profile. Each of the boundary layers is then considered in turn, with the integral boundary layer parameters calculated using a numerical integration method based on the trapezium rule. The results obtained should be treated with some caution, since the calculations are particularly sensitive to the extrapolation of the velocity profile to the wall. Furthermore, it is acknowledged that the use of a cubic interpolatory spline in the near wall region can lead to significant under/over estimates of the true data points. However, with careful interpretation of the results, this method has been shown to give excellent agreement with the detailed boundary layer data of Stevens (1970).

3.3.3 Overall Performance Parameters

Changes in the spatially averaged pressure between various planes within the diffuser system are expressed in terms of the stagnation pressure loss (λ) and static pressure recovery (C_p) coefficients which for incompressible flow are;

$$\lambda_{a-b} = \frac{\tilde{P}_a - \tilde{P}_b}{\tilde{P}_a - \tilde{p}_a} \qquad \text{(Eqn.3.42)}$$

$$Cp_{a-b} = \frac{\tilde{p}_b - \tilde{p}_a}{\tilde{P}_a - \tilde{p}_a} \qquad \text{(Eqn.3.43)}$$

where 'a' and 'b' are the upstream and downstream planes respectively. However, it should be noted that the definition of these quantities has been the subject of some discussion, due to the way that the performance of a duct varies with inlet conditions. For example, as reviewed earlier, Britchford et. al. (1994) have shown that blade wakes can have a favourable effect by re-energising boundary layer flow due to enhanced mixing. However, the presence and mixing out of such flow non-uniformities will lead to an increase in the systems mass weighted pressure loss. Klein (1988), in tests on short combustor pre-diffusers with blade wakes at inlet, suggested performance be defined in terms of momentum-mix weighted values in order to reduce the pressure loss variation with inlet conditions. In this case, the mean stagnation and static pressures at the inlet and exit planes are calculated as those which would occur if the respective velocity profiles were allowed to mix out in a frictionless duct of constant area. The mean total pressure calculated using this method therefore contains the losses associated with the mixing out of the blade wakes, while the calculated mean static pressure will be higher than that measured due to the rise in pressure during the mixing process. However, the theory is based on the assumption that the flow mixes out in a constant area duct and at constant pressure which will not always be valid, since in reality mixing continues while wakes are decelerated or accelerated. Thus, for example, the momentum-mix approach takes no account of the extra losses associated with wakes mixing out in adverse pressure gradients as outlined by Denton (1993). It should be noted that the overall performance data in this report is presented in terms of mass weighted pressures as defined in Eqn.3.42. The data therefore includes not only the favourable effects of wake mixing, on boundary layer flow, but also any mixing losses associated with the non-uniform inlet flow. It is also thought that the

representative inlet conditions mean that the mass weighted pressure loss data reflects that which would be recorded within a modern gas turbine engine.

In addition to the overall stagnation pressure loss within the duct, its radial distribution can be determined by considering the change in pressure along a streamline between traverse planes. This can be obtained by dividing the flow across the duct, at the upstream and downstream traverse planes, into 1% increments of mass flow. At the corresponding radial locations, the values of stagnation pressure can then be interpolated and used to define the loss along each streamline. The radial distribution of loss and its development can therefore be described by monitoring the change in stagnation pressure along streamlines at each traverse plane within the duct. Furthermore, the area under the radial distribution of stagnation pressure loss represents the overall stagnation pressure loss of the flow up to that plane, with the loss obtained from numerical integration of the radial distribution being in excellent agreement with the overall pressure loss obtained using the spatially averaged values.

3.3.4 Balancing of the Momentum Equations

In order to identify the relative importance of pressure gradient and streamline curvature effects on streamwise velocity, an analysis of the mean momentum equation has been performed. For example, at a given location, the main determinants of the mean streamwise velocity can be resolved by considering the various terms in the mean streamwise momentum equation.

Bradshaw (1973) indicates that while it is desirable to assume that surfaces are flat for small values of boundary layer thickness to radius ratio (δ/r), the extra terms introduced into the governing equations of curved flows are not insignificant. It is therefore thought that the governing equations of the flow within an annular S-shaped duct should be expressed within an s,n,ϕ coordinate system. In such a coordinate system (Fig3.10) s is the distance measured along a reference streamline (taken as the inner casing in this investigation), and n is measured along straight lines normal to the reference line. The third coordinate, ϕ, is measured as an angular rotation normal to the (s,n) plane. The radius of curvature of the reference streamline (R) is in general a function of **s** ($\partial s = R\partial\theta$) in which case the coordinates become non-unique on the locus of the centre of curvature, while if R is constant the system reduces to cylindrical polar coordinates. The mean velocity components in the s, n, and ϕ directions are U, V and W respectively, with u', v' and w' being the corresponding fluctuating velocity

components.

The Navier-Stokes equations of motion are well documented for cartesian, cylindrical polar and spherical polar coordinate systems. However, since Howarth (1951) first developed a coordinate system for flow along a general curved surface, very little work has been published on the s,n coordinate system. Bradshaw (1973) developed the continuity and momentum equations for incompressible two-dimensional flow in the s,n coordinate system and a number of authors (Irwin and Smith, 1975, Gibson et. al., 1981, Rodi and Scheuerer, 1983) have also presented work using similar equations. Eghlima and Kleinstreuer (1985) have presented the incompressible form of the axisymmetric equations, although there is some doubt as to whether an order of magnitude study has been performed on the equations in order to simplify them. Unfortunately, it has not been possible to find a single example, in the published literature, of the full three dimensional equations of motion in the s,n,ϕ coordinate system. It has therefore been necessary in this investigation to derive the equations (Appendix 2) from a general orthogonal coordinate system (Rosenhead, 1963). For example, for turbulent, incompressible, three dimensional flow, the continuity equation for a general orthogonal coordinate system can be written as;

$$div\vec{V} = \frac{1}{h_1 h_2 h_3}\left(\frac{\partial}{\partial x_1}(h_2 h_3 V_1) + \frac{\partial}{\partial x_2}(h_3 h_1 V_2) + \frac{\partial}{\partial x_3}(h_1 h_2 V_3)\right) = 0 \qquad \text{(Eqn.3.44)}$$

where the total velocity vector V has components (V_1,V_2,V_3) corresponding to the orthogonal velocity components U,V,W in the streamwise, normal and circumferential directions respectively. Furthermore, the metrics (h_1,h_2,h_3) are derived from elemental lengths in the streamwise ($x_1=\theta$), normal ($x_2=n$) and circumferential ($x_3=\phi$) directions such that;

$$h_1 = R + n \qquad h_2 = 1 \qquad h_3 = r \qquad \text{(Eqn.3.45)}$$

The continuity equation for incompressible three dimensional flow can therefore be shown to be;

$$\frac{1}{h}\frac{\partial U}{\partial s} + \frac{1}{rh}\frac{\partial r}{\partial s}U + \frac{\partial V}{\partial n} + \frac{1}{r}\frac{\partial r}{\partial n}V + \frac{V}{Rh} + \frac{1}{r}\frac{\partial W}{\partial \phi} + \frac{1}{rh}\frac{\partial h}{\partial \phi}W + \frac{1}{Rr}\frac{\partial R}{\partial \phi}W = 0 \qquad \text{(Eqn.3.46)}$$

where h =1+n/R is the ratio of local (R+n) to reference (R) radius of curvature.

In addition, the mean momentum equations in the s, n and ϕ directions have also been developed for turbulent incompressible flow. Neglecting outside forces, the momentum equations can be written in vector form as;

$$\frac{\partial \vec{V}}{\partial t} + grad\left(\frac{1}{2}\vec{V}^2\right) - \vec{V} \times \vec{\omega} = -\frac{1}{\rho} grad\,(p) + \nu \nabla^2 \vec{V} \qquad \text{(Eqn.3.47)}$$

from which the three component (s,n,ϕ) equations can be derived. For example, neglecting the viscous stresses, since they are thought to be insignificant over the range of experimental data acquired, the time averaged s-component momentum equation can be written as;

$$\frac{1}{h}\frac{\partial \overline{U}^2}{\partial s} + \frac{1}{r}\frac{\partial}{\partial n}(\overline{U}\overline{V}r) + \frac{2\overline{U}\overline{V}}{Rh} + \frac{1}{r}\frac{\partial}{\partial \phi}(\overline{U}\overline{W}) + \frac{1}{rh}\frac{\partial r}{\partial s}(\overline{U}^2 - \overline{W}^2) =$$

$$-\frac{1}{\rho h}\frac{\partial \overline{p}}{\partial s} - \left(\frac{1}{h}\frac{\partial \overline{u'}^2}{\partial s} + \frac{1}{r}\frac{\partial}{\partial n}(\overline{u'v'}r) + \frac{2\overline{u'v'}}{Rh} + \frac{1}{r}\frac{\partial}{\partial \phi}(\overline{u'w'}) + \frac{1}{rh}\frac{\partial r}{\partial s}(\overline{u'}^2 - \overline{w'}^2)\right)$$

(Eqn.3.48)

Having derived the equations of motion, it has therefore been possible to calculate each of the terms, at a given point in the flow, using the experimental data. The convection terms and the forces due to streamwise pressure gradients have been evaluated from mean velocity and static pressure data obtained using five hole pressure probes. In addition, it has also been possible to calculate the turbulent stress terms using the laser doppler anemometry measurements of all 6 Reynolds stresses.

Each of the terms in the streamwise momentum equation (Eqn.3.48), for example, has been calculated using a computer program. Initially, the program reads in the experimental data obtained at all of the traverse stations using both 5 hole pressure probes and the LDA system. The data is then interpolated onto common traverse locations and extrapolated to the wall. Each of the terms in the streamwise differential equation are then calculated at every point in the traverse, with each radial traverse being considered in turn. The streamwise derivatives have been calculated by fitting

cubic interpolatory splines to the data at fixed heights along the traverse stations. The streamwise derivative then being found by central differencing of the interpolated data immediately upstream and downstream of the actual data point. Derivatives in the normal and circumferential directions have been calculated using a 3rd order Lagrange polynomial (Gerald, 1980) fitted to the data. Results from the program are presented in the form of the radial distribution of the various terms at each traverse plane, along with any imbalance in the calculated terms. The results indicate that the dominant force on the fluid, due to the Reynolds stresses, is produced by the primary (uv) shear stress gradient which is at least an order of magnitude larger than the other stress terms along the duct. Thus, for reasons of clarity the smaller stress components have been neglected from most of the analysis presented, though it should be noted that they do feature in the evaluation of any imbalance in the equations.

The experimental data has therefore been used to identify the most significant terms in the momentum equations, for the flow within the S-shaped duct, and in the s,n directions these are

$$\frac{D\bar{U}}{Dt} + \frac{2\bar{U}\bar{V}}{Rh} - \frac{\bar{W}^2}{rh}\frac{\partial r}{\partial s} = -\frac{1}{\rho h}\frac{\partial \bar{p}}{\partial s} - \frac{1}{r}\frac{\partial}{\partial n}(\overline{u'v'}r) \qquad \text{(Eqn.3.49)}$$

$$\frac{D\bar{V}}{Dt} - \frac{\bar{U}^2}{Rh} - \frac{\bar{W}^2}{r}\frac{\partial r}{\partial n} = -\frac{1}{\rho}\frac{\partial \bar{p}}{\partial n} - \frac{1}{rh}\frac{\partial}{\partial s}(\overline{u'v'}r) \qquad \text{(Eqn.3.50)}$$

For example, with no swirl present, the fluid element (Fig.3.11) is subjected to centripetal (U^2/Rh) and coriolis ($2UV/Rh$) acceleration in addition to the particles acceleration in the streamwise and normal directions ($\partial U^2/\partial s$, $\partial V^2/\partial n$). With the introduction of swirl an additional centripetal acceleration arises (W^2/r), and it should be noted that this has components in both the streamwise ($W^2/rh \times \partial r/\partial s$) and normal ($W^2/r \times \partial r/\partial n$) directions (Fig.3.11). The forces associated with these accelerations are, of course, provided by the pressure gradients, turbulent and viscous stresses. For example, in the streamwise direction the shear force is associated with the turbulent shear stress gradient ($1/r\partial(\overline{u'v'}r/\partial n$) whilst the pressure force is obtained from the streamwise gradient ($1/\rho h\ \partial p/\partial s$). Furthermore, in order to permit comparisons between tests with different inlet conditions, these terms are expressed relative to the streamwise momentum at duct inlet.

As already shown, extra terms are generated in the governing equations derived

in the s,n,ϕ coordinate system which was chosen in preference to the more conventional coordinate systems. However, Finnigan (1983) indicates that the s,n system has the disadvantage that the coordinate lines in the normal direction can be parallel to the reference streamline only. Thus, at all other streamlines there will be mean velocity components that are not parallel with the normal direction. Finnigan suggests such problems can be resolved by using a doubly curvilinear coordinate system, in which the streamwise coordinate lines are everywhere orthogonal to the curvilinear normal lines (Fig.3.12). However, it was felt in this investigation, that a coordinate system was required which incorporated the traverse planes in order to minimise interpolation of the data. It is therefore thought important to acknowledge that whilst every care has been taken in the derivation of the governing equations there are some concerns as to their suitability.

Chapter 4 Results and Discussion

4.0 Results and Discussion

4.1 Two-dimensional Axisymmetric ("Clean") Inlet Condition

The two dimensional axisymmetric case, termed the "clean" inlet condition, forms the first phase of a continuing investigation at Loughborough University of Technology. As already discussed in Section 1.5 Britchford (1997) undertook this first phase of the investigation and obtained measurements using both five hole pressure probes and a 3 component LDA system. Thus, the complex flows which are the subject of this investigation can be explained relative to the flow features of Britchford's two dimensional case. For example, by examining the pressure distribution within the duct for the "clean" inlet condition, the effect due to the presence of a radial strut can be discerned. It is therefore important to note that some of the results presented in this section have already been broadly outlined by Britchford, as indicated by the relevant references, although the actual data presented here is derived from Britchford's raw experimental data. Further analysis has been performed though on this data which is of significance to the geometries tested in this investigation. For example, measurements of both the mean and fluctuating flow field, obtained by Britchford, have been used to identify the most significant terms in the momentum equations.

4.1.1 Inlet Condition

The two dimensional axisymmetric inlet condition for the datum test case was obtained by allowing boundary layers to develop along an upstream entry length. As initially outlined by Britchford & Carrotte (1994), the inlet conditions to the working section displayed excellent circumferential uniformity and were virtually swirl free. At x/L=-0.55, the turbulent boundary layers that have developed along the inner and outer casings of the entry length occupy approximately 22% and 23% of the passage height respectively (Fig.4.1.1). For an annulus height of 71.1mm this gives a boundary layer thickness (δ) of approximately 15.5mm and 16.6mm for the inner and outer casings respectively. The displacement thickness (δ^*) calculated for each boundary layer, using the method discussed in Chapter 3, was 2.4mm (inner) and 2.3mm (outer). In addition, the momentum thickness (θ) values were approximately 1.8mm (inner) and 1.7mm (outer) with corresponding shape parameters ($H=\delta^*/\theta$) of 1.36 and 1.34. These inner and outer casing boundary layers were isolated by a potential core region with a velocity of approximately 30.3m/s, giving a Reynolds number (Re_θ) for each boundary layer of approximately 3700 based on this velocity and the momentum thickness. The

spatial average velocity for the annular passage (U_{Mean}) was 28.3 m/s, this being used as a reference value for non-dimensionalising the mean velocity and Reynolds stress data at this and subsequent downstream traverse planes.

The mean streamwise data are also presented in log-law coordinates (Fig.4.1.2) from which a skin friction coefficient ($C_f = \tau_w / \frac{1}{2}\rho U_{Max}^2$) of approximately 0.0033 was obtained. With a Reynolds number of 3700 based on momentum thickness and the boundary layer edge velocity this is in excellent agreement with the value (C_f) of 0.0033 derived from a skin friction relationship based on the 1/7th power law (Young, 1989);

$$C_f = 0.026 Re_\theta^{-1/4} \qquad \text{(Eqn.4.1.1)}$$

However, Fig.4.1.2 does illustrate one of the problems associated with making measurements within relatively small annular passages typical of those found within gas turbine engines. The closest point to a casing surface at which LDA measurements could be obtained was typically 0.5mm ($y^+ = 35$), while pressure probe measurements could only be made to within 1mm of each casing. However, the edge of the viscous sub-layer was typically only 0.1mm ($y^+ = 10$) from the casing surface, with the fully turbulent region of each boundary layer occurring at a height greater than 0.8mm from each casing surface. Thus, due to the constraints of a practically sized test facility, it has not been possible to acquire measurements in all regions of the boundary layer.

The distribution of all 6 Reynolds stresses across the annular passage are also presented (Fig.4.1.3). As might be expected, the ($\overline{v'w'}$) and ($\overline{u'w'}$) shear stresses are nominally zero, across the passage, which indicates the quality of the experimental data. Within the central region of the passage, the primary ($\overline{u'v'}$) shear stress is also virtually zero. However, the development of boundary layers within the entry length has produced near linear distributions of the primary ($\overline{u'v'}$) shear stress towards each casing. Values of shear stress at the wall, extrapolated from the measured shear stress distribution, have been used to calculate a skin friction coefficient (C_f) of 0.0034 and 0.0035 for the inner and outer casing boundary layers respectively. These values are in good agreement with the results presented earlier. Close to each casing the radial normal stress component ($\overline{v'v'}$) shows some evidence of decreasing, thereby indicating

measurements within the boundary layer transition region. However, no such reductions are observed in the other components of Reynolds stress which will occur at smaller distances from the surface than those at which measurements have been obtained. Furthermore, while the normal stresses are small within the central region of the duct, some differences are evident. As noted by Carrotte et. al. (1993) the fluctuating component of radial velocity ($\sqrt{\overline{v'^2}}$=0.3m/s) is slightly greater than the corresponding streamwise ($\sqrt{\overline{u'^2}}$) and circumferential ($\sqrt{\overline{w'^2}}$) fluctuating components of approximately 0.2 m/s. However, in this region turbulence should be isotropic. This difference in the measured normal stress components is due to both the finite resolution to which each component can be measured and to errors introduced during the transformation of the measured velocity components into the three mutually orthogonal components aligned with the rig axis (as discussed in Chapter 3).

4.1.2 Mean Static Pressure and Velocity Distributions

Consideration of the momentum equation (e.g. Schlichting, 1968) indicates that the streamwise pressure gradients have a direct effect on the mean streamwise velocity (U). With this in mind the static pressure distribution along each casing wall, and at various heights across the duct, is presented (Fig.4.1.4). The data is expressed in terms of a coefficient (C_p) defined using the mass weighted stagnation and static pressures at inlet to the working section (x/L=-0.55) as outlined in Chapter 3. Differences between the static pressures across the duct reflect how the pressure field adjusts to provide the required radial forces to turn the flow. Hence across the first bend the static pressure adjacent to the outer casing is higher than that adjacent to the inner. However this situation reverses within the second bend as the flow is returned to the axial direction. As a result of these changes in the radial pressure gradient, significant streamwise pressure gradients occur. Hence, the flow along the inner casing is subjected to a predominantly positive (i.e. adverse) gradient as the static pressure coefficient rises, from -0.33 to +0.24 along approximately 70% of the duct length. In contrast, the pressure gradient is mostly negative (i.e. favourable) adjacent to the outer casing with the coefficient reducing from +0.20 to -0.26 along a similar length. Note also how these gradients vary significantly across the height of each boundary layer, with the maximum streamwise variations occurring along each casing.

Relative to the pressure field the mean streamwise velocity profiles (Fig.4.1.5) are presented which show the presence of a potential core region, along the entire length of the duct, which isolates each casing boundary layer. Within the inviscid core

the near linear variation of velocity indicates the response of the flow to the pressure field associated with the duct curvature. However, the most critical regions of flow development are associated with each boundary layer. It can be seen that along both walls the flow remains attached, although significant regions of boundary layer growth are apparent. The boundary layer integral parameters (δ^*, θ, H) have been calculated (Table 4.1), using the method outlined in Chapter 3, and indicate how the boundary layers develop along the inner and outer casings. This data shows that the boundary layer development is broadly similar to that which would be expected due to the applied streamwise pressure gradient. For example, the significant variation of each boundary layer's shape parameter (H) along the duct (Fig.4.1.6) indicates that it is the flow adjacent to the inner casing that is most likely to separate, reaching a maximum value of 1.66 at x/L = 0.75. This boundary layer growth occurs within the region of adverse pressure gradient previously described. It should be noted however, that this value is significantly below the value of 2.7 that Schubauer and Klebanoff (1951), amongst others discussed in Chapter 1, associate with imminent turbulent flow separation.

Although the static pressure distribution appears broadly responsible for the observed mean velocity profiles, the development of each boundary layer must also be influenced by the turbulent flow field which is directly affected by streamline curvature. As initially suggested by Britchford et. al. (1994), the relative magnitude of these effects can be assessed from a plot (Fig.4.1.7) of the non-dimensional pressure gradient parameter (δ^*/τ_w. dp/dx) versus the curvature parameter (δ/R). Gillis & Johnston (1983) and Barlow & Johnston (1988) suggest that the ratio of boundary layer thickness (δ) to wall radius of curvature (R) is the widely accepted parameter describing the magnitude of the curvature effects on the outer layer of the flow. They suggest that for $\delta/R < 0.01$ these effects are generally weak, but are strong for $\delta/R > 0.1$. Thus, the inner wall boundary layer in this investigation is initially subject to relatively strong convex curvature, the maximum value of curvature parameter ($\delta/R=0.11$) occurring at x/L = 0.125. However by x/L = 0.50 curvature is in the opposite sense (i.e. concave), increasing up to a maximum value ($\delta/R=0.12$) at x/L=0.80. Along the outer casing, the boundary layer is subjected to similar effects but in this case concave curvature precedes the convex curvature with maximum values of $\delta/R=0.08$ and $\delta/R=0.09$ respectively.

4.1.3 Turbulent Flow Field

The magnitude of the curvature parameter (δ/R), indicates that significant regions within each boundary layer are experiencing relatively strong curvature. Hence in order to assess the relative importance of this effect on the mean velocity field it is necessary to consider the shear stress as well as the pressure field distributions within the duct. For reasons to be outlined in Section 4.1.4, the turbulent flow field is mainly considered in terms of the primary ($\overline{u'v'}$) shear stress distribution. The measured distributions (Fig.4.1.8) show that while the development of boundary layers within the entry length has produced the near linear distributions of shear stress at x/L=-0.55 described earlier, these rapidly change to produce complex distributions within the S-shaped duct. It should be noted that wall shear stress values have been obtained from fits of the mean velocity profiles to the "log law" distribution. Hence, these diagrams represent the total shear stress (τ_{ij}) where it is assumed that in regions where LDA measurements have been made this shear stress is composed of entirely the turbulent ($\overline{u'v'}$) component. Close to each casing these turbulent stresses, of course, reduce in magnitude with the viscous component becoming dominant.

The distribution of shear stress ($\overline{u'v'}$) throughout the boundary layer is modified by both streamwise pressure gradients and streamline curvature, although these two effects are more apparent in different parts of the layer. For example, by considering the production terms in the 2D transport equations for the turbulent kinetic energy (k) and the primary shear stress ($\overline{u'v'}$), as presented by Bradshaw (1973) in the special s,n coordinate system. i.e.:

$$Production\,(k) = -h\frac{\partial U}{\partial n}\overline{uv} - (\overline{u}^2 - \overline{v}^2)\left[\frac{\partial U}{\partial s} + \frac{V}{R}\right] - \overline{uv}\left[\frac{\partial V}{\partial s} - \frac{U}{R}\right] \quad \text{(Eqn.4.1.2)}$$

$$Production\,(uv) = \overline{u}^2\left(\frac{\partial V}{\partial s} - \frac{U}{R}\right) + h\overline{v}^2\frac{\partial U}{\partial n} - (\overline{u}^2 - \overline{v}^2)\frac{U}{R} \quad \text{(Eqn.4.1.3)}$$

It can be seen that the pressure gradient can only exert an indirect influence on the shear stress distribution, through modification of the mean velocity gradient ($\partial U/\partial n$). However, while the mean velocity profile responds quickly to the applied pressure gradient, the turbulence reacts relatively slower causing the development of the shear stress profile to lag behind that of the mean velocity profile. The production

terms (Eqn.4.1.2 and 3) further indicate that the effect of the applied pressure gradient is mainly confined to the region adjacent to each wall where the flow is of relatively low momentum, but the velocity gradients ($\partial U/\partial n$) are high. Baskaran et. al. (1991), reviewed earlier in Chapter 1, have shown that the shear production of turbulent kinetic energy ($\overline{u'v'}.\partial U/\partial n$) and shear stress generation ($\overline{v'^2}.\partial U/\partial n$) as well as the normal stress production of turbulent kinetic energy (($\overline{u'^2}-\overline{v'^2}$).$\partial U/\partial s$) are also important in this region. In contrast, streamwise curvature is seen mainly to affect the outer layer since the extra strain rate (U/R) is relatively large in comparison with $\partial U/\partial n$. This leads to an increase or decrease, depending on the sign of the curvature, of both the turbulent kinetic energy and shear stress. The production terms can therefore be used to indicate where pressure gradient and streamline curvature effects are significant in the development of the observed shear stress distribution (Fig.4.1.8).

4.1.3.1 Pressure Gradient Effects

Initially, along the inner wall, there is a short period of favourable pressure gradient throughout which the wall shear stress increases (Fig.4.1.8) due to the relative increase in momentum. However, between x/L=0.25 and x/L=0.75 the sustained adverse pressure gradient along the inner casing reduces the wall shear stress, with the peak value increasing in magnitude and moving away from the wall. Schubauer and Klebanoff (1951), reviewed earlier in Chapter 1, have shown that such a fall in the shear stress towards the surface (Fig.1.7) is evidence that the shear stress is acting to prevent separation. The long region of adverse pressure gradient along the inner casing is then followed by a further favourable pressure gradient throughout which the wall shear stress increases. In contrast, for the outer casing, the pressure gradient is adverse along the initial and latter stages of the duct, resulting in the peak shear stress moving away from the surface and a low wall value. However along most of the surface (x/L=0.25 to x/L=0.75) the pressure gradient is favourable during which the wall shear stress increases. Schubauer and Klebanoff have shown that when the pressure gradient is either constant or falling, all pull is ultimately exerted on the surface and the shear stress would be expected to be a maximum there. However, the conclusions of Schubauer and Klebanoff were obtained from boundary layers being subjected to pressure gradients of constant sign. It can be seen that within the S-shaped duct complex distributions of shear stress develop, adjacent to each casing, as each boundary layer responds to the varying pressure gradients along the duct.

4.1.3.2 Streamline Curvature Effects

The Reynolds shear stress ($\overline{u'v'}$) distributions are further modified by the direct effect of streamline curvature on the turbulence field. Wattendorf (1935) described how the imbalance that exists between the centripetal acceleration of a turbulent fluid element and its surrounding pressure field gives rise, over a convex surface, to reduced turbulence levels. In contrast, over a concave surface increased turbulence mixing is observed. Along the inner wall of the S-shaped duct (Fig.4.1.8), the flow reacts quickly to the onset of convex curvature at x/L=0.0 leading to an initial suppression of shear stress in the outer region of the boundary layer, evident (at x/L=0.125) within 2 boundary layer thicknesses (Fig.4.1.8). As already noted, effects due to curvature on the primary shear stress ($\overline{u'v'}$) are most substantial in the outer layer, where the streamwise velocity component (U) is greatest. Concave curvature commences at x/L=0.50, though it is not until x/L=0.75, over 3 boundary layer thicknesses, that enhanced shear stress values are observed. As the flow exits the duct (x/L=1.0), the curvature is very small and the shear stress distribution is similar to that seen at x/L=0.75 due to the inherent lag of the turbulence structure relative to the mean velocity. For the outer casing, similar effects are observed, except in this case turbulence mixing and shear stress levels are initially enhanced in the outer part of the boundary layer by the concave curvature, prior to the suppression of the shear stress in the outer layer after the onset of convex curvature at x/L=0.50. Differences in the rate of response of the turbulence to the onset of concave and convex curvature have been seen in previous studies. Bandyopadhyay & Ahmed (1993), amongst many others reviewed in Chapter 1, confirmed that a turbulent boundary layer is slower to respond to concave curvature than to convex. They showed that when the preceeding section is flat, the onset of concave curvature produces a change in wall shear stress after a delay of over 4 boundary layer thicknesses, while in contrast the lag was less than 3 boundary layer thicknesses for convex curvature. Similar responses are evident in the complex distributions of shear stress measured in the S-shaped duct, as each boundary layer responds to the curvature along each casing.

4.1.4 Analysis of Momentum Equation

In order to assess the impact of the turbulent flow field on mean velocity relative to the pressure field, an analysis of the mean momentum equation has been performed. For example, at a given location, the main determinants of the mean streamwise velocity can be resolved by considering the various terms in the mean streamwise

momentum equation. Section 3.3.4 describes how the equations of continuity and motion have been derived in the s,n,ϕ coordinate system. For the "clean" inlet condition, the equations can be expressed in the two-dimensional axisymmetric form. For example, the continuity equation for incompressible flow can be shown to be;

$$\frac{1}{rh}\left(\frac{\partial}{\partial s}(Ur) + \frac{\partial}{\partial n}(Vrh)\right) = 0 \qquad \text{(Eqn.4.1.4)}$$

where h =1+n/R is the ratio of local (R+n) to reference (R) radius of curvature and the mean velocity components in the s, n, and ϕ directions are U, V and W respectively. Furthermore, for incompressible two-dimensional axisymmetric flow, the s-component momentum equation can be written as;

$$\frac{1}{h}\frac{\partial}{\partial s}(\overline{U}^2 r) + \frac{1}{r}\frac{\partial}{\partial n}(\overline{U}\overline{V}r) + \frac{2\overline{U}\overline{V}}{Rh} = -\frac{1}{\rho h}\frac{\partial \overline{p}}{\partial s} - \left(\frac{1}{rh}\frac{\partial}{\partial s}(\overline{u'}^2 r) + \frac{1}{r}\frac{\partial}{\partial n}(\overline{u'v'}r) + \frac{2\overline{u'v'}}{Rh}\right)$$

(Eqn.4.1.5)

It should be noted that the viscous terms have been neglected, since they are thought to be insignificant over the region where experimental data has been acquired. An analysis of the s-component momentum equation has therefore been performed by calculating each of the terms, at a given point in the flow, using the experimental data.

The terms on the left hand side of Eqn.4.1.5 and the forces due to streamwise pressure gradients ($1/\rho h\ \partial p/\partial s$) have been evaluated from mean velocity and static pressure data obtained using five hole pressure probes. In addition, it has also been possible to calculate the turbulent stress terms using Britchford's LDA measurements of all 6 Reynolds stresses. The various interpolatory and differencing methods used to calculate the differential terms are discussed in more detail in Section 3.3.4. The results indicate that the dominant force on the fluid, due to the Reynolds stresses, is produced by the primary shear stress gradient ($1/r\partial(\overline{u'v'}r)/\partial n$). For example, the forces associated with the turbulent stresses in the s-component momentum equation at x/L=0.75 (Fig.4.1.9) indicate that the primary shear stress gradient is at least an order of magnitude larger than the other stress terms. Thus, for reasons of clarity the smaller stress components have been neglected from most of the analysis presented, though it

should be noted that they do feature in the evaluation of any imbalance in the equations.

The experimental data has been used to identify the most significant terms in the momentum equations for the flow within the S-shaped duct. With no swirl present, the fluid is subjected to a coriolis (2UV/Rh) acceleration in addition to the acceleration in the streamwise direction (1/rh $\partial(U^2r)/\partial s$). The forces associated with these accelerations are, of course, provided by the pressure gradients, turbulent and viscous stresses. For example, in the streamwise direction the shear force is associated with the turbulent shear stress gradient ($1/r\partial(\overline{u'v'}r)/\partial n$) whilst the pressure force is obtained from the streamwise gradient ($1/\rho h\ \partial p/\partial s$). The analysis has been restricted to the region between the traverse stations at x/L=0.0 and x/L=1.0. In addition, to permit comparisons between tests with different inlet conditions these terms are expressed relative to the streamwise momentum at duct inlet. Using these techniques the relative magnitude of the pressure ($1/\rho h\ \partial p/\partial s$) and shear stress ($1/r\ \partial(\overline{u'v'}r)/\partial n$) forces applied to the flow can be assessed which, together with the convection term ($1/r\ \partial(UVr)/\partial n$), give rise to the changes in mean streamwise velocity ($1/rh\ \partial(U^2r)/\partial s$) observed.

4.1.4.1 Momentum Equation Balance

Whilst the objective of the analysis is to identify the impact of shear forces on the mean velocity, relative to the pressure forces, all of the terms in the streamwise momentum equation (Eqn.4.1.5) have been calculated (though not all are presented) and contribute to the resulting balance. However, examination of the significant terms in the s-component mean momentum equation at inlet (x/L=0.0) to the S-shaped duct (Fig. 4.1.10), shows that there is a large imbalance of the evaluated terms. Furthermore, it should be noted that the imbalance is relatively large compared with the magnitude of the individual terms and is typical of the imbalance that exists at other downstream traverse locations. Furthermore, a significant imbalance can be seen in similar analysis of the continuity equation at x/L=0.0 (Fig.4.1.11).

However, the magnitude of the imbalance in this investigation is cause for some concern. It is thought that neither the coriolis (2UV/Rh) or turbulent terms are likely to generate such a large imbalance in the s-component momentum equation. Furthermore, the streamwise derivatives of both pressure ($1/\rho h\ \partial p/\partial s$) and velocity $1/rh\ \partial(U^2r)/\partial s$) are confidently thought to be calculated to sufficient accuracy not to cause such a large imbalance. However, it can be seen (Fig.4.1.10) that the radial distribution of the

imbalance is similar to that of the convection term (1/r ∂(UVr)/∂n). It is therefore thought that the imbalance in the s-component momentum equation is sensitive to the calculation of this convection term which can be expanded to give;

$$\frac{1}{r}\frac{\partial}{\partial n}(UVr) = U\frac{\partial V}{\partial n} + V\frac{\partial U}{\partial n} + \frac{UV}{r}\frac{\partial r}{\partial n} \qquad \text{(Eqn.4.1.6)}$$

From the experimental data each component can be calculated separately. The results indicate that the U∂V/∂n term is significantly larger than the other two terms. It is therefore thought that the convection term (1/r ∂(UVr)/∂n) is particularly sensitive to the calculation of the gradient of the radial velocity component (∂V/∂n). With hindsight, it might be unreasonable to expect to calculate the gradient of the relatively small radial velocity (V) with the same accuracy to which the gradients of both the relatively large streamwise velocity (U) and pressure (p) can be calculated from experimental data. While it is difficult to estimate the error on a single measurement, as indicated in Chapter 3, measurements obtained using a 5 hole pressure probe were repeatable to within 0.5mm H_2O. While such an error is unlikely to significantly effect the calculation of the differential terms including the relatively large streamwise velocity (U), a similar error on the relatively small radial component of velocity is likely to be of greater significance. Such errors on the radial velocity component are therefore likely to be significant in the calculation of the gradient ∂V/∂n, with these errors being most appreciable in the near wall regions where gradients are highest but with the measurements more likely to be in error.

As a means of assessing the sensitivity of the imbalance to the radial velocity gradient, the distribution of radial velocity across the passage required to satisfy mass flow continuity can be calculated. This can be achieved by balancing the term describing the radial transport of mass flow (1/rh ∂(Vrh)/∂n) with the term describing the net streamwise transport of mass flow (1/rh ∂(Ur)/∂s). As in the case of the convective term in the s-component momentum equation, the term ∂(Vrh)/∂n can be expanded to;

$$\frac{1}{rh}\frac{\partial}{\partial n}(Vrh) = \frac{\partial V}{\partial n} + \frac{V}{r}\frac{\partial r}{\partial n} + \frac{V}{Rh} \qquad \text{(Eqn.4.1.7)}$$

and shown to be dominated by the gradient $\partial V/\partial n$ (Fig.4.1.12). Thus, assuming that $\partial V/\partial n$ is approximately equal to $1/rh\ \partial(Ur)/\partial s$, a profile of radial velocity can be calculated which balances the continuity equation. It should be noted that this method depends on assuming an initial velocity at some point in the flow. Thus, while the distribution of radial velocity across the passage height is predicted, the overall levels of the predicted velocity are arbitrary. In this investigation, the radial velocity profile has been generated by assuming a value at mid passage height equal to the measured value as the measurement at this location is thought to be least in error. The radial velocity at subsequent locations across the passage height can then be calculated from;

$$V_n = V_{n+\delta n} + \frac{\partial V}{\partial n}\delta n \qquad \text{(Eqn.4.1.8)}$$

At x/L=0.0 (Fig.4.1.13), it can be seen that the calculated radial velocity is not too dissimilar from the measured radial velocity. At most of the traverse planes, the adjustment of the radial velocity profile required to balance the continuity equation is small and within experimental error. For example, at x/L=0.50 (Fig.4.1.13), the calculated radial velocity profile lies very close to the measured profile with slight differences observed in the near wall regions. It is acknowledged that the measured radial velocity profiles presented do not tend towards zero in the near wall region. This is thought to be due to a number of effects. For example, the experimental error associated with the relatively low levels of radial velocity is thought to be significant in the near wall region. Furthermore, while the traverse planes are normal to a line through the S-shaped duct at mid-annulus height, this is not thought to be the case at the inner and outer walls where the casing profiles might be expected to diverge marginally.

The balance of the s-component momentum equation obtained using a profile of radial velocity calculated to ensure mass flow continuity is presented (Fig.4.1.14.a) at inlet to the S-shaped duct (x/L=0.0). It can be seen that the imbalance has reduced significantly when compared with that presented earlier (Fig.4.1.10) for analysis performed using the measured radial velocity profile. However, it should be noted that whilst similar reductions of the imbalance have been obtained at each of the downstream planes, a degree of imbalance remains in the analysis. For example, at x/L=0.5 (Fig.4.1.14.b) it can be seen that while the balance is agreeable over 60% of

the passage height, a small imbalance can be observed towards each casing. Clauser (1954) has indicated that a number of authors have experienced considerable difficulty in attempts to balance the two-dimensional momentum equations for flows in pressure gradients. Coles (1969) found that a balance is rare for flows developing in an adverse pressure gradient and attributed this to three-dimensional effects. For example, Clauser observed lateral movement within boundary layers subjected to an adverse pressure gradient. A number of authors have also experienced difficulties in obtaining two dimensional flow on concave surfaces. As already discussed in Section 1.2.1.2, several authors (e.g. So and Mellor 1975, Barlow and Johnston 1988) have reported large spanwise variations in boundary layers on concave surfaces. Meroney and Bradshaw (1975) observed repeatable stationary patterns and attributed these to longitudinal vortices. However, Barlow and Johnston (1988) suggest that if the flow is relatively free of upstream disturbances the concave curvature leads to the formation of large scale structures which wander with no fixed spatial location and would be difficult to identify from time averaged measurements. It is therefore thought that in this investigation, with both varying pressure gradients and streamline curvature effects, that some imbalance of the momentum equation is to be expected. However, whilst the balance at each station has been achieved using the calculated profile of radial velocity rather than using the measured radial profile, the pressure and turbulent shear stress terms presented in the following analysis remain unaffected.

4.1.4.2 Streamwise Pressure and Shear Forces.

It is thought that a discussion of the respective significance of the streamwise pressure ($1/\rho h\ \partial p/\partial s$) and shear forces ($1/r\ \partial(\overline{u'v'}r)/\partial n$) is best concentrated towards the flow within the inner casing boundary layer although data is presented for both boundary layers. As already shown, it is in the region of the inner casing, towards the rear of the duct, where the flow is most likely to separate. It should however be noted that data is limited close to each casing, where the primary shear stress ($\overline{u'v'}$) might be expected to be high. Furthermore, since no data has been obtained within the near wall regions, the data presented represents the shear force due to the turbulent and not the viscous stresses. At the wall, of course, the streamwise pressure gradient ($\partial p/\partial s$) should balance the total shear stress gradient ($\partial\tau/\partial n$). However, since it is thought difficult to calculate the shear stress gradient at the wall accurately in a flow subjected to both variable streamwise pressure gradients and curvature, the wall values are not presented.

At inlet (x/L=0.0) to the S-shaped duct (Fig. 4.1.15), a strong favourable

pressure gradient exists throughout the inner casing boundary layer, while in contrast a relatively weak adverse pressure gradient exists throughout the outer casing boundary layer. It should also be noted how the streamwise gradients of static pressure ($1/\rho h\ \partial p/\partial s$) vary significantly across the height of each boundary layer, with the maximum values occurring at each casing. Such complex distributions of the streamwise pressure gradient ($1/\rho h\ \partial p/\partial s$) are evident at all of the downstream traverse stations, with positive and negative values indicating that the streamwise pressure gradient is acting to decelerate and accelerate the flow respectively. Thus, along the inner casing, the streamwise pressure gradient can be seen to be negative (favourable) at x/L=0.0 prior to the long region of positive (adverse) pressure gradient between x/L=0.25 and x/L=0.75. At x/L=0.875 the streamwise pressure gradient reverts to negative (favourable) as the flow is returned to the axial direction in the second bend.

The effects of both the streamwise pressure gradient and streamline curvature on the development of the shear stress distribution (Fig.4.1.8) have already been discussed in Section 4.1.3. Similar effects can also be seen in the distribution of the primary shear force ($1/r\ \partial(\overline{u'v'}r)/\partial n$). At inlet to the S-shaped duct (x/L=0.0) it can be seen that the primary shear force is negligible towards the inner casing, where the streamwise pressure gradient is acting to accelerate the flow. However, at x/L=0.125, the primary shear stress is more discernable as the wall shear stress increases in response to the favourable pressure gradient. The flow is subjected to a strong adverse pressure gradient, between x/L=0.25 and x/L=0.75, with the primary shear stress gradient exhibiting similar effects to those already observed in the Reynolds shear stress distributions (Fig.4.1.8). For example, at x/L=0.625, the positive and negative values of the primary shear stress gradient in the outer and inner regions of the boundary layer indicate that the peak value of shear stress has moved away from the wall and exists at the zero crossing point. Analogous to the streamwise pressure gradient ($1/\rho h\ \partial p/\partial s$), the negative values of the primary shear force act to accelerate the flow in this region. Furthermore, it can be seen that at the critical point (x/L=0.75) where the flow is most likely to separate the negative values of the primary shear force are of a similar magnitude to the positive values of the streamwise pressure force acting to decelerate the flow. Thus, while the streamwise pressure force might be considered to dominate much of the flow, in this critical region the primary shear force is significant and acts to prevent separation. While this may be relatively unimportant in this particular case, this may be more important in less well behaved flows where

separation is more imminent.

It is important to note that whilst such an analysis of the s-component momentum equation has proved difficult, with some parts of the analysis having been compromised, the objective of identifying the relative importance of pressure gradient and streamline curvature effects has been achieved. It has been shown that while the streamwise pressure forces are dominant in much of the duct, the primary shear force is comparable in the most critical region of the duct. These results also provide a datum against which, for example, the pressure and shear forces that exist for a duct with swirling flow can be compared.

4.1.5 Stagnation Pressure Loss

The streamwise momentum equation for incompressible two-dimensional axisymmetric flow (Eqn.4.1.5) can be further used to assess the change in stagnation pressure along streamlines within the S-shaped duct. For example, for flow along a streamline (i.e. V=0, v'≠0), the s-component momentum equation reduces to;

$$\frac{1}{h}\frac{\partial \overline{U}^2}{\partial s} + \frac{\overline{U}^2}{rh}\frac{\partial r}{\partial s} = -\frac{1}{\rho h}\frac{\partial \bar{p}}{\partial s} - \left(\frac{1}{r}\frac{\partial \overline{u'}^2}{\partial s} + \frac{\overline{u'}^2}{rh}\frac{\partial r}{\partial s} + \frac{\partial}{\partial n}(\overline{u'v'}) + \frac{\overline{u'v'}}{r}\frac{\partial r}{\partial n} + \frac{2\overline{u'v'}}{Rh}\right) \quad \text{(Eqn.4.1.9)}$$

while the continuity equation (Eqn.4.1.4) reduces to;

$$\frac{1}{h}\frac{\partial U}{\partial s} + \frac{U}{rh}\frac{\partial r}{\partial s} = 0 \quad \text{(Eqn.4.1.10)}$$

Multiplying Eqn.4.1.10 through by U and time averaging produces;

$$\frac{1}{2h}\frac{\partial \overline{U}^2}{\partial s} + \frac{\overline{U}^2}{rh}\frac{\partial r}{\partial s} + \frac{1}{2h}\frac{\partial \overline{u'}^2}{\partial s} + \frac{\overline{u'}^2}{rh}\frac{\partial r}{\partial s} = 0 \quad \text{(Eqn.4.1.11)}$$

and substituting Eqn.4.1.11 into Eqn.4.1.9 leads to;

$$\frac{1}{2h}\frac{\partial \overline{U}^2}{\partial s} + \frac{1}{2h}\frac{\partial \overline{u'}^2}{\partial s} = -\frac{1}{\rho h}\frac{\partial \bar{p}}{\partial s} - \frac{\partial}{\partial n}(\overline{u'v'}) - \frac{\overline{u'v'}}{r}\frac{\partial r}{\partial n} - \frac{2\overline{u'v'}}{Rh} \quad \text{(Eqn.4.1.12)}$$

If stagnation pressure is now defined in terms of;

$$\frac{\partial P}{\partial s} = \frac{\partial}{\partial s}\left(p + \frac{1}{2}\rho\left(\overline{U}^2 + \overline{u'}^2\right)\right) \qquad \text{(Eqn.4.1.13)}$$

then, Eqn.4.1.12 can be written as;

$$\frac{\partial P}{\partial s} = -\frac{1}{h}\frac{\partial}{\partial n}(\rho\overline{u'v'}) - \frac{\rho\overline{u'v'}}{rh}\frac{\partial r}{\partial n} - \frac{2\rho\overline{u'v'}}{R} \qquad \text{(Eqn.4.1.14)}$$

Neglecting the first order terms, since in general $\partial(\rho\overline{u'v'})/\partial n >> \rho\overline{u'v'}$, and defining the total shear stress $\tau = -\rho\overline{u'v'}$, gives;

$$\frac{\partial P}{\partial s} = \frac{1}{h}\frac{\partial \tau}{\partial n} \qquad \text{(Eqn.4.1.15)}$$

Thus, the change in stagnation pressure along streamlines between the inlet and exit planes (where $h \approx 1$) can be described by;

$$\frac{\partial P}{\partial s} = \frac{\partial \tau}{\partial n} \qquad \text{(Eqn.4.1.16)}$$

with this definition being in agreement with Gillis and Johnston's (1983) definition for two-dimensional flow.

The significant effect of streamwise curvature and pressure gradients on the shear stress distribution (τ) within the S-shaped duct has already been discussed (Section 4.1.3). Thus, whilst the avoidance of flow separation from the casings of the S-shaped duct is of immediate concern to the gas turbine engineer, of secondary concern is the level of stagnation pressure loss that may be generated within the duct due to these effects.

The radial distribution of loss and its development within the duct can be described by monitoring the change in stagnation pressure along streamlines. At every plane the mass flow is therefore divided into 1% increments across the duct, with the stagnation pressures at these locations being determined by interpolation of the

measured data as discussed in Chapter 3. At several planes the loss distributions across the duct are presented (Fig.4.1.16), based on the pressure loss along each streamline, with the integrated area under each curve representing the overall stagnation pressure loss incurred by the flow up to that plane. As indicated by Eqn.4.16, these changes in stagnation pressure are a result of the shear stress gradients that exist within the duct, which can be integrated along each streamline to give the stagnation pressure loss. Note how in certain regions of the duct, stagnation pressure can increase along a streamline and that the loss associated with each boundary layer is different in both magnitude and distribution. For example, along the inner wall the loss is mostly associated with the adverse pressure gradient applied over a significant length of the duct, with this high loss region moving away from the casing as the flow proceeds towards duct exit. Alternatively for the outer casing the majority of the loss is located in the outer regions of the boundary layer and is thought mainly due to the initial concave curvature. This enhances turbulence levels with the production of turbulent energy resulting in a stagnation pressure loss, with these enhanced turbulence levels only gradually being suppressed by the convex curvature in the latter half of the duct. For the central core region the stagnation pressure loss should be zero with the minor variations observed being within experimental error of this value.

Within the working section of the test facility the loss coefficient (λ) is 0.04. This being based on the mass weighted stagnation pressure loss between x/L=-0.55 and x/L=1.40 relative to the mean dynamic head at the upstream plane ($\frac{1}{2}\rho U_{mean}^2$). Based on the conditions between duct inlet (x/L=0.0) and exit (x/L=1.0) the loss coefficient (λ) is approximately 0.02. This value represents approximately half of the stagnation pressure loss incurred between x/L=-0.55 and x/L=1.40, the duct length between these planes being almost double that between x/L=0.0 and x/L=1.0. However, the relative magnitude of the S-shaped duct loss can be more easily assessed by evaluating the loss incurred by the flow between rig inlet and the traverse plane being considered. This is non-dimensionalised by the dynamic head ($\frac{1}{2}\rho U^2$), and is presented relative to axial location (x/L) within the facility (Fig.4.1.17). Note the experimental scatter due to the relatively small changes in pressure that are taking place and the finite resolution to which the pressures can be measured. It can be seen that stagnation pressure loss within the inlet section results in a loss coefficient of 0.09 at x/L = -0.55 which rises to 0.13 at x/L = 1.40. Within the parallel sided inlet section, the rate of loss increase will initially be high and decrease towards the end of this section. However, a prediction of the

flows development within the inlet section, using a Reynolds stress model, indicates that the loss increase does not differ significantly from that of a linear distribution (Bailey et. al. 1995). Consequently, it can be seen that the rate of loss increase through the S-shaped duct does not appear to be significantly different from that of the inlet section. Thus despite strong curvature and pressure gradient effects the stagnation pressure loss within the duct appears to be comparable with that which would be obtained within a parallel sided duct. This is, of course, for a duct in which the flow is well behaved and flow separation is avoided. However, as already noted the radial distribution of loss (Fig.4.1.16) produced within the duct is very different to that which would be generated by a parallel sided duct.

The relatively small duct pressure loss is difficult to establish experimentally, whilst significant variations of shear stress within the duct have already been described. It is therefore desirable to validate the shear stress and pressure measurements to ensure both sets of data are consistent with each other. Based on Eqn.4.15 the derivatives $\partial(\overline{u'v'})/\partial n$ and $\partial P/\partial s$ from both sets of measurements were compared and found to be in good agreement, as shown for example at x/L=0.50 (Fig.4.1.18). Furthermore, based on the shear stress gradients and using Eqn.4.16, an estimated value of the duct stagnation pressure loss (λ) of 0.055 was obtained between x/L = -0.55 and 1.4. Allowing for the inherent inaccuracies associated with the differentiation of experimental data this is thought to be in excellent agreement with the value of 0.04 obtained directly from the pressure measurements.

4.2 Compressor Generated Inlet Condition

The flow entering an annular S-shaped duct within a gas turbine engine contains large scale flow features such as blade wakes and the remnants of rotor tip vortices. As already discussed, in Chapter 1, a number of investigations have shown how the performance of annular diffusers are influenced by the structure of the flow delivered by an upstream compressor. In this investigation, representative flow structures have been generated using a single stage compressor, comprising a rotor and an outlet guide vane (OGV) row. It is thought that such a configuration gives a good compromise between providing representative inlet conditions whilst avoiding the expense and complexity of using a multistage compressor. The aim of this section is therefore to assess the response of this more complex mean and turbulent velocity field to the pressure gradients and curvature effects within the duct, with the more detailed objectives being identified as;

- to investigate the effect of both OGV blade wakes and rotor tip leakage on the casing boundary layers.

- To assess the size of the OGV blade wakes and to identify any influences on the rate at which the wakes mix out.

- To assess the effect of representative inlet conditions on the stagnation pressure loss within the duct, both in terms of its magnitude and distribution.

The results presented in this section have been mostly acquired from measurements using a 3D Laser Doppler Anemometry system, with data being obtained at the inlet plane (x/L=0.0) and at 3 other stations (x/L=0.375, 0.75 and 1.40) along the duct. The LDA traverse stations have been installed at various circumferential locations around the test facility in order to accommodate the relatively bulky traverse mechanism whilst also distributing the associated stresses around the duct casing. Hence, it should be noted that any observed circumferential movement of the wake reflects merely an error in traverse alignment. In addition, the presented data are based on a simple time average with no attempt being made to phase lock the measurements to the passing of the upstream rotor blades. Hence, turbulence quantities such as the Reynolds stresses include not only fluctuations of the flow about the mean stress field but also additional 'pseudo' stresses due to the passing of rotor wakes through the measurement volume whilst data was being acquired. Furthermore, the

well defined "clean" inlet conditions (Section 4.1), and the subsequent flow field that develops, have been used to provide some basis for comparison when results are obtained for the more complex compressor generated inlet condition.

4.2.1 Inlet Condition

Measurements have been obtained at a traverse plane 0.3 chord lengths downstream of the OGV trailing edge (x/L=0.0), thus defining the inlet conditions to the S-shaped duct with the upstream single stage rotor and OGV row present. These measurements provide information on both the mean velocities and the turbulent flow field. Although only examples pertinent to the text are referred to, the intention is to make the data available in electronic format, as it is thought this data may be suited to CFD validation exercises.

Streamwise velocity contours (Fig.4.2.1) indicate the circumferential and radial distribution of fluid at inlet to the S-shaped duct (x/L=0.0). In addition to boundary layers on each casing, well defined blade wakes are present from the upstream compressor outlet guide vanes. The mass flow at this plane was found to be within 1.5% of that recorded upstream of the single stage compressor. The spatial average streamwise velocity (U_{Mean}) for the annular passage was 38.06 m/s. This value was used as a reference value for normalising the mean velocity, while the Reynolds stresses at this and subsequent traverse planes have been normalised by U_{Mean}^2. The distributions of streamwise (Fig.4.2.2), radial (Fig.4.2.3) and circumferential (Fig.4.2.4) turbulence intensity ($\sqrt{\overline{u'_i}^2}/U_{Mean}$) indicate that a core region exists of nearly isotropic turbulence with a level of approximately 5% as compared to 1% for the "clean" inlet condition. Higher levels of turbulence intensity can be seen in the OGV wake, with a prominent region being evident on the suction side of the blade, near the outer casing, where turbulence intensities exceed 30%. Furthermore, the distribution of turbulent kinetic energy (Fig.4.2.5) also indicates the presence of a large amount of turbulent energy close to the outer casing. This complex turbulence distribution is thought to be associated with rotor tip leakage effects, with similar results having been seen by Prato et. al. (1995). Furthermore, the primary shear stress ($\overline{u'v'}$) also shows how the rotor tip leakage dominates this distribution (Fig.4.2.6), with very high values being recorded at the outer casing.

In generating more representative inlet conditions, a more complex mean and turbulent velocity field has therefore been produced in comparison to the "clean" inlet

conditions discussed in Section 4.1. For these more complex inlet conditions the development of the mean velocity profile in response to the pressure gradients and curvature effects within the S-shaped duct has therefore been investigated.

4.2.2 Mean Static Pressure and Velocity Distributions

The axial variation of static pressure along each casing wall is presented (Fig.4.2.7) in terms of a coefficient (C_p) defined using the mass weighted stagnation and static pressures at inlet to the duct (x/L=0.0). As shown earlier (Section 4.1.2), differences in static pressure across the duct reflect how the pressure field adjusts to provide the required radial forces to turn the flow. As a result of these changes in the radial pressure gradient, significant streamwise pressure gradients occur. Comparison with the results obtained for the datum test case indicates similar distributions, although slight differences can be observed. These are thought to be associated with effects such as the mixing out of blade wakes and the change in kinetic energy flux at inlet to the duct. The energy parameter (α) describes the additional kinetic energy the flow contains due to radial and circumferential non-uniformity compared to a flow with a flat profile. Thus, mixing out of OGV blade wakes in the early part of the duct (with a corresponding reduction in α) may account for the generally higher static pressure levels observed within the first bend.

The radial variation of the streamwise velocity has been obtained by averaging circumferentially over one OGV blade spacing. This method has been used in order to extract information from the highly complex flow field, although clearly, some of the flow features associated with circumferential variations of the flow field will be concealed. However, this method does form a starting point for the analysis and facilitates a direct comparison of the data with the results of the datum test case obtained using the "clean" inlet conditions.

The circumferentially averaged streamwise velocity profiles (Fig.4.2.8) are of a similar nature to those obtained in the datum test case. At inlet to the S-shaped duct (x/L=0.0) the mean velocity data indicates that along the inner and outer casing turbulent boundary layers have developed, each occupying approximately 25% and 23% of the passage height respectively. For an annulus height of 71.1mm this gave respective boundary layer thicknesses (δ) of approximately 17.6mm and 16.2mm. These boundary layers are isolated by what appears to be a potential core region, the presence of which can be seen along the entire length of the duct. It should however be

noted that within this region circumferential variations of the flow field do occur which are associated with the OGV wakes. It can be seen that the flow remains attached along both walls with the velocity profiles indicating similar responses to the duct curvature as those seen in the datum case. However, some differences are apparent. For example, along the inner wall, at x/L=0.75, comparison with the datum case reveals higher velocities close to the casing (< 5% annulus height) but lower velocities in the outer regions of the boundary layer. In addition, the flow along the outer casing exhibits much fuller velocity profiles with high velocities present throughout the boundary layer.

The boundary layer integral parameters (δ^*,θ,H) have been calculated, using the method outlined in Chapter 3, from the circumferentially averaged properties at each of the traverse stations (Table 4.2). The displacement thickness (δ^*), which is a measure of the mass flow deficit of each boundary layer, has been calculated from the area weighted circumferentially averaged streamwise velocity profile. Also calculated has been the momentum thickness (θ) of the circumferentially averaged profile. It is acknowledged that, since the momentum thickness (θ) is a measure of the boundary layers deficit in momentum, this value based on the circumferentially averaged profile will differ from that of an average based on the momentum calculated at each circumferential location. However, a study of this effect revealed only minor variations and the data presented in this investigation is therefore based on the circumferentially averaged profile.

The significant variation of each boundary layer's shape parameter ($H=\delta^*/\theta$) along the duct (Fig.4.2.9) indicates that, as in the datum case, it is the flow adjacent to the inner casing that is most likely to separate. The shape parameter attains a maximum value of 1.47 at x/L=0.75, although it should be noted that these results have been obtained for circumferentially averaged profiles and local deviations can be expected. At x/L=0.75, where the averaged shape parameter has a maximum of 1.47, the circumferential variation of shape parameter (Fig.4.2.10) indicates local values in the range of 1.3 to 1.55. However, compared with the maximum value of 1.66 obtained at x/L=0.75 for the "clean" inlet condition, this indicates that the tendency of the flow to separate is reduced for the compressor generated inlet conditions. Furthermore, this implies that the streamwise pressure gradients could be increased, for example by reducing the duct length for the same change in mean radius, without necessarily incurring flow separation. Along the outer casing a slight reduction in shape parameter

is also observed, compared with the datum case, consistent with the much fuller velocity profile noted earlier. As will subsequently be discussed, this is thought to be due to the enhanced turbulence levels associated with rotor tip leakage effects.

4.2.3 Turbulent Flow Field

The radial variation of the primary shear stress distribution ($\overline{u'v'}$) has been obtained by averaging circumferentially over one blade spacing (Fig.4.2.11). The extent of the circumferential variation is indicated, for example, at x/L=0.0 (Fig.4.2.6). As also noted for the mean velocity distribution this is a somewhat simplistic approach, but it does give an approximate indication of the magnitude and distribution of the stresses present. This averaging of the data forms the starting point of the analysis and enables tentative comparisons to be made with the datum test case obtained using naturally developed inlet conditions. In most regions of the duct the shear stress ($\overline{u'v'}$) distributions are broadly similar to those measured for the "clean" inlet condition (Fig.4.2.11). For example, a region of low shear stress exists all along the duct, in the central passage region, whilst the distributions are also comparable at most locations within each boundary layer. This indicates how despite the different inlet conditions, with non-axisymmetric boundary layers etc., the overall flow field is exhibiting similar responses to the applied pressure gradients and curvature effects within the duct. However, these profiles also indicate regions where significant differences are apparent relative to the datum test case. Enhanced levels of shear stress exist in the outer casing boundary layer corresponding to the region in which rotor tip clearance effects exist. However, these enhanced shear stresses in the outer casing boundary layer mix out rapidly and, by x/L=0.375, the profiles are broadly similar. As the flow develops further downstream, the circumferentially averaged shear stress profiles at subsequent traverse locations (x/L=0.75, x/L=1.4) are comparable. The radial variation of the $\overline{v'w'}$ (Fig.4.2.12) and $\overline{u'w'}$ (Fig.4.2.13) Reynolds shear stress exhibit similar effects at inlet to the S-shaped duct. Once again, rapid mixing takes place as the flow moves downstream to x/L=0.375, with corresponding reductions in both of the additional shear stress components. However, there is still some evidence of rotor tip leakage effects in the $\overline{v'w'}$ and $\overline{u'w'}$ components of Reynolds shear stress at x/L=0.75 and x/L=1.4 when compared with the approximately zero values obtained for the "clean" condition.

Having considered the various influences on flow development through an analysis of the circumferentially averaged flow features, strong evidence has been

found to explain the much fuller velocity profiles present along the outer casing. However, it is still not immediately clear as to why there is an improvement of the shape parameter in the more critical inner casing boundary layer. It is thought that while circumferential averaging has provided a means for examining the "global" flow features a more detailed analysis of the development of the OGV wakes through the S-shaped duct is also required.

4.2.4 OGV Wake Development

An investigation into the development of the OGV wake is important for providing information for the prediction of both the losses and the possible impact on the downstream blade rows. The mixing and dissipation of the OGV wake produces a loss of energy, while the velocity defect in the wake is an important consideration for the design of subsequent blade rows. It is thought that mixing out of the OGV wake, in this investigation, is likely to be influenced by both the streamwise pressure gradients that occur within the S-shaped duct and the effects of streamline curvature on the turbulent structure.

The inlet conditions to the S-shaped duct are defined over a single OGV blade space at a traverse station 0.3 blade chords downstream of the OGV trailing edge. As already shown, the streamwise velocity contours (Fig.4.2.1) indicate the presence of a wake formed from the merging together of the OGV surface boundary layers, subdividing the core region of high velocity flow which persists well into the four corners of the blade passage. Further distinctions can be made between the exit flow from the suction and pressure surfaces. If we consider the wake to be bisected between the flow associated between the pressure and suction sides of the blade, then the wake from the suction side of the passage possesses a nearly constant width in the region from 15% to 75% passage height, which thickens towards the end wall regions. This wake thickening is thought to be due to secondary flows which cause the casing boundary layers to accumulate on the suction surface of the blade as observed by Stevens and Young (1987). This view is supported by the way in which the casing boundary layers tend to be thinner on the pressure side of the blade passage. Further evidence of these effects can be seen in the circumferential distributions of streamwise velocity (Fig.4.2.14), presented at 10%, 50% and 90% passage heights, which indicate an appreciably thicker wake in the outer casing region of the suction surface boundary layer. It can therefore be seen that the OGV wake differs across the height of the duct due to the upstream conditions in which the flow has developed.

Wake in Mid-Passage Mixing out of the compressor OGV wake in the mid passage region, where pressure gradients are relatively small, is indicated by the wake velocity profiles (Fig.4.2.15). It can be seen that the majority of the wake mixing has occurred before x/L=0.375 which is within 1.9 OGV axial chord lengths. A further way in which the mean streamwise velocity component (U) of the wake can be described is by means of normalised wake distributions. Several authors (Raj and Lakshminarayana 1976, Lakshminarayana and Davino 1980, Stevens and Young 1987) have shown that similarity exists for blade wake profiles where the velocity defect across the wake (U) is normalised by the maximum defect in the wake (U_c). Circumferential normalisation is carried out based upon the suction (L_{ss}) and pressure surface (L_{ps}) semi-wake widths which are defined as the distance between the wake centre line and the location of half the maximum defect (Fig.4.2.16).

At inlet to the duct (x/L=0.0) the normalised wake distribution (Fig.4.2.17), at mid annulus height, is in excellent agreement with a Gaussian distribution defined as;

$$\frac{U}{U_c} = exp\,(-0.693\eta^2) \qquad \text{(Eqn.4.2.1)}$$

The wake profile (Fig.4.2.15) at this plane, some 0.3 blade chords downstream of the OGV trailing edge, is clearly defined and the semi-wake widths can be calculated accurately. However, at the subsequent downstream planes, the OGV wake has undergone significant levels of mixing. The wake profile is therefore less clearly defined (Fig.4.2.15) which makes accurate calculation of the semi-wake width difficult. This is thought to indicate why the level of agreement, even within a semi-wake width, generally decreases as the wake progresses downstream.

Although it is acknowledged the calculation of the OGV semi-wake width is questionable at some of the planes downstream of the duct inlet, the axial variation of the wake width is included for completeness. The axial variation of the OGV wake width is presented (Fig.4.2.18) in terms of a characteristic width (L) defined by Lakshminarayana and Davino (1980) as;

$$L = \frac{2 \times (L_{ss} + L_{ps})}{s} \qquad \text{(Eqn.4.2.2)}$$

where (s) is taken to be the blade pitch. The axial variation of the characteristic wake width (L) has been obtained at 40%, 50% and 60% annulus heights (Fig.4.2.18). Hence, the analysis is restricted to regions where some level of similarity of the normalised wake distributions has been obtained. Whilst it is difficult to draw firm conclusions, a clear trend is exhibited by the data. At inlet to the duct (x/L=0.0, x/c=0.3), the values of the characteristic wake width at these heights are similar and comparable with those obtained by Raj and Lakshminarayana (1976) in tests on a cascade, and with Lakshminarayana and Davino's (1980) data obtained for both stator and IGV wakes. The characteristic wake width (L) at all three heights then increases with axial distance as the wake mixes out downstream. However, the rate at which the wake width increases, which indicates the rate of decay of the OGV wake, can be seen to differ at each of the heights. For example, at x/c=2.175 (corresponding to x/L=0.375), the wake width varies from 0.51 to 0.55 at 40% and 60% annulus height respectively, thus indicating a significantly larger rate of wake mixing at 60% annulus height. It should be noted though that the rate of wake mixing is expected to vary with passage height even in the core region. For example, streamwise pressure gradients vary with radial location as does the influence of rotor tip leakage effects and streamline curvature. Furthermore, the streamwise pressure gradients vary along the length of the duct and, depending on axial location, at a given passage height may be either favourable or adverse. As already discussed though, it is difficult to accurately determine the semi-wake widths at locations downstream of the duct inlet (x/L=0.0) where the wake profiles are less clearly defined. Thus, while the axial variation of the characteristic wake width (L) is included for completeness, it is difficult to draw any firm conclusions on the factors that effect mixing of the OGV wake.

Whilst the difficulties in determining the characteristic wake width (L) from the experimental data have been acknowledged, it is thought the velocity defect in the wake can be calculated relatively accurately. The axial variation of the velocity defect behind the OGV, at mid annulus height, is presented (Fig.4.2.19) in terms of the streamwise velocity defect normalised by the edge velocity;

$$\Lambda = \frac{U_{edge} - U_c}{U_{edge}} \qquad \text{(Eqn.4.2.3)}$$

The axial variation of the OGV velocity defect has, again, been obtained at 40%, 50%

and 60% annulus heights (Fig.4.2.19). As already noted the wake at these heights is subjected to contrasting streamwise pressure gradients. However, the effect of these contrasting streamwise pressure gradients on the velocity defect appears small, with little variation in the calculated velocity defects at each height. In addition, for the limited data available, there is favourable agreement with the measurements of Lakshminarayana and Davino (1980) for both IGV and stator blades. The velocity defect decays rapidly between x/c=0.0 and x/c=0.4, while after this region the decay rate is significantly slower. Lakshminarayana and Davino (1980) suggest that for x/c>0.4 the decay rate of the velocity defect is very slow, with the results in this investigation extending the published data and indicating that an asymptotic value is approached at larger distances (x/c>7) from the OGV trailing edge.

It is generally felt that while discrepancies have been acknowledged, a significant degree of similarity is exhibited by the blade wake profiles, which simplifies the problem of predicting and validating the wakes development.

Wake in Casing Boundary Layers The streamwise velocity (U) contours at x/L=0.375 (Fig.4.2.20) and x/L=0.75 (Fig.4.2.21), indicate the expected recovery of the OGV wake and boundary layer in the regions close to the outer casing. This is supported by the circumferential distributions of streamwise velocity, presented at 90% annulus height (Fig.4.2.22), which show how much of the wakes velocity defect has mixed out by x/L=0.375. Furthermore, the flow outside of the influence of the OGV blade wake exhibits an increase in velocity. It should however be noted that wake mixing in the region up to x/L=0.375 must be largely assisted by the rotor tip leakage effects discussed earlier. As the flow moves downstream to x/L=0.75, further mixing out of the wake is assisted by the favourable pressure gradient, which also contributes to further boundary layer recovery along the outer casing. In contrast, the circumferential distribution of streamwise velocity at 10% annulus height (Fig.4.2.23), indicates the effect of the adverse streamwise pressure gradients. Significant mixing out of the well defined OGV wake profile, which exists at inlet to the S-shaped duct, occurs by x/L=0.375. In addition, an appreciable reduction in streamwise velocity in the regions between OGV blades is indicative of thickening of the inner casing boundary layer due to the adverse pressure gradient. However, it has already been shown (Section 4.2.2) that compared with the datum "clean" case there is a beneficial reduction in shape parameter along the inner wall, with this effect having been previously noted by Britchford (1993). It is therefore desirable to gain an

understanding of the mechanism by which this improvement has been brought about. Britchford (1993) indicated that slower moving wake fluid may move radially inward in the first bend due to the applied radial pressure gradient. Furthermore, Britchford recognised that if this fluid is of higher energy than the boundary layer fluid, then this fluid can help to re-energise the inner casing boundary layer. However, Britchford could only draw tentative conclusions due to the lack of turbulent flow field information, with evidence provided by pressure probe data close to the OGV trailing edge.

With Britchford's tentative conclusions in mind, the flow vectors at inlet to the S-shaped duct (Fig.4.2.24) show similar evidence, with fluid within the wake being seen to move radially towards the inner casing. However, although some radial movement is indicated by the flow vectors (Fig.4.2.24), the flow has not had sufficient time to react to the pressure gradient. Further downstream, at x/L=0.375 and x/L=0.75, the flow vectors (Fig.4.2.25 and Fig.4.2.26) indicate the flow in the outer casing boundary layer is still dominated by rotor tip leakage effects. However, at these downstream locations it is difficult to identify movement of the fluid relative to the bulk motion. The radial movement of the wake fluid can be more easily illustrated by considering the flows streamwise vorticity. In this investigation, streamwise vorticity (Ω_s) has been calculated from the experimental data, using Rosenheads (1963) definition of;

$$\Omega_s = \frac{1}{r}\left[\frac{\partial}{\partial n}(Wr) + \frac{\partial V}{\partial \phi}\right] \qquad \text{(Eqn.4.2.4)}$$

The contours of streamwise vorticity (Ω_s) at inlet to the duct (x/L=0.0) clearly indicate regions of high vorticity towards the outer casing where rotor tip leakage effects have already been observed (Fig.4.2.27). Furthermore, there is some indication of regions of relatively high vorticity within the inner casing boundary layer where secondary flow vortices might be expected to exist. However, the streamwise vorticity contours also appear to indicate features which are associated with a radial movement of fluid within the OGV wake. This radial movement of fluid within the wake is also evident further downstream, at x/L=0.375, where the streamwise vorticity contours (Fig.4.2.28) indicate the transport of fluid in regions within the inner casing boundary layer. Now, it has already been shown (for the "clean" case) how the radial movement

of fluid is generated by the radial pressure gradients that are established within the duct. With no swirl present, the fluid is subjected to a centripetal acceleration (U^2/Rh) which is associated with the radial pressure gradient ($1/\rho\partial p/\partial n$). These radial pressure gradients within the duct though are established to turn the "mainstream" flow, giving;

$$\frac{\partial p}{\partial n} \approx \frac{\rho U^2}{Rh} \qquad \text{(Eqn.4.2.5)}$$

It is therefore thought that in the region of the wake, where the streamwise velocity and hence the centripetal acceleration is much lower, there is an imbalance and the flow is not in radial equilibrium. This imbalance has been calculated and is an order of magnitude greater than any forces generated by the turbulent flow field (e.g. due to the shear stress gradients). It is therefore thought that this data, which includes turbulence information, provides confirmation of this mechanism which generates the radial movement of fluid within the duct. As already noted this fluid has a total pressure deficit, but it is less than the deficit resident in the inner wall boundary layer. Thus, the radial movement of fluid with the OGV wakes acts to re-energise significant regions of the inner casing boundary layer. This accounts for the observed reduction in shape parameter, compared with that of the datum case, in the more critical region of the inner casing boundary layer where the flow may otherwise be most likely to separate.

4.2.5 Stagnation Pressure Loss

As noted earlier (Section 4.1.5), of secondary consideration to the gas turbine engineer, after the avoidance of flow separation, is the stagnation pressure loss occurring within the duct. For the case with compressor generated inlet conditions, overall performance can only be assessed between x/L=0.0 (0.3 chord lengths downstream of the OGV trailing edge) and the downstream traverse planes. Thus, for comparison purposes, the clean inlet performance is also defined from data obtained at these same locations. It should however be noted that pressure gradient and streamline curvature effects are present upstream of duct inlet (x/L=0.0).

The overall mass weighted stagnation pressure loss (λ) with a complete compressor stage at inlet is approximately 0.035 between x/L=0.0 and 1.0 which compares with 0.020 for the clean inlet condition. However, this pressure loss is still relatively small and can only be defined to within ±0.0075 of its true value. Most of the

additional loss though is thought to be attributable to mixing of the OGV wakes within the duct. As described by Denton (1994), this loss can normally be estimated by assuming mixing occurs at constant momentum in a parallel sided duct. Although not strictly true here, this approach has been applied to the wake profiles observed at duct inlet and, in particular, to the wakes in the central passage region which have not been distorted by any boundary layer influences. This yielded a mixing loss value of 0.015 which is the correct order of magnitude to account for the observed increase in loss. It should also be noted that mixing will occur rapidly downstream of the blade row, and so the actual mixing and overall duct loss depend on the axial location of the traverse plane with respect to the OGV trailing edge. It should therefore be noted that the loss values presented here are optimistic.

The radial distribution of pressure loss along streamlines for both the clean and compressor generated inlet conditions are presented (Fig.4.2.29). As discussed in Chapter 3, streamlines have been obtained by dividing the mass flow at the upstream (x/L=0.0) and downstream (x/L=1.0) planes into 1% increments across the duct. However, it should be noted that this is not strictly correct since some fluid will move radially although it is assumed that the magnitude of this effect is small relative to the overall flow field.

Note the finite loss now occurring in the centre of the duct due to wake mixing. However, the similar distributions of loss within each boundary indicate the same flow mechanisms are present and contributing to the generation of stagnation pressure loss. The only exception to this is in the outer regions of the inner wall boundary layer, where a relatively high loss is apparent. This develops as the boundary layer is subjected to the sustained adverse pressure gradient within the duct and is located at the wake-boundary layer intersection.

4.3 Strutted S-Shaped Duct

The annular S-shaped ducts within modern gas turbine engines commonly incorporate radial struts such as those, for example, within the Rolls Royce Trent engine (Fig.1.2) which carry loads and engine services. Such struts are necessarily sizeable and are likely to have a significant impact on the flow field that develops within the S-shaped duct. In addition, since the axial length of the duct must be minimised in order to reduce the weight penalties associated with engine length, the gas turbine engineer will also be concerned with any possible effect on the upstream and downstream compressor spools. The aim of this section of the investigation is therefore to provide information pertaining to the design of S-shaped ducts which incorporate radial struts, the more detailed objectives being identified as;

- To investigate the upstream influence of a radial strut.
- To assess the impact of a radial strut on the development of the casing boundary layers, especially in terms of the more critical inner casing boundary layer which is more prone to separation.
- To identify the effect of the significant streamwise pressure gradients that arise within the duct, due to flow curvature, on the static pressure distribution along the strut surface.
- To assess the size of the strut wake and to identify any influences on the rate at which the wake mixes out.
- To assess the impact of the strut wake on a downstream compressor spool in terms of the distortion that the strut wake represents.

For this part of the investigation measurements have been obtained, at several stations within the S-shaped duct, both for the two-dimensional axisymmetric ("Clean") inlet conditions (described in more detail in Section 4.1) and for inlet conditions generated by a single stage axial compressor. Measurements have been obtained using both five hole pressure probes and static pressure tappings located on the surface of the strut.

4.3.1. Flow Development Upstream of Strut

Axisymmetric Inlet Conditions At inlet to the working section (x/L=-0.55) the conditions are essentially the same as those reported in Section 4.1.1, with turbulent boundary layers along the inner and outer casings occupying approximately 22% and

23% of the passage height respectively (Fig.4.3.1). The streamwise velocity contours form an area traverse approximately 0.85 chord lengths upstream of the strut (Fig.4.3.2.a) and indicate excellent circumferential uniformity, while the flow vectors (Fig.4.3.2.b) show the density of the experimental data points recorded. These axisymmetric conditions indicate any upstream effect on the flow field due to the strut is not apparent at this location (x/L=-0.55). However at inlet to the S-shaped duct (x/L=0.0), which at 50% annulus height is approximately 0.16 strut chord lengths upstream of the strut, the effect due to the downstream strut blockage is clearly evident. The streamwise velocity contours (Fig.4.3.3.a) indicate that, compared with the surrounding flow, the casing boundary layers immediately upstream of the strut are of increased thickness with a smaller core region of high velocity flow. This result can be clarified by comparing the streamwise velocity profile directly upstream of the strut with that obtained outside of the struts influence (Fig.4.3.4). Such a comparison indicates that the inner and outer casing boundary layers are affected to different degrees. Most noticeably, the greatest reduction in flow momentum occurs within the inner casing boundary layer directly upstream of the strut. This is because of the variation in axial location of the strut leading edge (Fig.4.3.5), relative to the traverse station, with the strut leading edge close to the outer wall being relatively further downstream (0.19 chord lengths) than the leading edge close to the inner wall (0.13 chord lengths). The effect of the blockage presented by the strut is therefore more prevalent in the inner wall region at this location.

Although no measurements have been made between inlet to the S-shaped duct (x/L=0.0) and the strut leading edge (x/L=0.125), the upstream effects of the strut will continue to increase resulting in large circumferential variations of the flow field in this region.

Compressor Generated Inlet Conditions More engine representative inlet conditions were obtained by incorporating a single stage rotor and OGV row at inlet to the S-shaped duct, these inlet conditions having been described in more detail in section 4.2. At duct inlet (x/L=0.0), the mean streamwise velocity contours (Fig.4.3.6.a) indicate not only boundary layers on each casing, but also well defined blade wakes from the upstream OGV blade row. The flow vectors (Fig.4.3.6.b) indicate the magnitude and direction of the velocity component parallel to the traverse plane. It can be seen there is a bulk radial movement of fluid towards the inner casing as the flow reacts to the radial pressure gradient associated with duct curvature. In

terms of the circumferential component of velocity, the secondary flow seems to be the dominant feature. The circumferentially averaged swirl angle distribution (Fig.4.3.7) also indicates increased angles towards the hub and tip due to the remnants of secondary flows within the OGV passages. However it is also important to note that within the central passage region (10% to 70% annulus height) there is some 3 degrees underturning by the OGVs. The spatial average mean streamwise velocity for the annular passage was 37.03 m/s and this was used as a reference value for nondimensionalising the mean velocity data at subsequent traverse stations.

It has already been indicated, for the case with axisymmetric inlet conditions, that the upstream effect of the strut is apparent at duct inlet (x/L=0.0). It is therefore not surprising that this downstream blockage presented by the strut, located 0.16 chord lengths downstream of the traverse plane and directly between OGV blade wakes, is evident. The streamwise velocity contours (Fig.4.3.6.a) indicate that, compared with the adjacent OGV passages, the casing boundary layers in the passage immediately upstream of the strut are relatively thicker with a smaller core region of high velocity flow.

In order to assess the effect of the downstream blockage presented by the strut, measurements were performed with the strut removed, the area traversed corresponding to the same two OGV blade spaces. Comparison of the mean velocity distributions obtained from measurements with and without the strut (Figs. 4.3.6.a and 4.3.8.a), indicates that not only is the OGV passage immediately upstream of the strut affected by the presence of the strut, but also the adjacent passages. Within these passages, a larger core region of high velocity flow is present when the strut is in place, compared with the strut removed, indicating that these passages are accepting some of the mass flow displaced from the OGV passage directly in line with the strut. Based on these measurements it has been estimated that the mass flow through the OGV passage directly upstream of the strut is 11% less than that through the corresponding passage with the strut removed.

Of further concern to the gas turbine engineer is the diffusion factor (DF), which provides a convenient way of assessing the overall loading of the blades. Lieblein (1965) defined the diffusion factor as;

$$DF = 1 - \frac{V_2}{V_1} + \frac{\Delta V_\theta}{2\sigma V_1} \qquad \text{(Eqn.4.3.1)}$$

where V_1 and V_2 are the mean velocities into and out of the blade row, $\Delta V\theta$ is the change in swirl velocity in the blade row and (σ=c/s) is the solidity. Cumpsty (1989) indicates that values of DF in excess of 0.6 are thought to indicate blade stall and that a value of 0.45 might be taken as a typical design choice. With the strut removed, the diffusion factor of the OGV has been estimated to be 0.26, which indicates the relatively low loading of the blades in this investigation. However, for the OGV passage directly upstream of the strut, it is estimated the diffusion factor increases to 0.36. This is derived by considering the local increase in static pressure at OGV exit, directly in line with the strut, and assumes a uniform static pressure distribution at inlet to the blade row. While such a value is still well within the design criteria, it should be noted that this is for relatively lightly loaded blades. Thus, for blades designed with a more representative diffusion factor of 0.45, a comparable increase may have more serious implications. It also follows that for a highly loaded blade row separation will initially be associated with the blade passages in line with the struts. The axial location of the strut, relative to the upstream blade row, should therefore be an important design consideration.

4.3.2 Flow Development Around the Strut

Axisymmetric Inlet Conditions Although measurements with pressure probes were made along the strut surface between its leading and trailing edges, these results are not presented. This is because the probe size was large relative to the boundary layers that developed along the strut and hence there are reservations as to the accuracy of the results. However, the pressure distribution could be obtained from the static pressure tappings along the strut surface.

The axial static pressure distributions measured along the strut at 10%, 50% and 90% annulus heights are presented (Fig.4.3.9) in terms of a nondimensional pressure coefficient (C_p) referenced to the conditions at x/L=-0.55. The distributions along both sides of the strut are comparable, as expected for an essentially swirl free flow. Thus, for clarity, the data from only one side of the strut is considered further.

At 50% strut height (Fig.4.3.10) the pressure gradients along the strut are favourable up to the 45% chord location, downstream of which the static pressure increases. This is in reasonable agreement with the pressure distribution deduced from the data of Abbott and Von Doenhoff (1949) based on measurements of the NACA65T profile under "freestream" conditions. However, at 10% strut height (Fig.4.3.11) an

unfavourable pressure gradient is present over 80% of the strut chord, whereas towards the outer casing (90% strut height, Fig.4.3.12) the gradient is favourable over most of the strut length. Although variations will occur due to the changing profile across the strut height, the observed differences between the distributions are mainly due to the superposition of the S-shaped duct streamwise pressure gradients onto the strut surface. This is illustrated by subtracting the static pressure distribution within the duct, as already presented, from the distribution measured along the strut. At 10% (Fig.4.3.11) and 90% (Fig.4.3.12) strut height, the resulting distribution is a good approximation to that of the freestream distribution for the corresponding profile as outlined by Abbott and Von Doenhoff (1949). Hence, the static pressure distribution surrounding the strut is not only a function of the strut profile but also the pressure distribution of the duct in which it is located. Furthermore, this result indicates that rather than using a standard profile, the strut design could be modified to account for the pressure field within which it operates. In doing so, favourable pressure gradients (i.e. close to the outer casing) could be taken advantage of whilst off-loading regions in which the pressure gradient is mostly adverse (i.e. close to the inner casing). Such an integrated design approach would be of even greater benefit if cambered struts were to be incorporated within the duct in order to accommodate swirling flows.

Compressor Generated Inlet Conditions The axial pressure distributions measured along the strut at 10%, 50% and 90% annulus heights are presented (Fig.4.3.13) in terms of a nondimensional pressure coefficient (Cp) referenced to the conditions at x/L=0.0. Comparison of the pressure distributions with those obtained with naturally developed inlet conditions (Fig.4.3.14) shows that the two sets of data exhibit similar trends. It should also be noted that although the distributions either side of the strut are similar (Fig.4.3.13), it can be seen that there are differences in the magnitude of the calculated pressure coefficient. These differences can be attributed to the circumferentially averaged swirl angle distribution (Fig.4.3.15) presented at exit from the OGV (x/L=0.0), indicating that the flow is at nominally 3 degrees incidence to the strut leading edge over the majority of the passage height. This incidence onto the strut though will vary radially across the passage height due to the effect of the secondary flows within the OGV passage, with swirl angles of up to 6 and 8 degrees being seen in the hub and tip regions respectively (Fig.4.3.15). Also presented is the swirl angle distribution (Fig.4.3.15) at the strut trailing edge (x/L=0.875) obtained by averaging circumferentially over two OGV blade spaces. The circumferential pressure

gradient which is established across the strut, as already shown in the pressure distributions along the strut surface, therefore provides a tangential force which acts to straighten the flow. As a result the swirl angles are therefore significantly reduced by x/L=0.875, with swirl angles of less than one degree over 80% of the annulus height.

4.3.3 Flow Development Downstream of Strut

Axisymmetric Inlet Conditions An investigation into the development of the strut wake is important for providing information on the prediction of both the losses and the optimum spacing between the strut trailing edge and the downstream blade rows. The mixing and dissipation of the strut wake produces a loss of energy, while the velocity defect in the wake, which is a function of the distance from the strut trailing edge, is an important consideration for the design of subsequent blade rows. It is thought that mixing out of the strut wake, in this investigation, is likely to be influenced by both the significant streamwise pressure gradients that occur within the S-shaped duct and the local turbulent structure which itself is influenced by streamline curvature effects.

At a traverse plane 2mm downstream of the strut trailing edge (x/L=0.875), the core region of high velocity flow (Fig.4.3.16) is now subdivided by the wake formed from the merging together of the strut surface boundary layers. Also indicated is the mean flow field that is produced, close to each casing, associated with the interaction of the strut and casing boundary layers. These effects are further indicated by the circumferential distributions of velocity (Fig.4.3.17) close to the strut trailing edge (x/L=0.875), presented at 10%, 50% and 90% passage heights, which show how the contrasting upstream conditions have affected development of the wake and boundary layers along the inner and outer casings. For example, prior to the trailing edge the strut and casing boundary layers in the inner wall regions have undergone a strong deceleration, although no significant regions of flow separation are evident. However, the flow in this location is much closer to separation relative to the outer wall region which has been subjected to a favourable pressure gradient. Thus, a thinner boundary layer is evident in the outer casing region, indicated (Fig.4.3.17) by the relatively faster moving fluid present in locations outside of the struts influence. Furthermore, the outer casing strut wake is thin and its effects are localised, relative to the wake at the inner casing which is much thicker and dominates more of the surrounding flow field (Fig.4.3.17). It can therefore be seen that, not surprisingly, the strut wake differs across the height of the duct due to the upstream conditions in which the flow has developed.

It is expected that mixing out of the wake will vary according to the downstream conditions being experienced. For example, the critical inner wall region is helped by the trailing edge being positioned at the point in the duct where the pressure gradients are changing sign. Hence the favourable downstream pressure gradient along the inner casing will therefore produce an acceleration of the flow, and thus a recovery of the boundary layer. In addition the concave curvature of the inner casing, downstream of x/L=0.5, enhances turbulence levels and will therefore further help in mixing out of the wake. In contrast, near the outer casing wake mixing is hindered by the adverse pressure gradient in this region with turbulence levels, and hence mixing, also being reduced by the convex curvature. It is therefore thought necessary to investigate the OGV wake development in the mid-passage and casing boundary layers separately.

Wake in Mid-Passage Mixing out of the strut wake in the mid passage region, where pressure gradients are relatively small, is indicated by the wake velocity profiles at several downstream axial locations (Fig.4.3.18). It can be seen that substantial mixing out of the wake has occurred by x/L=1.4, which is within 0.7 strut chord lengths. It has already been shown (Section 4.2.4) that a further way in which the mean streamwise velocity component (U) of the wake can be described is by means of normalised wake distributions. Circumferential normalisation is carried out based upon the semi-wake widths (L_{ss},L_{ps} see Fig.4.2.16) which, for a single uncambered strut, should be nominally the same and are commonly designated ($b_{1/2}$) for a single body. At mid annulus height, the normalised wake distributions (Fig.4.3.19) are in good agreement for all of the downstream planes within a semi-wake width of the centreline. Agreement is also favourable, within a semi-wake width, with a Gaussian distribution (Eqn.4.2.1). However, immediately downstream of the strut trailing edge (x/L=0.875), there is a significant discrepancy from the Gaussian distribution at distances further than a semi-wake width from the wake centre line. Ravindrinath and Lakshminarayana (1980) attribute a similar discrepancy to the complex vortex system that forms at the trailing edge and note that similarity has not been proven in such regions. Although not presented here, the deviation of the strut wake defect from the Gaussian distribution is also appreciable outside of the mid-passage region near the casing boundary layers.

It is not thought meaningful to present the axial variation of the wake width behind a single strut in terms of Lakshminarayana and Davino's (1980) characteristic width (L), as described in Section 4.2.4 for the OGV wake. This is because the characteristic wake width (L) is referenced to the blade pitch (s) of the associated blade

row. However, it is thought possible to compare the data with Schlichtings (1968) observations of the two-dimensional wake behind a single body. Schlichting suggests that the semi-wake width ($b_{1/2}$) behind a circular cylinder varies with distance (x) according to;

$$b_{1/2} \approx B \times (x \times C_D \times d)^{1/2} \qquad \text{(Eqn.4.3.2)}$$

where the drag coefficient (C_D) of a cylinder with diameter (d) and height (h) is given by;

$$C_D = \frac{D}{0.5\rho U_\infty^2 hd} \qquad \text{(Eqn.4.3.3)}$$

The semi-wake width ($b_{1/2}$) behind the strut with chord (c) can be similarly defined as;

$$b_{1/2} \approx B \times (x \times C_D \times c)^{1/2} \qquad \text{(Eqn.4.3.4)}$$

where Schlichting suggests the constant (B) is a function of the mixing length (l) and, assuming a Gaussian distribution of the wake profile, has obtained a value of 0.25 from measurements. The drag force on the strut (D) has been calculated from the measured deficit of the momentum flux in the strut wake in a similar method to that outlined by Roach and Turner (1985). Due to the proximity of the measurement stations to the strut trailing edge, it has also been necessary to take into account the contribution due to the static pressure perturbation. A drag coefficient (C_D) for the strut of approximately 0.01 has been calculated from the experimental data at x/L=1.0, where the drag force (D) has been normalised by the freestream dynamic head and the planform area ($0.5\rho U_\infty^2 ch$). The strut drag coefficient (C_D) of 0.01 compares with values of 0.024 and 0.0172 quoted by Lakshminarayana and Davino (1980) for an IGV and a stator blade respectively, with these relatively higher drag coefficients reflecting the levels of turning such blades perform.

The axial variation of the measured strut semi-wake widths ($b_{1/2}$) are presented at 40%, 50% and 60% annulus heights (Fig.4.3.20), and are comparable with a theoretical distribution, based on Eqn.4.3.4, which is given by;

$$b_{1/2} = 0.25\,(0.0019x)^{1/2} \qquad \text{(Eqn.4.3.5)}$$

It should be noted that the semi-wake widths obtained from either side of the strut are nominally the same and therefore data from only one side of the strut is presented. Immediately downstream of the strut trailing edge, at an axial distance normalised by the strut chord (x/c) of 0.01, the semi-wake widths at 40%, 50% and 60% annulus heights are comparable. The semi-wake width at all three heights increases with axial distance as the wake mixes out downstream. However, the rate at which the wake width increases, which indicates the rate of decay of the strut wake, is different at each of the heights. For example, at x/c=0.66, the semi-wake width varies from 3.6mm to 4.6mm at 60% and 40% annulus height respectively, thus indicating a significantly larger rate of wake mixing at 40% annulus height. However, it should be remembered that the wake at these heights is subjected to contrasting streamwise pressure gradients. Whilst a nominally zero pressure gradient exists at 50% height, the wake at 40% height undergoes a favourable pressure gradient, while the wake at 60% annulus height is subjected to an adverse pressure gradient. Thus, there is a radial variation in wake width as the wake develops downstream, with the rate of wake mixing increasing with proximity to the inner casing, consistent with the effects of the streamwise pressure gradient. It should also be noted that the radial variation of the rate of wake mixing due to this effect will be more significant close to each casing, where the streamwise pressure gradients are greater.

The axial variation of the velocity defect behind the strut is presented (Fig.4.3.21) in terms of the streamwise velocity defect normalised by the edge velocity as discussed earlier in Section 4.2.4 (Eqn.4.2.3). The axial variation of the strut velocity defect, at three heights within the core region, can be seen to be in good agreement with the measurements of Lakshminarayana and Davino (1980) for both IGV and stator blades. It has already been shown, in similar analysis for the OGV wake, that the velocity defect decays rapidly between x/c=0.0 and x/c=0.4, while after this region the decay rate is significantly slower and approaches an asymptotic value. The broadly similar values obtained, for the strut case, at 40%, 50% and 60% annulus heights indicates that the effect of the contrasting streamwise pressure gradients on this parameter is small. It can be seen that approximately 50% of the strut wakes velocity defect has mixed out within 0.01 chord lengths, while over 70% of the defect has mixed out within 0.16 chord lengths. Within this region it is thought the effect of the pressure gradient is small compared with the shear forces, while after this region the velocity defect has recovered to such an extent that the effect of pressure gradient is not

discernible.

The axial variations of both the struts streamwise velocity defect and wake width are thought to be of use to the gas turbine engineer, in the context of designing struts within an S-shaped duct. Gostelow (1984) has shown how the axial spacing between blade rows can have a significant effect on performance, including changes in efficiency, stall margin and vibration. It is therefore thought the data presented in this investigation can be used to define the spacing between the strut trailing edge and a downstream blade row in order to minimise potential wake interactions.

Wake in Casing Boundary Layers The streamwise velocity contours at x/L=1.0 (Fig.4.3.22) and x/L=1.40 (Fig.4.3.23), indicate the expected recovery of the strut wake in the more critical inner wall region. The wake-velocity profiles (Fig.4.3.24) at 10% annulus height show how by x/L=1.0, much of the wakes velocity defect has mixed out, while the flow in the regions outside of the struts influence also exhibits an increase in velocity. As the wake progresses to x/L=1.40, further boundary layer recovery and wake mixing occurs. Although the outer casing wake and boundary layer flow has undergone the beneficial effects of a sustained favourable pressure gradient upstream of the strut trailing edge, it is to be expected that its subsequent downstream development will be hindered by the adverse pressure gradient generated as the flow is returned to the axial direction. At 90% height the wake velocity profiles (Fig.4.3.25) indicate how, outside of the struts influence, the boundary layer velocity decreases between x/L=0.875 and x/L=1.40 in response to the applied pressure gradient. This is the opposite effect to that observed, for example, along the inner casing. What can also be observed though is the mixing out of the strut wake by the shear forces in this region. Now, what would normally be expected is a general increase in the wake velocity until its magnitude corresponds to that of the surrounding flow field. In this instance, however, by x/L=1.40 the velocities in line with the strut are actually greater than those of the surrounding flow. This effect is in contrast with the more conventional wake mixing exhibited in the wake-velocity profiles at 10% annulus height (Fig.4.3.24), where both wake and boundary layers undergo recovery. Another mechanism must therefore be responsible for producing these regions in the outer casing wake flow, which have recovered to a greater extent than the surrounding flow field.

The streamwise vorticity distribution, calculated using a similar method to that already shown in Section 4.2.4, is presented (Fig.4.3.26) downstream of the trailing

edge (x/L=1.0). In flow about a strut and casing intersection, vorticity in the upstream boundary layer is converted into streamwise vorticity as the vortex tube takes the form of a horseshoe around the strut (Fig.4.3.27). Thus, counter-rotating vortices exist on either side of the blade at both the inner and outer casing junctures. The contours of streamwise vorticity (Fig.4.3.26) clearly indicate regions of high vorticity in the four strut-casing corners. In the region of the outer casing, the corner vortices are merged with the vorticity associated with the strut wake, while more distinct regions of vorticity are apparent towards the inner casing. Furthermore, secondary vortices can be seen within the inner casing boundary layer. Chang and Gessner (1991) have reported the formation of secondary vortices, in addition to the horseshoe vortex, in the flow about a strut-endwall intersection. They concluded that the secondary vortex is formed as a result of the transverse pressure gradients acting on the curved flow between the convex surface of the strut and the end-wall casing. The results in this investigation similarly show the secondary vortices to be comparable in magnitude and counter rotating. The vortices observed at both the inner and outer casings are thought to distort the mean flow field and turbulence structure and may also contribute to the radial movement of fluid within the strut wake. However, what the streamwise vorticity contours clearly indicate is a general radial movement of fluid within the wake, with very high levels evident towards the outer casing. The flow vectors (Fig.4.3.28), at the same location, further indicate why the streamwise velocity within the wake recovers to reach levels greater than those in the surrounding flow field. Fluid within the wake can be seen to be moving radially, towards the outer casing, from approximately 70% annulus height.

It has already been shown, in Section 4.2.4, how the radial pressure forces within the duct are established to turn the mainstream flow, with the radial pressure gradient ($1/\rho\partial p/\partial n$) balancing the centripetal acceleration (U^2/Rh). However, within the strut wake, where the streamwise velocity and hence the centripetal forces are much lower, there is an imbalance with the pressure forces. Thus, the pressure forces act to drive the wake fluid radially outwards and, while this fluid has a velocity deficit, as indicated by the wake velocity profiles at x/L=0.875 (Fig.4.3.17), it is less than the deficit existing in the outer casing boundary layer. This radial movement of fluid, within the strut wake, therefore acts to re-energise the outer casing boundary layer-wake flow. It is therefore thought that the combined effects of both vorticity and the radial force imbalance act to drive higher energy fluid towards the outer casing, with the flow in

line with the strut therefore being less likely to separate compared with the fluid outside of the influence of the strut wake.

Compressor Generated Inlet Conditions Whilst much of the strut wake data presented for the axisymmetric inlet conditions is equally applicable to the case where a single stage compressor was placed at inlet to the S-shaped duct, what is of interest is the relative size of the strut and OGV wakes presented to the downstream compressor. At the strut trailing edge (x/L=0.875) the distortion of the streamwise velocity contours (Fig.4.3.29), obtained from an area traverse over four OGV blade spaces, indicates that only the remnants of OGV blade wakes are present. The circumferential distribution of velocity at the same axial location, presented at 10%, 50% and 90% annulus height (Fig.4.3.30), further indicates the relative magnitude of the strut and OGV wakes. However, by x/L=1.0 (Fig.4.3.31), much of the strut wakes velocity defect at mid annulus height has mixed out, while at x/L=1.4 (Fig.4.3.32), the circumferential distribution of streamwise velocity indicates that the strut and OGV wakes within both casing boundary layers are comparable.

It has already been shown how significant streamwise pressure gradients are established within the S-shaped duct, producing successive regions of acceleration and deceleration. Thus along approximately 70% the inner casing, for example, the boundary layer thickens as the flow progresses downstream. One effect of this is to reduce the effective flow area relative to the geometric area of the annulus, which has a considerable effect on the streamwise velocity through the duct. Thus, axisymmetric through-flow calculations which make no attempt to model the casing boundary layers use an "end-wall" blockage factor which reflects the reduction in the area available for flow. In a similar way, the presence of blade wakes also reduces the area available for flow and must therefore be allowed for in the design process. Dring et. al. (1983) suggest a "tangential" blockage which reflects all departures from axisymmetry across the blade passage including wake profiles, corner stalls and hub and tip clearances. According to Dring et. al. the tangential blockage (K), at a given radial location, is the ratio of the circumferentially area weighted streamwise velocity (U^{aw}) to the streamwise velocity (U^{mw}) based on the mass weighted total and static pressures;

$$\overline{K} = \overline{U}^{aw} / \tilde{U}^{mw} \qquad \text{(Eqn.4.3.6)}$$

where for incompressible flow;

$$\tilde{U}^{mw} = \sqrt{\left(\tilde{P}_t^{mw} - \tilde{p}_s^{mw}\right) / \frac{\rho}{2}} \qquad \text{(Eqn.4.3.7)}$$

In this investigation, the radial distribution of tangential blockage (K) has been calculated, at exit from the S-shaped duct (x/L=1.0), by circumferentially averaging over two OGV blade spaces. Distributions are presented (Fig.4.3.33) both for the strutted duct with compressor generated inlet conditions and with axisymmetric inlet conditions, with the data being comparable with that presented by a number of authors (Dring et. al. 1983, Joslyn and Dring 1985). The distribution for the axisymmetric case indicates a finite level of blockage across the passage, due to the strut wake, which increases towards the hub and tip. Relatively high levels of blockage can be seen in the outer regions of the inner casing boundary layer, at approximately 30% height, where the wake and boundary layer intersect (Fig.4.3.22). The radial distribution of blockage is similar for the compressor generated inlet condition, with the generally higher levels across the passage reflecting the additional blockage of the OGV wakes.

4.3.4 Stagnation Pressure Loss

Loss coefficients have been determined for both the clean and compressor generated inlet conditions. However it should be noted that for the clean inlet condition the loss values are referenced to x/L=-0.55, at which the upstream effect of the strut is not evident, but with the compressor only the duct inlet plane (x/L=0.0) is available.

The influence of a single strut on overall performance is relatively small. For example, it is estimated that the clean inlet loss coefficient increases from 0.040 to 0.042 when a single strut is incorporated, with corresponding values of 0.035 and 0.038 with the compressor present. Now it has already been stated that the duct pressure loss can only be defined within ±0.005 and ±0.0075 of its true value for the clean and compressor generated inlet conditions respectively, and the incremental loss due to the strut falls within these tolerances. However, whilst the additional loss due to a single strut is relatively small in terms of the overall performance, it should be remembered that the localised effect is relatively large. For example, the circumferential variation of stagnation pressure loss for the clean inlet condition is presented (Fig.4.3.34) with the loss values referenced to x/L=-0.55 (where the upstream effect of the strut is not evident). Thus for the sector traversed, of

approximately 11.6 degrees, a loss coefficient can be calculated (e.g. λ=0.090) for this sector. It can also be assumed that the profile at the extremity of this sector is present around the remaining 348.4 degrees of the annulus for which a loss coefficient (e.g. λ=0.040) can be calculated. Mass weighting of these coefficients then allows the overall duct loss, with a single strut present, to be calculated (λ=0.042). Using this technique it is thought meaningful in this investigation to quote the additional loss due to a single strut.

A modern gas turbine engine is likely to incorporate a significant number of struts. For example, 8 struts are incorporated within the compressor inter-connecting duct of the Rolls Royce Trent engine, which are designed to carry both loads and engine services. The overall effect on performance of such a number of struts can be broadly estimated in this investigation if it is assumed the duct geometry is varied to account for the blockage associated with a given number of struts, and the flow associated with each strut is independent of its nearest neighbour. For example, with compressor generated inlet conditions, 8 struts would increase the duct loss from 0.035 to approximately 0.058, while with 12 struts the loss would be 0.070.

4.4 Compressor Generated Swirl Inlet

In a gas turbine engine potential benefits could arise, in terms of the compression system length and overall performance, if swirling flow were allowed to pass between the upstream and downstream compressor spools linked by the S-shaped duct. For example, the gas turbine engineer may be able to reduce the loading on the upstream stage, by allowing the last stator row to release some swirl into the duct. Furthermore, by controlling the swirl distribution throughout the duct, it may be possible to remove any inlet guide vanes to the downstream compressor, thus shortening the overall compression system length. However, although such benefits potentially exist, there is little published data available.

This investigation is an initial attempt to assess the effect of swirl on the flow within an annular S-shaped duct without struts. Removing the outlet guide vanes from the upstream single stage compressor allows approximately 30 degrees of rotor exit swirl to enter the duct. It should be noted that the method by which the swirl in this investigation has been generated is mainly dictated by both time and financial considerations. However, whilst a 2D axisymmetric swirling inlet condition might be thought to be more preferable, swirl provided directly by a rotor is of obvious interest to the gas turbine engineer. With this in mind it should also be noted that all the data is based on a simple time average with no attempts being made to isolate, for example, the rotor blade wakes passing down the duct.

The results in this section mainly concentrate on the global flow field and how this is affected by the introduction of swirl. The well defined "clean" inlet conditions (Section 4.1), and the subsequent flow field that develops, have been used to provide some basis for comparison when results are obtained for the more complex swirl inlet condition. Although a large amount of detailed data have been collected attempts can only be made to identify the most significant factors. Particular effort has therefore been made to ensure that these factors are directly associated with swirl, and not as a consequence of the way in which swirl has been introduced.

4.4.1 Inlet Conditions

At nominally the same traverse plane the mean streamwise velocity (U) profiles obtained with an axial compressor upstream of the duct are presented (Fig.4.4.1). Note that data are presented both for when no OGV's are present (i.e. "swirl" case), and the circumferentially averaged profile obtained for the complete compressor stage.

Relative to the "clean" condition the profiles indicate that similar streamwise curvature effects are observed (Fig.4.4.1), with the near linear variation of the velocity profiles in the central region indicating the response of the inviscid core flow to this streamwise curvature. However, differences are apparent, particularly towards the inner casing boundary layer. It should also be noted that, as discussed later, the downstream flow field development will be affected by the different turbulent structure presented by the upstream compressor. At the same traverse plane turbulent kinetic energy profiles are presented, with the complete compressor stage data being based on a mass weighted circumferential average (Fig.4.4.2). Significant differences are clearly apparent between, for example, the "clean" and swirling flow cases. It is important to note that most of these differences are not directly associated with the swirl component but are mainly a consequence of the method by which this swirl has been introduced. Hence, the effects of such changes need to be acknowledged, when comparing the data sets, before any conclusions can be made concerning the effects of swirl.

The measurements presented in this section, as already noted, have been based on a simple time average. Thus, with the rotor present, any turbulence data includes both the periodic fluctuations associated with the rotor wakes passing through the measurement volume and a random component associated with the more "conventional" turbulence. Measurements have been performed, using a single hot wire anemometer, at inlet (x/L=0.0) and exit (x/L=1.0) from the S-shaped duct at a number of radial locations. At inlet to the S-shaped duct, the autocorrelation function obtained at 50% annulus height (Fig.4.4.3) is periodic about the blade passing frequency. The blade passing frequency and its harmonics are further indicated by a plot of the power spectral density obtained at the same location (Fig.4.4.4), with a blade passing frequency of 1580 Hz being consistent with the rotor speed of approximately 2200rpm. This periodic component of the velocity signal is evident over approximately 90% of the annulus height, although the signal becomes less periodic and more random towards each casing. For example, at 96% annulus height, the blade passing frequency cannot be seen in either the autocorrelation function (Fig.4.4.5) nor the power spectral density (Fig.4.4.6). However, the periodicity observed over 90% of the annulus height at inlet (x/L=0.0) to the duct is also evident at exit (x/L=1.0). At duct exit, the autocorrelation function obtained at mid-annulus height (Fig.4.4.7) exhibits similar trends to that obtained at inlet to the duct (Fig.4.4.3). Thus the periodicity associated with the rotor passing frequency is still observed at exit as the

rotor wakes are convected through the duct. Furthermore, this periodicity is again evident (though to a lesser degree) over approximately 90% of the annulus height. Whilst the presence of such features make it more representative of engine conditions t is recommended that future work should aim to isolate the turbulent fluctuations associated with these rotor wakes for the swirling flow case.

The differences between the "clean" and swirling test cases, due to the method by which swirl has been introduced into the rig, have been acknowledged. However, this investigation is concerned with the impact of the mean swirl velocity component (W) on the flow field development. A significant swirl component has been generated, by removing the OGV blade row, with swirl angles in excess of 30 degrees entering the duct.

4.4.2 Swirl Distribution

The development of the mean swirl velocity profiles (Fig.4.4.8) within the duct is governed by the conservation of tangential momentum (Wr) which, in the absence of friction, would be constant along streamlines. The total tangential momentum (M_θ) entering and leaving the duct is based on the equation presented by Dring (1992);

$$M_\theta = \int_{r_{inner}}^{r_{outer}} \rho \overline{U}^{aw} \overline{W}^{mw} r dA \qquad \text{(Eqn.4.4.1)}$$

where (U^{aw}) and (W^{mw}) are, for a given radial location, the area weighted streamwise and mass weighted swirl velocities respectively. Using this definition the total tangential momentum (M_θ) at duct exit (x/L=1.0) and in the downstream settling length (x/L=1.40) was found to be within 1% of that entering the duct (x/L=0.0). In addition to approximately conserving overall tangential momentum though, the local distribution of this momentum across the duct may also be considered. For example, at duct inlet (x/L=0.0) the swirl distribution (Fig.4.4.8) is compared with that of a distribution representing a constant level of local tangential momentum between the inner and outer casings (i.e. Wr = constant) based on the value at 50% passage height. However, a better representation is provided at duct inlet (x/L=0.0), exit (x/L=1.0) and in the downstream settling length (x/L=1.4) by plotting the tangential momentum (Wr) against stream function, obtained by interpolation of the data to give values at 1% increments of mass flow across the duct (Fig.4.4.9). It can be seen that the rotor stage at inlet, between approximately 20% and 95% of passage height, produces a slightly

increasing level of tangential momentum with radius. Towards the inner casing though tangential momentum also increases due to the upstream influence of the spinning rotor hub. The exit profiles show that through the duct the tangential momentum adjacent to each casing reduces with a corresponding small increase occurring in the central passage region. However the broadly similar profiles indicate that not only is the overall tangential momentum conserved but the radial transport of momentum across stream surfaces is relatively weak. Hence, not only do the overall swirl (W) levels increase through the duct as the mean radius (r) decreases, but these increases in tangential velocity will be greater towards the inner casing where the relative change in radius is greatest (Fig.4.4.8). Since the observed changes in swirl (W) velocity are governed by the need to conserve tangential momentum, the decreasing radius means that the swirl component in this case predominantly accelerates. However, similar results concerning the conservation of tangential momentum were obtained by Lohmann et. al.(1979) in annular diffusers within which the flow was subjected to an increasing radius. Such results indicate that diffusion or acceleration of the tangential velocity, as produced by the change in radius of a duct, is an efficient process. As was also noted by Lohmann et. al. (1979), this also represents an efficient mechanism by which the static pressure, associated with the swirl component, will also vary.

Of further significance to the gas turbine engineer is the local swirl angles of the mean flow, due to the presence of the swirl velocity, which now occur within the S-shaped duct. These are not only of significance for the design of the downstream compressor spool, but S-shaped ducts often have to accommodate radial struts carrying loads or engine services. The swirl angles at duct inlet (x/L=0.0), exit (x/L=1.0) and in the downstream settling length (x/L=1.4) are presented (Fig.4.4.10). Note the increasing swirl angles through the duct, with the observed variation being a function of changes to both the axial and swirl velocity components.

4.4.3 Mean Static Pressure Distribution

The static pressure distribution along each casing for the "clean" and swirling flow cases are presented, with the complete compressor stage producing a similar distribution to that observed for the "clean" configuration (Fig.4.4.11). The distributions are presented relative to the mass weighted static pressure at duct inlet (p_2) and, as is usual, the total dynamic pressure ($P_2 - p_2$) entering the duct. The indicated streamwise pressure gradients though, and their effect on the streamwise velocity (U), is better reflected by referencing these pressure changes to a dynamic pressure based

on the axial rather than total velocity component (Fig.4.4.12). In this context the presence of swirl is seen to have a significant effect on the streamwise pressure gradients along both casings.

As already discussed for the "clean" inlet condition, differences between the casing pressures at a given axial location reflect how the pressure field adjusts to provide a radial force, thereby turning the flow in response to the streamwise curvature of the duct. As a result significant streamwise pressure gradients occur, with the flow along the inner casing being subjected to a predominately positive (i.e. adverse) gradient as the pressure coefficient rises along approximately 70% of the duct length. It has already been shown (Section 4.1) that it is towards the end of this region of increasing pressure where the inner casing boundary layer is most likely to separate. With swirl present the measured streamwise pressure gradients within the duct (Figs.4.4.11 and 4.4.12) are modified by the introduction of curvature effects in the circumferential direction about the rig centreline (r). Inspection of the n-component momentum equation, indicates that the radial pressure gradient ($\partial p/\partial n$) is now mainly a function of the centripetal forces associated with circumferential curvature ($\rho W^2/r\ \partial r/\partial n$), as well as streamwise curvature ($\rho U^2/Rh$);

$$\frac{\partial p}{\partial n} \approx \frac{\rho U^2}{Rh} + \frac{\rho W^2}{r}\frac{\partial r}{\partial n} \qquad \text{(Eqn.4.4.2)}$$

Normalising these terms by the axial momentum (M_x) at inlet (x/L=0.0) to the duct enables comparisons to be made between the swirl and "clean" inlet conditions;

$$\frac{\partial C_p}{\partial n} \approx \frac{\rho U^2}{RhM_x} + \frac{\rho W^2}{rM_x}\frac{\partial r}{\partial n} \qquad \text{(Eqn.4.4.3)}$$

where the radial pressure gradient is defined in terms of a static pressure coefficient (C_p) such that;

$$C_p = \frac{p - \tilde{p}_2}{\rho U^2_{Mean} A} \qquad \text{(Eqn.4.4.4)}$$

The experimental data, for both the "clean" and swirl inlet conditions, has been used to calculate each of the terms in Eqn.4.4.3. These terms have been integrated across the duct to obtain the actual difference in pressure (ΔC_p), between the casings, associated with some of these components;

$$\Delta C_p = \int_{n_i}^{n_o} \left(\frac{\rho U^2}{RhM_x} \right) dn + \int_{n_i}^{n_o} \left(\frac{\rho W^2}{rM_x} \frac{\partial r}{\partial n} \right) dn \qquad \text{(Eqn.4.4.5)}$$

For example, it can be seen (Fig.4.4.13) that at each plane the overall change in pressure across the duct associated with the streamwise curvature (U^2/Rh) is broadly similar for the "clean" and swirling flow cases. Also presented for the clean case is the actual difference in pressure (ΔC_p (Clean)) between the casings, at each plane, which represents the sum of the various terms. Furthermore, what is important to note is that addition of the extra component ($W^2/r\ \partial r/\partial n$), to the clean case, approximately yields the pressure difference (between each casing) for the swirling flow case (ΔC_p (Swirl)). The relative changes in pressure (Fig.4.4.11 and 4.4.12) are therefore dominated by the swirl component and, furthermore, this component ($W^2/r\ \partial r/\partial n$) increases through the duct due to the higher swirl velocities generated as the mean duct radius decreases. As a result of these effects the streamwise pressure gradients must also change, with the modification varying with height across the duct. For example, relatively large increases occur in the swirl component towards the inner casing. Thus along the inner casing the region of positive (i.e. adverse) pressure gradient only occurs along approximately 50% of the duct, after which the increasing swirl component causes the pressure gradient to become negative (Fig.4.4.11 and 4.4.12). Whilst this would appear to reduce the possibility of flow separation it must be remembered that, as indicated by the most significant terms in the s-component momentum equation,

$$\frac{DU}{Dt} - \frac{W^2}{rh}\frac{\partial r}{\partial s} = -\frac{1}{\rho h}\frac{\partial p}{\partial s} - \frac{1}{r}\frac{\partial}{\partial n}(\overline{u'v'}r) \qquad \text{(Eqn.4.4.6)}$$

part of this pressure gradient is associated with an additional centripetal force ($W^2/rh\ \partial r/\partial s$) acting along the streamwise direction. Thus, forces generated by the pressure and shear stress gradients represent the total change in momentum but, for the swirling case, subtraction of this centripetal component is required in order to obtain the net change of flow momentum in the streamwise direction (DU/Dt). To illustrate this

effect on the swirl case, the radial distribution of the streamwise pressure and shear forces acting on the mean flow are presented at x/L=0.50 (Fig.4.4.14). The various terms have, again, been normalised by the inlet axial momentum (M_x) in order that comparisons can be made between the "clean" and swirl cases. For example, the forces associated with the primary shear stress gradient ($1/r\ \partial(\overline{u'v'}r)/\partial n$), for both cases, are comparable over most of the annulus height. For the swirl case, it can be seen that close to the inner casing the pressure gradient ($1/\rho h\ \partial p/\partial s$) is only slightly adverse, but when the centripetal component is superimposed ($1/\rho h\ \partial p/\partial s - W^2/rh\ \partial r/\partial s$) the decelerating force affecting the streamwise velocity is much greater and is comparable with that of the clean case. It should be noted though that a small difference can be observed with the net decelerating force being less than that indicated for the "clean" case. This is thought to show how development of the streamwise velocity profile can, to some extent, be directly influenced by the swirl (W) component.

The influence of the swirl component of velocity (W) on the streamwise component (U) can be illustrated by considering the flow along a streamline. If we assume the flow to be inviscid and that stagnation pressure is conserved then, for flow in the streamwise direction, Bernoulli's equation gives;

$$P_t = p + \frac{1}{2}\rho U^2 \qquad \text{(Eqn.4.4.7)}$$

For a constant level of stagnation pressure in the normal direction $\partial P_t/\partial n=0$, then;

$$\frac{\partial p}{\partial n} + \rho U\frac{\partial U}{\partial n} = 0 \qquad \text{(Eqn.4.4.8)}$$

The same analysis can be applied to the swirling flow case, from which we obtain;

$$\frac{\partial p}{\partial n} + \rho U\frac{\partial U}{\partial n} + \rho W\frac{\partial W}{\partial n} = 0 \qquad \text{(Eqn.4.4.9)}$$

If we now consider that the pressure gradient ($\partial p/\partial n$) consists of components

associated with both the streamwise (U) and the swirl velocity (W) then;

$$\left.\frac{\partial p}{\partial n}\right|_U + \left.\frac{\partial p}{\partial n}\right|_W + \rho U\frac{\partial U}{\partial n} + \rho W\frac{\partial W}{\partial n} = 0 \qquad \text{(Eqn.4.4.10)}$$

It has already been shown, in comparisons of the axisymmetric and swirling flow cases, how the pressure gradient associated with the swirl velocity ($\partial p/\partial n|_W$) balances the centripetal acceleration ($\rho W^2/r\ \partial r/\partial n$), thus;

$$\left.\frac{\partial p}{\partial n}\right|_U + \frac{\rho W^2}{r}\frac{\partial r}{\partial n} + \rho U\frac{\partial U}{\partial n} + \rho W\frac{\partial W}{\partial n} = 0 \qquad \text{(Eqn.4.4.11)}$$

If we now consider a constant level of tangential momentum across the duct then;

$$\frac{\partial}{\partial n}(Wr) = 0 \qquad \text{(Eqn.4.4.12)}$$

which when expanded gives;

$$W\frac{\partial r}{\partial n} + r\frac{\partial W}{\partial n} = 0 \qquad \text{(Eqn.4.4.13)}$$

resulting in;

$$\frac{\partial W}{\partial n} = -\frac{W}{r}\frac{\partial r}{\partial n} \qquad \text{(Eqn.4.4.14)}$$

Substitution of Eqn.4.4.14 into Eqn.4.4.11 gives;

$$\left.\frac{\partial p}{\partial n}\right|_U + \frac{\rho W^2}{r}\frac{\partial r}{\partial n} + \rho U\frac{\partial U}{\partial n} - \frac{\rho W^2}{r}\frac{\partial r}{\partial n} = 0 \qquad \text{(Eqn.4.4.15)}$$

This simple case is therefore thought to illustrate that if tangential momentum (Wr) is constant in the radial direction within the duct, the mean streamwise (U) and swirling (W) velocity components will be mainly independent. This is because changes in static

pressure, produced by the swirl component, generate the necessary pressure gradients that provide the centripetal forces associated with this swirl component (W^2/r). When this is not the case though, additional pressure changes are required thereby affecting the streamwise velocity (U) component. Thus, as the radius decreases through the duct so the swirl velocity changes, and the streamwise velocity must therefore respond to provide the necessary centripetal forces. This coupling of the streamwise (U) velocity to the swirl (W) component is thought responsible for the observed local changes in streamwise flow acceleration relative to the clean case. Analysis shows that these effects are particularly evident in the latter half of the duct towards the inner casing. Furthermore, the observed changes reflect the tangential momentum profile generated by the upstream rotor, and so a profile could be generated to maximise potential benefits associated with the streamwise velocity field.

4.4.4 Shear Stress Distribution

The measured distributions of the shear stress component ($\overline{u'v'}$) along the duct are presented (Fig.4.4.15). It is the gradient of this component ($\partial(\overline{u'v'})/\partial n$) which is of most significance to the mean flow field development in the streamwise (U) direction. For the "clean" inlet condition, two factors which have a significant effect on the development of this shear stress distribution have already been described in detail (Section 4.1.3). Firstly, the streamwise pressure distribution has a direct influence on the mean velocity (U) and hence, through the mean velocity gradient ($\partial U/\partial n$), has an indirect influence on the shear stress. Secondly, a more direct effect on the turbulent flow field is that due to the relatively strong streamline curvature effects. It has also been noted that the effect of the streamwise pressure gradient, on the shear stress distribution, is more apparent in the near wall region adjacent to each casing. In contrast, the more direct influence of streamline curvature on the turbulent flow field is more apparent in the outer part of each boundary layer. Relative to this data, the swirling flow distributions can be compared. However, due to the way in which swirl has been generated, such effects as rotor wakes and tip leakage have also been introduced into the rig. It should therefore, again, be emphasised that only tentative conclusions can be drawn from this data.

For reference purposes the shear stress distributions, at 4 stations, are presented for the case with a complete compressor stage (i.e. rotor and OGV row) thereby producing a different turbulent structure at duct inlet. The mean flow field and turbulent kinetic energy distribution at this location (x/L=0.0) have already been

presented (Section 4.2.1). Although there are significant circumferential variations in the flow field, due to OGV wakes, the ($\overline{u'v'}$) shear stresses have been circumferentially averaged. This is a somewhat simplistic approach but it does give an approximate indication of the magnitude and distribution of the stresses present. At duct inlet, the rotor tip leakage effects result in enhanced stress levels adjacent to the outer casing. Nevertheless, over most of the duct the stress distributions are broadly similar to that measured for the "clean" inlet condition. For example, a region of low shear stress exists all along the duct, in the central passage region, whilst the distributions are also comparable within the inner wall boundary layer. The exception to this is adjacent to the outer casing, between duct inlet and x/L = 0.375, where rotor tip leakage effects result in enhanced stress levels.

With the OGV row removed from the single stage compressor (i.e "swirl" case) shear stresses of appreciable magnitude are observed for all 3 components but only the ($\overline{u'v'}$) component is presented here. For the swirling flow case the shear stress distribution at duct inlet is significantly different, though the shear stress is still virtually zero in the central passage region. For example, differences are apparent in the magnitude and distribution adjacent to the inner casing, whilst the enhanced stress levels associated with rotor tip leakage effects are now even higher. However, by x/L=0.375, these differences have reduced, but downstream of this location much larger differences then develop relative to the other cases presented.

Although differences are apparent at duct inlet it is thought they cannot account for the large differences in the shear stress distributions that develop within the duct relative to the other cases presented. It is to be expected, for example, that gradients of shear stress adjacent to the inner casing will be affected by the different streamwise pressure gradients. However, this cannot account for the large shear stresses that develop in the latter half of the duct, which are associated with the inner casing boundary layer, with there also no longer being a region of zero shear stress in the central portion of the duct. One likely possibility is that these stresses are associated with the additional curvature effects introduced by the swirl component.

It has already been shown (Section 4.1.3) that, in the latter half of the duct, streamline curvature effects produced enhanced turbulence levels in the outer part of the inner casing boundary layer. This being due to the decrease in angular momentum (URh) as the radius of curvature (Rh) increases. With swirling flow much larger stresses in this region are observed, and a region of zero shear stress is no longer

present in the central portion of the duct. In addition to the higher turbulence levels at the commencement of this region, it is thought that further enhancement of the shear stress is occurring. This is likely to be due to curvature components in both the streamwise (Rh) and circumferential (r) directions. Flow stability or instability therefore depends on the streamwise (U) and circumferential (W) mean velocity profiles. In the latter half of the duct these may combine to provide an unstable flow with large stresses being generated.

4.4.5 Mean Streamwise Velocity Distribution

As already described in Section 4.1.2, the mean streamwise velocity at a given location is a function of the centripetal forces, streamwise pressure gradients and the applied shear stress gradients. It has been shown that the duct curvature directly affects the streamwise velocity profile through the static pressure field, and indirectly through the modified turbulent structure.

For the "clean" inlet condition the mean velocity profiles (Fig.4.4.16) show the presence of a potential core region, along the entire length of the duct. At each location the gradient of velocity in this region reflects the curvature (Rh) which is being undertaken by the flow in the streamwise direction. This core region isolates the boundary layers adjacent to each casing and, as noted earlier (Section 4.1.2), the variation of each boundary layers shape parameter (H) along the duct shows that it is the flow adjacent to the inner casing that is most likely to separate. This is due to the combined influence of the sustained adverse pressure gradient and curvature effects on the boundary layer development. This gives rise to a rapid growth in shape parameter which reaches a maximum value of 1.66 at x/L=0.75, although as already noted this is well below the value of approximately 2.7 associated with flow nearing separation. At the same location, but with the complete compressor stage present, a slight reduction in the circumferentially averaged boundary layer shape parameter was observed. However, for that configuration the flow field was not axisymmetric and, as discussed earlier (Section 4.3), this improvement was associated with an interaction between the OGV wakes and the boundary layer. Also noted for this case was the more fuller velocity profiles observed adjacent to the outer casing.

The streamwise velocity profiles for the swirling flow case are also presented (Fig.4.4.16) with broadly similar regions of accelerating and decelerating flow being observed. For example, despite the observed changes to the static pressure distribution

along the inner casing, the boundary layer profiles indicate broadly similar streamwise velocity changes along the duct due to the reasons already described. However, some variations are apparent at duct inlet with larger differences developing further downstream. These changes in profile are apparent not only in the core region, but relatively high velocities are observed adjacent to each casing. For the outer casing boundary layer these higher velocities develop quickly and can be observed along most of the duct length. In contrast, the increased velocities adjacent to the inner casing are only observed in the latter half of the duct. Nevertheless, at the critical location along the inner wall (x/L=0.75) the fuller profile is reflected by the favourable change in the boundary layer shape parameter, based on the streamwise velocity profile, which has reduced from 1.66 to 1.40.

Although large changes are observed in the shear stress distribution within the core region and inner casing boundary layers these are not of sufficient magnitude to produce the observed changes to the streamwise pressure field. Data already presented at x/L=0.50 (Fig.4.4.14) has illustrated this, in which the relative magnitude of the shear and pressure forces has been assessed. Although changes in the shear forces are observed they are relatively small and, if anything, reduce the accelerating shear force which is adjacent to the inner casing over a significant part of its length. It is therefore thought that it is the streamwise velocity and how it is coupled with the swirl component which is of significance in this region. In contrast, along the larger diameter outer casing, the data such as that at x/L=0.50 (Fig.4.4.14) indicates relatively small changes in the pressure gradients. In the outer casing boundary layer, the observed changes are mainly due to the greatly enhanced shear forces indicated, for example, by the data at x/L=0.125 (Fig.4.4.17). These large shear forces are associated with rotor tip leakage effects and, for the swirling flow case, this effect is of greater significance than any effects associated with coupling of the streamwise and swirl velocity components.

The only results to which some comparisons can be made is that of swirling flow in annular passages of relatively constant radius such as that described by Lohmann et al. (1979) and Scott et al. (1973). In these cases changes in the streamwise (U) profile were due to variations in the turbulence field brought about by the stabilising and destabilising curvature effects introduced by the tangential momentum profile. For the results presented in this investigation, changes in the turbulence levels brought about by the swirl component are evident. However, in this investigation swirl has been

introduced by an upstream axial rotor which also introduces localised changes in turbulence such as that associated with rotor tip leakage effects. Furthermore, of greater significance is the change in radius within the duct which, together with the tangential momentum profile produced by the upstream rotor, influences the streamwise velocity profile.

4.4.6 Stagnation pressure loss

Knowledge of the important mechanisms which determine the flow field within the S-shaped duct allow methods to be developed for optimising the design of such ducts. However, of further practical significance is the overall stagnation pressure loss within the duct for which very little published data is available. In this case the loss coefficient (λ) is based on the difference in mass weighted stagnation pressure between duct inlet (x/L=0.0) and the downstream settling length (x/L=1.4), relative to the total mass weighted dynamic head at duct inlet. For the "clean" condition the loss value (λ) of 0.02 is relatively low and, as noted earlier (Section 4.1.6), is comparable with that which would occur if the duct was replaced by a parallel sided annular passage. Also noted (Section 4.3.5) was the increase in loss, to approximately 0.035, for the complete compressor stage with this extra loss being attributed to the mixing out of OGV wakes within the duct. However, for the swirling flow case the OGV's were removed and a loss value of 0.045 was obtained. This reflects the higher levels of turbulence generated within the duct when the swirling flow is introduced. Furthermore, in this case the loss value can also be expressed with respect to the axial dynamic head at duct inlet ($\frac{1}{2}\rho U^2$) which yields a value of 0.115. This illustrates the relatively high loss that arises, for a given axial dynamic head, when a swirl component of this magnitude is introduced. However, whilst the duct loss can be evaluated for these different inlet conditions what cannot be assessed is the change in overall performance of a compression system which incorporates a duct operating under such conditions.

In addition to the overall stagnation pressure loss within the duct, its radial distribution is presented in terms of the change in pressure along "nominal" streamlines (Fig.4.4.18). As discussed in more detail in Chapter 3, this was obtained by dividing the flow at each plane into 1% increments, across the duct, and at these locations stagnation pressure values could be interpolated. It should be noted that the definition of "true" streamlines is difficult for both the compressor and swirl cases as some radial convection of fluid, across these "nominal" streamlines, can be expected due to the presence of blade wakes and rotor tip leakage effects. However, it is thought this

analysis indicates the broad trends. More detailed results presented earlier (Section 4.1.6) for the "clean" condition show how along the inner wall the loss is mostly associated with the adverse pressure gradient applied over a significant length of the duct. Hence, at duct exit the region of high loss is situated relatively close to the inner casing surface. In contrast, for the outer casing the majority of the loss is in the outer region of the boundary layer and is mainly due to the initial concave curvature. This enhances turbulence levels which are only gradually suppressed in the latter half of the duct. With the complete compressor stage present the loss distribution indicates that similar flow mechanisms within each boundary layer are contributing to the generation of stagnation pressure loss. Furthermore, a finite loss exists in the central passage region which can be associated with the mixing out of the compressor OGV wakes. For the swirling flow case higher losses are generated within the outer casing boundary layer, although higher stress levels have already been noted in this region at duct inlet. However, whilst the levels of loss have increased, the comparable distributions again indicates that similar loss generating mechanisms are present. Within the core region data already presented has shown the development of significant levels of turbulence within the duct and so, as to be expected, a finite pressure loss is indicated in this region. However, the most significant change in the magnitude and distribution of the loss occurs within the inner casing boundary layer, with particularly high loss levels occurring adjacent to the inner casing.

High losses reflect the work done by the mean flow field, against both the viscous and turbulent stresses, as it passes through the duct. Thus, loss is generated as energy from the mean flow field is transferred to the turbulent motion. This is numerically equal to the production term in the turbulence kinetic energy transport equation which, in a cartesian coordinate system can be shown (e.g. Young, 1989) to be;

$$-\rho \overline{u_i u_j} \frac{\partial U_i}{\partial x_j} \qquad \text{(Eqn.4.4.16)}$$

In order to generate loss, this term must be numerically positive. For example, for the clean inlet condition, the duct loss is mainly associated with the boundary layer shear term ($-\rho\overline{u'v'}\partial U/\partial y$). A significant region of loss is generated within the inner casing boundary layer where the velocity gradient ($\partial U/\partial y$) is positive and the shear stress

($\overline{u'v'}$) is negative. This term ($-\rho\overline{u'v'}\partial U/\partial y$) is also significant for the swirl inlet condition, but for this case comparable levels of all three shear stress components have been measured. However, as Eqn.4.4.16 indicates, loss production is a function of not only the local shear stress (u_iu_j) but also of the velocity gradient ($\partial U_i/\partial x_j$). In the region of the inner casing, where high loss levels have been observed for the swirl case, the velocity gradient ($\partial W/\partial y$) is large and positive (Fig.4.4.8, x/L=625 for example) while the $\overline{v'w'}$ shear stress (Fig.4.4.19, x/L=0.625) is negative up to approximately 8% annulus height. Furthermore, the velocity gradient ($\partial W/\partial y$) is large compared with the other velocity gradients ($\partial U_i/\partial x_j$), while the levels of the $\overline{v'w'}$ shear stress close to the inner casing are comparable with the other stresses ($\overline{u_iu_j}$). The mechanism for the term ($-\rho\overline{v'w'}\partial W/\partial y$) is analogous to the more obvious boundary layer shear term ($-\rho\overline{u'v'}\partial U/\partial y$), and thus might similarly be expected to have a significant effect on loss generation. Thus, the increased loss levels adjacent to the inner casing are thought to be due to the additional boundary layer shear term ($-\rho\overline{v'w'}\partial W/\partial y$). It should be noted that further loss generation mechanisms might be expected to contribute to the high loss levels observed adjacent to the inner casing, although it is thought that the two boundary layer shear terms discussed ($-\rho\overline{u'v'}\partial U/\partial y$, $-\rho\overline{v'w'}\partial W/\partial y$) are of most significance. Thus while only tentative conclusions can be drawn from the data, as with the data already presented, this is thought to indicate how the development of the boundary layer in this region is significantly affected by the presence of swirl.

4.5 Summary of Results and Discussion

The overall performance of the annular S-shaped duct has been evaluated both in terms of boundary layer development and stagnation pressure loss. Furthermore, the complex three dimensional flows that occur with compressor generated inlet conditions and the presence of struts have been explained in terms of the variation of the flow features from the two dimensional case. The "clean" case has been used to identify the significant effects on boundary layer development, which have provided a datum to which the more complex test cases could be compared. For example, it has been shown that the static pressure distribution around the strut is determined not only by the strut profile, but also the pressure distribution imposed by the duct itself. It is hoped that such information will encourage the gas turbine engineer to modify the design of struts to account for the pressure field within which the strut operates. Similarly, it has also been shown that the boundary layers can be re-energised when engine representative conditions are provided by an axial compressor at inlet, implying that for the same change in mean radius a shorter duct could be designed without necessarily incurring flow separation. Of further concern to the gas turbine engineer is the stagnation pressure loss within the duct, and this has been presented both in terms of the overall levels of loss and in terms of the radial distribution of loss. In addition, the flow mechanisms that contribute to the generation of stagnation pressure loss within the duct have been identified. The effects of inlet swirl on the flow field that develops within an annular S-shaped duct have been identified and should be of consequence to the gas turbine engineer both for the design of the downstream compressor spool and of any radial struts which may be located within the duct. It is therefore hoped that the information provided by this investigation will assist in the design of compressor inter-connecting ducts.

Chapter 5 Conclusions

5.0 Conclusions

An experimental investigation has been carried out to determine the aerodynamic performance of an annular S-shaped duct representative of that used to connect the compressor spools of aircraft gas turbine engines. Measurements of both the mean and turbulent flow field have been obtained using both five hole pressure probes and a 3 component Laser Doppler Anemometry (LDA) system. Results are presented both for a single stage compressor, operating immediately upstream of the duct, and for when the outlet guide vane (OGV) row was removed. In this latter case swirl angles in excess of 30 degrees were generated by the rotor. To provide a basis for comparison, results have also been presented for axisymmetric inlet conditions (termed the "clean" or datum case) obtained by allowing boundary layers to develop within an upstream entry length. In addition, both for the inlet conditions provided by a single stage compressor and for the "clean" inlet condition, the effect of placing a single radial strut within the duct, typical of that used for carrying loads and engine services, has been assessed.

For the "clean" case significant streamwise pressure gradients arise within the duct due to flow curvature, which also has a direct influence on the turbulent flow field. This effect results in the flow adjacent to the inner casing being more liable to separate. Through an analysis of the most significant terms in the momentum equations, it has been shown that whilst the streamwise pressure forces might be considered to dominate much of the flow, in this critical region the primary shear force is significant and acts to prevent separation. While this may be relatively unimportant in this particular case, this may be more important in less well behaved flows where separation is more imminent. With no flow separation present the stagnation pressure loss within the duct was of a similar magnitude to that which would be obtained within a parallel sided passage. The magnitude and radial distribution of loss was consistent with the measured shear stress distribution within the duct.

For the case where a single stage compressor was operated immediately upstream of the S-shaped duct, the following conclusions have been drawn;

- Similar streamwise pressure gradients, to those observed for the datum case, arise within the duct due to flow curvature, which also has a direct influence on the turbulent flow field. The significant variation of each boundary layer's shape parameter along the duct indicates that, as in the

datum case, it is the flow adjacent to the inner casing that is most likely to separate.

• When representative inlet conditions are presented by an axial compressor at duct inlet, radial movement of fluid with the OGV wakes acts to re-energise significant regions of the inner casing boundary layer. This implies that the streamwise pressure gradients could be increased, for example by reducing the duct length for the same change in mean radius, without necessarily incurring flow separation.

• Along the outer casing a slight reduction in shape parameter is also observed, compared with the datum case. This is due to the enhanced turbulence levels associated with rotor tip leakage effects.

• The OGV wake velocity defect decays rapidly between x/c=0.0 and x/c=0.4, while after this region the decay rate is significantly slower approaching an asymptotic value at larger distances (x/c>7) from the OGV trailing edge.

• The overall mass weighted stagnation pressure loss (λ) with a complete compressor stage at inlet increases due to mixing of the OGV wakes within the duct. It should be noted that mixing occurs rapidly downstream of the blade row, and so the loss values presented in this investigation are optimistic.

For the case where a single radial strut was placed within the S-shaped duct, the following conclusions have been drawn;

• The strut has an upstream influence on the flow, which in this investigation varies across the passage due to the relative streamwise location of the strut leading edge. The effect of the blockage presented by the strut is therefore more prevalent in the inner wall region.

• When representative inlet conditions are presented by an axial compressor at duct inlet, not only is the OGV passage immediately upstream of the strut affected by the presence of the strut, but also the adjacent passages. Within these passages, a larger core region of high velocity flow is present when the strut is in place, compared with the strut removed, indicating that these passages are accepting some of the mass

flow displaced from the OGV passage directly in line with the strut. Based on these measurements it has been estimated that the mass flow through the OGV passage directly upstream of the strut is 11% less than that through the corresponding passage with the strut removed.

• Attached flow was observed over the entire surface of the radial strut. The static pressure distribution is determined not only by the strut profile, but also the pressure distribution imposed by the duct on the strut. Such a result indicates that rather than using a standard profile, the strut design can be modified to account for the pressure field within which it operates.

• As observed for the OGV wake, radial movement of fluid within the strut wake, acts to drive higher energy fluid towards the outer casing. The flow in line with the strut being less likely to separate compared with the fluid outside of the influence of the strut wake.

• The influence of a single strut on overall performance is relatively small. For example, the clean inlet loss coefficient increases from 0.040 to 0.042 when a single strut is incorporated, with corresponding values of 0.035 and 0.038 with the compressor present. However, with compressor generated inlet conditions, it is estimated that 8 struts would increase the duct loss from 0.035 to approximately 0.058.

For the case where swirl angles in excess of 30 degrees were generated by a rotor immediately upstream of the S-shaped duct, the following conclusions have been drawn;

• Tangential momentum is conserved within the duct which, as the duct radius decreases, results in increasing swirl velocities. These changes are highest towards the inner casing where the relative change in radius is greatest.

• Streamwise velocity profiles are broadly similar despite large changes in the measured streamwise pressure gradients. It should be remembered though that a component of centripetal acceleration, associated with the swirl velocity, acts in the streamwise direction.

• Towards the rear of the duct some differences in the streamwise velocity distribution develop in the core region, with higher velocities occurring

adjacent to the critical inner wall casing. Results indicate this is the response of the streamwise velocity component to changes in the swirl velocity. These changes will also be a function of the tangential momentum profile produced by the upstream rotor.

• Higher velocities along the outer casing are mainly due to the enhanced mixing associated with tip leakage effects from the upstream rotor. Hence, these effects are due to the rotor presence rather than being a direct consequence of the presence of swirl.

• For the swirling flow case a loss value of 0.045 was obtained. This reflects the higher levels of turbulence generated within the duct when the swirling flow is introduced. Furthermore, in this case the loss value can also be expressed with respect to the axial dynamic head at duct inlet ($\frac{1}{2}\rho U^2$) which yields a value of 0.115. This illustrates the relatively high loss that arises, for a given axial dynamic head, when a swirl component of this magnitude is introduced.

• The most significant change in the magnitude and distribution of the loss occurs within the inner casing boundary layer, with particularly high loss levels occurring adjacent to the inner casing. The increased loss levels adjacent to the inner casing are thought to be due an additional boundary layer shear term.

Chapter 6 Recommendations for Further Work

6.0 Recommendations for Further Work

This thesis is part of a continuing investigation at Loughborough, which includes a comprehensive measurement of the mean flow and turbulence structure within an annular S-shaped duct. The experimental data presented in this investigation should be used to validate and assist in the development of CFD codes, with the long term objective to apply such methods to the design of S-shaped ducts for a variety of engine configurations. It is also recommended that a series of measurements are obtained with the LDA system phase-locked to the passing upstream rotor blades, in order to remove the additional "pseudo" stresses associated with the passing of rotor wakes through the measurement volume. Such data would also assist in the development of turbulence models.

CFD codes should be used to design a new radial strut within the duct. The strut profile could be modified to account for the pressure field within which it operates. Favourable pressure gradients should be taken advantage of while off-loading regions in which the pressure gradient is mostly adverse. Such an integrated design approach would be of even more interest if cambered struts were incorporated within the duct, although it should be noted that the significant aerodynamic blockage associated with a number of struts would entail extensive modifications to the test facility. The testing of a new radial strut should also include turbulence measurements in order to examine further the radial movement of fluid within the strut wake.

A joint experimental and CFD programme should investigate further the findings of this investigation of the effect of swirl on the S-shaped duct. Futher work should look at the effects of variations in the radial distribution of tangential momentum at inlet to the duct. Of particular interest would be the effect of a constant tangential momentum profile, at inlet to the duct, on the development of the streamwise velocity profile.

References

Abbott, I.H. and Von Doenhoff, A.E., 1949, "Theory of wing sections.", Dover Publications Inc., New York.

Ahmed, N.A., Forster,C.P. and Elder, R.L., 1991, "Laser anemometry in turbomachines", Proceedings of the Institution of Mechanical Engineers, Vol.205.

Bailey, D.W., Britchford, K.M., Carrotte, J.F. and Stevens, S.J., 1995, "Performance assessment of an annular S-shaped duct.", ASME Paper No. 95-GT-242, IGTI Aeroengine Congress, Houston, Texas.

Bailey, D.W. and Carrotte, J.F., 1996, "The influence of inlet swirl on the flow within an annular S-shaped duct.", ASME Paper No. 96-GT-60, IGTI Aeroengine Congress, Birmingham, United Kingdom.

Bandyopadhyay, P.R.and Ahmed, A., 1993, "Turbulent boundary layers subjected to multiple curvatures and pressure gradients.", Journal of Fluid Mechanics, Vol.246, pp.503-527.

Barlow, R.S. and Johnston, J.P., 1988, "Structure of a turbulent boundary layer on a concave surface.", Journal of Fluid Mechanics, Vol.191.

Baskaran, V., Smits, A.J. and Joubert, P.N., 1987, "A turbulent flow over a curved hill. Part 1. Growth of an internal boundary layer.", Journal of Fluid Mechanics, Vol.182, pp.47-83.

Baskaran, V., Smits, A.J. and Joubert, P.N., 1991, "A turbulent flow over a curved hill. Part 2. Effects of streamline curvature and streamwise pressure gradient.", Journal of Fluid Mechanics, Vol.232, pp.377-402.

Bradshaw, P., 1969, "The analogy between streamline curvature and bouyancy in turbulent shear flow.", Journal of Fluid Mechanics, Vol.36, pp.177.

Bradshaw, P., 1972, "The understanding and prediction of turbulent flow.", Aeronautical Journal, Vol.76, pp.403-417.

Bradshaw, P., 1973, "Effects of streamline curvature on turbulent flow.", AGARD AG-169.

Bradshaw, P., Launder, N.E. and Lumley, J.L., 1996, "Collaborative testing of turbulence models.", Transactions of the ASME, Journal of Fluids Engineering, Vol.118, pp.243-247.

Britchford, K.M., 1997, Ph.D Thesis, To be submitted, Loughborough University of Technology.

Britchford, K.M., Manners, A.P., McGuirk, J.J. and Stevens, S.J., 1993, "Measurements and prediction of flow in annular s-shaped ducts.", Proceedings of the Second International Symposium on Engineering Turbulence Modelling and Measurements, Lisbon.

Britchford, K.M, Carrotte, J.F., Stevens, S.J. and McGuirk, J.J., 1994, "The development of the mean flow and turbulence structure in an annular S-shaped duct." ASME Paper No. 94-GT-457, IGTI Aeroengine Congress, The Hague, Netherlands.

Bryer, D.W. and Pankhurst, R.C., 1971, "Pressure probe methods for determining wind speed and flow direction.", HMSO.

Buchave, P., 1979, "The measurement of turbulence with the burst-type laser Doppler anemometer - errors and correction methods.", Report No. TRL-106, State University of New York at Buffalo.

Burrill, K.F. and Barnes, R.W., 1971, "Complex annular ducts for use in gas turbine engines - current problem areas in their design.", Paper No.20, A Symposium on Internal Flows, University of Salford.

Burstware Version 3.0, 1991, "Burstware User Guide.", Dantec Elektronik, Denmark.

Carrotte, J.F., 1990, "The mixing characteristics of dilution jets issuing into a confined cross-flow", Ph.D. Thesis, Department of Transport Technology, Loughborough University of Technology.

Carrotte, J.F., Britchford, K.M. and Wray, A.P., 1993, "Three component LDA measurements of annulus wall boundary layers upstream of an annular S-shaped duct.", Proceedings of the Fifth International Conference on Laser Anemometry Advances and Applications, Veldhoven, The Netherlands, pp.111-118.

Carrotte, J.F. and Britchford, K.M., 1994, "The effect of laser beam orientation on the accuracy of 3D LDA measurements within an annular test facility.", Proceedings of the Seventh International Symposium, Lisbon.

Carrotte, J.F., Baliey, D.W. and Frodsham, C.W., 1995, "Detailed measurements on a modern combustor dump diffuser system.", Transactions of the ASME, Journal of Engineering for Gas Turbines and Power, Vol.117, pp.678-685.

Carrotte, J.F., McGuirk, J.J. and Stevens, S.J., 1995, "Diffuser aerodynamic design - The impact of developments in combustor technology.", International Symposium on Air Breathing Engines, Melbourne, Australia.

Cebecci, T, Hirsh, R.S. and Whitelaw, H., 1979, "On the calculation of laminar and turbulent boundary-layers on longitudinally curved surfaces." AIAA Vol.17, p.434.

Chang, P.S. and Gessner, F.B., 1991, "Experimental investigation of flow about a strut-endwall interaction.", AIAA Journal, Vol.29, pp.2105-2114.

Clauser, F.H., 1953, "Turbulent boundary layers in adverse pressure gradient", Journal of the Aeronautical Sciences, Vol.21, pp.91-108

Coles, D.E., "Proceedings Computation of Turbulent Boundary Layers - 1968 AFOSR-IFP-Stanford Conference", Vol.II, Stanford University, 1969.

Craft, T.J., Launder, B.E. and Suga, K., 1996, "Development and application of a cubic eddy-viscosity model of turbulence.", International Journal of Heat and Fluid Flow, Vol.17, No.2, pp.108-115.

Cumpsty, N.A., 1989, "Compressor aerodynamics.", Longman Scientific & Technical, England.

Daly, B.J. and Harlow, F.H., 1970, "Transport equations in turbulence.", The Physics of Fluids, Vol.13, pp.2634-2649.

Dantec Elektronik, 1991, "Burst Spectrum Analyser User Guide.", Model 57N10/57N14/57N25, Denmark.

Denton, J.D., 1994, "Loss mechanisms in turbomachines.", Transactions of the ASME, Journal of Turbomachinery, Vol.115.

Dominy, R.G. and Kirkham, D.A., 1996, "The influence of blade wakes on the performance of interturbine diffusers.", Journal of Turbomachinery, Vol.118, pp.347-352.

Dring, R.P., 1992, "Radial transport and momentum exchange in an axial compressor.", ASME 92-GT-364, Aeroengine congress, Cologne.

Dring, R.P. and Spear,D.A., 1991, "The effects of wake mixing on compressor aerodynamics.", Transactions of the ASME, Journal of Turbomachinery, Vol.113, No.4, pp.600-607.

Dring, R.P., Joslyn, D.H. and Wagner, J.H., 1983, "Compressor rotor aerodynamics.", Viscous Effects in Turbomachines, AGARD-CP-351.

Durst F. , Jovanovic, J. and Sender,J., 1995, "Measurements in the near-wall region of a turbulent pipe flow.", Journal of Fluid Mechanics, Vol.295, pp.303-335.

Edwards, R.V., 1987, "Report of the special panel on statistical particle bias problems in laser anemometry.", Transactions of the ASME, Journal of Fluids Engineering, Vol.109, pp.89-93.

Eghlima, A. and Kleinstreuer, C., 1985, "Numerical analysis of attached turbulent boundary layers along strongly curved surfaces.", AIAA Journal, Vol.23, No.2, pp.177-184.

El Kersh, A.M.R., 1983, "Investigations into design and performance of annular diffusers." Ph.D. Thesis, Paisley College of Technology.

Ellis, L.B. and Joubert, P.N., 1974, "Turbulent shear flow in a curved duct.", Journal of Fluid Mechanics, Vol.62, pp.65-84.

Eskinazi, S. and Yeh, H., 1956, "An investigation on fully developed turbulent flows in a curved channel.", Journal of Aeronautical Science, Vol.23, p.23.

Finnigan, J.J., 1983, "A streamline coordinate system for distorted two-dimensional shear flows.", Journal of Fluid Mechanics, Vol.130, pp.241-258.

Gerald, C.F., 1980, "Applied numerical analysis - Second Edition.", Addison-Wesley Publishing Company, ISBN 0-201-02696-1.

Gibson, M.M., Jones, W.P. and Younis, B.A., 1981, "Calculation of turbulent boundary layers on curved surfaces.", Physics of Fluids, Vol.24, pp.386-395.

Gibson M.M., and Younis, B.A., 1986, "Calculation of swirling jets with a Reynolds-stress closure", Physics of Fluids, Vol.29, pp.38-48.

Giel, T. and Barnett, D., 1979, "Analytical and Experimental study of statistical bias in laser velocimetry.", Laser Velocimetry and Particle Sizing, Hemisphere Publishing Corp., Washington, pp.86-99.

Gillis, J.C. and Johnston, J.P., 1983, "Turbulent boundary layer flow and structure on a convex wall and its redevelopment on a flat wall.", Journal of Fluid Mechanics, Vol.135.

Gostelow, J.P., 1984, "Cascade aerodynamics.", Pergamon Press Ltd., England, ISBN 0-08-020427-9.

Hanjalic, K. and Launder, B.E., 1976, "A contribution towards a Reynolds stress closure for low Reynolds number turbulence.", Journal of Fluid Mechanics, Vol.74, pp593-610.

Himmelskamp, H., 1945, " Profiluntersuchungen an einem umlaufenden Propellor." Diss. Gottingen 1945, Reports of the Max-Planck-Institit fur Stromungsforschung, Gottingen, No.2, 1950.

Hinze, J.O., 1959, "Turbulence.", McGraw-Hill Book Company, New York.

Hoadley, D., 1970, "Three dimensional turbulent boundary layers in an annular diffuser.", Ph.D. Thesis, Department of Engineering, Cambridge University.

Hoffman, P.H. and Bradshaw, P., 1978, "Turbulent boundary layers on surfaces of mild longitudinal curvature.", IC Aero Report No. 78-04, Department of Aeronautics, Imperial College, London.

Hogg, S. and Leschziner, M.A., 1989, "Computation of highly swirling confined flow with a Reynolds stress turbulence model.", AIAA Journal, Vol.27, No.1, pp57.63.

Irwin, H.P.A.H. and Smith, P.A., 1975, "Prediction of the effect of streamline curvature on turbulence.", Physics of Fluids, Vol.18, No.6, pp.624-630.

Japikse, D., 1984, "Turbomachinery diffuser design technology.", Concepts ETI.

Japikse, D. and Pampreen, R., 1979, "Annular diffuser performance for an automotive gas turbine.", Transactions of the ASME, Journal of Engineering for Power, Vol.101, pp.358-372.

Jeans, A.H. and Johnston, J.P., 1983, "The effects of concave curvature on turbulent boundary layer structure.", Thermosciences Division, Report No. MD-40, Department of Mechanical Engineering, Stanford University.

Johnston, J.P. and Eide, S.A., 1976, "Turbulent boundary layers on centrifugal compressor blades: Prediction of the effects of surface curvature and rotation.", Transactions of the ASME, Journal of Fluids Engineering, pp.374-381.

Jones, W.P. and Launder, B.E., 1972, "The prediction of laminarization with a two-equation model of turbulence.", International Journal of Heat and Mass transfer, Vol.15, pp.301.-314.

Jones, W.P., and Launder, B.E., 1973, "The calculation of low Reynolds number phenomena with a two equation model of turbulence.", International Journal of Heat and Mass Transfer, Vol.16, pp.1119-1130.

Jones, W.P. and Manners, A.P., 1989, "The calculation of the flow through a two dimensional faired diffuser.", Proceedings of the Sixth Symposium on Turbulent Shear Flows, Toulouse, France, pp.17.7.1-17.7.5.

Jones, W.P. and Pascau, A., 1989, "Calculation of confined swirling flows with second moment closure.", Transactions of the ASME, Journal of Fluids Engineering, Vol.111, pp.248-255.

Joslyn, D.H. and Dring, R.P., 1985, "Axial compressor stator aerodynamics.", Transactions of the ASME, Journal of Engineering for Gas Turbines and Power, Vol.107, p.485.

Klebanoff, P.S., 1955, "Characteristics of turbulence in a boundary layer with zero pressure gradient.", NACA Report No.1247.

Klein, A., 1981, "Review: Effects of inlet conditions on Conical-diffuser performance.", Transactions of the ASME, Journal of Fluids Engineering, Vol.103, pp.250-257.

Klein, A., 1988, "The relation between losses and entry flow conditions in short dump diffusers for combustors.", Z Flugwiss Weltraumforsch, Aeronautical Journal.

Klein, A., 1995, "Characteristics of combustor diffusers.", Progress in Aerospace Science, Vol.31, pp.171-271.

Kline, S.J., Cantwell, B.J., and Lilley, G.M., 1981, "The 1980-81 AFSOR-HTTM-STANFORD Conference on complex turbulent flows.", Thermosciences Division, Mechanical Engineering Department, Stanford University.

Kreysig, E., 1988, "Advanced Engineering Mathematics.", John Wiley and Sons, 6th Edition, Chapter 24.

Kumar, D.S. and Kumar, K.L., 1980, "Effect of swirl on pressure recovery in annular diffusers.", I.Mech.E., Journal of Mechanical Engineering Science, Vol.22, pp.305-313.

Lakshminarayana, B. and Davino, R., 1980, "Mean velocity and decay characteristics of the guidevane and stator blade wake of an axial flow compressor.", Transactions of the ASME, Journal of Engineering for Power, Vol.102, pp.50-60.

Launder, B.E., 1988, "Turbulence modelling of three-dimensional shear flows.", Invited Paper 26-1, AGARD Conference Proceedings No.438, Fluid Dynamics of Three Dimensional Turbulent Shear Flows and Transition.

Launder, B.E., and Sharma, B.I., 1974, "Application of the energy-dissipation model of turbulence to the calculation of flow near a spinning disc.", Letters in Heat and Mass Transfer, Vol.1, pp.131-138.

Launder, B.E., and Spalding, D.B., 1974, "The numerical computation of turbulent flows.", Computer methods in applied mechanics and engineering, Vol.3, pp269-289

Launder, B.E., Reece, G. and Rodi, W., 1975,"Progress in the development of a Reynolds stress turbulence closure.", Journal of Fluid Mechanics, Vol.68, pp.537-566.

Launder, B.E. and Shima, N., 1989, "Second moment closure for the near-wall sublayer: Development and application." AIAA Journal, Vol.27, pp.1319-1325.

Leschziner, M.A., 1994, "Refined turbulence modelling for engineering flows.", Presented at ECCOMAS'94 Conference, 5-8 September, Stuttgart, Germany, also see Computational Fluid Dynamics'94, Wiley, p.33.

Leschziner, M.A., and Rodi, W., 1981, "Calculation of annular and twin parallel jets using various discretization schemes and turbulence-model variations.", Transactions of the ASME, Journal of Fluids Engineering, Vol.101, pp.352-360.

Lieblein, S., 1965, "Experimental flow in two dimensional cascades.", Aerodynamic Design of Axial Flow Compressors, NASA SP-36.

Lohmann, R.P., Markowski, S.J., and Brookman, E.T., June 1979, "Swirling flow through annular diffusers with conical walls.", Transactions of the ASME, Journal of Fluids Engineering, pp.224-229.

McLaughlin D.K. and Teiderman W.G., 1973, "Biasing correction for individual realization laser anemometer measurements in turbulent flows.", Physics of Fluids, Vol.16, pp.2082-2088.

Meroney, R.N. and Bradsaw, P., 1975, "Trubulent boundary layer growth over a longitudinally curved surface.", AIAA Journal, Vol.175, pp.479-510.

Moser, R.D. and Moin, P., 1987, "The effect of curvature in wall-bounded turbulent flows.", Journal of Fluid Mechanics, Vol.175, pp.479-510.

Muck, K.C., Hoffman, P.H. and Bradshaw, P., 1985, "The effect of convex surface curvature on turbulent boundary layers.", Journal of Fluid Mechanics, Vol.161, pp.347-369.

Nikuradse, J., 1929, "Untersuchungen uber die Stromungen des Wassers in konvergenten und divergenten Kanalen.", Forschungsarbeiten of the VDI, No.289.

Pfeil, H. and Going, M., 1987, "Measurements of the turbulent boundary layer in the diffuser behind an axial compressor.", Transactions of the ASME, Journal of Turbomachinery, Vol.109, pp.405-412.

Prabhu A., Narasimha, R. and Rao, B.N.S., 1983, "Structure and mean flow similarity in curved turbulent boundary layers.", Proceedings of the IUTAM Symposium on the Structure of Complex Turbulent Shear Flows, Marseille.

Prandtl, L., 1925, "Uber die ausgebildete Turbulenz.", ZAMM, Vol.5, pp136-139, and Proceedings of the Second International Congress of Applied Mechanics, Zurich.

Prato, J., Lakshminarayana, B. and Suryavamshi, H., 1995, "Experimental investigation of the mean flow field at the exit of an embedded stator in a multistage axial flow compressor.", ISABE 95-7061.

Raj, R. and Lakshminarayana, B., 1973, "Characteristics of the wake behind a cascade of aerofoils.", Journal of Fluid Mechanics, Vol.61, pp.707-730.

Ramaprian, B.R. and Shivaprasad, B.G., 1977, "Mean flow measurements in turbulent boundary layers along mildly curved surfaces", AIAA Journal, Vol.15, pp.189-196.

Ravindrinath, A. and Lakshminarayana, B., 1980, "Mean velocity and decay characteristics of the near and far-wake of a compressor rotor blade of moderate loading.", Transactions of the ASME, Journal of Engineering for Power, Vol.102, pp.535-548.

Reynolds, W.C., 1970, "Computation of turbulent flows - state of the art.", Stanford University, Thermosciences Division, Report No. MD-27.

Roach, P.E. and Turner, J.T., 1985, "Secondary loss generation by gas turbine support struts.", International Journal of Heat and Fluid FLow, Vol.6, No.2, pp.79-88.

Rodi, W. and Scheuerer, G., 1983, "Calculation of curved shear layers with two-equation turbulence models.", Physics of Fluids, Vol.26, pp.1422-1436.

Rodi, W. and Scheuerer, G., 1986, "Scrutinizing the k-ε turbulence model under adverse pressure gradient conditions.", Transactions of the ASME, Journal of Fluids Engineering, Vol.108, pp.174-179.

Rosenhead, L., 1963, "Laminar Boundary Layers.", Clarendon Press, Oxford.

Rotta,J.C., 1951, "Statistische Theorie nichthomogener Turbulenz.", Z.Phys., Vol.129, p.547.

Schlichting, H., "Boundary layer theory.", McGraw-Hill Book Company, 1968.

Schubauer, G.B. and Klebanoff, P.S., 1951, "Investigation of separation of the turbulent boundary layer", NACA Report No.1030.

Schwartz, I.R., 1948, "Investigation of an annular diffuser-fan combination handling rotating flow.", NACA RM No. L9B28.

Scott, C.J. and Rask, D.R., 1973, "Turbulent viscosities for swirling flow in a stationary annulus.", Transactions of the ASME, Journal of Fluids Engineering, pp.557-566.

Senoo, Y., Kawaguchi, N., Kojima, T. and Nishi, M., 1981, "Optimum strut-configuration for downstream annular diffusers with variable swirling inlet flow.", Transactions of the ASME, Journal of Fluids Engineering, Vol.103, pp.294-298.

Shima, N., 1993, "Prediction of turbulent boundary layers with a second-moment closure: Part I - Effects of periodic pressure gradient, wall transpiration and free-stream turbulence.", Transactions of the ASME, Journal of Fluids Engineering, Vol.115, pp.56-63.

Shima, N., 1993, "Prediction of turbulent boundary layers with a second-moment closure: Part II - Effects of streamline curvature and spanwise rotation.", Transactions of the ASME, Journal of Fluids Engineering, Vol.115, pp.64-69.

Shivaprasad, B.G. and Ramaprian, B.R., 1978, "Turbulence measurements in boundary layers along mildly curved surfaces.", Transactions of the ASME, Journal of Fluids Engineering, Vol.100, pp.37-46.

Sitaram, N., Lakshminarayana,B. and Ravidranath, A., 1981, "Conventional probes for the relative flow measurement in a turbomachinery rotor blade passage.", Transactions of the ASME, Journal of Engineering for Power, Vol.103.

Smits, A.J., Young, S.T.B., and Bradshaw, P., 1979, "The effect of short regions of high surface curvature on turbulent boundary layers.", Journal of Fluid Mechanics, Vol.94, pp.209-242.

So, R.M.C., 1975, "Momentum integral for curved shear layers.", Transactions of the ASME, Journal of Fluids Engineering, pp.253-256.

So, R.M.C. and Mellor, G.L., 1975, "Experiment on turbulent boundary layers on a concave wall.", Aeronautical Quarterly, Vol.26, pp.25-40.

So, R.M.C. and Mellor, G.L., 1973, "Experiment on convex curvature effects in turbulent boundary layers.", Journal of Fluid Mechanics, Vol.60, pp.43-62.

Sovran, G. and Klomp, E.D., 1967, "Experimentally determined optimum geometries for rectilinear diffusers with rectangular, conical or annular cross-section.", Fluid Dynamics of Internal Flow, ed. G.Sovran, Elsevier Publishing Co.

Srinath, T., 1968, "An investigation of the effects of swirl on the flow regimes and performance of annular diffusers with equal inner and outer cone angles.", M.Sc. Thesis, Mechanical Engineering Department, University of Waterloo.

Stevens, S.J., 1970, "Turbulent incompressible flow in annular diffusers", Ph.D. Thesis, Department of Transport Technology, Loughborough University of Technology.

Stevens, S.J. and Ecclestone, B., 1969, "The performance of combustion chamber annular diffusers.", Department of Transport Technology Report No. TT69R02, Loughborough University of Technology.

Stevens, S.J. and Fry, P., 1973, "Measurement of boundary layer growth in annular diffusers.", Journal of Aircraft, Vol.10, pp.73-80.

Stevens, S.J., Harasgama, S.P. and Wray, A.P., 1984, "The influence of blade wakes on the performance of combustor shortened pre-diffusers.", Journal of Aircraft, Vol.21., No.9, pp.641-648."

Stevens, S.J. and Markland, 1968, "The effect of inlet conditions on the performance of two annular diffusers.", ASME Paper No. 68-WA/FE-38.

Stevens, S.J., Williams, G.J., and Nayak, U.S.L., 1978, "The influence of inlet conditions on the performance of annular diffusers.", Proceedings of the Joint Sumposium on Design and Operation of Fluid Machinery, Colarado State University, USA.

Stevens, S.J. and Wray, A.P., 1985, "The influence of blade wakes on the performance of outwardly curved combustor pre-diffusers.", AIAA-85-1291., 21st Joint Propulsion Conference.

Stevens, S.J. and Young, K.F., 1987, "Axial compressor outlet guide vane aerodynamics.", AIAA-87-1744, 23rd Joint Propulsion Conference.

Swales, C., Rickards, J., Brake, C.J. and Barrett, R.V., 1993, "Development of a pin-hole meter for aligning 2D laser doppler anemometers.", Dantec Information, Vol.12, pp.2-5.

Tamigniaux, T.L.B. and Oates, G.C., 1986, "Effect of a nearby solid surface on a five-hole pressure probe.", AIAA Journal, Vol.24.

Tani, I., 1962, "Production of longitudinal vortices in the boundary layer along a concave wall.", Journal of Geographical Research, Vol.67, pp.3075-3080.

Taylor, G.I., 1915, "The transport of vorticity and heat through fluids in turbulent motion.", Philisophical transactions, Vol.215, pp.1-26.

Thayer, E.B., 1971, "Evaluation of curved-wall annular diffusers." ASME Paper No. 71-WA/FE-35.

Versteeg, H.K. and Malalasekera, W., 1995, "An introduction to computational fluid dynamics", Longman Scientific and Technical, England.

von Doenhoff, A.E. and Tetervin, N., 1943, "Determination of general relations for the behaviour of turbulent boundary layers.", NACA TR No. 772.

Von Karman, T., 1934, "Some aspects of the turbulence problem.", Proceedings of the 4th International Congress of Applied Mechanics, Cambridge, p.54.

Wattendorf, F.L., 1935, "A study of the effect of curvature on fully developed turbulent flow.", Proceeding of the Royal Society of Aeronautics, Vol.148, p.565.

Wilcken, H., 1930, "Effect of curved surfaces on turbulent boundary layers.", NASA TT F-11421, translation of Ing.-Arch., Vol.1,p.357.

Wilcox, D.C., 1993, "Comparison of two-equation turbulence models for boundary layers with pressure gradient.", AIAA Journal, Vol.31, No.8, pp.1414-1421.

Williams, G.J., 1972, "The influence of inlet conditions on the boundary layer growth and overall performance of annular diffusers.", Ph.D. Thesis, Department of Transport Technology, Loughborough University of Technology.

Williams, G.J., and Stevens, G.J., 1971, "The influence of initial turbulence on the performance of annular diffusers.", Loughborough University of Technology, Department of Transport Technology, Report No. TT 7101.

Wolf, S. and Johnston, J.P., 1966, "Effects of nonuniform velocity profiles on flow regimes and performance in two-dimensional diffusers.", ASME Paper No. 68-WA/FE-25.

Wray, A.P., 1986, "The analysis of 5-hole probe test data using generalised computer software.", Report No. TT86R06, Department of Transport Technology, Loughborough University of Technology.

Wray, A.P., 1997, Ph.D. Thesis, (to be submitted), Department of Transport Technology, Loughborough University of Technology.

Wray, A.P., Carrotte, J.F. and Wilson, C.W., 1993, "The development of a large annular facility for testing gas turbine combustor diffuser systems.", AIAA-93-2546, 29th Joint Propulsion Conference.

Yeh, H., 1958, "Boundary layers along annular walls in a swirling flow.", Transactions of the ASME, Vol.80, pp.767-776.

You, S.M., and Simon, T.W., and Kim,J., 1989, "Free-stream turbulence effects on convex-curved turbulent boundary layers.", Transactions of the ASME, Journal of Heat Transfer, Vol.111, pp.66-72.

Young, A.D., 1989, "Boundary layers.", BSP Professional Books, ISBN 0-632-02122-5, pp.156-159.

Tables

x/L	δ	δ^*	θ	H	δ	δ^*	θ	H
-0.550	15.44	2.42	1.78	1.36	16.62	2.31	1.72	1.34
0.000	14.53	1.61	1.27	1.27	18.87	3.24	2.35	1.38
0.125	15.26	1.67	1.31	1.28	18.66	3.43	2.44	1.40
0.250	14.83	1.86	1.40	1.33	20.73	3.43	2.54	1.35
0.375	19.45	3.23	2.20	1.47	17.98	2.57	2.00	1.28
0.500	22.30	4.35	2.81	1.55	19.66	2.31	1.85	1.25
0.625	26.04	6.35	3.72	1.64	20.97	1.81	1.50	1.21
0.750	28.73	7.36	4.43	1.66	20.40	2.08	1.65	1.26
0.875	30.34	7.73	4.77	1.62	23.42	2.22	1.80	1.23
1.000	27.80	5.72	3.99	1.43	23.65	3.14	2.41	1.30
1.400	27.50	4.97	3.62	1.37	25.43	3.52	2.63	1.34

Table 4.1: Integral Boundary Layer Parameters

x/L	δ	δ^*	θ	H	δ	δ^*	θ	H
0.0	17.60	1.99	1.52	1.31	16.19	2.17	1.56	1.38
0.375	23.57	3.59	2.58	1.40	22.43	1.87	1.53	1.22
0.750	37.12	8.43	5.73	1.47	18.77	1.00	0.81	1.23
1.40	31.53	5.44	4.05	1.34	24.43	2.44	1.78	1.37

Table 4.2: Integral Boundary Layer Parameters (Compressor)

Figures

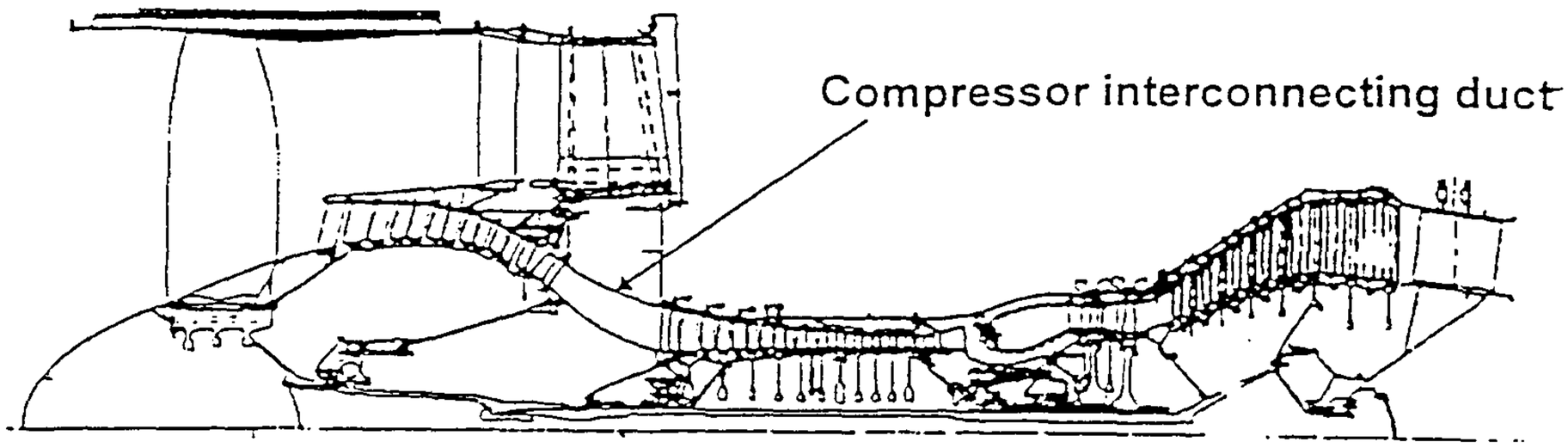

Fig.1.1.a Compressor interconnecting duct. (PW 4000)

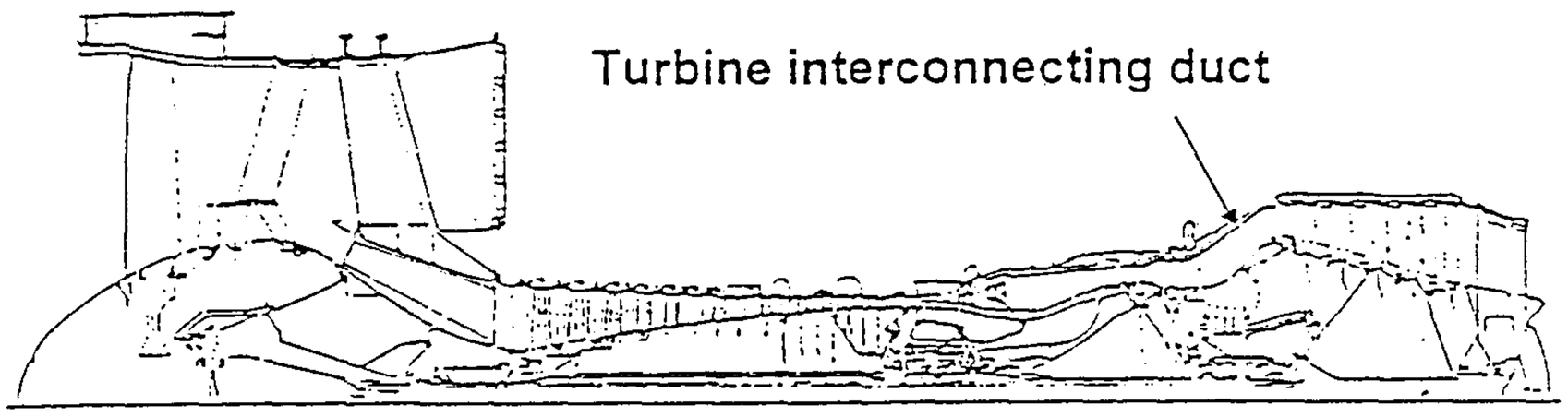

Fig.1.1.b Turbine interconnecting duct. (GE CF6)

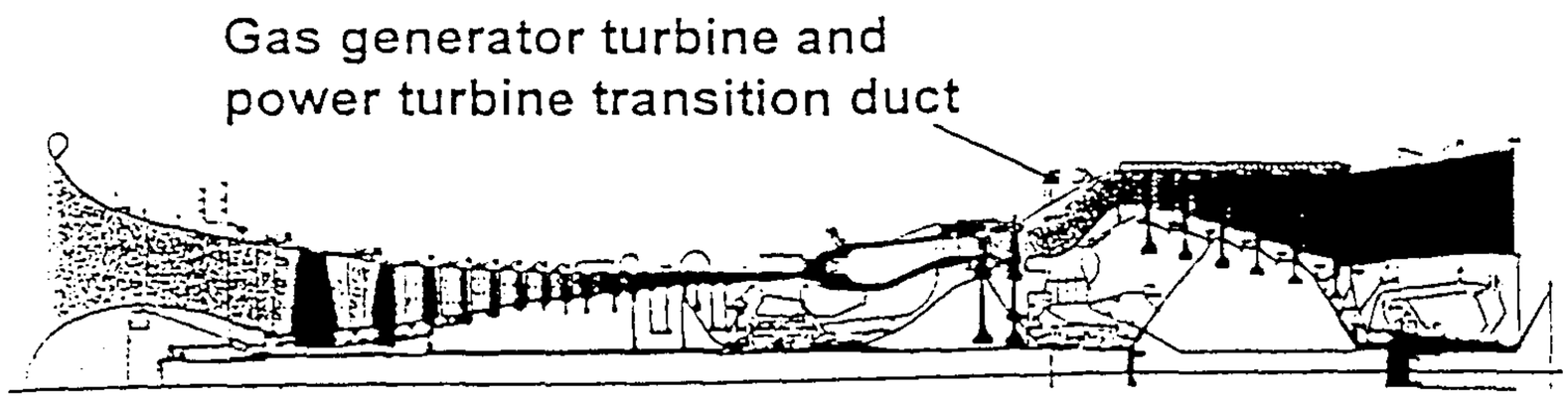

Fig.1.1.c Gas generator turbine and power turbine ducts. (GE LM2500+)

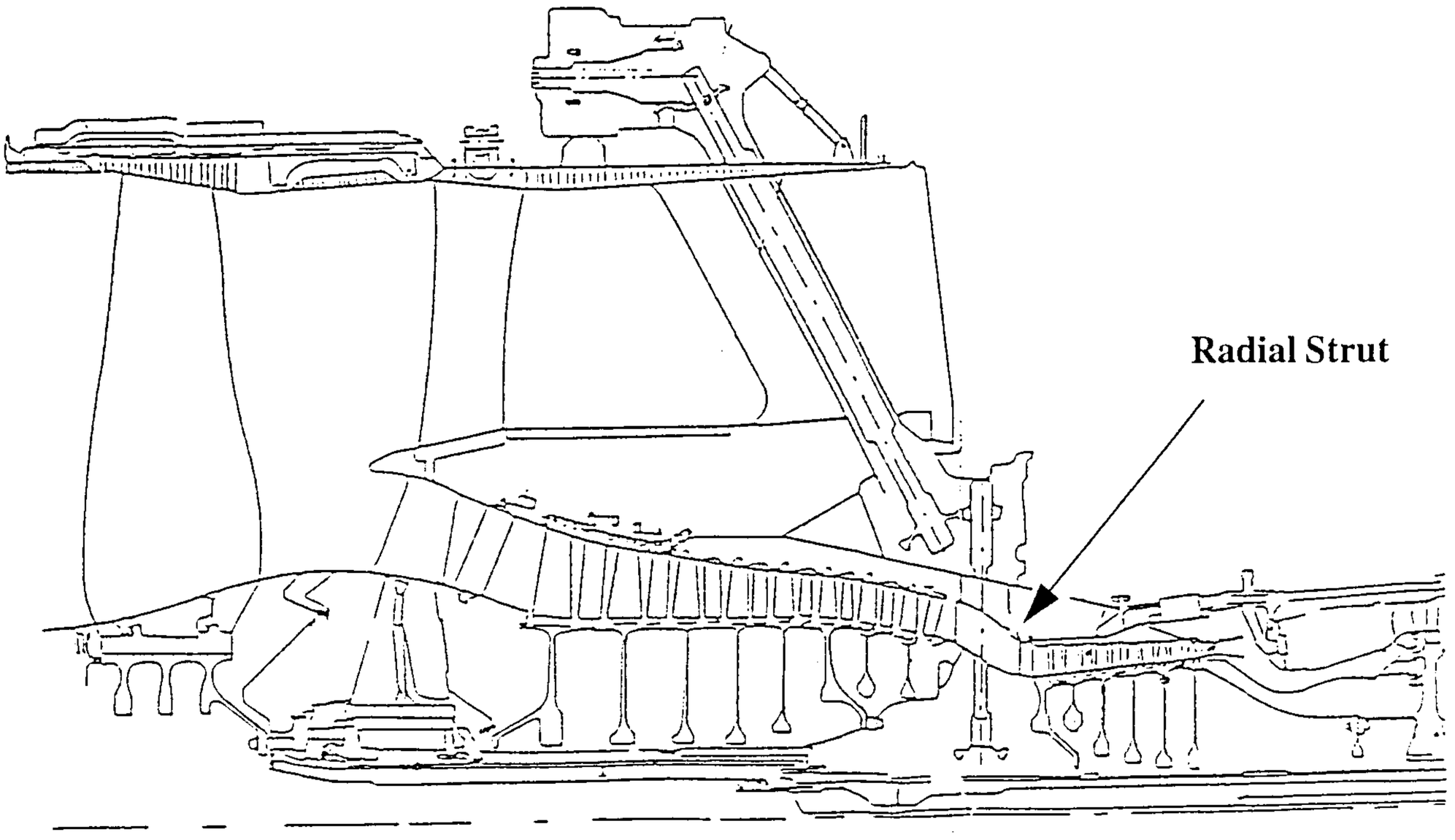

Fig.1.2 Radial strut within compressor interconnecting duct (RR Trent).

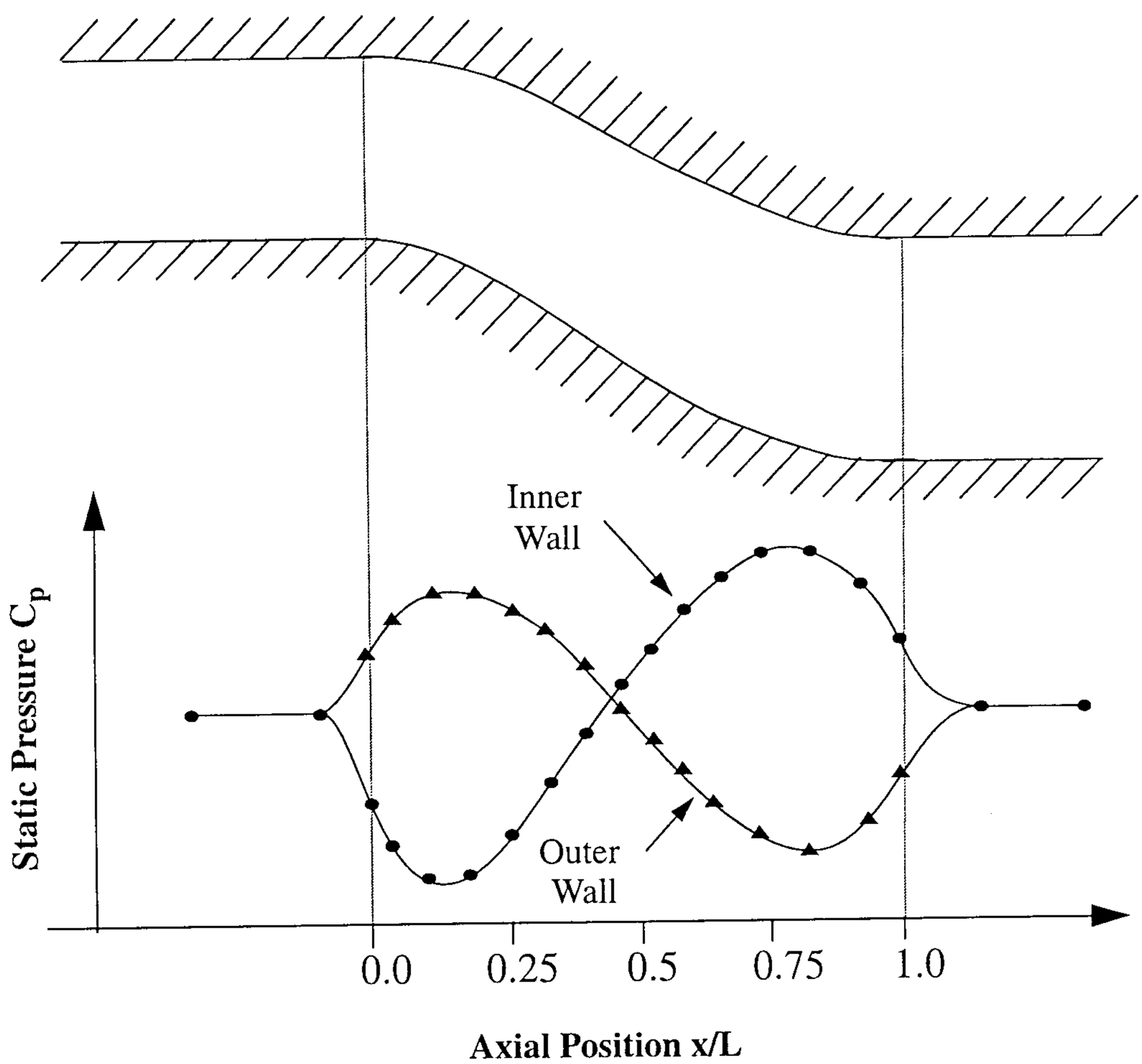

Fig.1.3 Schematic of the axial variation of wall static pressure within an S-shaped duct

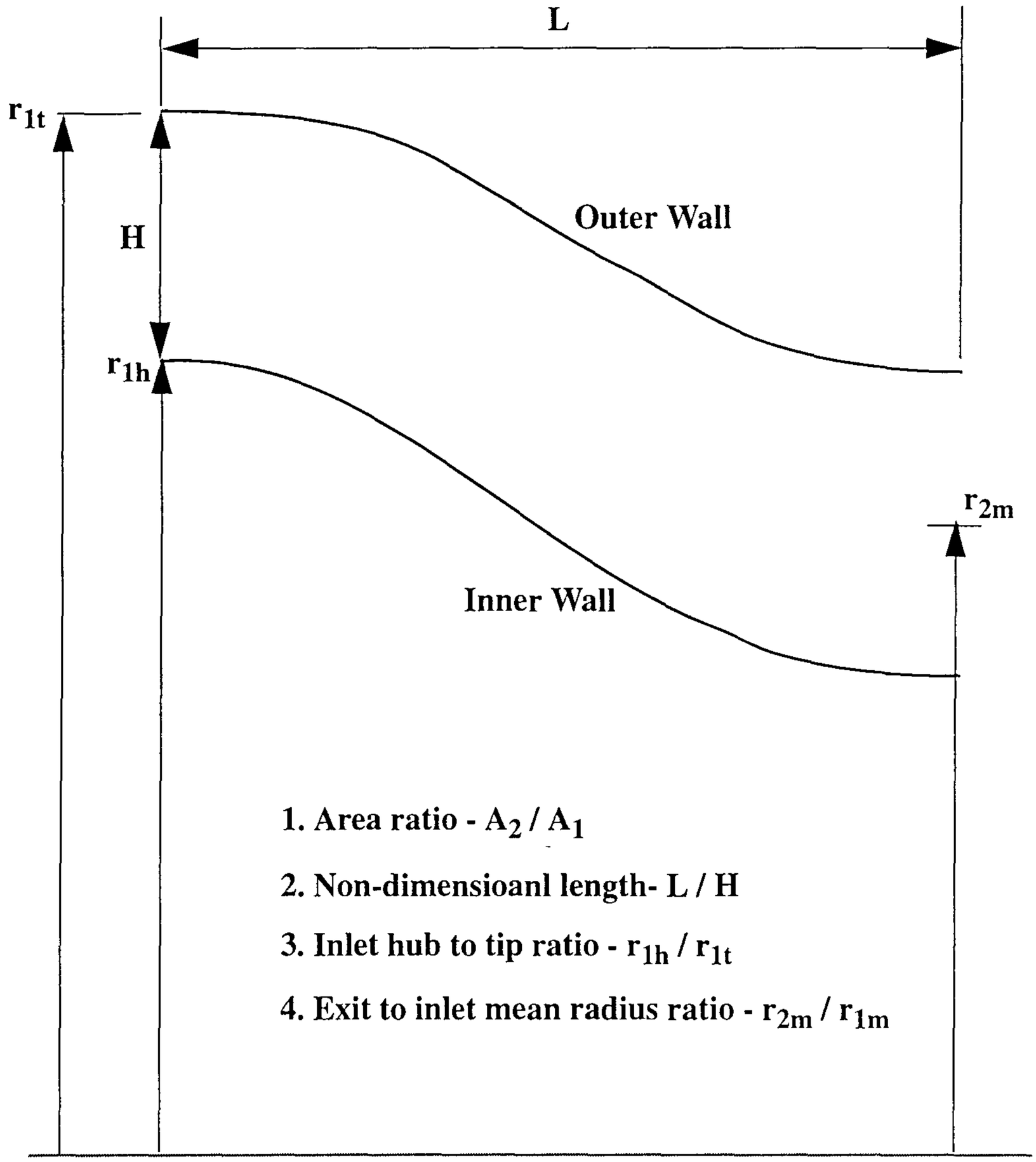

Fig.1.4 Definition of the S-shaped duct geometrical parameters.

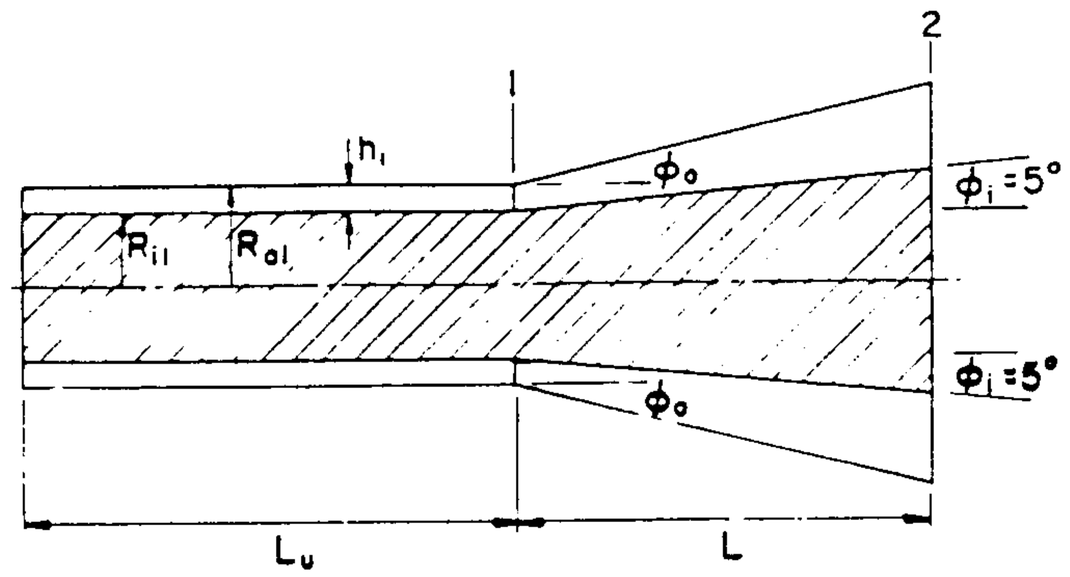

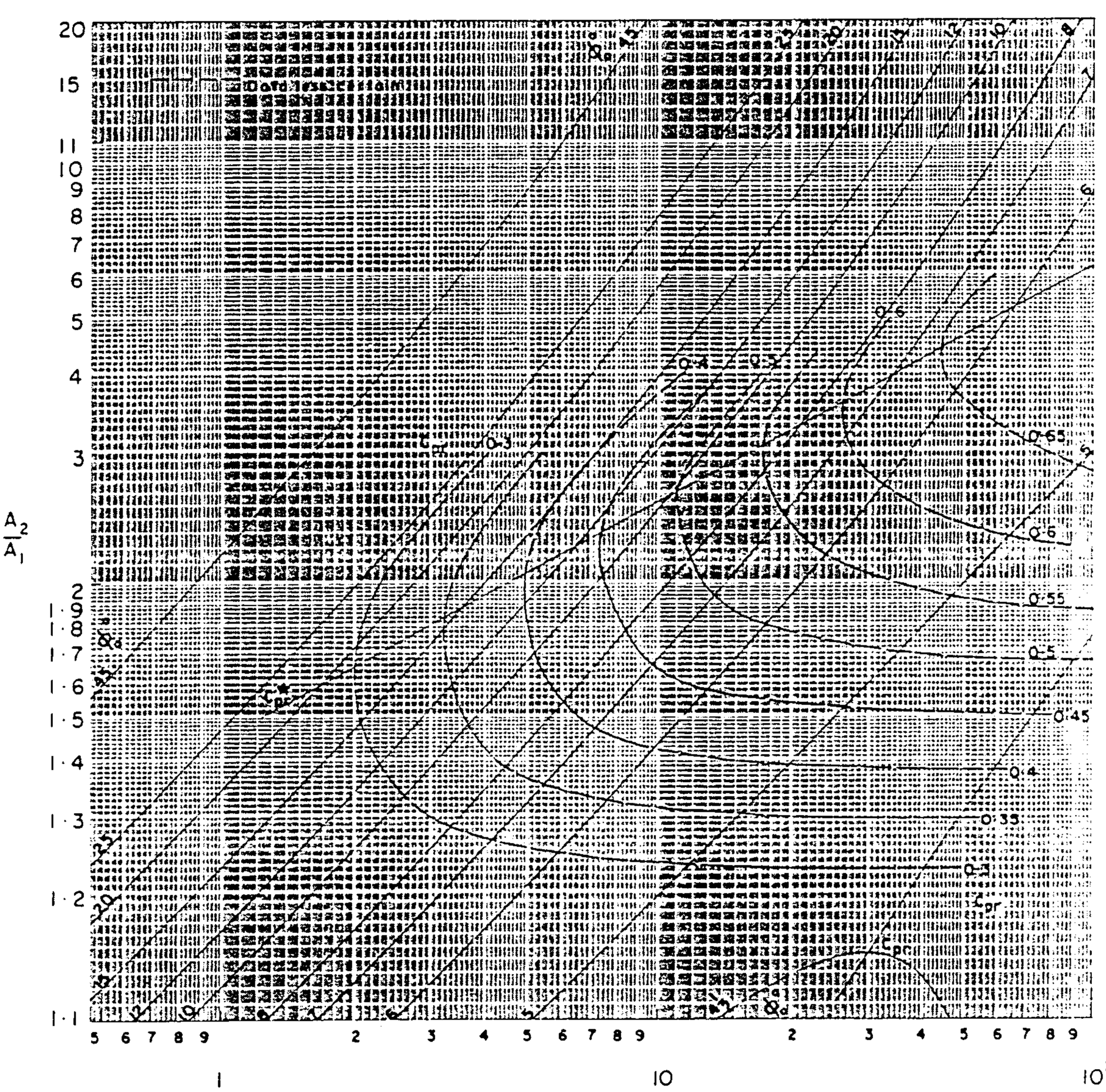

STATIC-PRESSURE RECOVERY COEFFICIENT, ANNULAR DIFFUSERS WITH $\phi_i = 5°$ AND $r_1 = 0·8$,
WITH TAILPIPES $\frac{L_d}{h_2} = 4$, FULLY-DEVELOPED ENTRY FLOW, $\frac{L_u}{h_1} \geqslant 100$

Fig.1.5 Static pressure recovery map for straight walled annular diffusers.

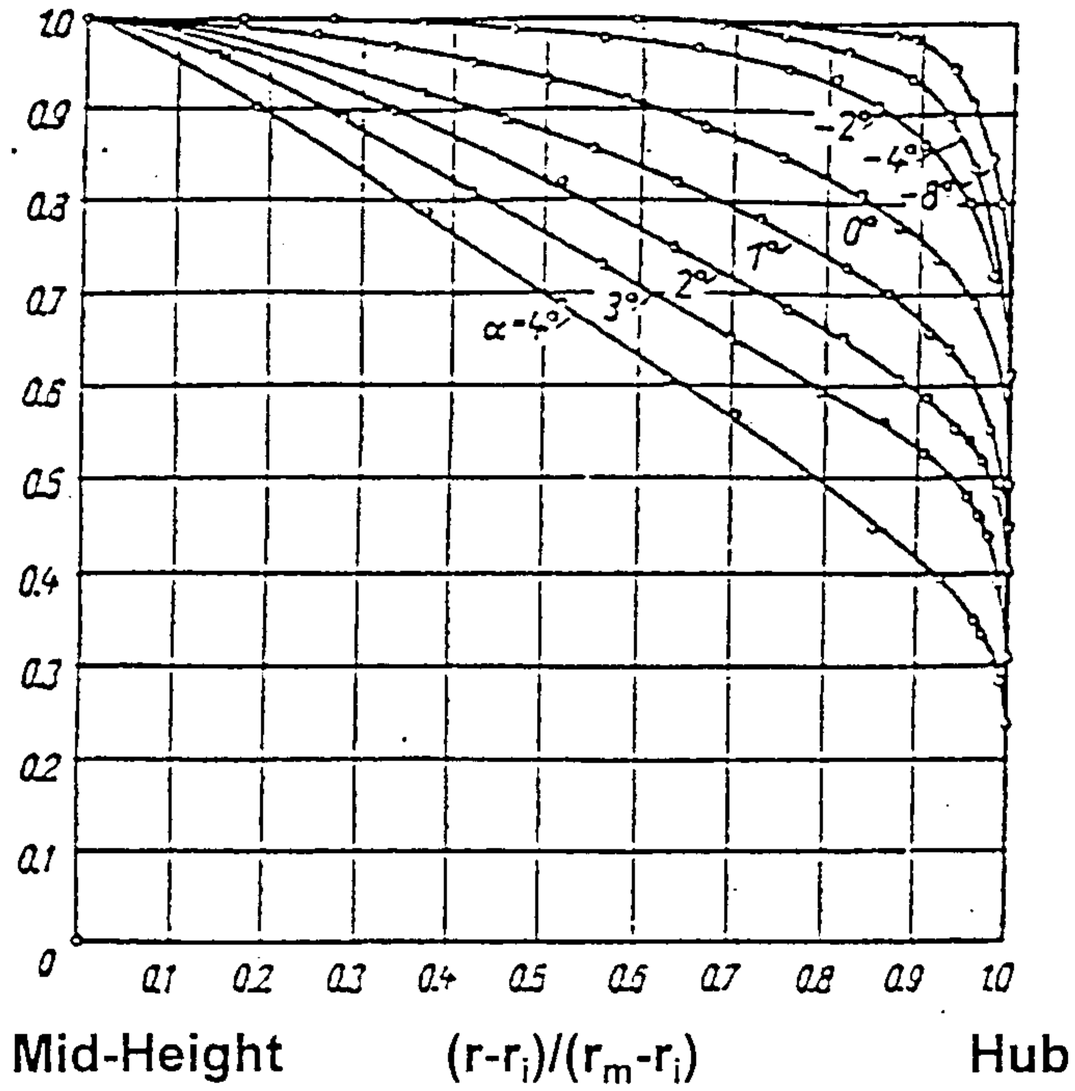

Fig.1.6.a Mean velocity distributions in convergent and divergent channels after Nikuradse (1929).

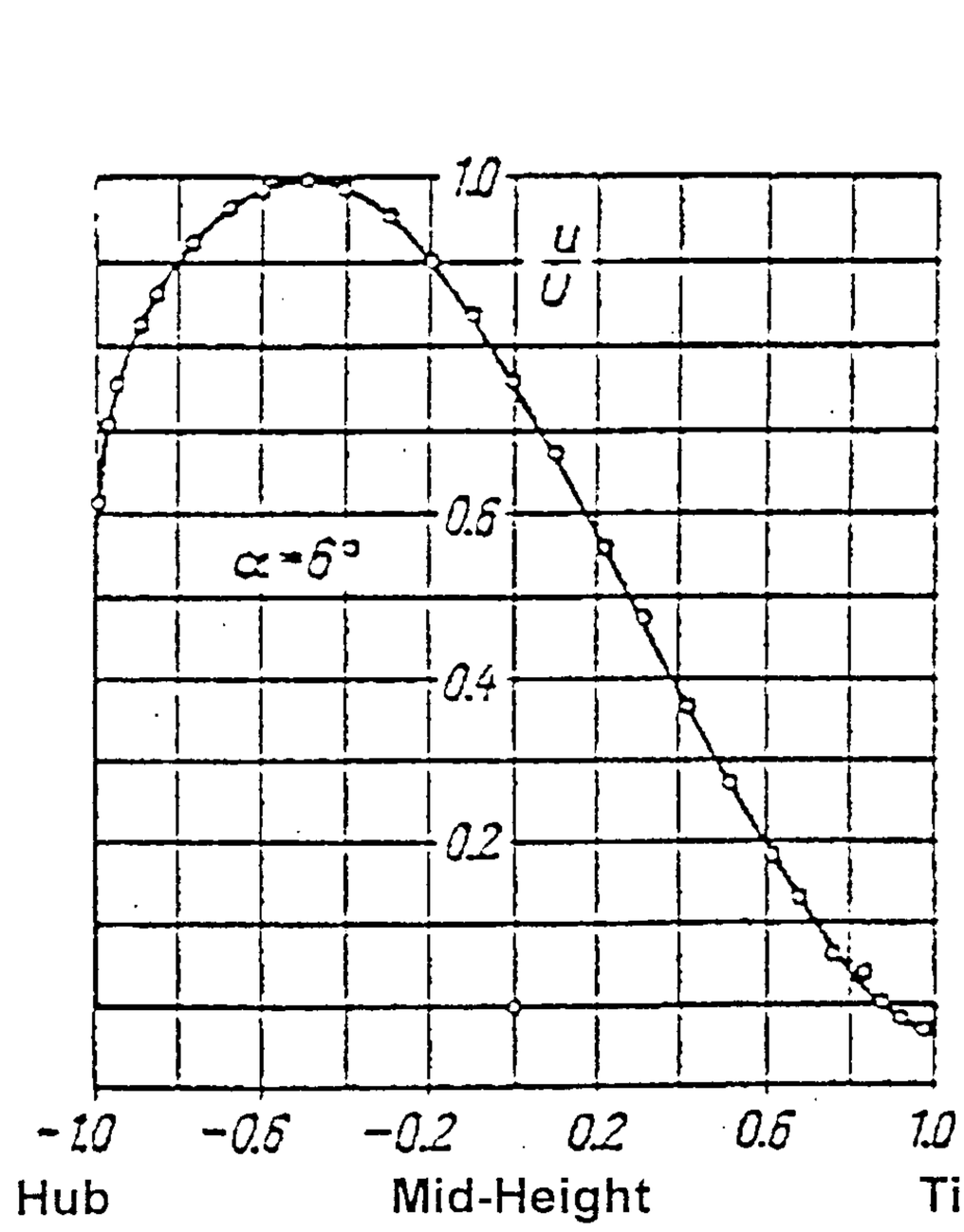

Fig.1.6.b Flow separation in a divergent channel (α=6 degrees) after Nikuradse (1929).

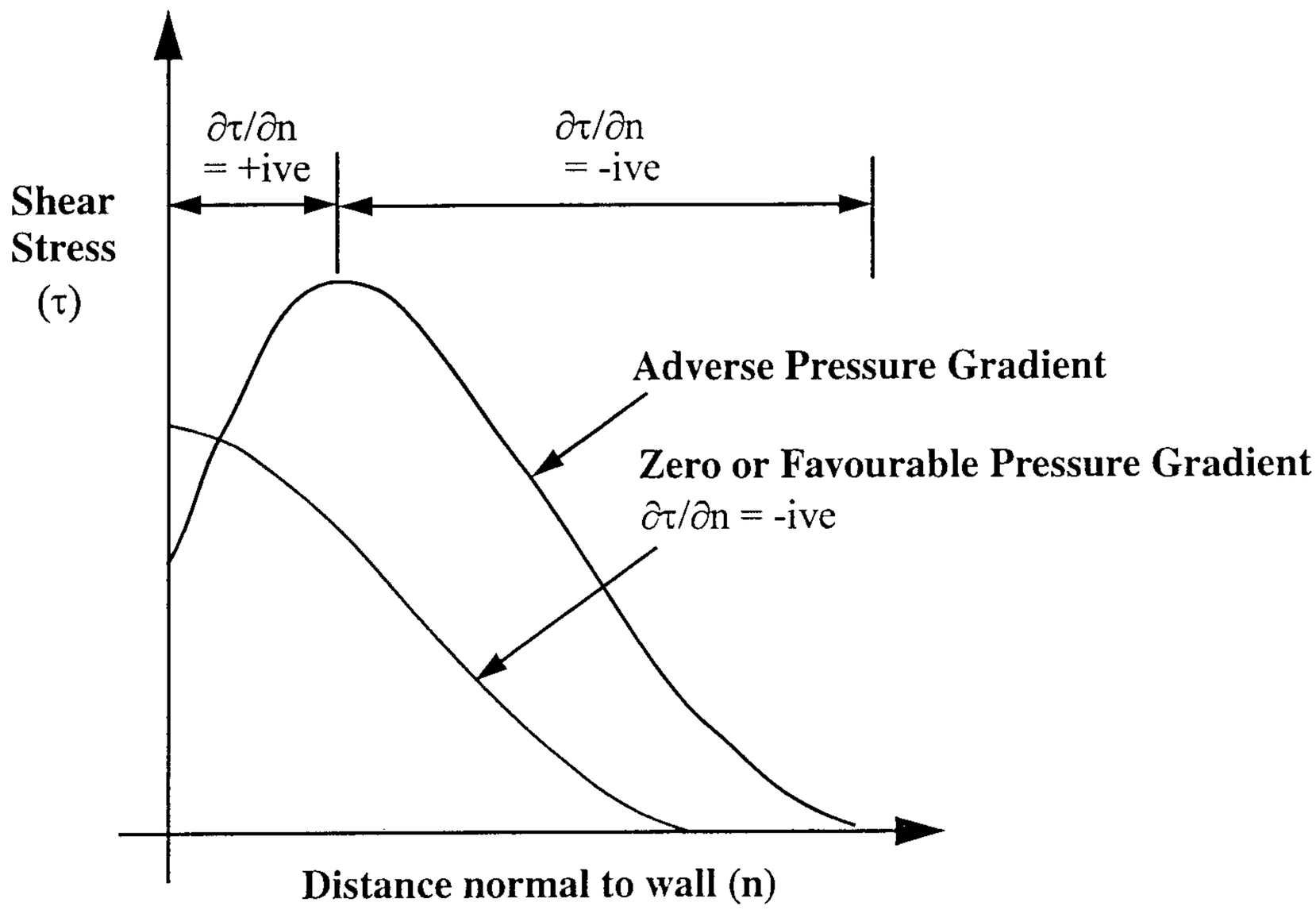

Fig.1.7 The effect of adverse pressure gradient on the shear stress distribution.

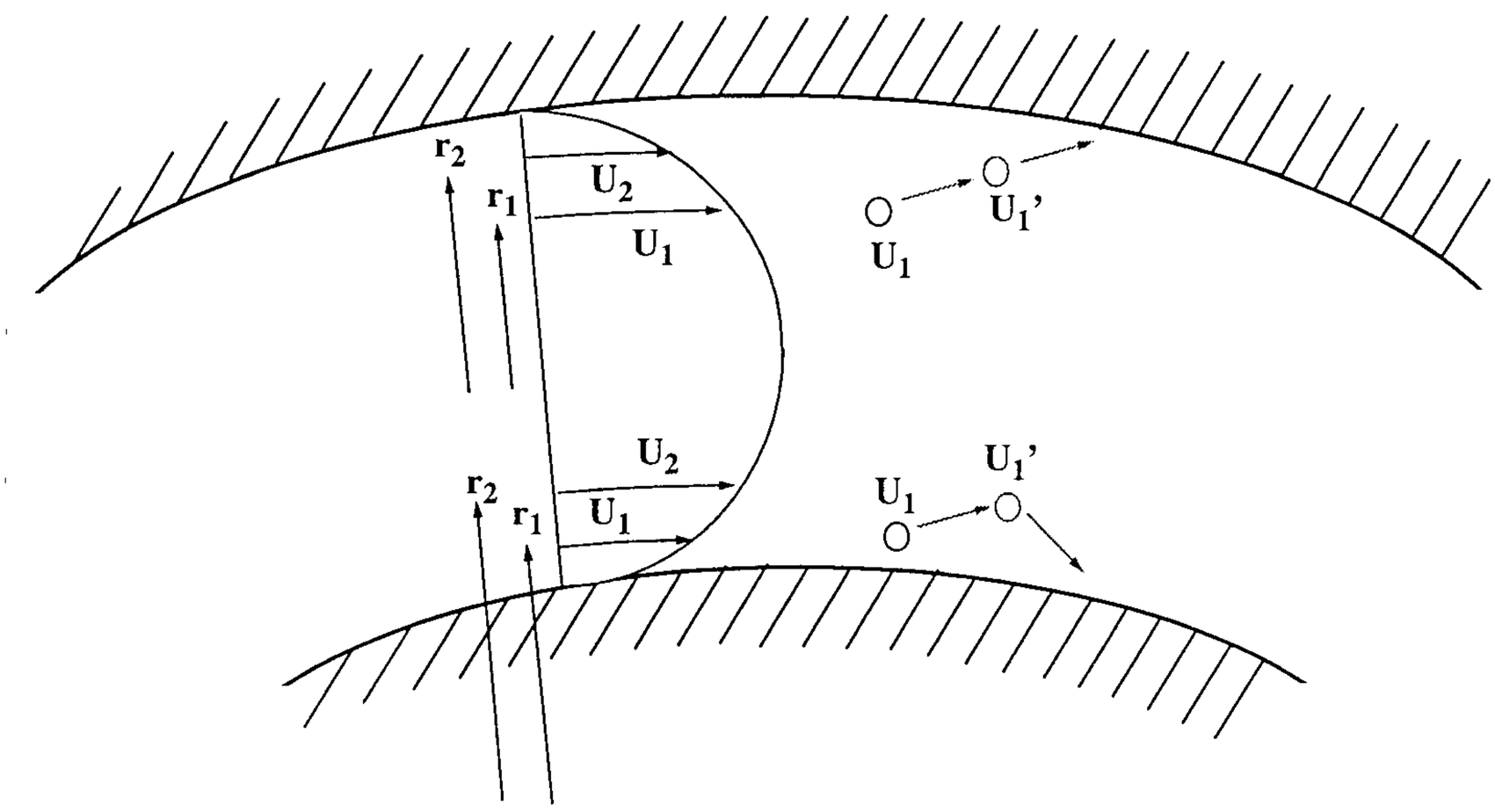

Fig.1.8 The motion of a displaced element in a curved flow.

Strain rate due to simple shear = $\left(1+\frac{n}{R}\right)\frac{\partial U}{\partial n}$

Extra strain rate due to streamwise curvature = $\frac{\partial V}{\partial s}-\frac{U}{R}$

Extra strain rate due to streamwise pressure gradient = $\frac{\partial U}{\partial s}+\frac{V}{R}$

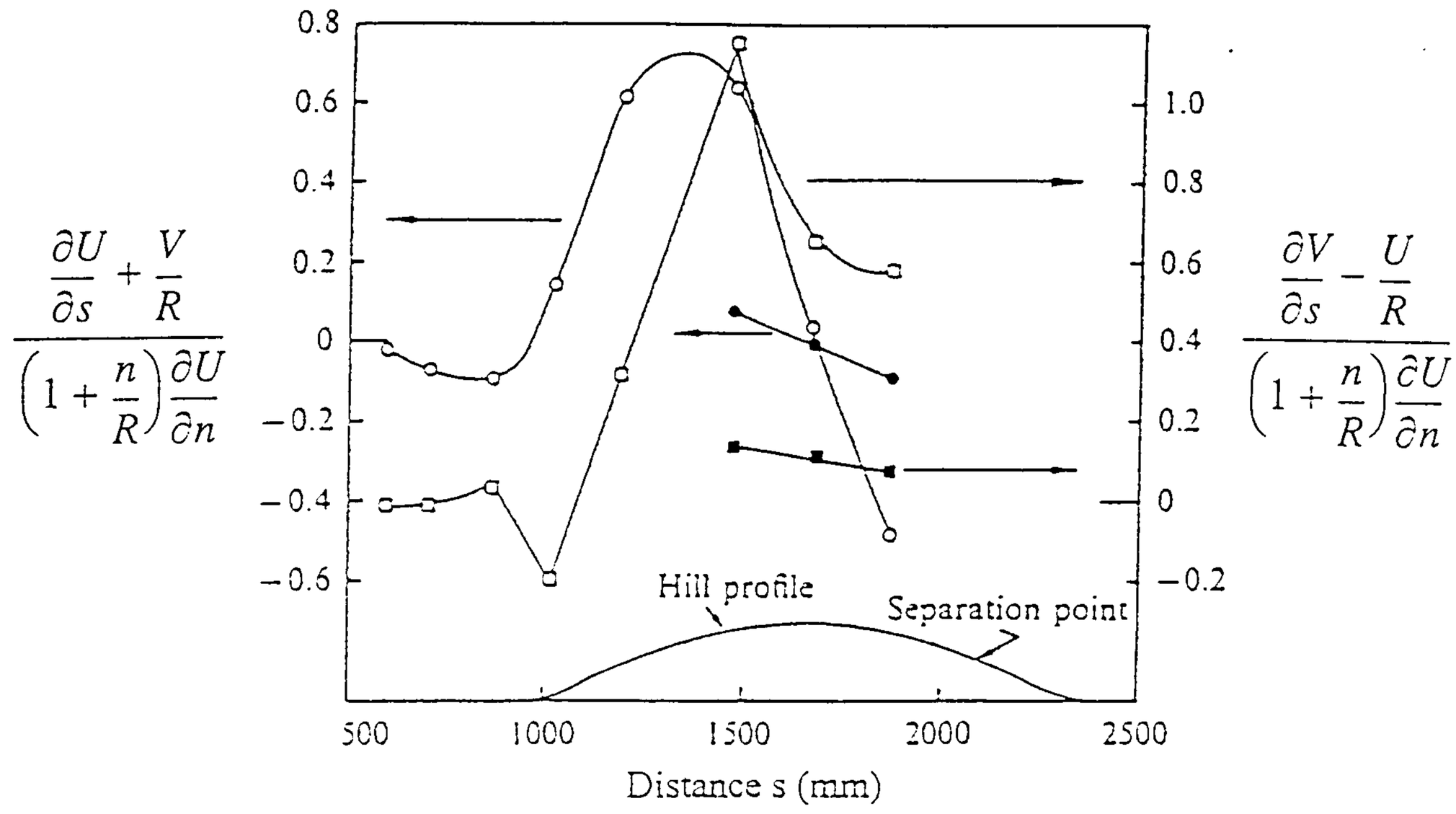

Open symbols refer to n/δ=0.5, solid symbols refer to n/δ=1.0

Fig.1.9 The ratio of the extra strain rates to simple shear after Baskaran et. al. (1991)

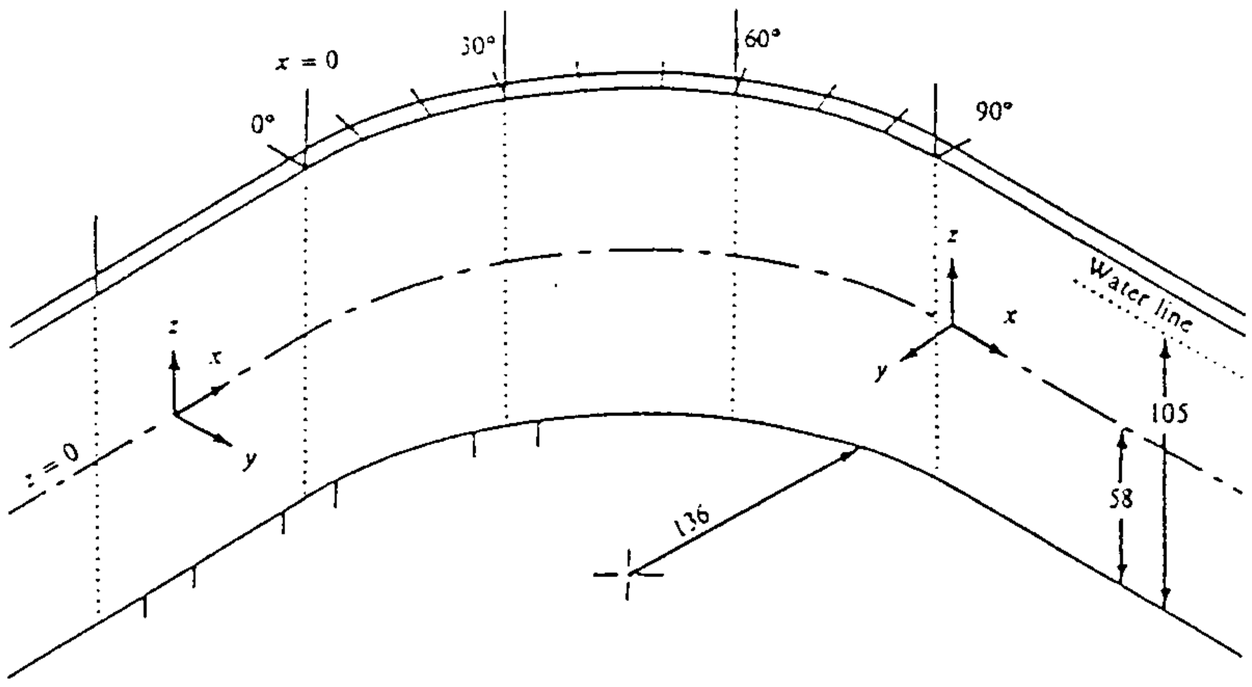

The Concave Test Wall

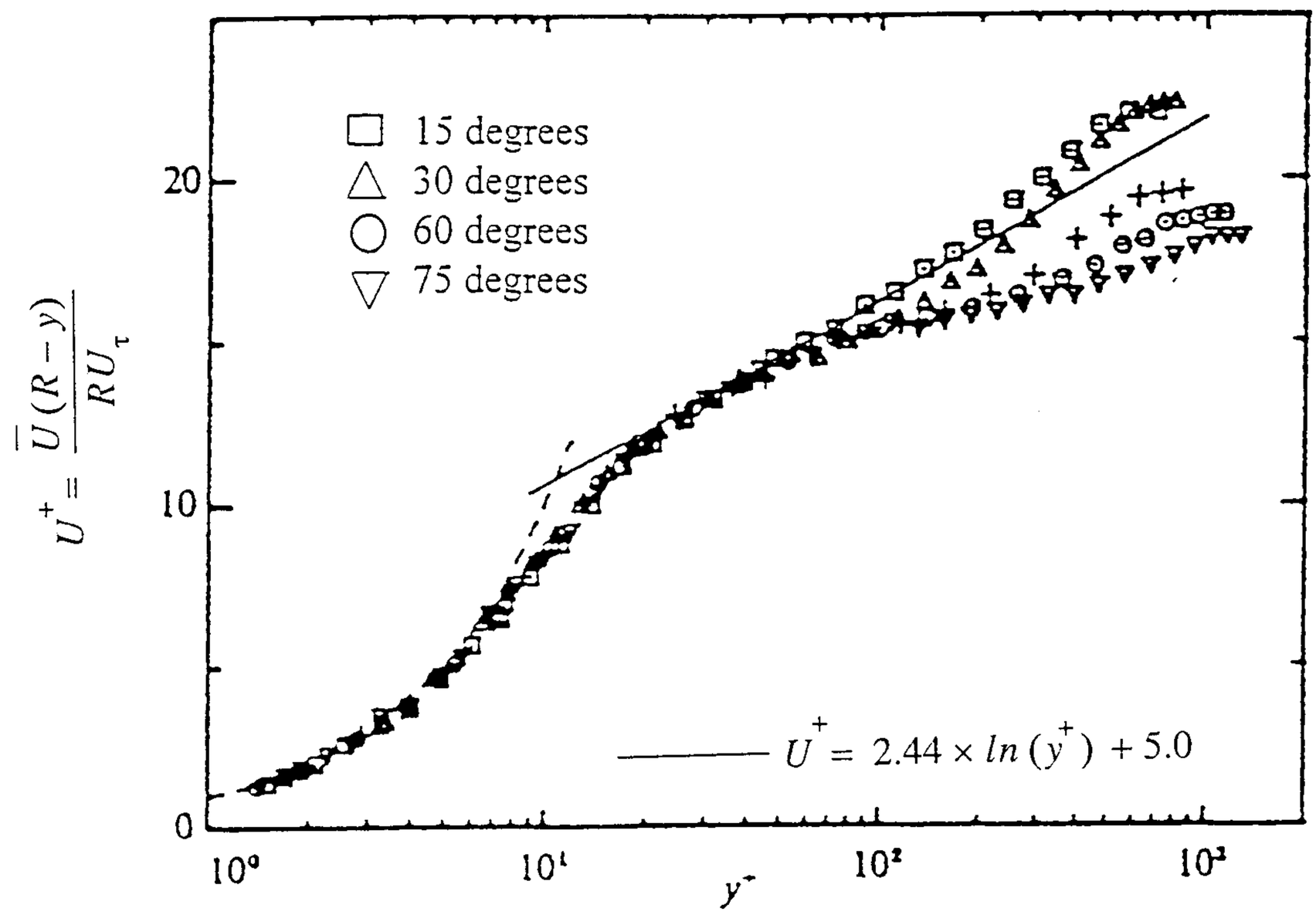

Fig.1.10 The effect of curvature on mean velocity profiles in log-law form after Barlow and Johnston (1988).

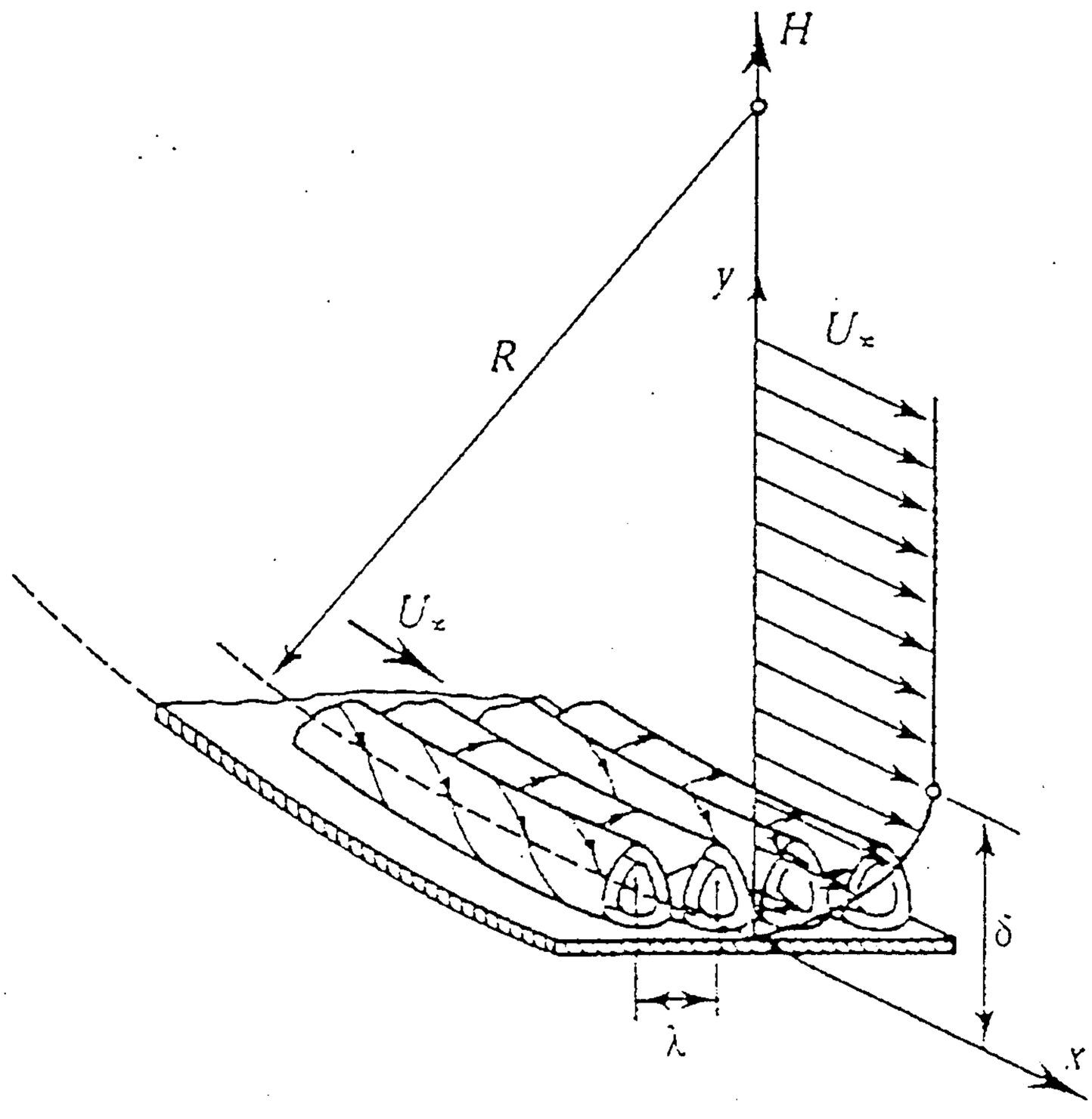

Fig.1.11 Taylor-Gortler vortices (reproduced from Schlichting, 1968).

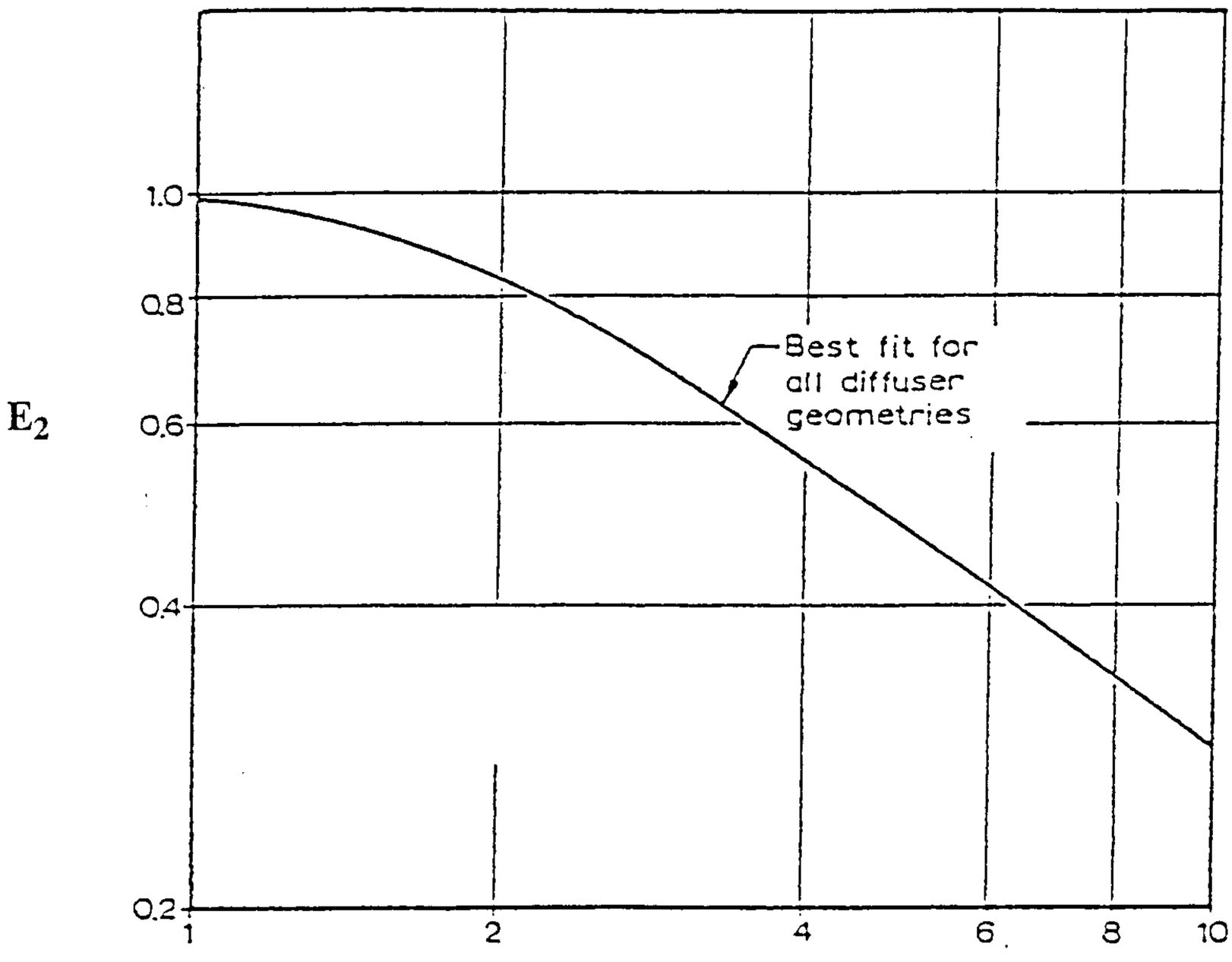

E_2

$$AR(100B_1)^{1/4}$$

where;

E_2 = effective area fraction

AR = ratio of exit to inlet area

B_1 = inlet blockage fraction

$AR(100B_1)^{1/4}$ = empirical parameter proportional to δ^*

Fig.1.12 The effect of inlet boundary layer blockage on optimun diffuser performance, after Sovran and Klomp (1967)

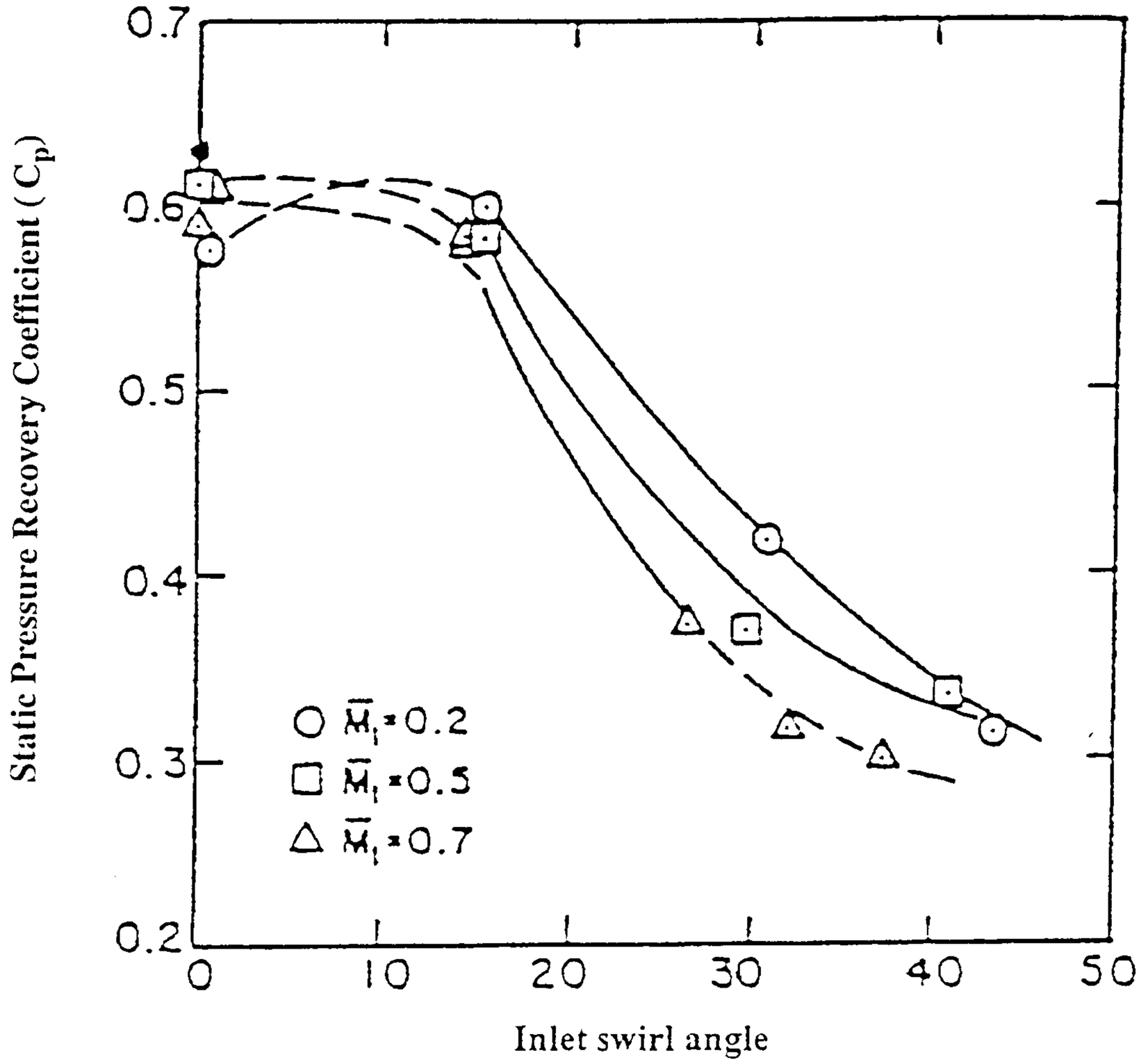

Fig.1.13 The variation of static pressure recovery (C_p) with both swirl angle and Mach number, after Japikse and Pampreen (1979)

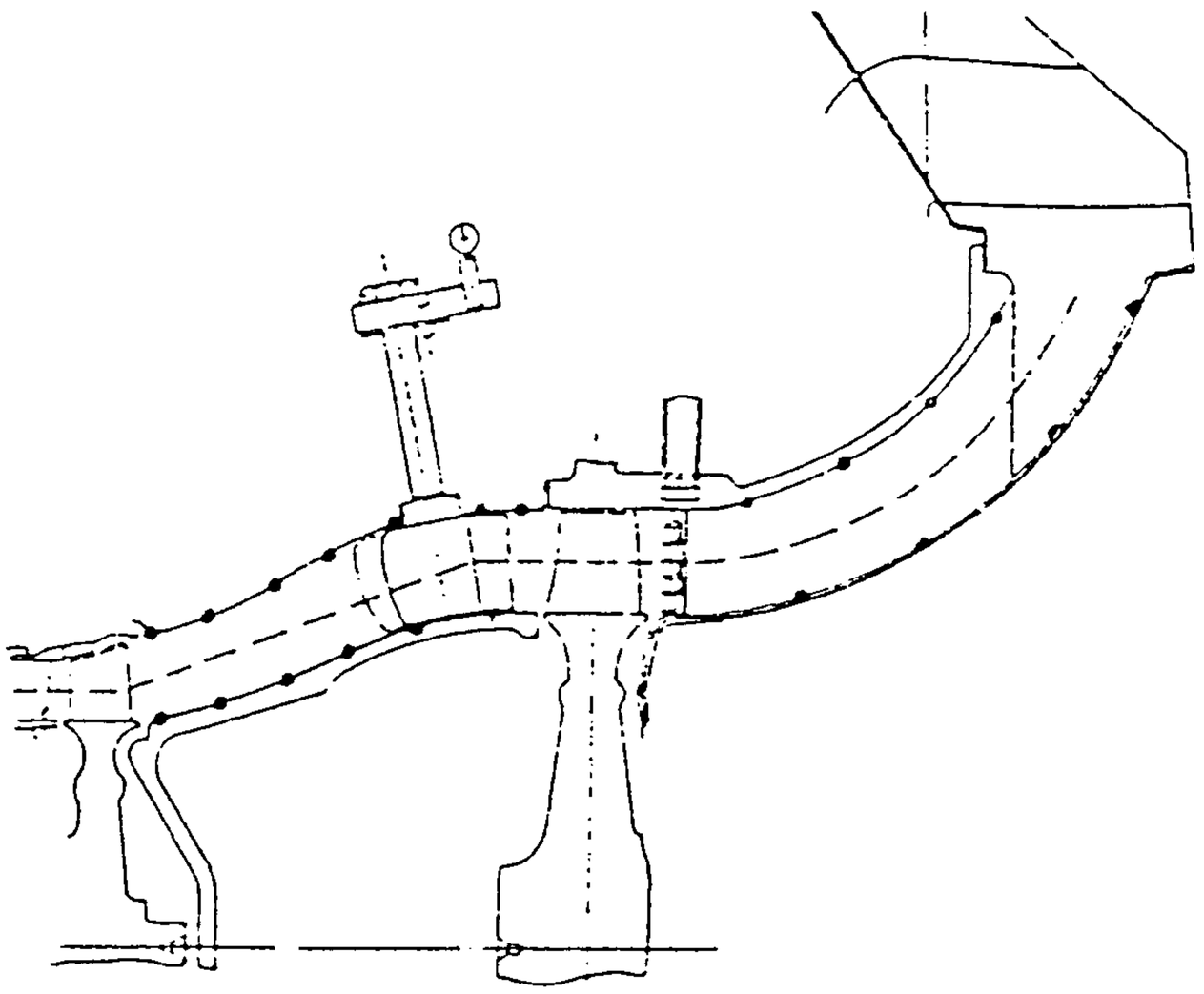

Fig.1.14.a Engine section drawing showing both the interstage diffuser and the exhaust diffuser, after Japikse and Pampreen (1979).

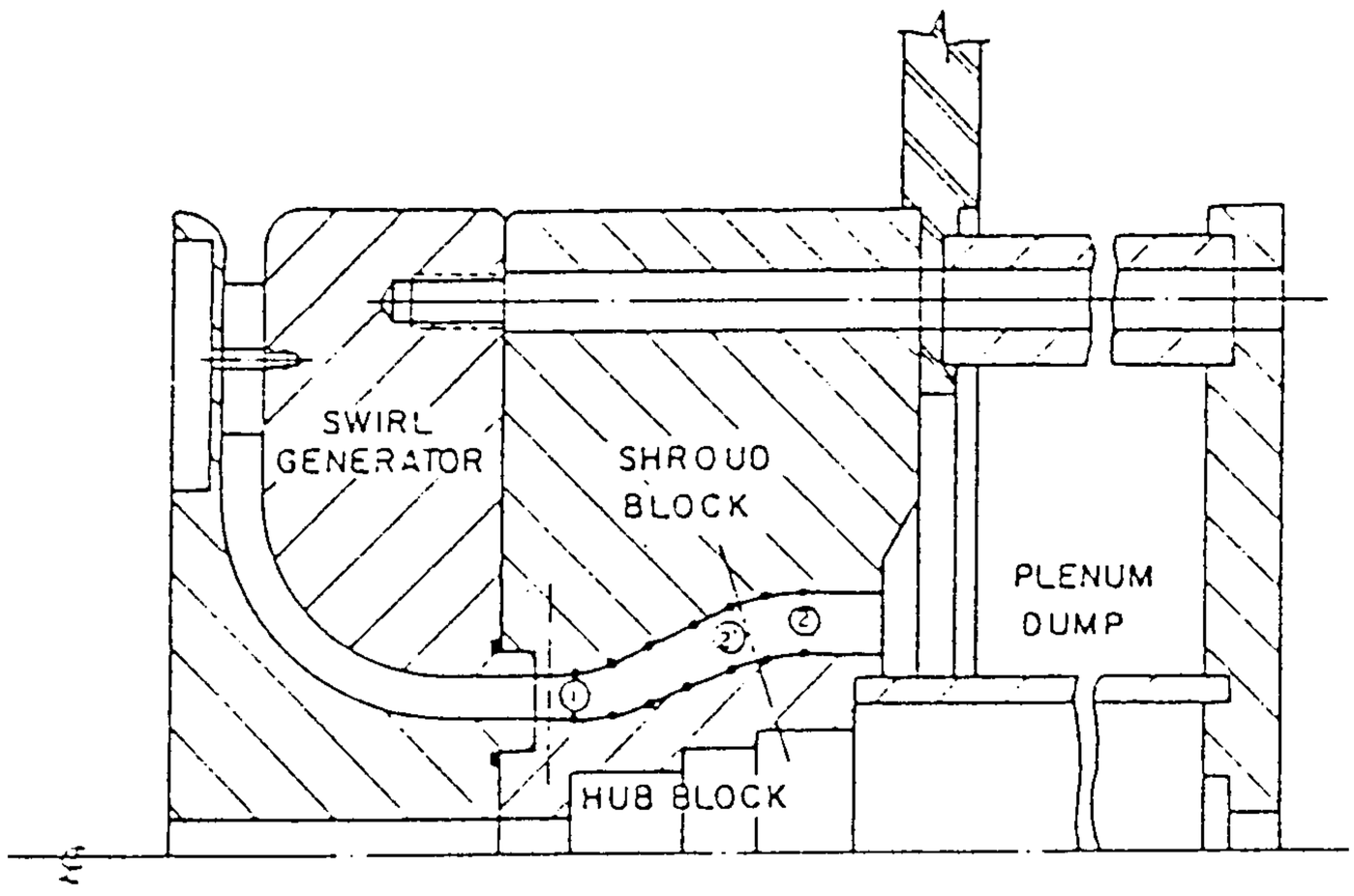

Fig.1.14.b Model of interstage diffuser (with swirl vanes) after Japikse and Pampreen (1979).

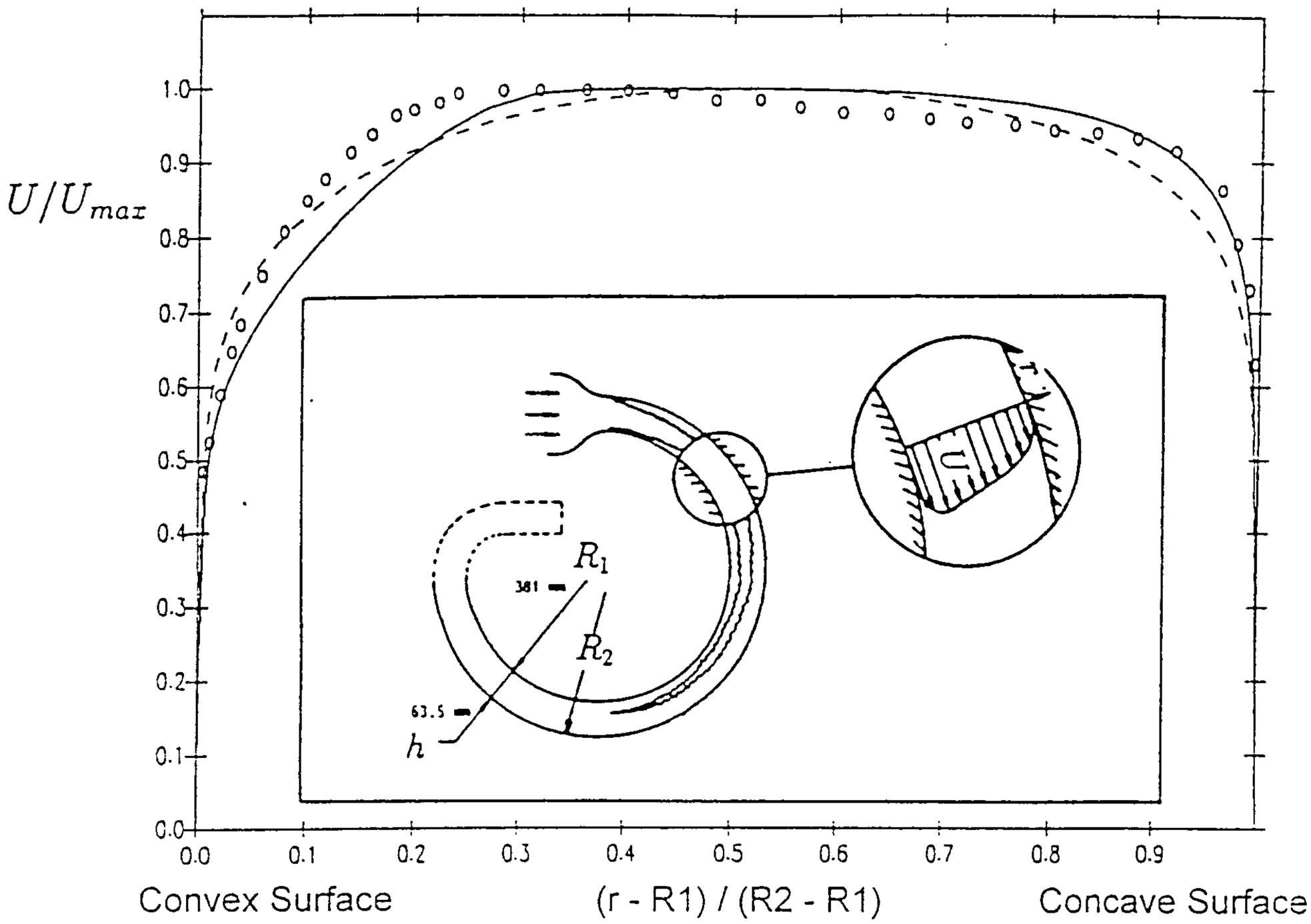

Fig.1.15 Measured and predicted mean velocity profile in fully developed curved channel flow, after Craft et. al. (1996).

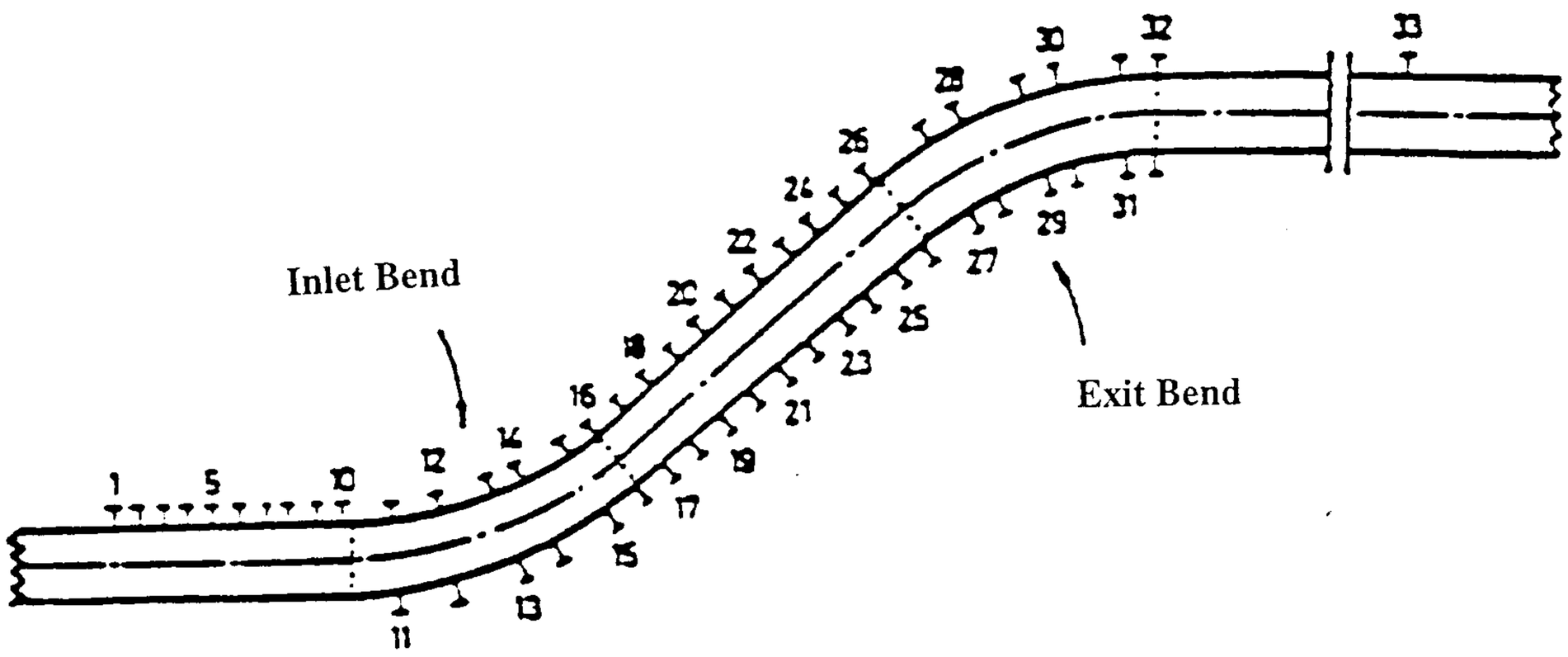

Fig.1.16 The Loughborough faired diffuser, after Stevens and Ecclestone (1969), Stevens and Fry (1973) and Jones and Manners (1989).

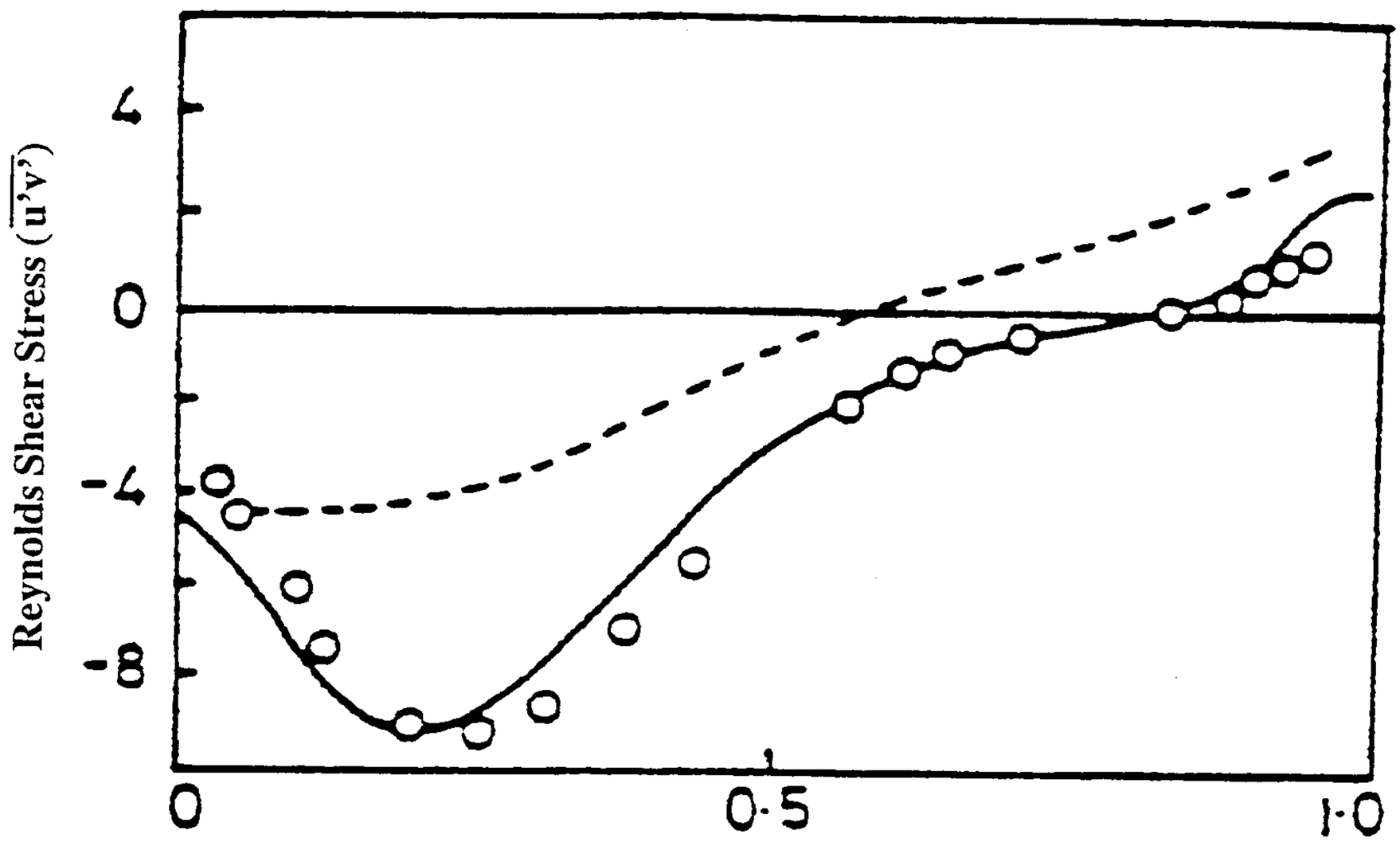

Fig.1.17 Measured and predicted shear stress ($\overline{uv}$) distributions in the inlet bend, after Jones and Manners (1989).

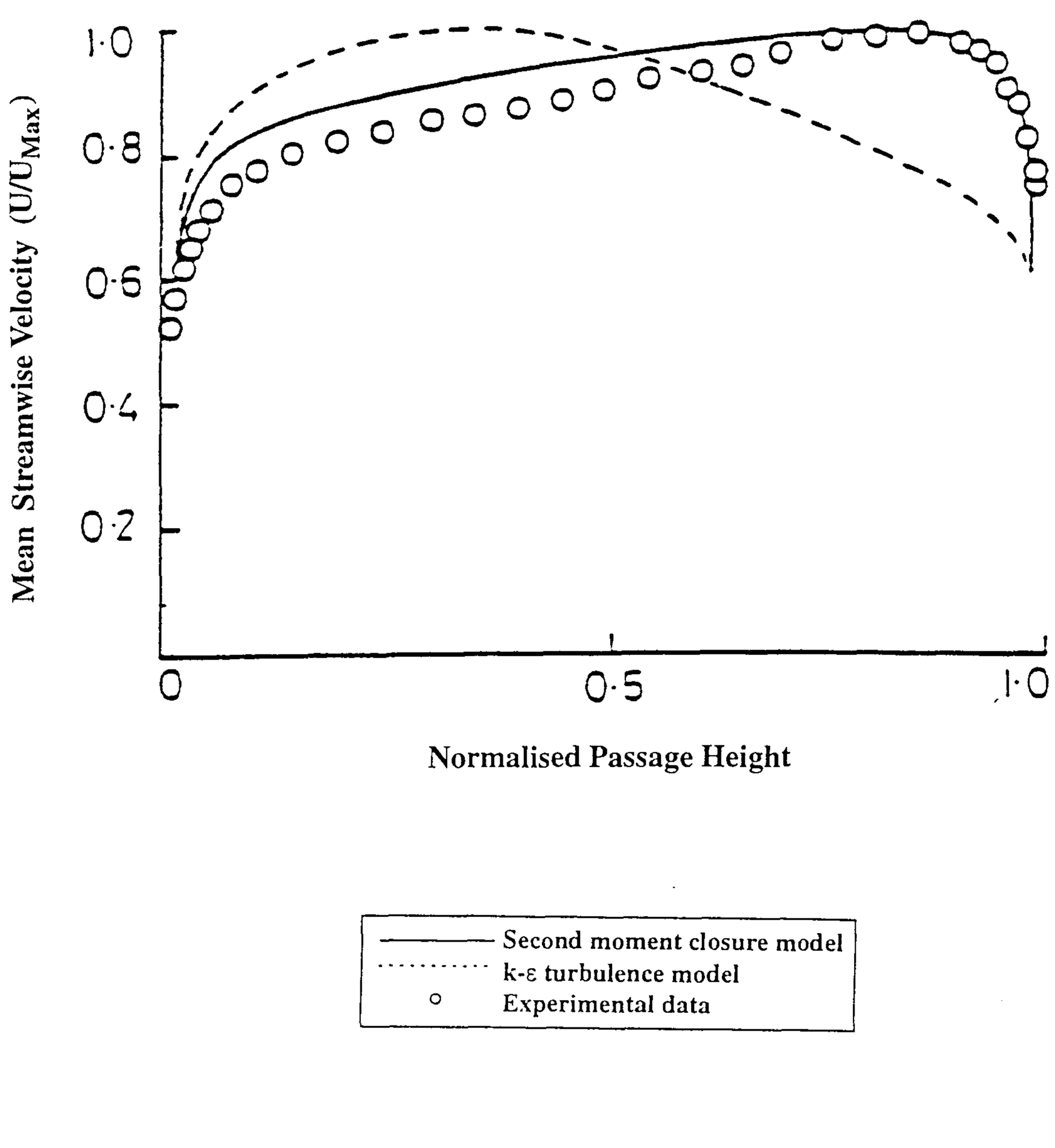

Fig.1.18 Measured and predicted mean velocity profiles at exit, after Jones and Manners (1989).

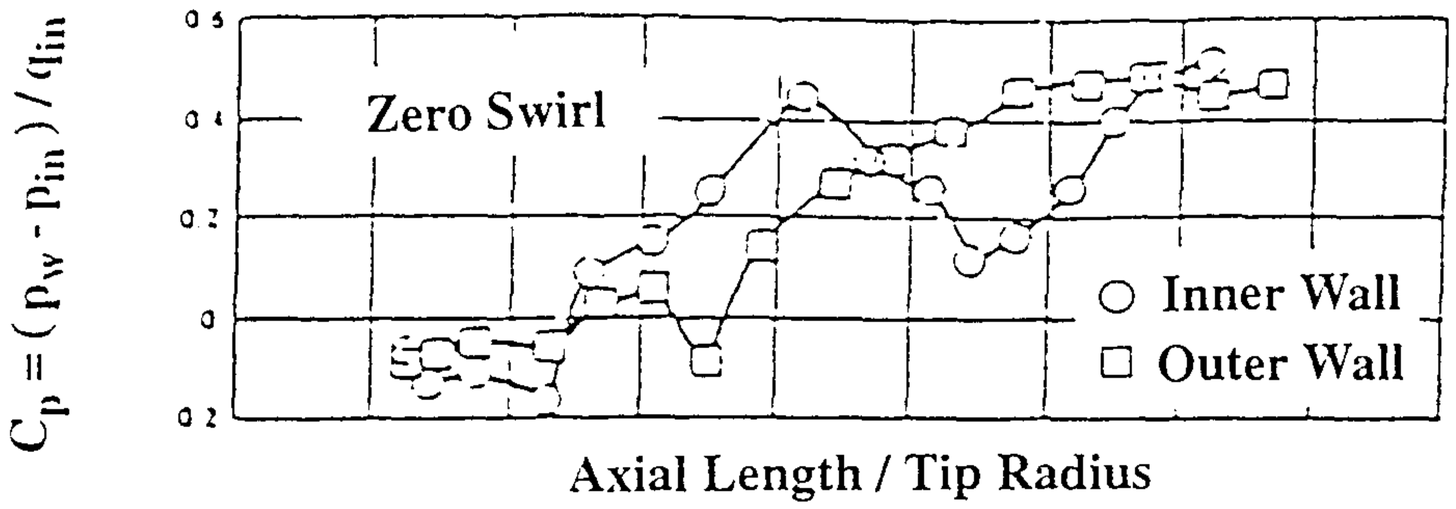

Fig.1.19.a Wall static pressure distribution without struts
after Thayer (1971)

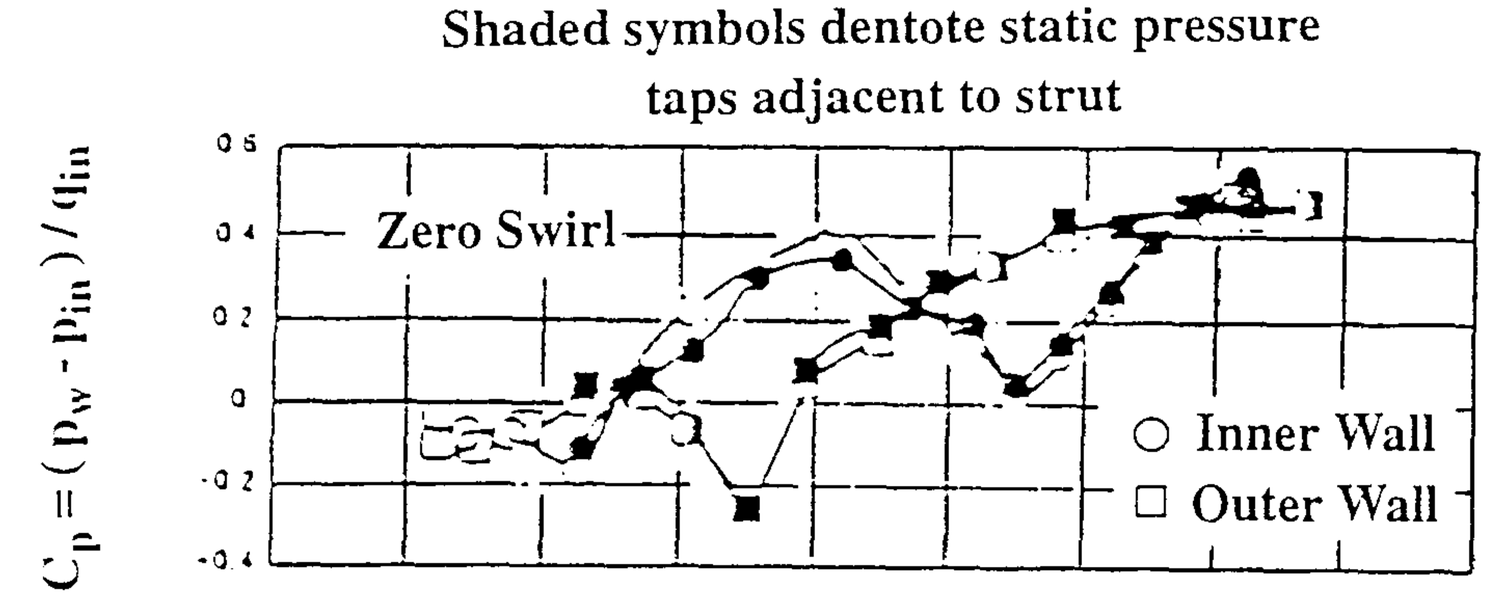

Fig.1.19.b Wall static pressure distribution with struts
after Thayer (1971)

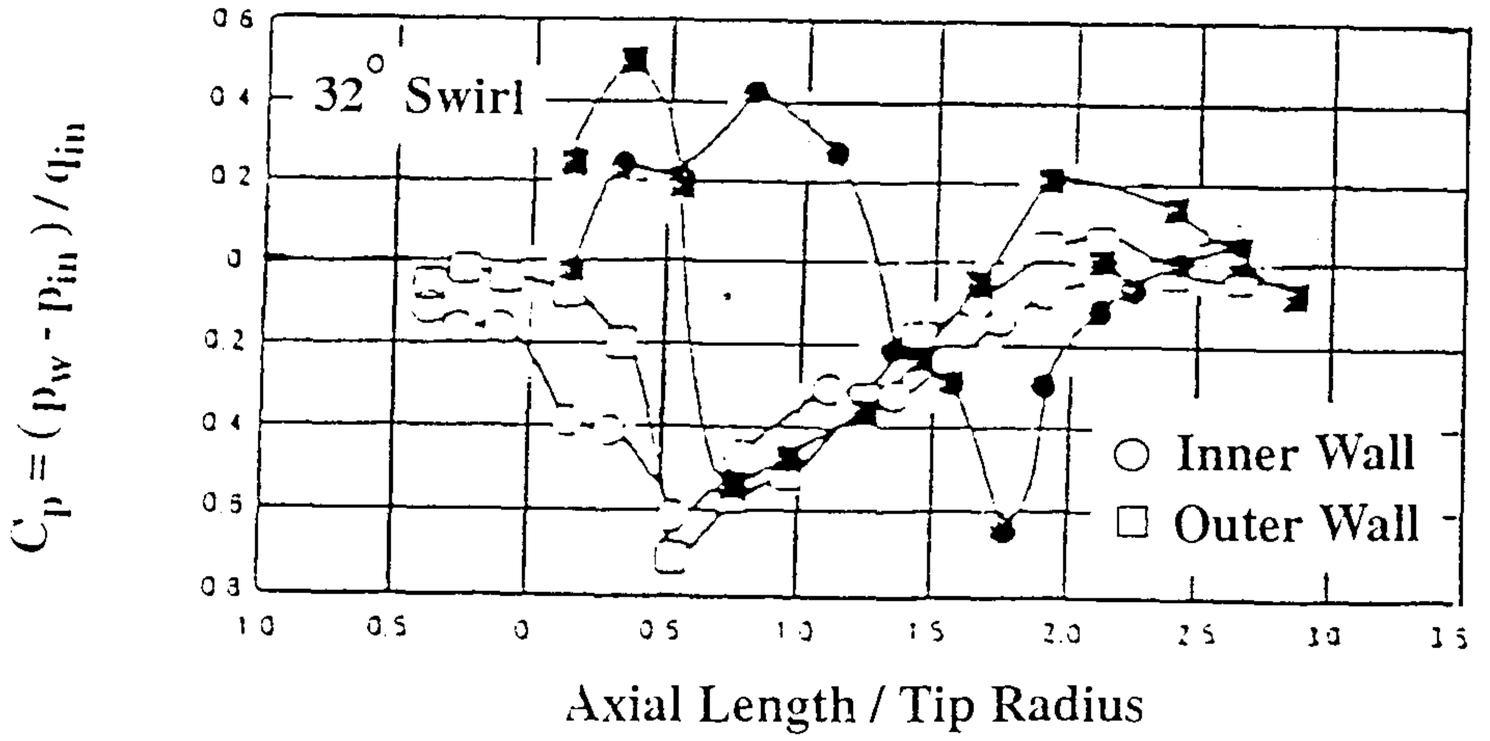

Fig.1.19.c Wall static pressure distribution with struts and 32 degrees swirl
after Thayer (1971)

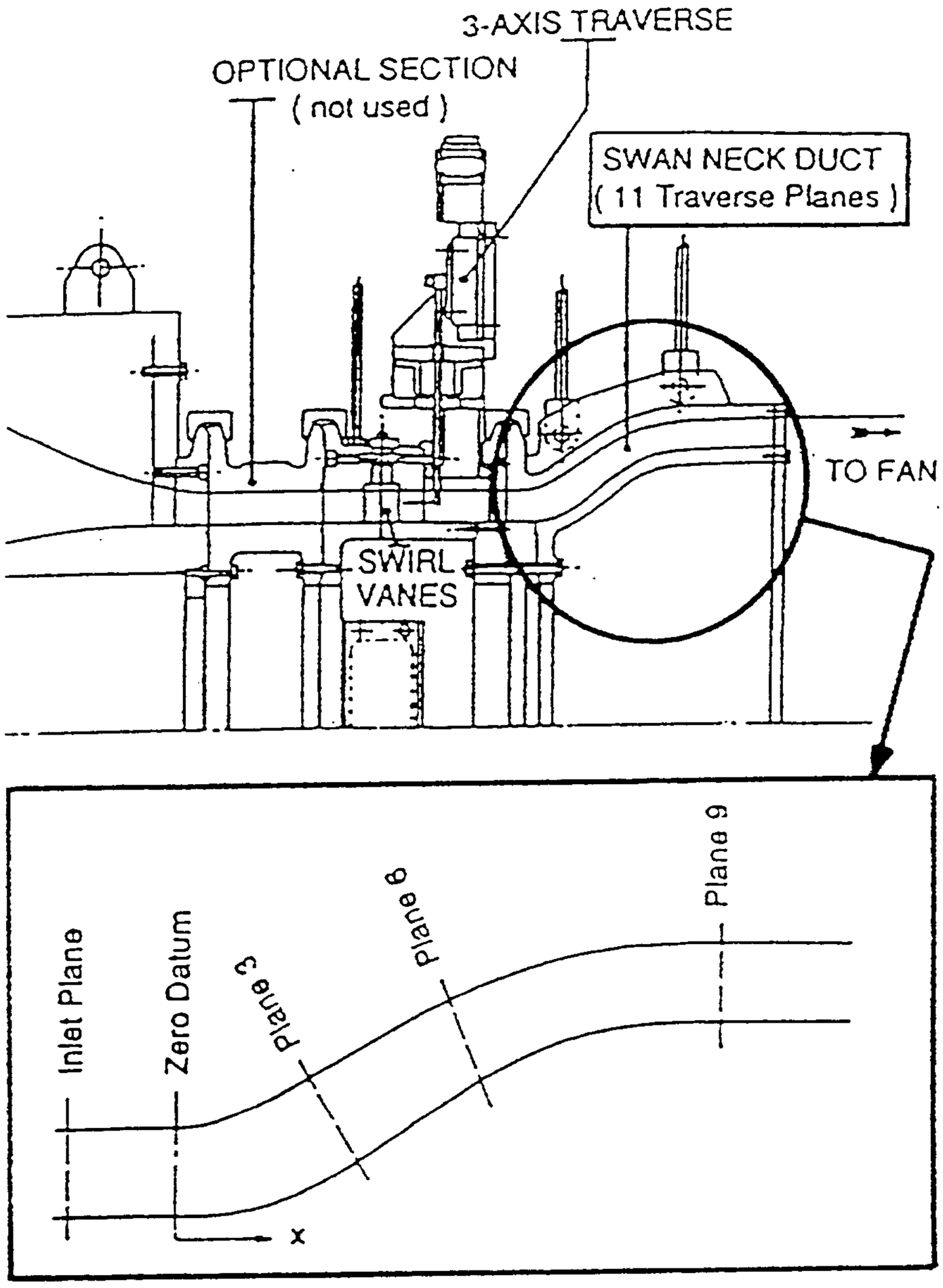

Fig.1.20 Turbine exhaust diffuser,
after Dominy and Kirkham (1996).

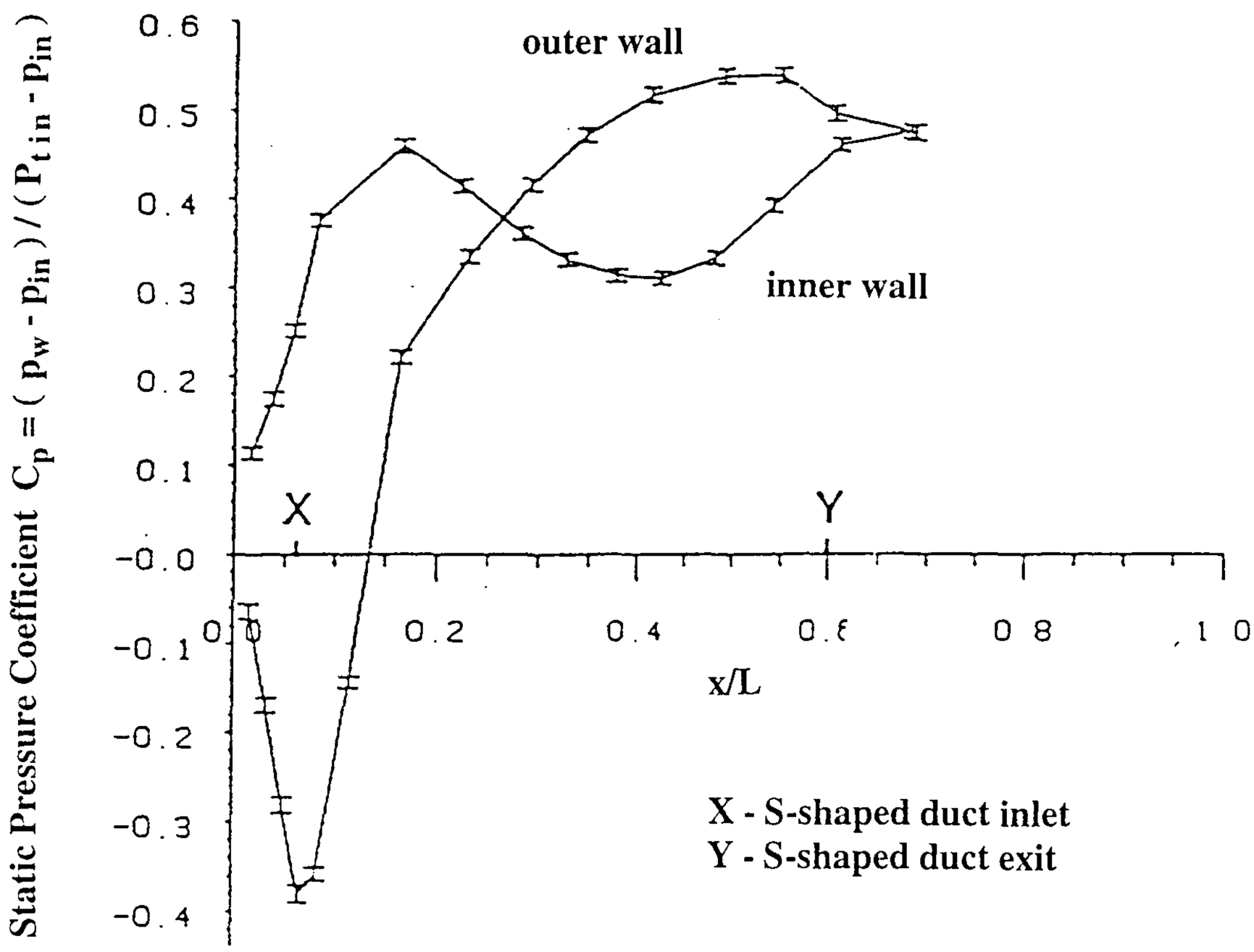

Fig.1.21 Wall static pressure (C_p) distribution,
after Dominy and Kirkham (1996).

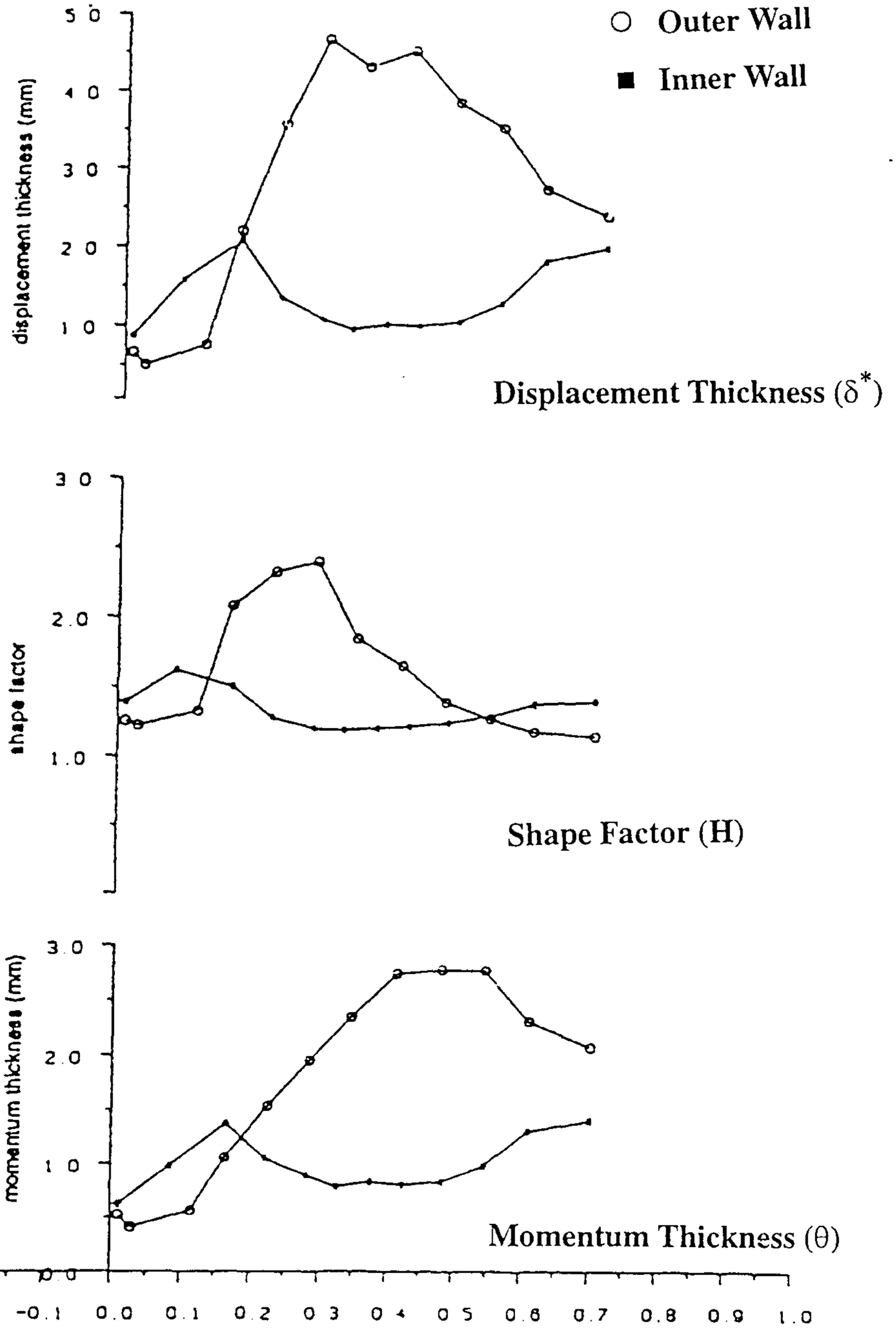

Fig.1.22 Axial variation of boundary layer integral parameters, after Dominy and Kirkham (1996).

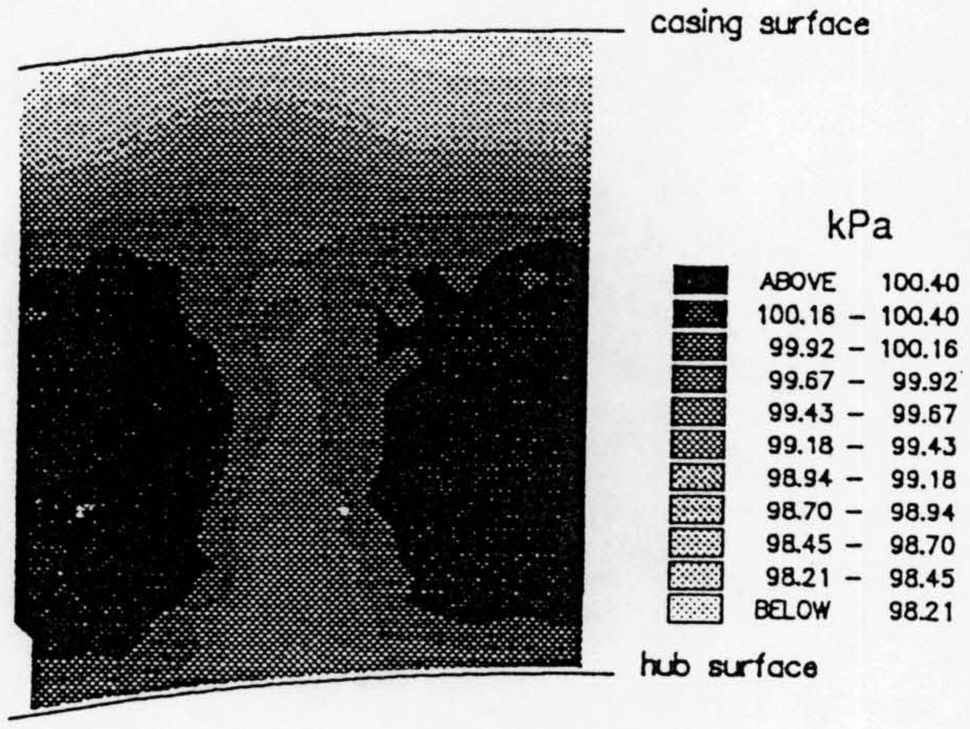

TOTAL PRESSURE

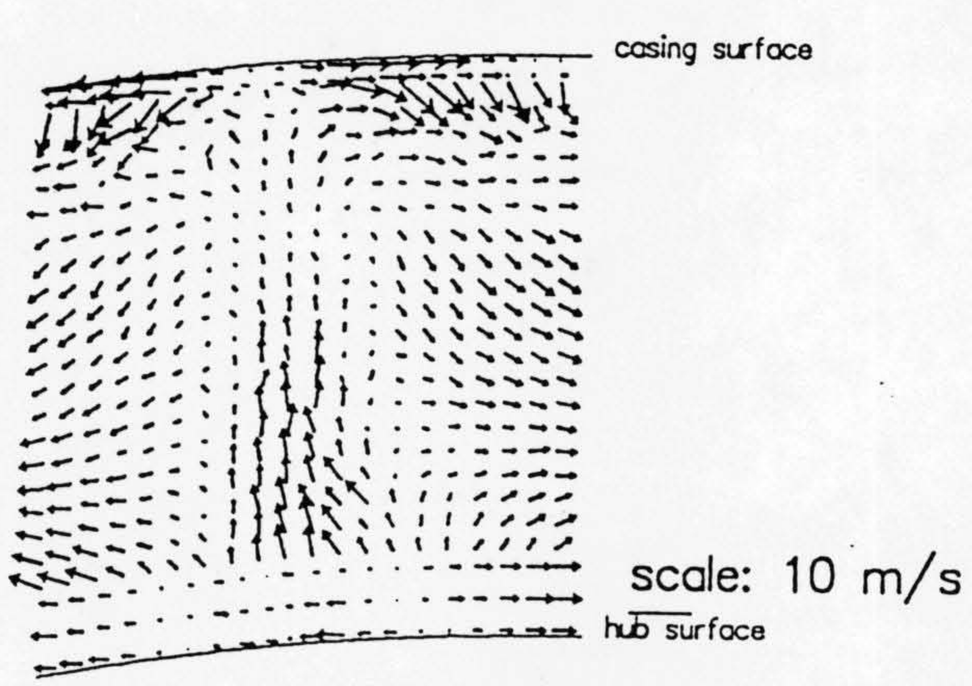

SECONDARY VELOCITY

Fig.1.23 Total pressure distribution and flow vectors, after Dominy and Kirkham (1996)

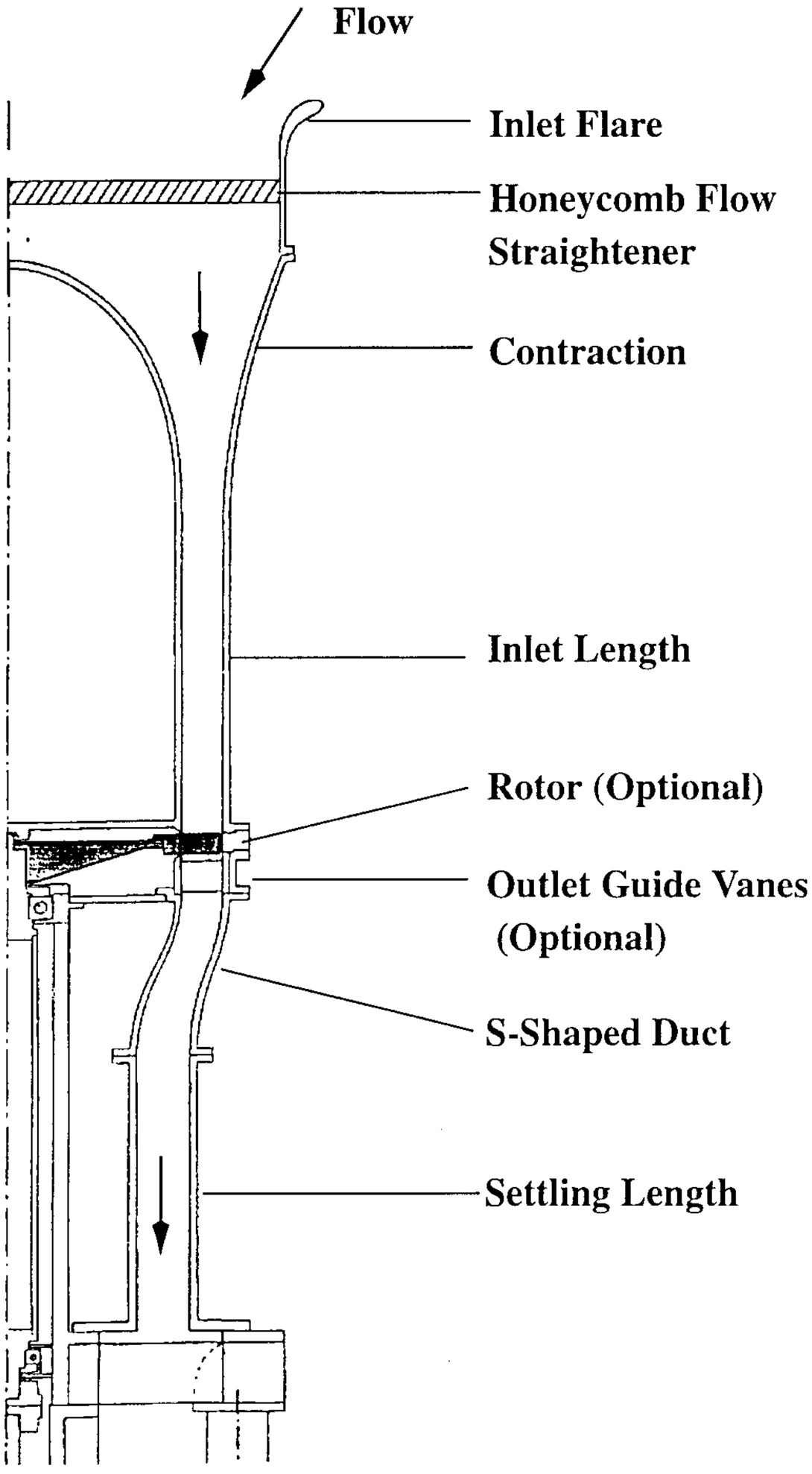

Fig.2.1 General layout

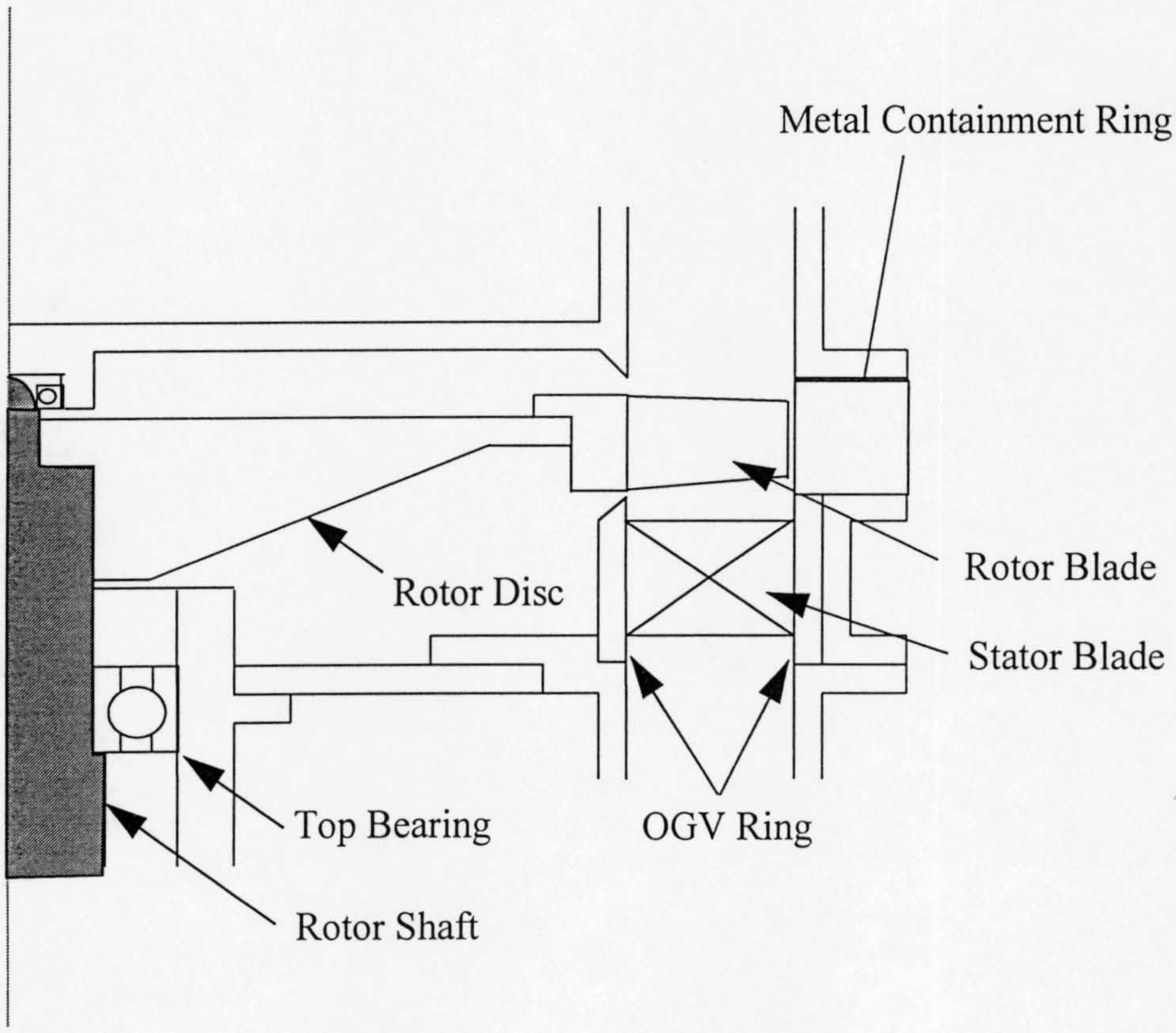

Fig.2.2 Single stage compressor

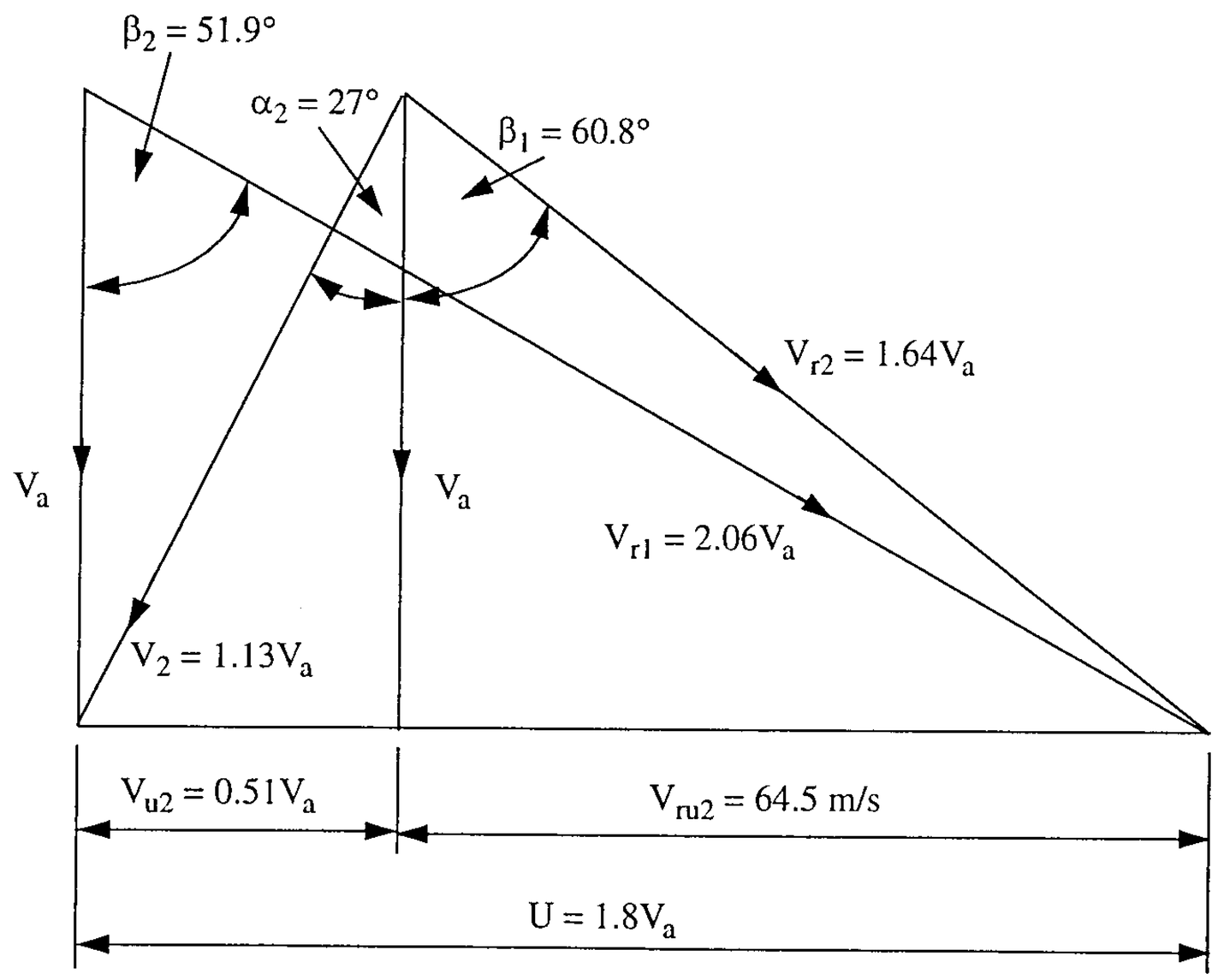

Fig.2.3 Velocity triangles at blade mid-height

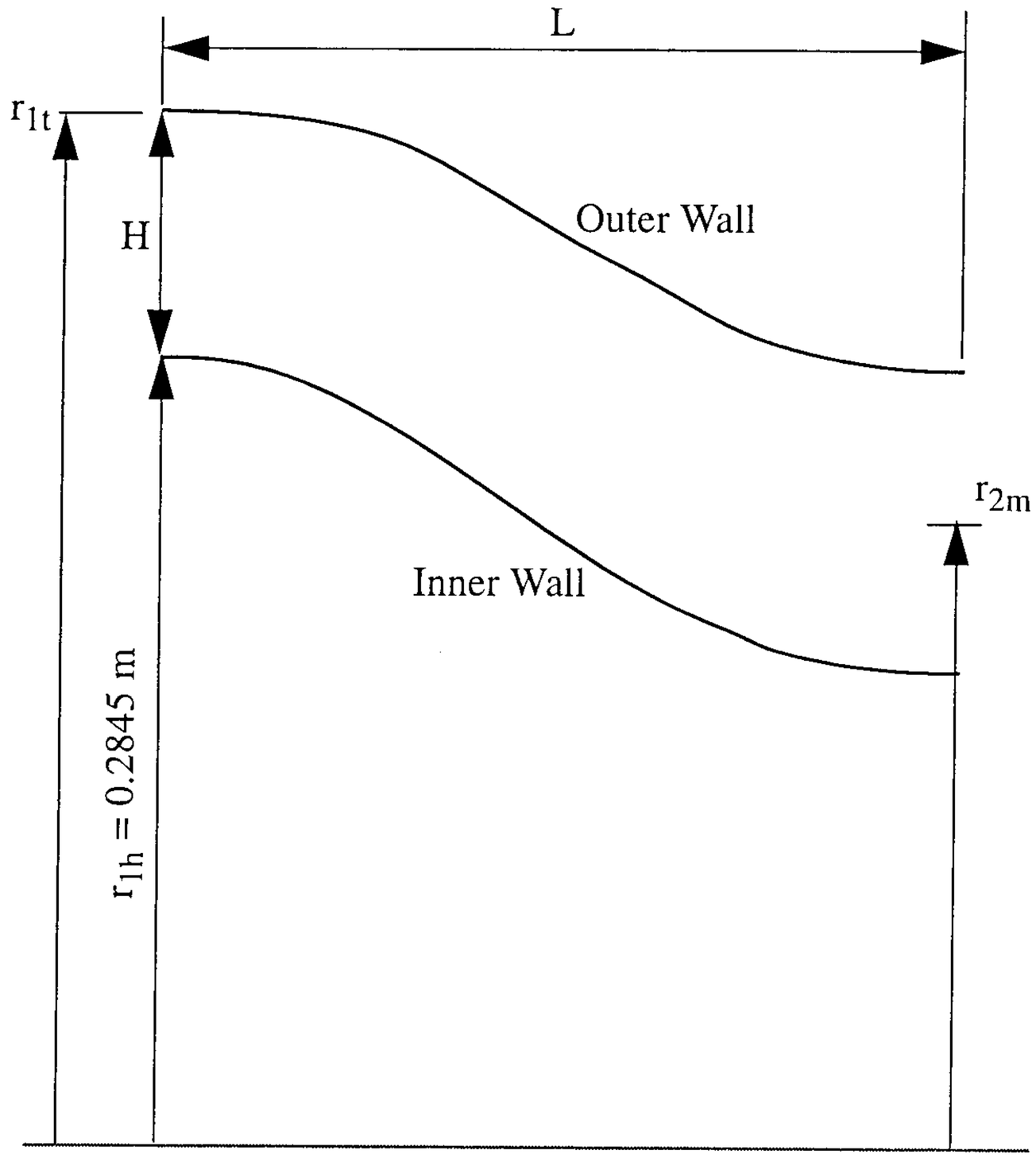

1. Area ratio (A_2 / A_1) = 1.0
2. Non-dimensioanl length (L / H) = 3.4
3. Inlet hub to tip ratio (r_{1h} / r_{1t}) = 0.8
4. Exit to inlet mean radius ratio (r_{2m} / r_{1m}) = 0.8

Fig.2.4 S-shaped duct geometry

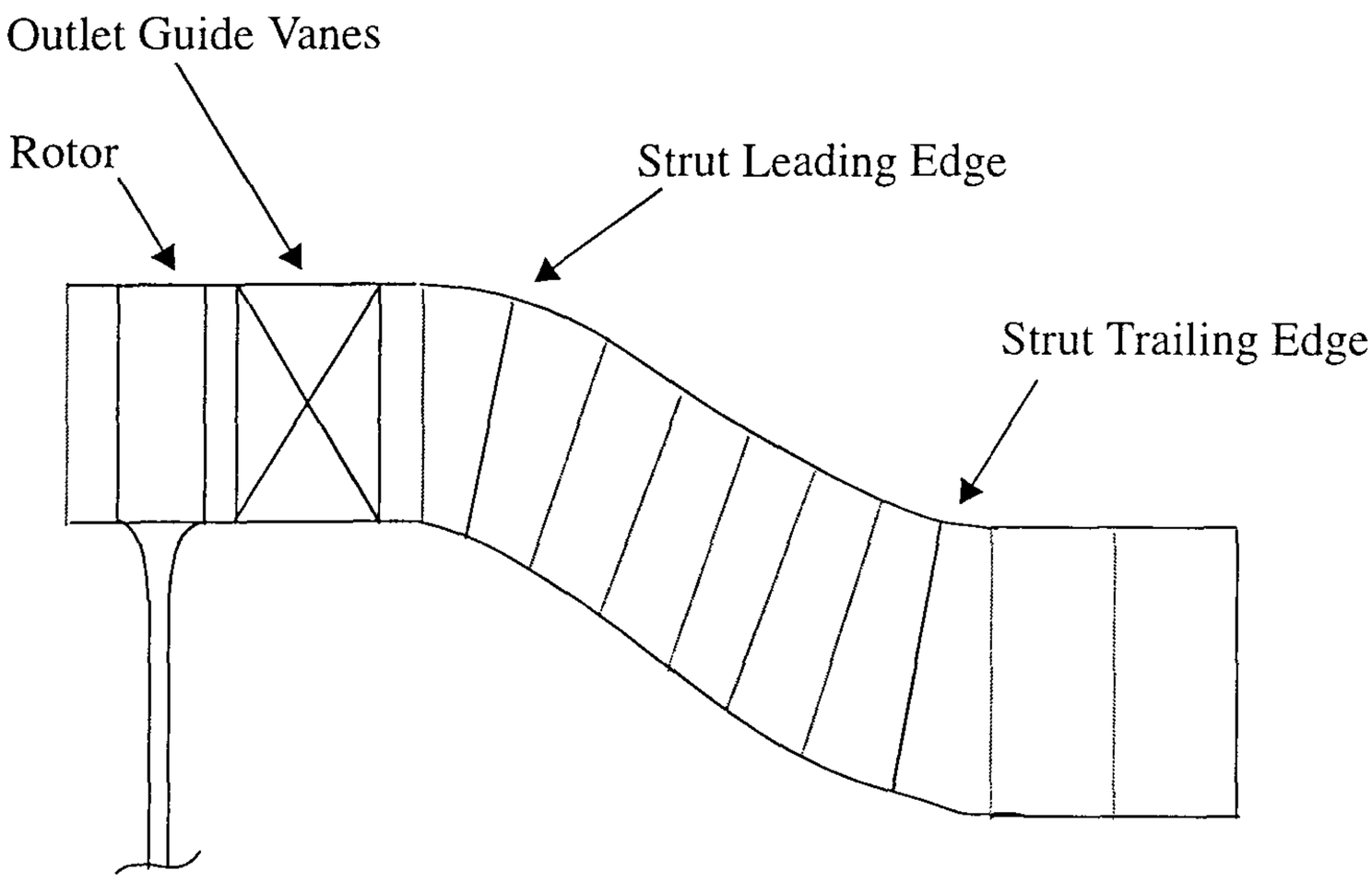

Fig.2.5 Position of radial strut within S-shaped duct

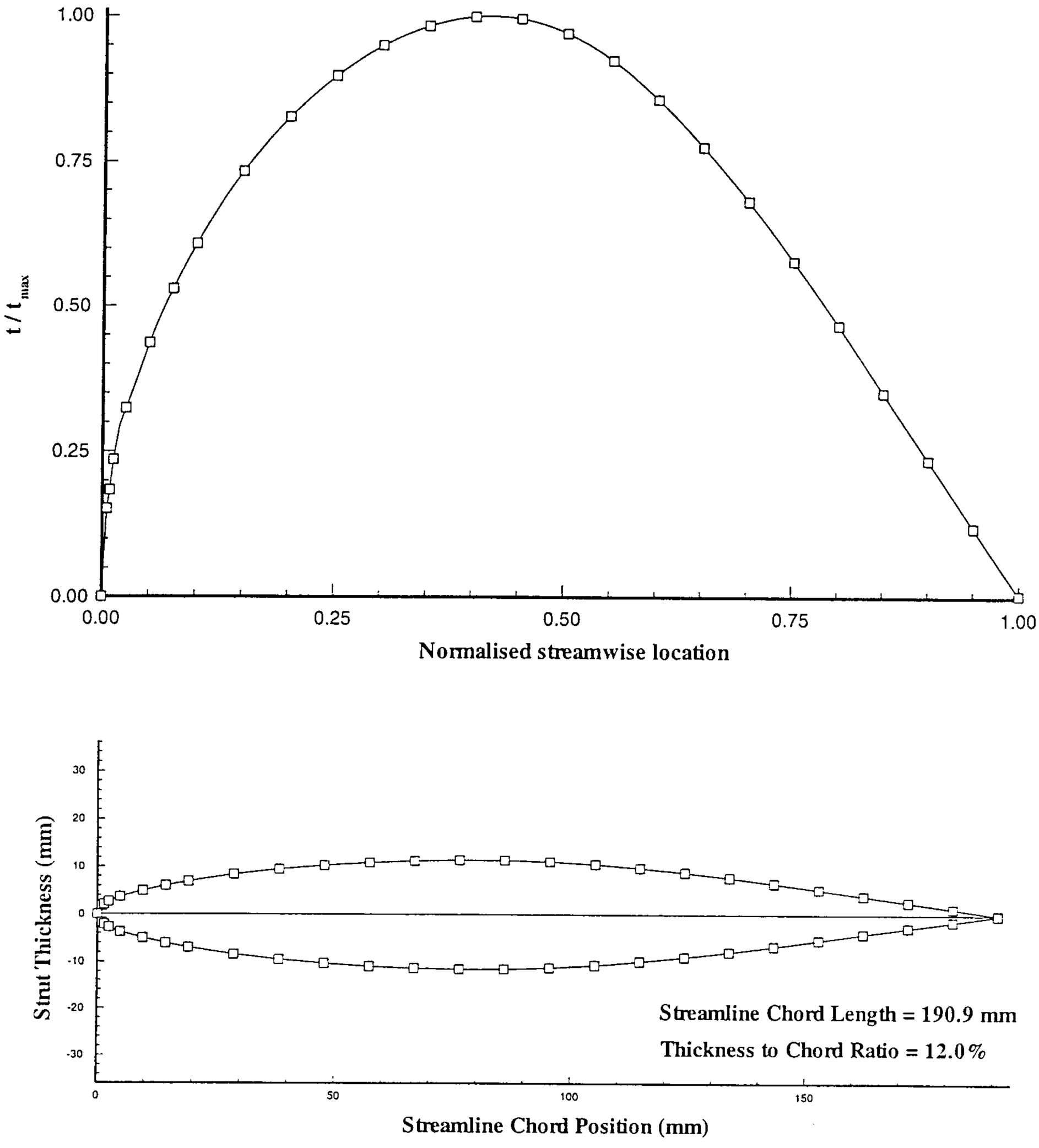

Fig.2.6 Blade profile (NACA65 - 012T)

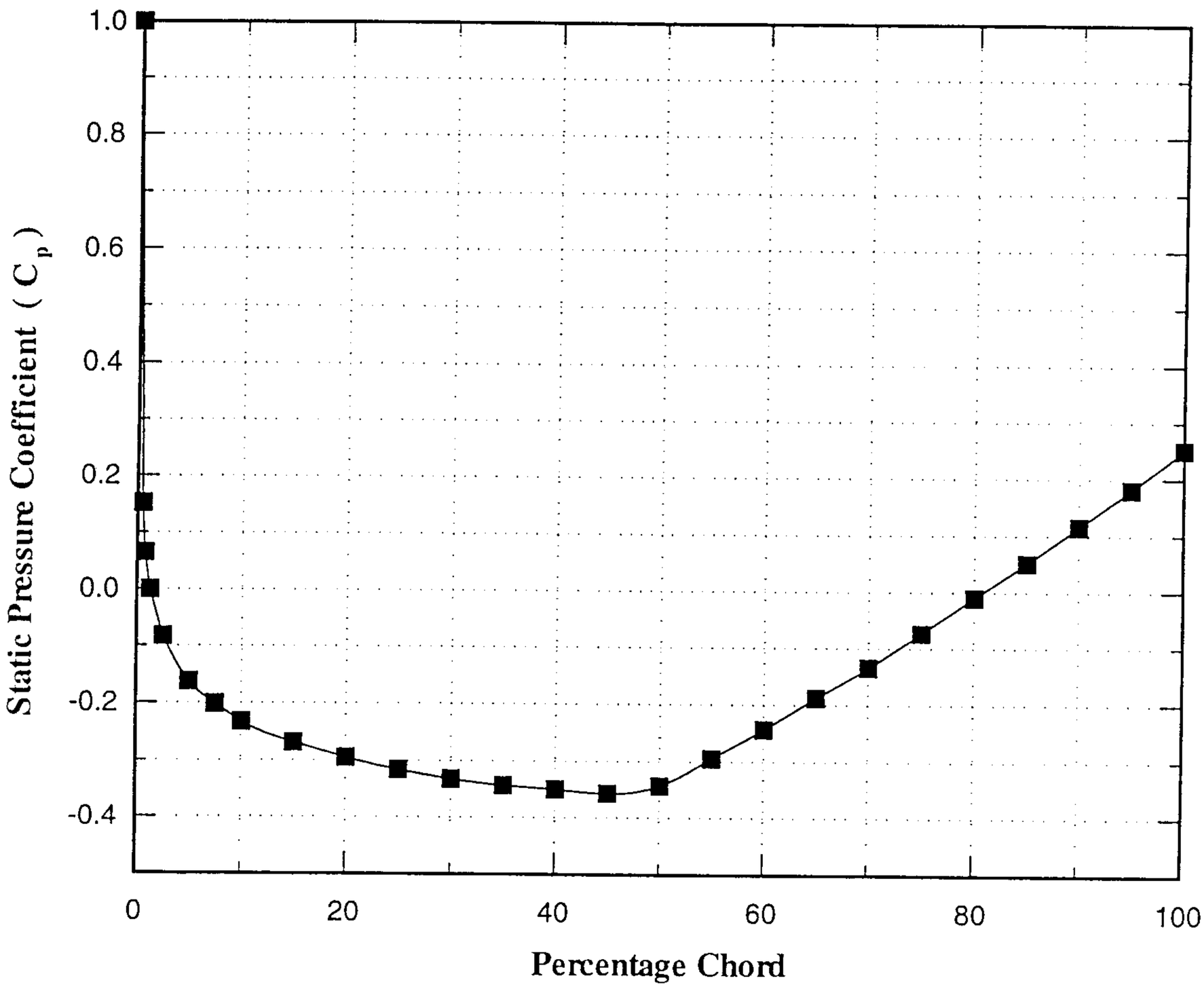

Fig.2.7 Surface static pressure distribution (NACA65 - 012T) after Abbott and Von Doenhoff (1949)

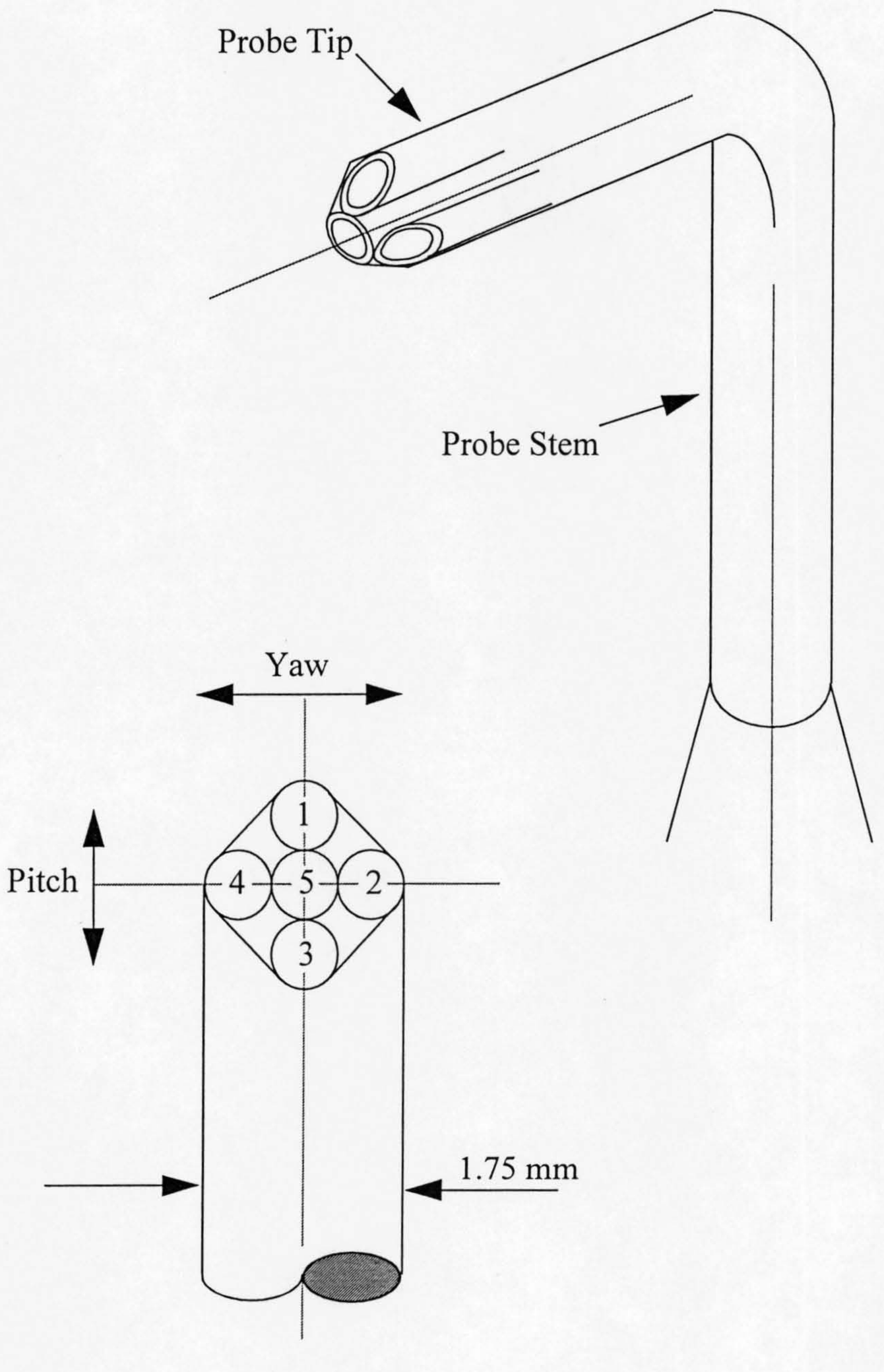

Fig.2.8 Five hole probe geometry

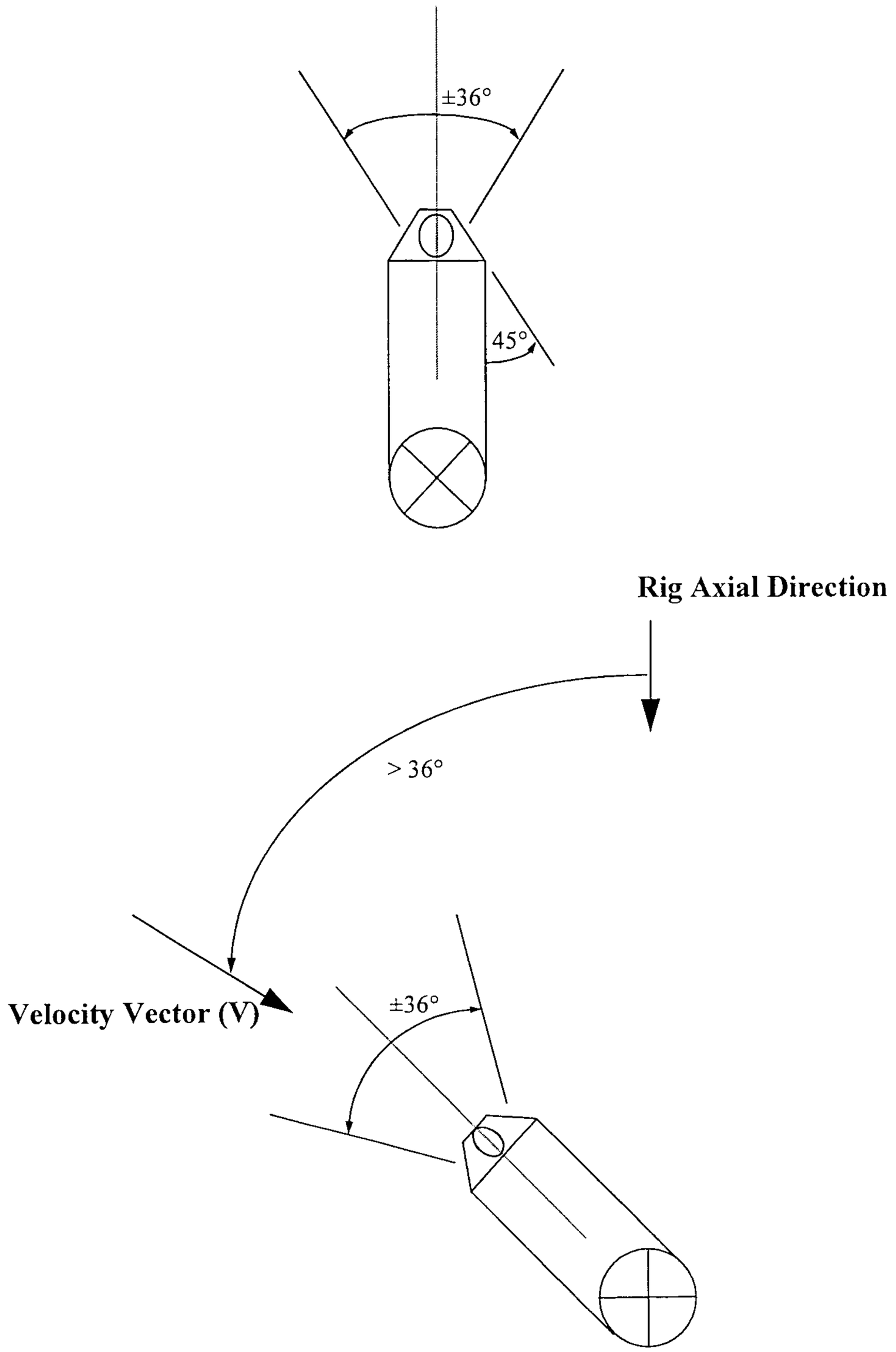

Fig.2.9 Positioning of 5 hole probe relative to velocity vector

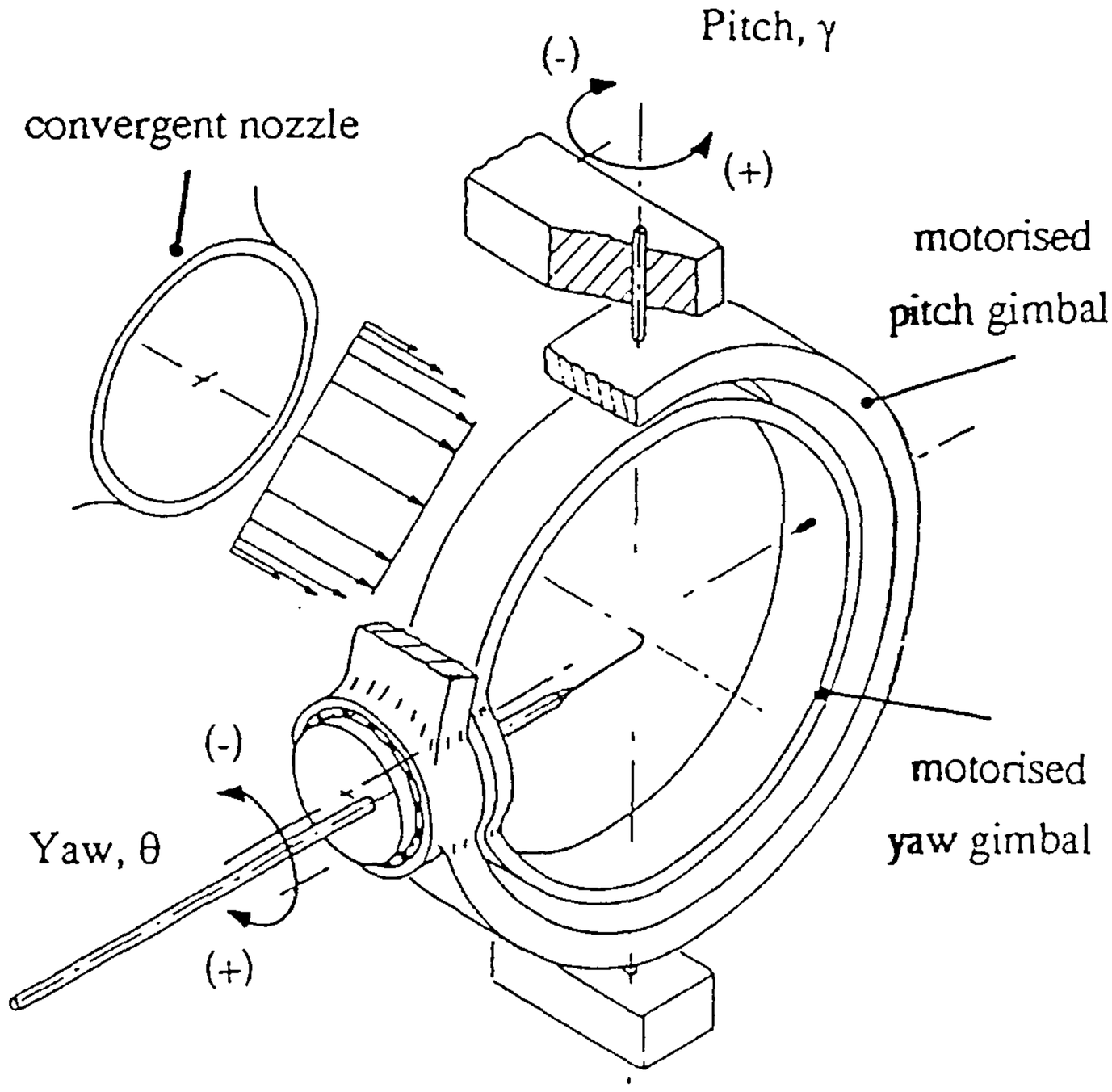

Fig.2.10 Calibration tunnel and twin axis gimbals

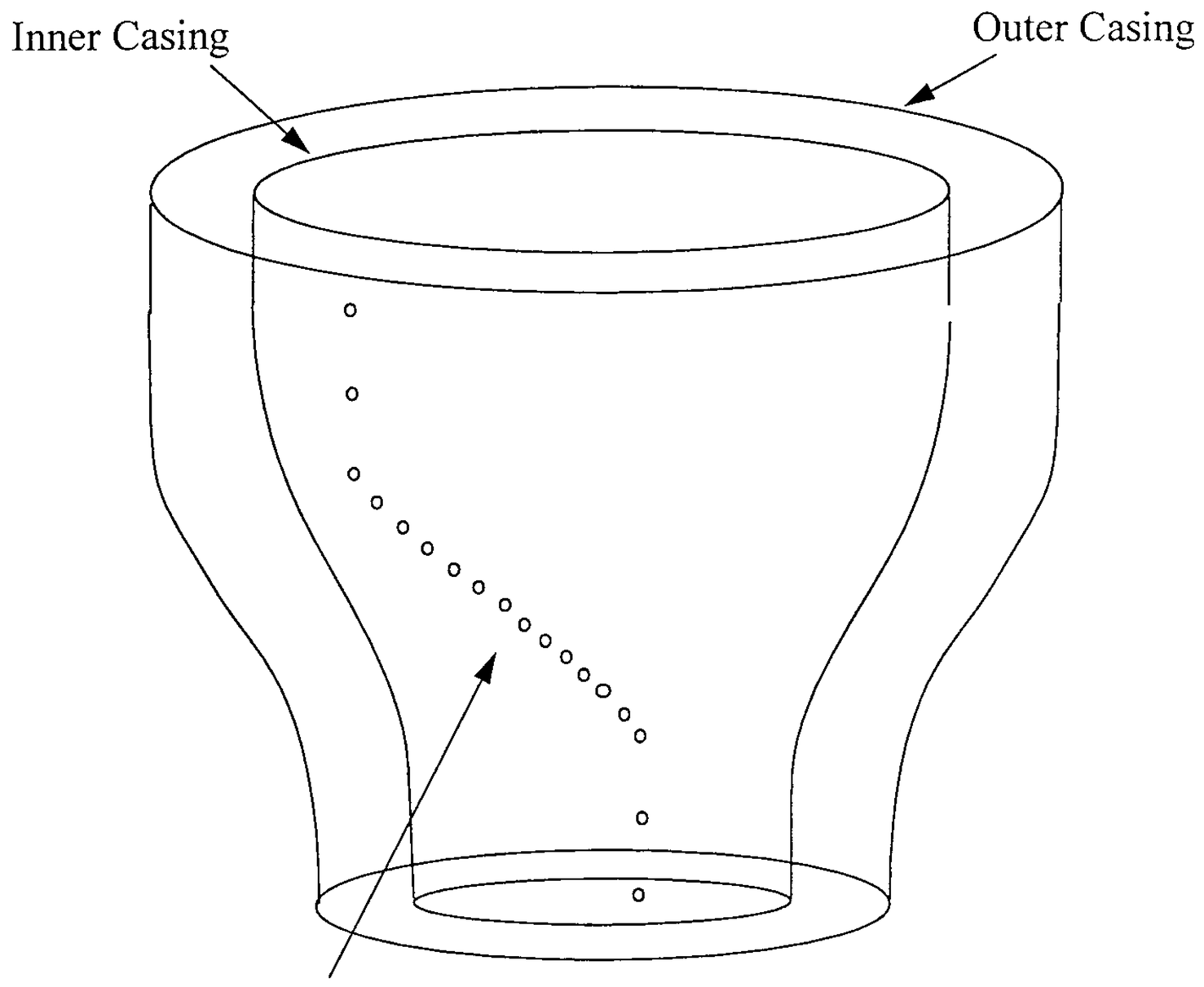

Fig.2.11 Helical wall static pressure tappings

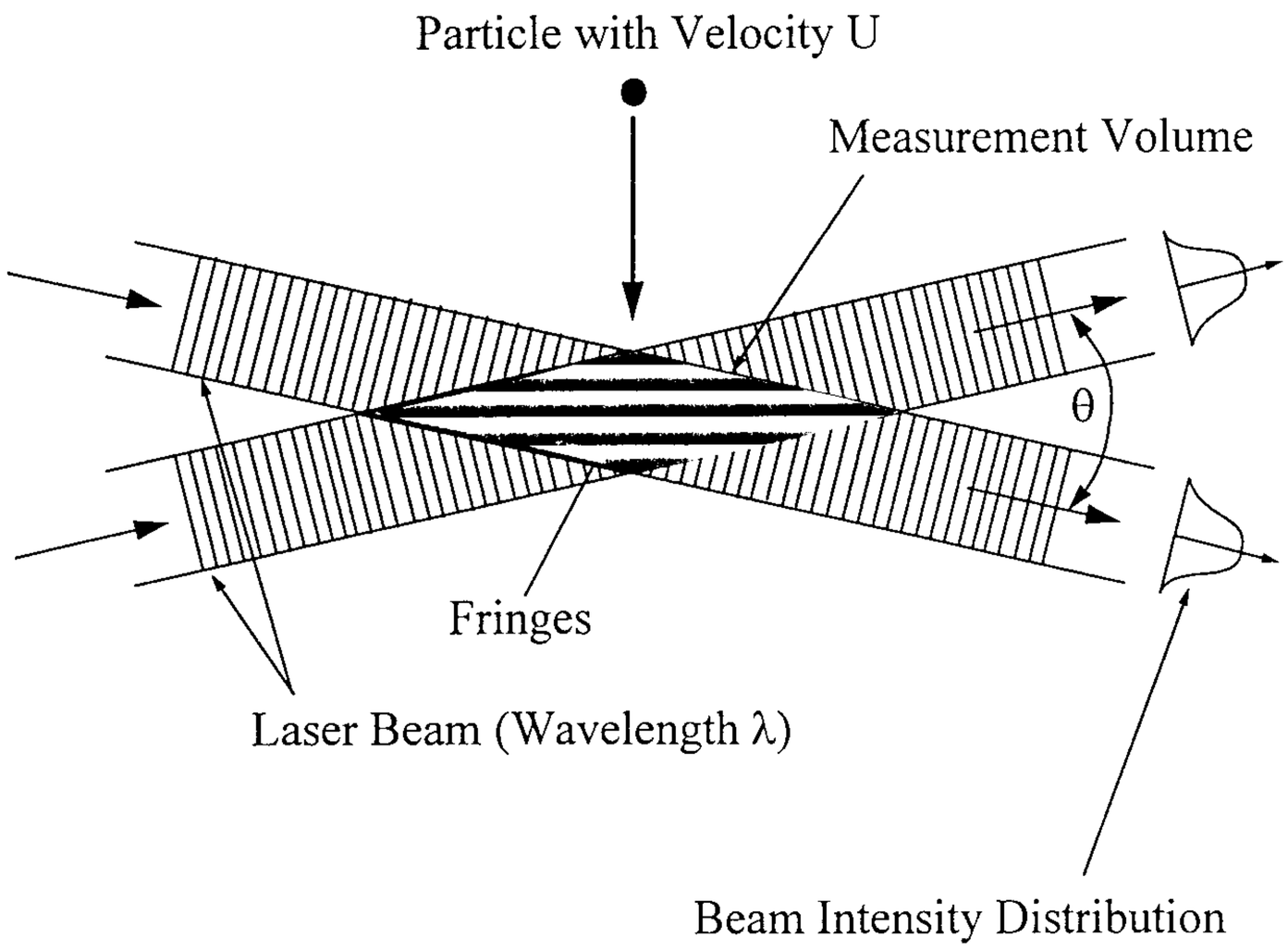

$$U = f_D \frac{(\lambda/2)}{\sin(\theta/2)}$$

Fig.2.12 Idealised principle of LDA

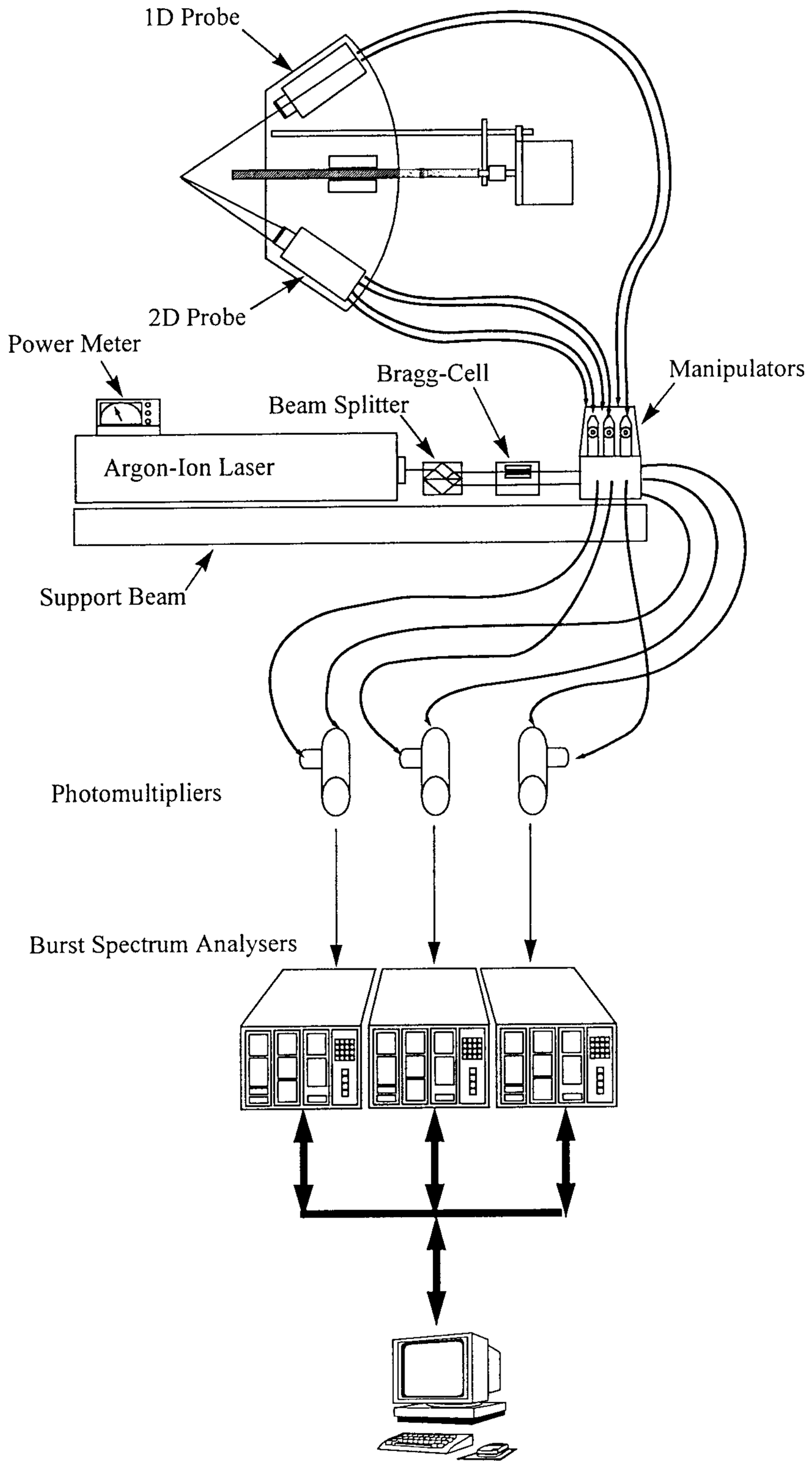

Fig.2.13 Schematic of LDA system

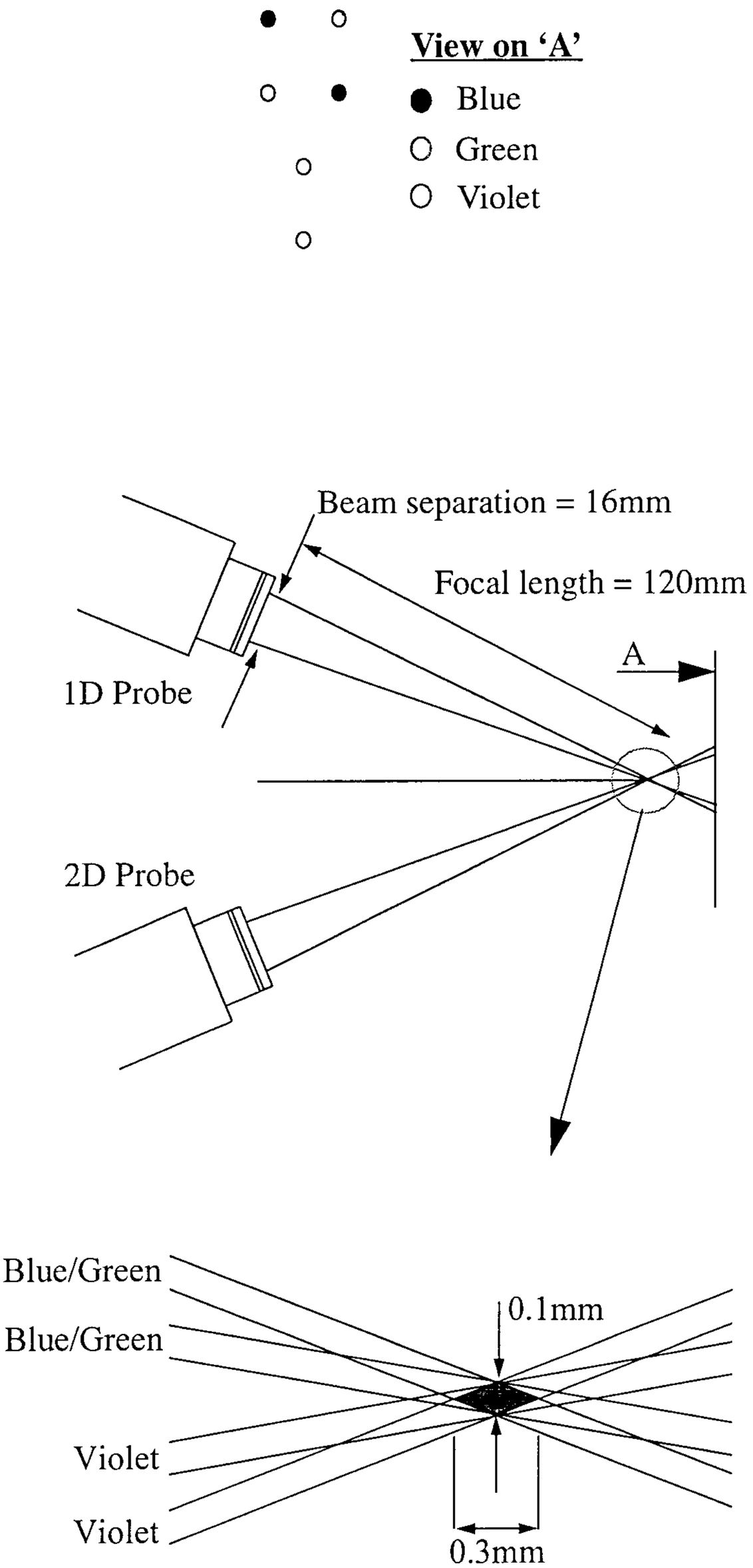

Fig.2.14 Optical geometry and the measurement volume

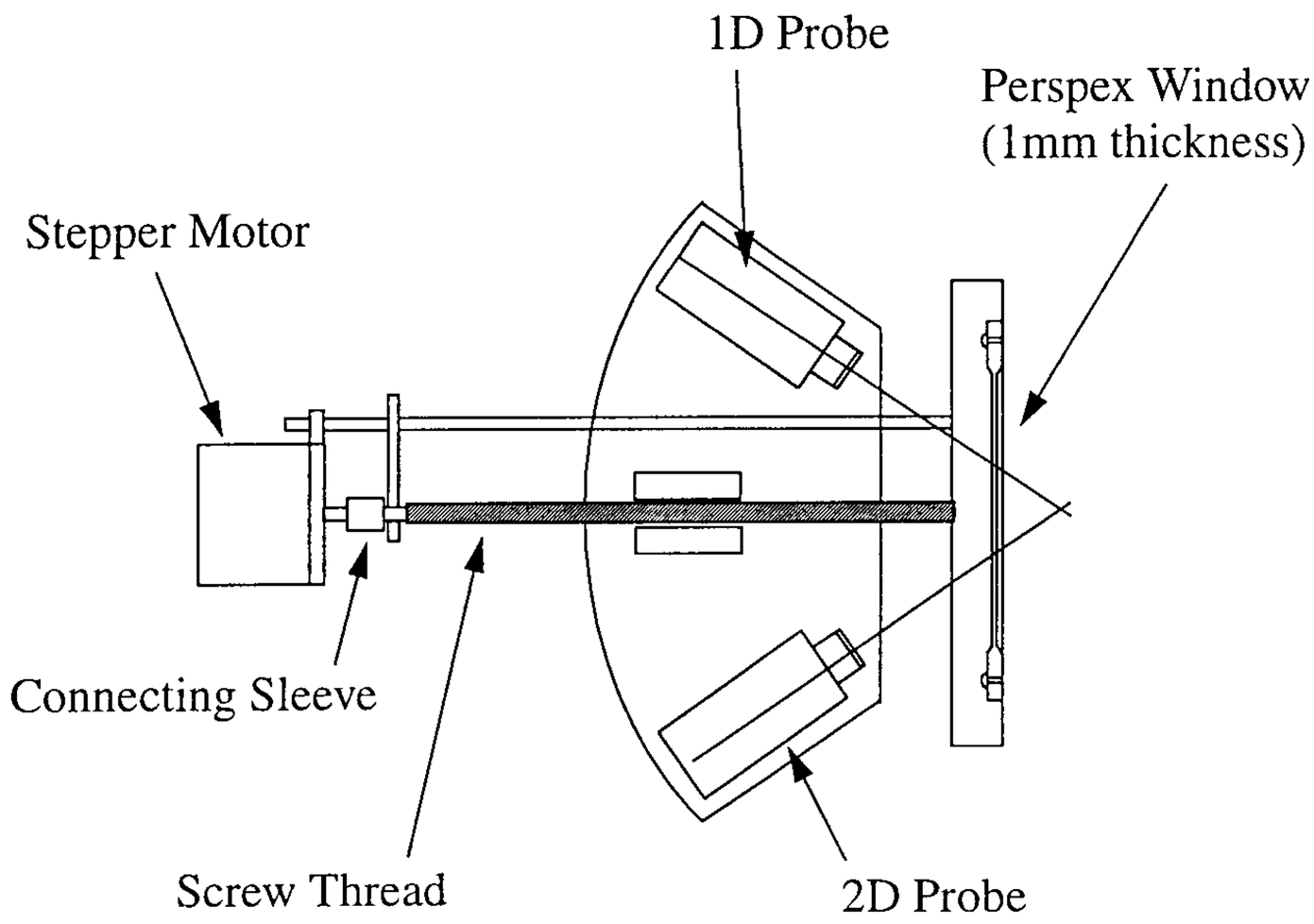

Fig.2.15 1D and 2D probes on traverse with window

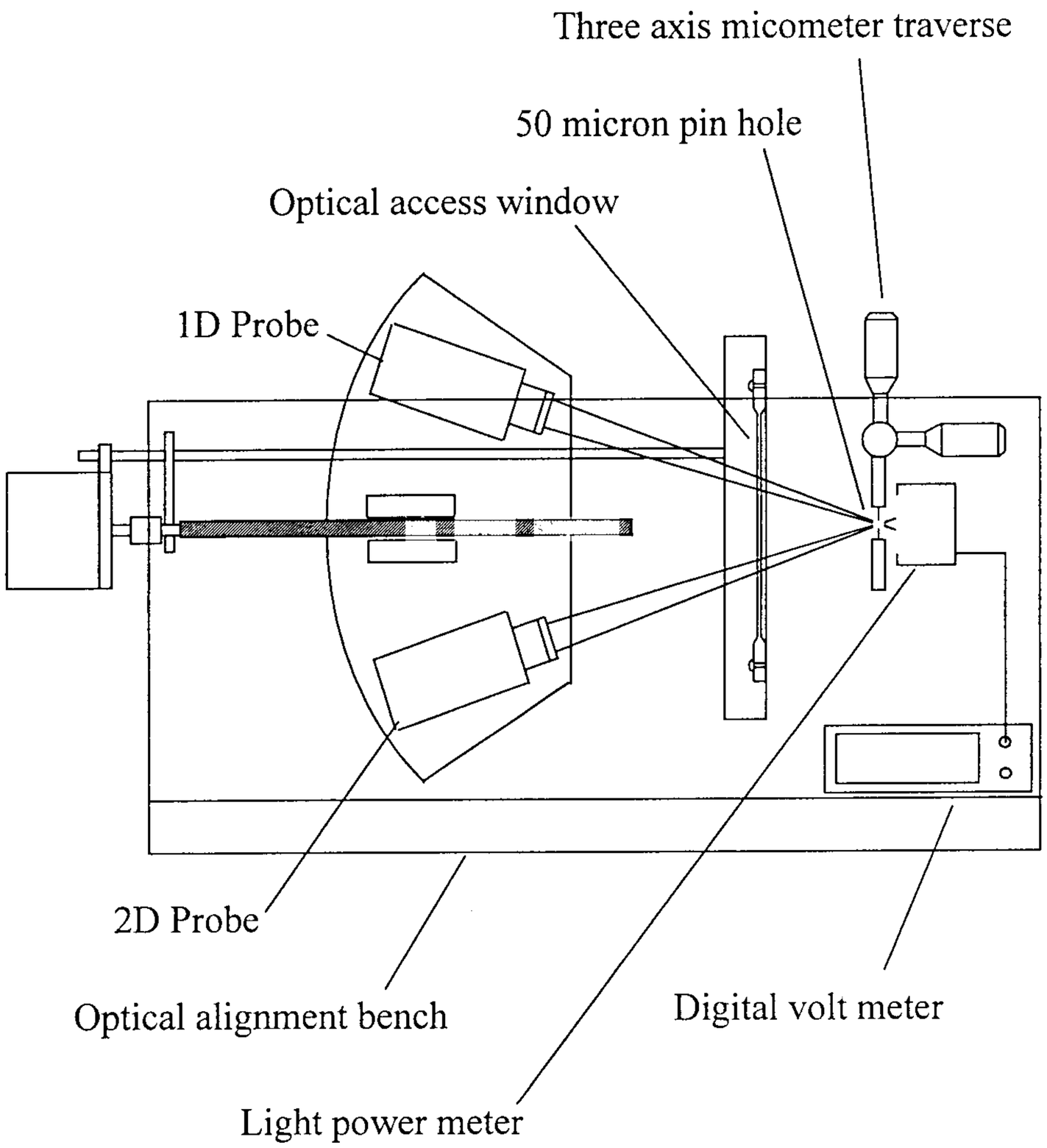

Fig.2.16 Laser beam alignment

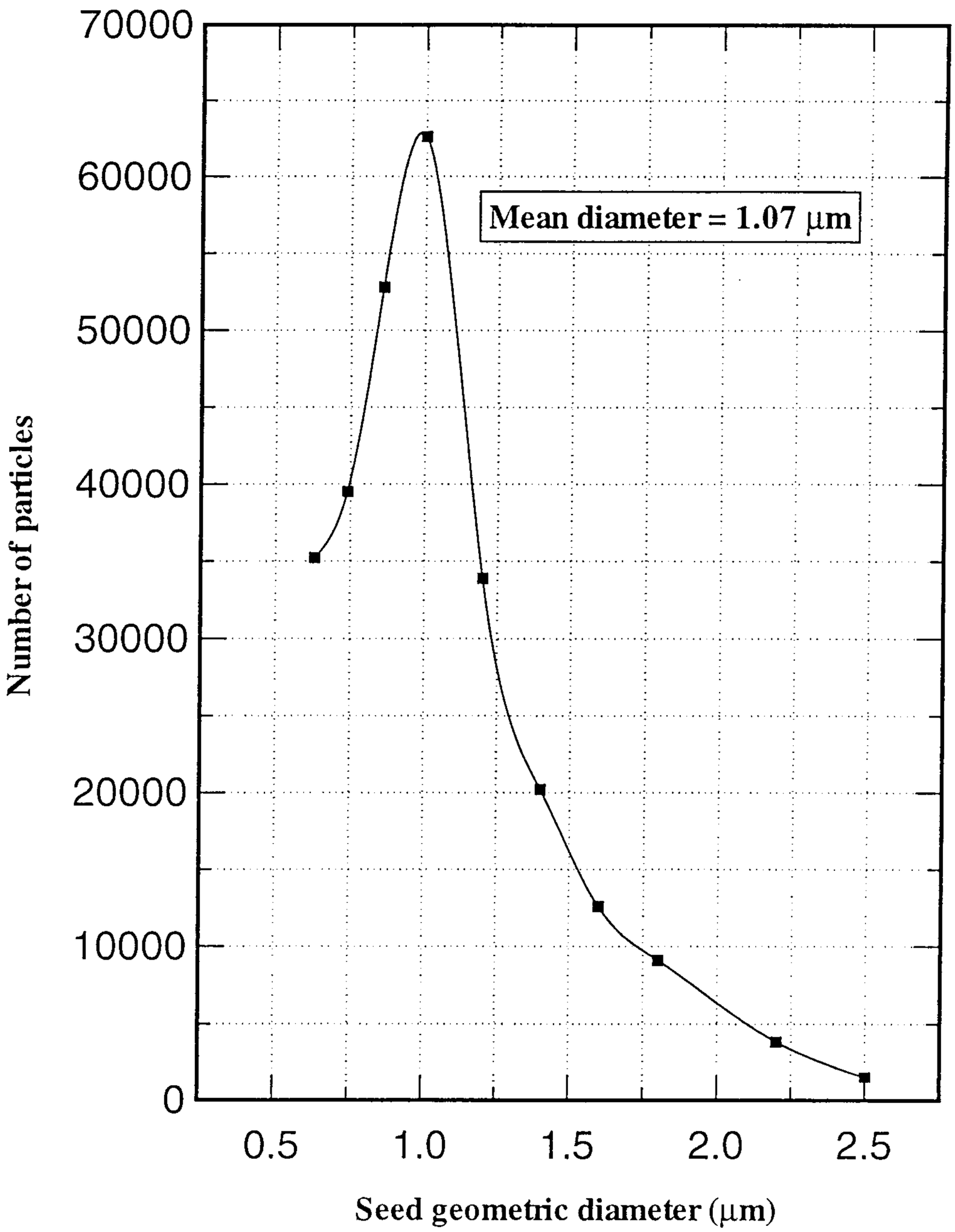

Fig.2.17 Size distribution of the seed sample

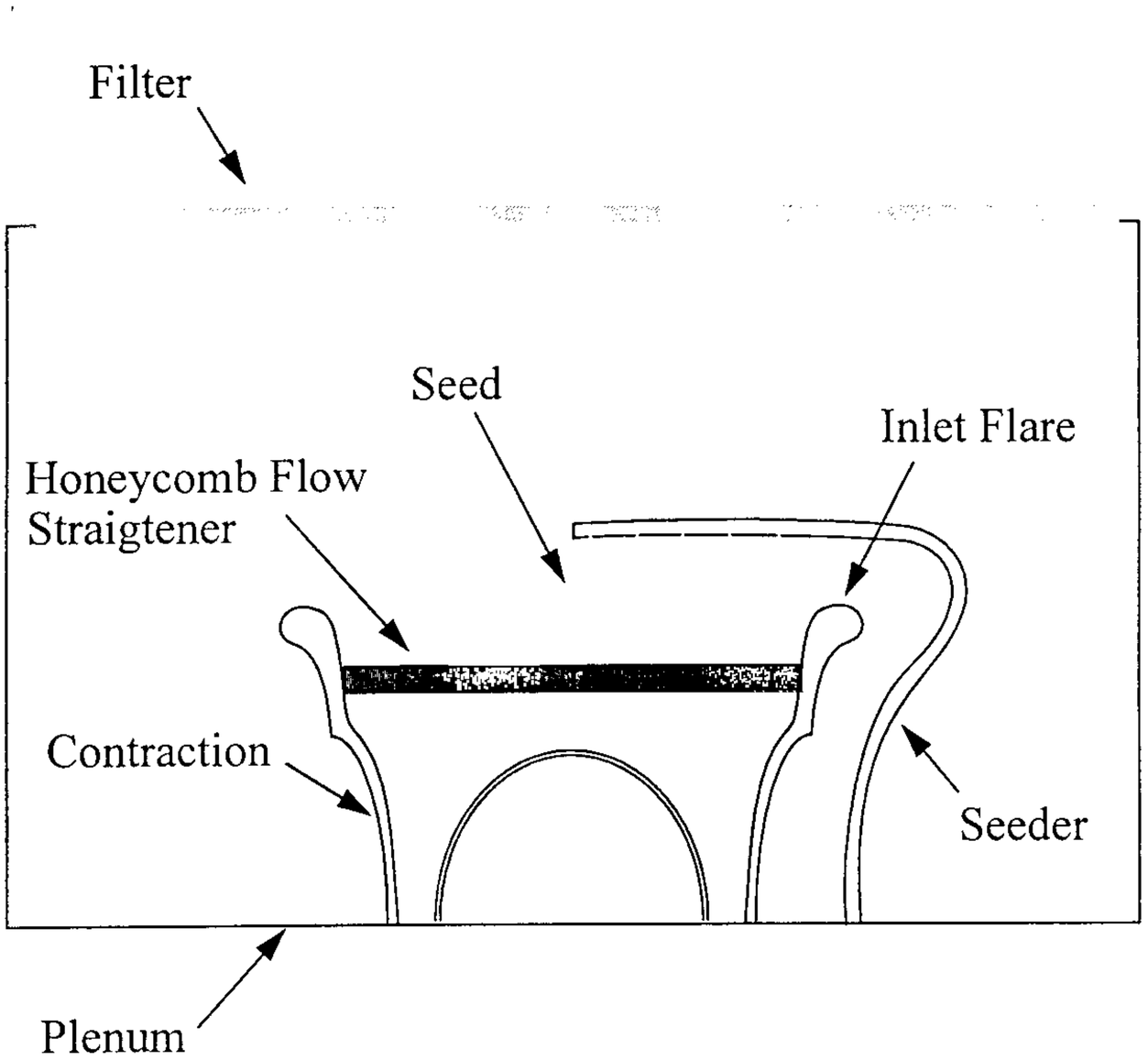

Fig.2.18 Seeder inside inlet plenum

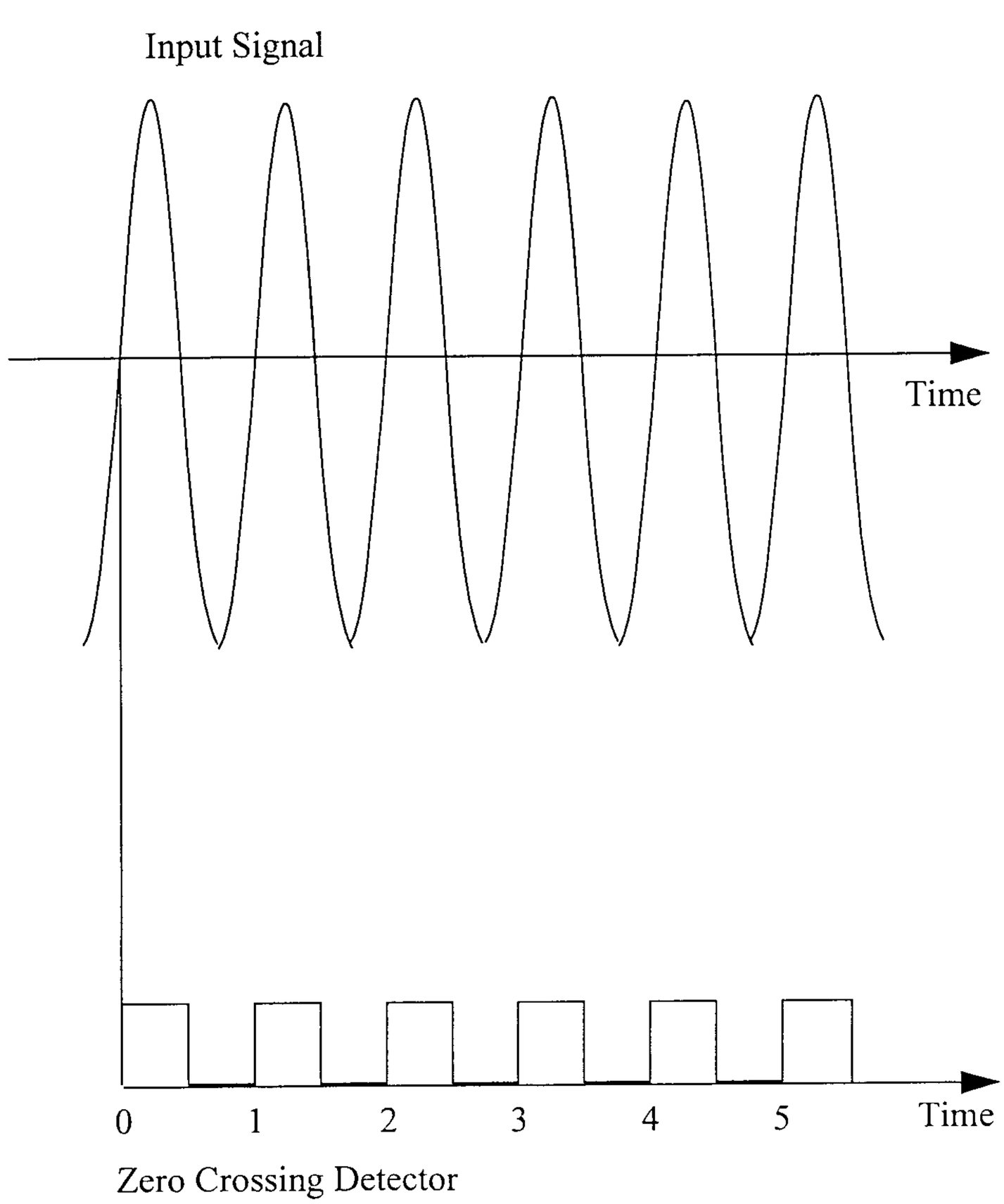

Fig.2.19 Signal zero crossings (counter processors)

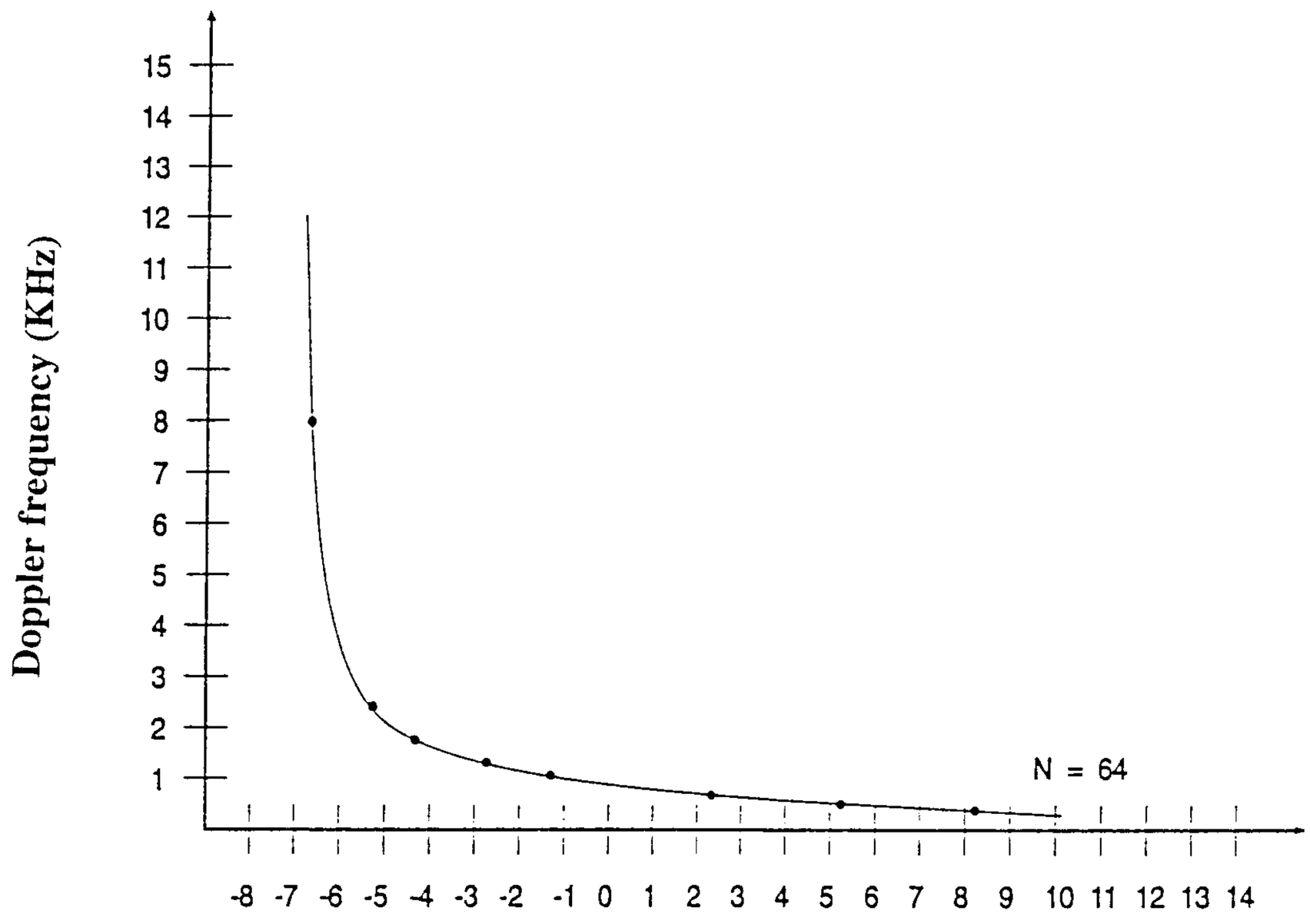

Fig.2.20 Variation of the Doppler frequency with signal to noise ratio (SNR).

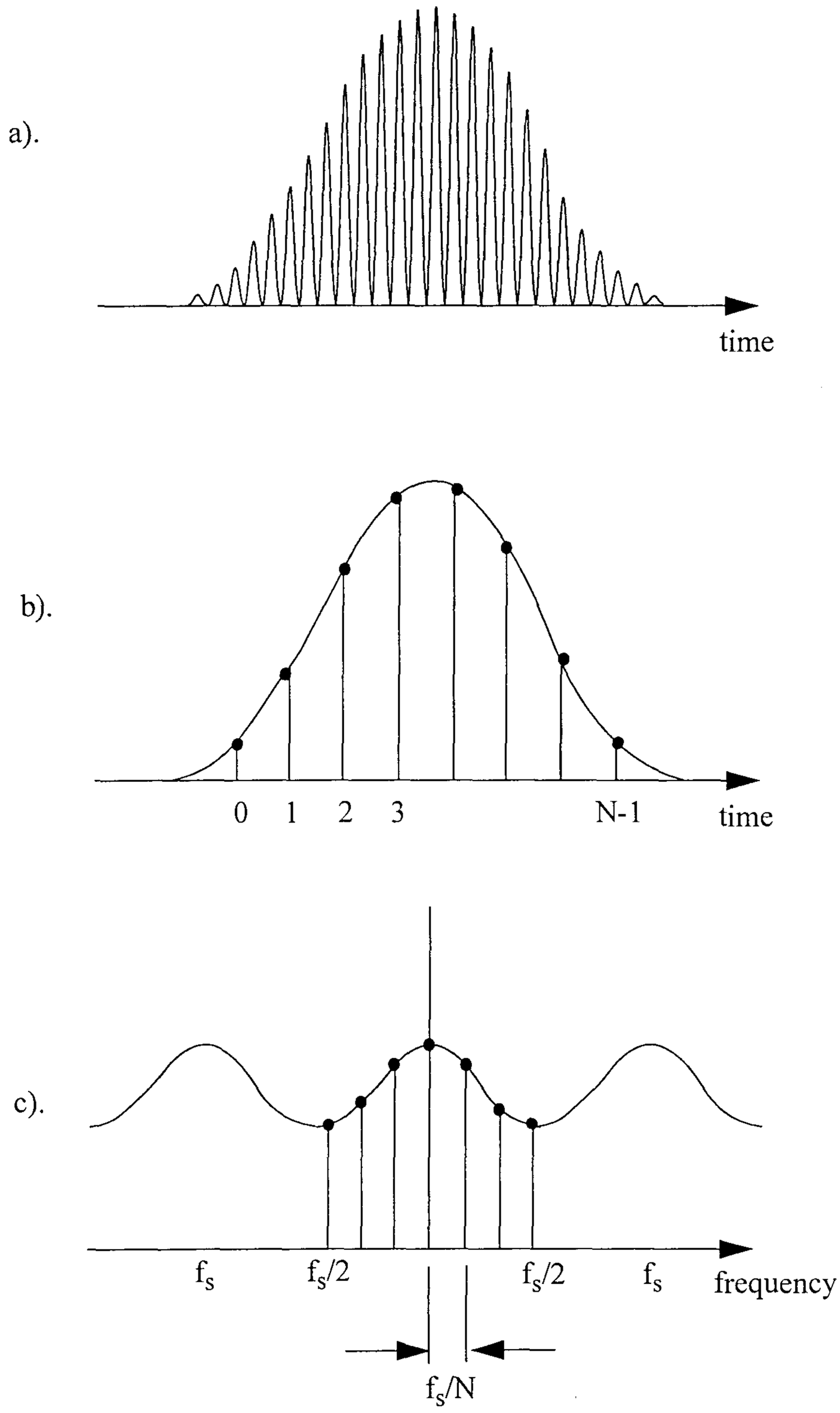

Fig.2.21 - a) Frequecy burst (Idealized)
b) Sampled time function (Idealized)
c) Sampled frequency function calculated using FFT (Idealized)

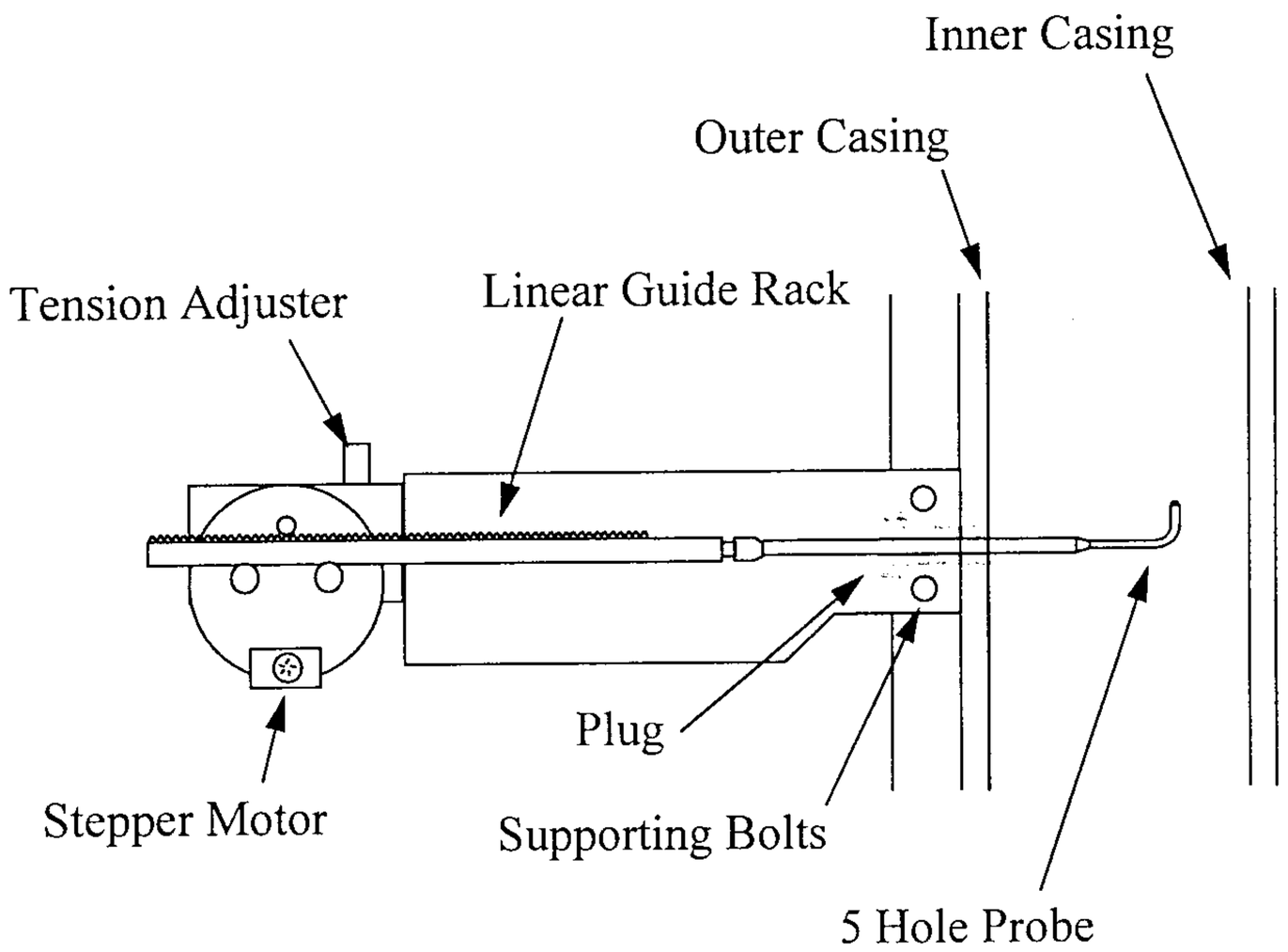

Fig.2.22 Radial Traverse

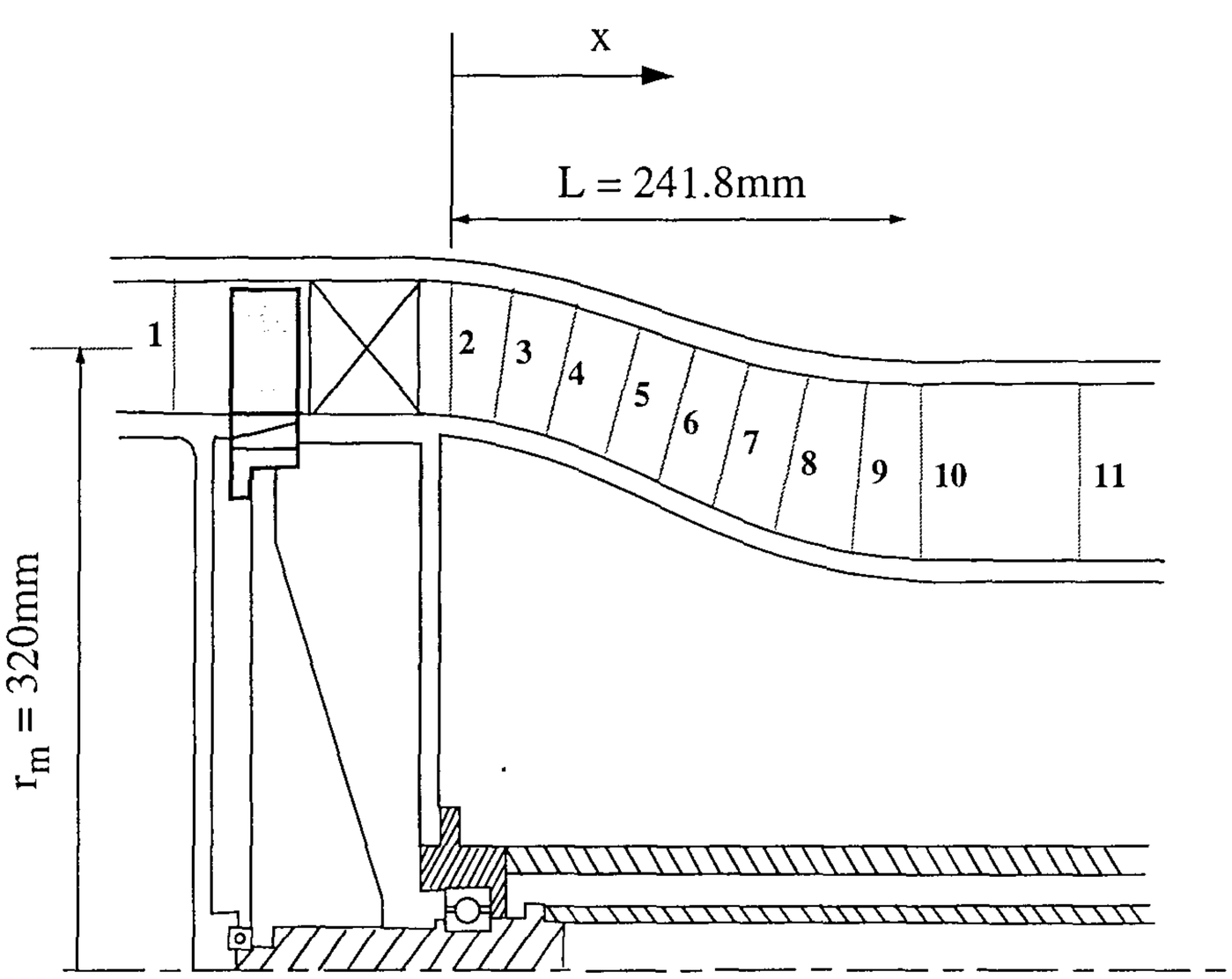

Traverse Locations at Mid Passage Height

STN	1	2	3	4	5	6	7	8	9	10	11
x/L	-0.55	0.00	0.125	0.250	0.375	0.500	0.625	0.750	0.875	1.000	1.400

Fig.2.23 Working section

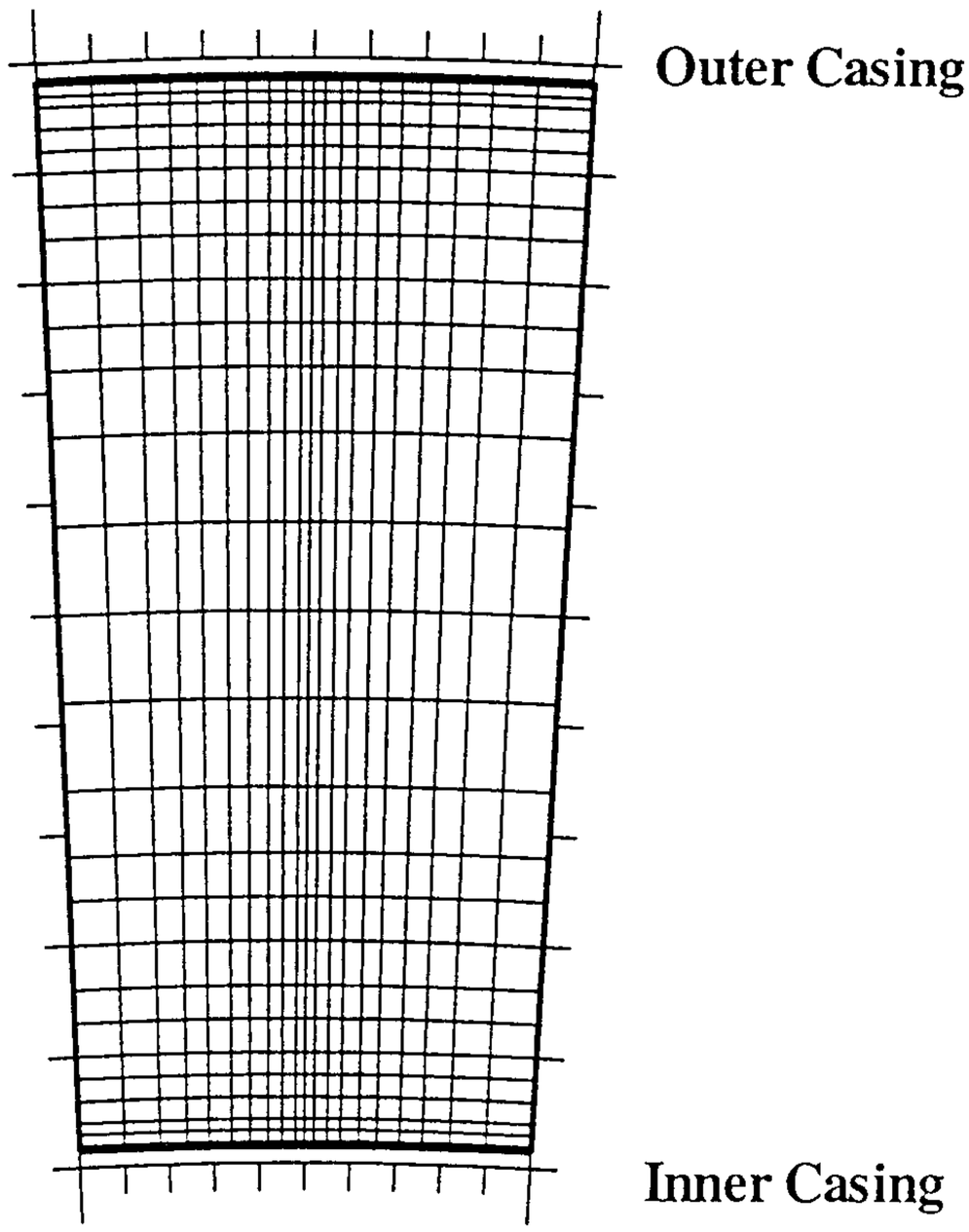

Fig.2.24 Typical area traverse

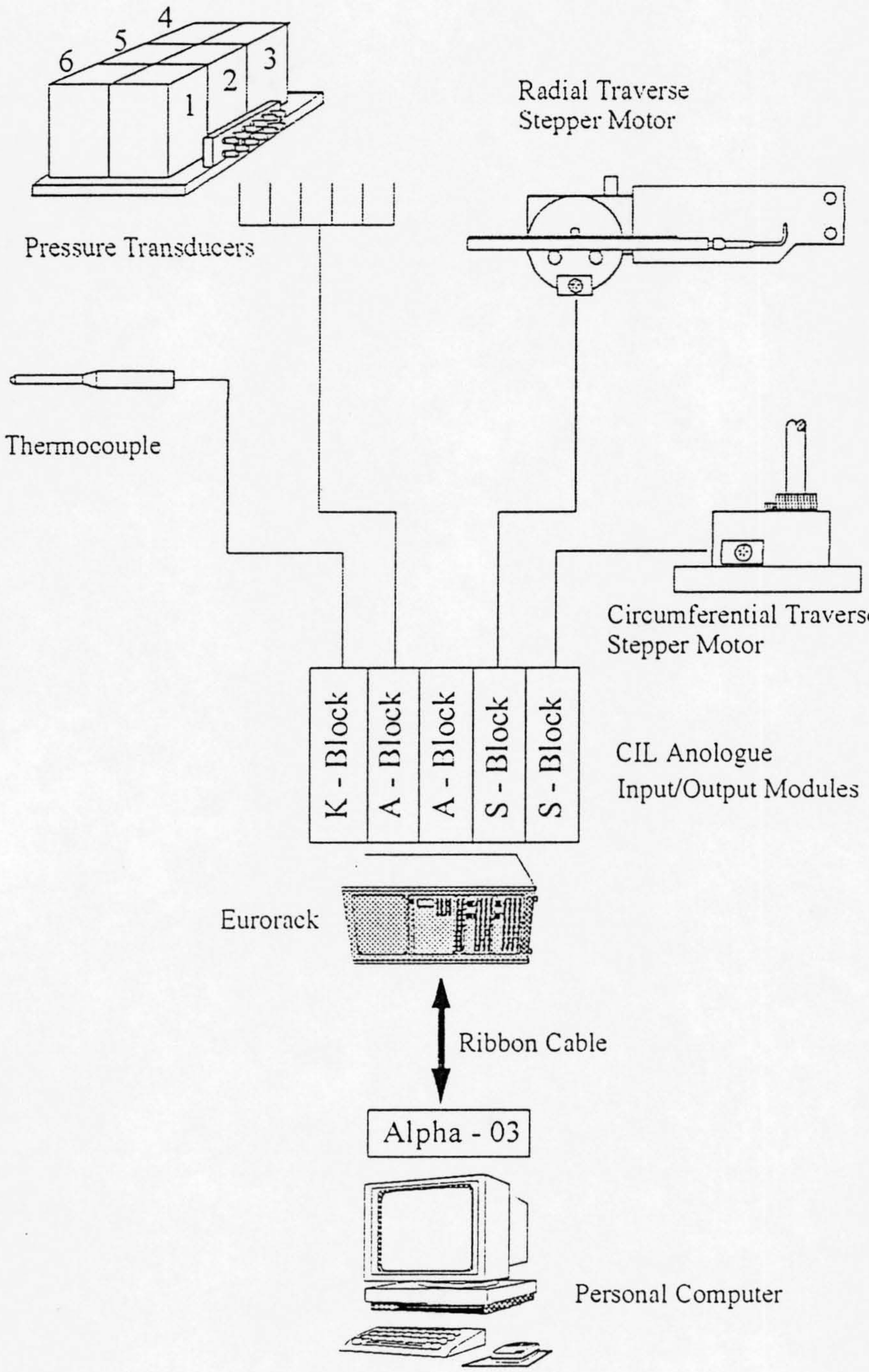

Fig.2.25 Data acquisition system (5 hole probe measurements)

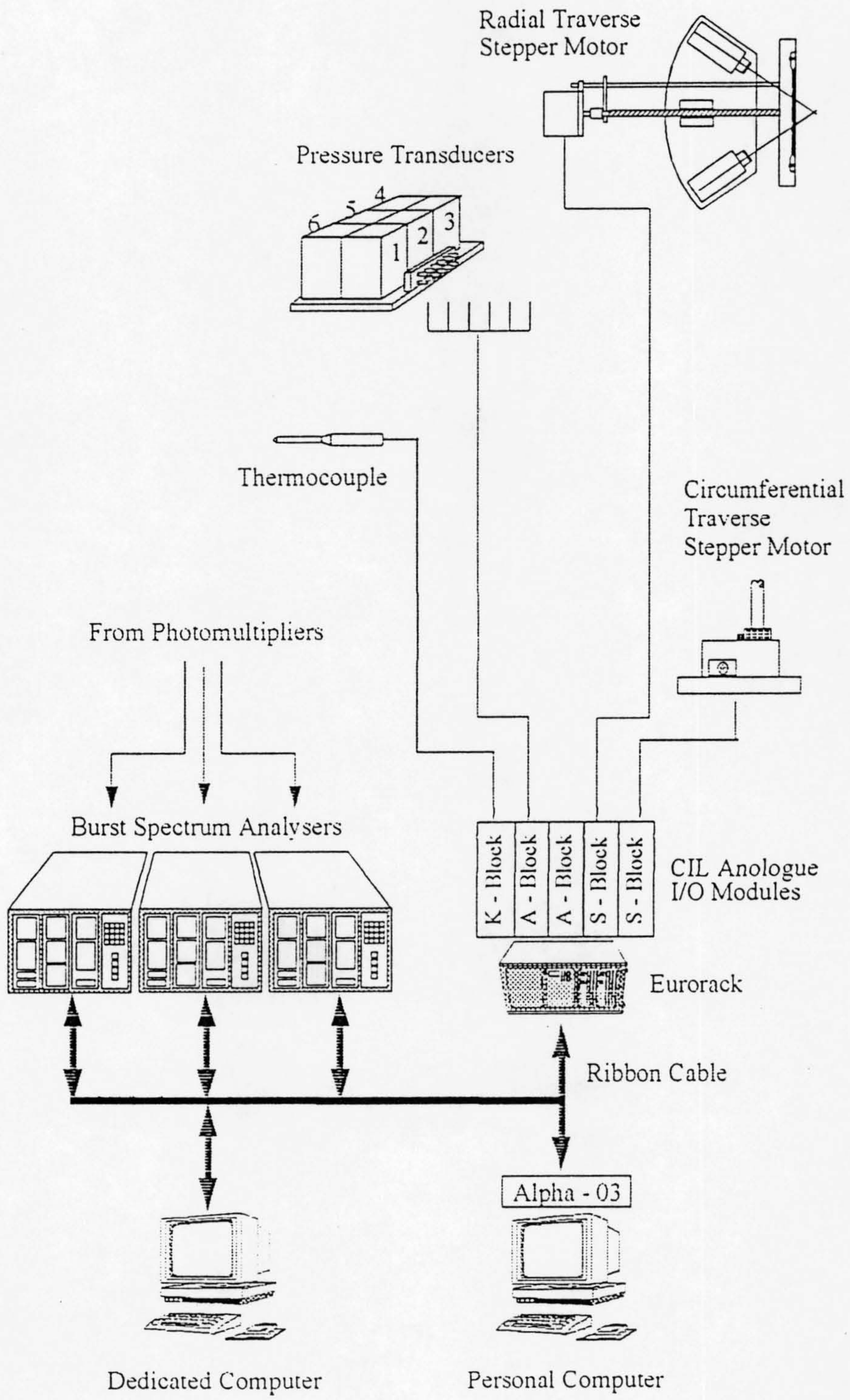

Fig.2.26 Data acquisition system (LDA measurements)

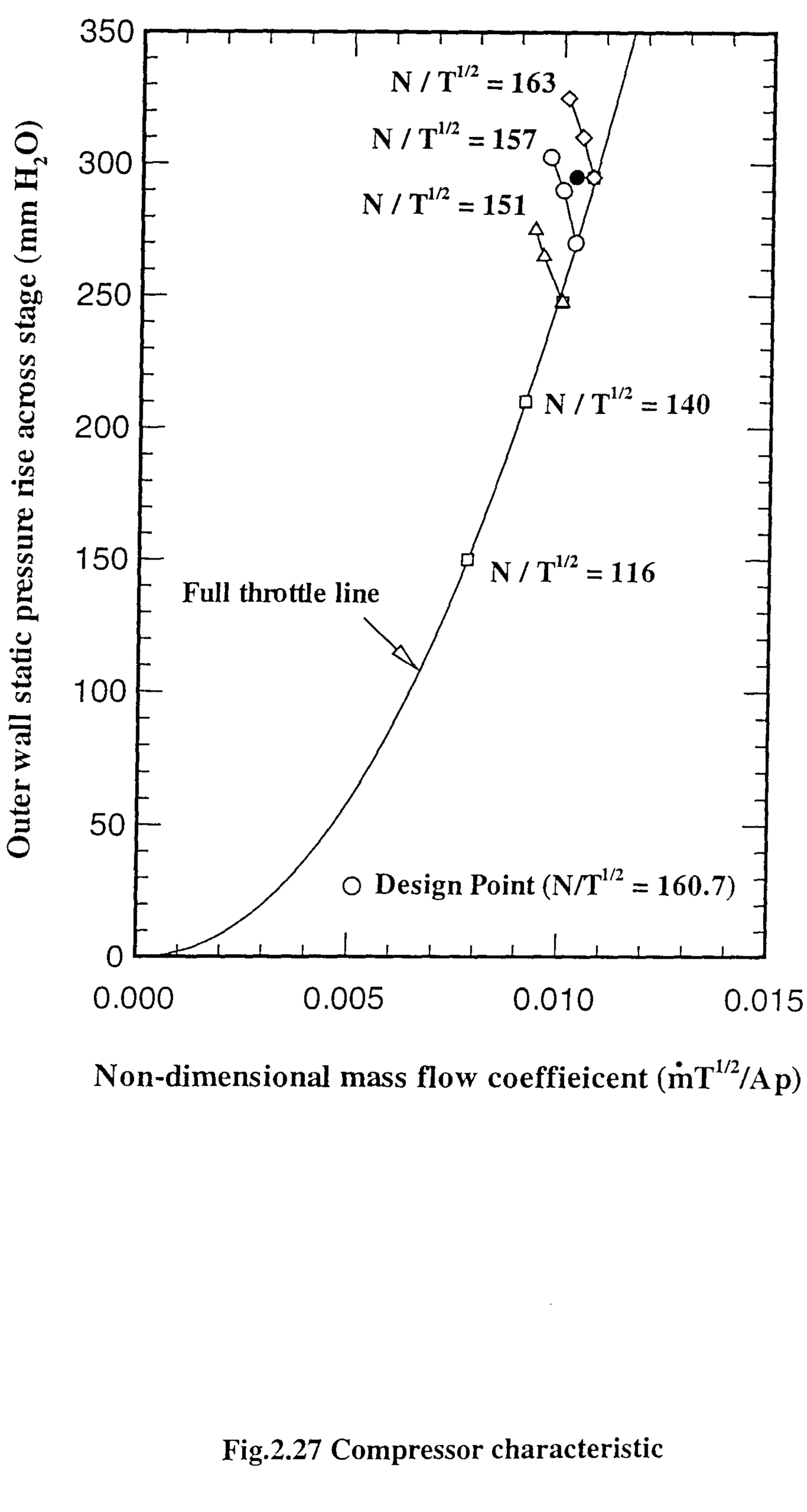

Fig.2.27 Compressor characteristic

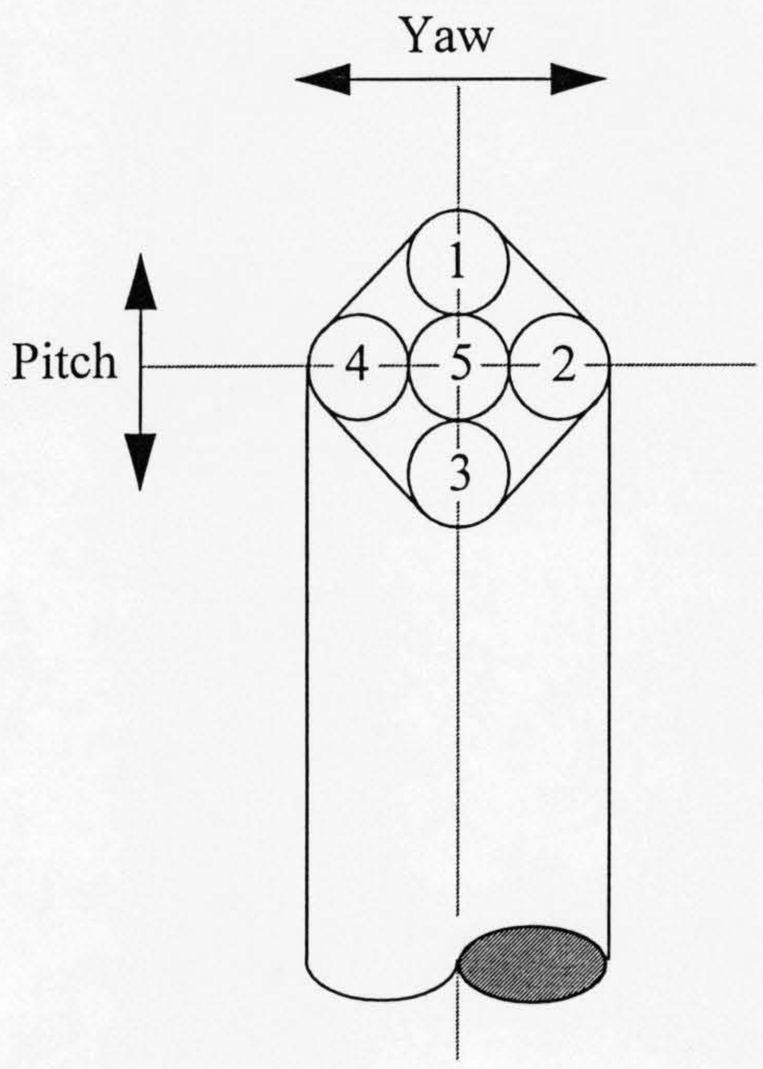

Fig.3.1 Five hole probe geometry.

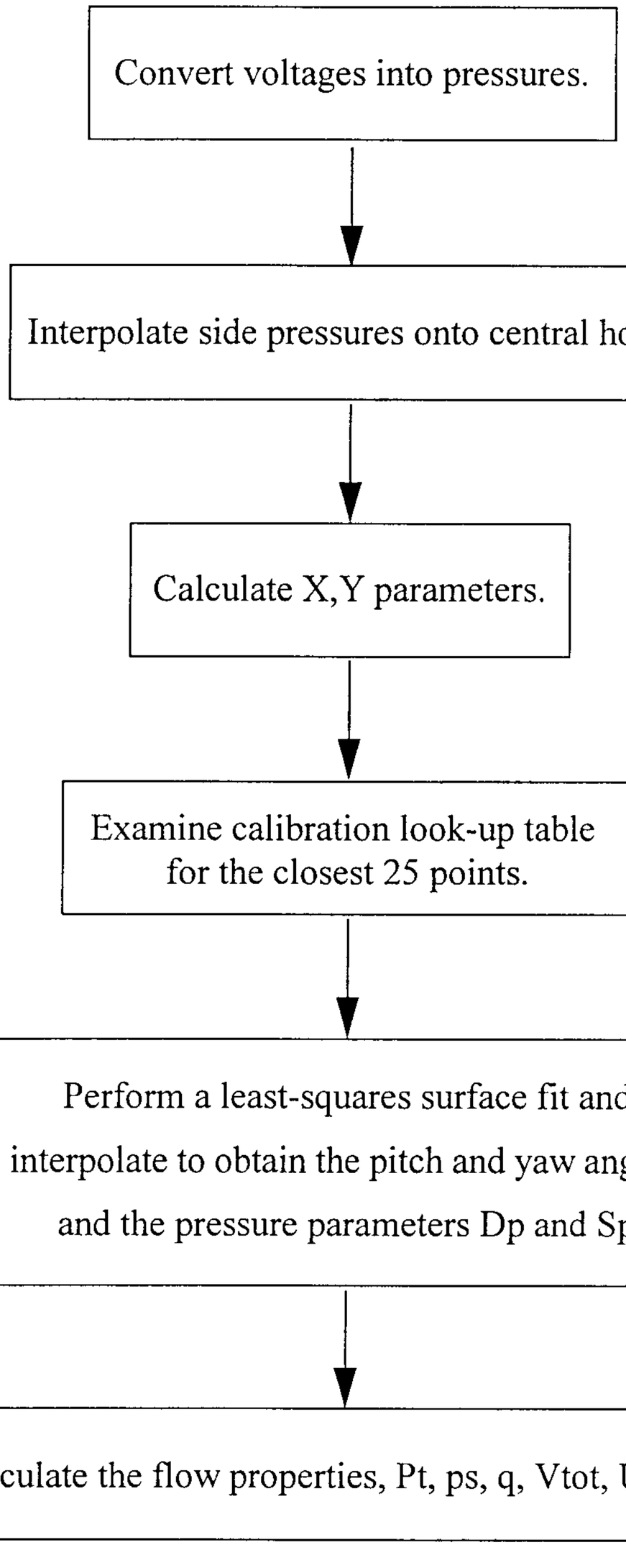

Fig.3.2 Procedure for deriving flow properties (5 hole probe)

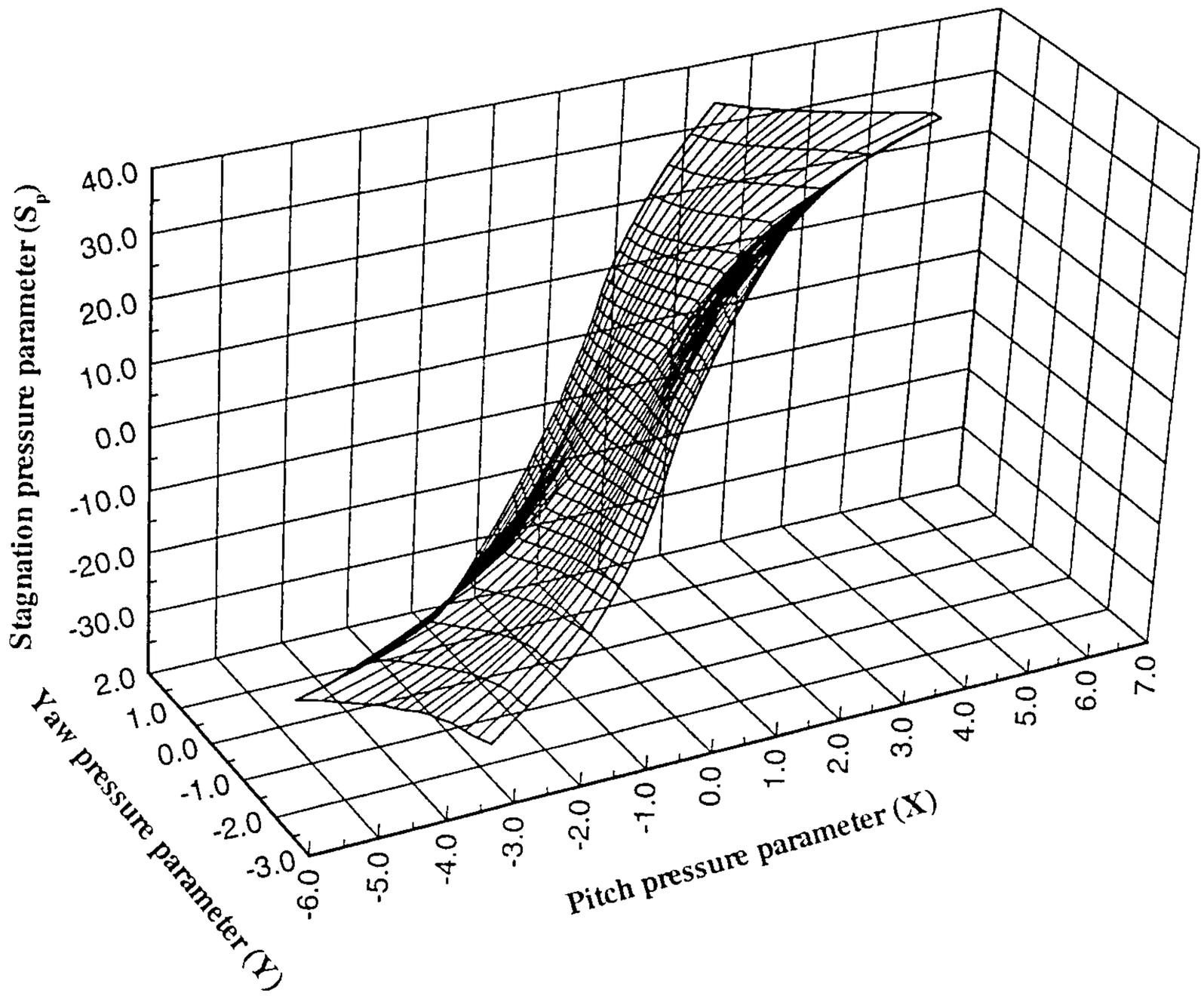

Fig.3.3 Five hole probe calibration X,Y,Z surface.

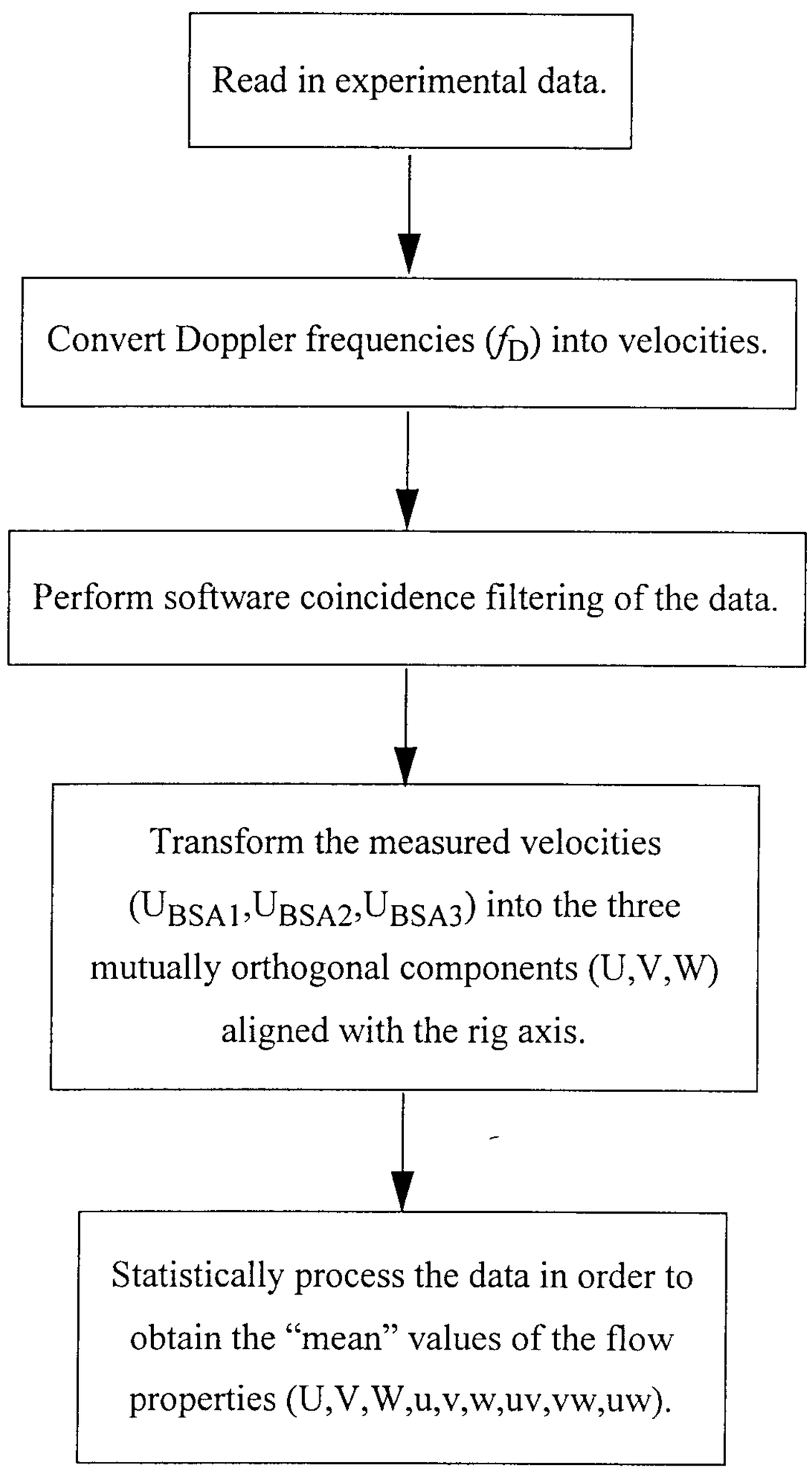

Fig.3.4 Procedure for deriving flow properties (LDA)

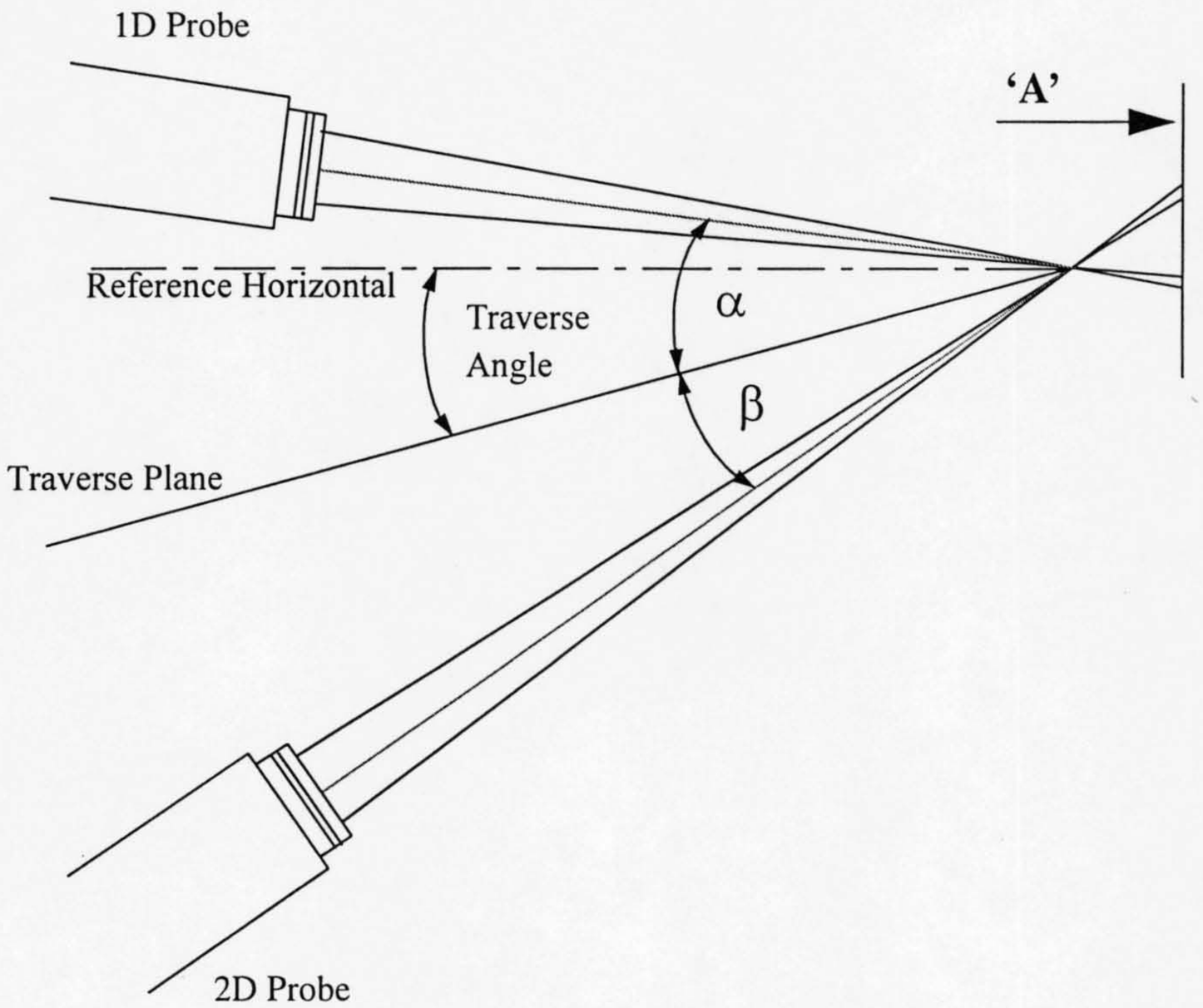

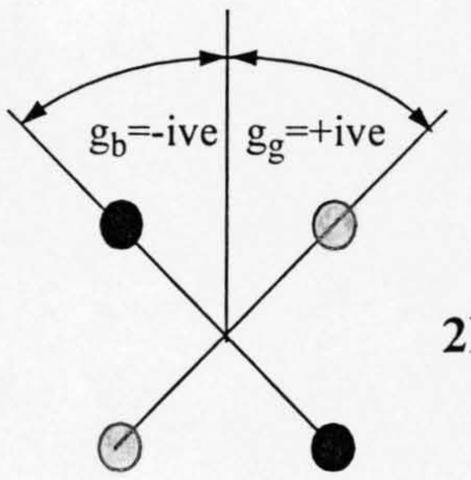

2D Beams

View on 'A'

Blue

Green

Violet

1D Beams

Fig.3.5 Laser beam alignment

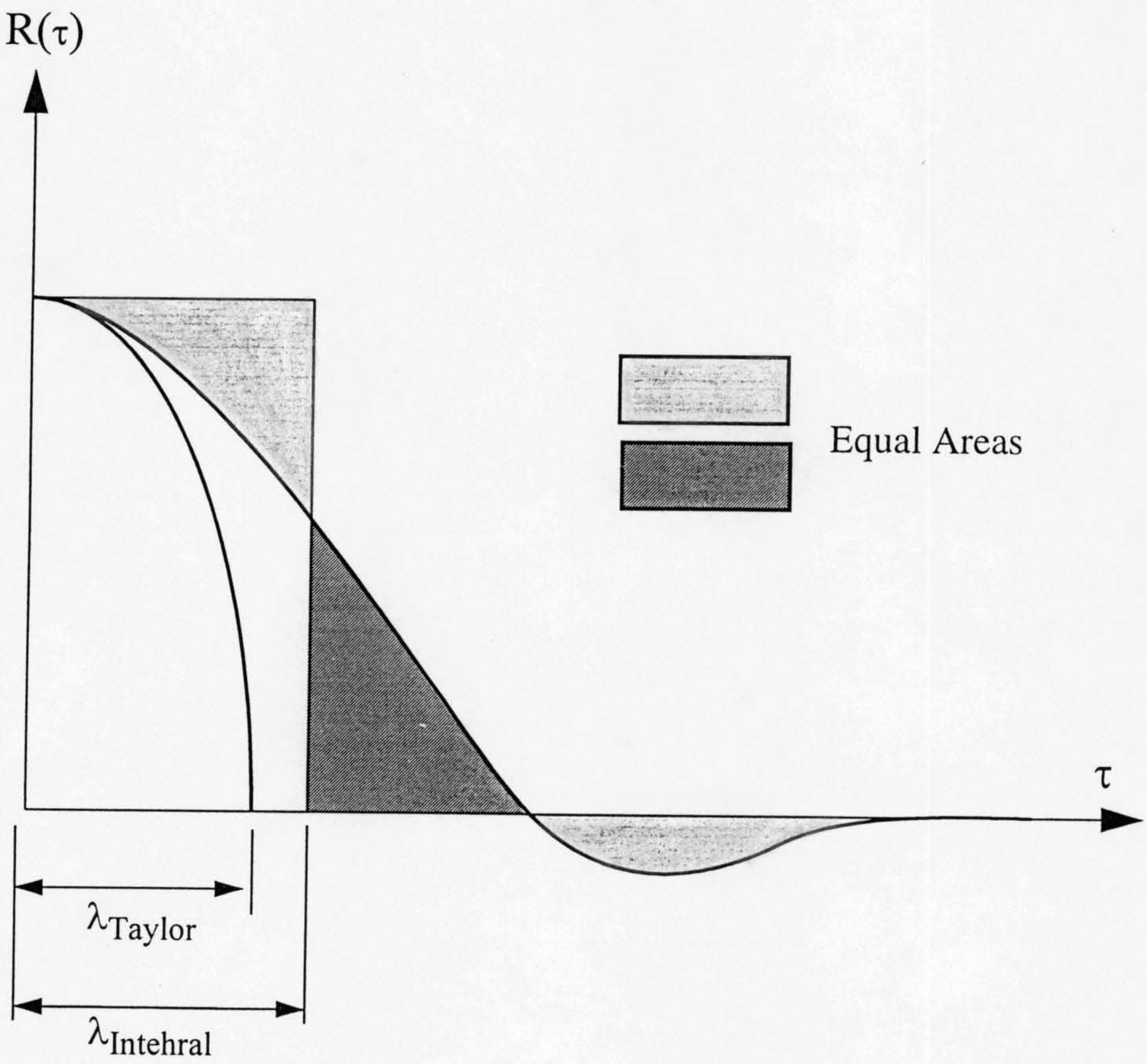

Fig.3.6 Autocorrelation of velocity signal.

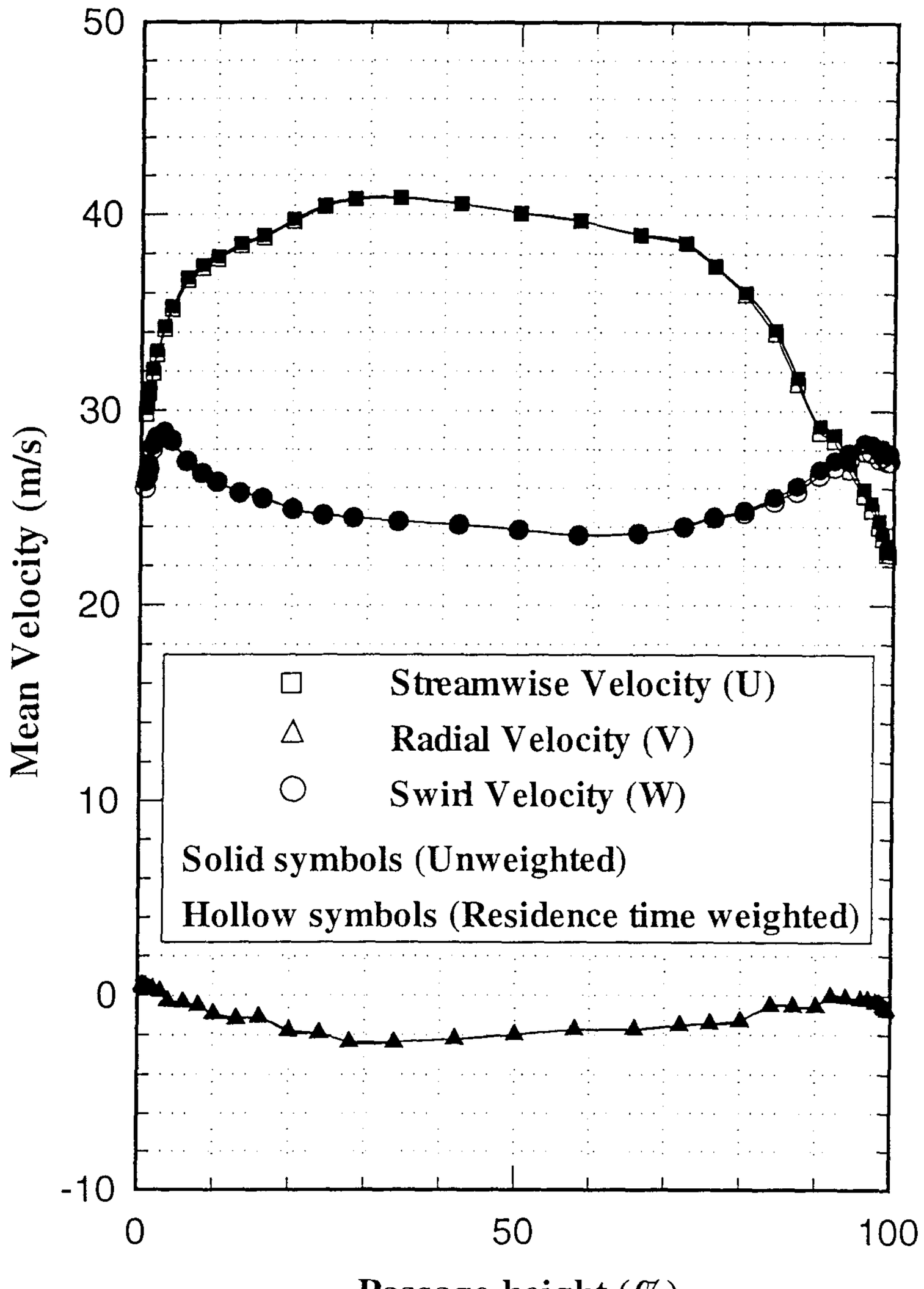

Fig.3.7 Comparison of residence time weighted and unweighted data.

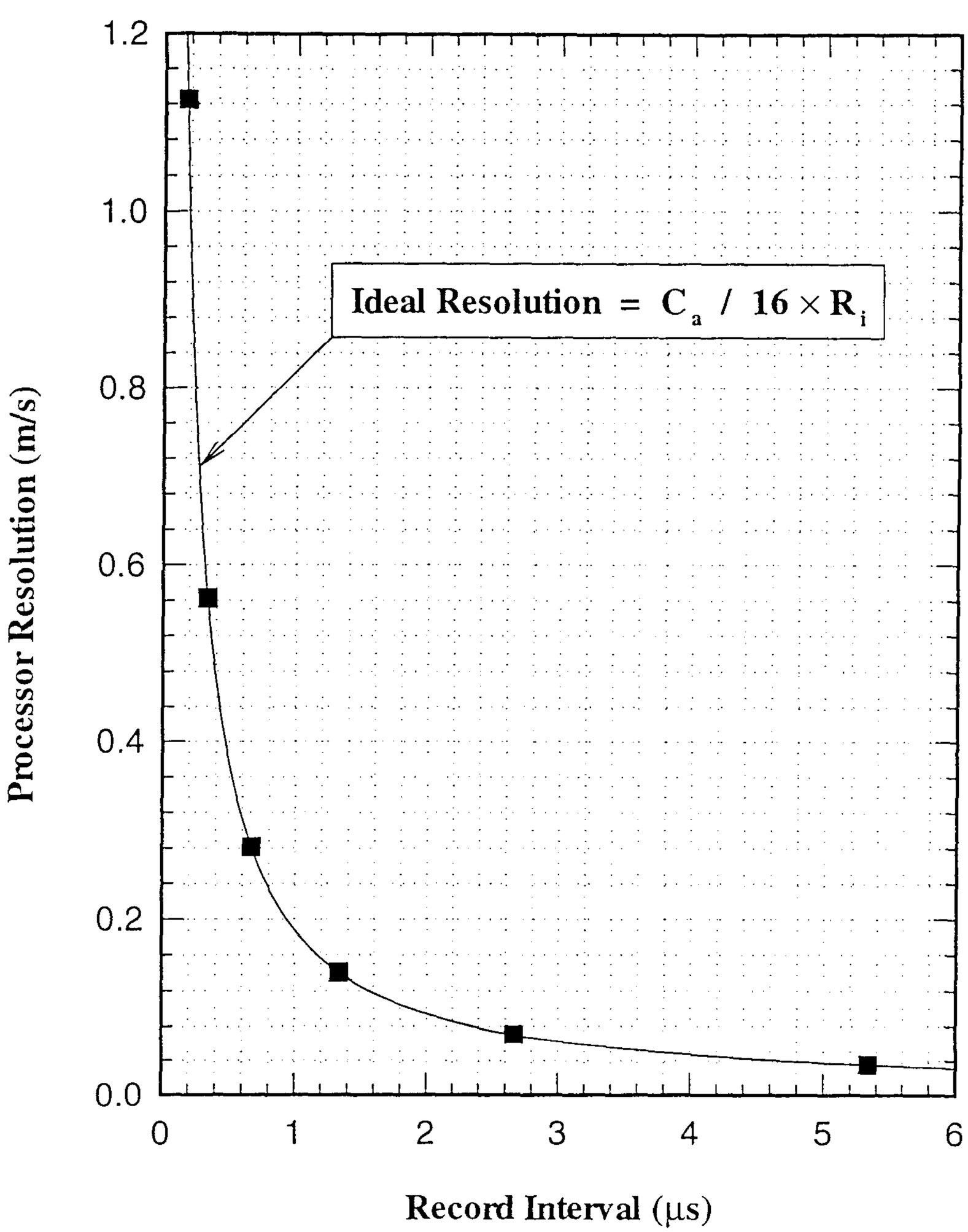

Fig.3.8 Processor resolution versus record interval.

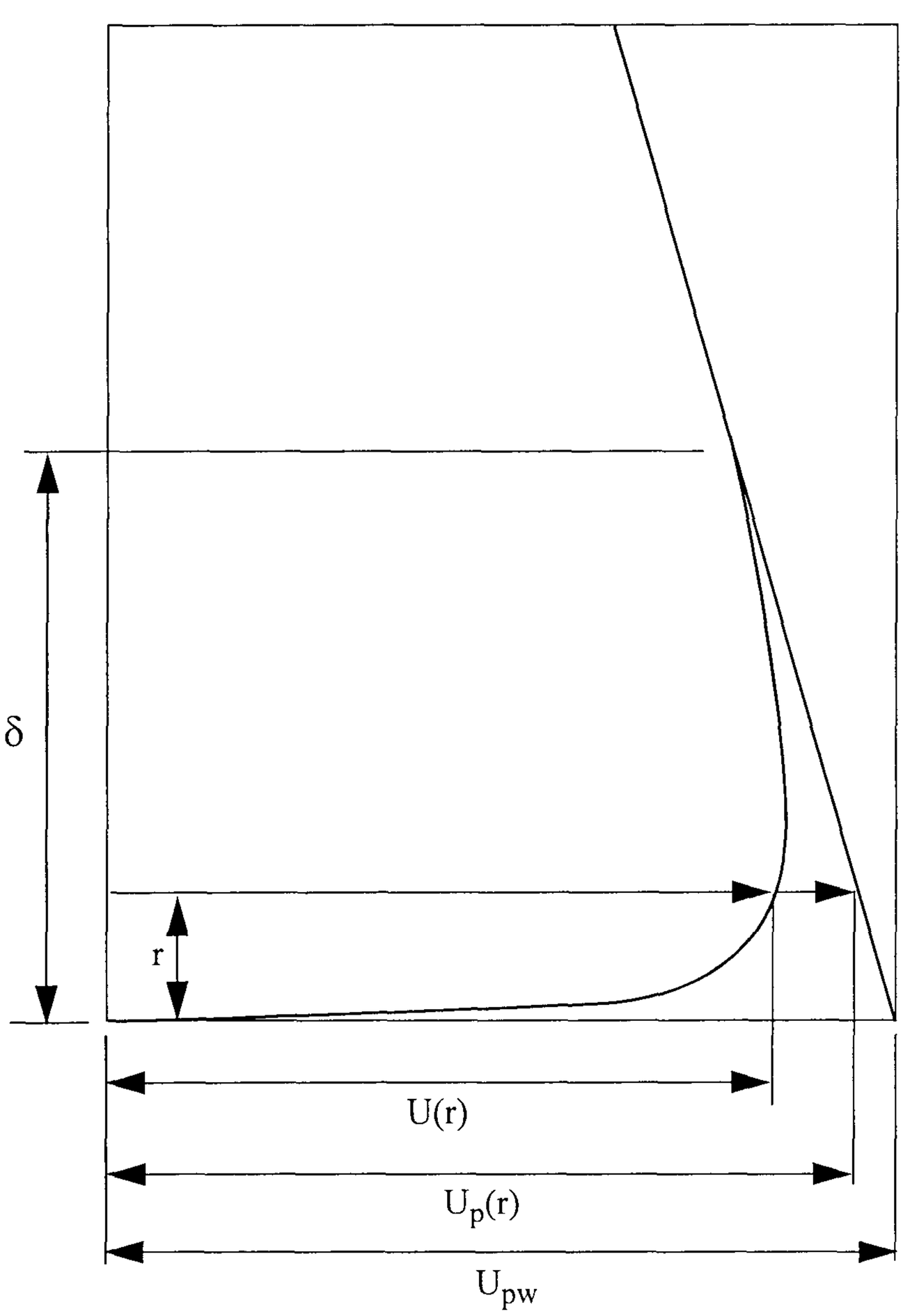

Fig.3.9 Boundary layer mean velocity profile

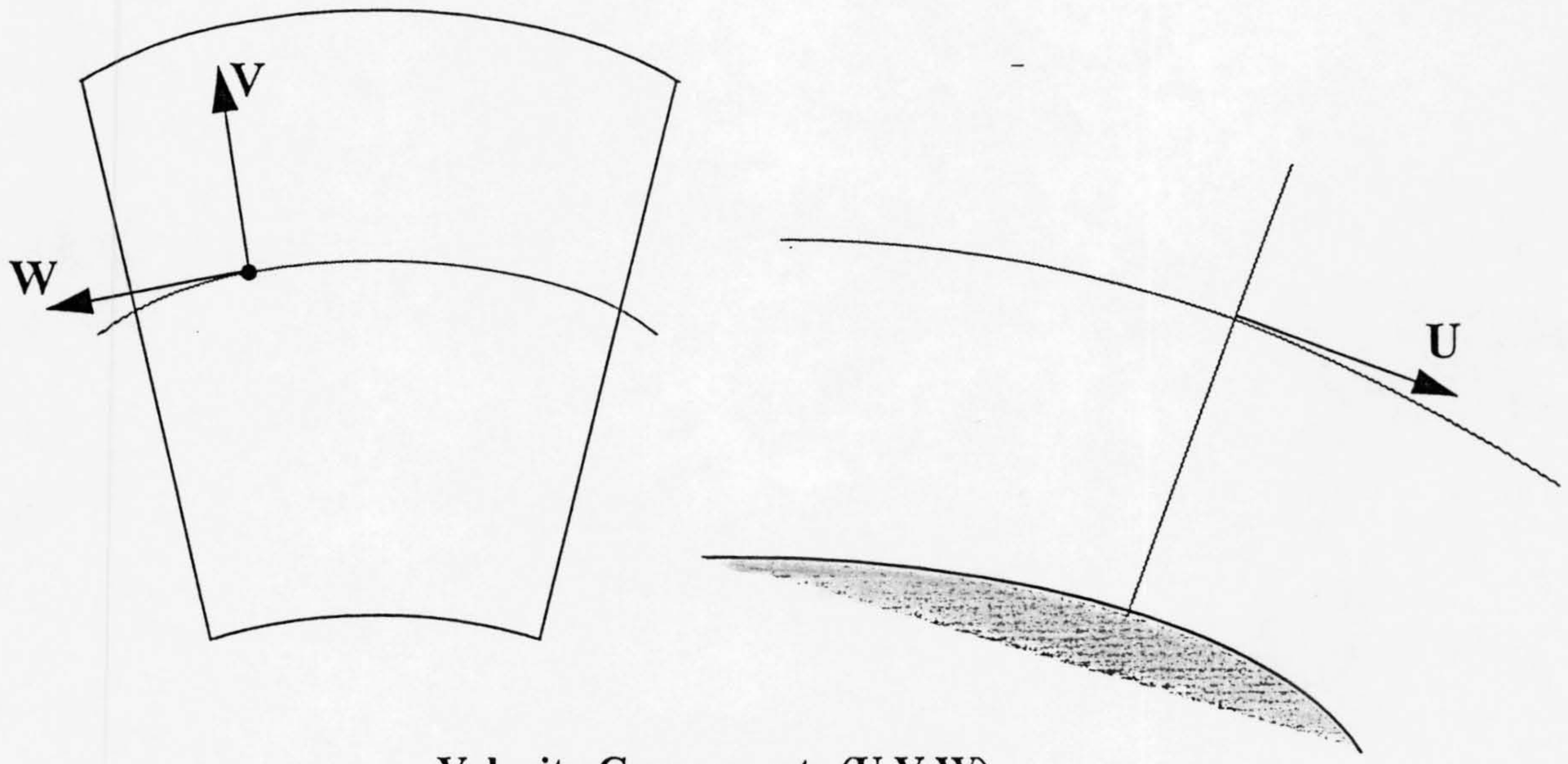

Velocity Components (U,V,W)

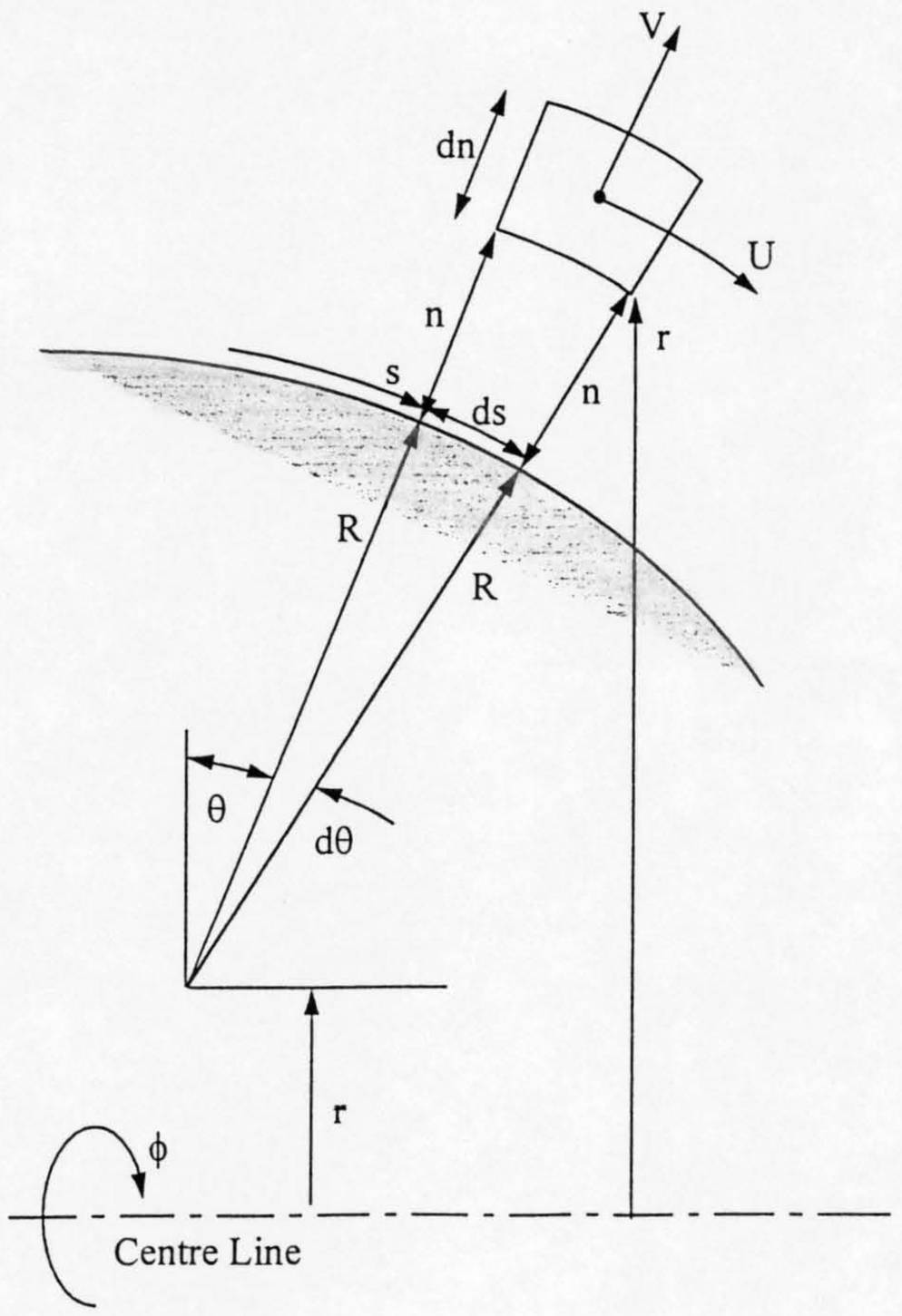

Fig.3.10 The s,n,ϕ coordinate system.

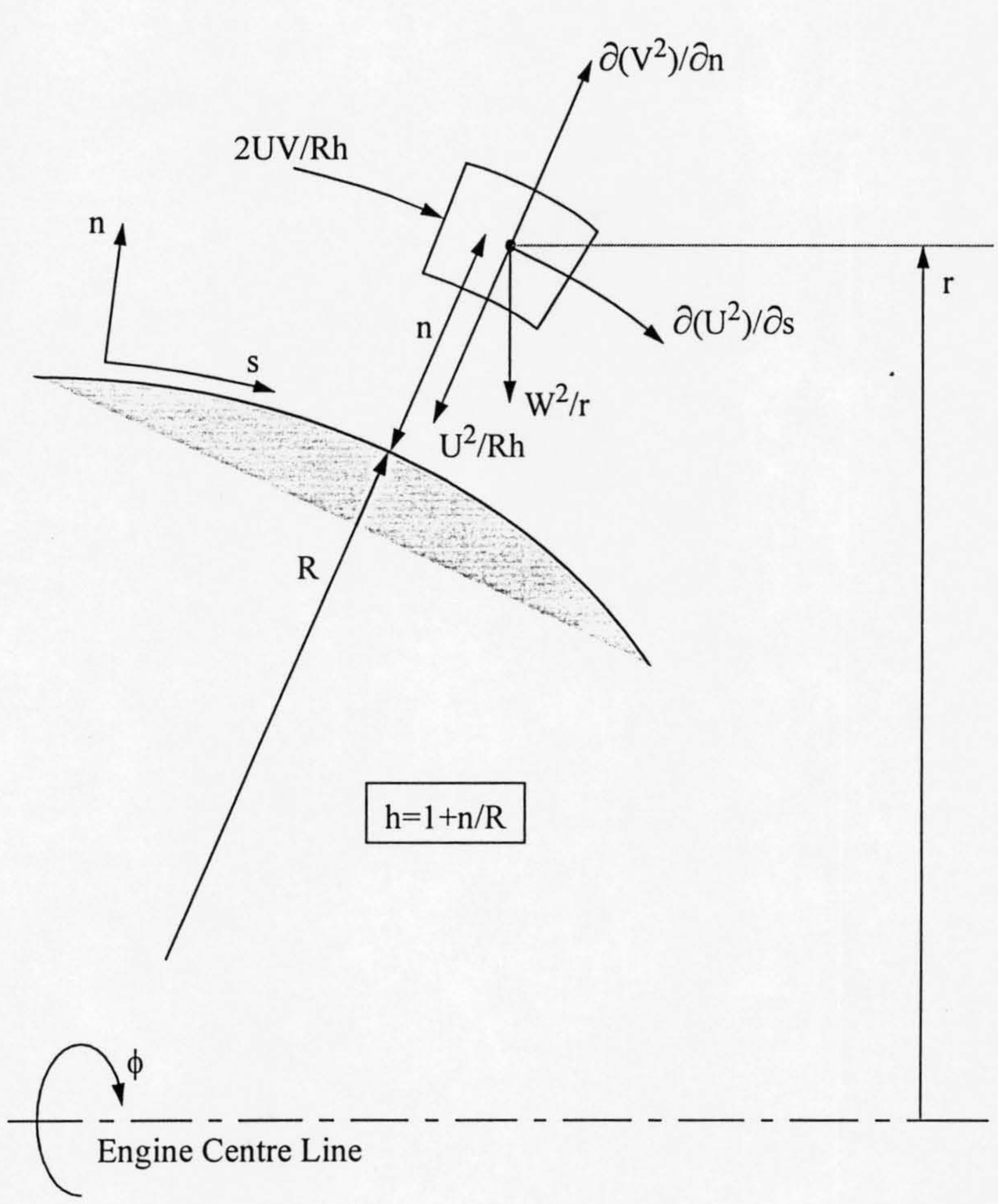

Fig.3.11 The accelerations on a fluid element.

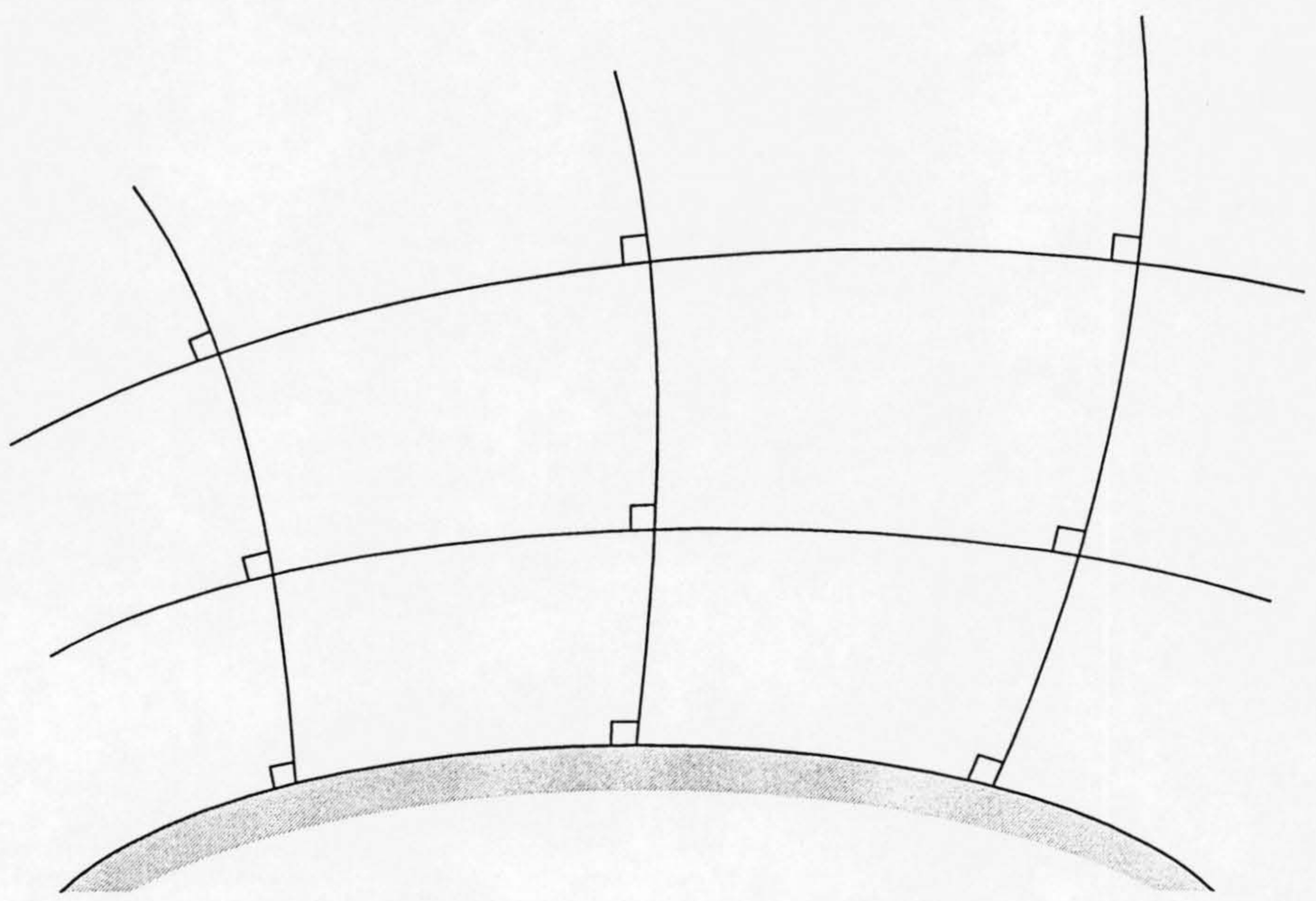

Fig.3.12 The doubly curvilinear orthogonal coordinate system.

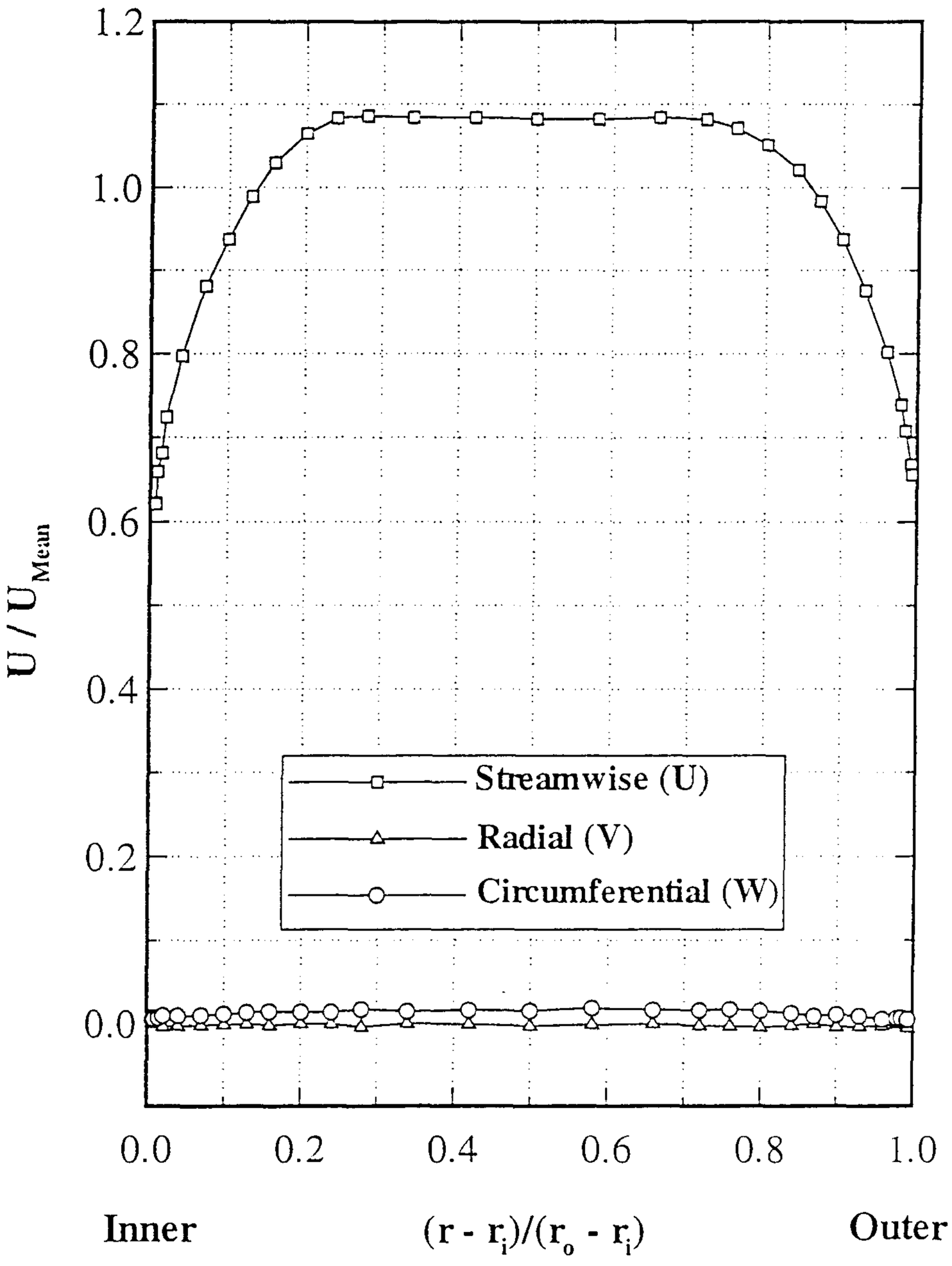

Fig.4.1.1 Mean velocity profiles (x/L=-0.55).

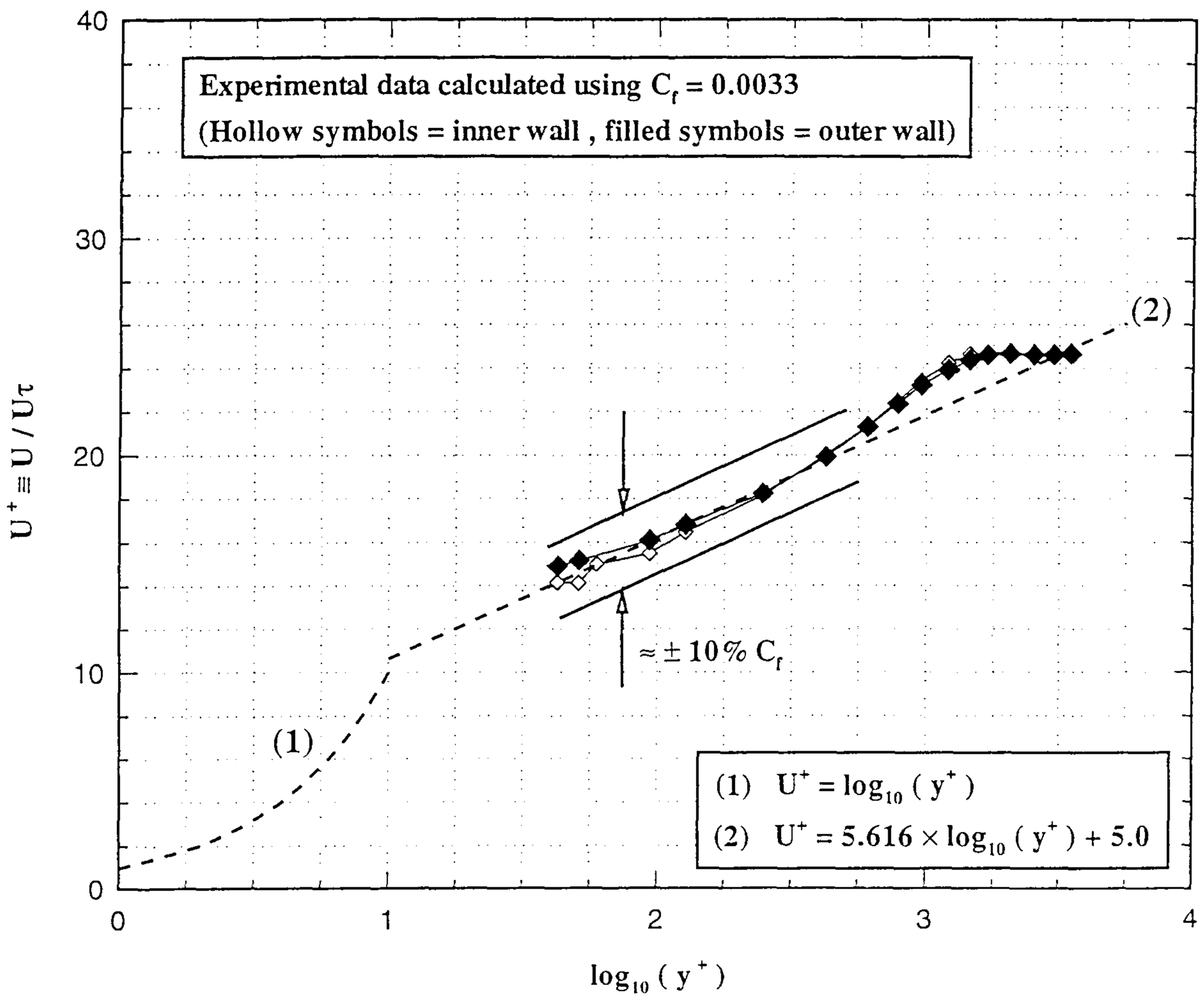

Fig.4.1.2 Log-law velocity profiles (x/L=-0.55).

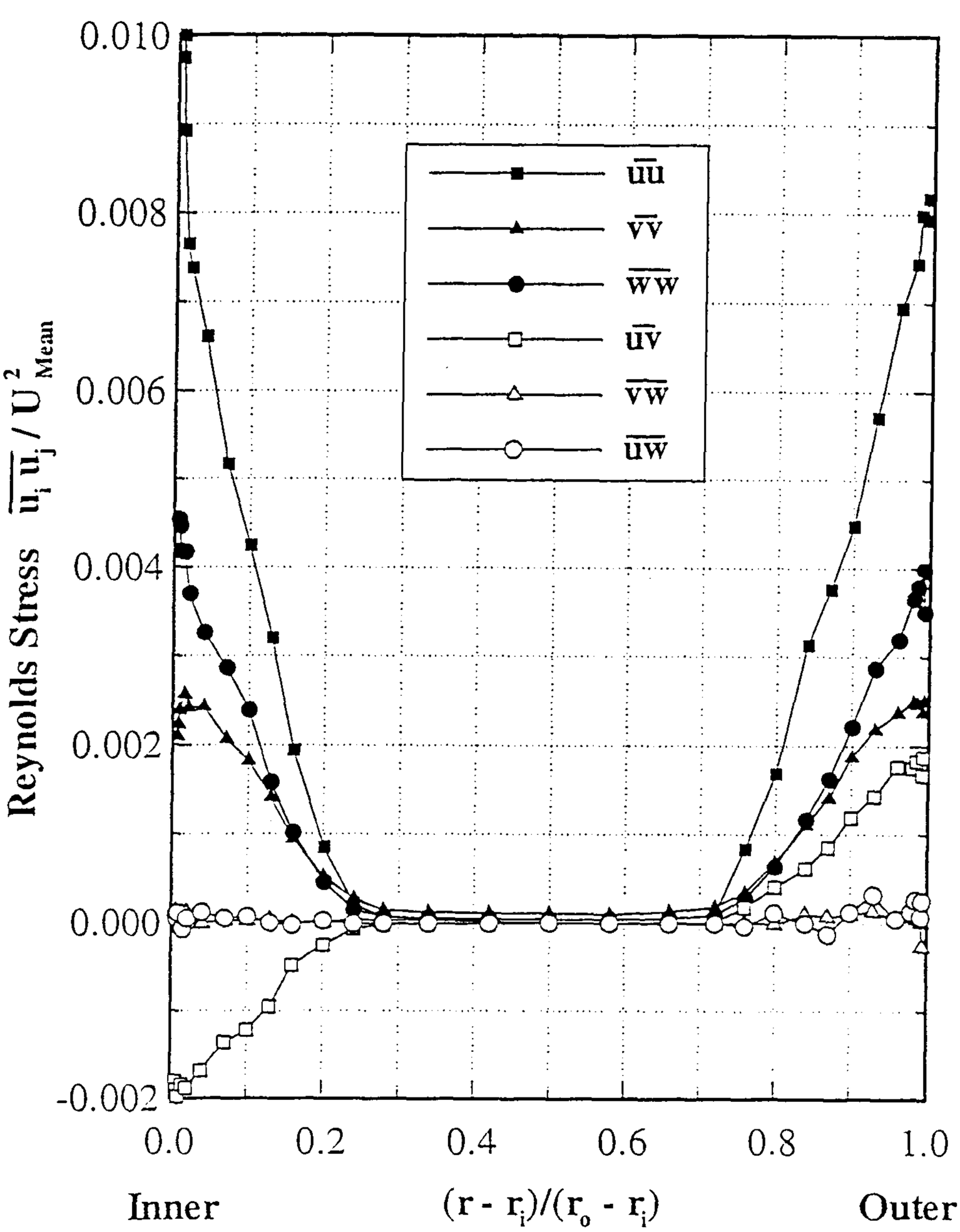

Fig.4.1.3 Reynolds stress profiles (x/L=-0.55).

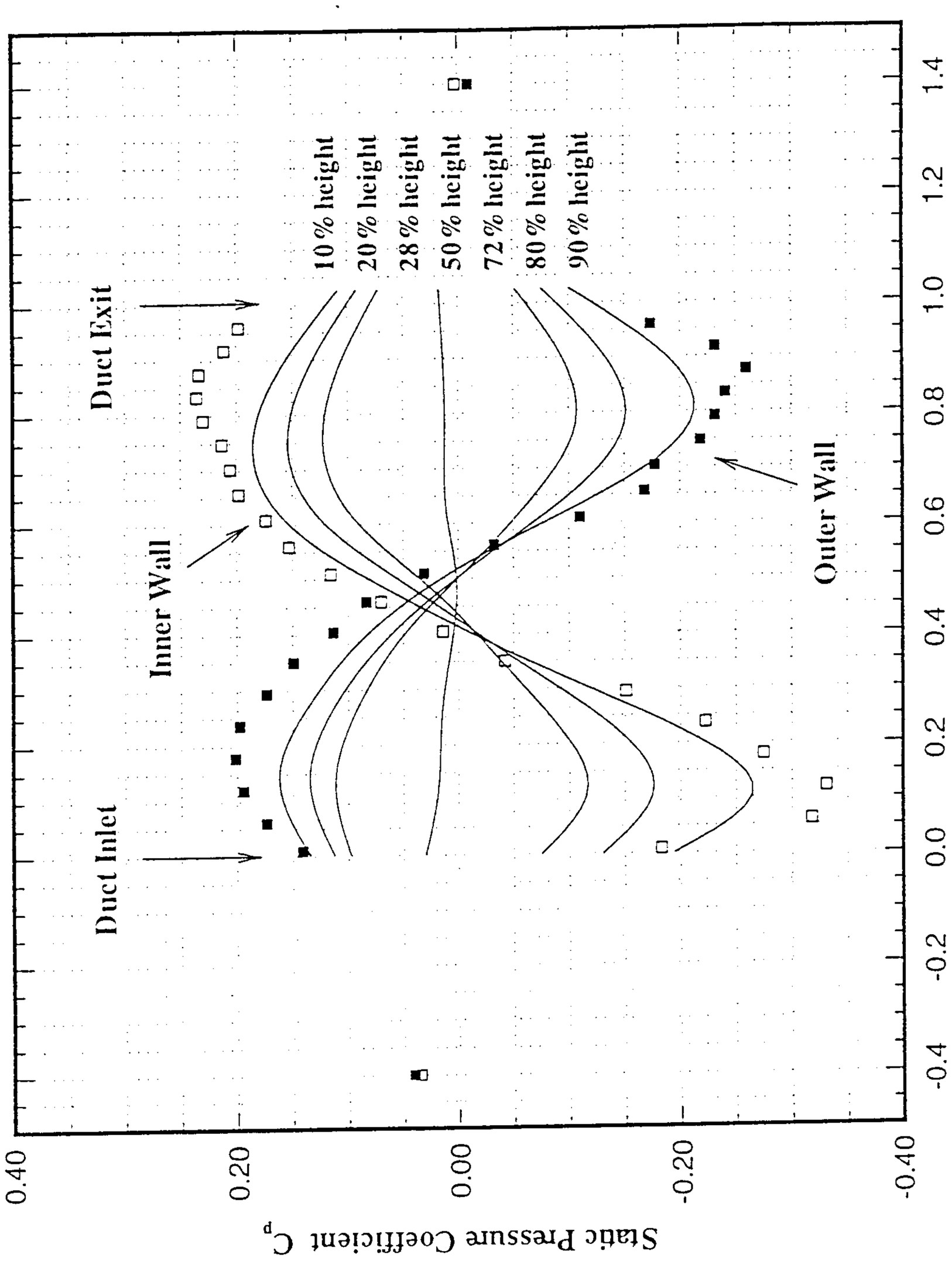

Fig.4.1.4 Axial distribution of static pressure coefficient (C_p).

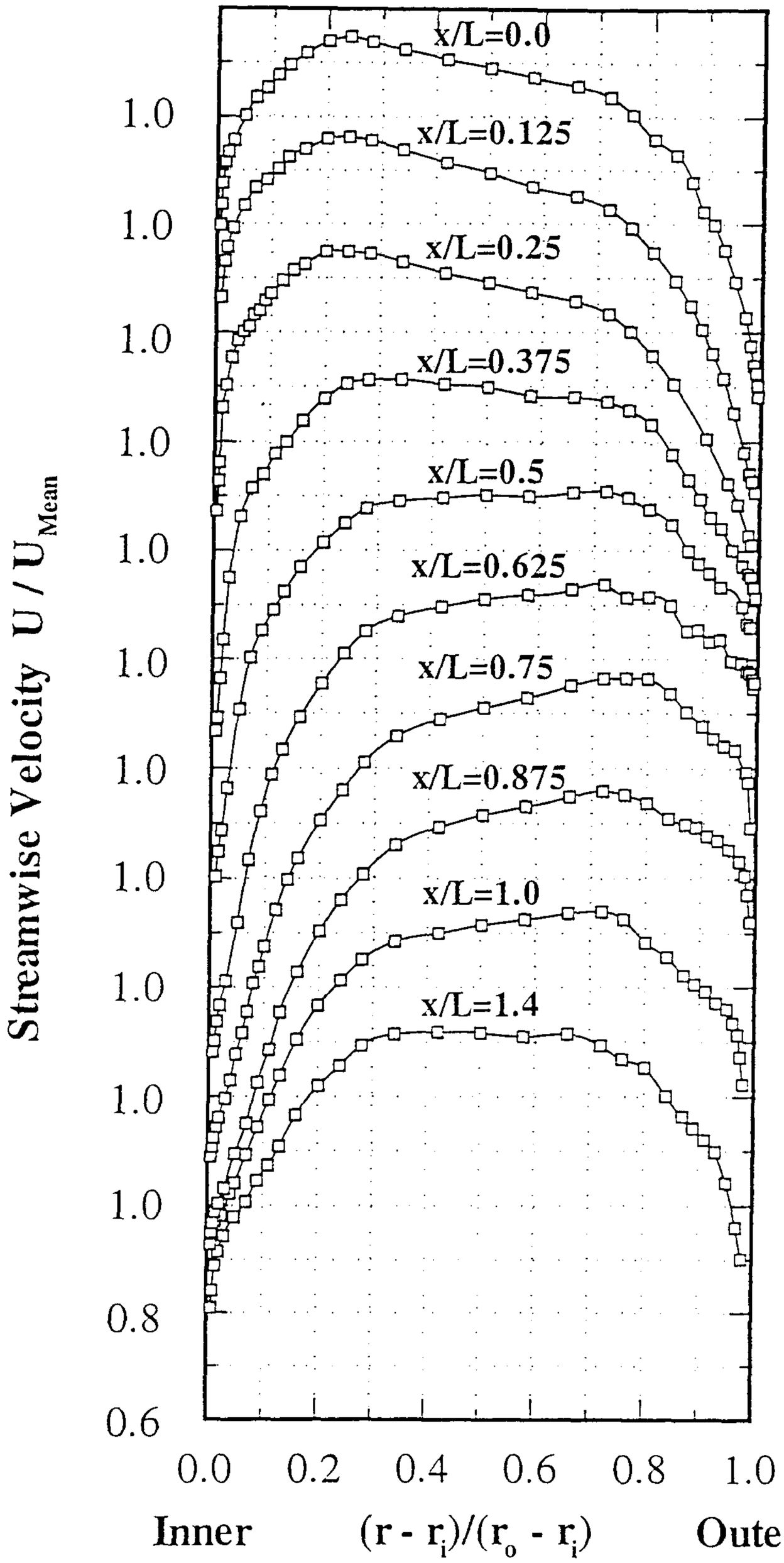

Fig.4.1.5 Development of streamwise velocity (U).

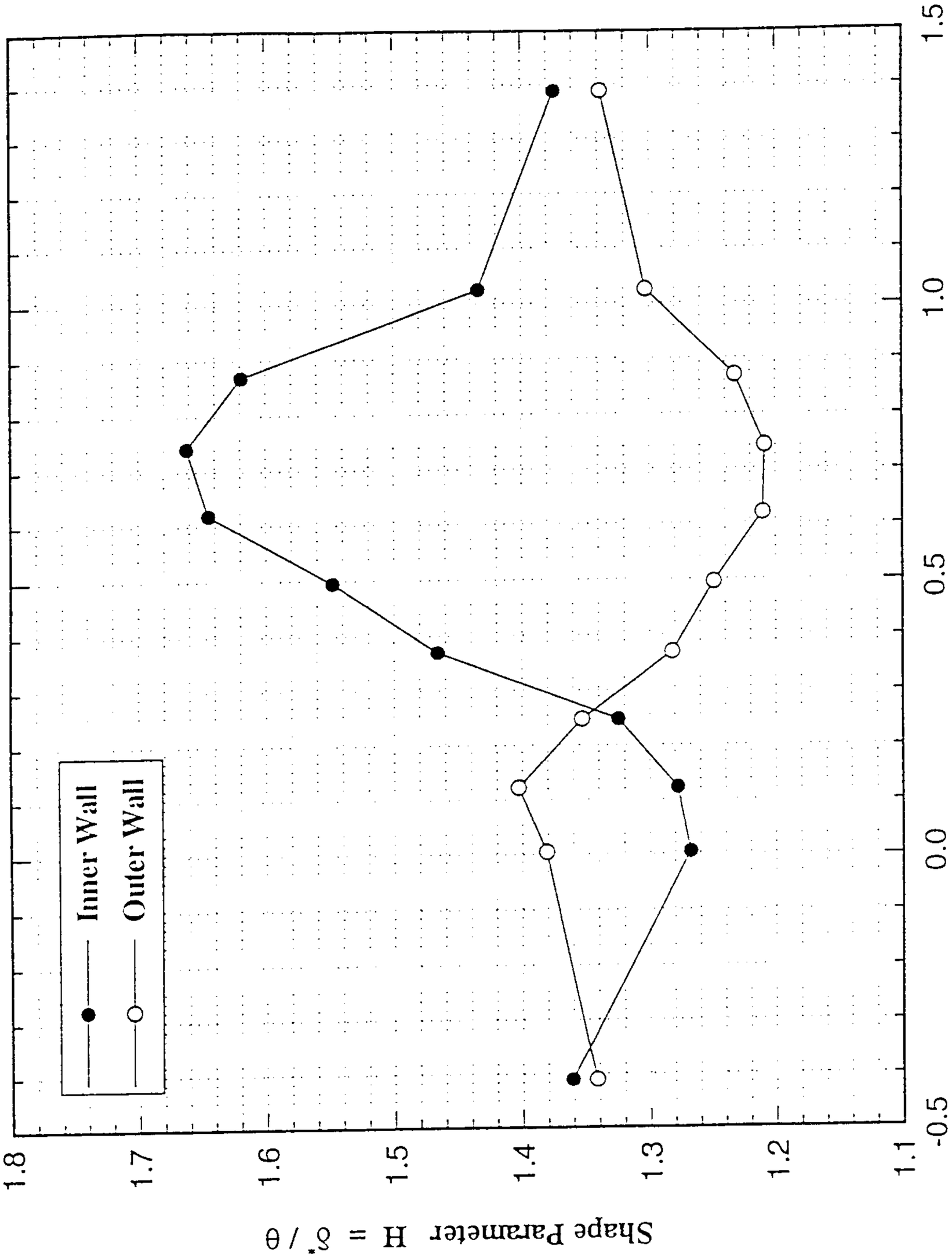

Fig.4.1.6 Axial variation of shape parameter (H).

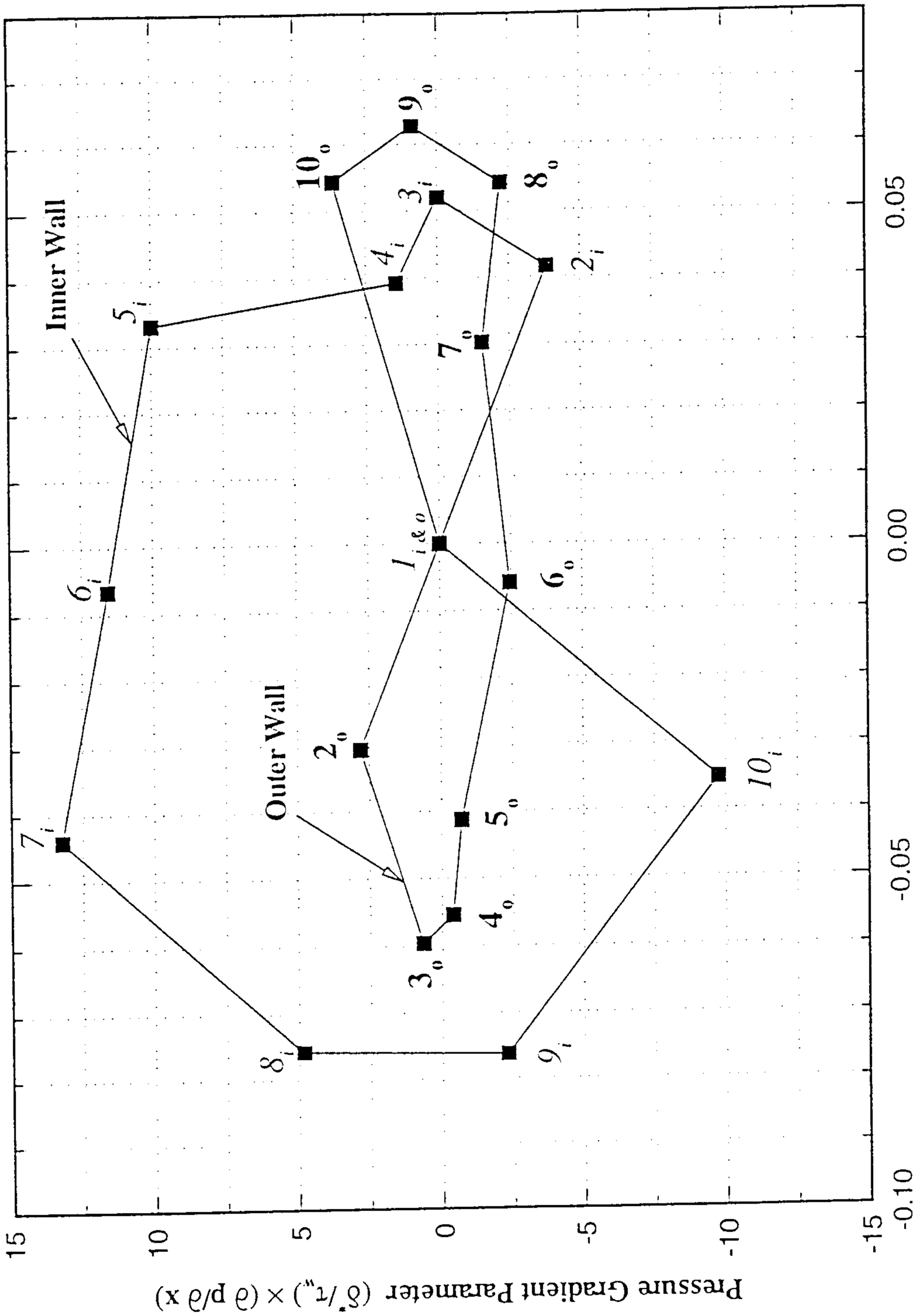

Fig.4.1.7 Variation of non-dimensional curvature and pressure gradient.

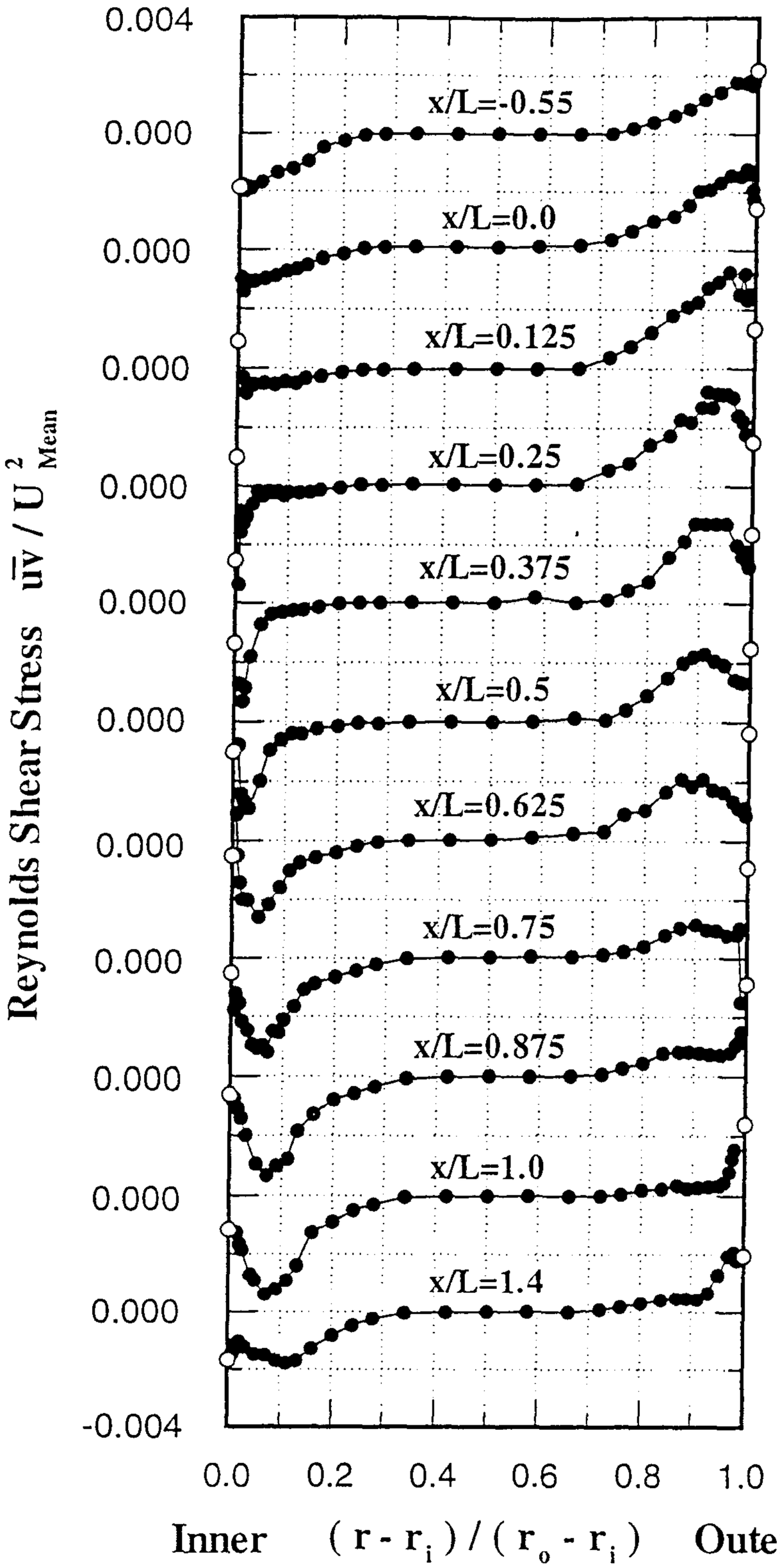

Fig.4.1.8 Development of Reynolds shear stress ($\overline{uv}$).

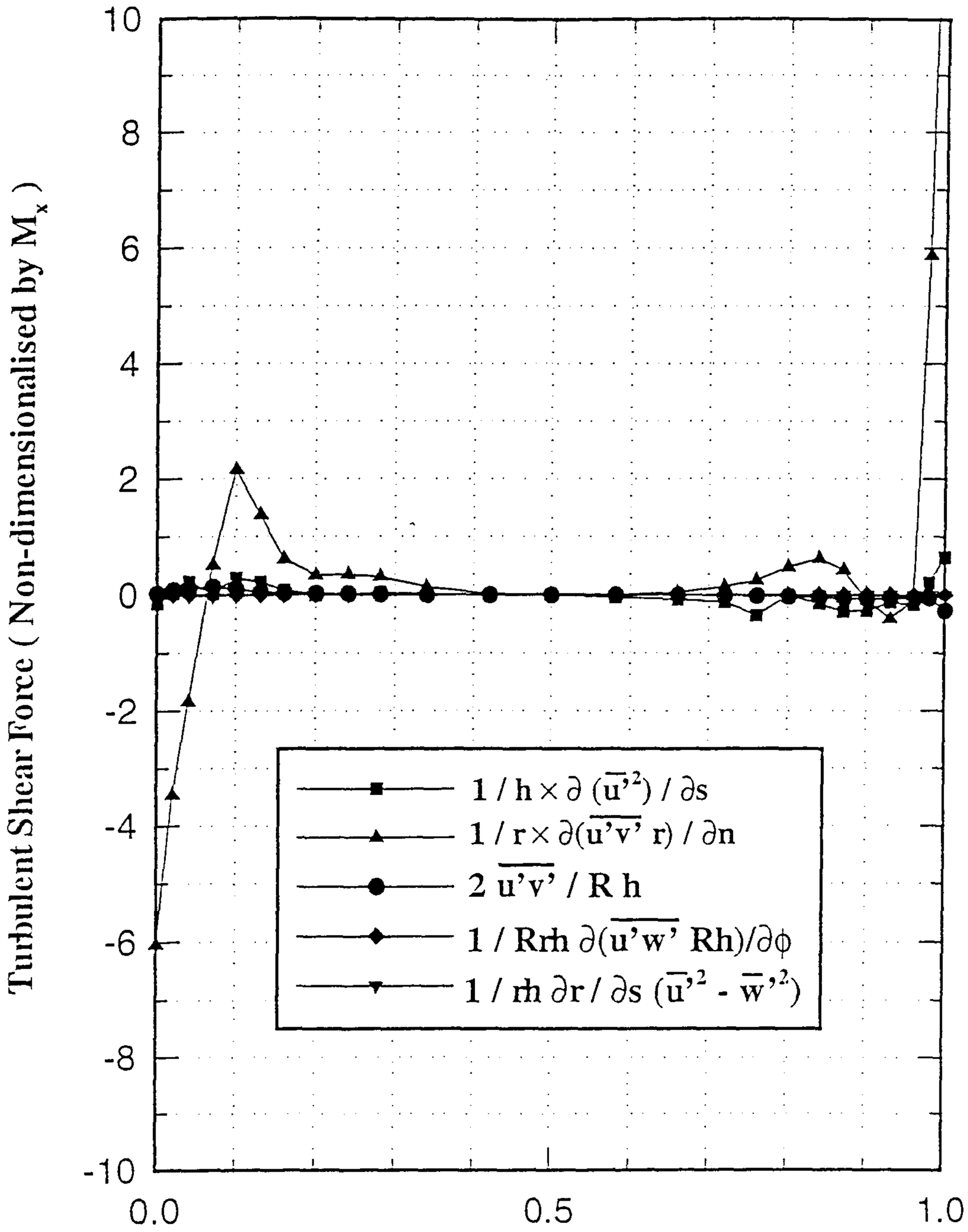

Fig.4.1.9 Radial distribution of turbulent terms (x/L=0.0).

$$\frac{1}{rh}\frac{\partial}{\partial s}(U^2 r) + \frac{1}{r}\frac{\partial}{\partial n}(UVr) + \frac{2UV}{Rh} = -\frac{1}{\rho h}\frac{\partial p}{\partial s} - \left(\frac{1}{rh}\frac{\partial}{\partial s}(\overline{u}^2 r) + \frac{1}{r}\frac{\partial}{\partial n}(\overline{u}\overline{v}r) + \frac{2\overline{u}\overline{v}}{Rh}\right)$$

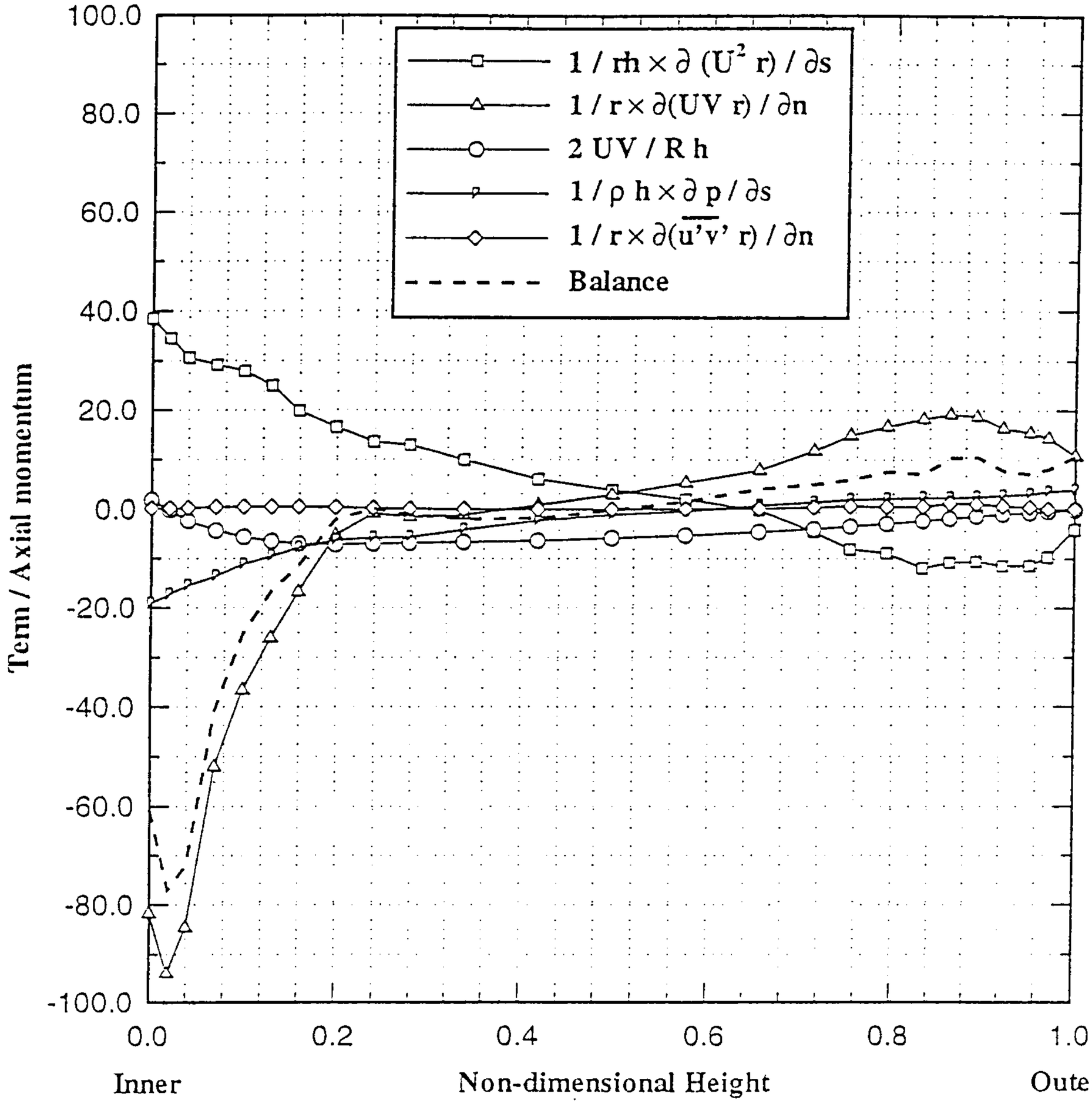

Fig.4.1.10 Radial distribution of terms in the s-momentum eqn (x/L=0.0).

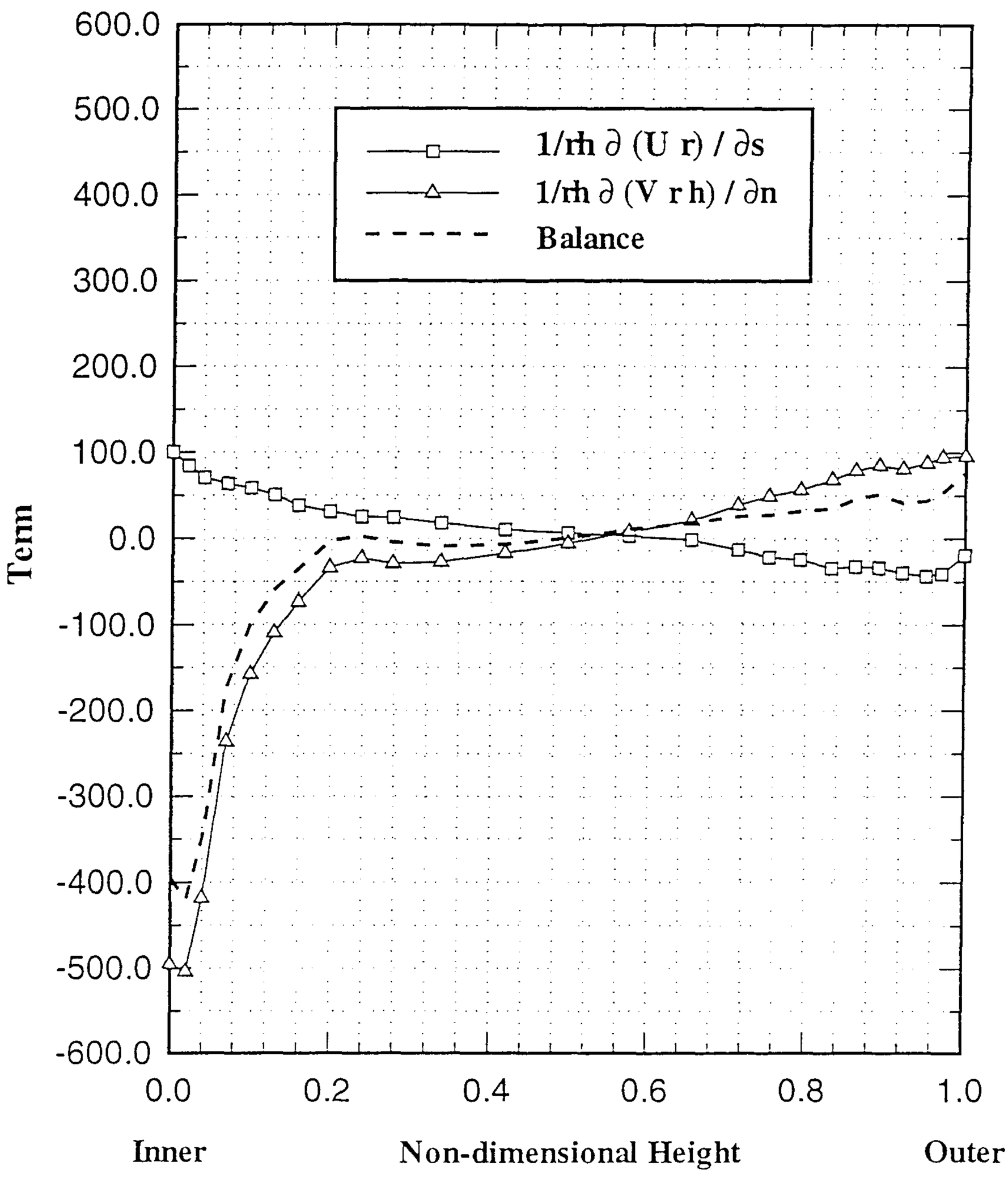

Fig.4.1.11 Radial distribution of terms in the continuity eqn (x/L=0.0).

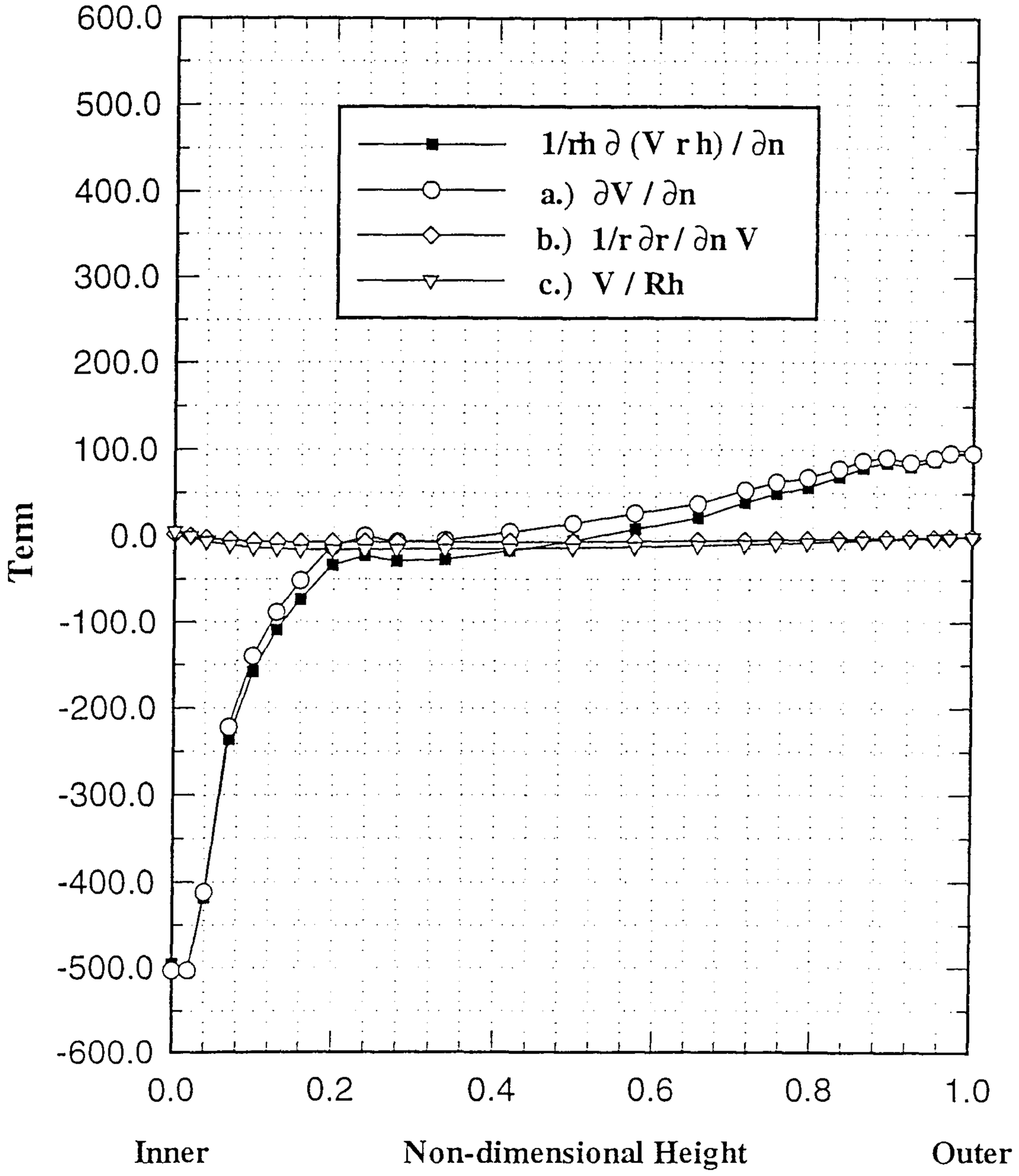

Fig.4.1.12 Radial distribution of the components of the convection term (x/L=0.0).

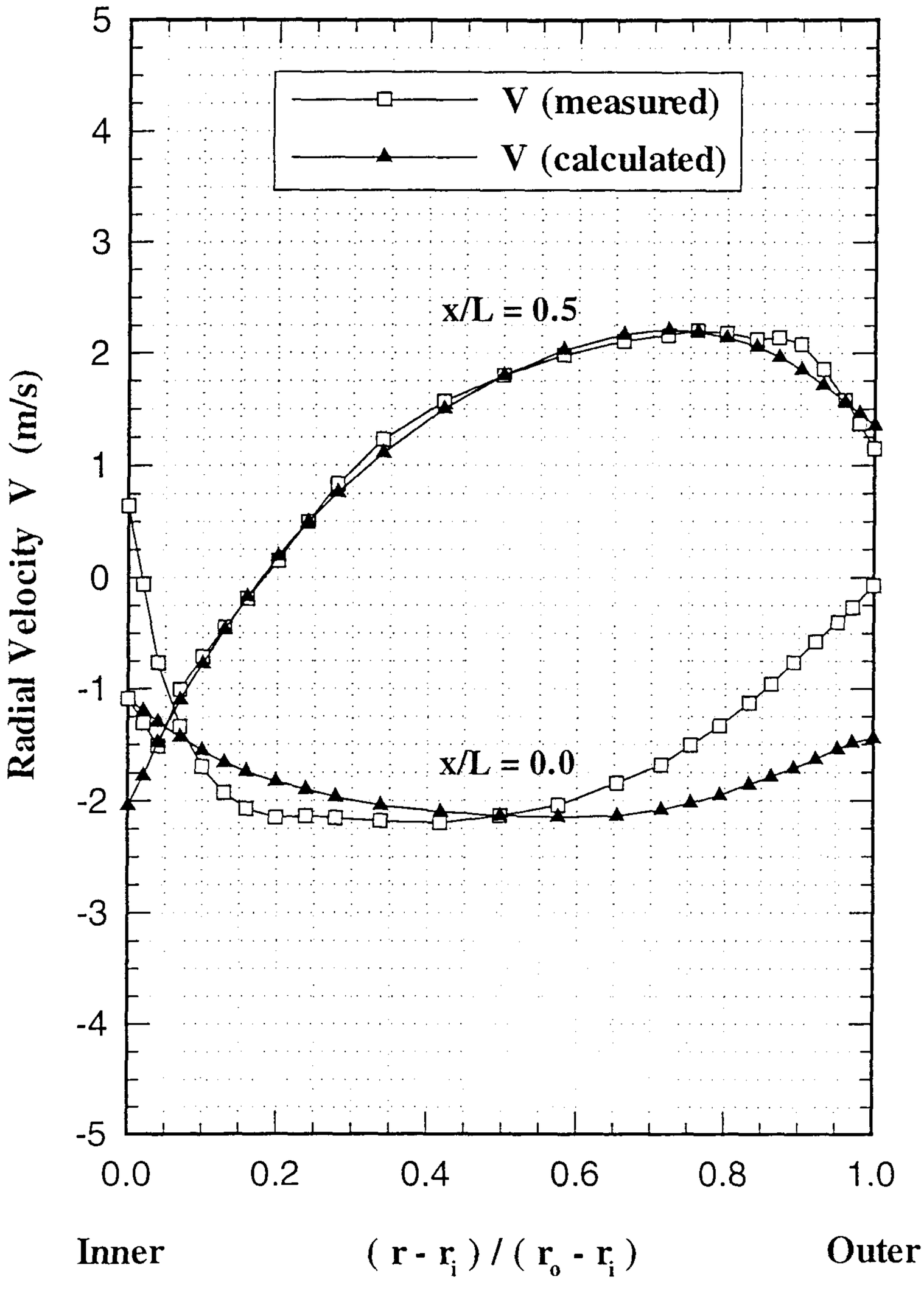

Fig.4.1.13 Measured and calculated radial velocity (V) profiles (x/L=0.0 and x/L=0.5).

$$\frac{1}{rh}\frac{\partial}{\partial s}(U^2 r) + \frac{1}{r}\frac{\partial}{\partial n}(UVr) + \frac{2UV}{Rh} = -\frac{1}{\rho h}\frac{\partial p}{\partial s} - \left(\frac{1}{rh}\frac{\partial}{\partial s}(\overline{u'^2} r) + \frac{1}{r}\frac{\partial}{\partial n}(\overline{u'v'} r) + \frac{2\overline{u'v'}}{Rh}\right)$$

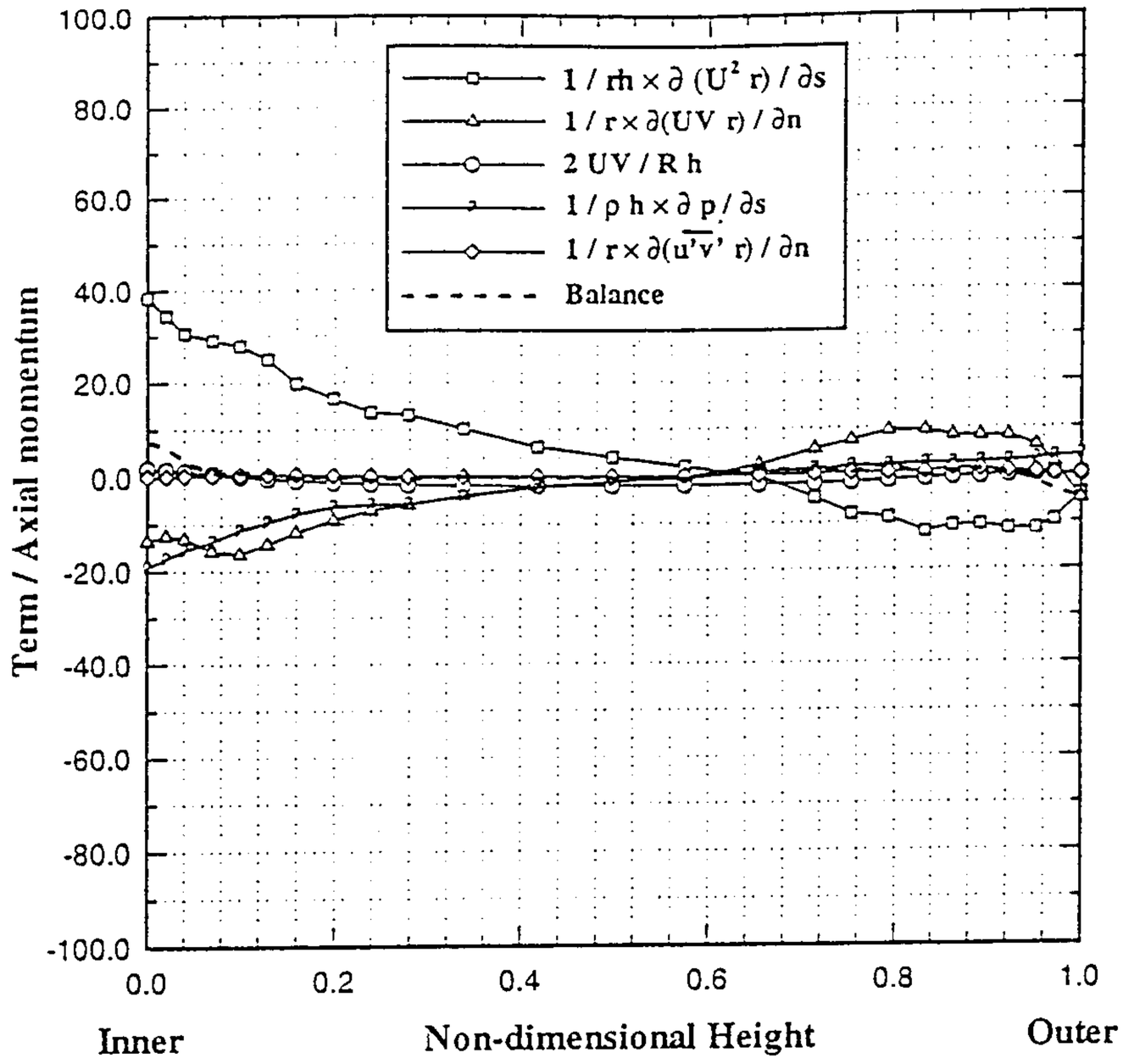

Fig.4.1.14.a Radial distribution of terms in the s-momentum equation (x/L=0.0) using radial velocity profile calculated to satisfy massflow continuity.

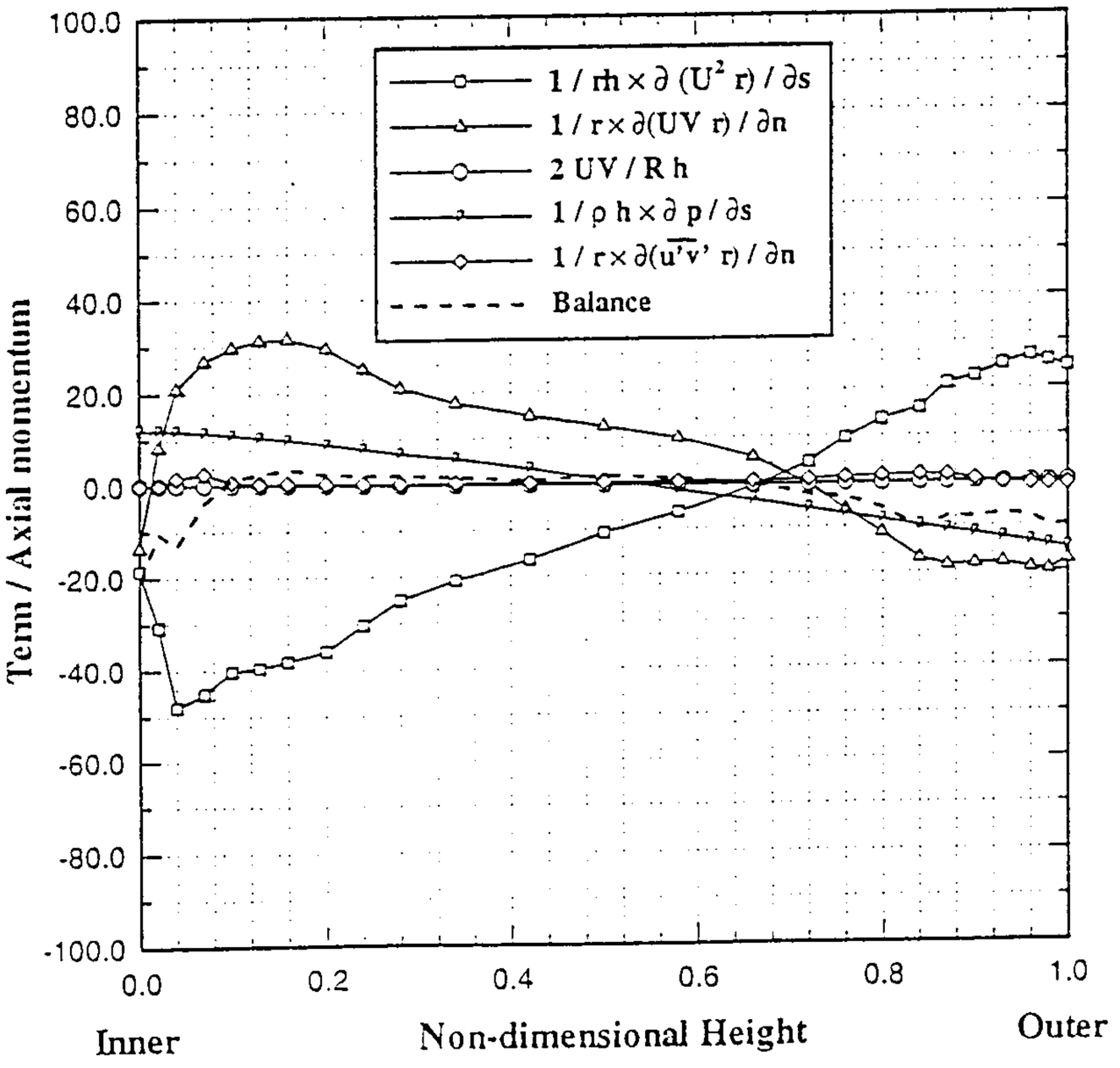

Fig.4.1.14.b Radial distribution of terms in the s-momentum equation (x/L=0.5) using radial velocity profile calculated to satisfy massflow continuity.

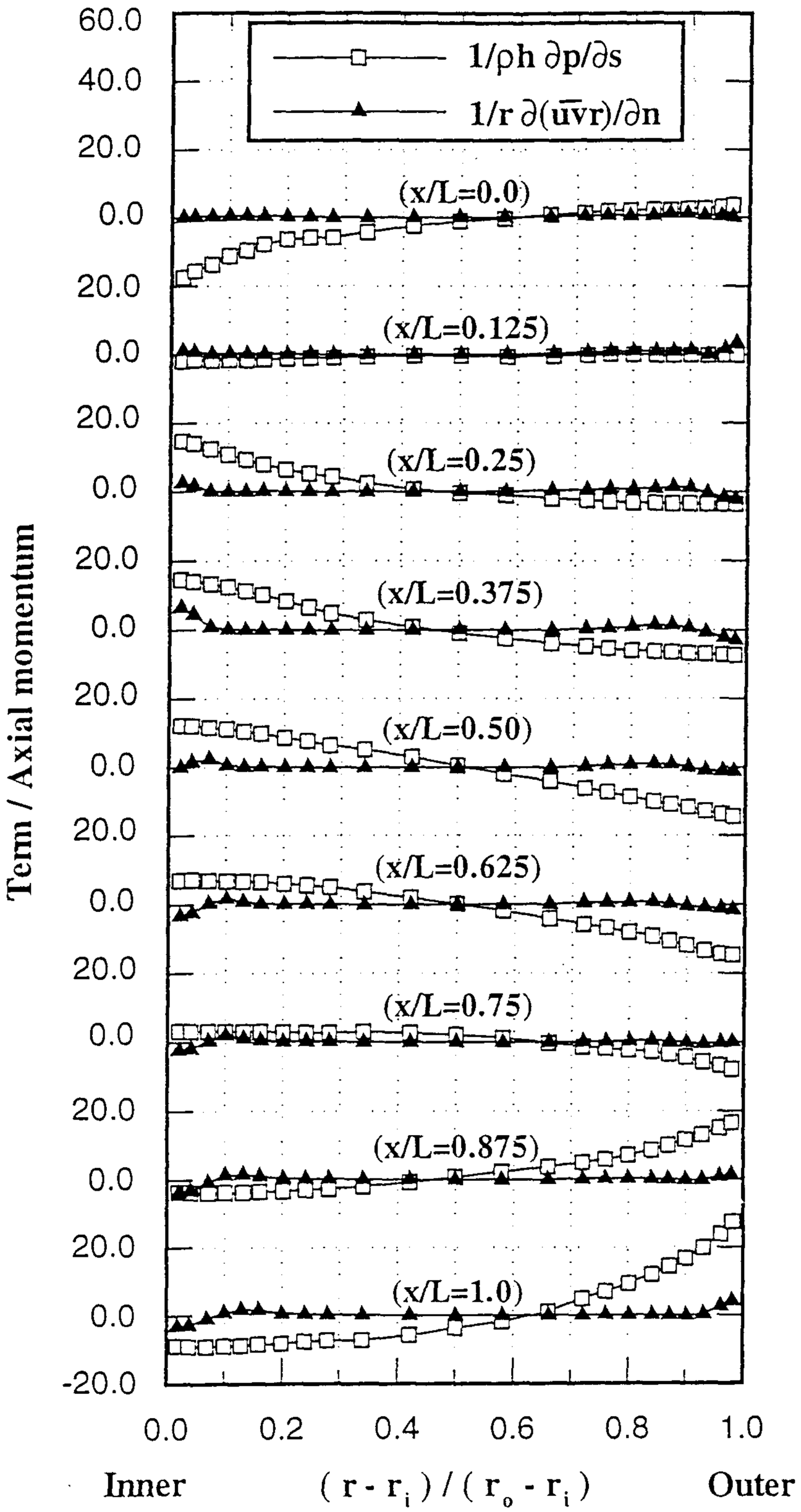

Fig.4.1.15 Development of pressure ($1/\rho h\ \partial p/\partial s$) and shear ($1/r\ \partial(\overline{uv}r)/\partial n$) forces.

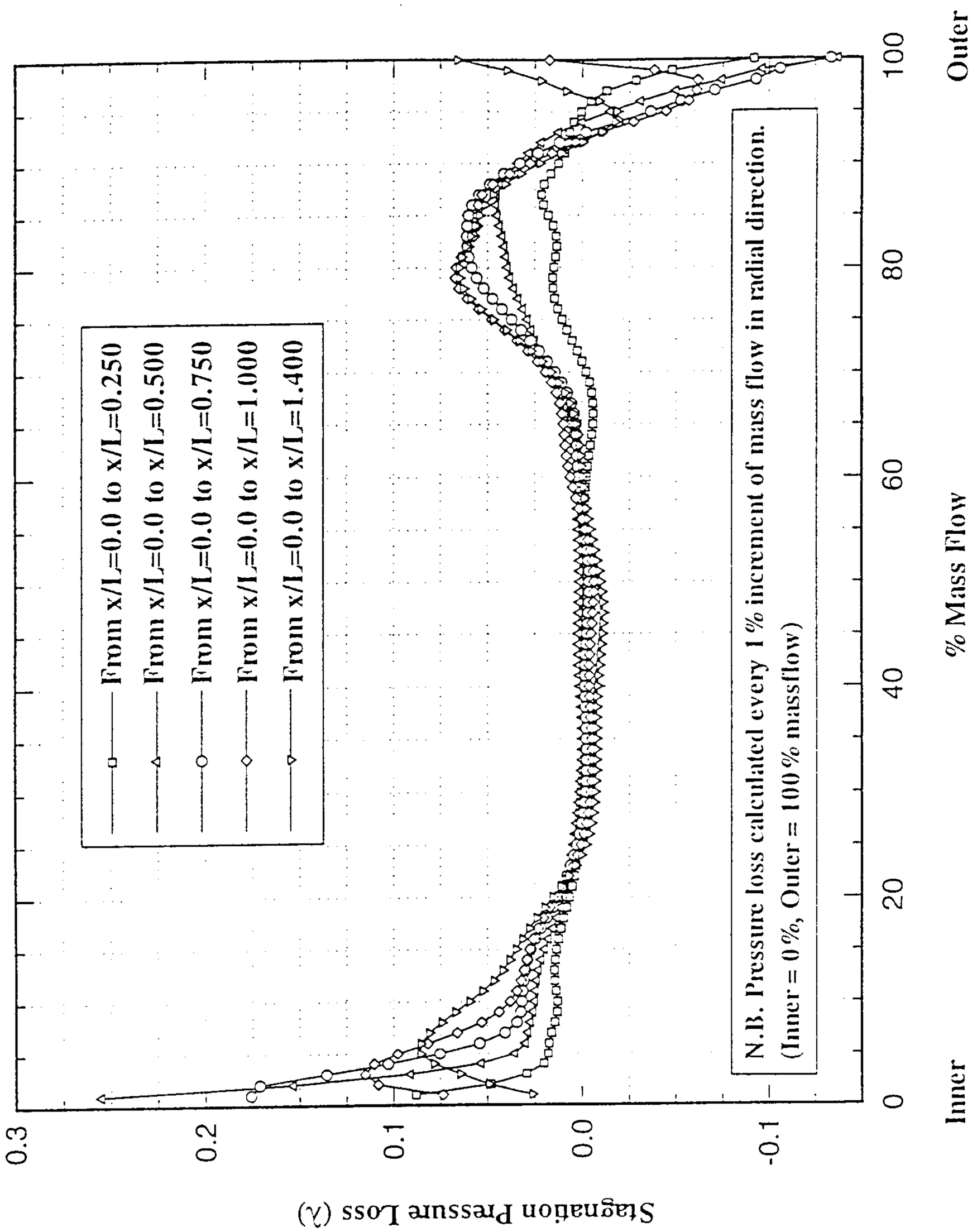

Fig.4.1.16 Development of the radial distribution of stagnation pressure loss

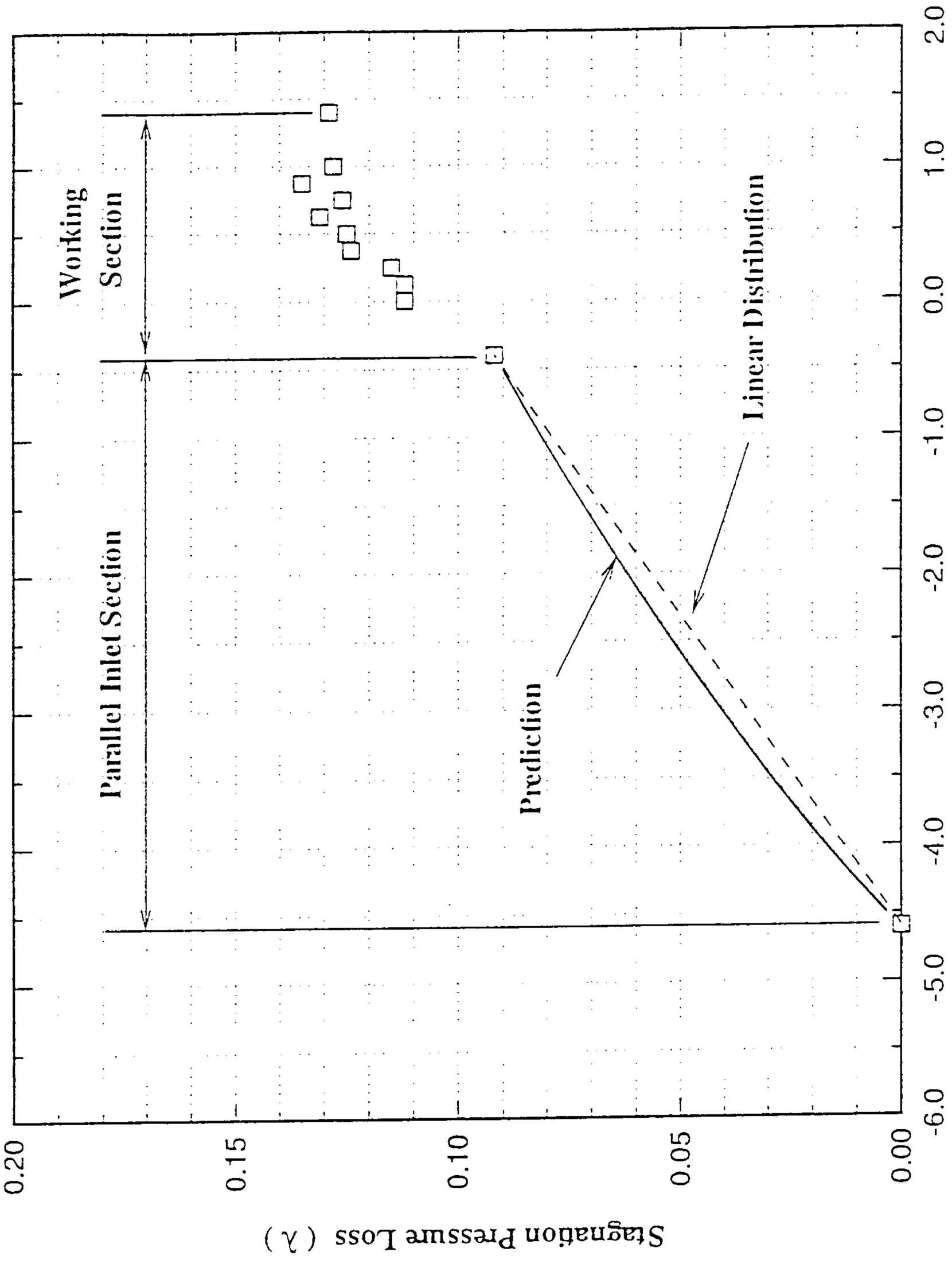

Fig.4.1.17 Axial variation of stagnation pressure loss (λ)

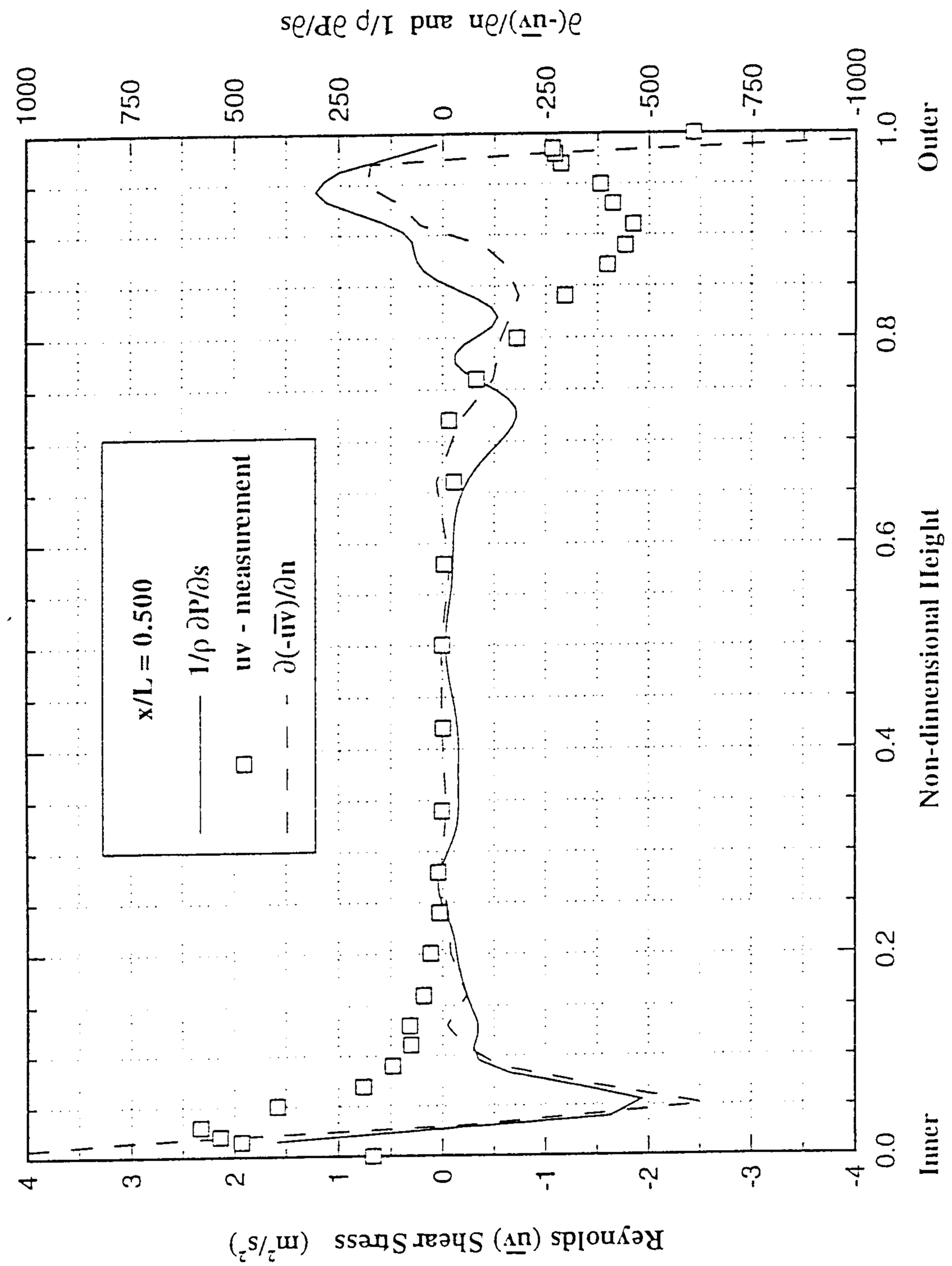

Fig.4.1.18 Profiles of $\partial(-\overline{uv})/\partial n$ and $1/\rho\ \partial P/\partial s$.

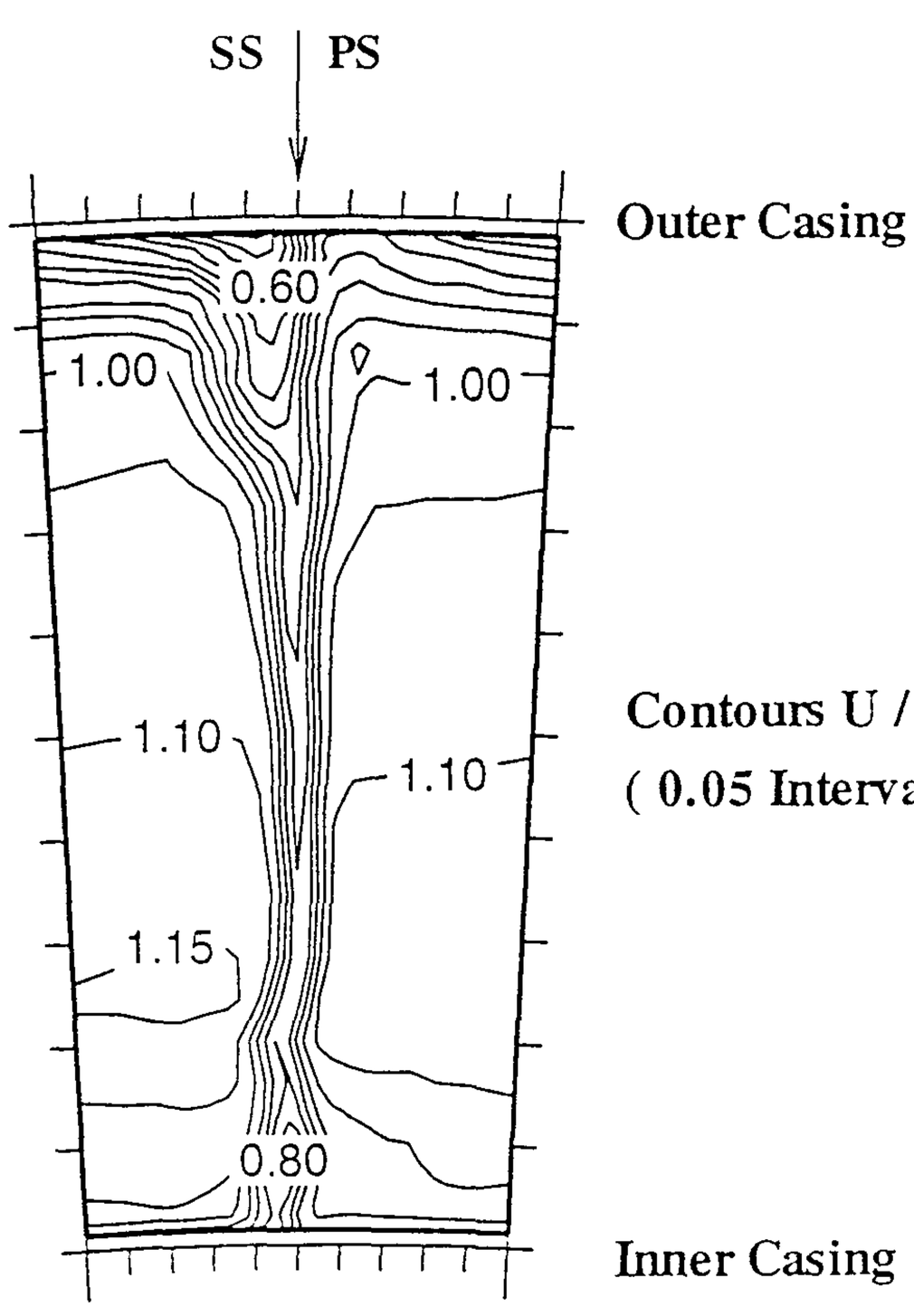

Fig.4.2.1 Streamwise velocity distribution (x/L=0.0).

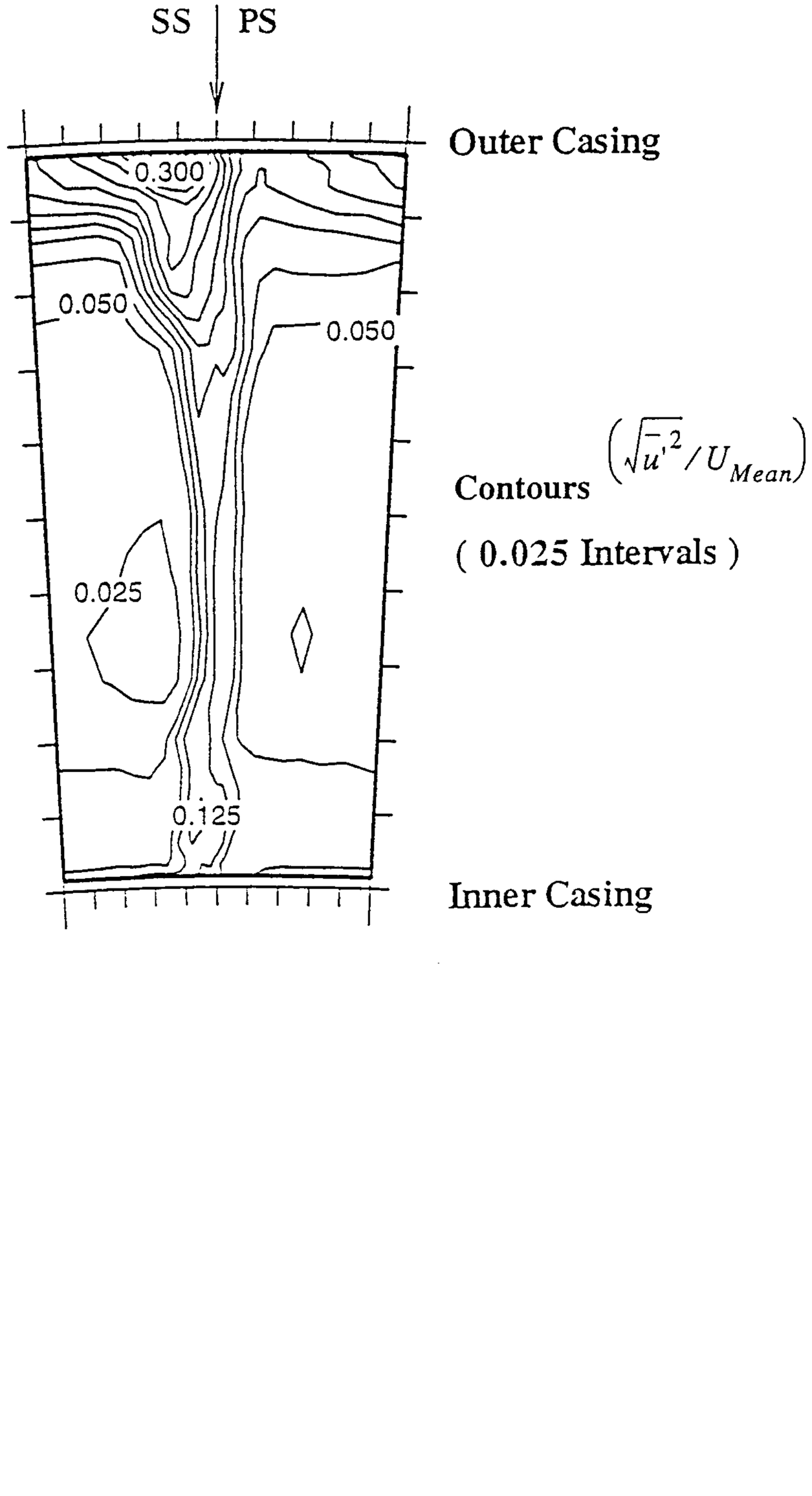

Fig.4.2.2 Turbulence intensity distribution - $\left(\sqrt{\overline{u'^2}}/U_{Mean}\right)$, x/L=0.0.

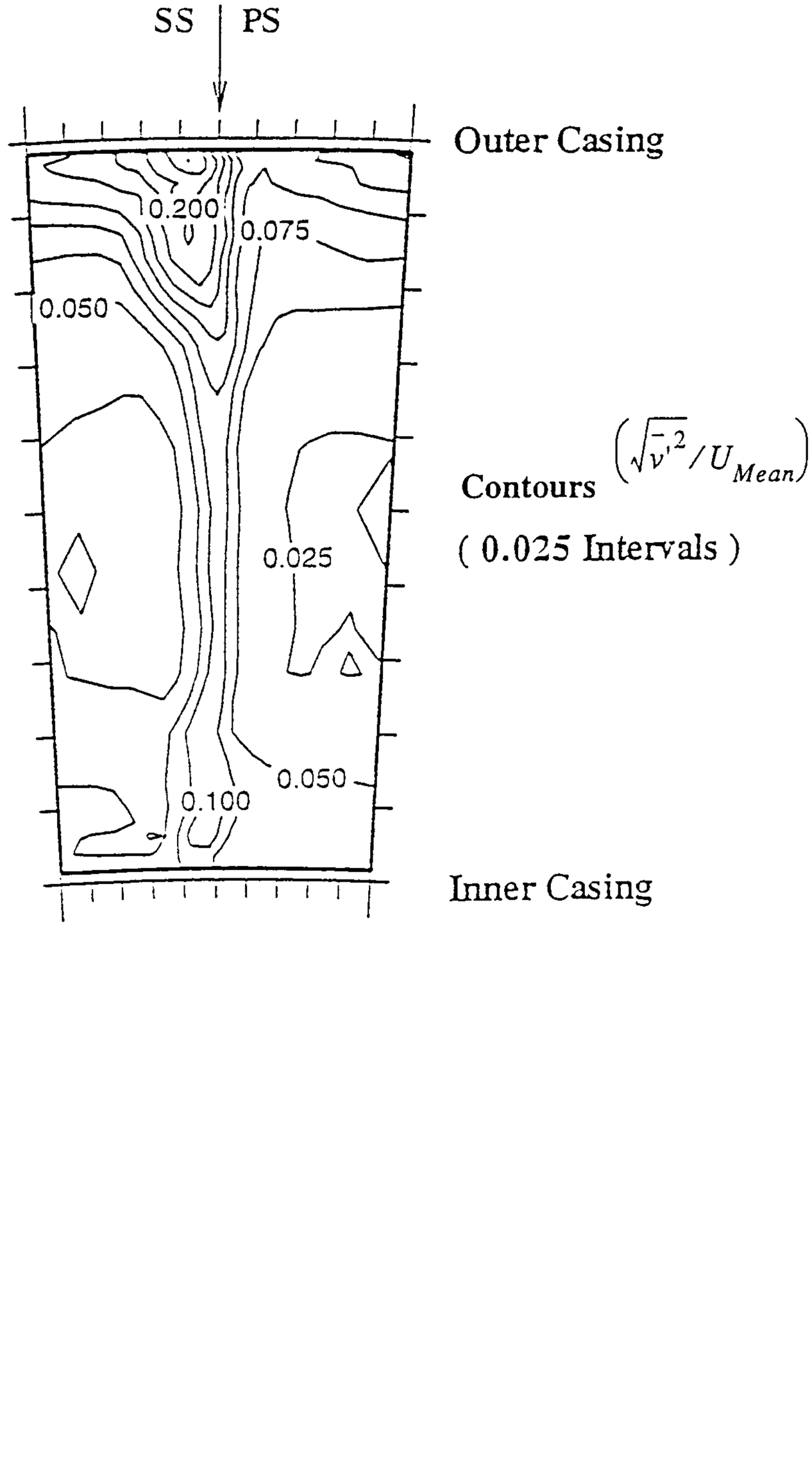

Fig.4.2.3 Turbulence intensity distribution - $\left(\sqrt{\overline{v'^2}}/U_{Mean}\right)$, x/L=0.0.

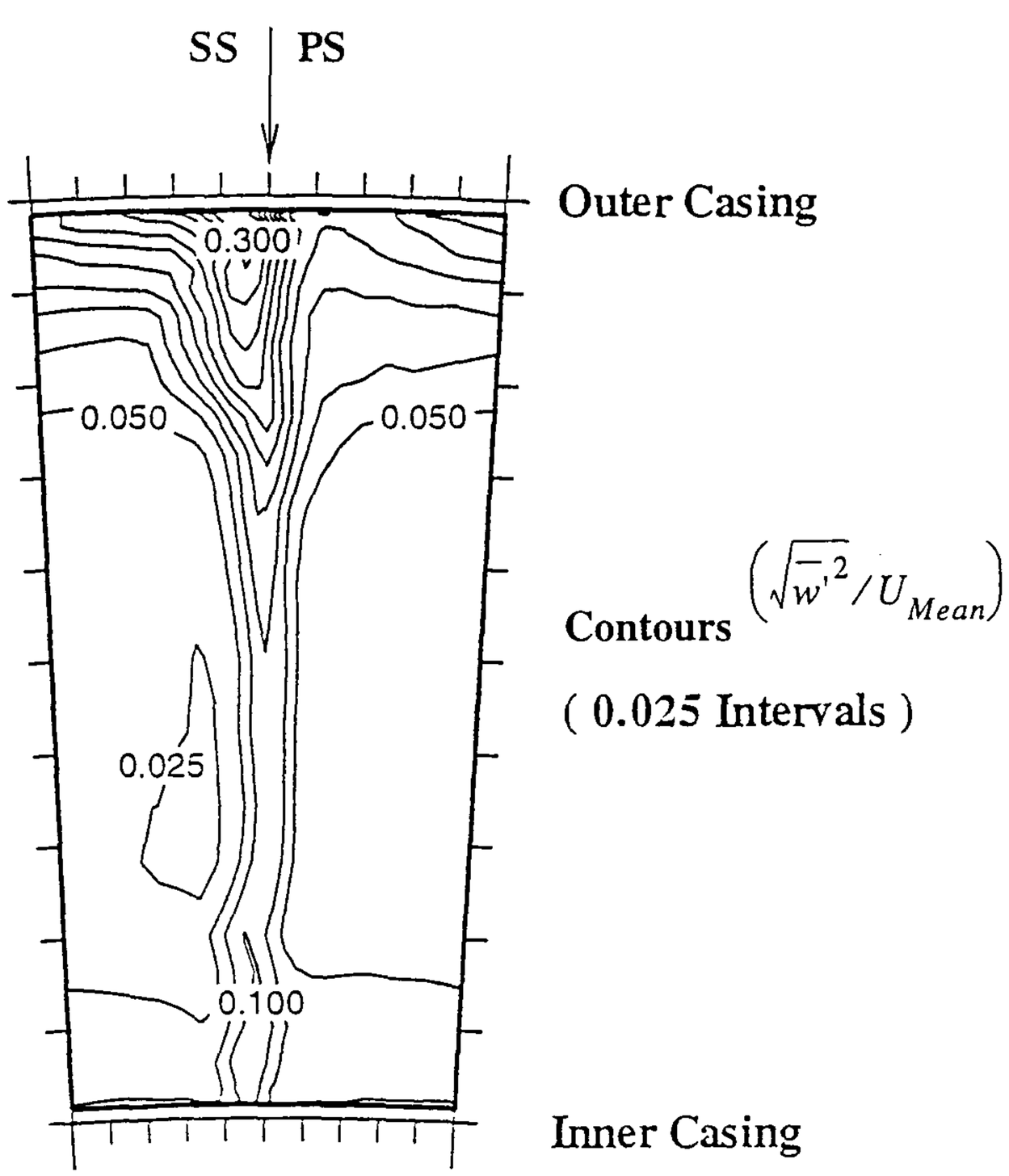

Fig.4.2.4 Turbulence intensity distribution - $\left(\sqrt{\overline{w'^2}}/U_{Mean}\right)$, x/L=0.0.

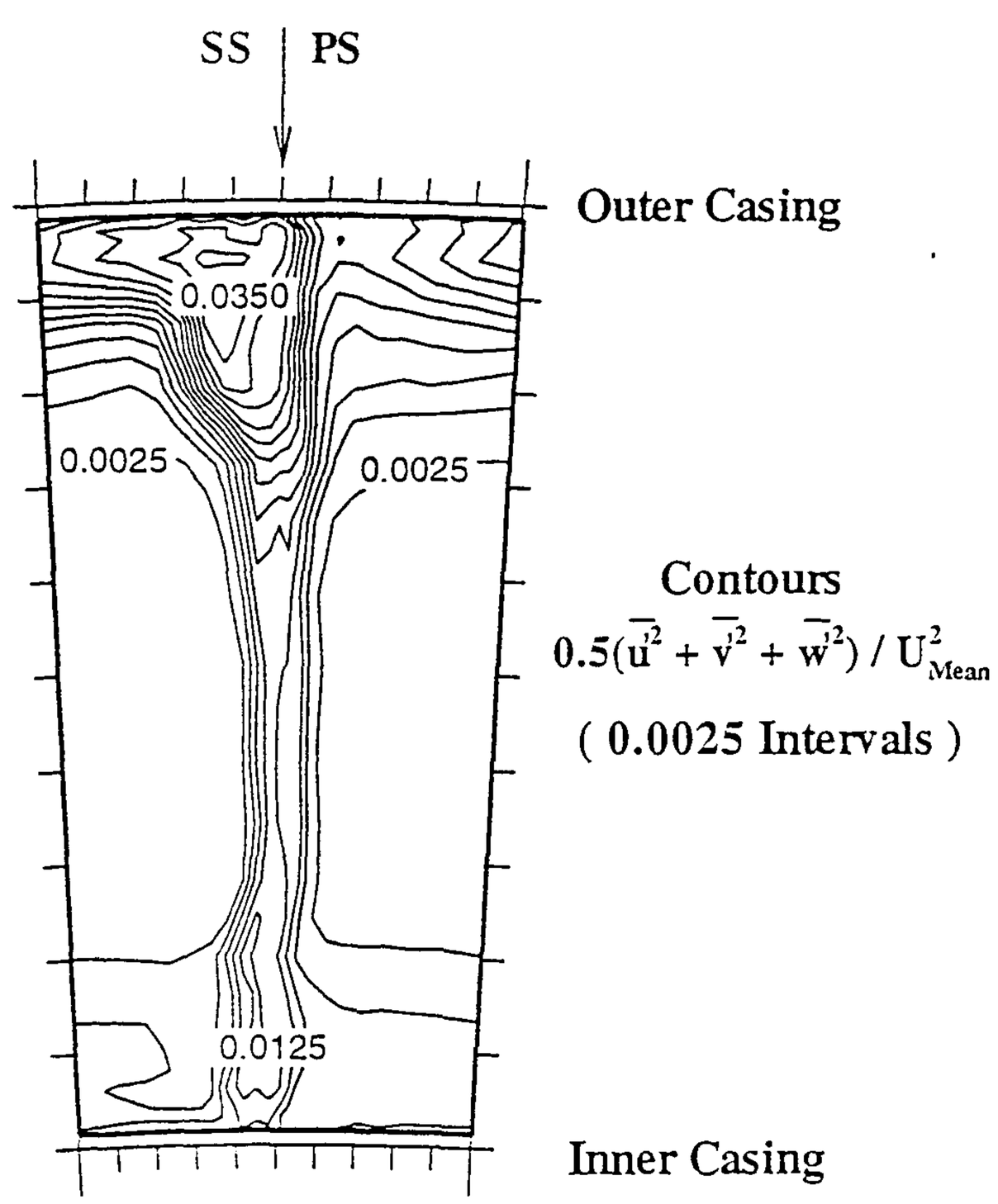

Fig.4.2.5 Turbulent kinetic energy distribution (x/L=0.0).

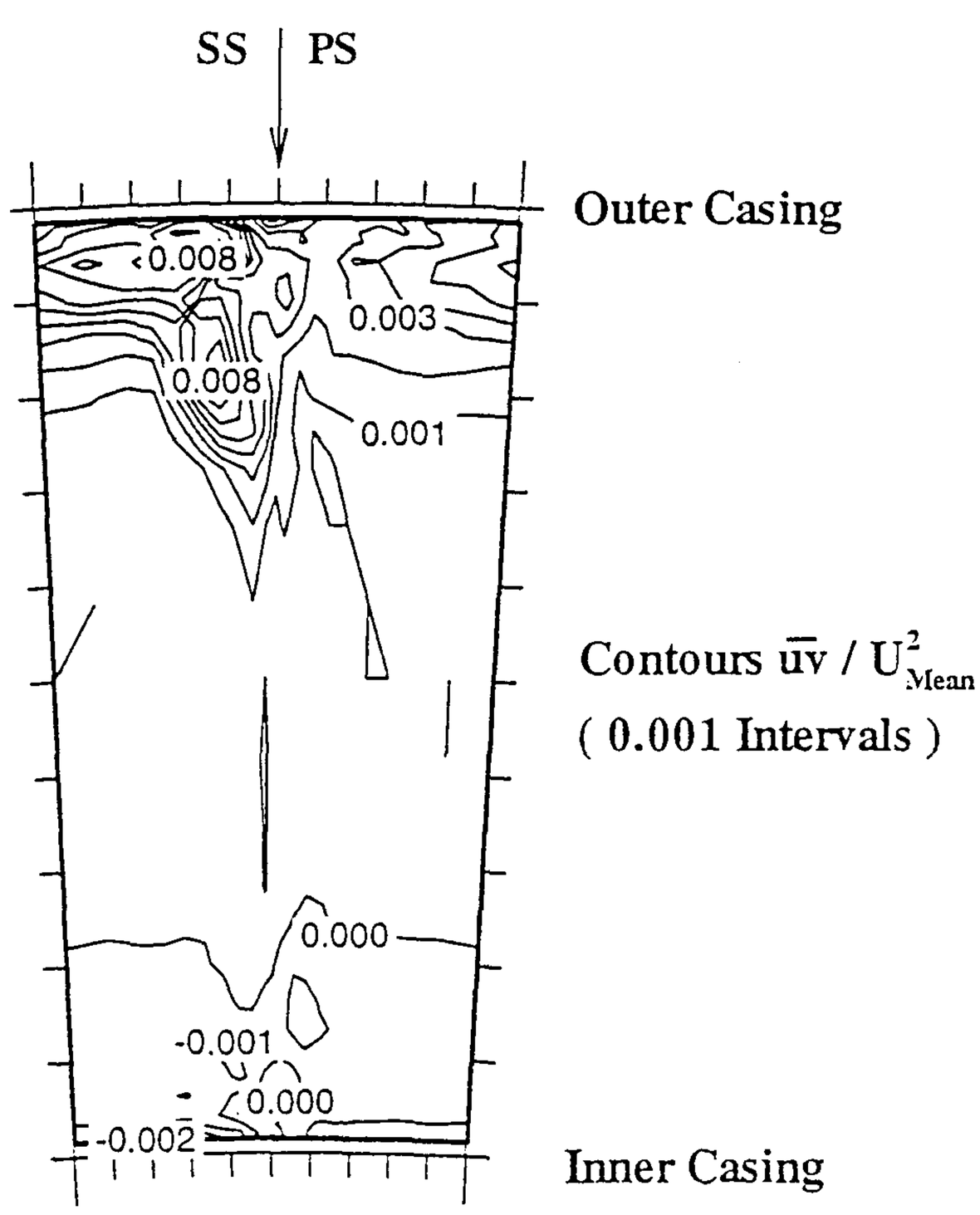

Fig.4.2.6 Reynolds shear stress distribution ($\overline{uv}$, x/L=0.0).

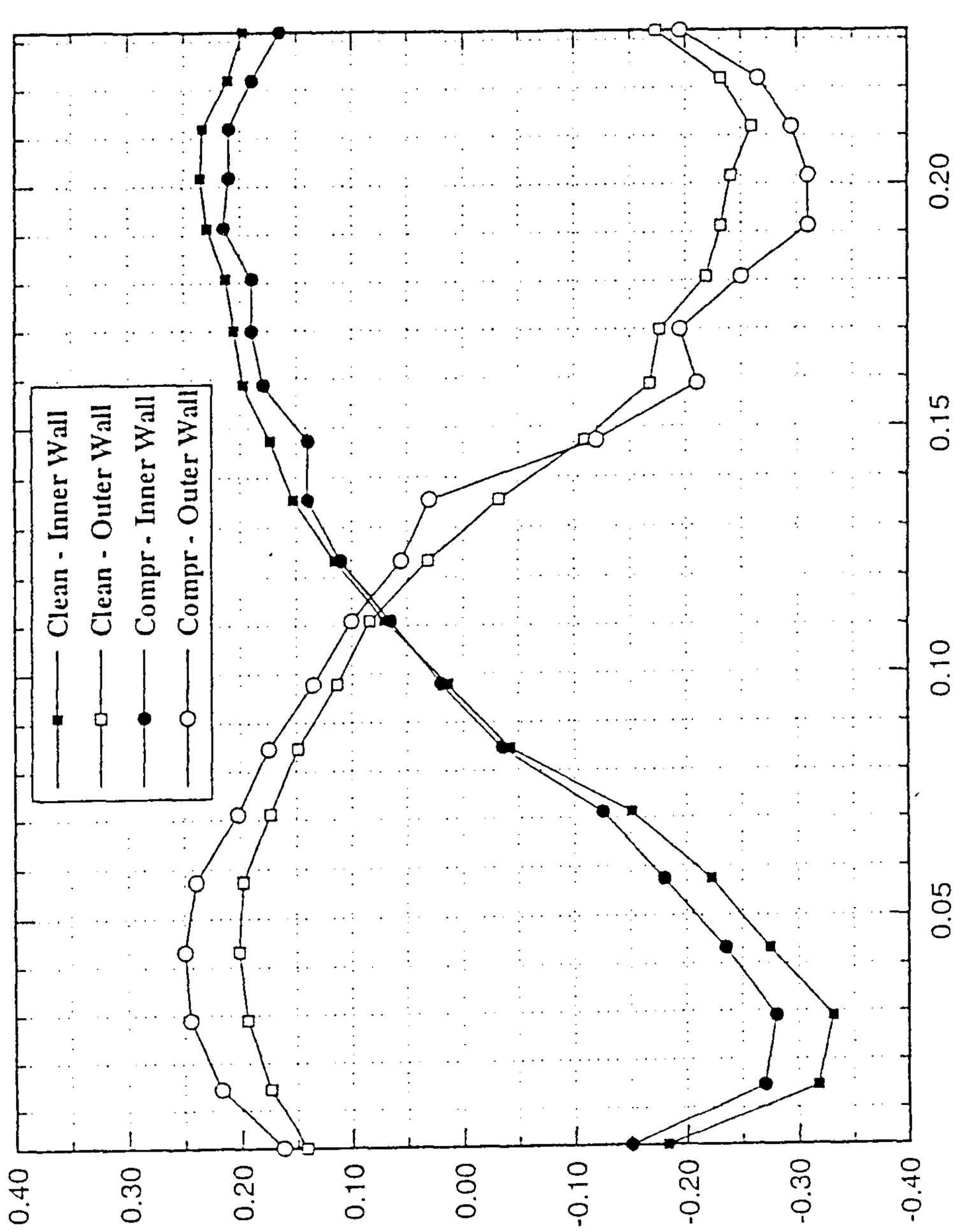

Fig.4.2.7 Axial variation of static pressure coefficient (C_p).

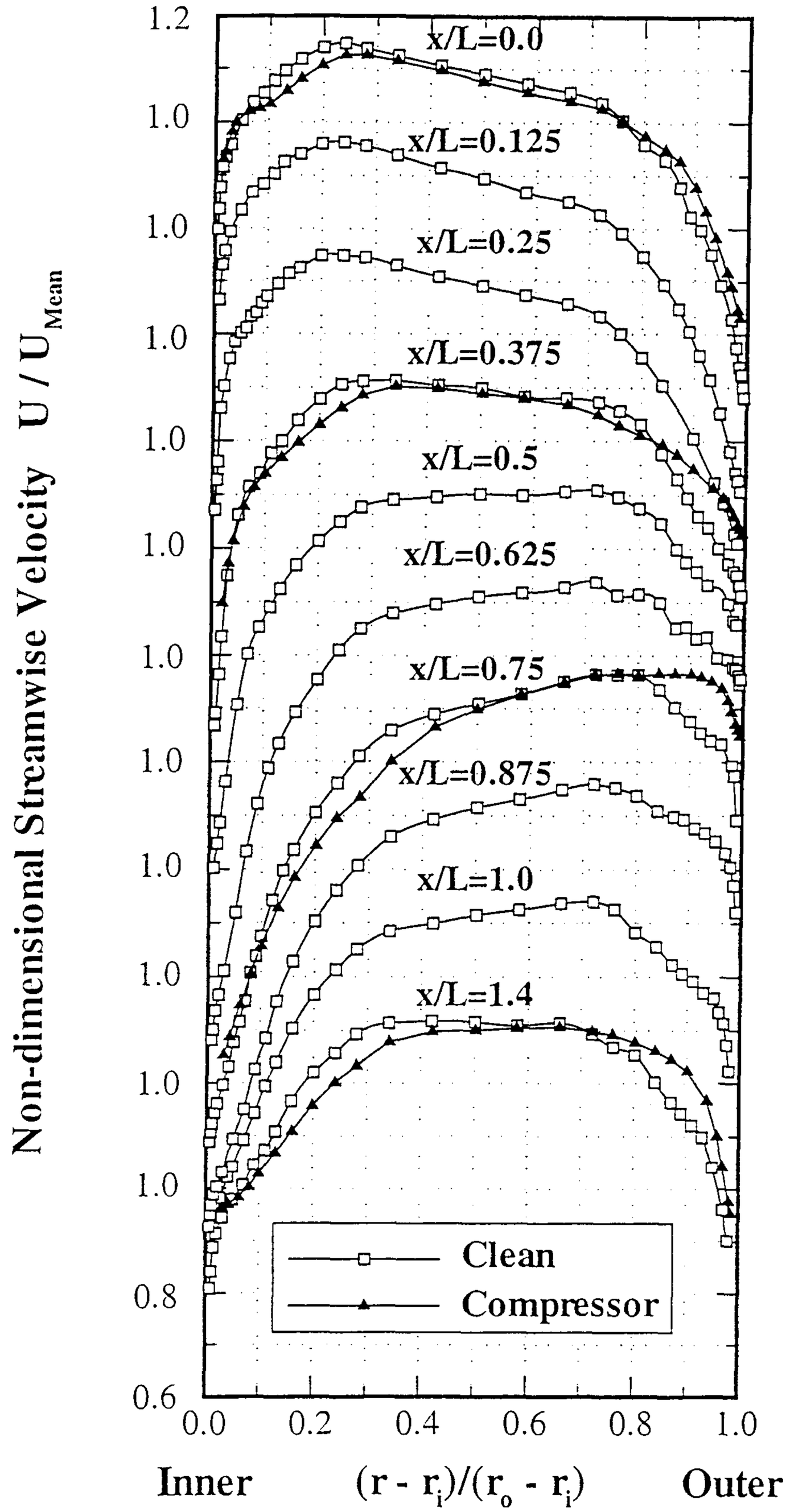

Fig.4.2.8 Development of pitch averaged streamwise velocity profiles.

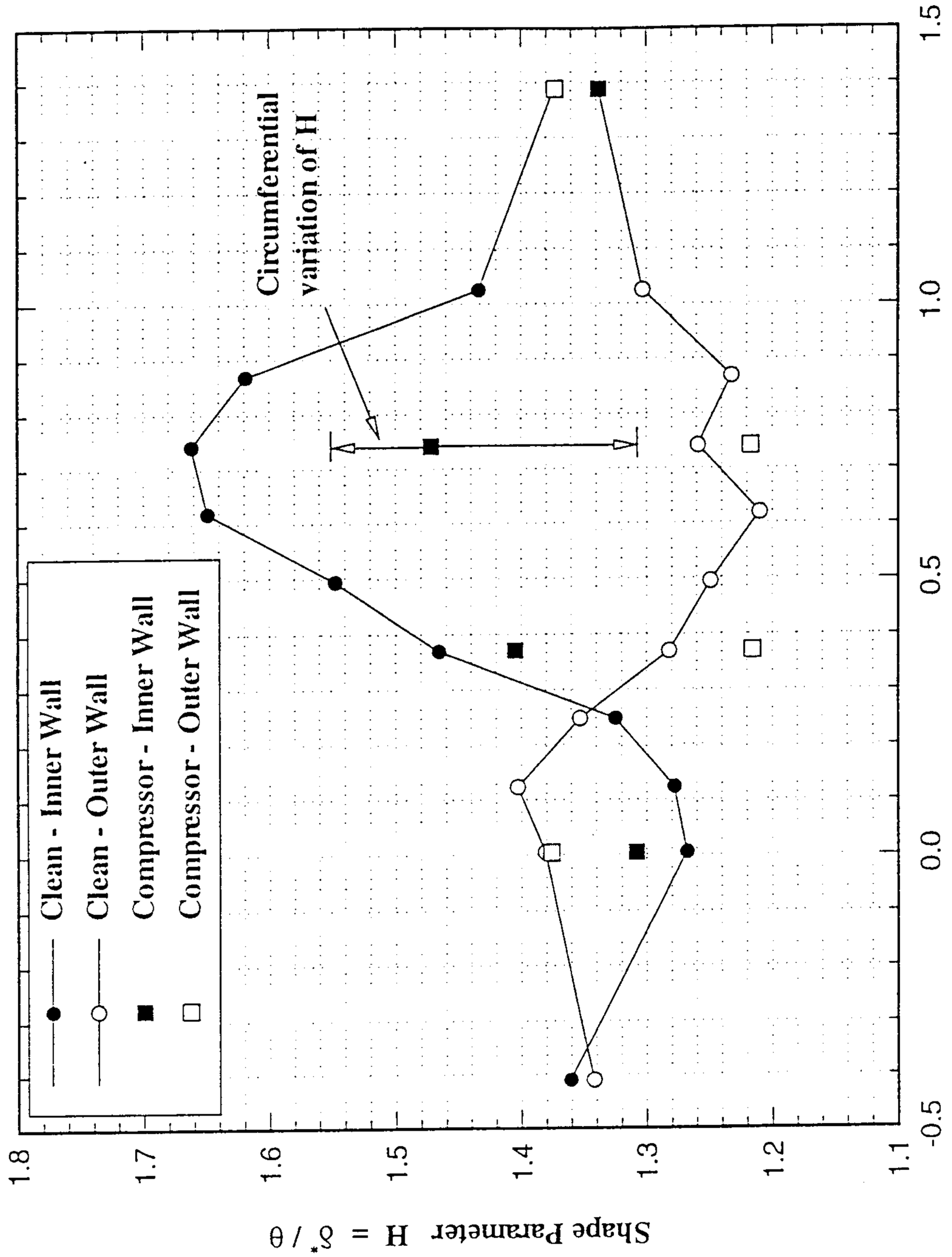

Fig.4.2.9 Axial variation of shape parameter (H)

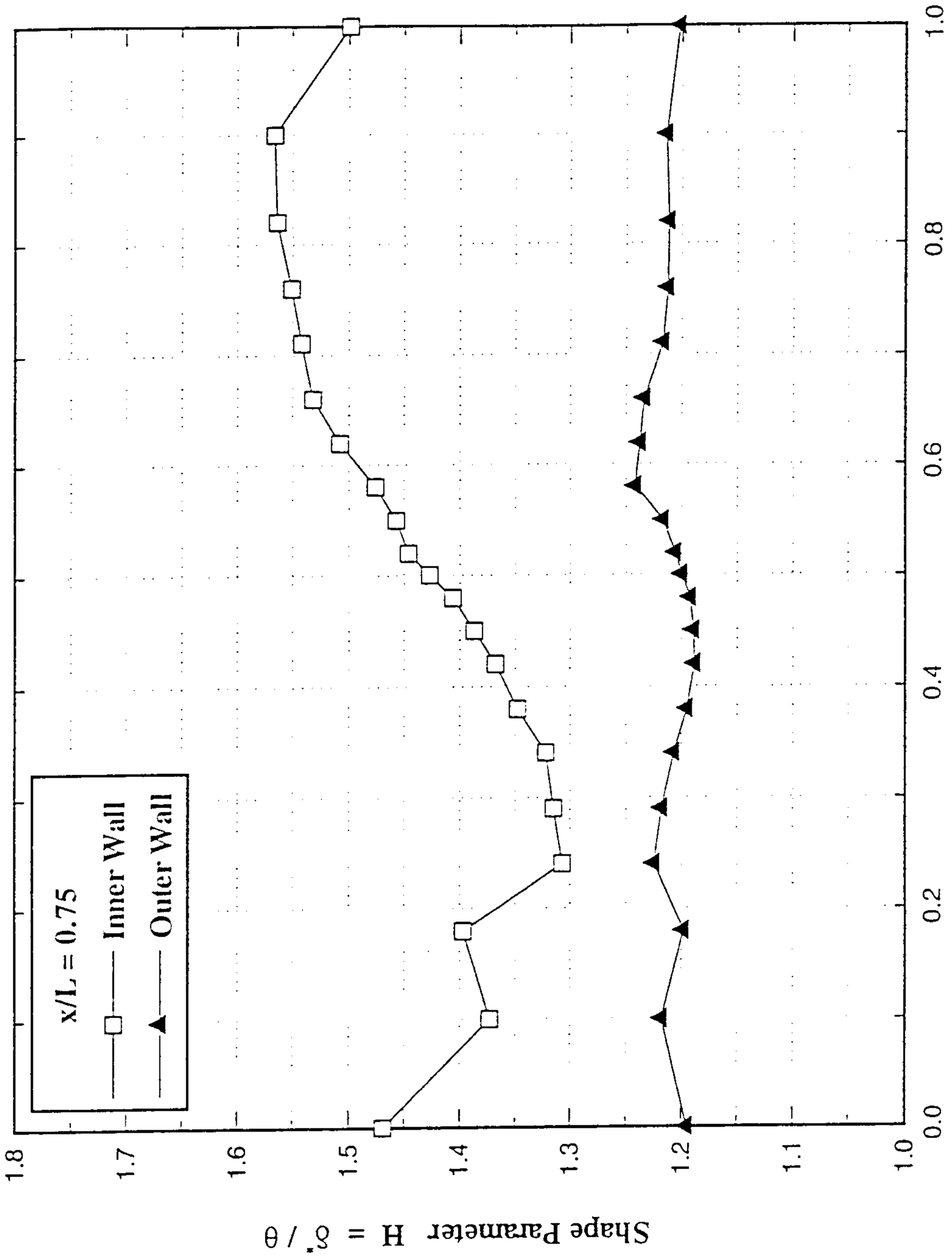

Fig.4.2.10 Circumferential variation of shape parameter H (x/L=0.75)

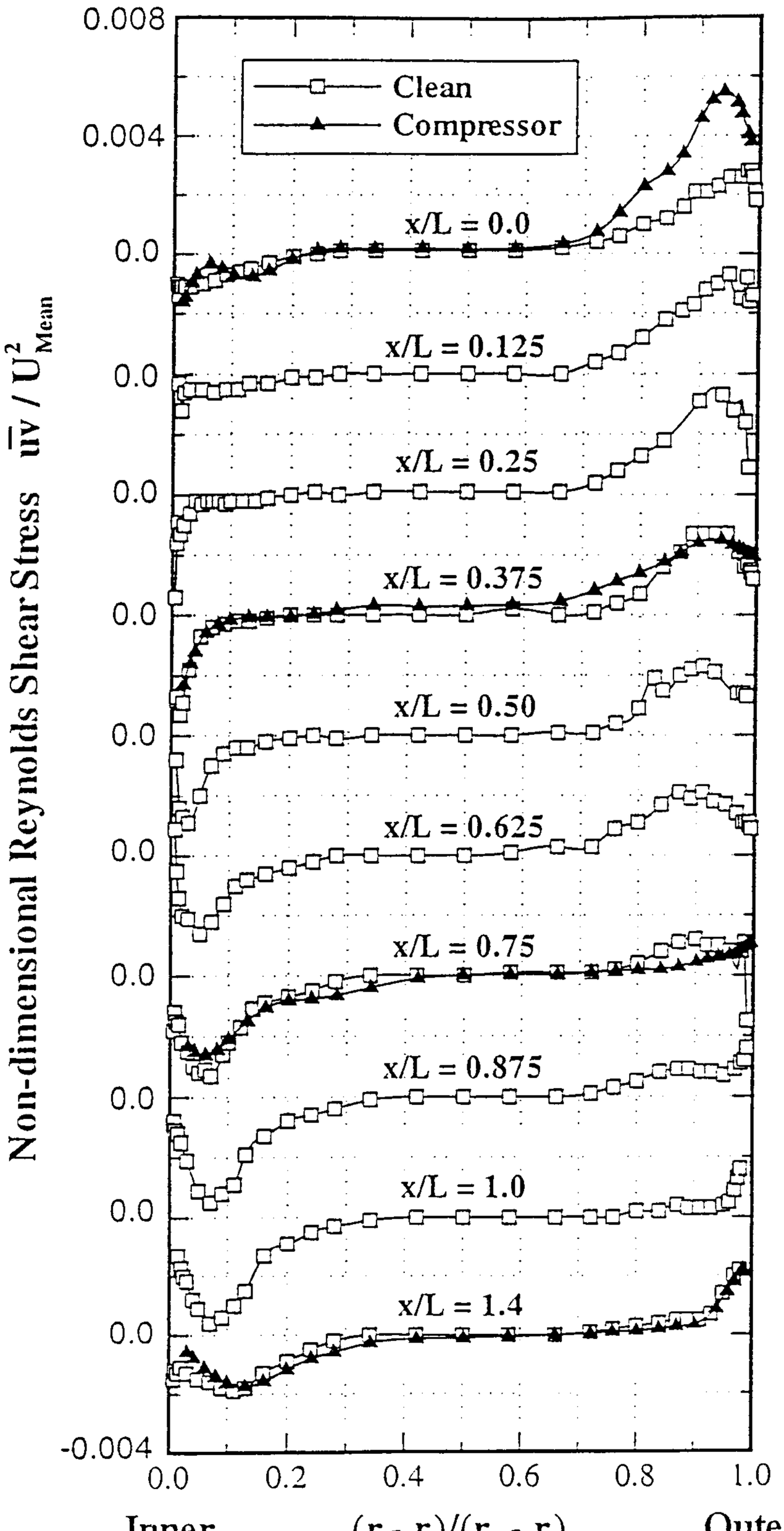

Fig.4.2.11 Development of Reynolds shear stress ($\overline{uv}$).

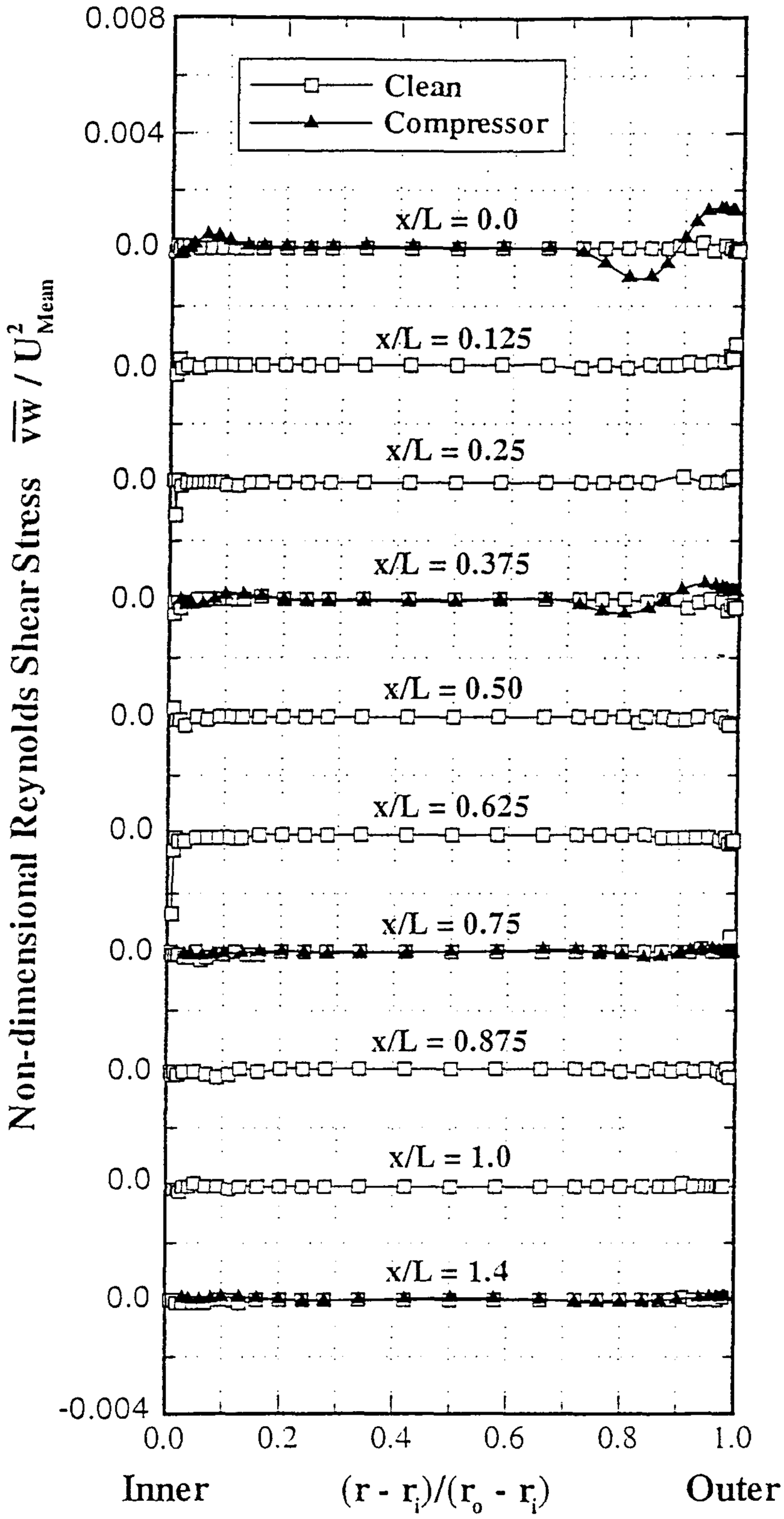

Fig.4.2.12 Development of Reynolds shear stress ($\overline{vw}$).

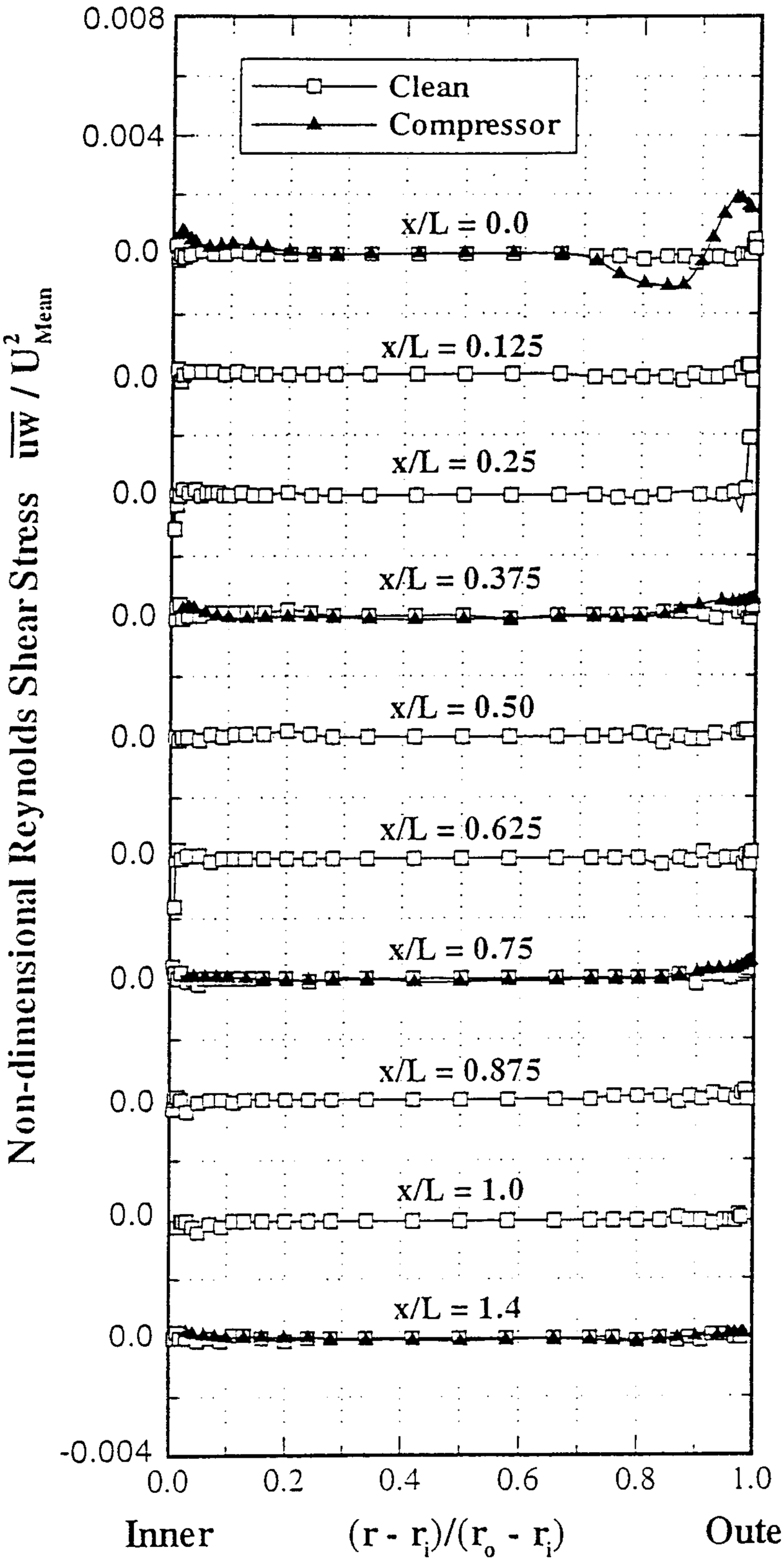

Fig.4.2.13 Development of Reynolds shear stress ($\overline{uw}$).

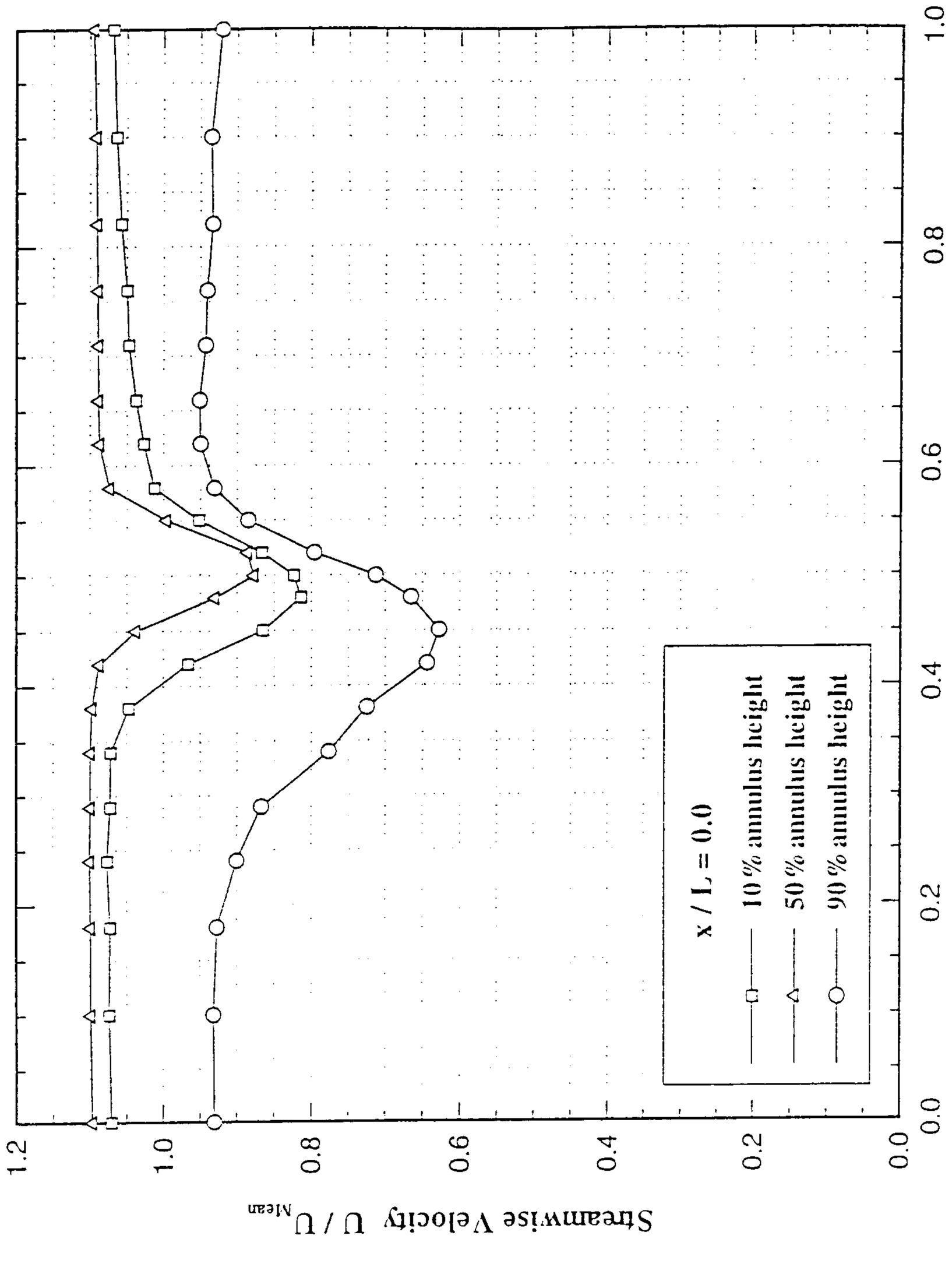

Fig.4.2.14 Circumferential distribution of streamwise velocity (x/L=0.0)

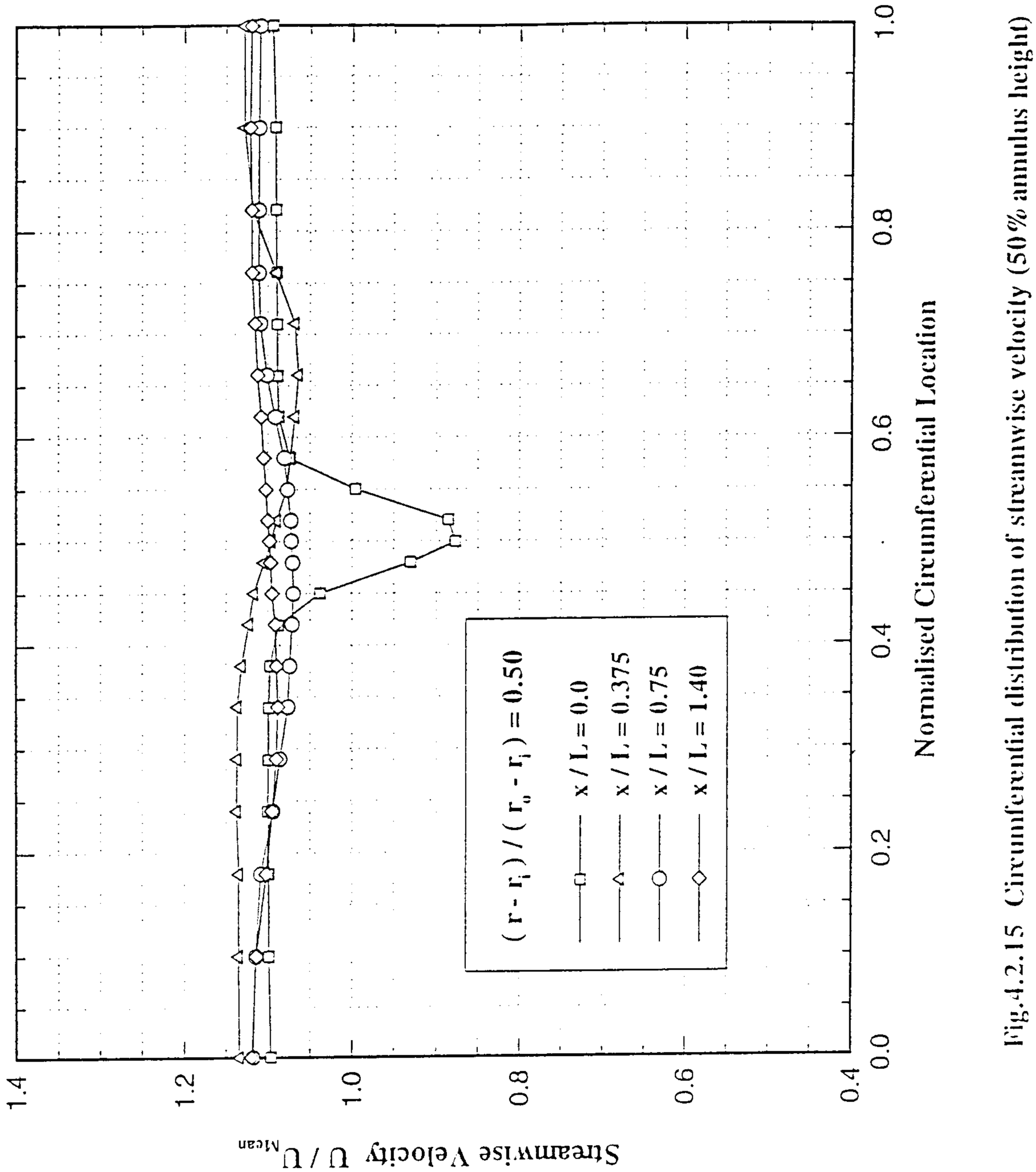

Fig.4.2.15 Circumferential distribution of streamwise velocity (50% annulus height)

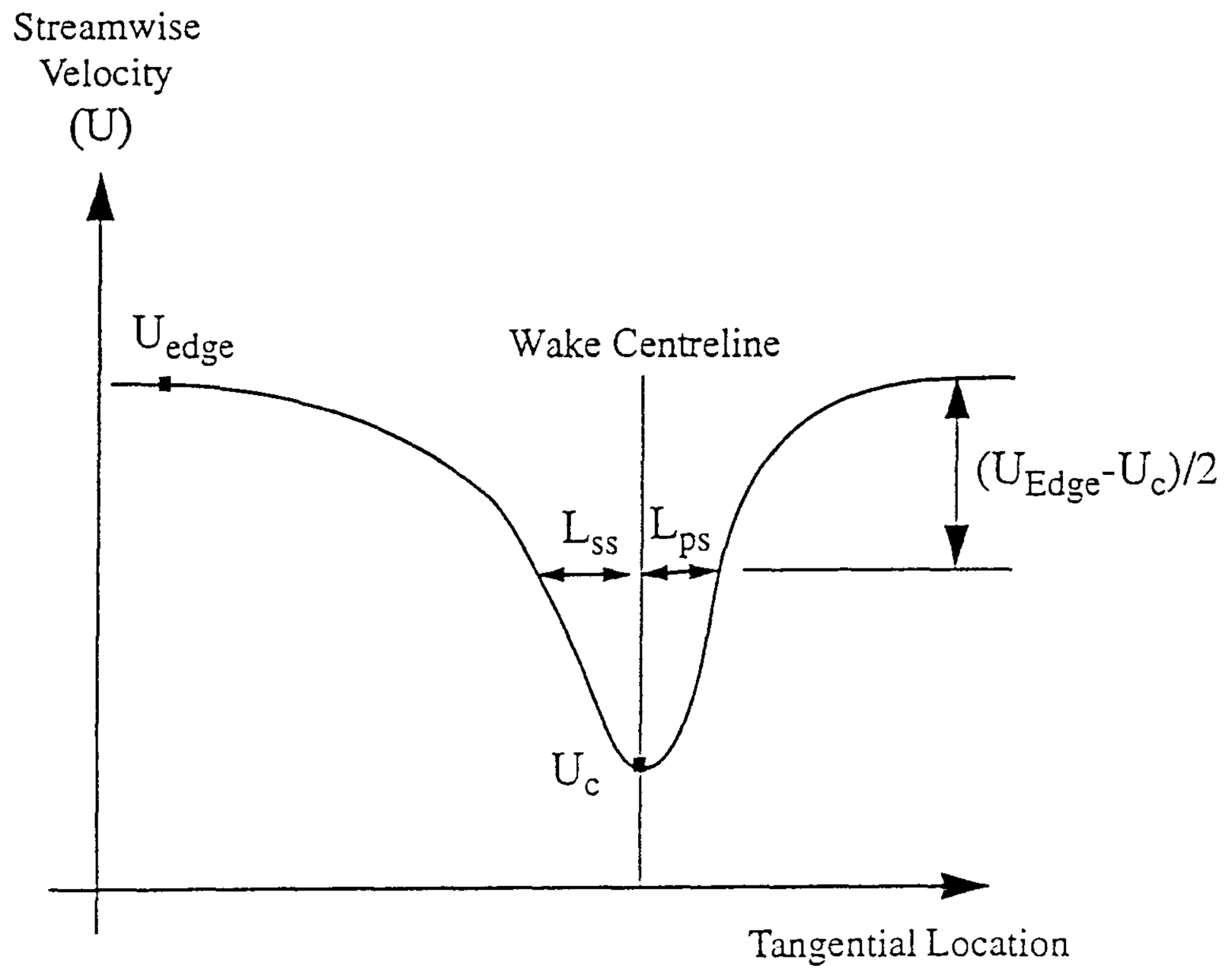

Fig.4.2.16 Definition of wake and velocity scales.

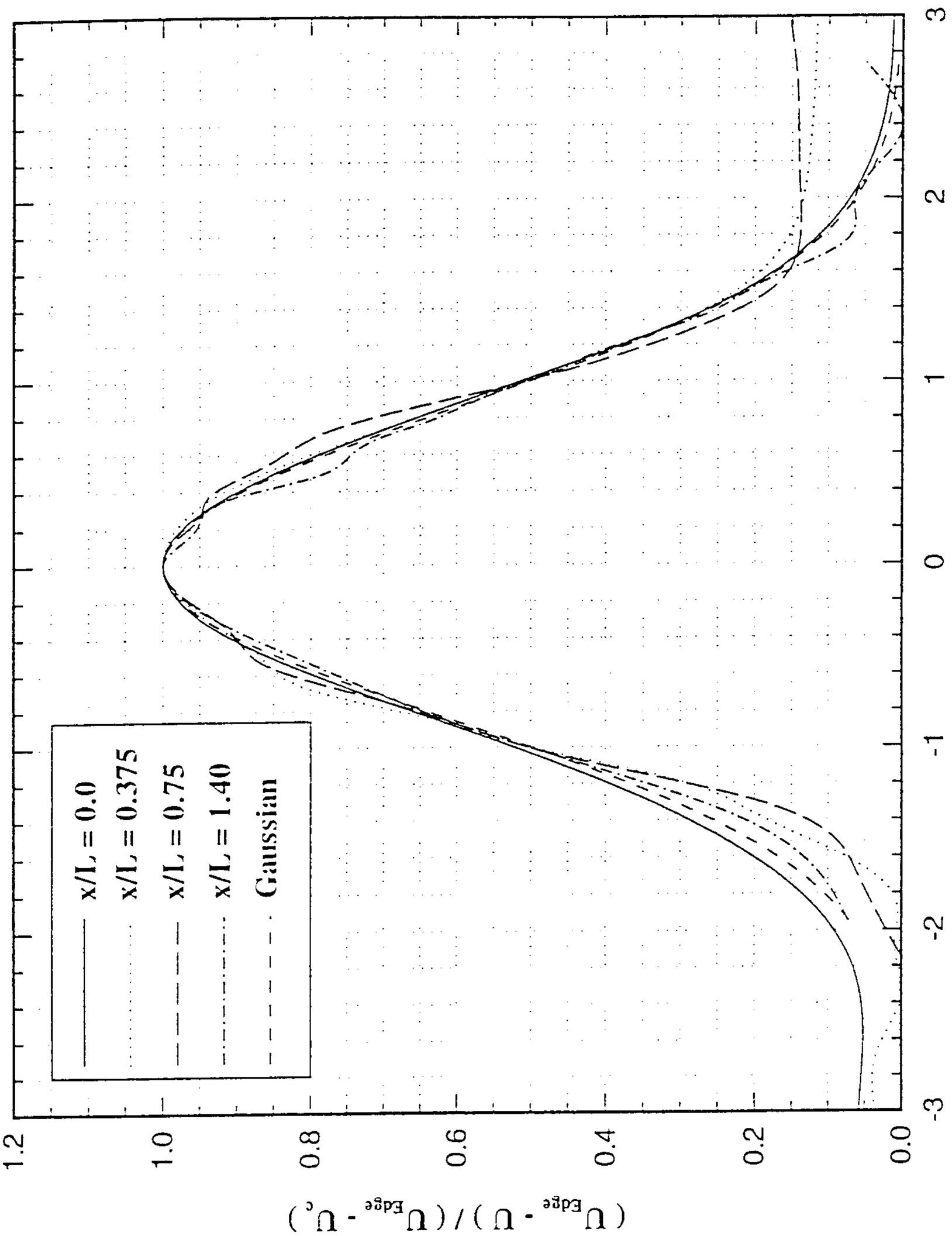

Fig.4.2.17 Normalised OGV wake profiles

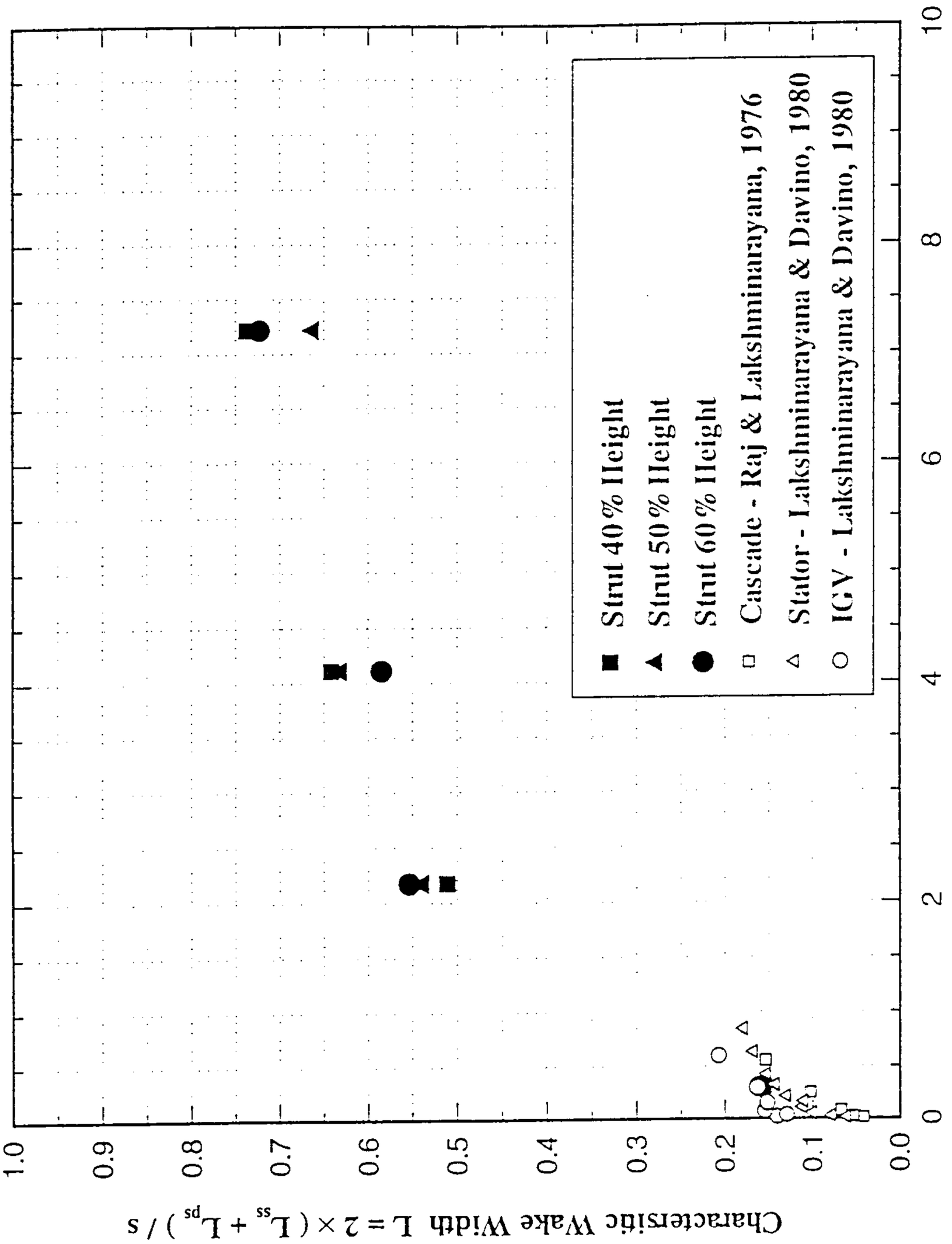

Fig.4.2.18 Axial variation of characteristic wake width (L)

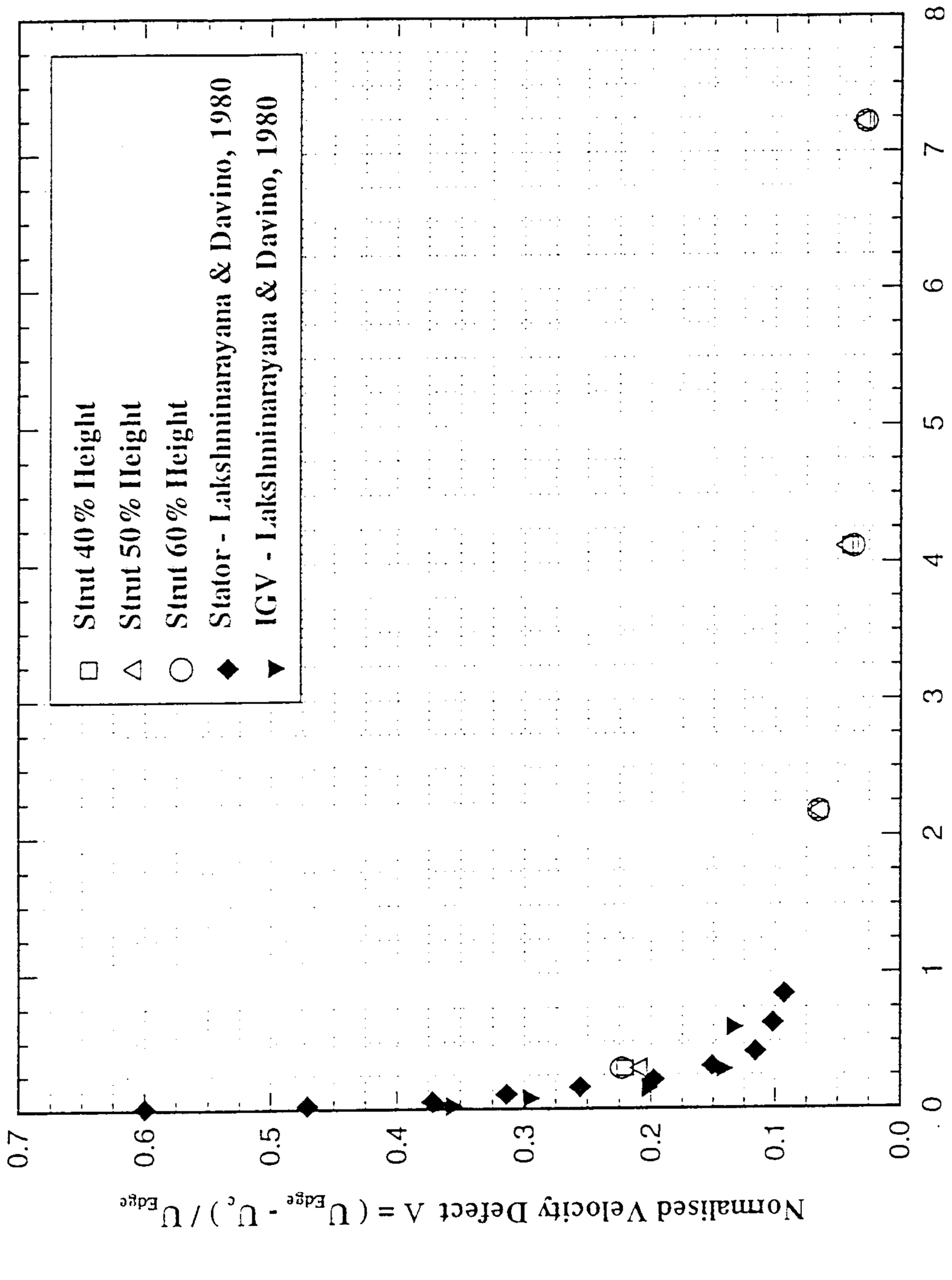

Fig.4.2.19 Axial variation of normalised velocity defect

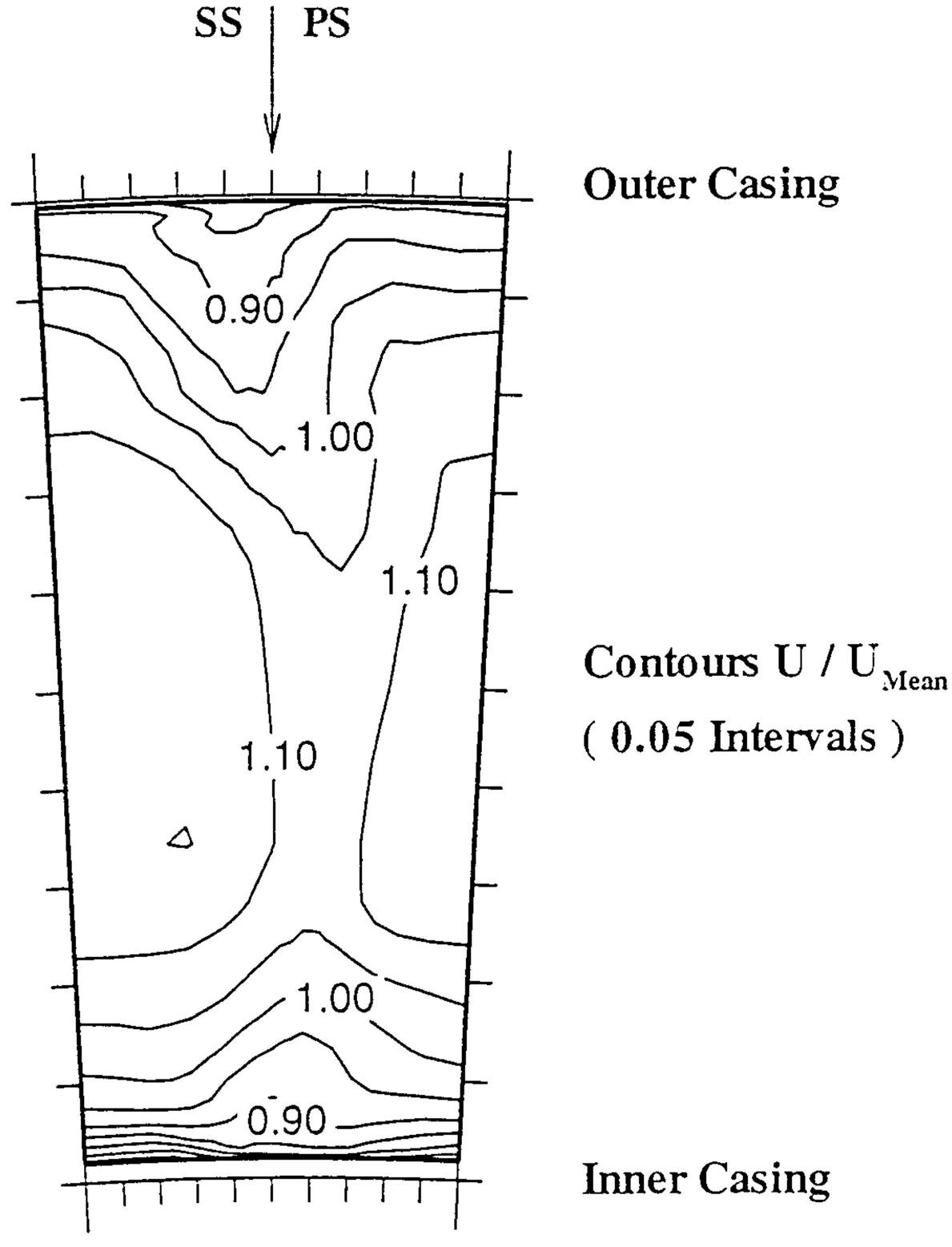

Fig.4.2.20 Streamwise velocity distribution (x/L=0.375).

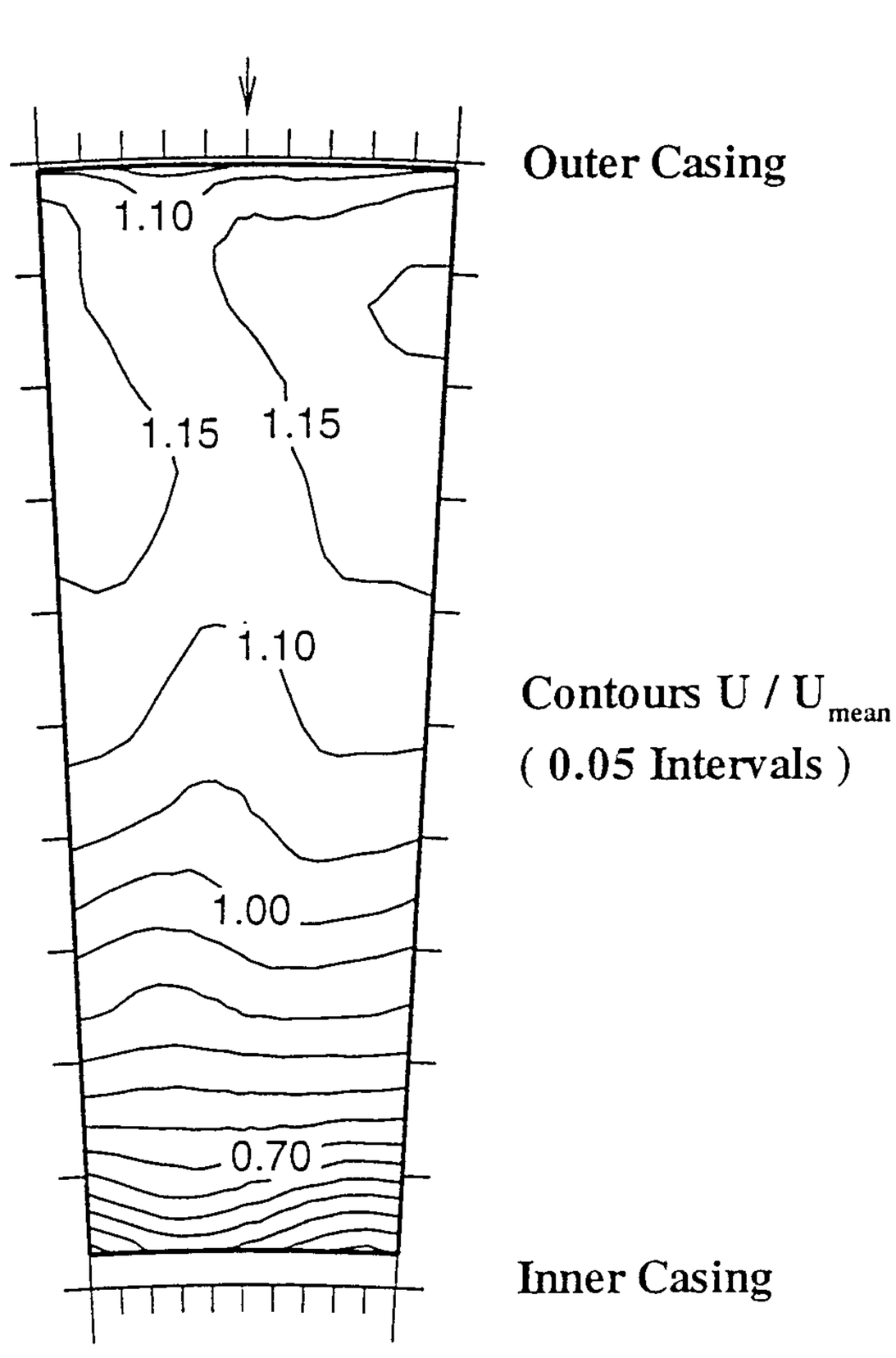

Fig.4.2.21 Streamwise velocity distribution (x/L=0.75).

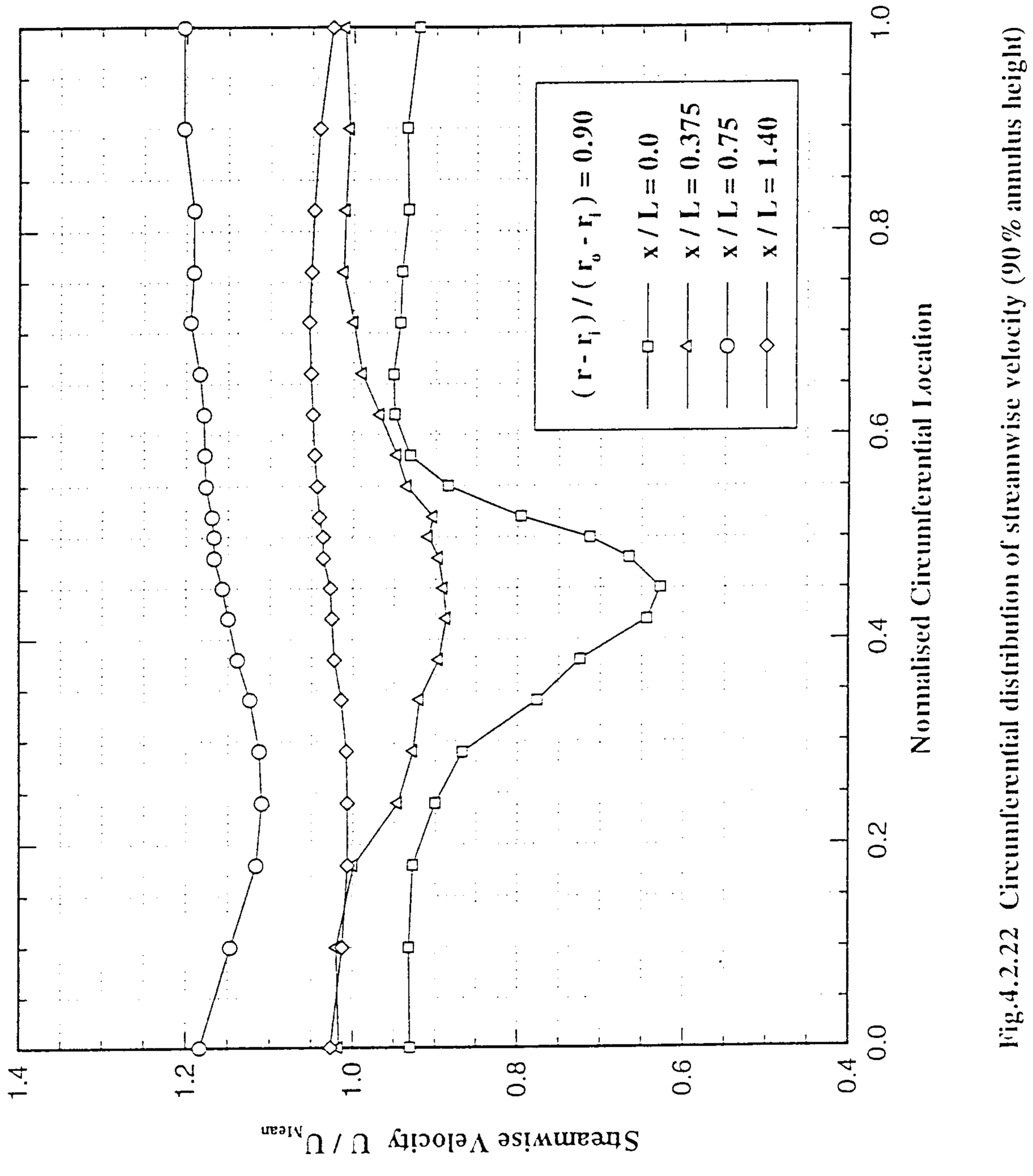

Fig.4.2.22 Circumferential distribution of streamwise velocity (90% annulus height)

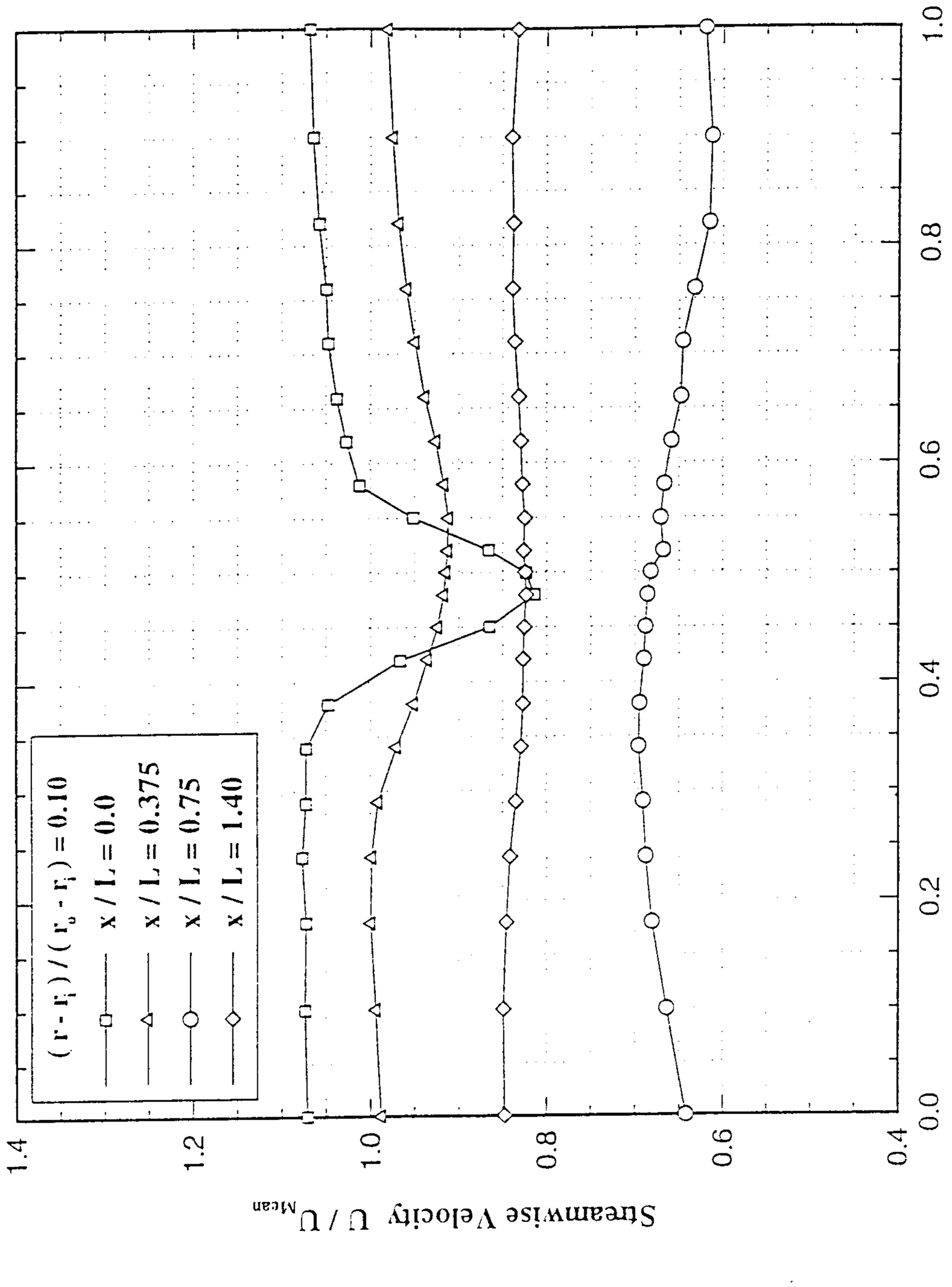

Fig.4.2.23 Circumferential distribution of streamwise velocity (10% annulus height)

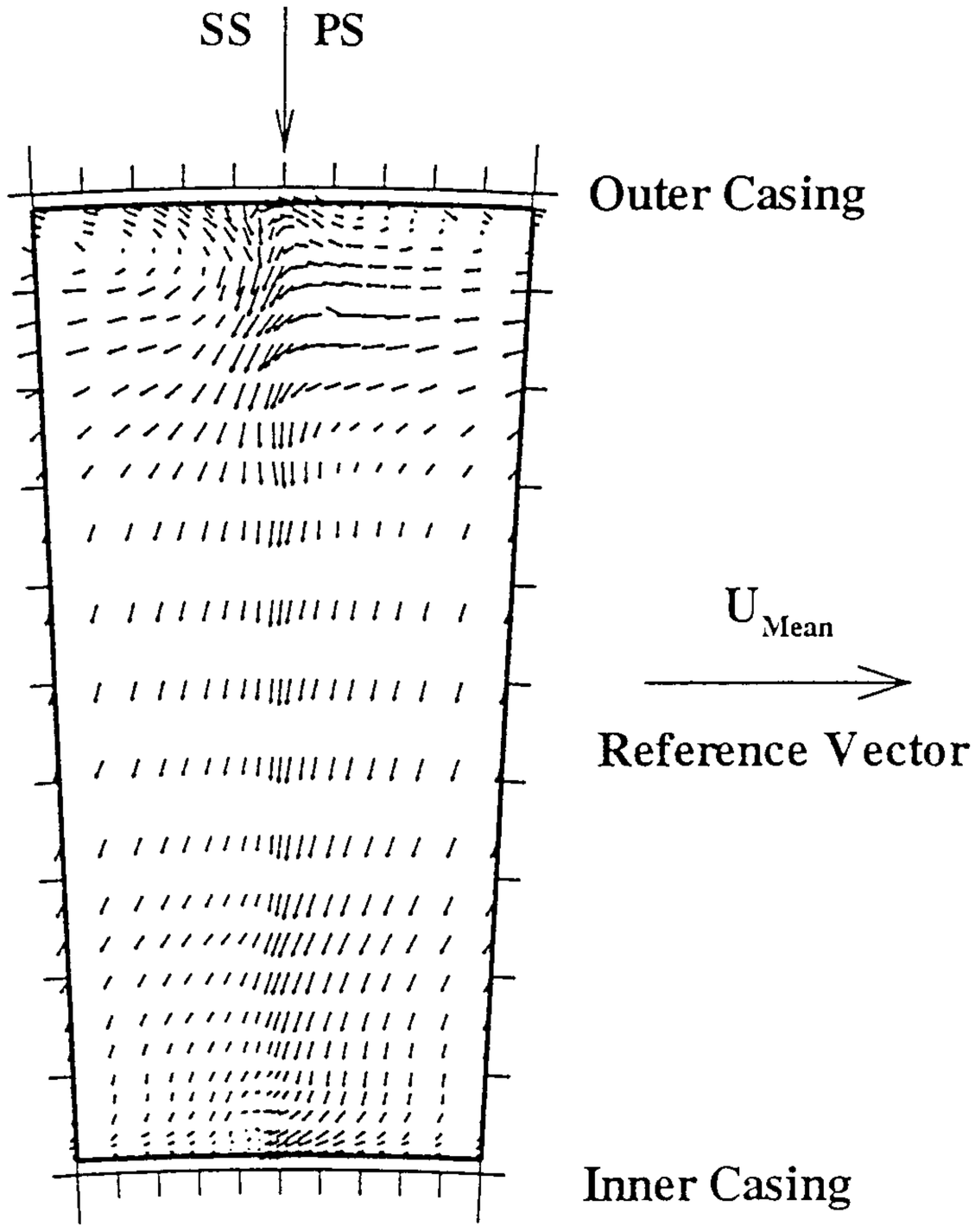

Fig.4.2.24 Flow vectors (x/L=0.0)

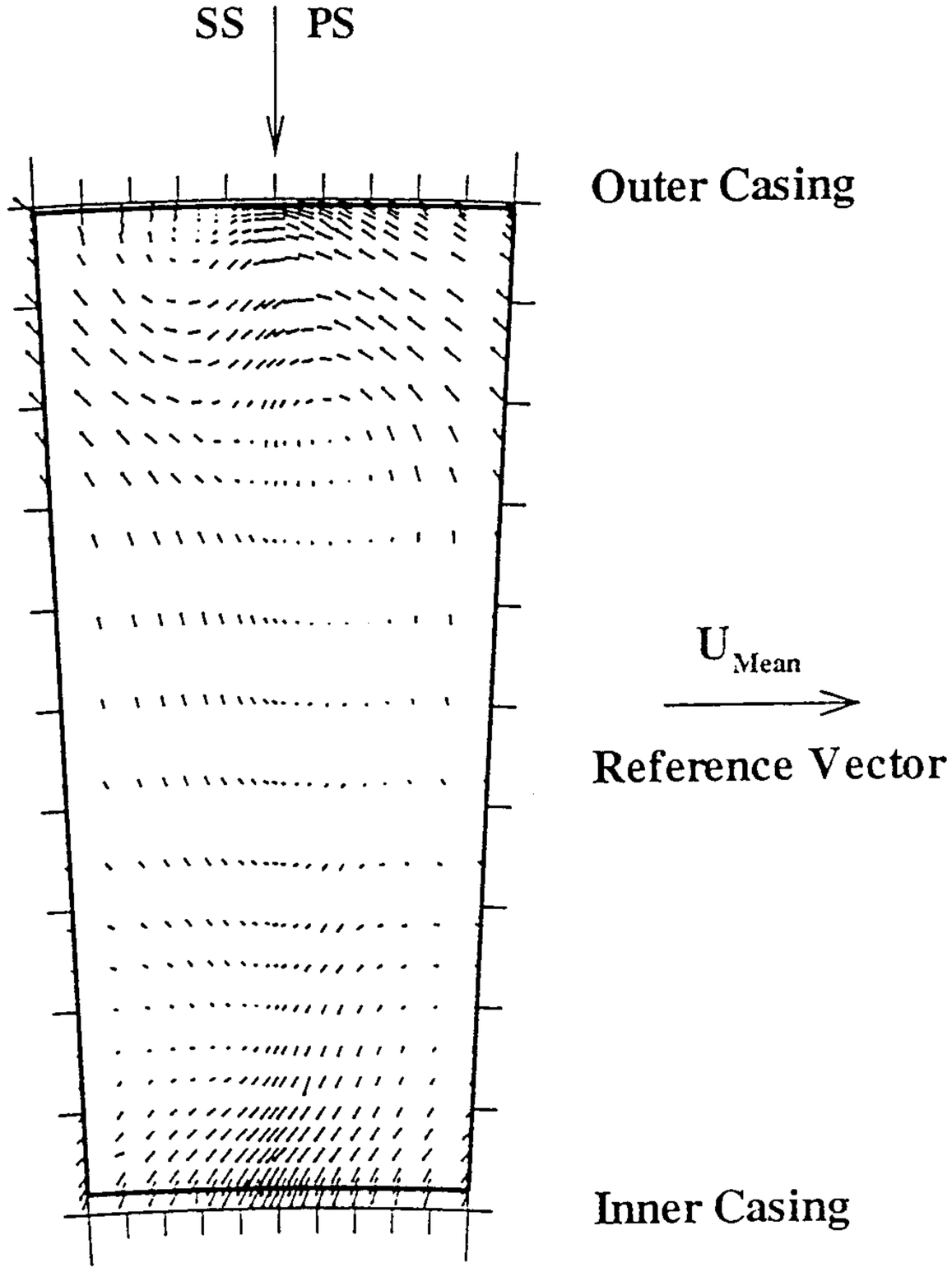

Fig.4.2.25 Flow vectors (x/L=0.375).

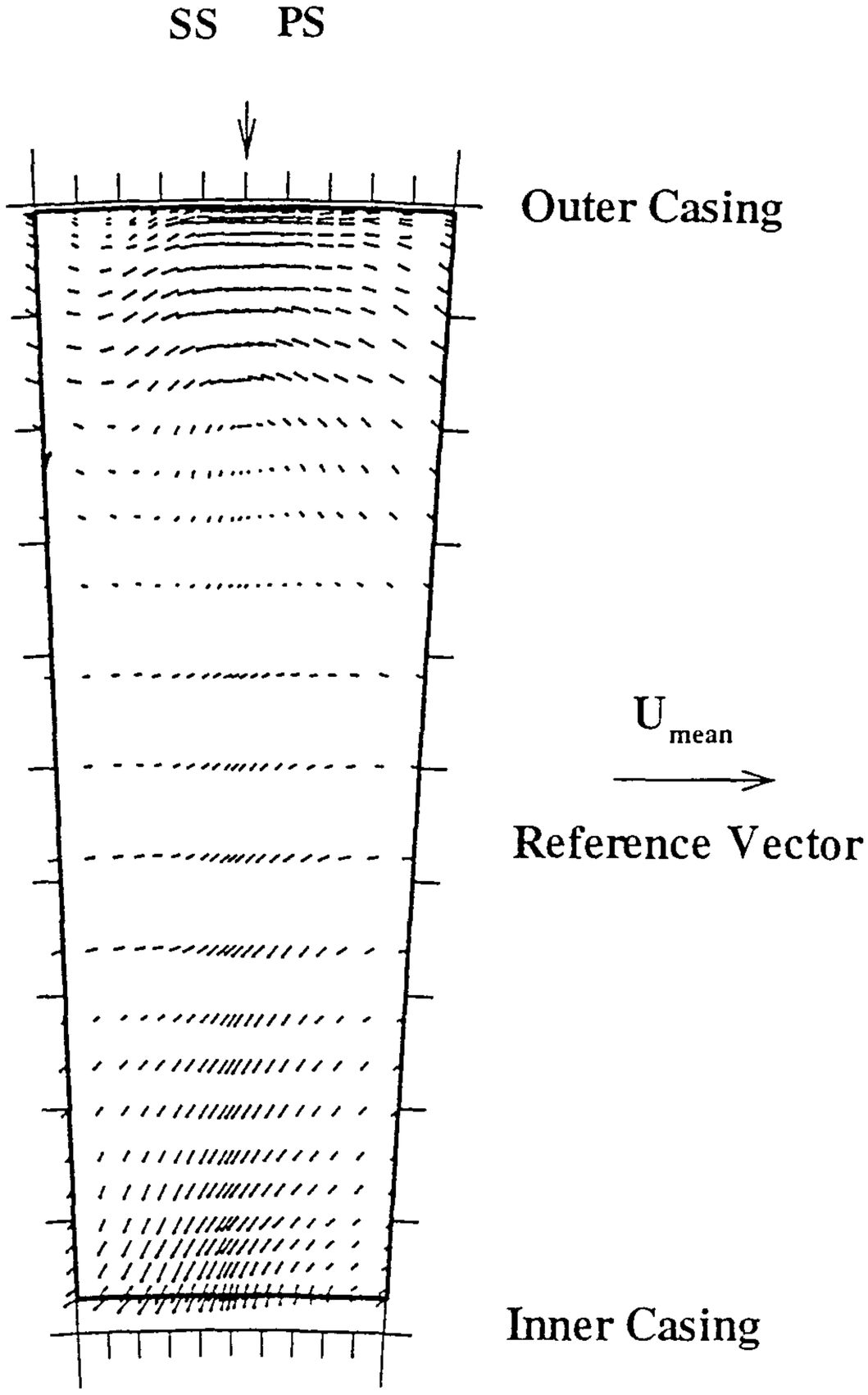

Fig.4.2.26 Flow vectors (x/L=0.75).

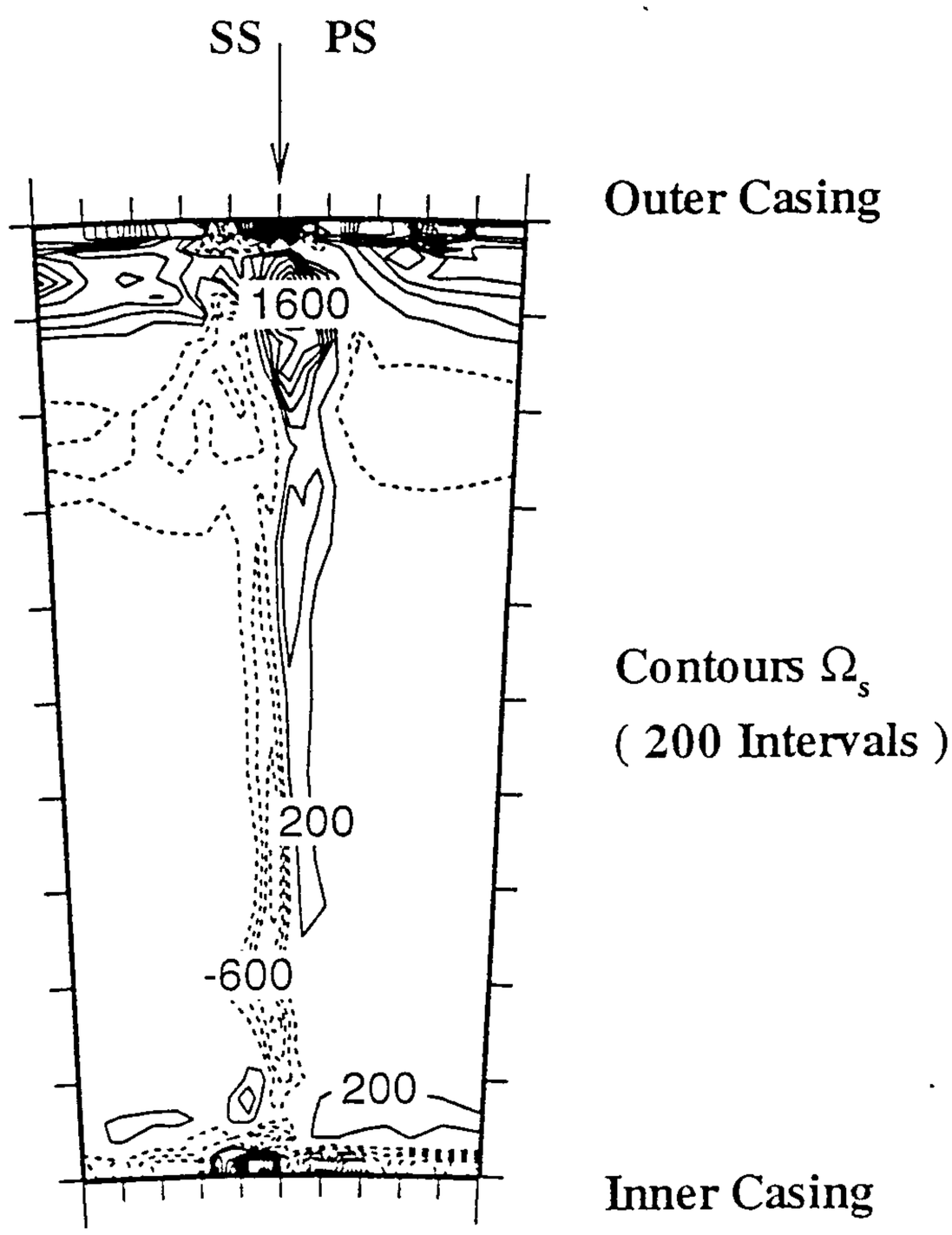

Fig.4.2.27 Streamwise vorticity distribution (x/L=0.0)

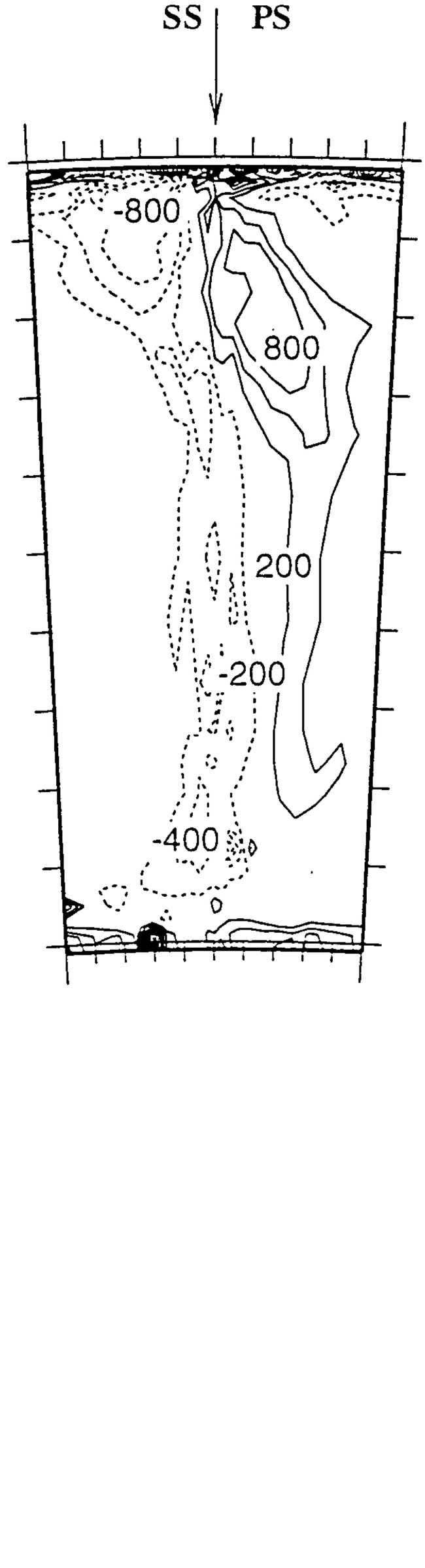

Fig.4.2.28 Streamwise vorticity distribution (x/L=0.375).

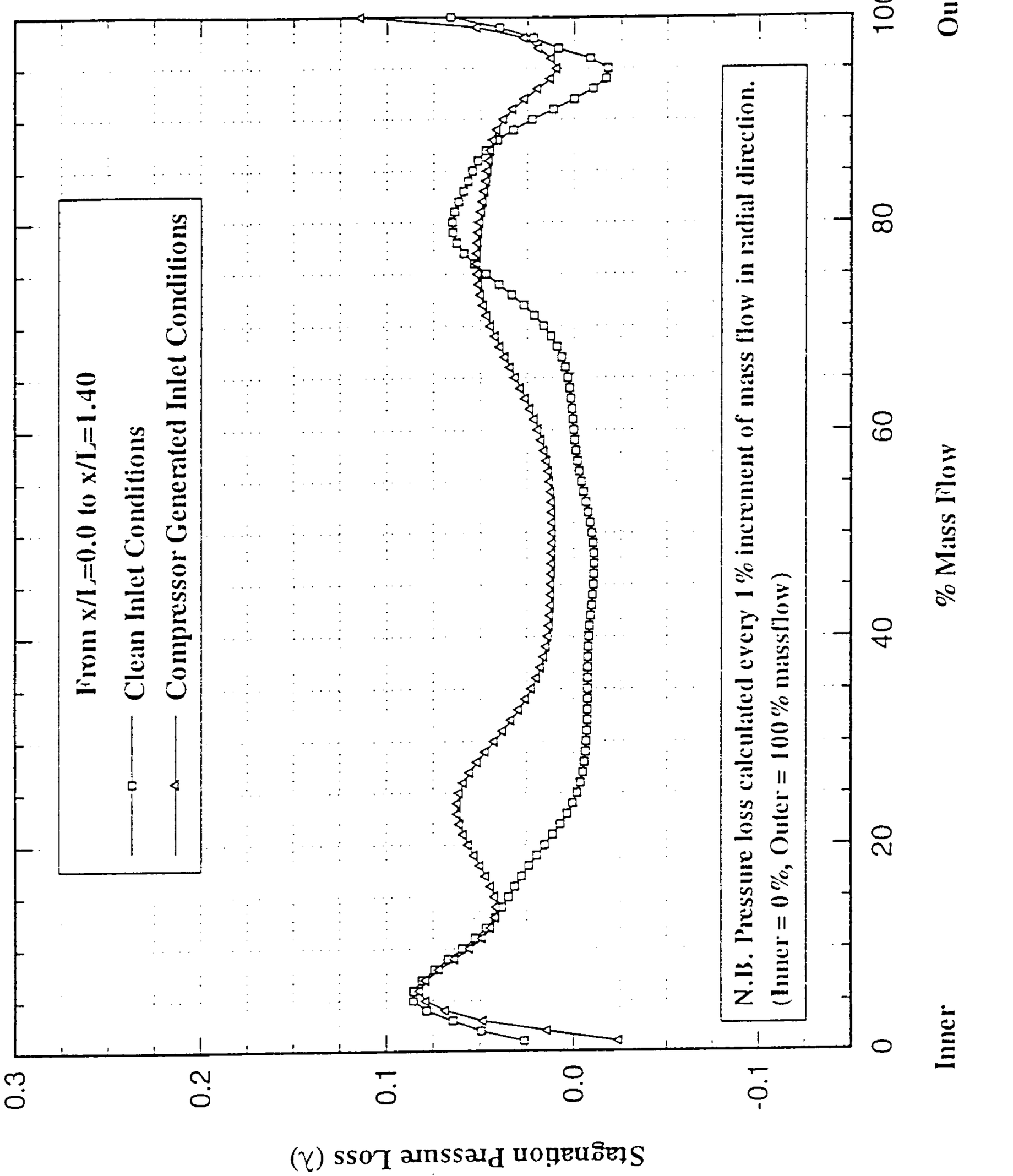

Fig.4.2.29 Radial distribution of stagnation pressure loss (x/L=0.0 to 1.4).

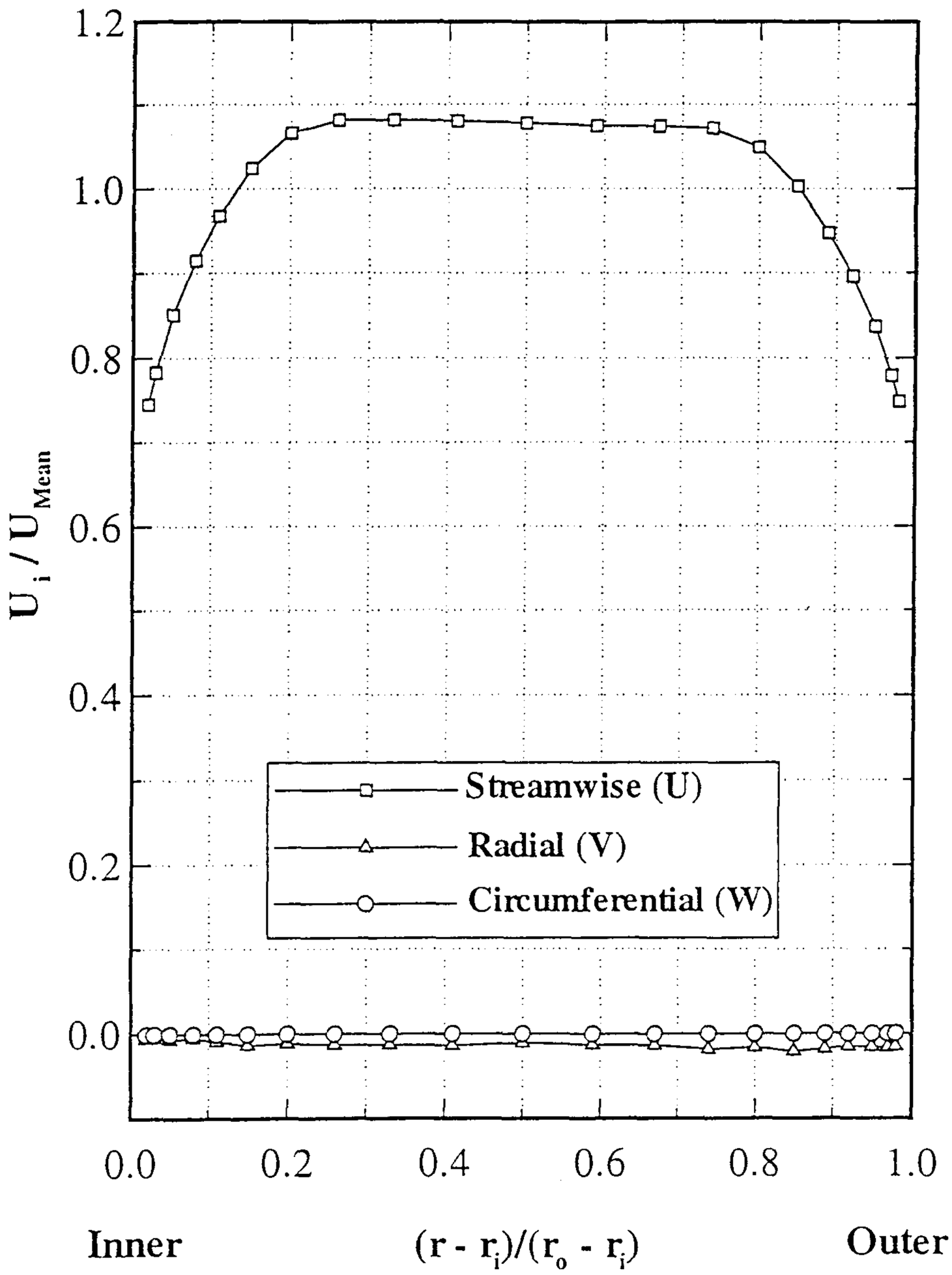

Fig.4.3.1 Mean velocity profiles (x/L=-0.55).

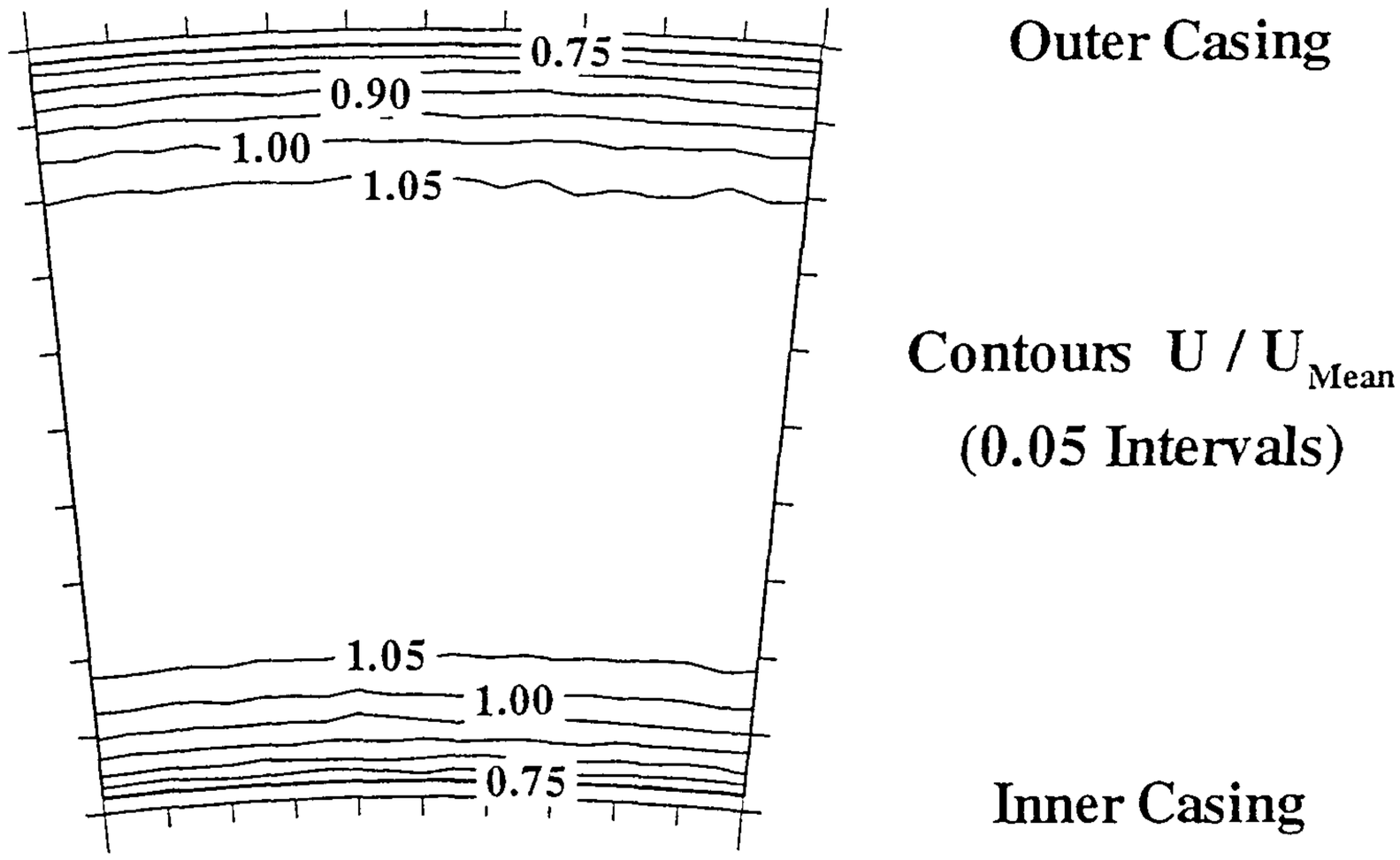

Fig.4.3.2.a Streamwise velocity distribution (x/L=-0.55).

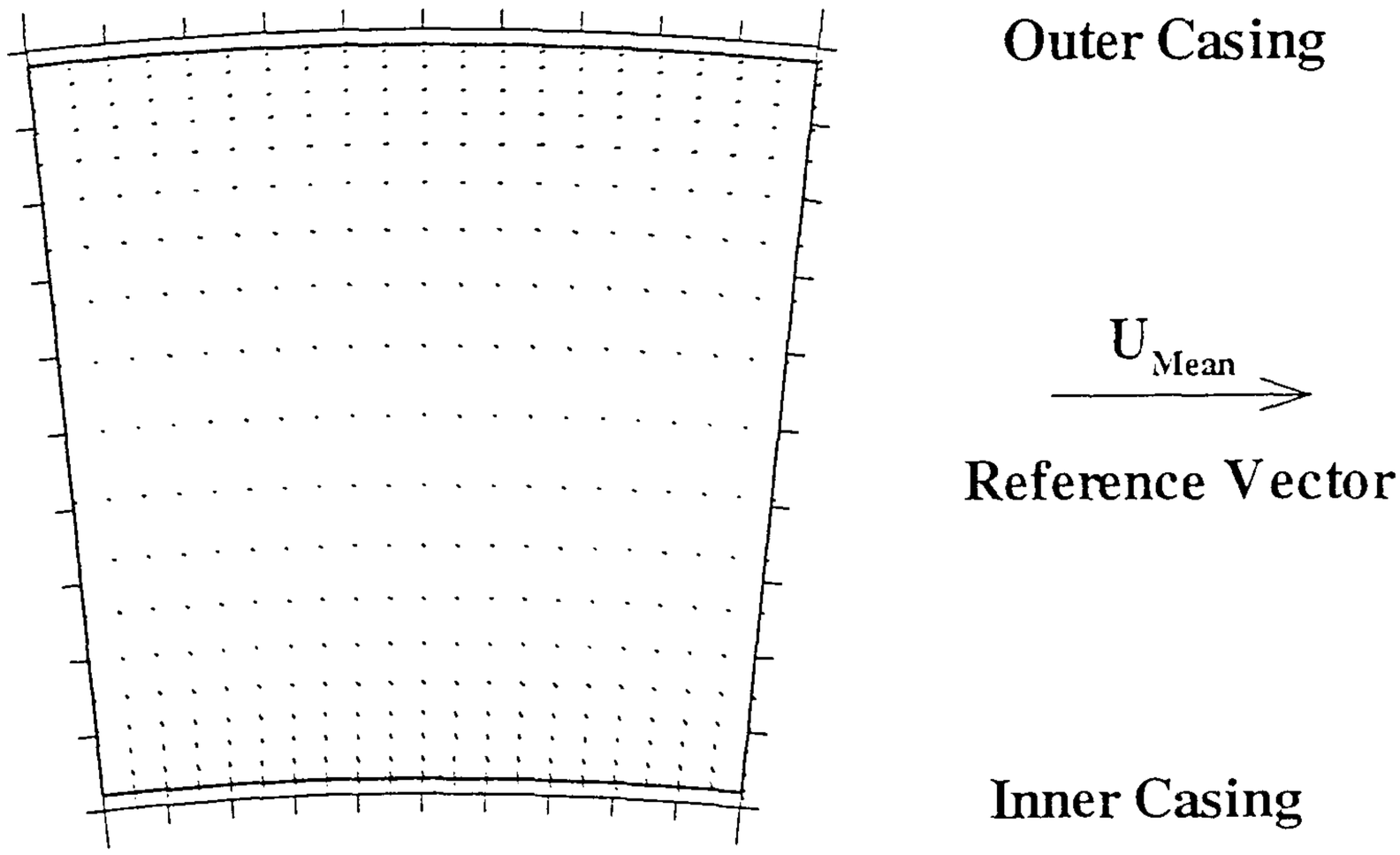

Fig.4.3.2.b Flow vectors (x/L=-0.55).

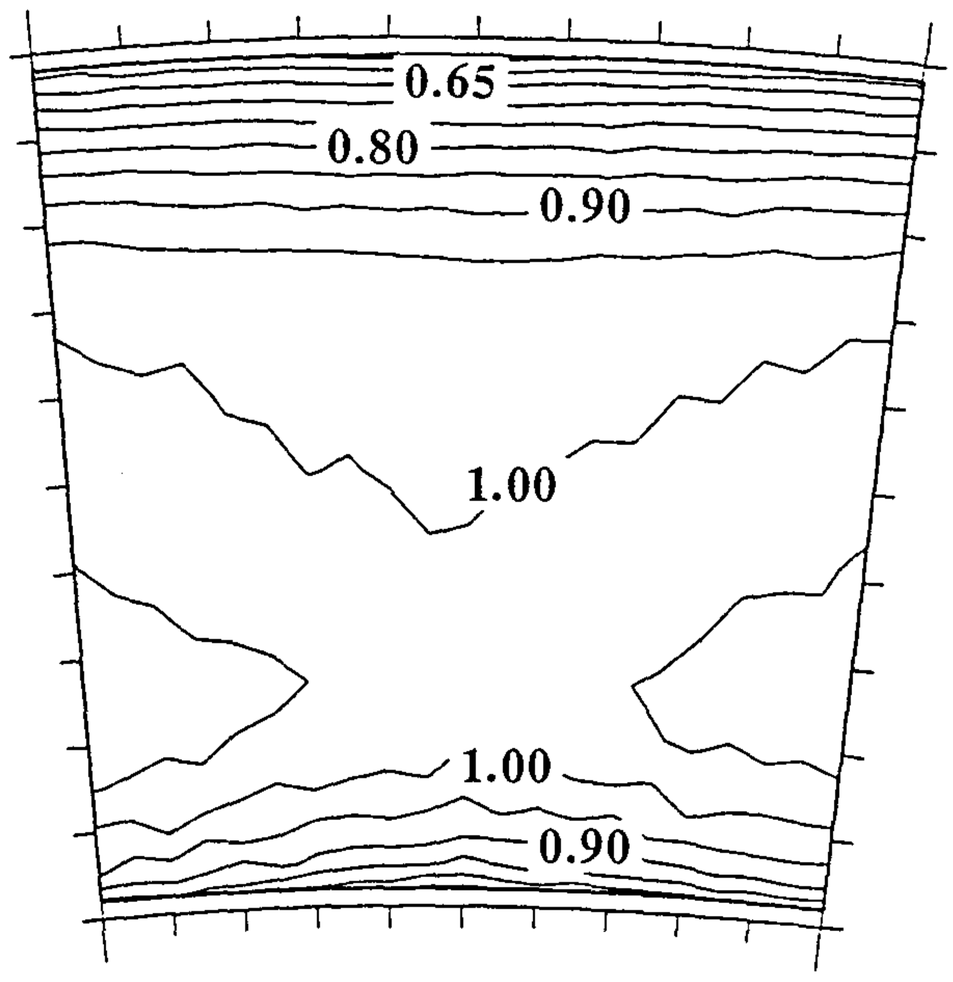

Fig.4.3.3.a Streamwise velocity distribution (x/L=0.0).

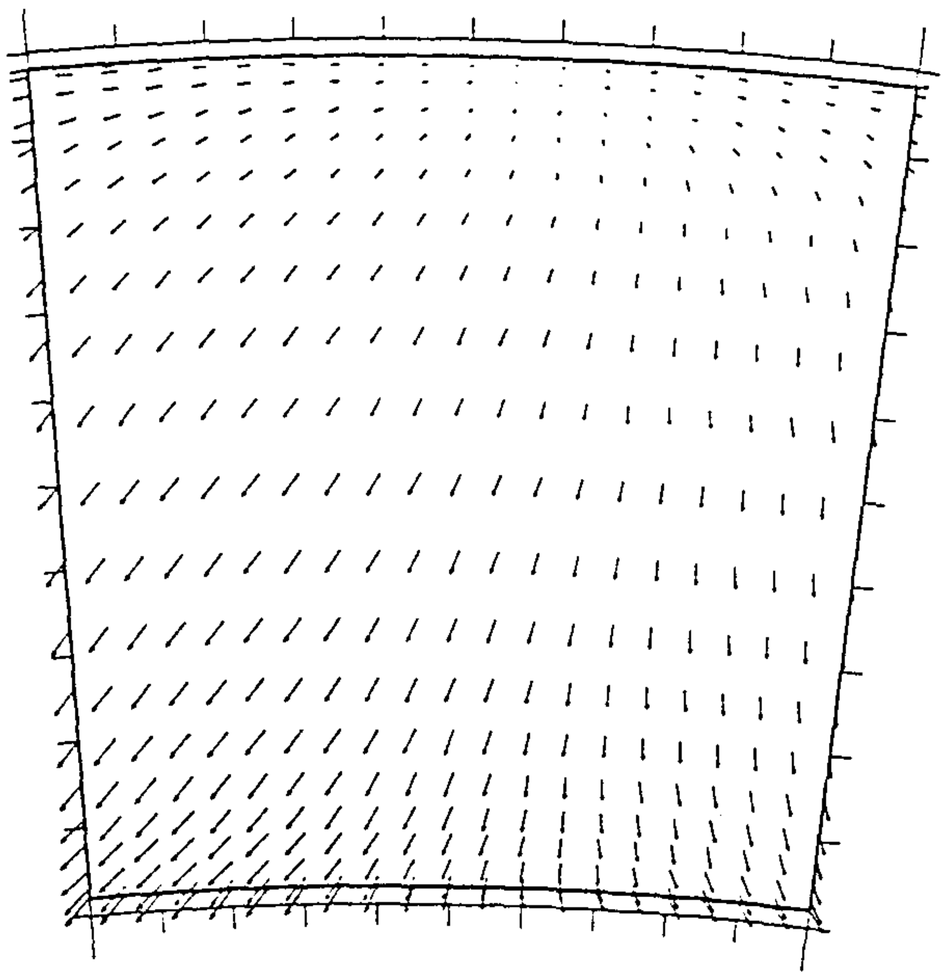

Fig4.3.3.b Flow vectors (x/L=0.0)

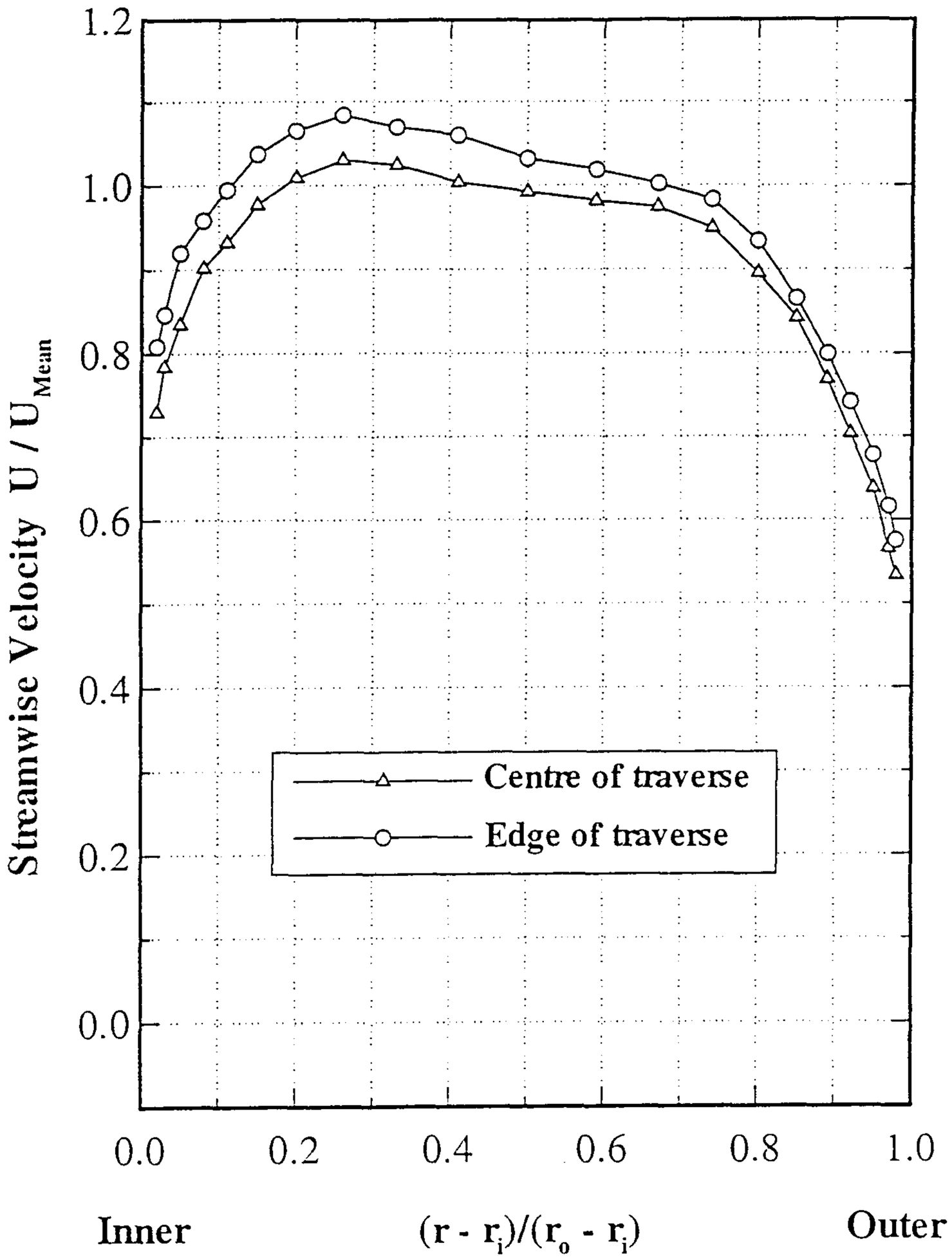

Fig.4.3.4 Streamwise velocity profiles (x/L=0.0).

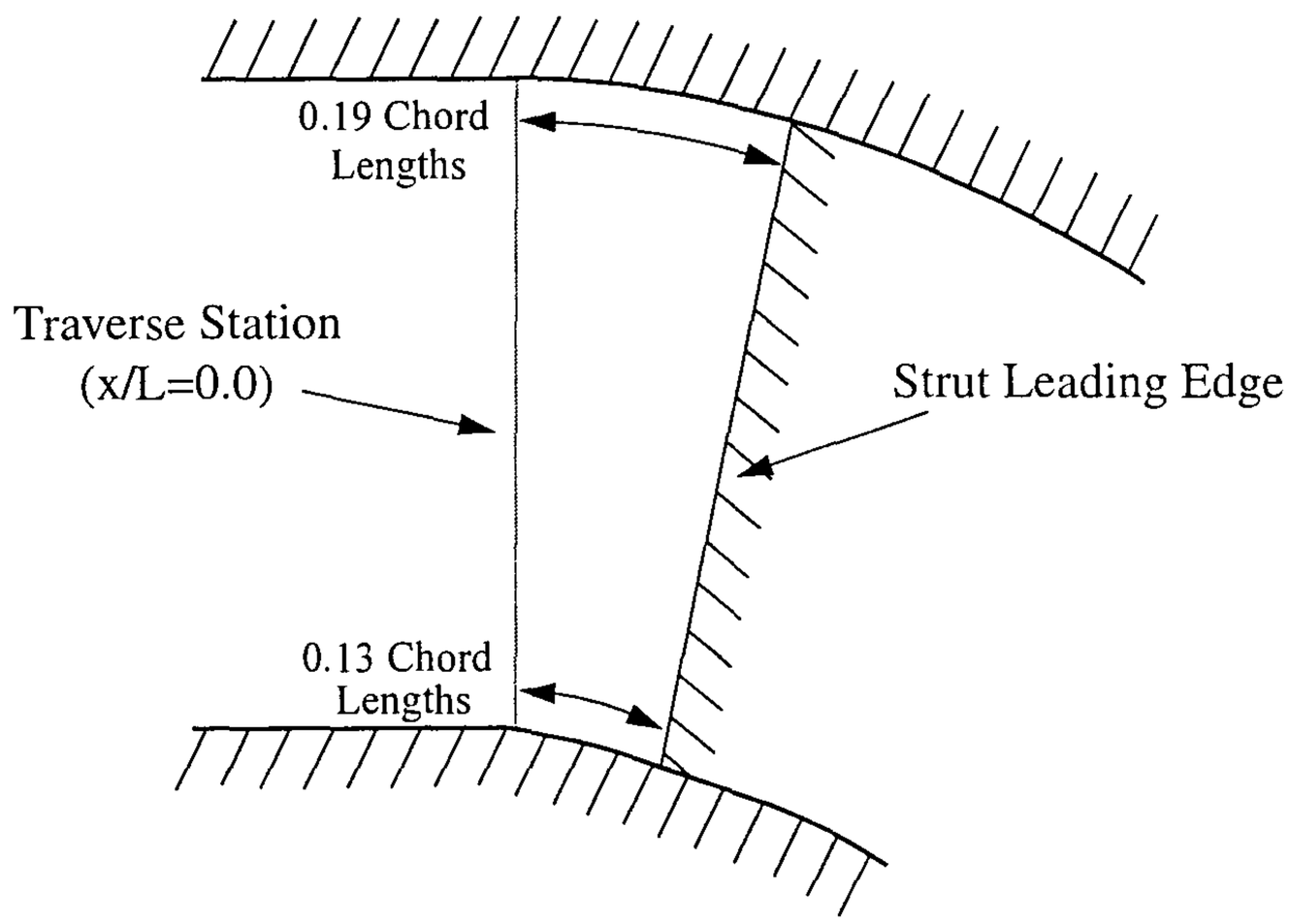

Fig.4.3.5 Position of strut leading edge within S-shaped duct

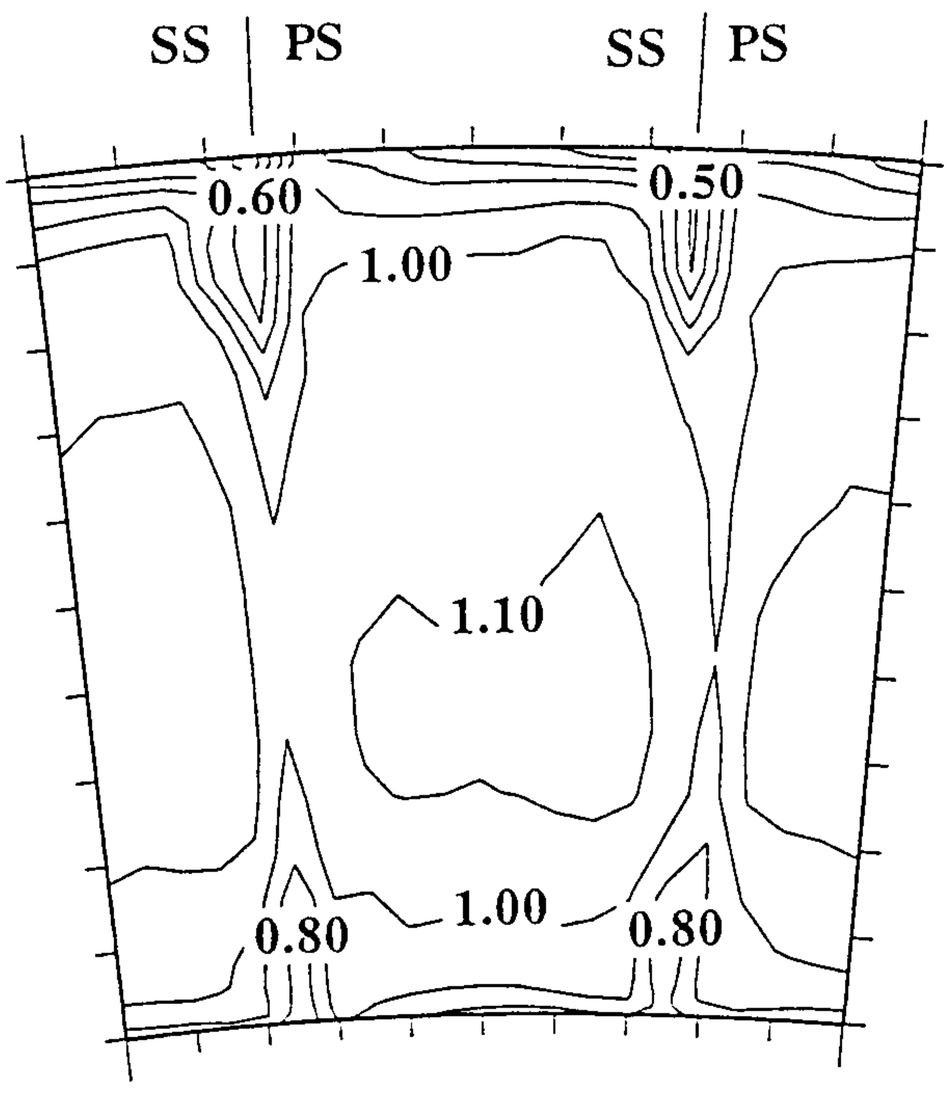

Fig.4.3.6.a Streamwise velocity distribution (x/L=0.0).

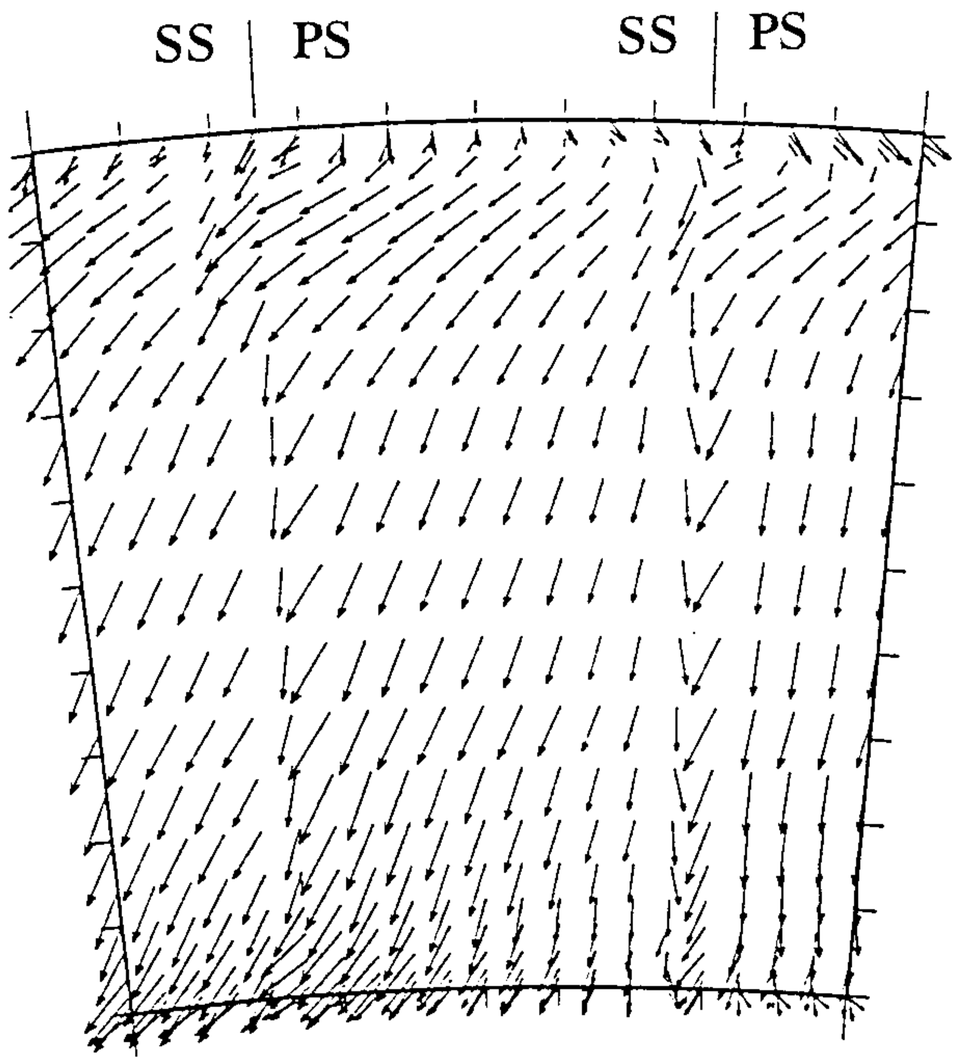

Fig.4.3.6.b Flow vectors (x/L=0.0).

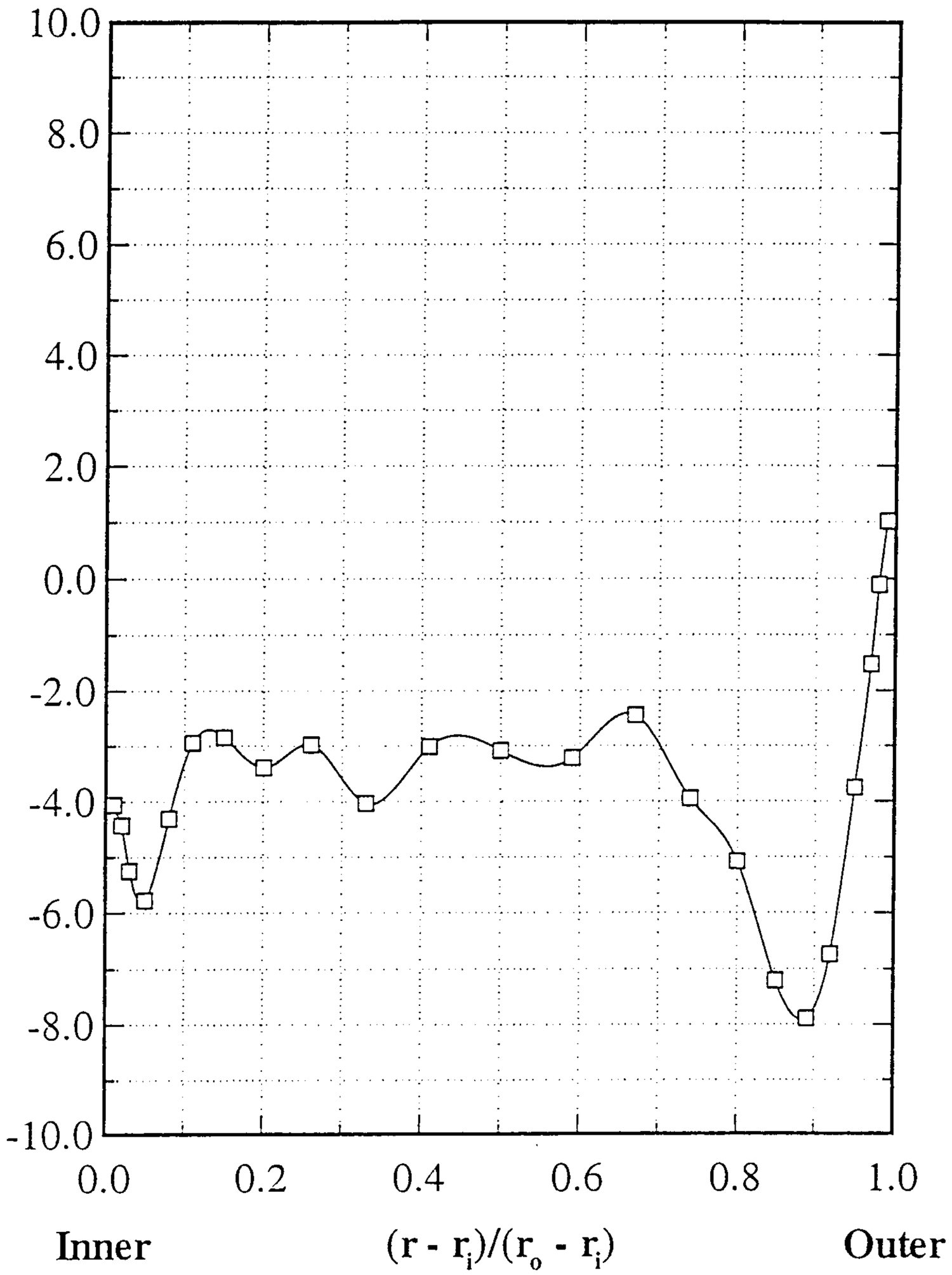

Fig.4.3.7 Radial distribution of pitch averaged swirl angle (x/L=0.0).

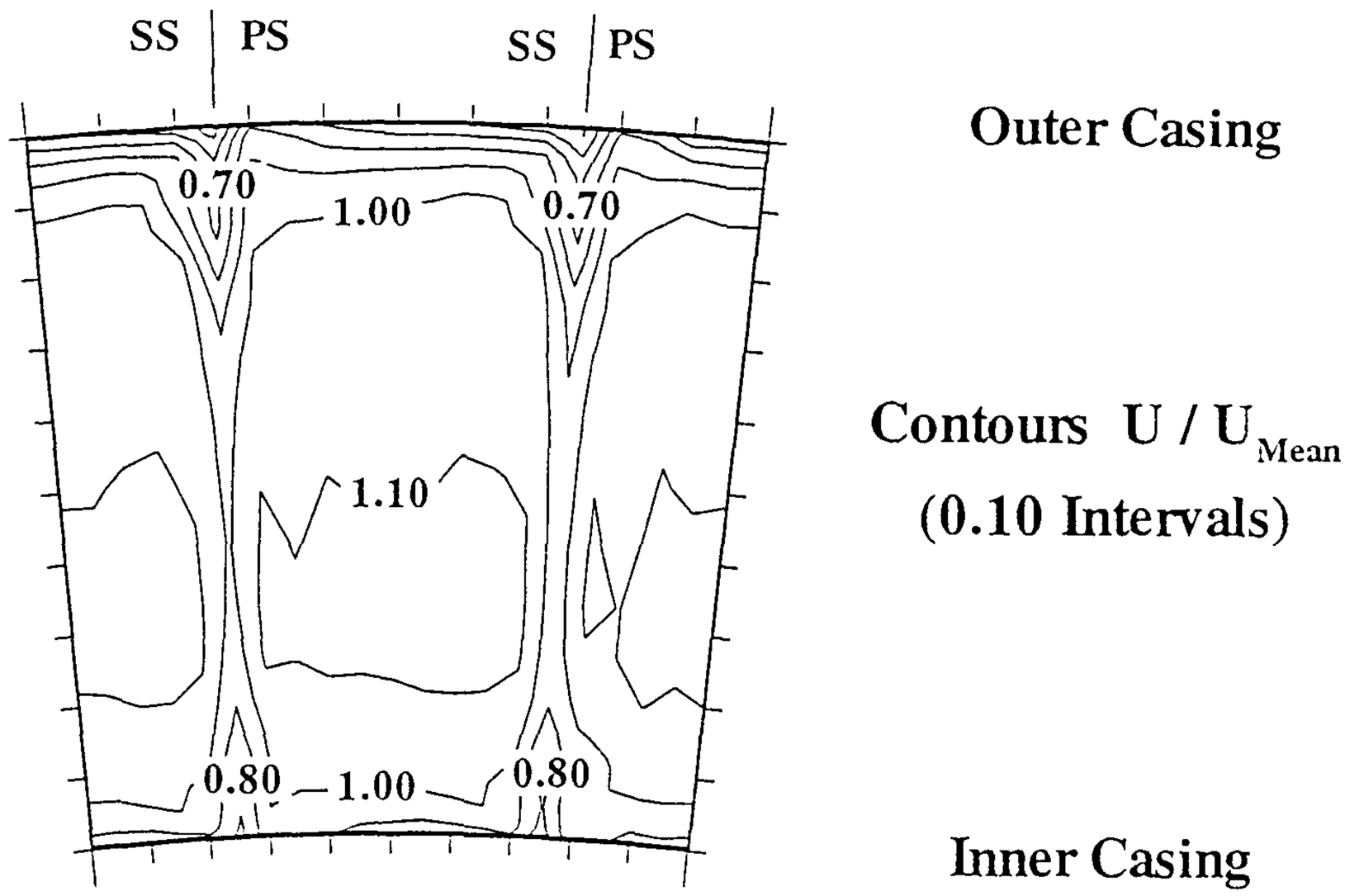

Fig.4.3.8.a Streamwise velocity distribution (Strut removed, x/L=0.0).

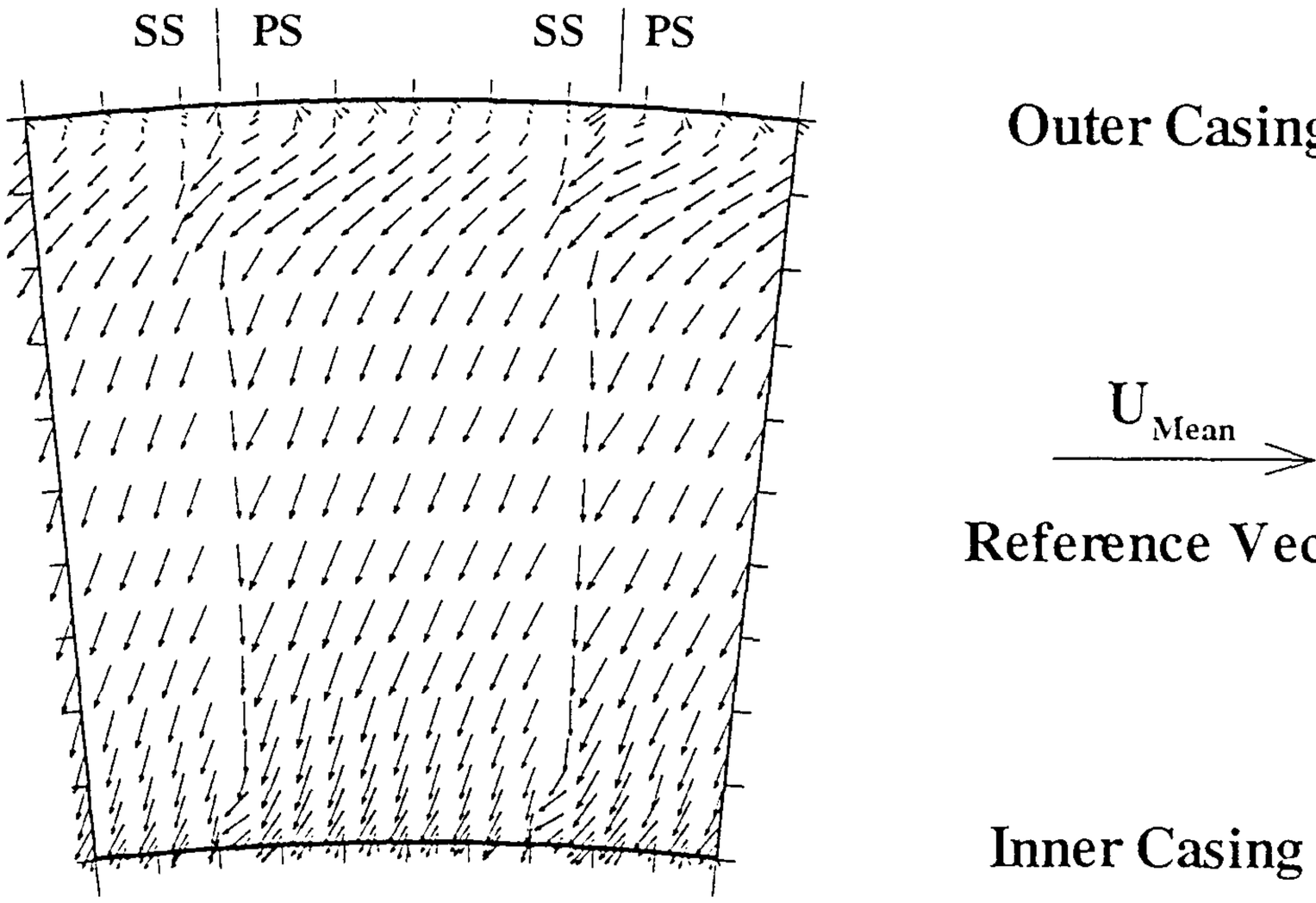

Fig.4.3.8.b Flow vectors (Strut removed, x/L=0.0).

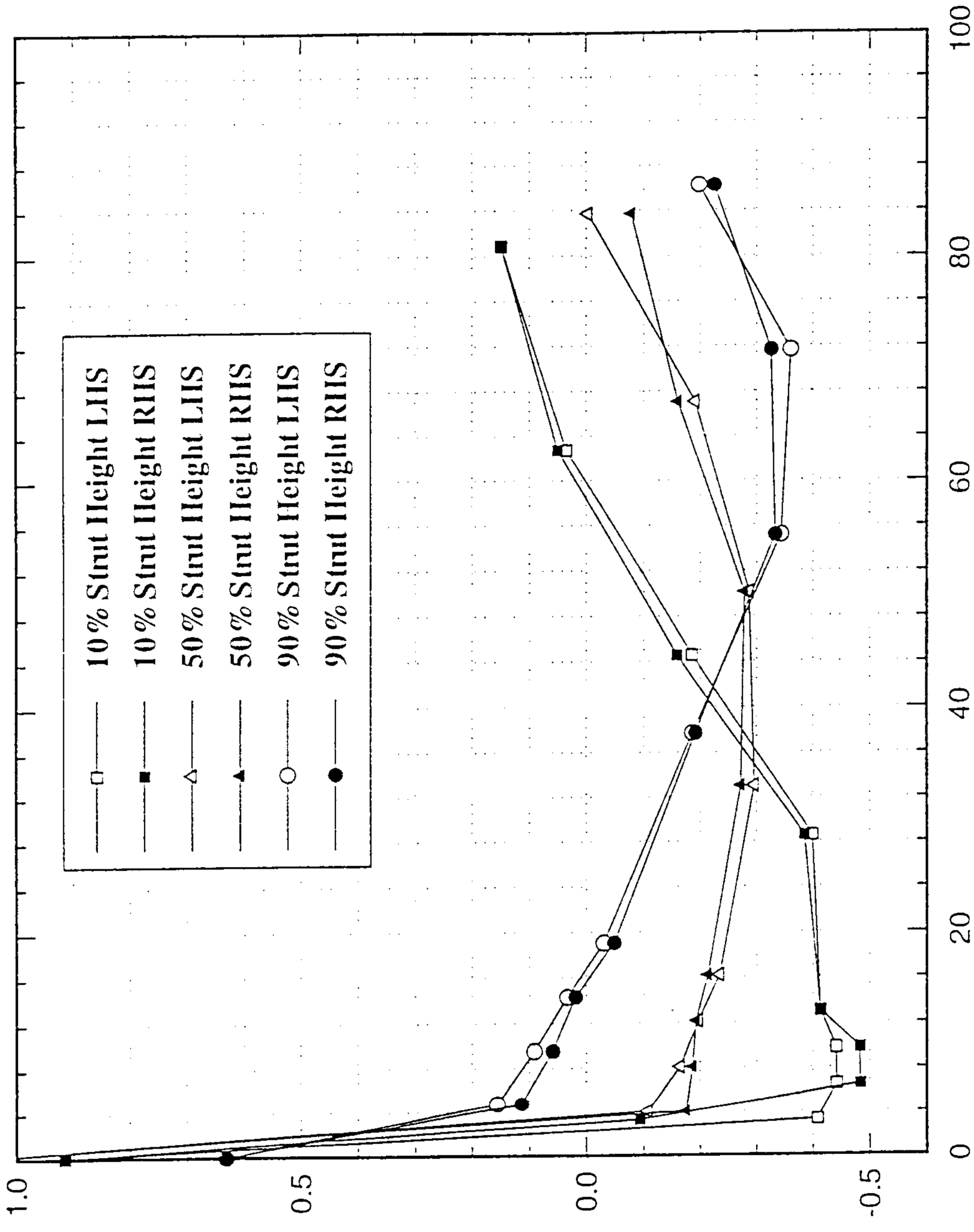

Fig.4.3.9 Static pressure distribution along strut surface.

$$C_p = (p - \bar{p}_1) / (\bar{P}_1 - \bar{p}_1)$$

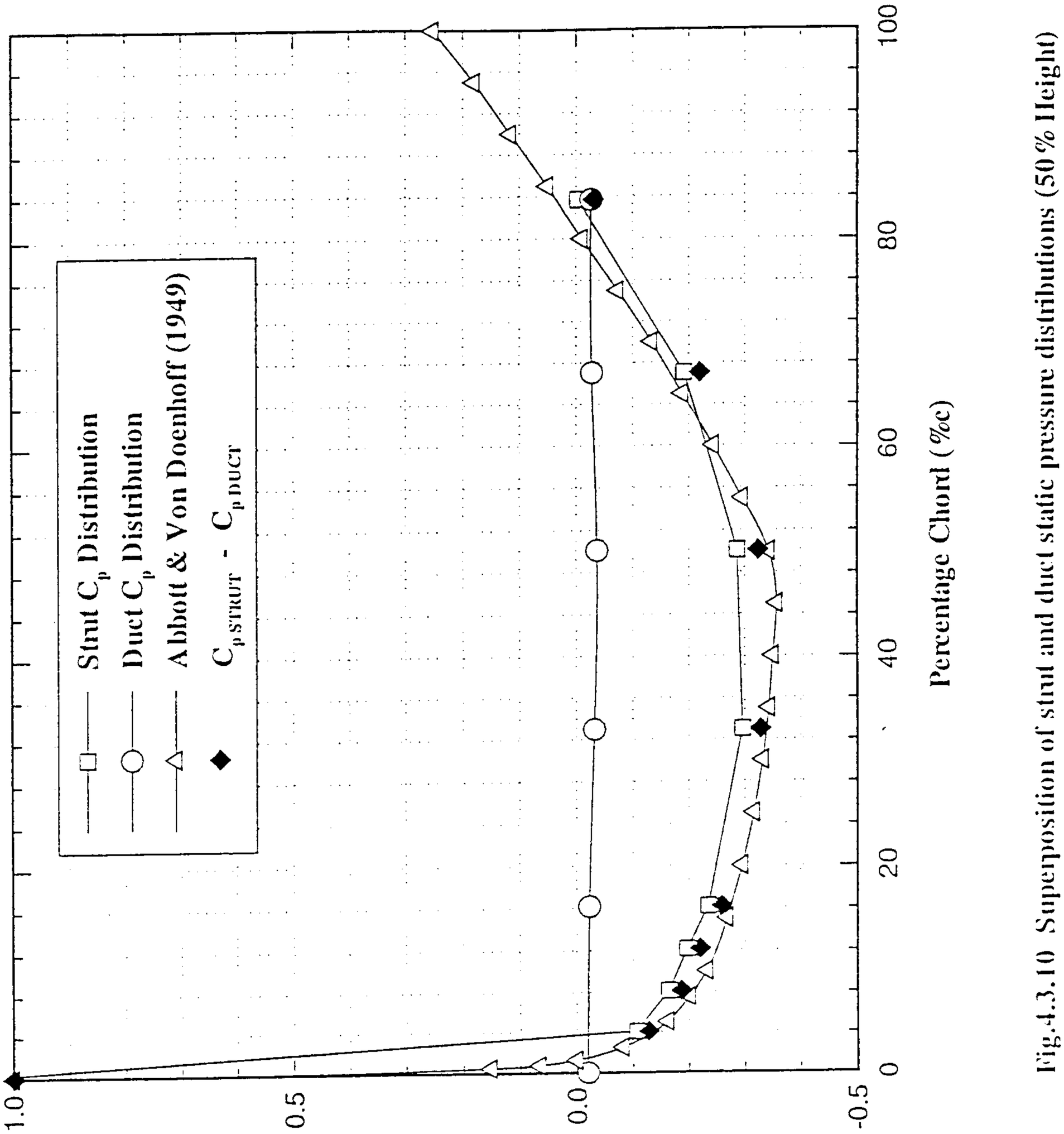

Fig.4.3.10 Superposition of strut and duct static pressure distributions (50 % Height)

$$C_p = (p - \bar{p}_1) / (\bar{P}_1 - \bar{p}_1)$$

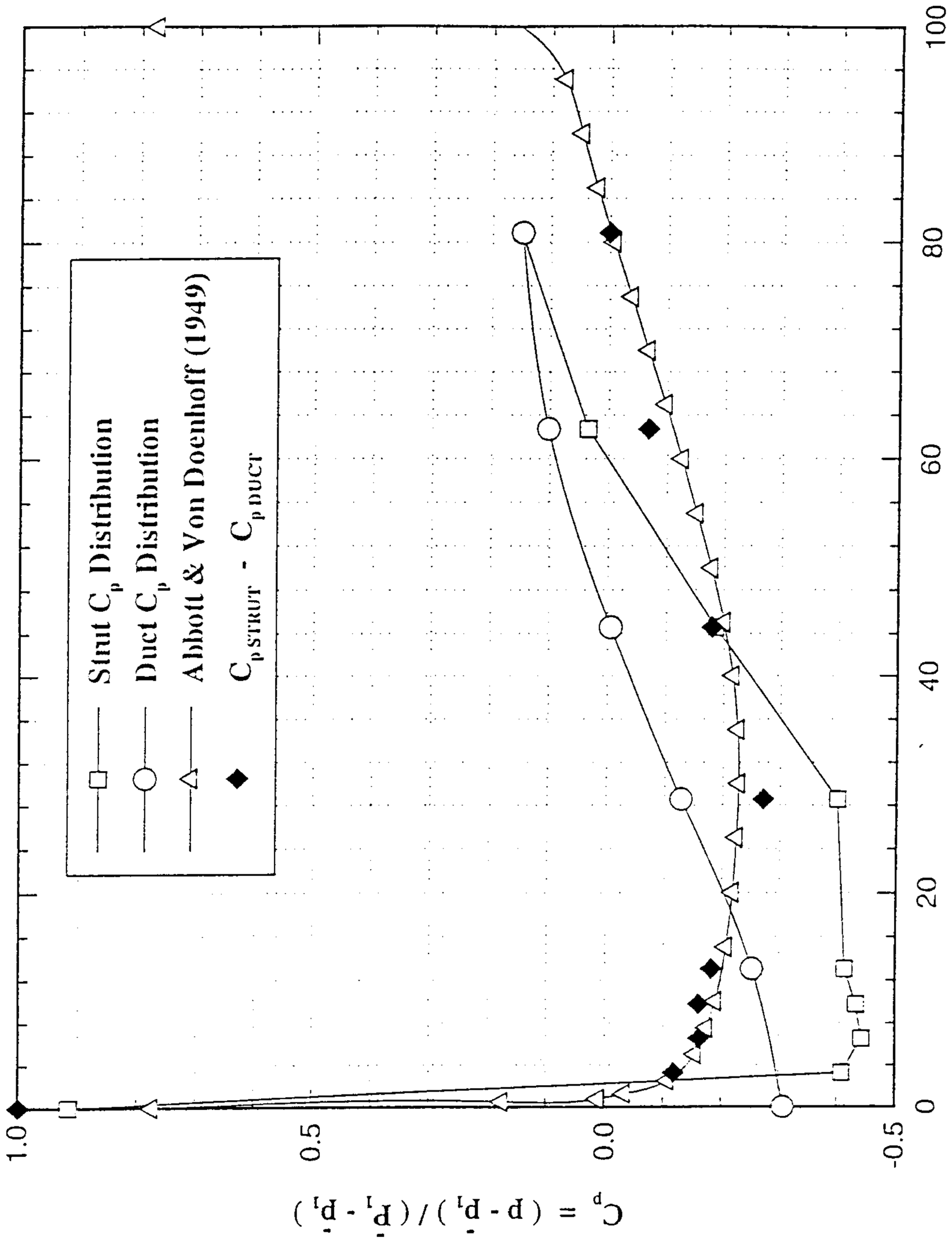

Fig.4.3.11 Superposition of strut and duct static pressure distributions (10% Height)

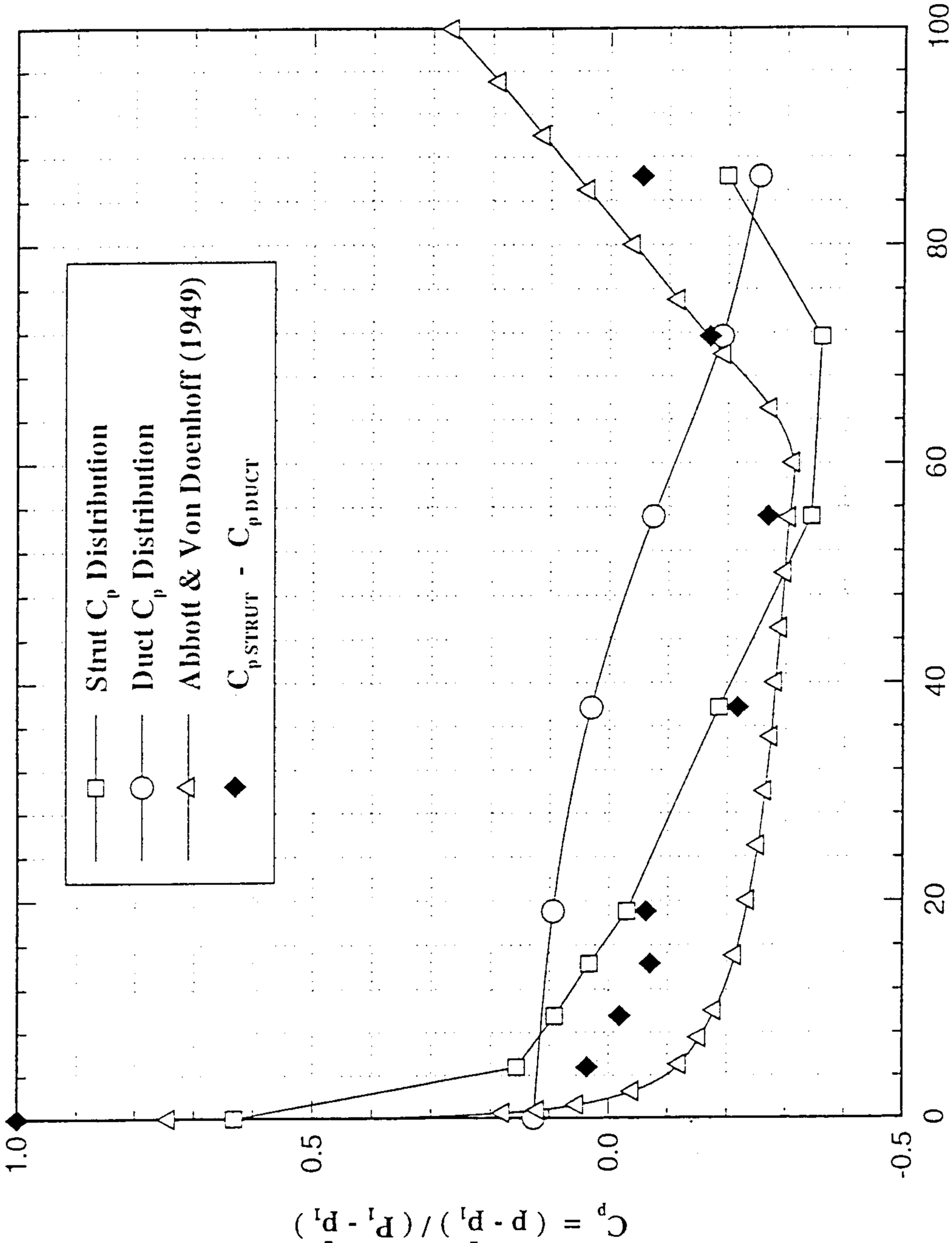

Fig.4.3.12 Superposition of strut and duct static pressure distributions (90% Height)

$$C_p = (p - \bar{p}_1) / (\bar{P}_1 - \bar{p}_1)$$

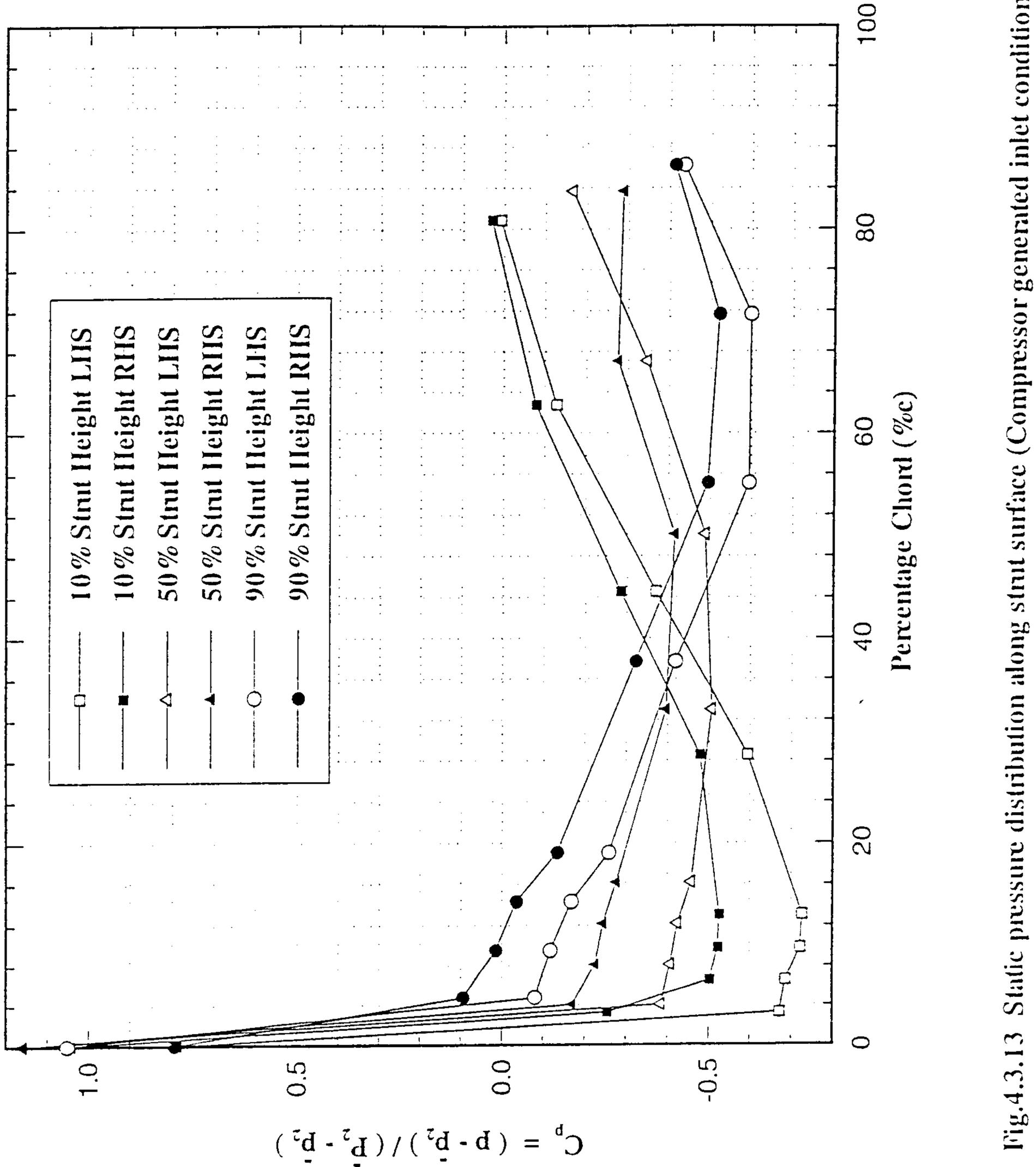

Fig. 4.3.13 Static pressure distribution along strut surface (Compressor generated inlet conditions)

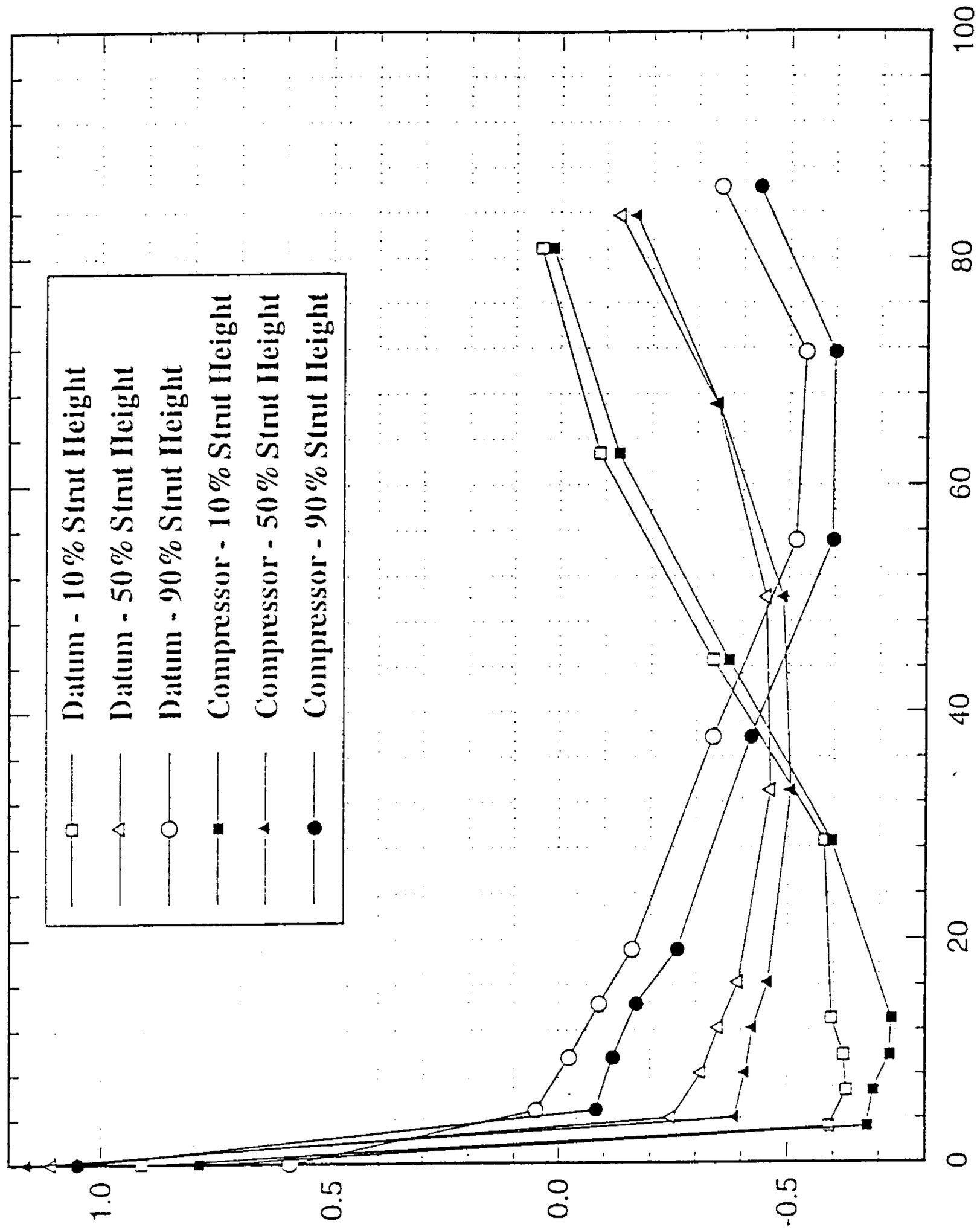

Fig.4.3.14 Comparison of strut surface static pressure distribution for the clean and compressor generated inlet conditions.

$$C_p = (p - \bar{p}_2) / (\bar{P}_2 - \bar{p}_2)$$

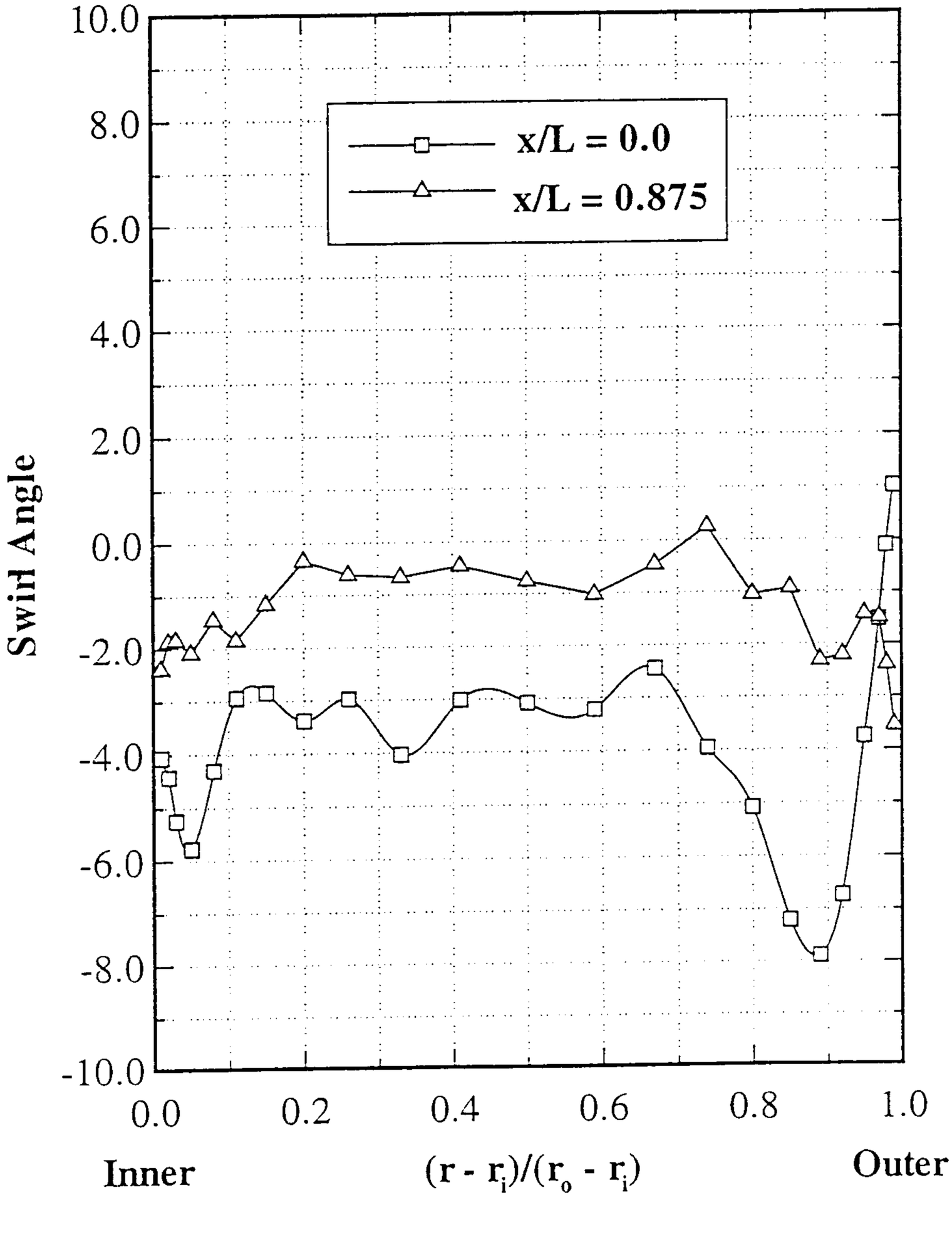

Fig.4.3.15 Radial distribution of pitch averaged swirl angle (x/L=0.0 and 0.875).

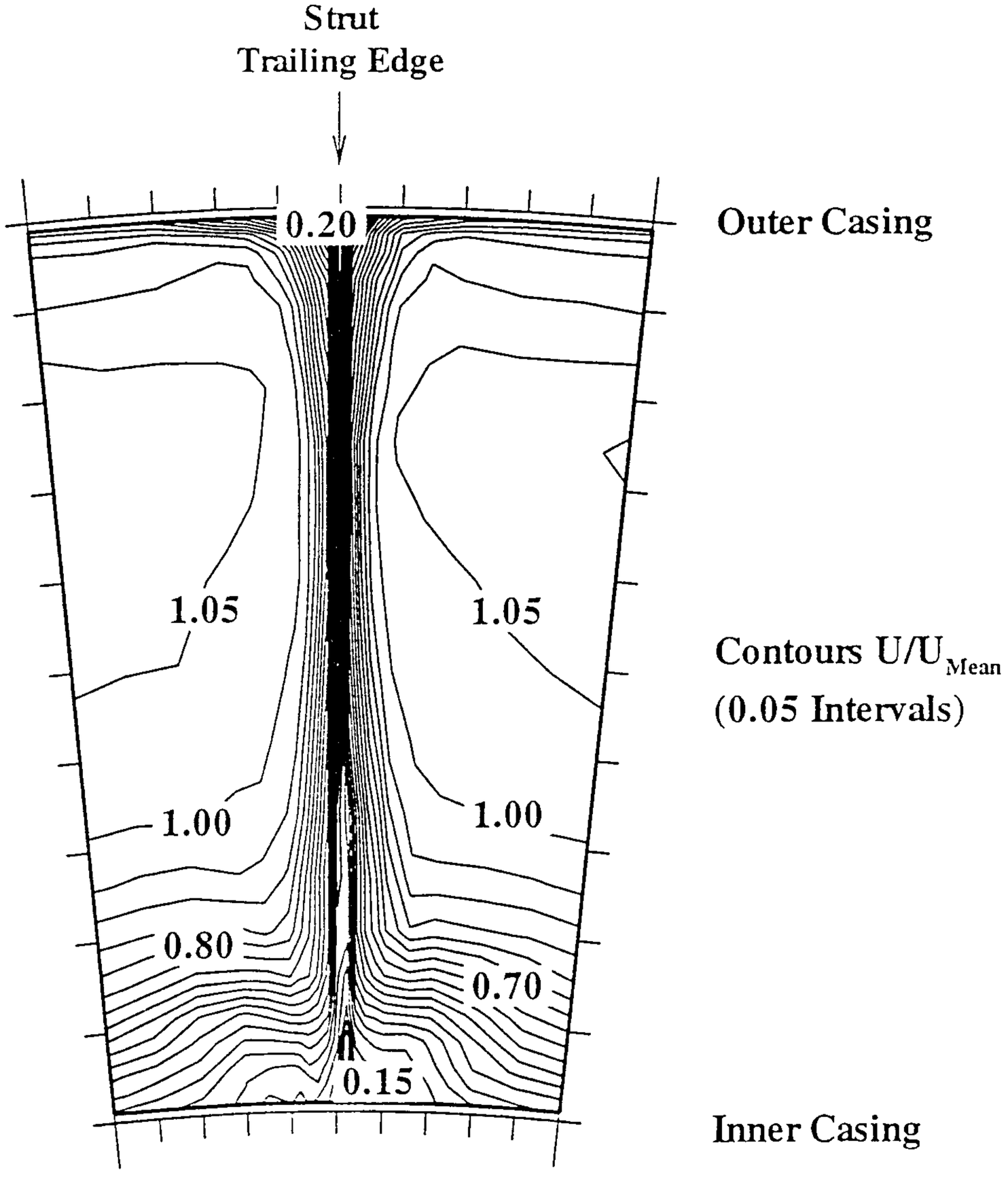

Fig.4.3.16 Streamwise velocity distribution (x/L=0.875).

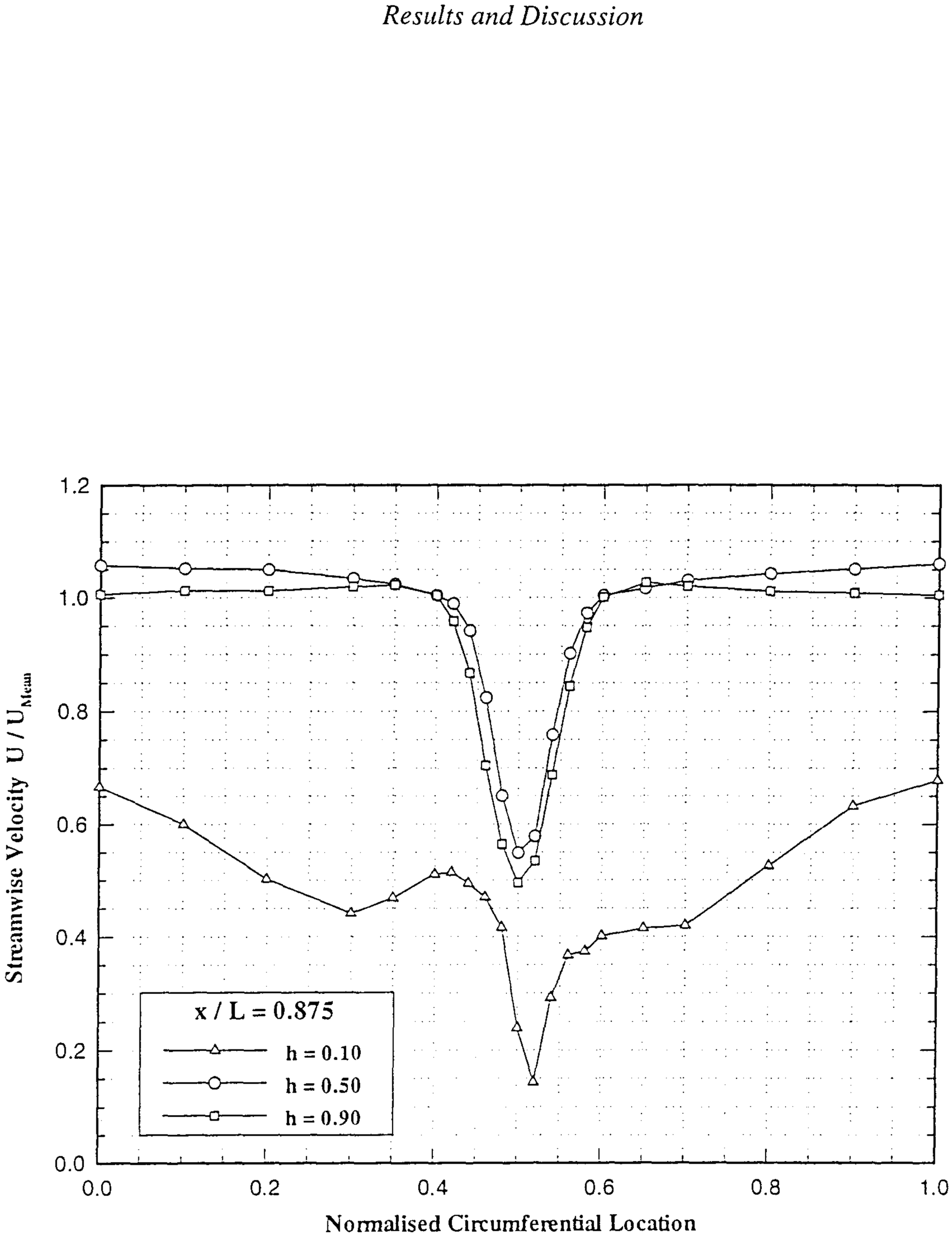

Fig.4.3.17 Circumferential distribution of streamwise velocity (x/L=0.875).

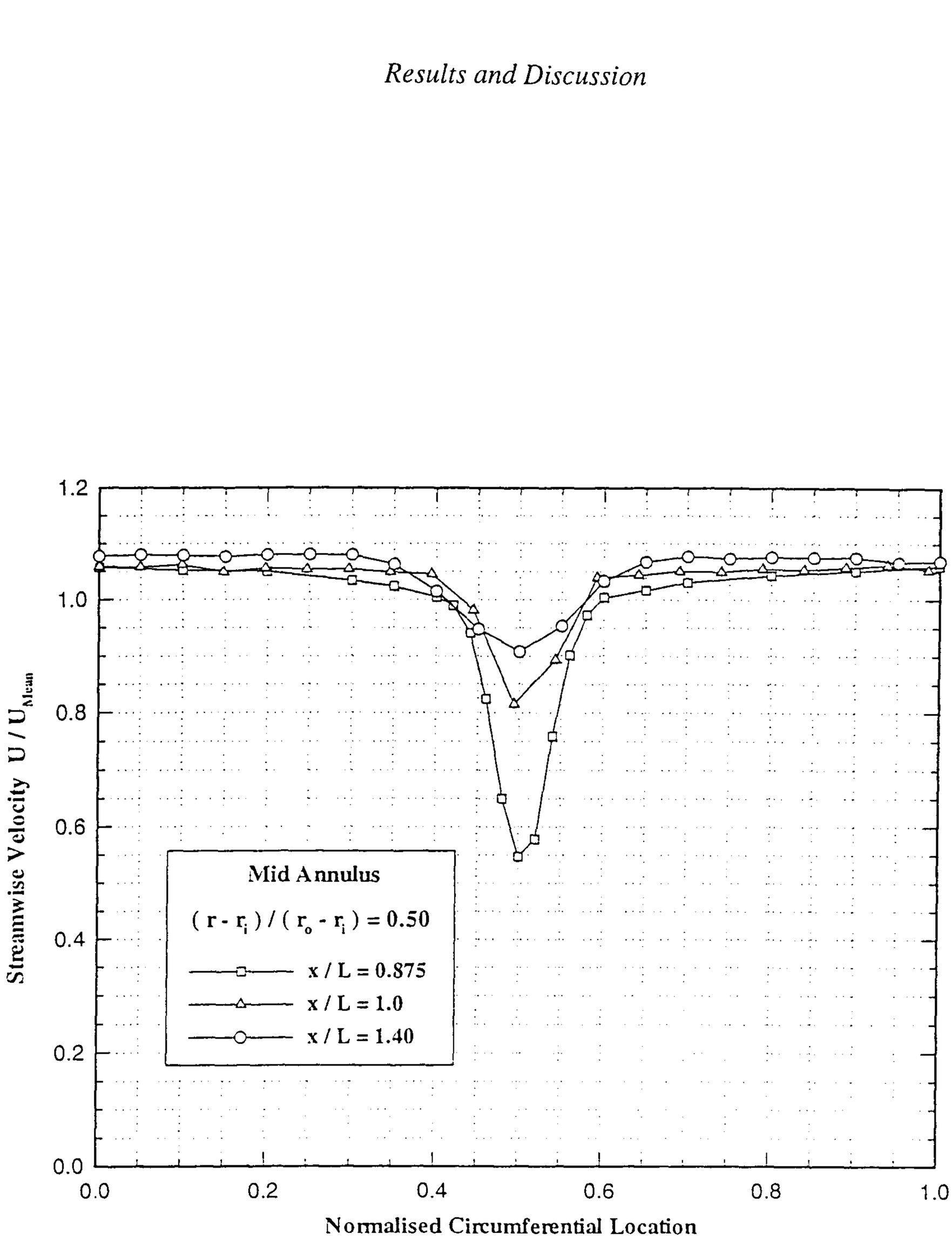

Fig.4.3.18 Circumferential distribution of streamwise velocity (50% annulus ht).

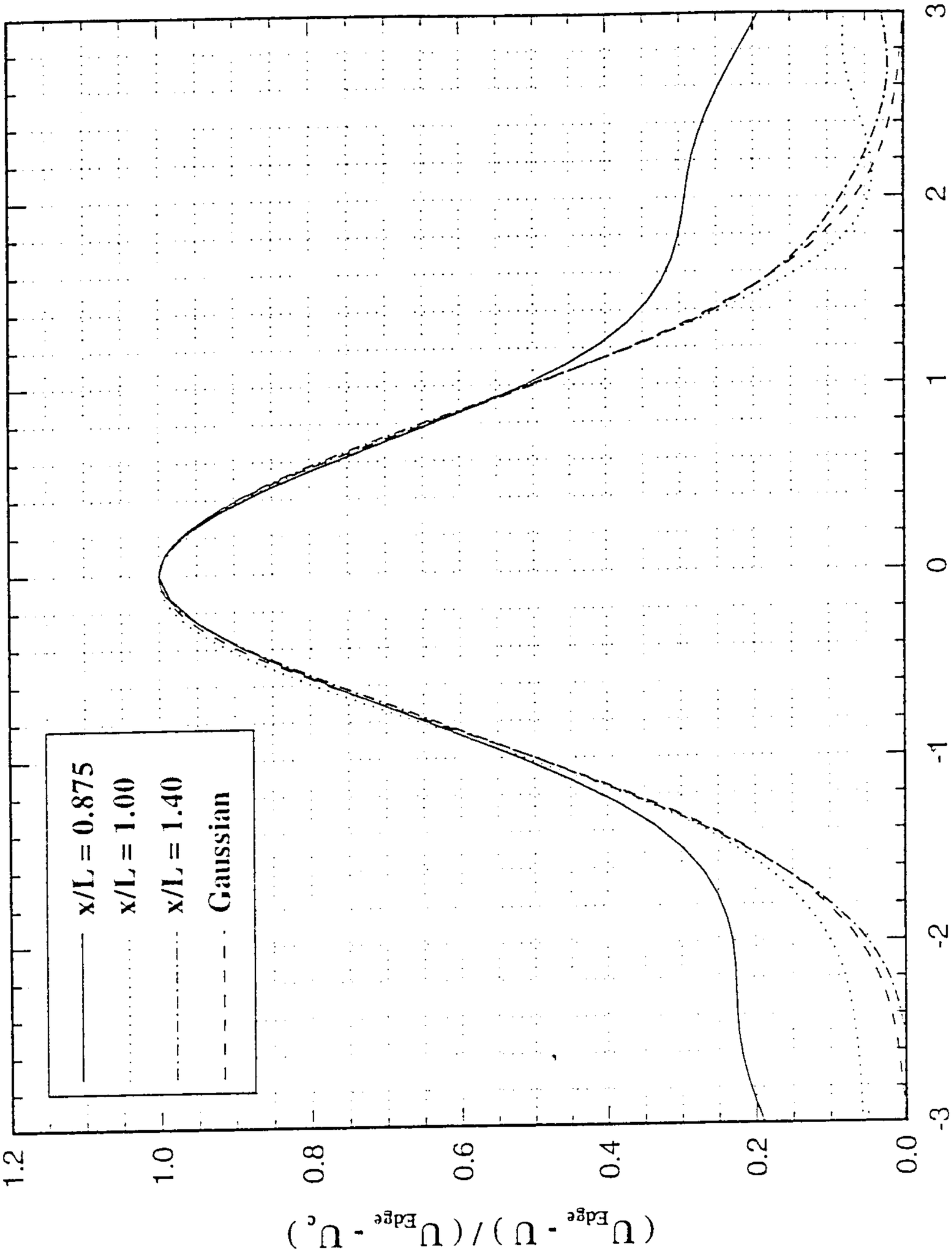

Fig.4.3.19 Normalised strut wake profiles

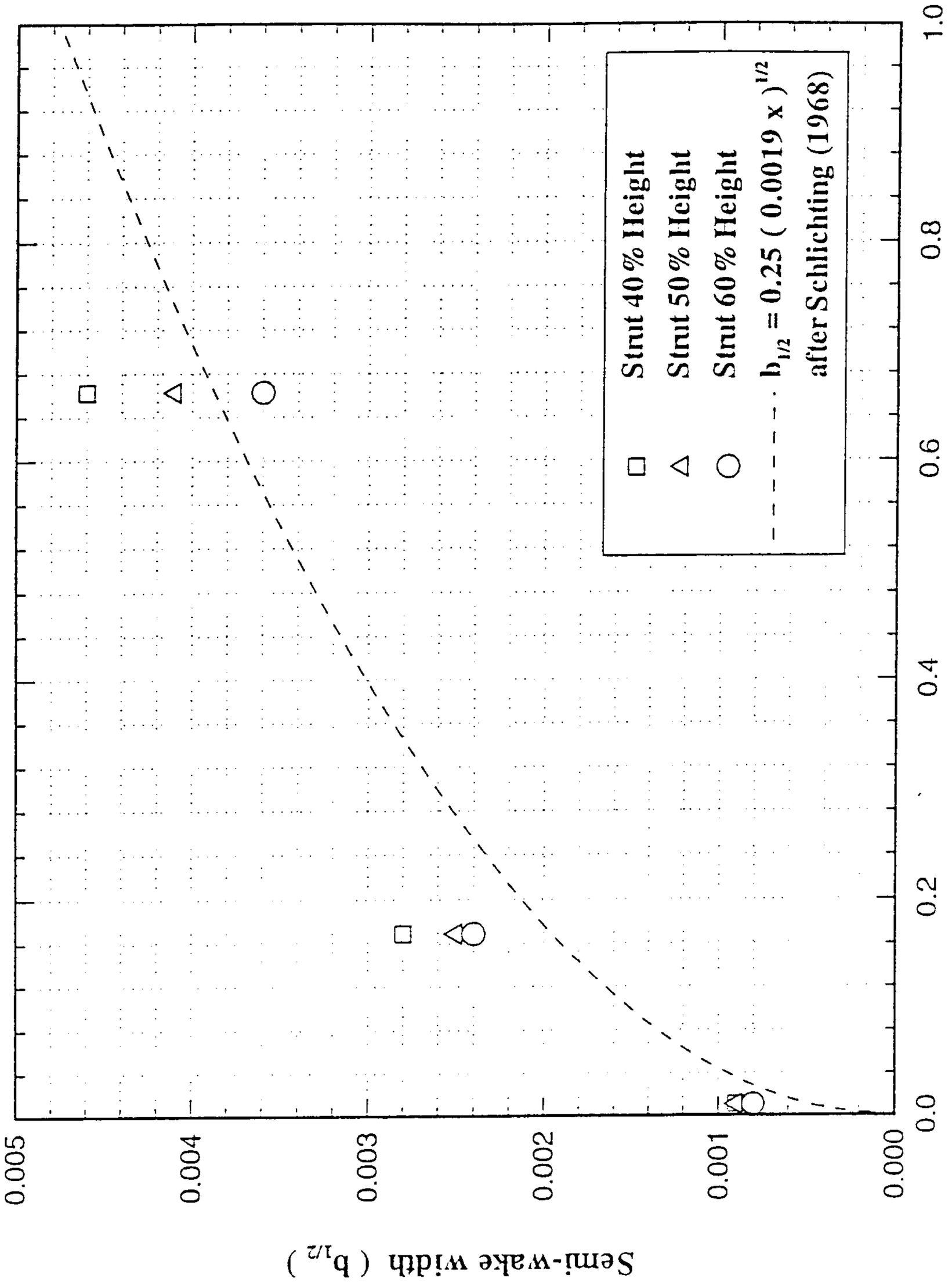

Fig.4.3.20 Axial variation of strut semi-wake width ($b_{1/2}$)

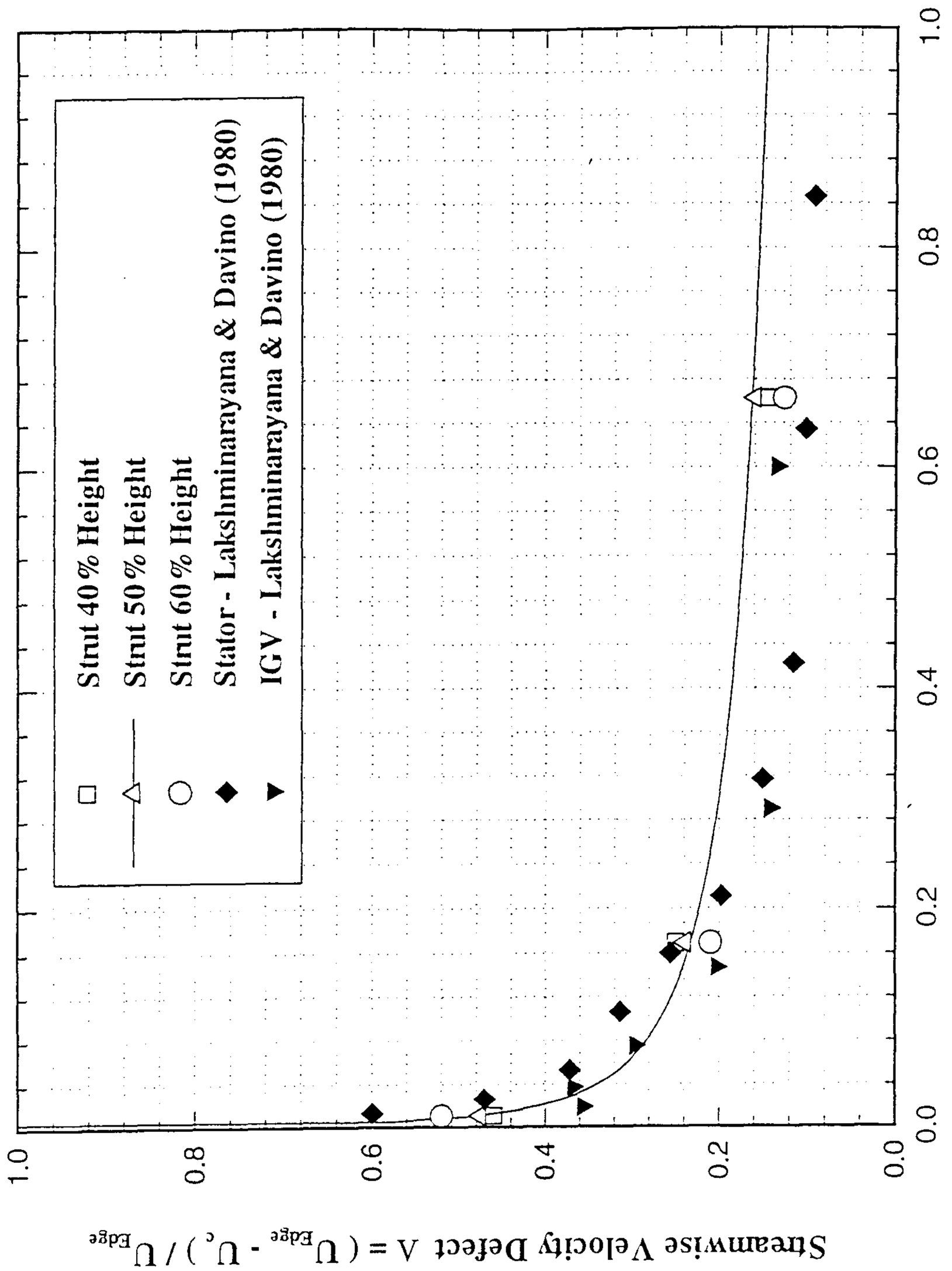

Fig.4.3.21 Axial variation of streamwise velocity defect

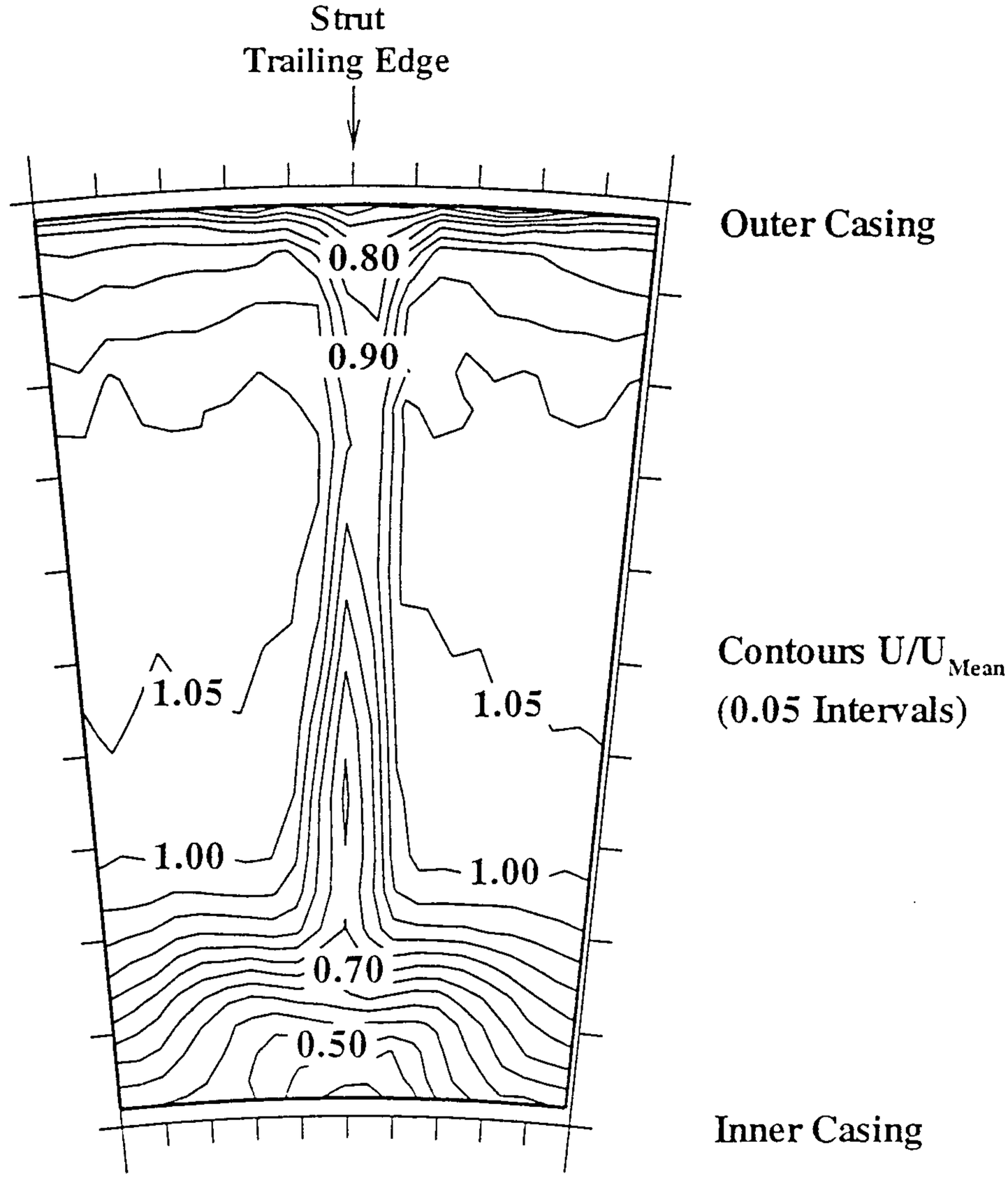

Fig.4.3.22 Streamwise velocity distribution (x/L=1.0).

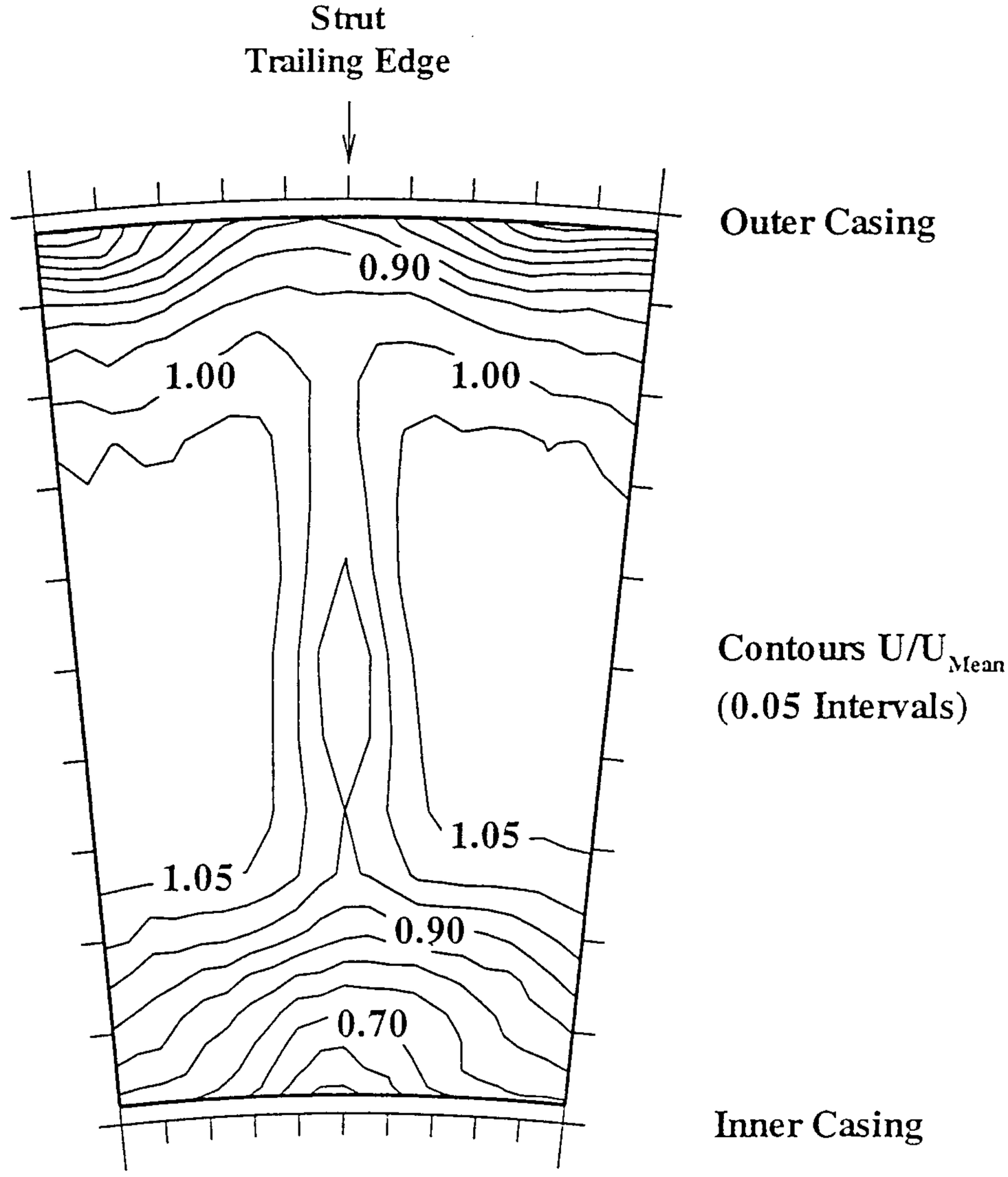

Fig.4.3.23 Streamwise velocity distribution (x/L=1.4).

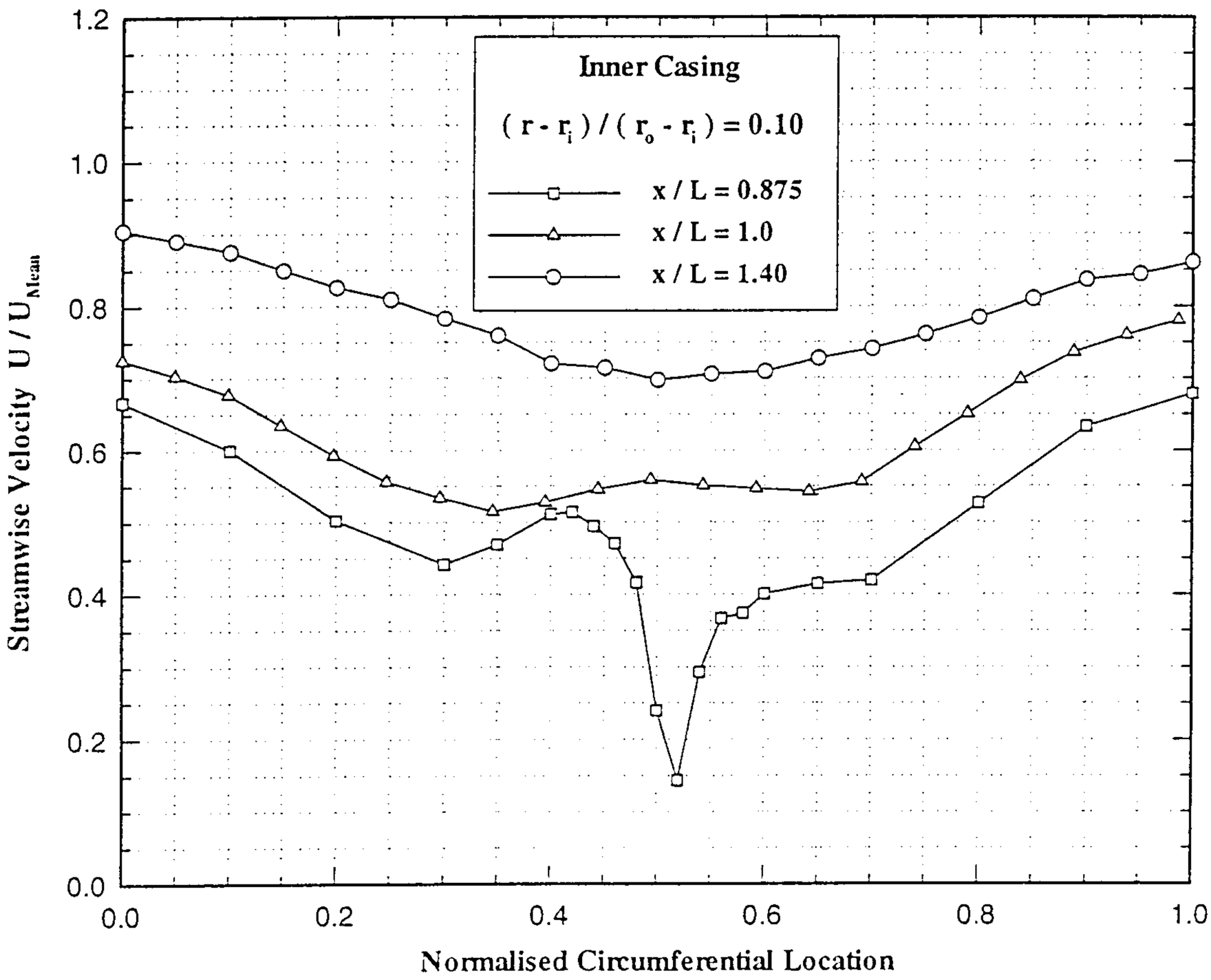

Fig.4.3.24 Circumferential distribution of streamwise velocity (10% annulus ht).

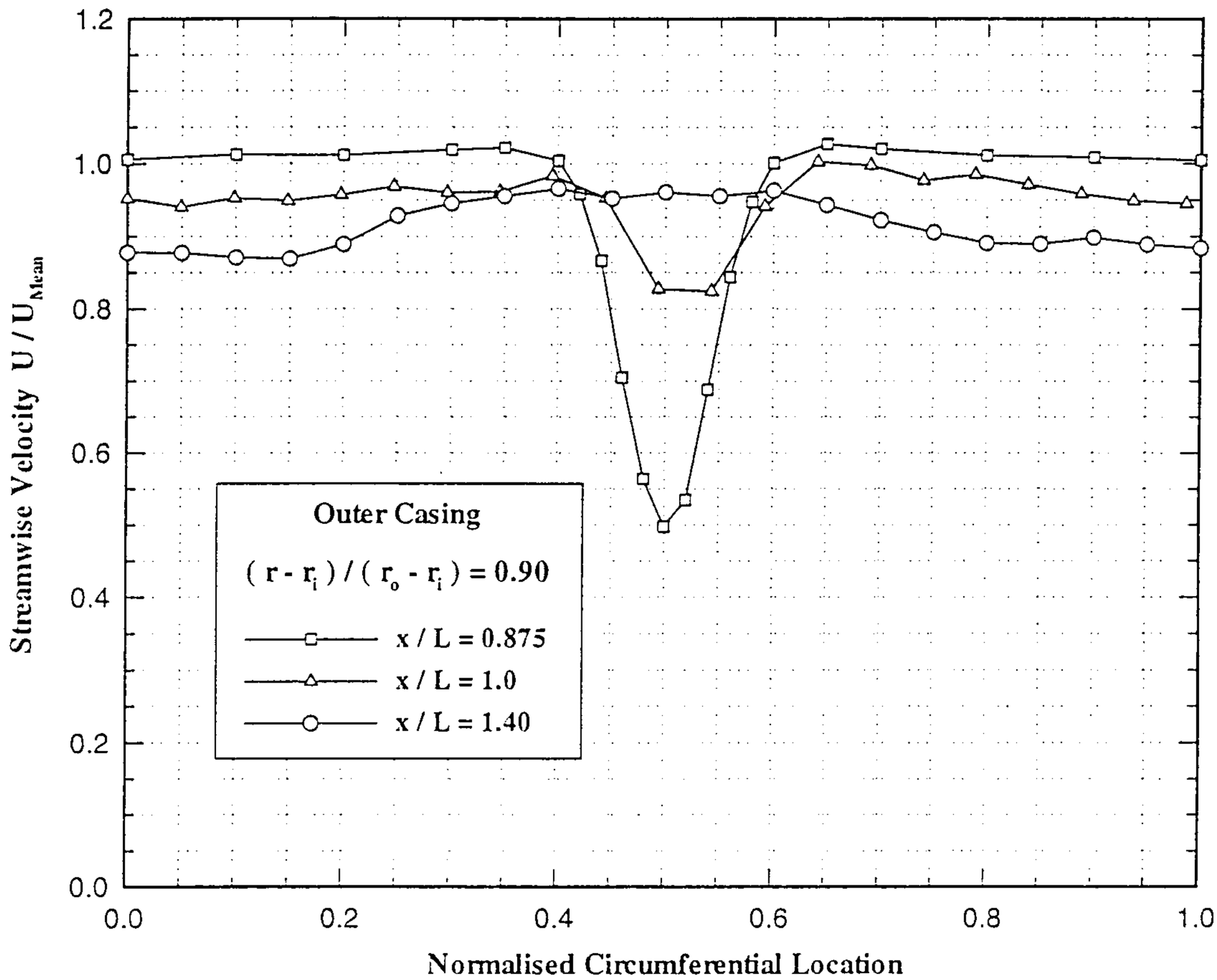

Fig.4.3.25 Circumferential distribution of streamwise velocity (90% annulus ht).

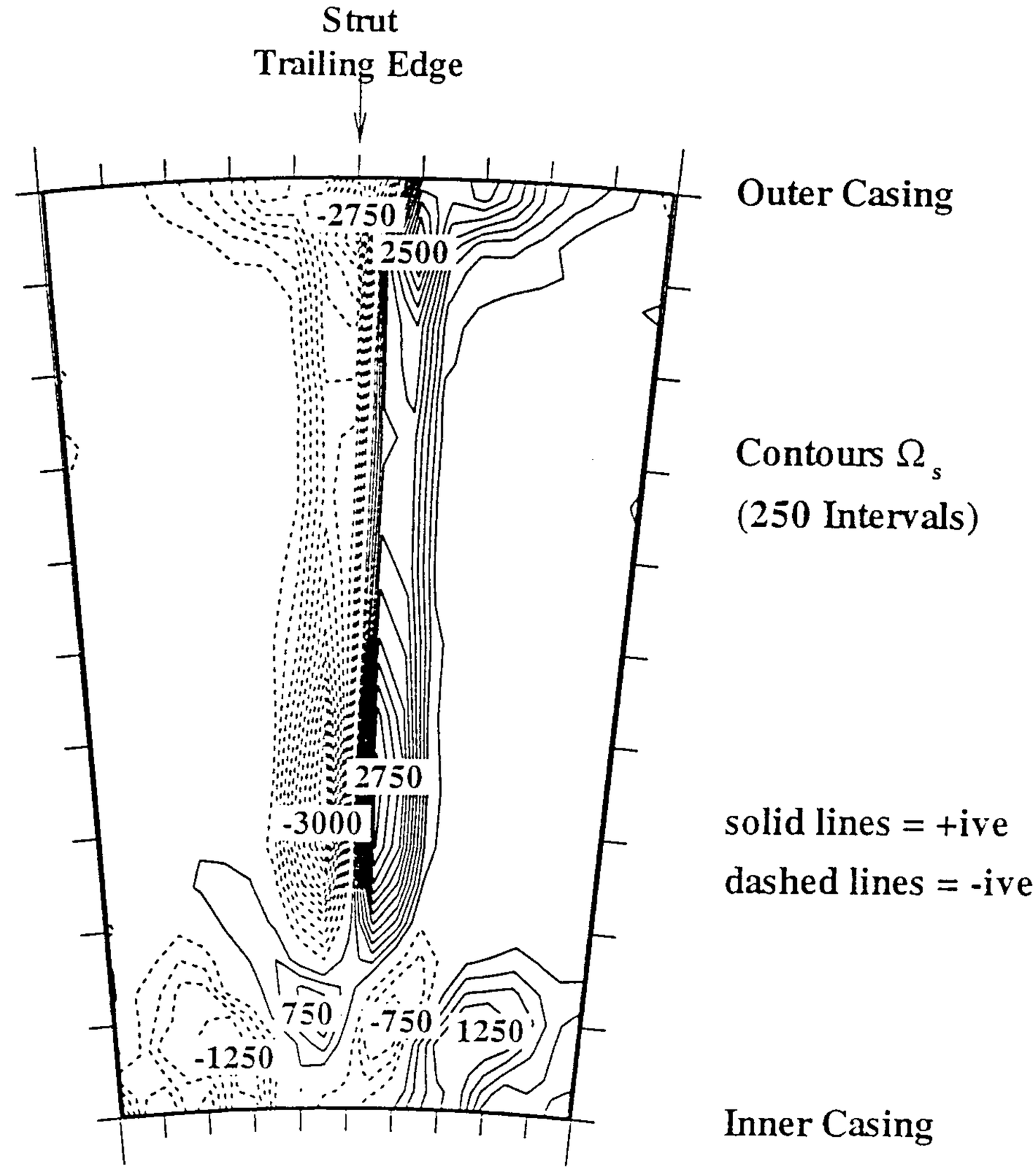

Fig.4.3.26 Streamwise vorticity distribution (x/L=0.875).

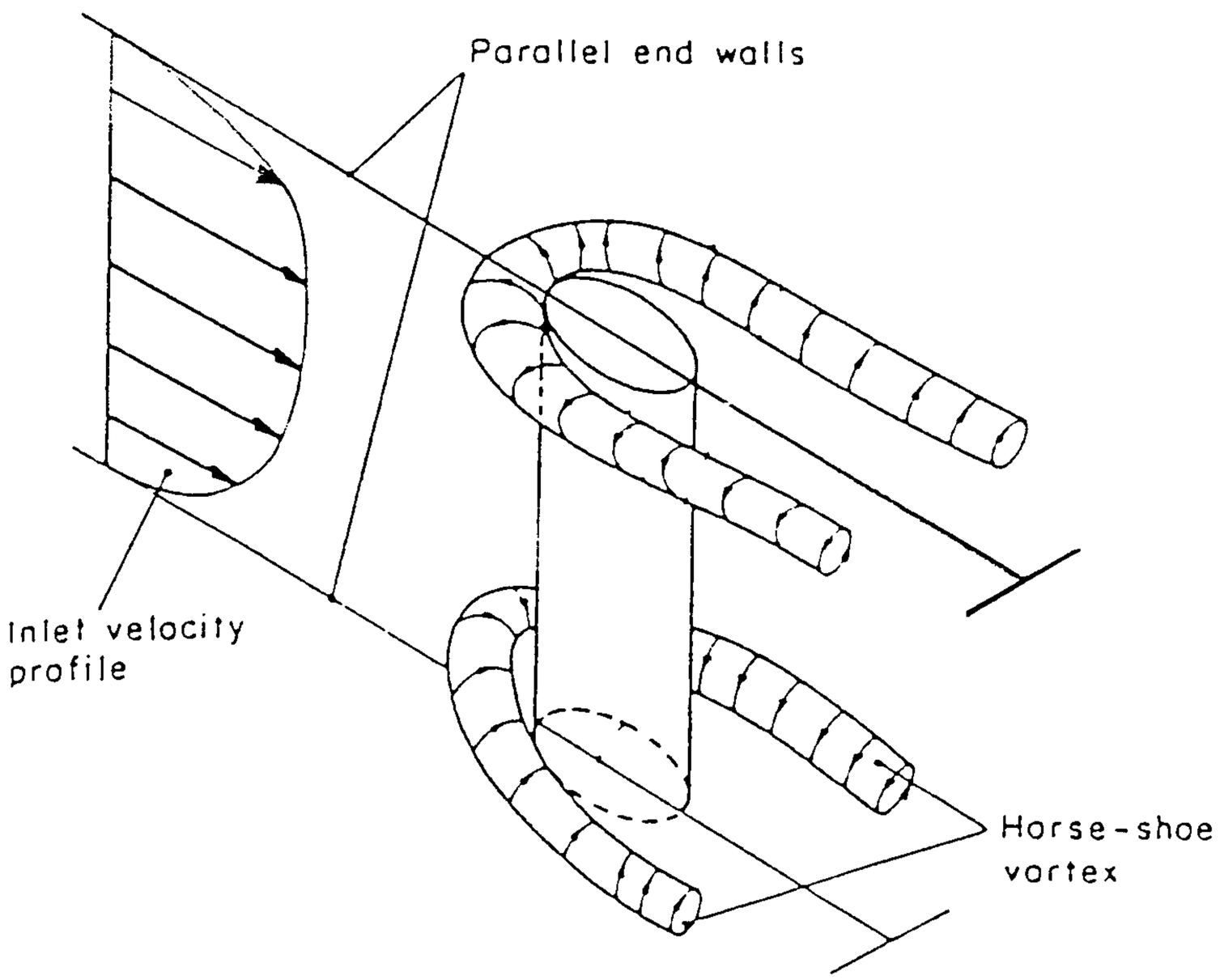

Fig.4.3.27 Diagram of horseshoe vortex system after Roach and Turner (1985).

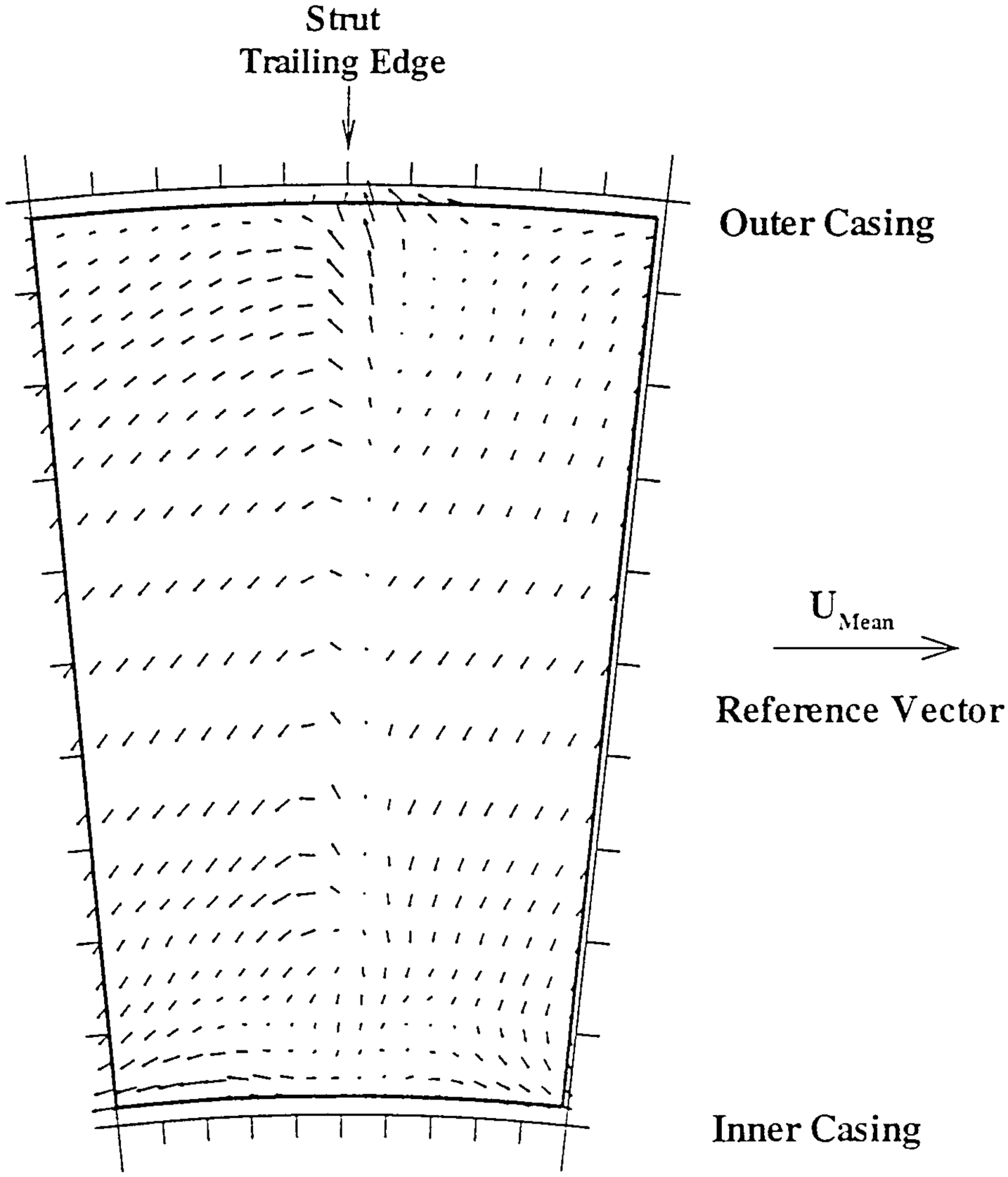

Fig.4.3.28 Flow vectors (x/L=1.00).

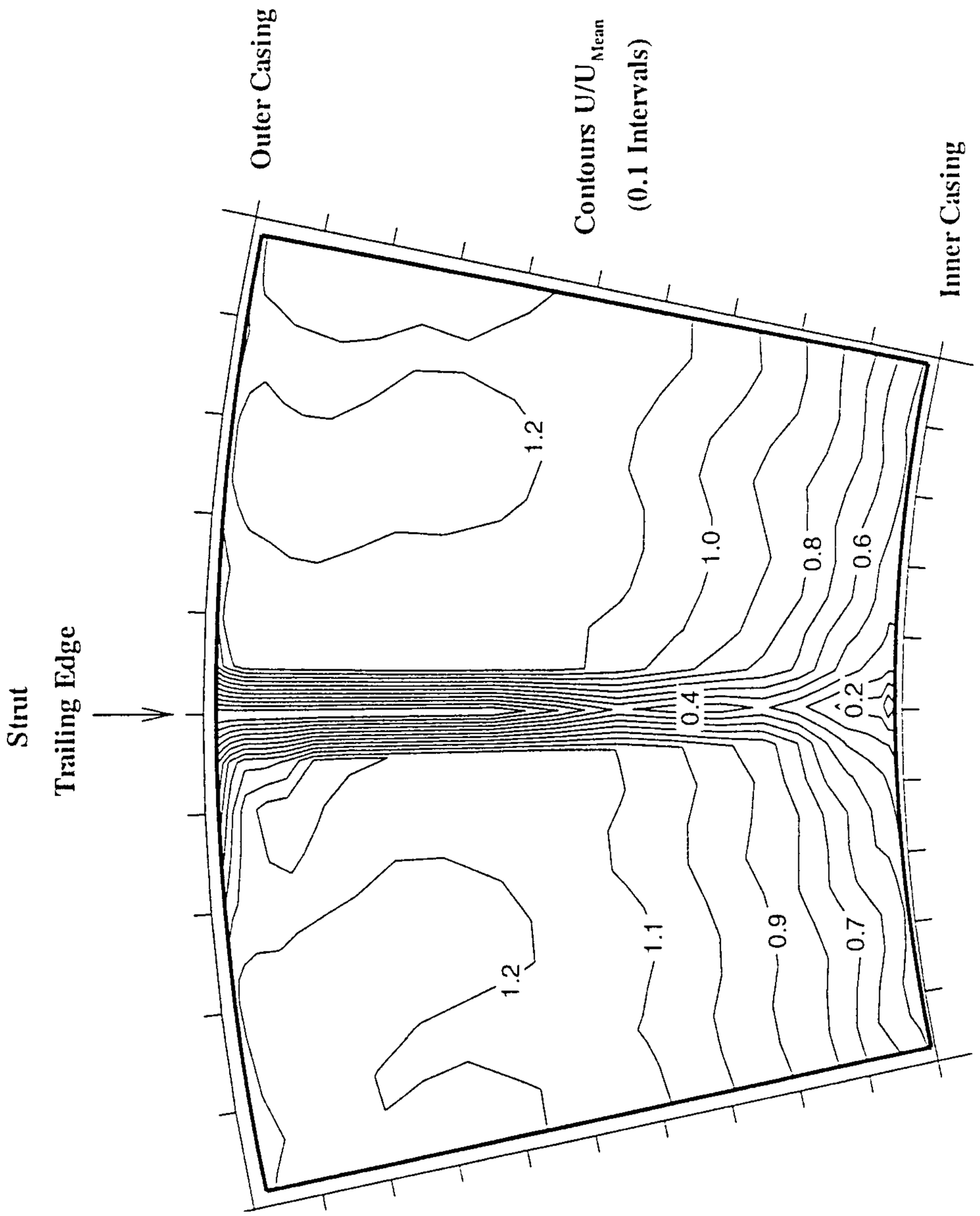

Fig.4.3.29 Streamwise velocity distribution (x/L=0.875)

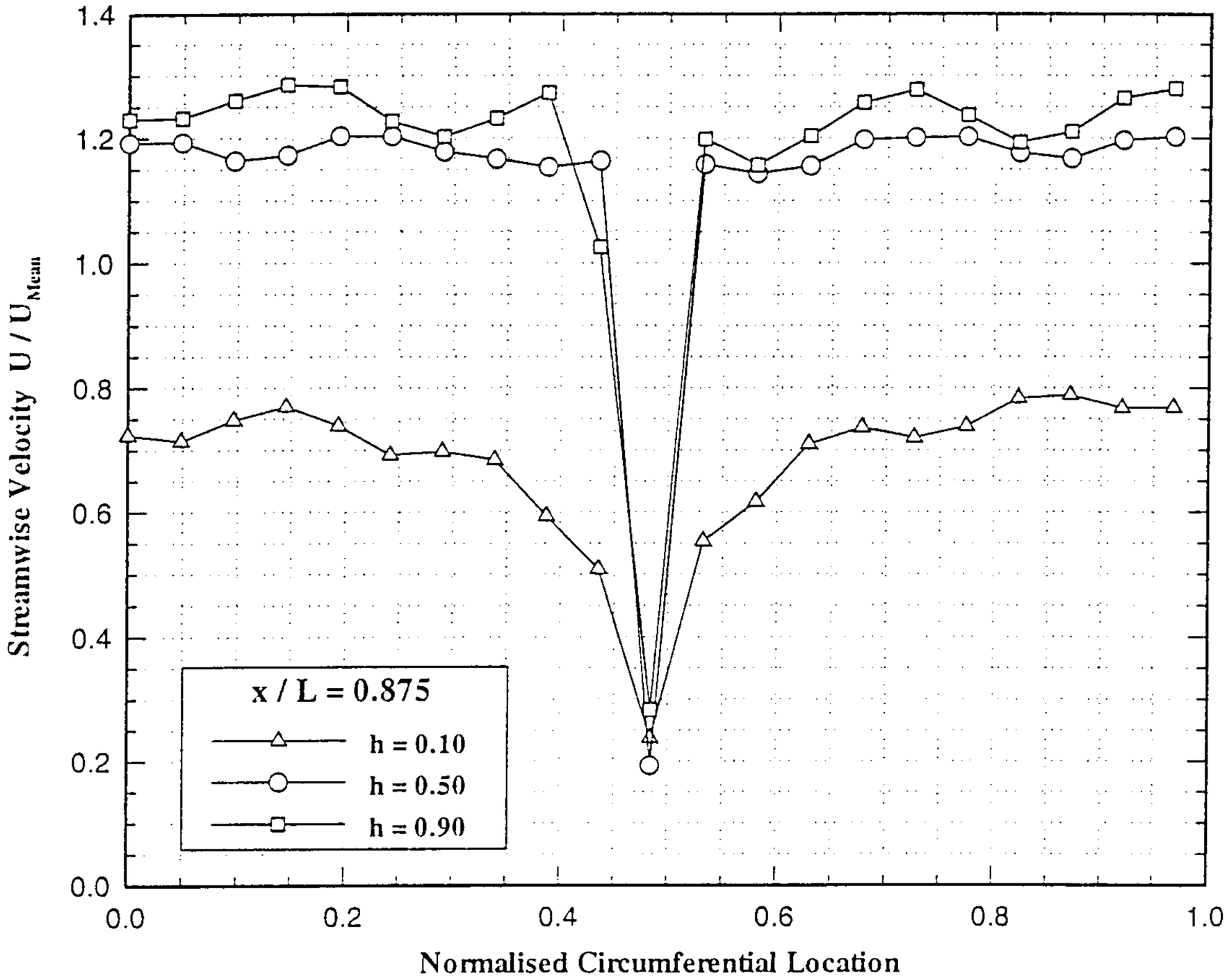

Fig.4.3.30 Circumferential distribution of streamwise velocity (x/L=0.875).

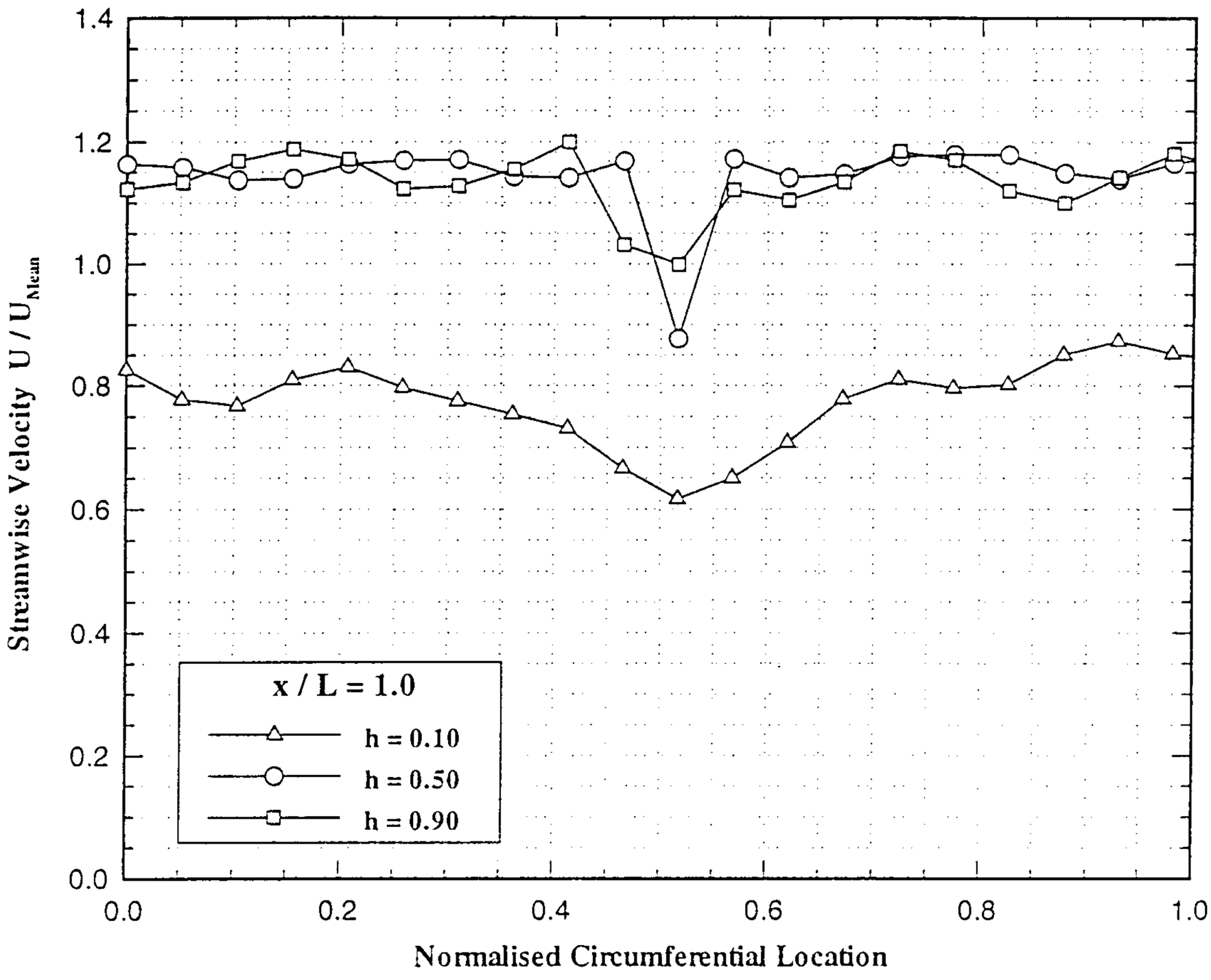

Fig.4.3.31 Circumferential distribution of streamwise velocity (x/L=1.0).

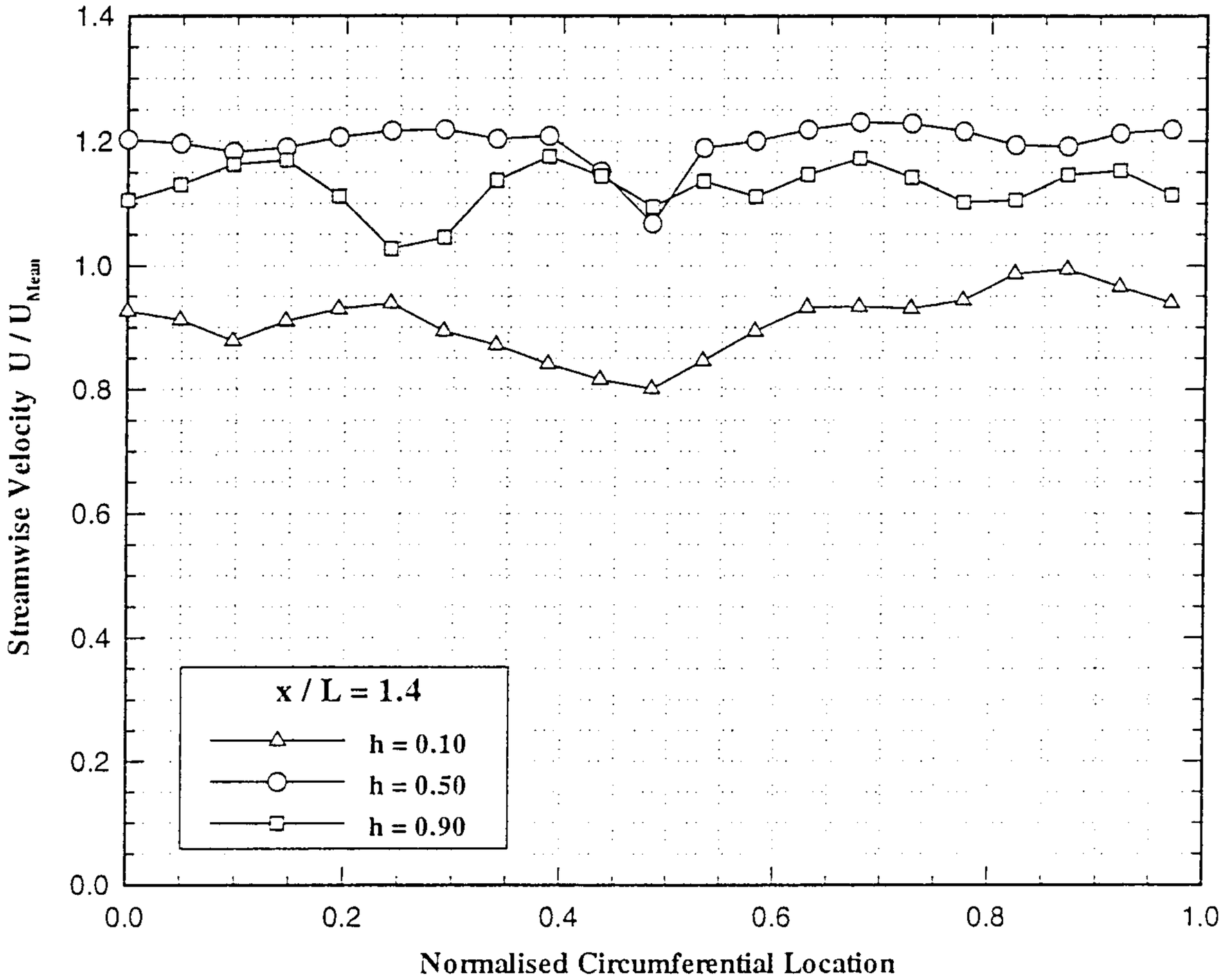

Fig.4.3.32 Circumferential distribution of streamwise velocity (x/L=1.4).

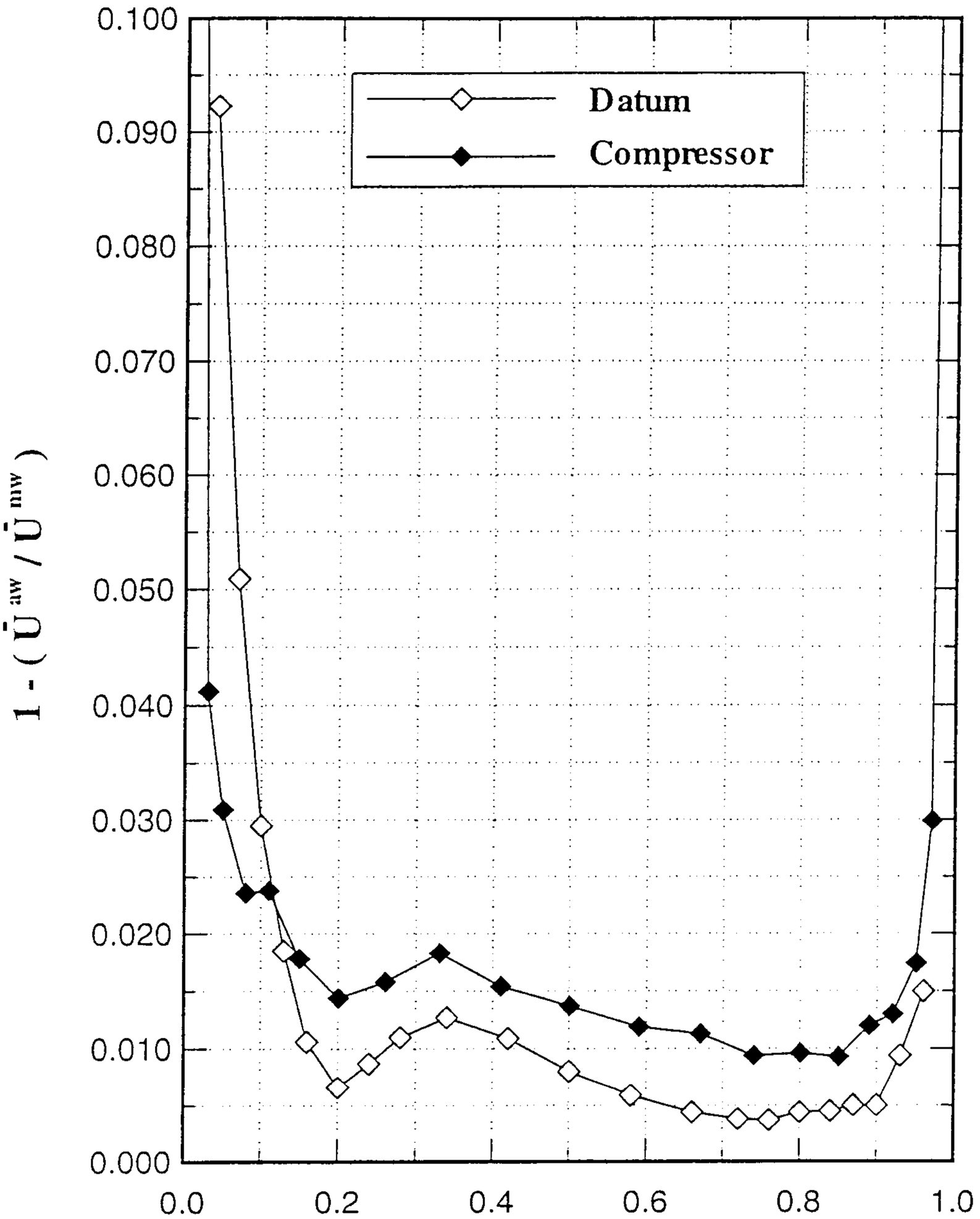

Fig.4.3.33 Radial distribution of tangential blockage (x/L=1.0).

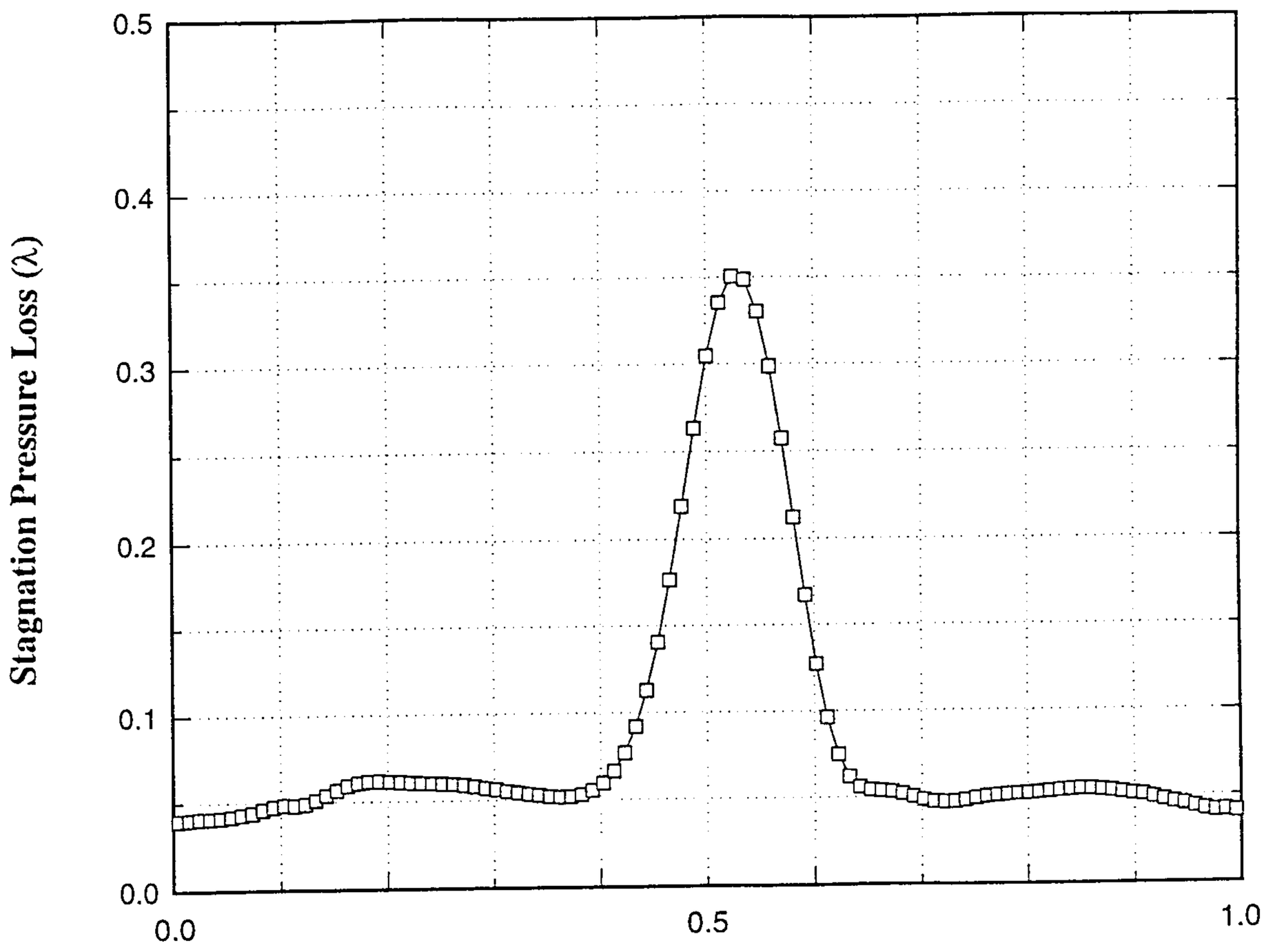

Fig.4.3.34 Circumferential variation of stagnation pressure loss.

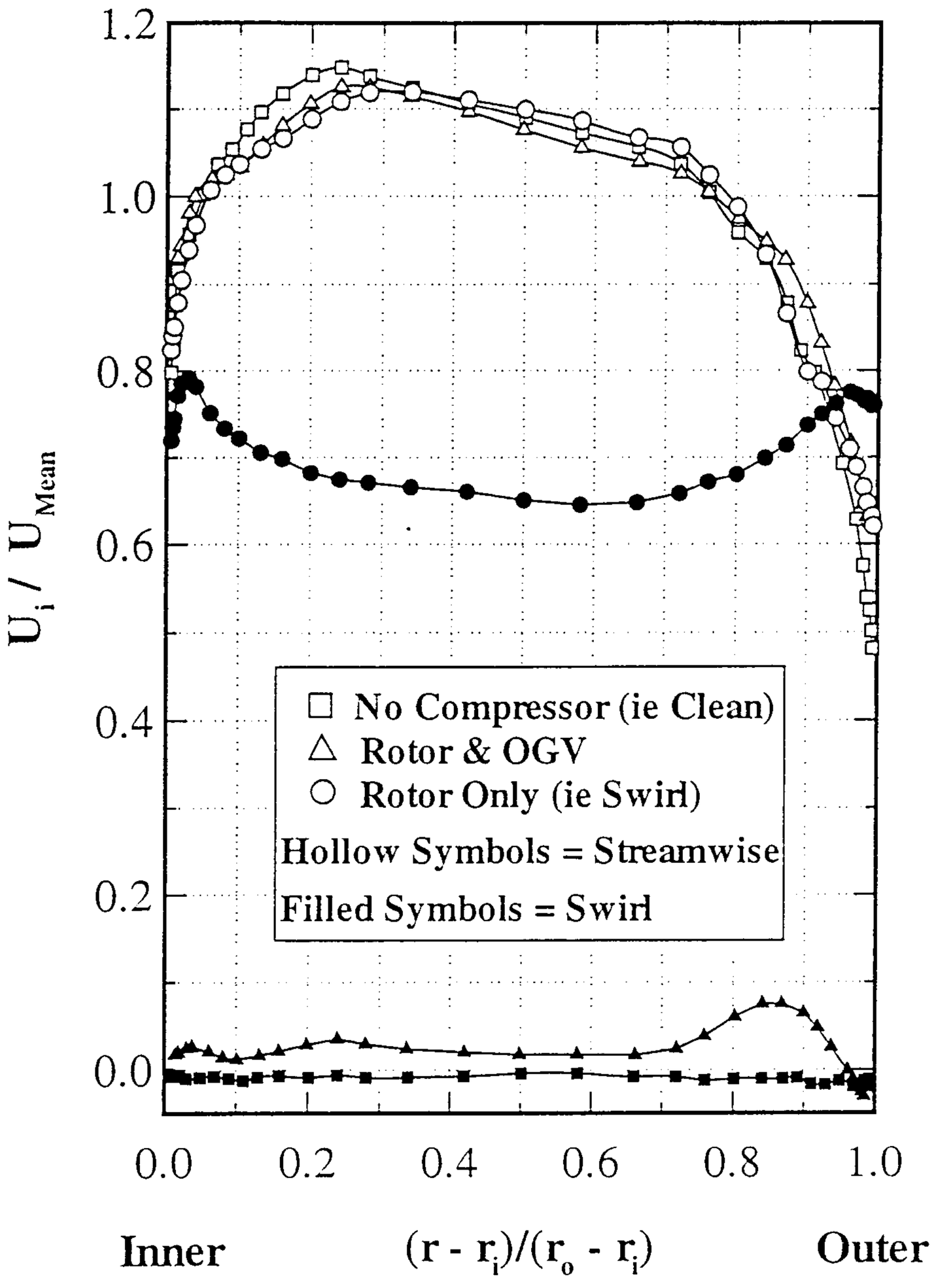

Fig.4.4.1 Streamwise and circumferential velocity profiles (x/L=0.0).

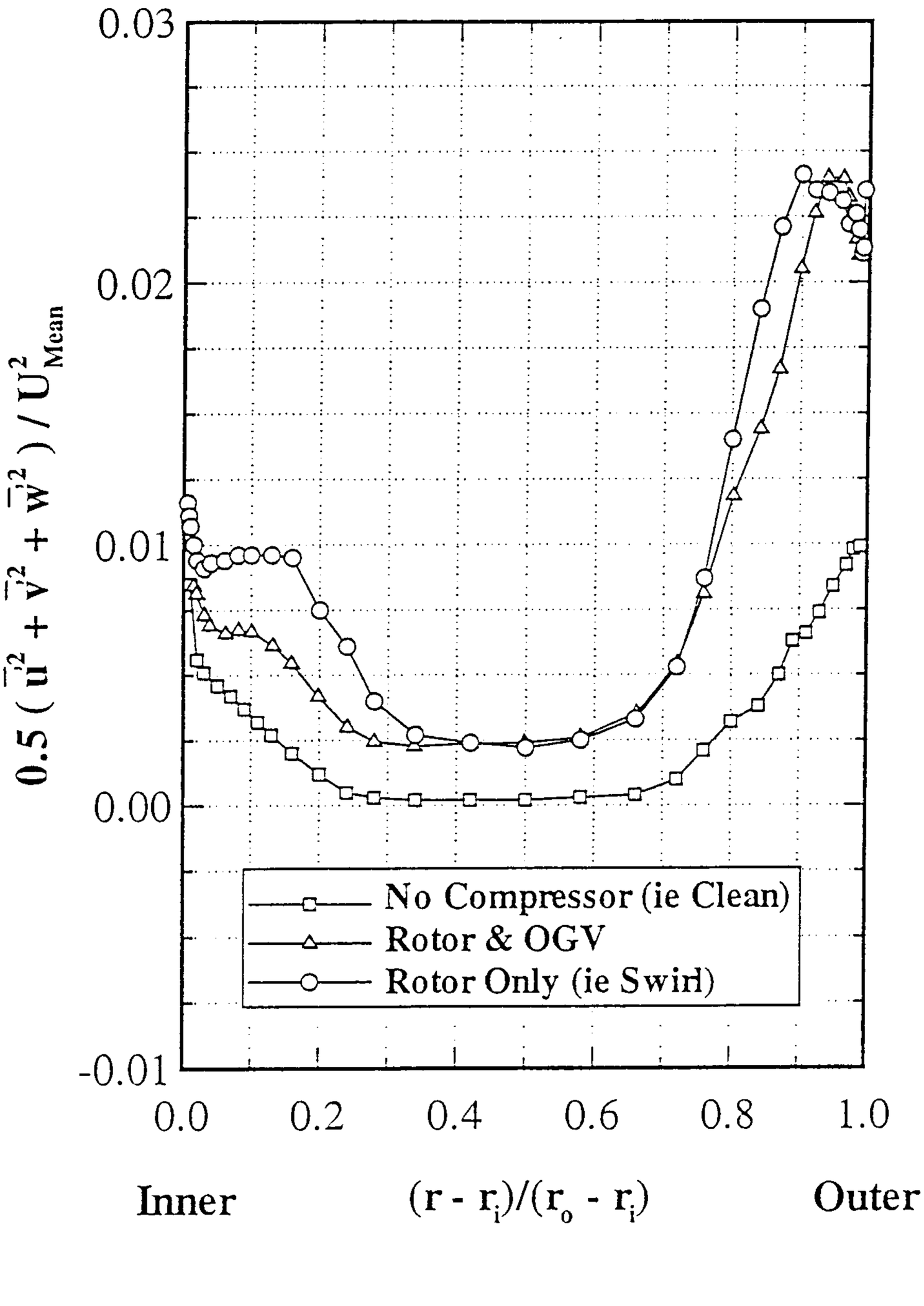

Fig.4.4.2 Turbulent kinetic energy profiles (x/L=0.0).

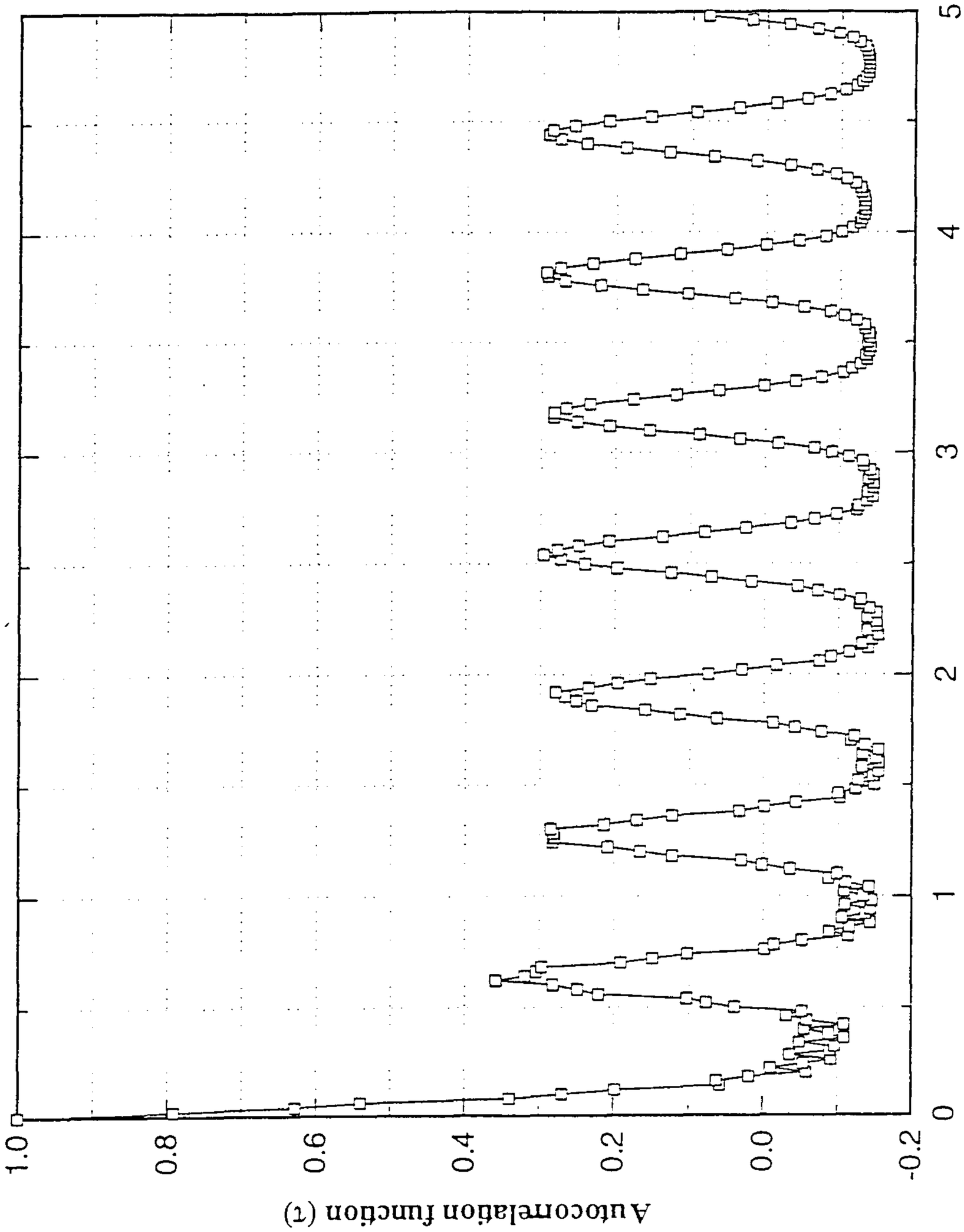

Fig.4.4.3 Autocorrelation function at 50% height (x/L=0.0).

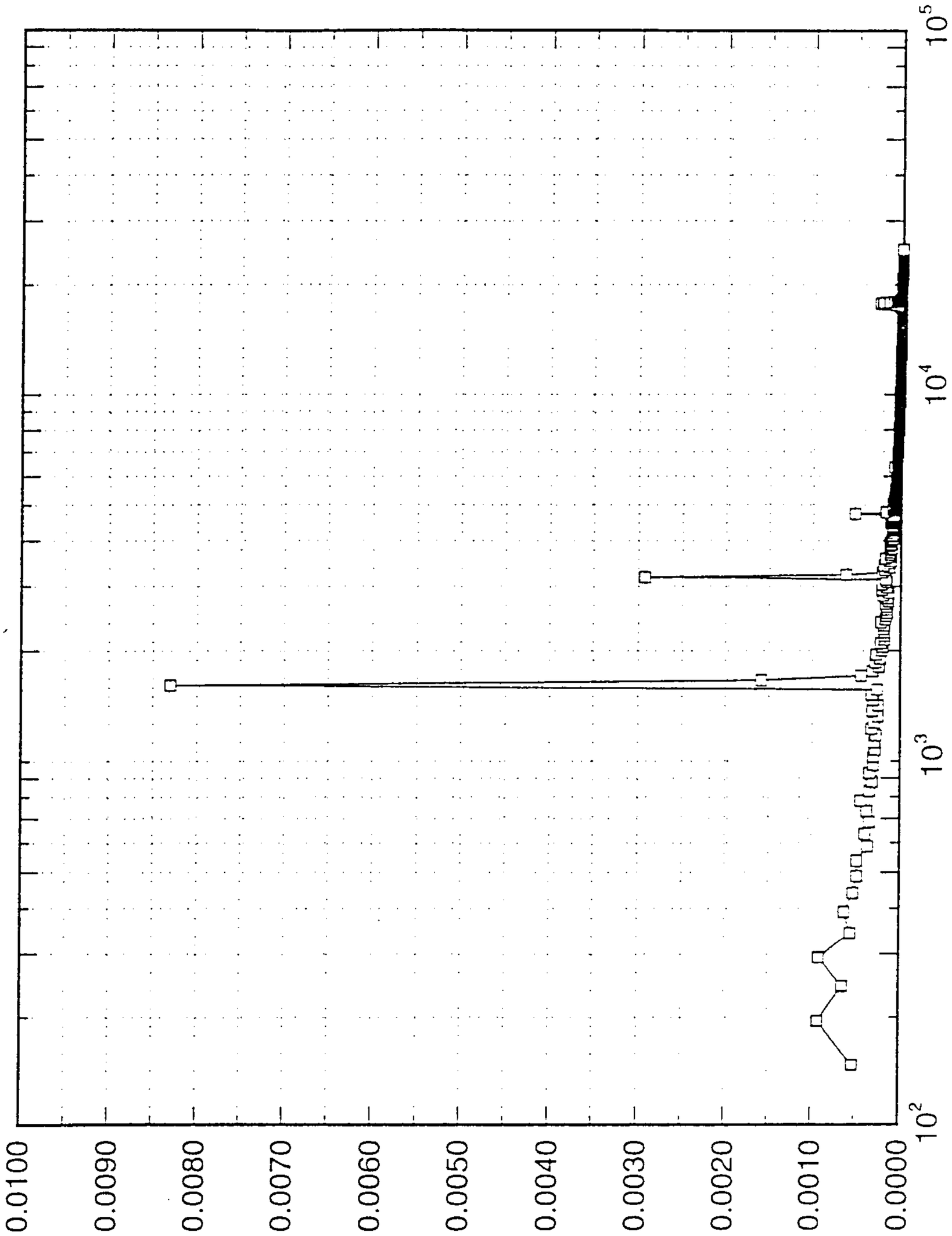

Fig.4.4.4 Power spectral density at 50% height (x/L=0.0).

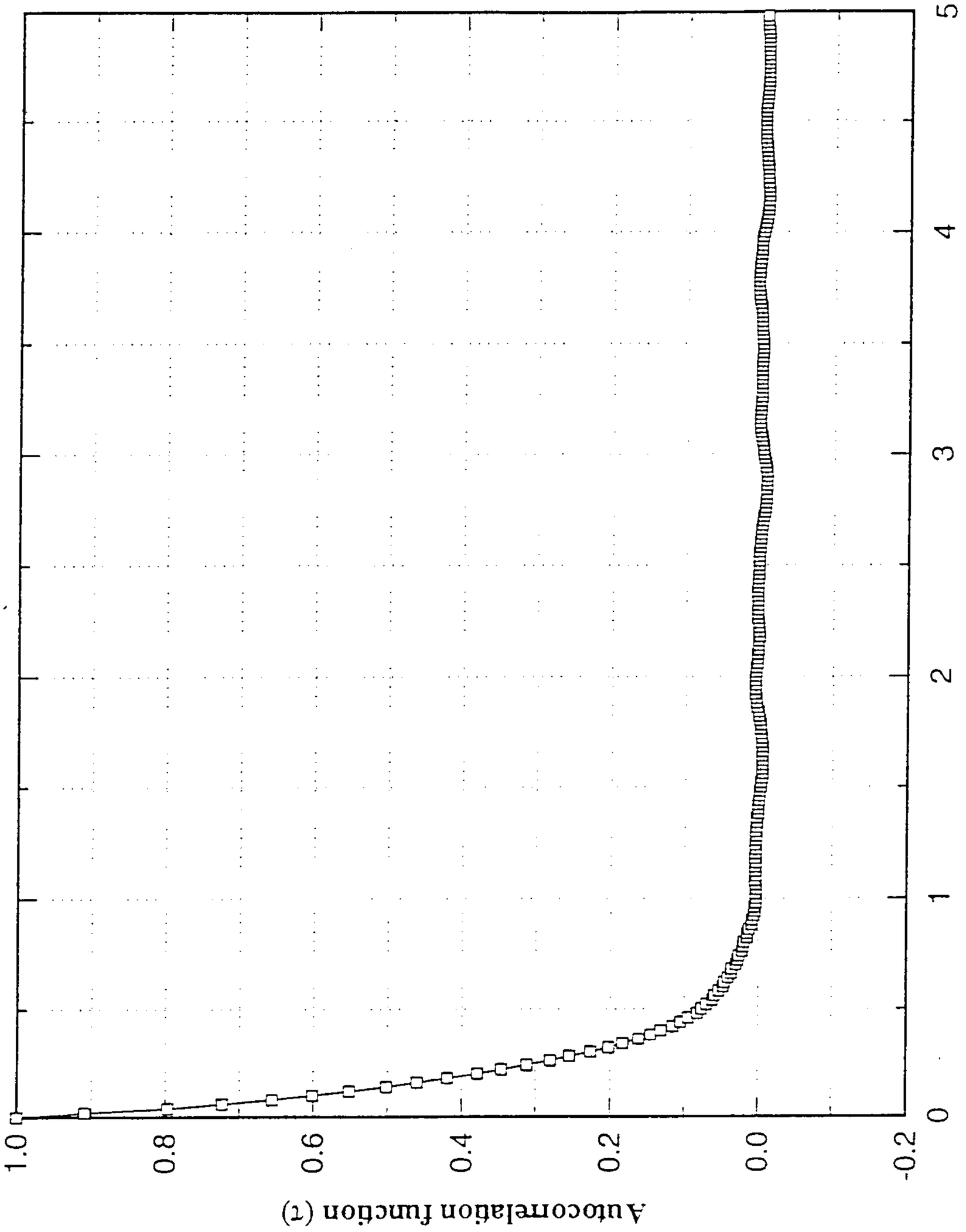

Fig.4.4.5 Autocorrelation function at 96% height (x/L=0.0).

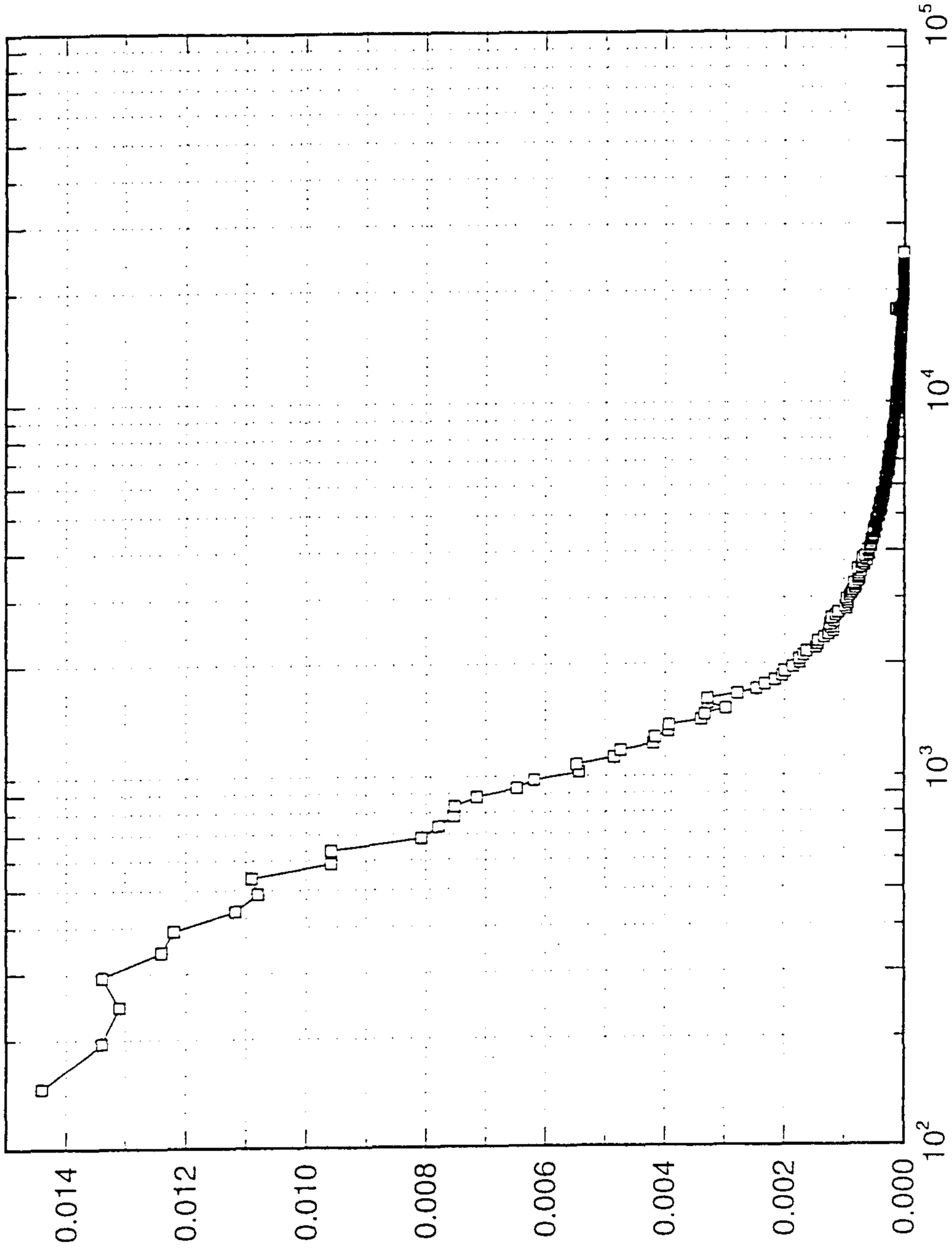

Fig.4.4.6 Power spectral density at 96% height (x/L=0.0).

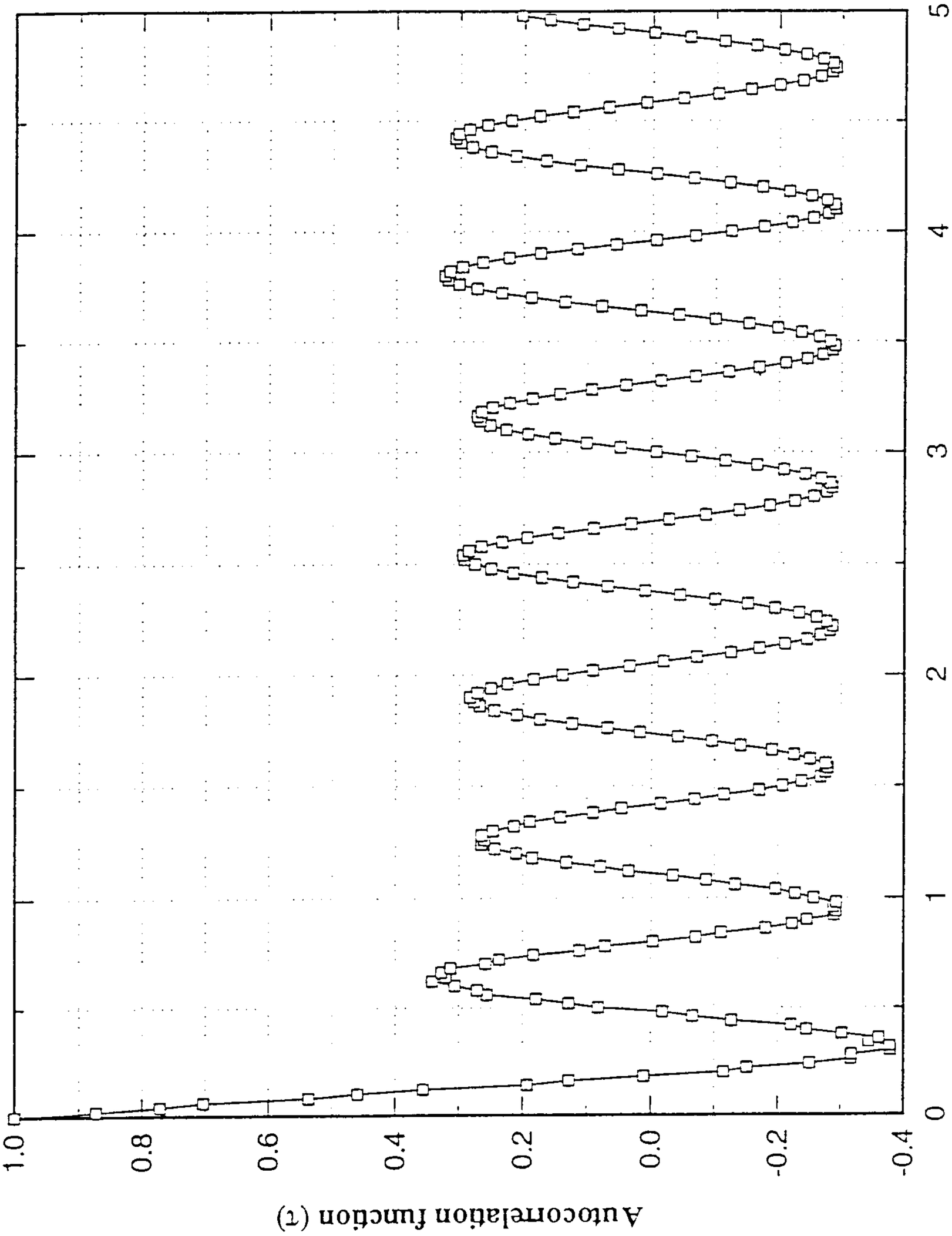

Fig.4.4.7 Autocorrelation function at 50% height (x/L=1.0).

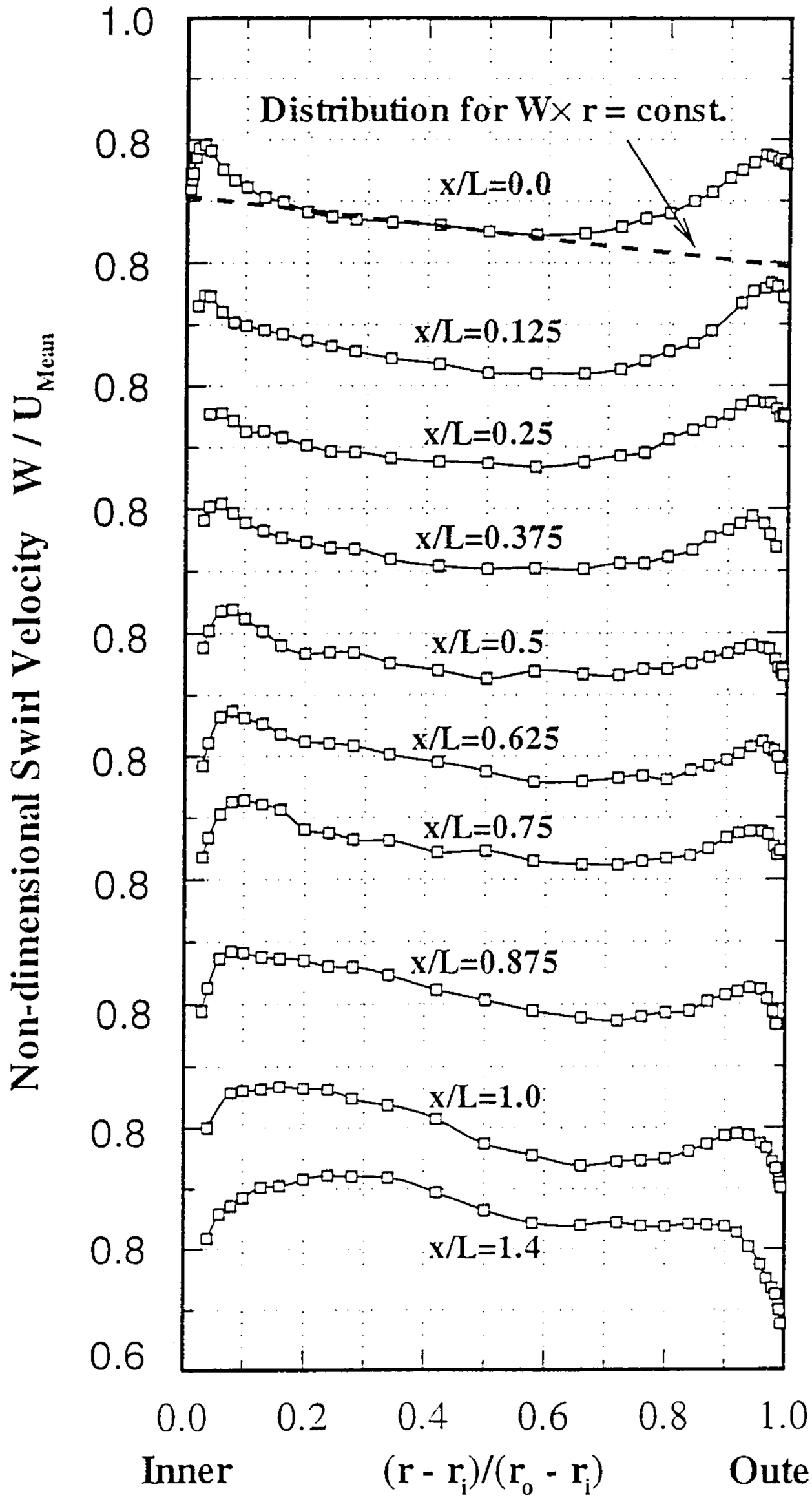

Fig.4.4.8 Development of the swirl velocity (W).

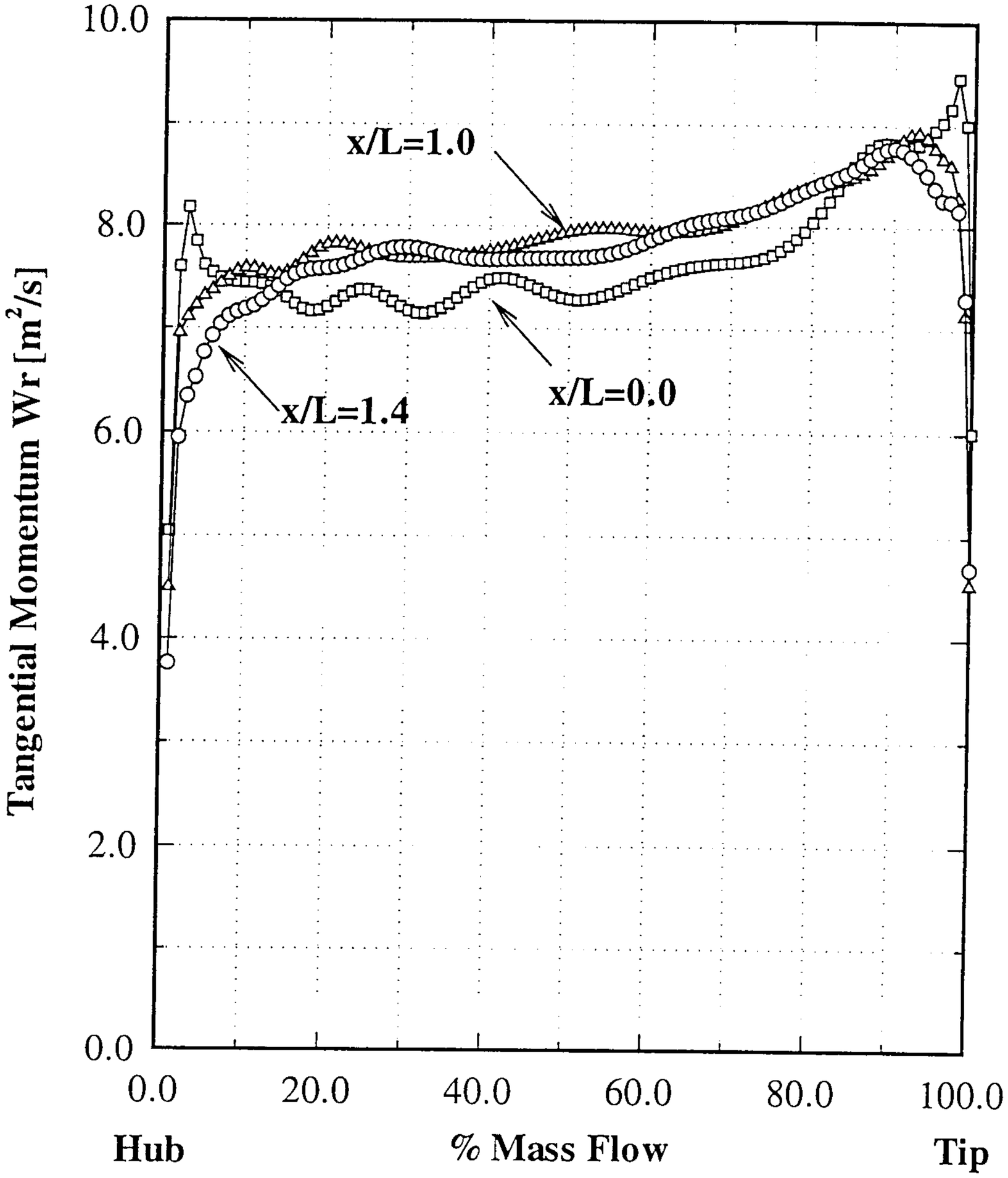

Fig.4.4.9 Radial distribution of tangential momemtum.

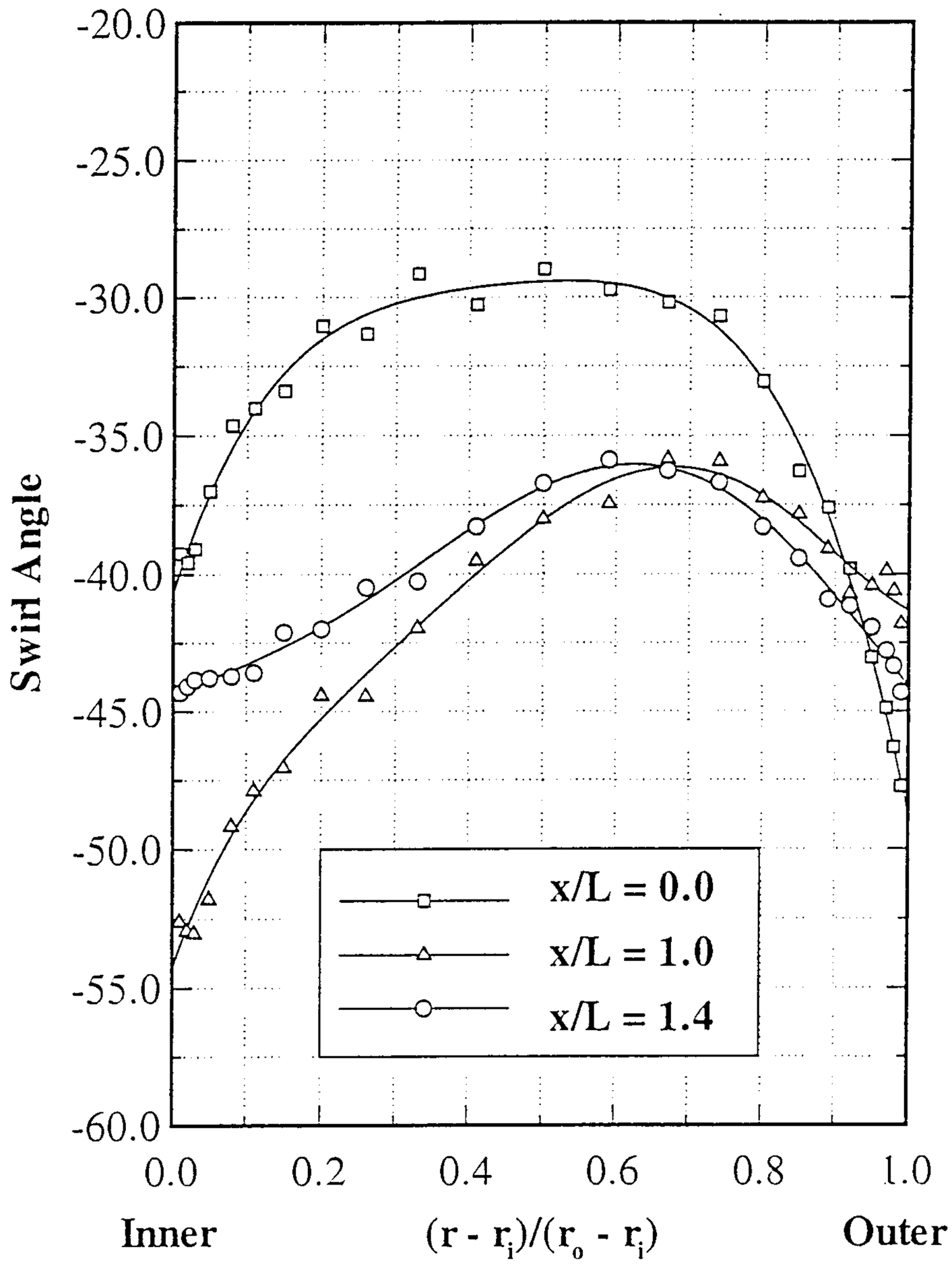

Fig.4.4.10 Radial distribution of swirl angle.

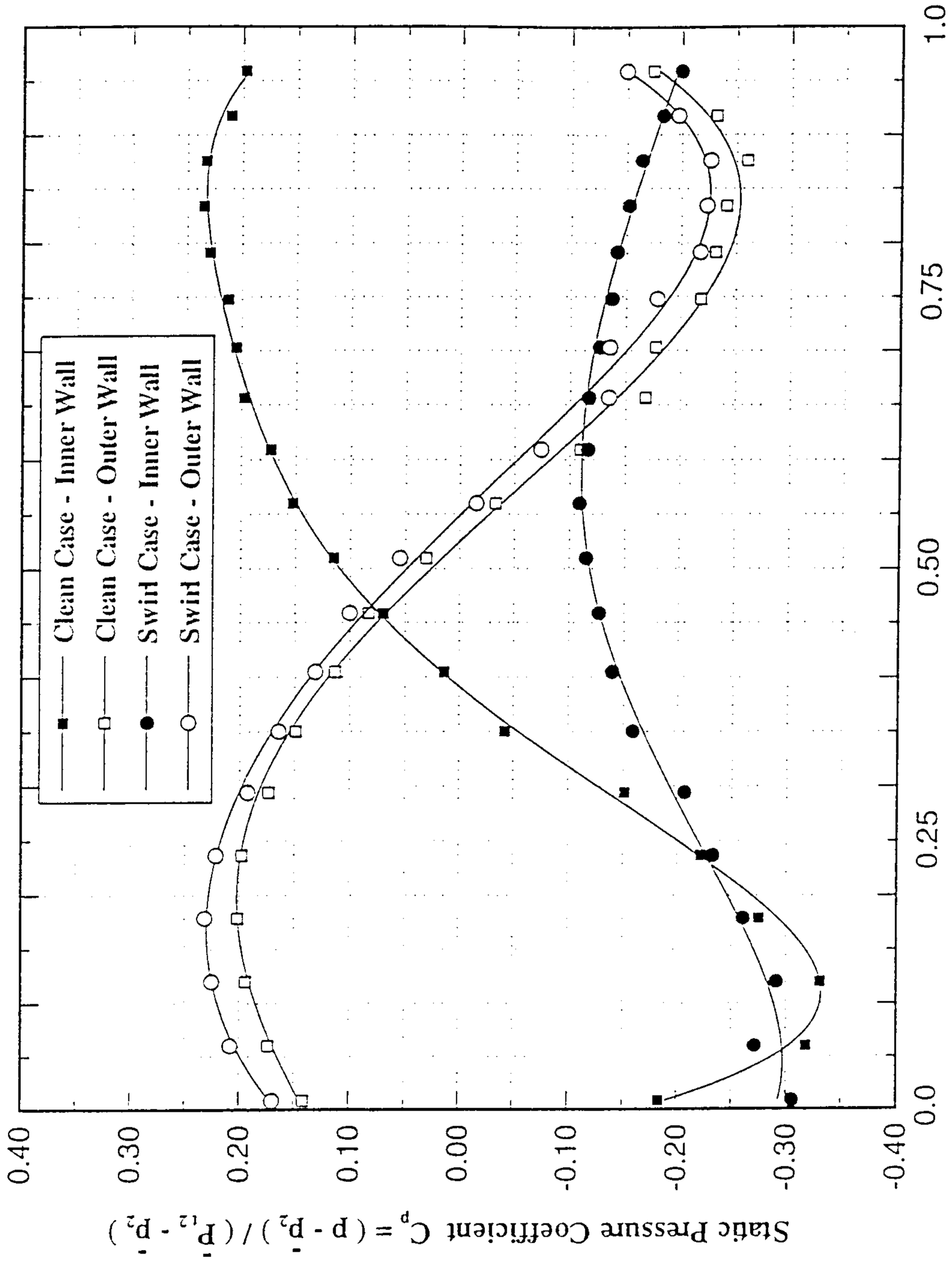

Fig.4.4.11 Axial variation of wall static pressure coefficient (C_p)
(Referenced to total dynamic head)

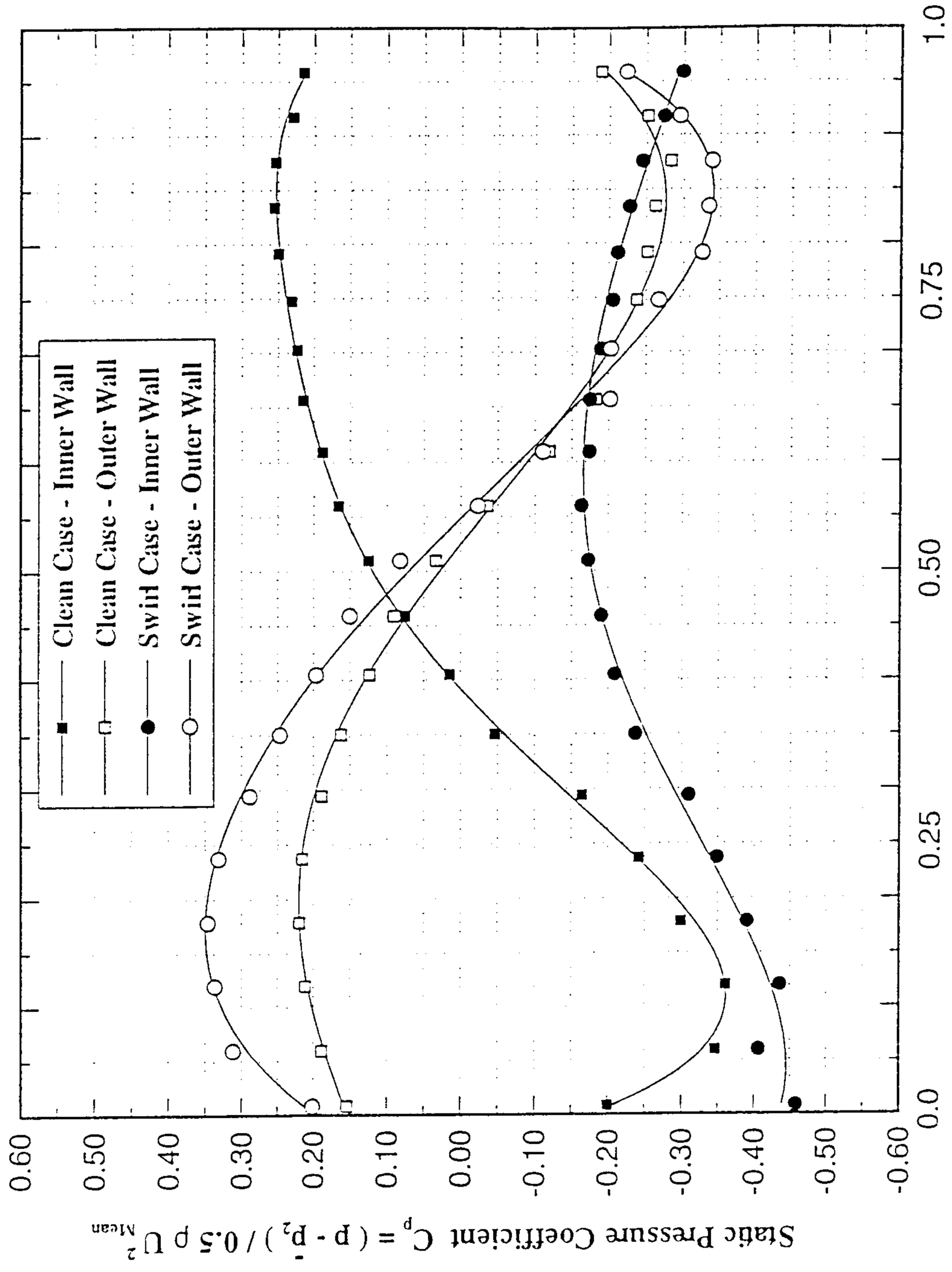

Fig.4.4.12 Axial variation of wall static pressure coefficient (C_p)
(Referenced to axial dynamic head)

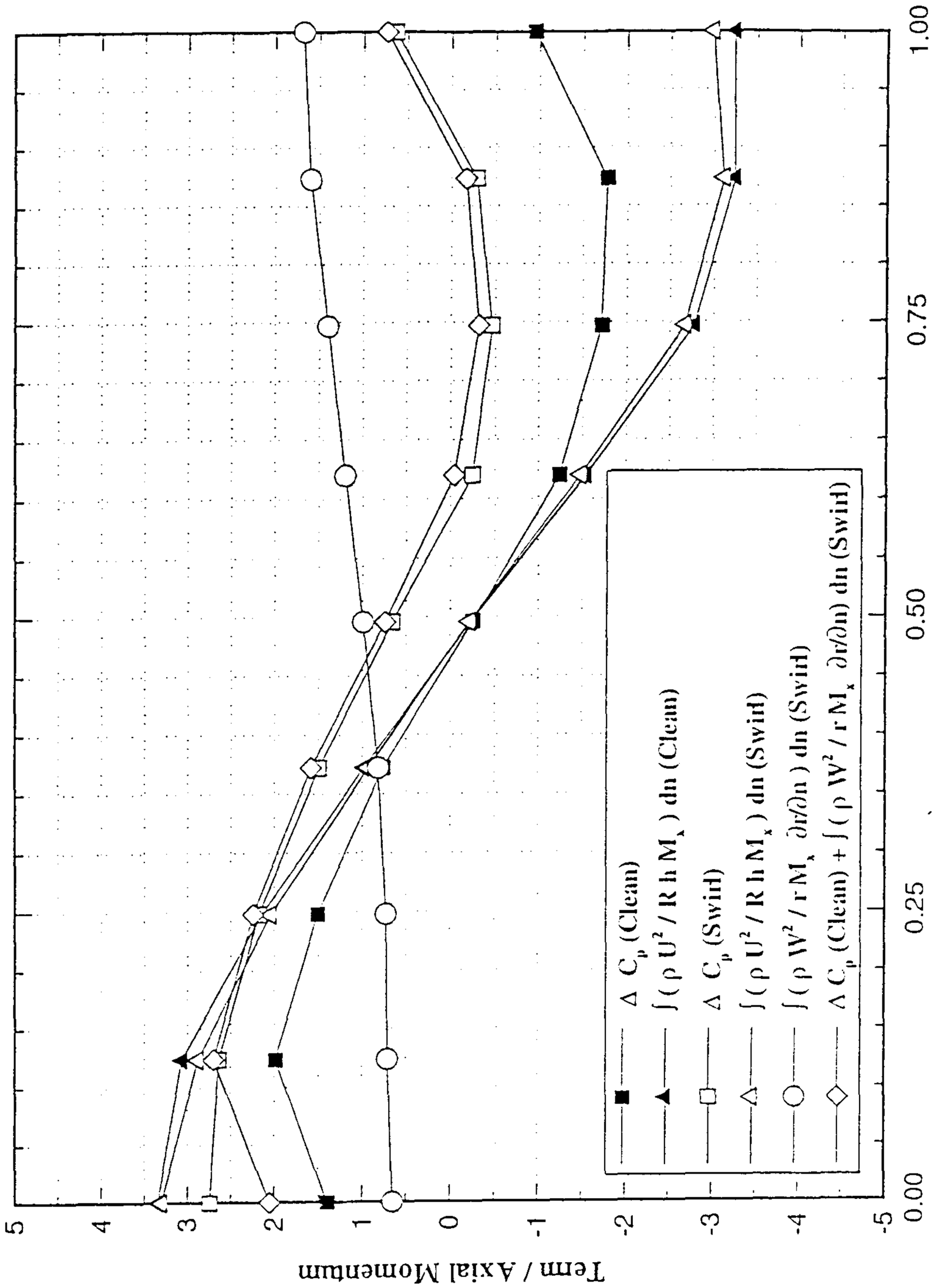

Fig.4.4.13 Axial distribution of the

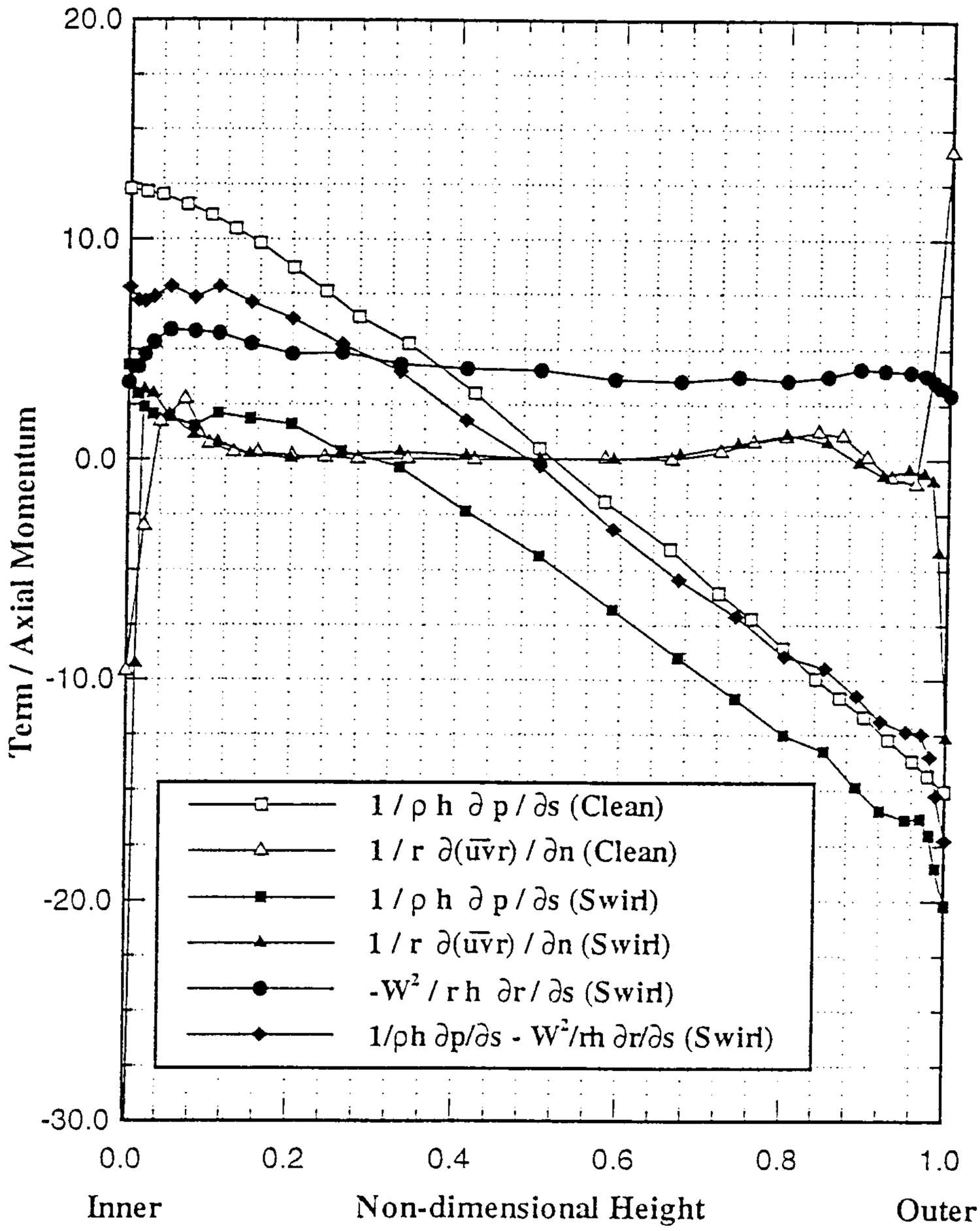

Fig.4.4.14 Radial distribution of terms in s-momentum equation (x/L=0.5).

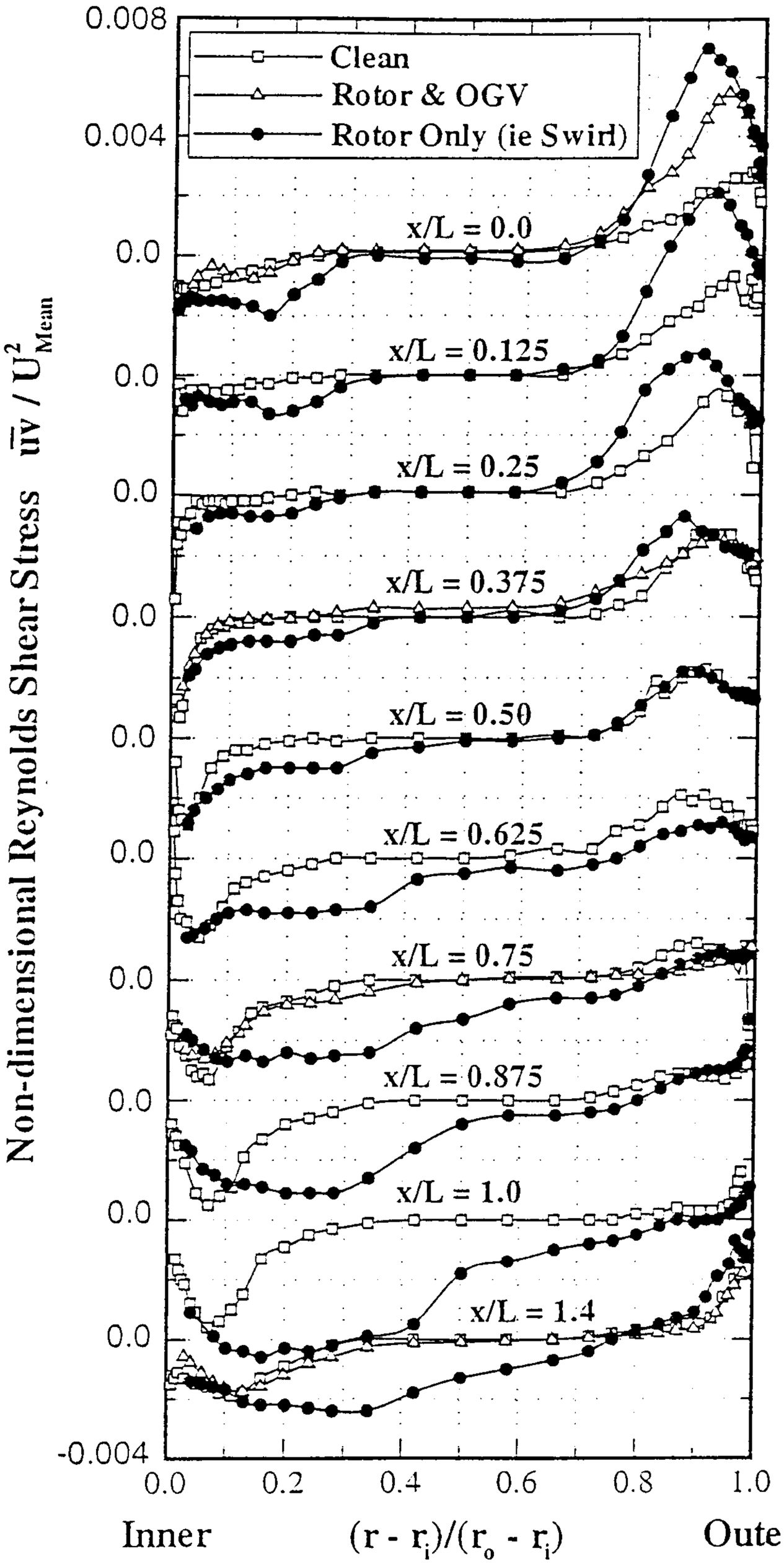

Fig.4.4.15 Development of the primary shear stress ($\overline{uv}$).

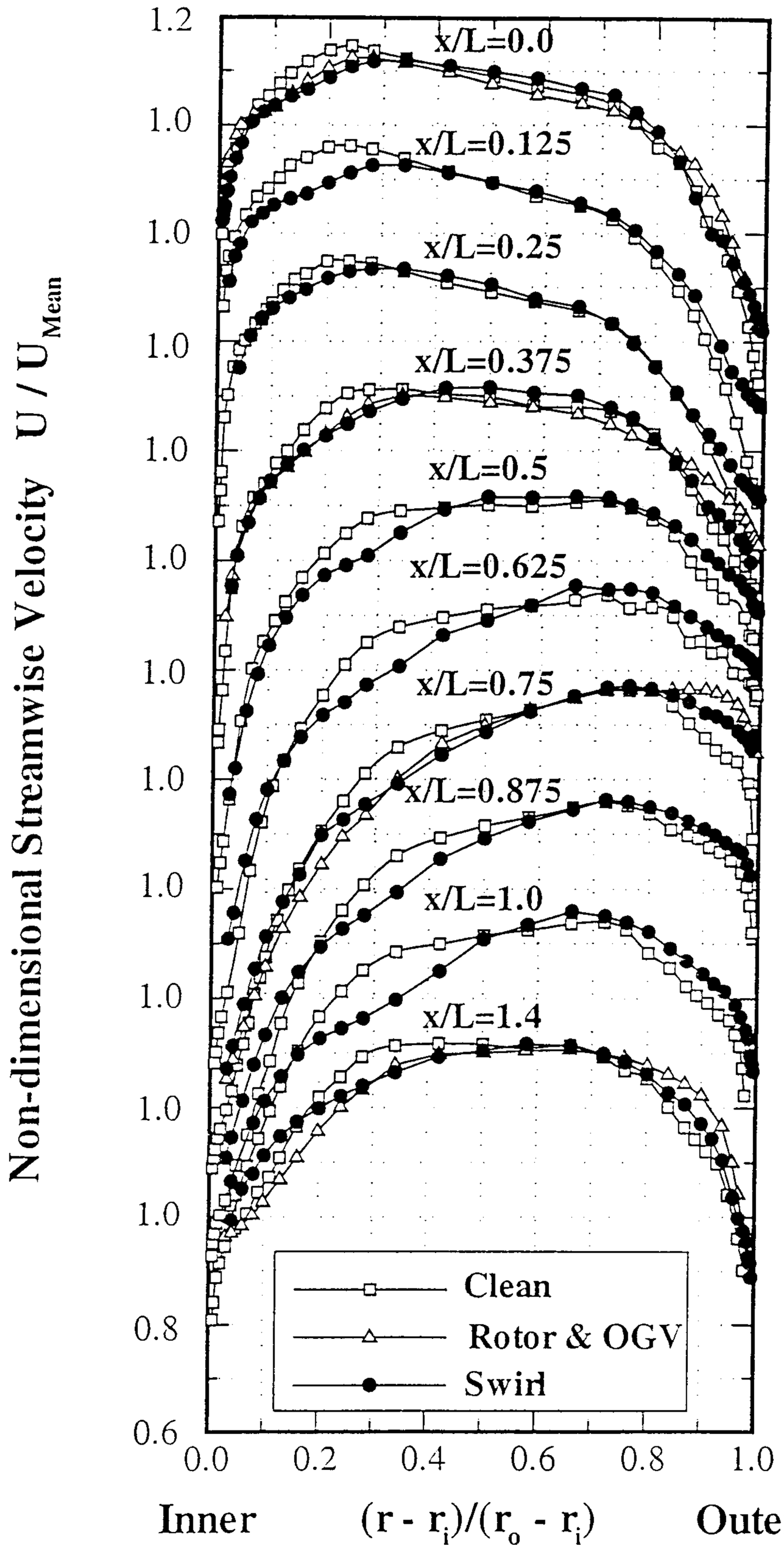

Fig.4.4.16 Development of the streamwise velocity.

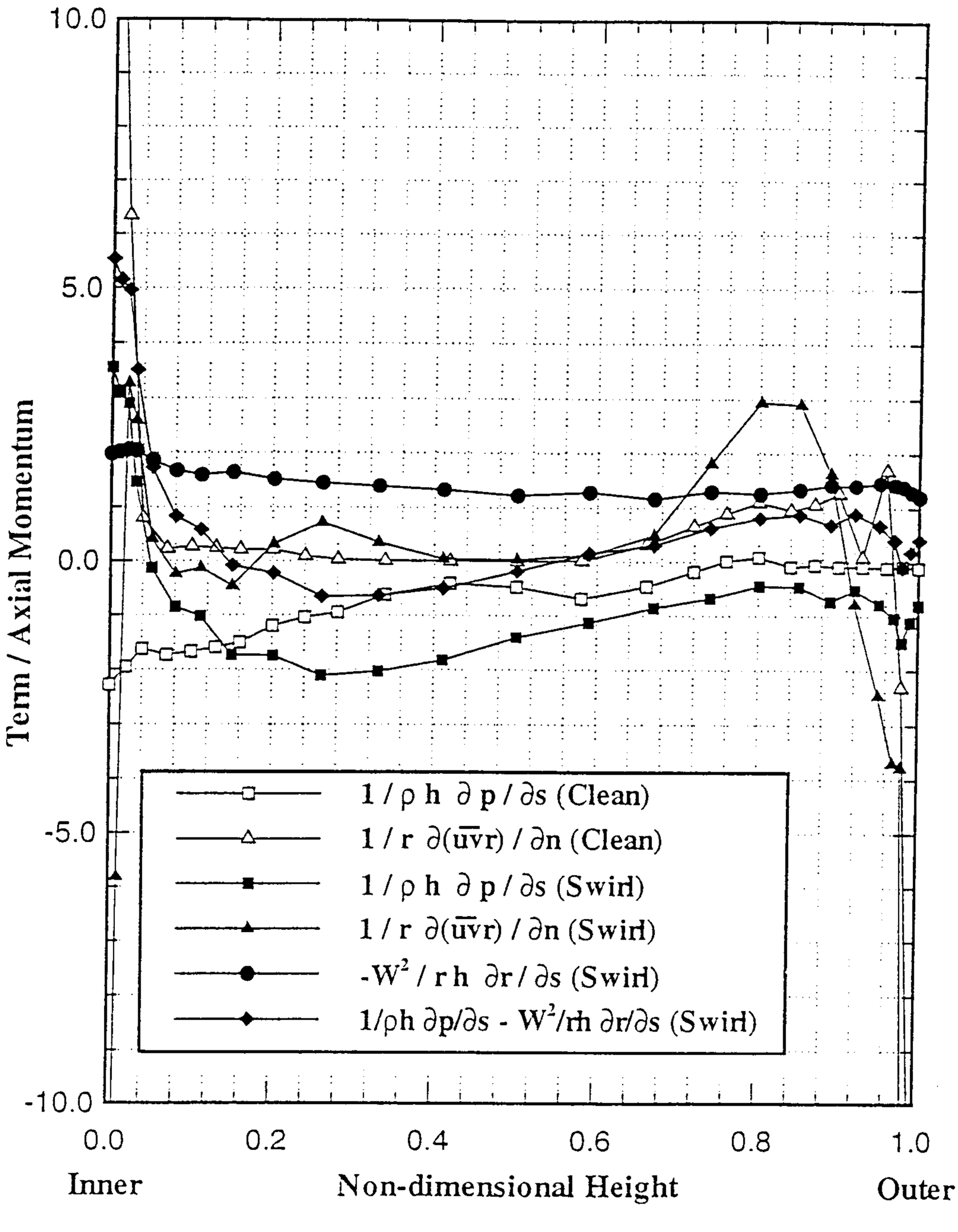

Fig.4.4.17 Radial distribution of terms in the s-momentum equation (x/L=0.125).

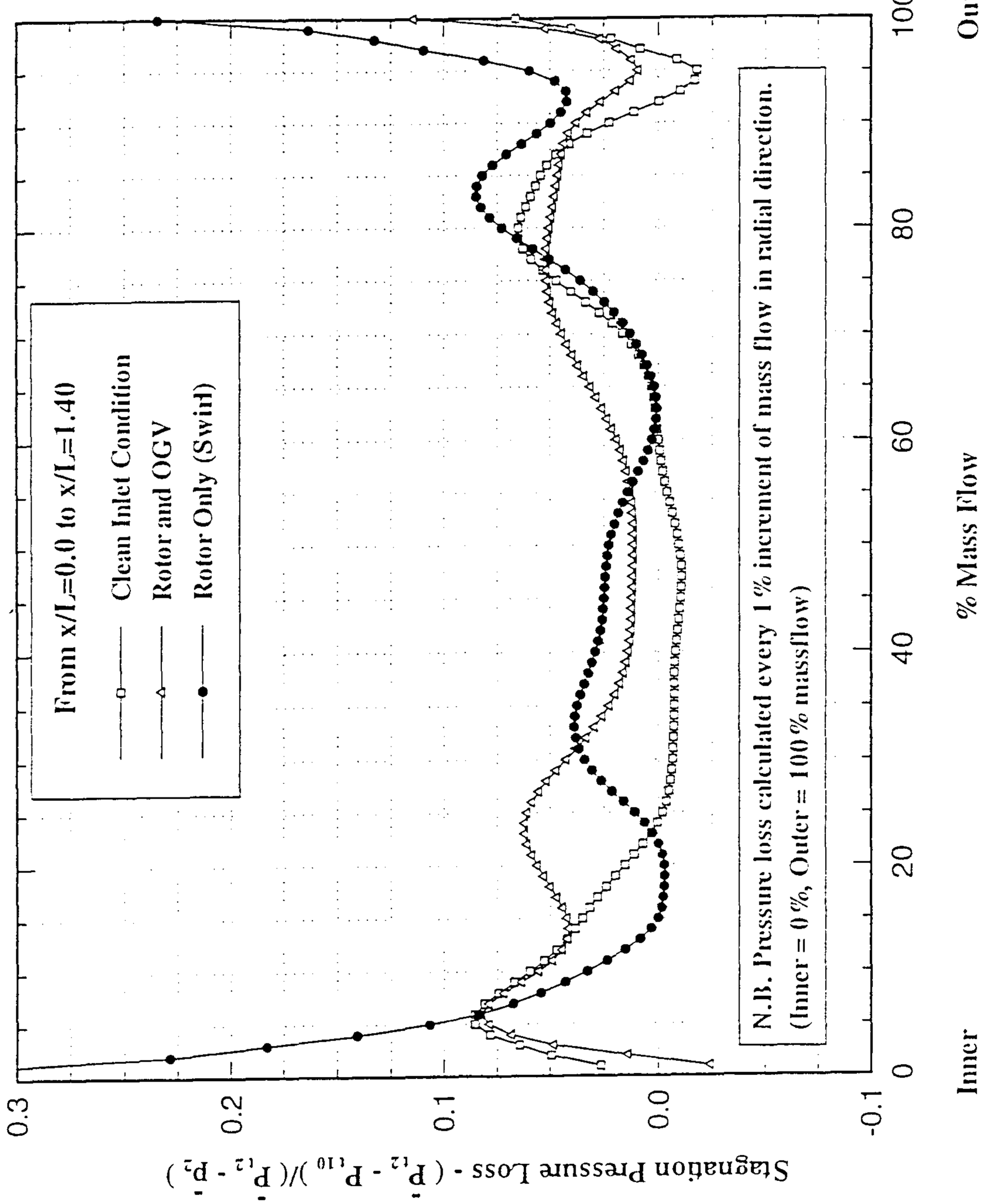

Fig.4.4.18 Radial distribution of stagnation pressure loss (x/L=0.0 to 1.4).

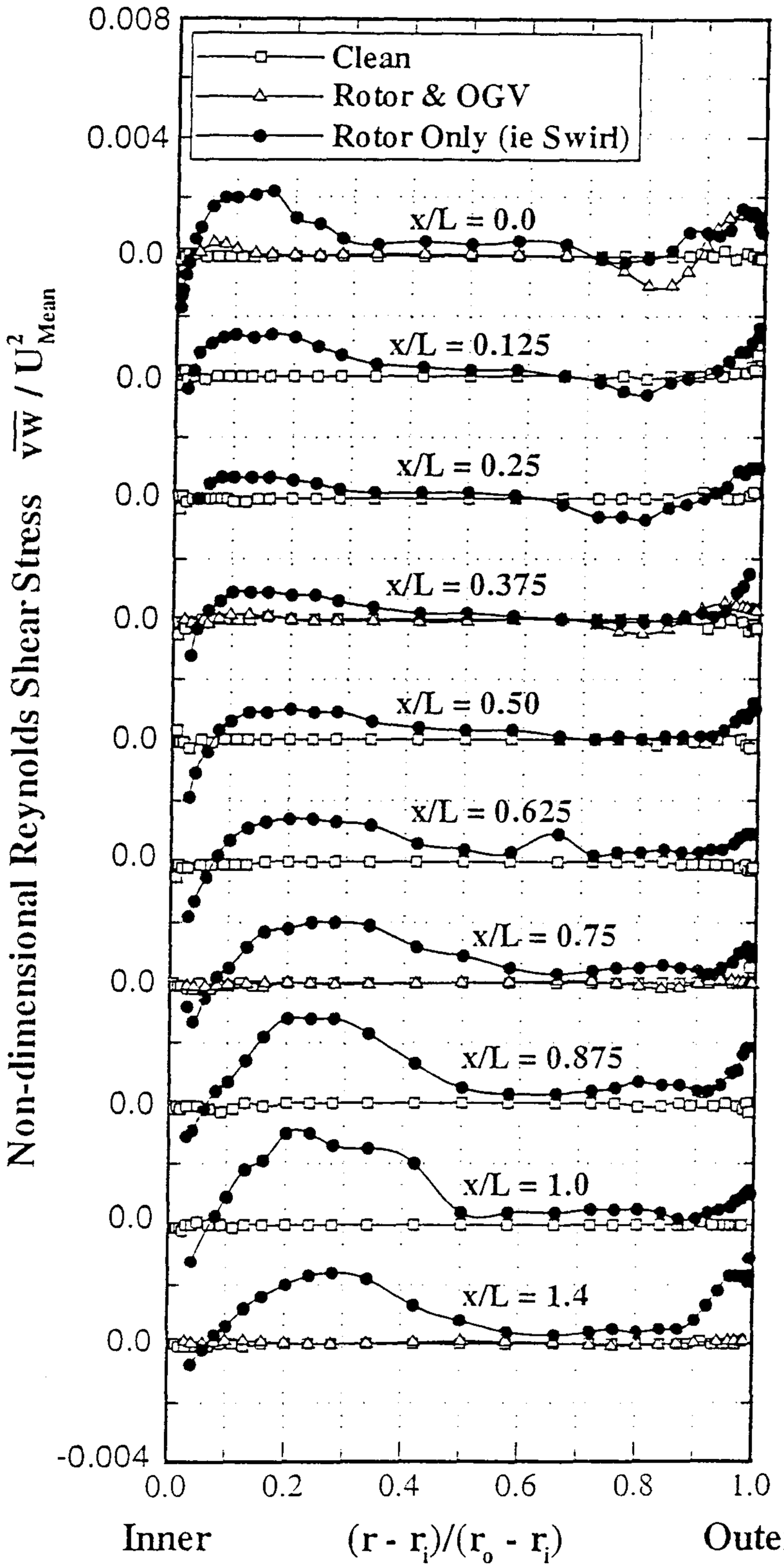

Fig.4.4.19 Development of Reynolds shear stress ($\overline{vw}$).

Appendix 1 The Optical Transformation Matrix

A.1 Derivation of the Optical Transformation Matrix.

The optical transformation matrix is used to transform the measured non-orthogonal velocities (U_{BSA1},U_{BSA2},U_{BSA3}) into the three mutually orthogonal components (U,V,W) alligned with the rig axis (Fig.A.1.1). The optical transformation matrix is comprised of 9 coefficients (or direction cosines a_{ij}) which can be derived from knowledge of the laser beam allignment;

$$\begin{bmatrix} U \\ V \\ W \end{bmatrix} = \begin{bmatrix} a_{11} & a_{12} & a_{13} \\ a_{21} & a_{22} & a_{23} \\ a_{31} & a_{32} & a_{33} \end{bmatrix} \begin{bmatrix} U_{BSA1} \\ U_{BSA2} \\ U_{BSA3} \end{bmatrix} \qquad \text{(Eqn.A.1.1)}$$

In this investigation, the 1D and 2D beams have been placed at angles (α) and (β) to the traverse plane respectively (Fig.A.1.2). The violet (1D) beam has been constrained to lie in the axial radial plane, while the green and blue (2D) beams have been rotated about the 2D probe axis by angles of (γ_g) and (γ_b) respectively (Fig.A.1.2).

If we consider the plane normal to the 2D probe (Fig.A.1.3.a), with velocity components U' and W in the plane, then the non-orthogonal velocity components U_{BSA1} and U_{BSA2} will be at angles (γ_g) and (γ_b) to the velocity component U'. If we further consider that a velocity (C) at an angle (θ) to U' direction can be resolved such that;

$$U' = C\cos\theta \qquad \text{(Eqn.A.1.2)}$$

$$W = C\sin\theta \qquad \text{(Eqn.A.1.3)}$$

Then;

$$U_{BSA1} = C\cos(\gamma_g - \theta)$$

$$U_{BSA1} = C(\cos\gamma_g\cos\theta + \sin\gamma_g\sin\theta)$$

$$U_{BSA1} = U'\cos\gamma_g + W\sin\gamma_g \qquad \text{(Eqn.A.1.4)}$$

and;

$$U_{BSA2} = C\cos(\theta + (-\gamma_b))$$

$$U_{BSA2} = C(\cos\theta\cos\gamma_b + \sin\theta\sin\gamma_b)$$

$$U_{BSA2} = U'\cos\gamma_b + W\sin\gamma_b \qquad \text{(Eqn.A.1.5)}$$

Equating Eqn.A.1.4 and Eqn.A.1.5 in order to remove U' leads to;

$$\frac{U_{BSA1} - W\sin\gamma_g}{\cos\gamma_g} = \frac{U_{BSA2} - W\sin\gamma_b}{\cos\gamma_b}$$

$$U_{BSA1}\cos\gamma_b - W\sin\gamma_g\cos\gamma_b = U_{BSA2}\cos\gamma_g - W\sin\gamma_b\cos\gamma_g$$

$$W(\sin\gamma_g\cos\gamma_b - \sin\gamma_b\cos\gamma_g) = \cos\gamma_b U_{BSA1} - \cos\gamma_g U_{BSA2}$$

$$W = \left(\frac{\cos\gamma_b}{\sin(\gamma_g - \gamma_b)}\right)U_{BSA1} + \left(\frac{-\cos\gamma_g}{\sin(\gamma_g - \gamma_b)}\right)U_{BSA2} \qquad \text{(Eqn.A.1.6)}$$

Now, from Eqn.A.1.4;

$$U'\cos\gamma_g = U_{BSA1} - W\sin\gamma_g$$

Substituting for W from Eqn.A.1.6 gives;

$$U'\cos\gamma_g = U_{BSA1} - \left(\frac{\cos\gamma_b\sin\gamma_g}{\sin(\gamma_g - \gamma_b)}\right)U_{BSA1} + \left(\frac{\cos\gamma_g\sin\gamma_g}{\sin(\gamma_g - \gamma_b)}\right)U_{BSA2}$$

$$U' = \left(\frac{1}{\cos\gamma_g} - \frac{\cos\gamma_b\sin\gamma_g}{\cos\gamma_g\sin(\gamma_g - \gamma_b)}\right)U_{BSA1} + \left(\frac{\sin\gamma_g}{\sin(\gamma_g - \gamma_b)}\right)U_{BSA2}$$

$$U' = \left(\frac{\sin(\gamma_g - \gamma_b) - \cos\gamma_b\sin\gamma_g}{\cos\gamma_g\sin(\gamma_g - \gamma_b)}\right)U_{BSA1} + \left(\frac{\sin\gamma_g}{\sin(\gamma_g - \gamma_b)}\right)U_{BSA2}$$

Now since;

$$\sin(\gamma_g - \gamma_b) = \sin\gamma_g\cos\gamma_b - \cos\gamma_g\sin\gamma_b$$

then;

$$U' = \left(\frac{-\sin\gamma_b}{\sin(\gamma_g - \gamma_b)}\right)U_{BSA1} + \left(\frac{\sin\gamma_g}{\sin(\gamma_g - \gamma_b)}\right)U_{BSA2} \qquad \text{(Eqn.A.1.7)}$$

If we now consider the x,r plane (Fig.A.1.3.b), with streamwise (U) and radial (V) velocity components in the x and r directions respectively, then the non-orthogonal velocity component U_{BSA3} will be at an angle (α) to the x-axis. If we further consider that a velocity (C) at an angle (θ) to the (x) direction can be resolved such that;

$$U = C\cos\theta \qquad \text{(Eqn.A.1.8)}$$

$$V = C\sin\theta \qquad \text{(Eqn.A.1.9)}$$

$$U' = C\cos(\theta - \beta)$$

$$U' = C(\cos\theta\cos\beta + \sin\theta\sin\beta)$$

$$U' = U\cos\beta + V\sin\beta \qquad \text{(Eqn.A.1.10)}$$

and;

$$U_{BSA3} = C\cos(\alpha - \theta)$$

$$U_{BSA3} = C(\cos\alpha\cos\theta + \sin\alpha\sin\theta)$$

$$U_{BSA3} = U\cos\alpha + V\sin\alpha \qquad \text{(Eqn.A.1.11)}$$

If we now equate Eqn.A.1.10 and Eqn.A.1.11 in order to remove V we obtain;

$$\frac{U' - U\cos\beta}{\sin\beta} = \frac{U_{BSA3} - U\cos\alpha}{\sin\alpha}$$

Thus;

$$U'\sin\alpha - U\cos\beta\sin\alpha = U_{BSA3}\sin\beta - U\cos\alpha\sin\beta$$

$$U(\sin\alpha\cos\beta - \cos\alpha\sin\beta) = U'\sin\alpha - U_{BSA3}\sin\beta$$

$$U\sin(\alpha - \beta) = U'\sin\alpha - U_{BSA3}\sin\beta$$

Now substituting Eqn.A.1.7 for U', we obtain;

$$U\sin(\alpha - \beta) = \left(\frac{-\sin\alpha\sin\gamma_b}{\sin(\gamma_g - \gamma_b)}\right)U_{BSA1} + \left(\frac{\sin\alpha\sin\gamma_g}{\sin(\gamma_g - \gamma_b)}\right)U_{BSA2} + (-\sin\beta)\,U_{BSA3}$$

$$U = \left(\frac{-\sin\alpha\sin\gamma_b}{\sin(\alpha - \beta)\sin(\gamma_g - \gamma_b)}\right)U_{BSA1} + \left(\frac{\sin\alpha\sin\gamma_g}{\sin(\alpha - \beta)\sin(\gamma_g - \gamma_b)}\right)U_{BSA2}$$

$$+ \left(\frac{-\sin\beta}{\sin(\alpha - \beta)}\right)U_{BSA3} \qquad \text{(Eqn.A.1.12)}$$

Now substituting U back in Eqn.A.1.11 we obtain;

$$V\sin\alpha = U_{BSA3} - \left(\frac{-\cos\alpha\sin\alpha\sin\gamma_b}{\sin(\alpha - \beta)\sin(\gamma_g - \gamma_b)}\right)U_{BSA1}$$

$$- \left(\frac{\cos\alpha\sin\alpha\sin\gamma_g}{\sin(\alpha - \beta)\sin(\gamma_g - \gamma_b)}\right)U_{BSA2} - \left(\frac{-\cos\alpha\sin\beta}{\sin(\alpha - \beta)}\right)U_{BSA3}$$

and therefore;

$$V = \left(\frac{\cos\alpha \sin\gamma_b}{\sin(\alpha-\beta)\sin(\gamma_g-\gamma_b)}\right)U_{BSA1} + \left(\frac{(-\cos\alpha)\sin\gamma_g}{\sin(\alpha-\beta)\sin(\gamma_g-\gamma_b)}\right)U_{BSA2}$$

$$+ \left(\frac{\cos\beta}{\sin(\alpha-\beta)}\right)U_{BSA3} \quad \text{(Eqn.A.1.13)}$$

Thus by combining Eqns.A.1.6, A.1.12 and A.1.13 we obtain the optical transformation matrix;

$$\begin{bmatrix} U \\ V \\ W \end{bmatrix} = \begin{bmatrix} \left(\frac{-\sin\alpha\sin\gamma_b}{\sin(\alpha-\beta)\sin(\gamma_g-\gamma_b)}\right) & \left(\frac{\sin\alpha\sin\gamma_g}{\sin(\alpha-\beta)\sin(\gamma_g-\gamma_b)}\right) & \left(\frac{-\sin\beta}{\sin(\alpha-\beta)}\right) \\ \left(\frac{\cos\alpha\sin\gamma_b}{\sin(\alpha-\beta)\sin(\gamma_g-\gamma_b)}\right) & \left(\frac{-\cos\alpha\sin\gamma_g}{\sin(\alpha-\beta)\sin(\gamma_g-\gamma_b)}\right) & \left(\frac{\cos\beta}{\sin(\alpha-\beta)}\right) \\ \left(\frac{\cos\gamma_b}{\sin(\gamma_g-\gamma_b)}\right) & \left(\frac{-\cos\gamma_g}{\sin(\gamma_g-\gamma_b)}\right) & 0 \end{bmatrix} \begin{bmatrix} U_{BSA1} \\ U_{BSA2} \\ U_{BSA3} \end{bmatrix}$$

(Eqn.A.1.14)

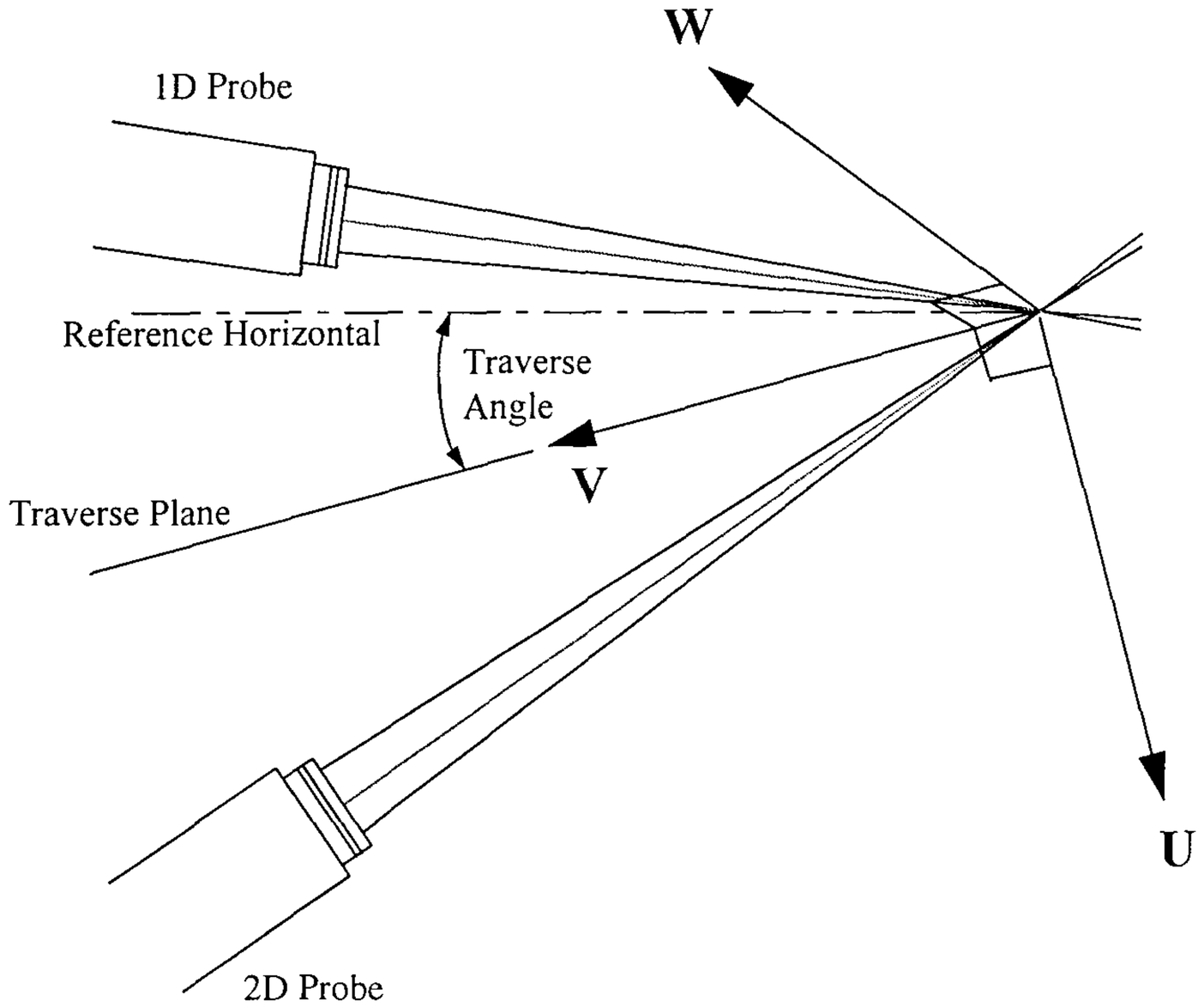

Fig.A.1.1 The orthogonal velocity components U,V and W

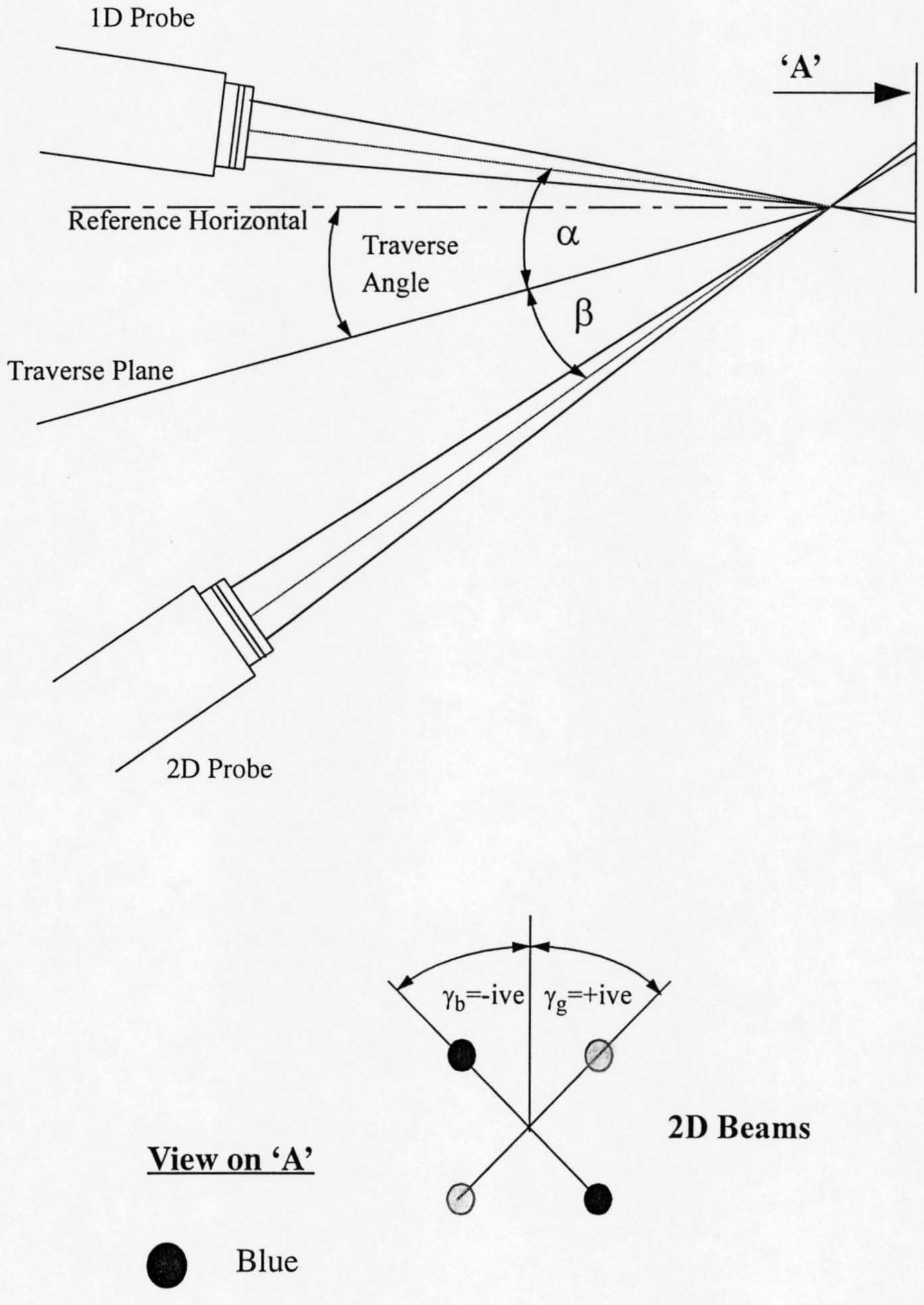

Fig.A.1.2 Laser beam alignment

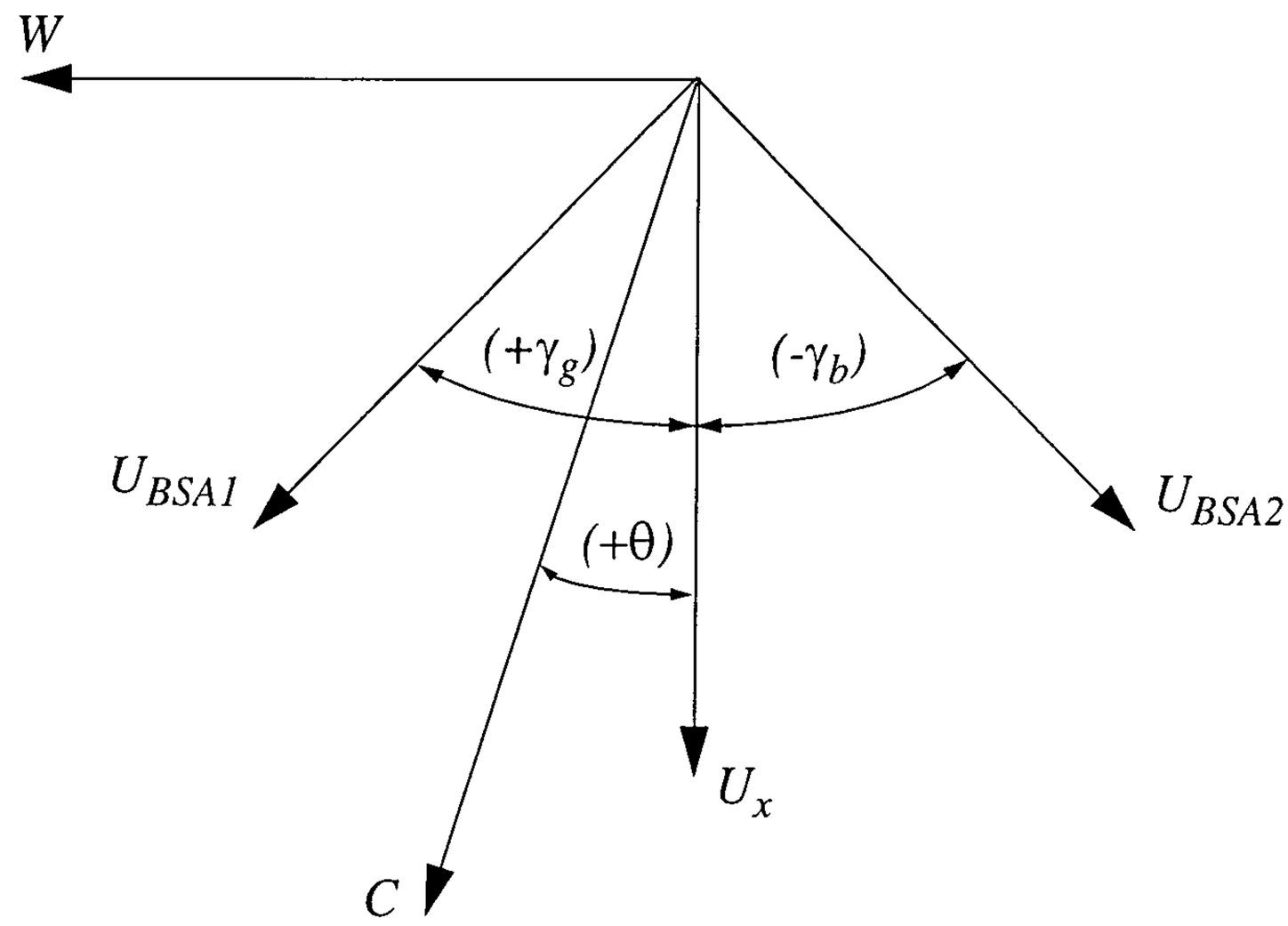

Fig.A.1.3.a The plane normal to the 2D probe.

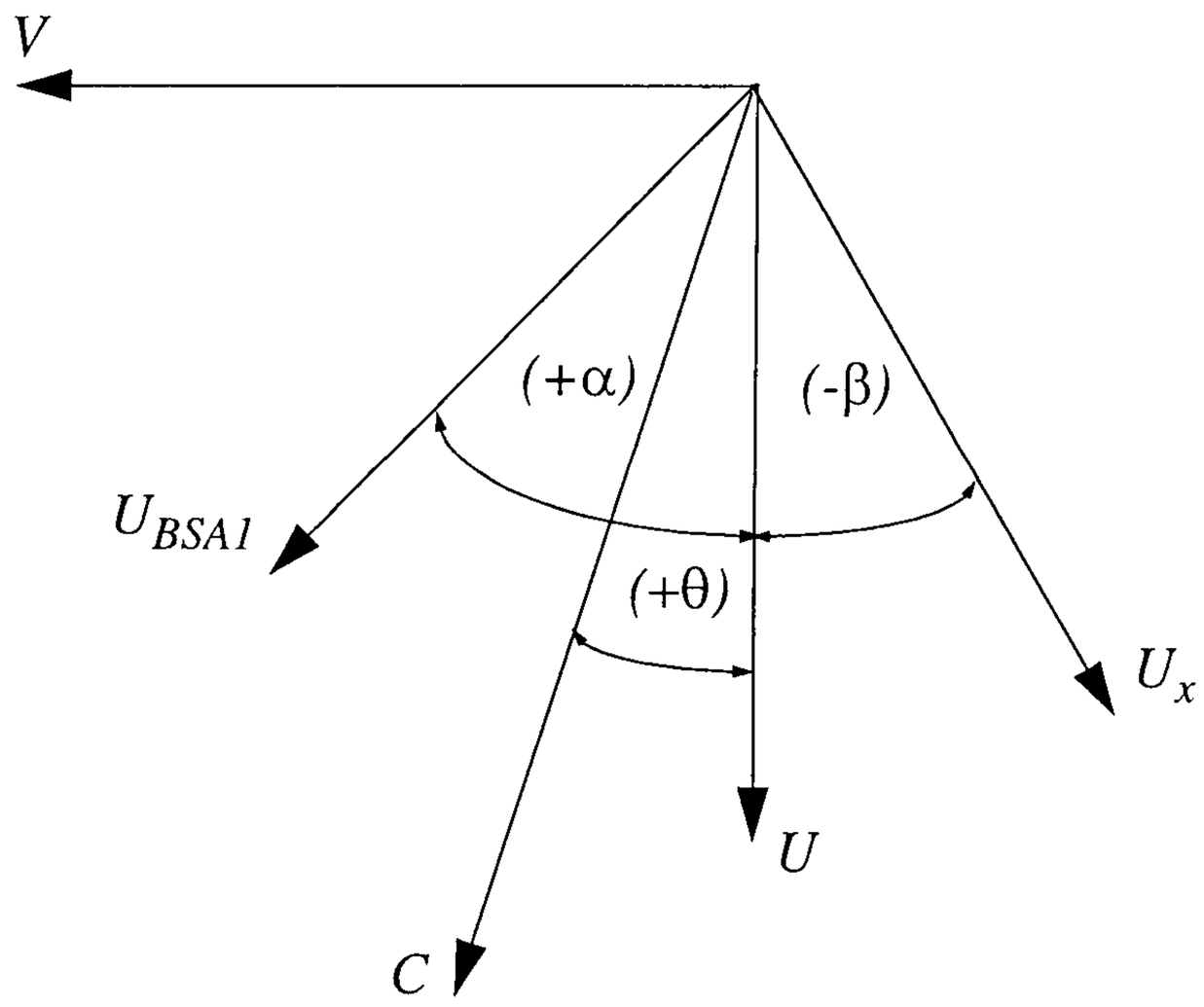

Fig.A.1.3.b The x-r plane.

Appendix 2

The Equations of Motion in the s,n,ϕ Coordinate System.

A.2. The Equations of Motion in the s,n,ϕ Coordinate System.

A.2.1 Comparison with Previously Published Work.

A.2 The Equations of Motion in the s,n ,ϕ Coordinate System .

Rosenhead (1963) has shown how the equations of motion (i.e. the continuity and momentum equations) for turbulent, incompressible flow can be written in vector form as;

$$div\vec{V} = 0 \qquad \text{(Eqn.A.2.1)}$$

$$\frac{\partial \vec{V}}{\partial t} + grad\left(\frac{1}{2}\vec{V}^2\right) - \vec{V} \times \vec{\omega} = -\frac{1}{\rho} grad\,(p) + \nu\nabla^2 \vec{V} \qquad \text{(Eqn.A.2.2}$$

where;

- V is the velocity vector
- ω is the curl of V and represents the vorticity of the fluid
- $\nabla^2 \vec{V}$ is the Laplace operator.

This invariant form of the equations applies for any coordinate system. Rosenhead (1963) has shown that to expand the equations for any particular system we require the formulae for the gradient of a scalar and the divergence and curl of a vector in the system. Rosenhead has obtained these formulae for a general orthogonal coordinate system, so that the divergence and curl of a vector V with components V_1,V_2 and V_3 are;

$$div\vec{V} = \frac{1}{h_1 h_2 h_3}\left(\frac{\partial}{\partial x_1}(h_2 h_3 V_1) + \frac{\partial}{\partial x_2}(h_3 h_1 V_2) + \frac{\partial}{\partial x_3}(h_1 h_2 V_3)\right) = 0 \qquad \text{(Eqn.A.2.3)}$$

$$\omega_1 = curl V_1 = \frac{1}{h_2 h_3}\left(\frac{\partial}{\partial x_2}(h_3 V_3) - \frac{\partial}{\partial x_3}(h_2 V_2)\right) \qquad \text{(Eqn.A.2.4)}$$

$$\omega_2 = curl V_2 = \frac{1}{h_1 h_3}\left(\frac{\partial}{\partial x_3}(h_1 V_1) - \frac{\partial}{\partial x_1}(h_3 V_3)\right) \qquad \text{(Eqn.A.2.5)}$$

$$\omega_3 = curl V_3 = \frac{1}{h_1 h_2}\left(\frac{\partial}{\partial x_1}(h_2 V_2) - \frac{\partial}{\partial x_2}(h_1 V_1)\right) \qquad \text{(Eqn.A.2.6)}$$

where $h_1\partial x_1$, $h_2\partial x_2$ and $h_3\partial x_3$ are elements of length at the point (x_1,x_2,x_3) in the directions of increasing x_1,x_2 and x_3 respectively.

The orthogonal coordinate system chosen in this investigation, alligned with the traverse stations of the test facility, is the s,n,ϕ coordinate system (Fig.A.2.1). The elemental lengths in the s,n,ϕ directions are therefore;

$$h_1 dx_1 = (R+n)\, d\theta \qquad \text{(Eqn.A.2.7)}$$

$$h_2 dx_2 = dn \qquad \text{(Eqn.A.2.8)}$$

$$h_3 dx_3 = r d\phi \qquad \text{(Eqn.A.2.9)}$$

Rosenhead (1963) has also shown how the components of the gradient of a scalar (Φ) are given by;

$$\frac{1}{h_1}\frac{\partial \Phi}{\partial x_1} \qquad \frac{1}{h_2}\frac{\partial \Phi}{\partial x_2} \qquad \frac{1}{h_3}\frac{\partial \Phi}{\partial x_3} \qquad \text{(Eqn.A.2.10)}$$

With these results the equation of continuity and the three components of the momentum equation can be derived for the s,n,ϕ coordinate system.

Taking the velocity vector V to have components U, V and W in the s, n and ϕ directions respectively then the continuity equation (Eqn.A.2.1) can be written as;

$$div\vec{V} = \frac{1}{h_1 h_2 h_3}\left(\frac{\partial}{\partial x_1}(h_2 h_3 U) + \frac{\partial}{\partial x_2}(h_3 h_1 V) + \frac{\partial}{\partial x_3}(h_1 h_2 W)\right) = 0 \qquad \text{(Eqn.A.2.11)}$$

Substituting the metric coefficients;

$$h_1 = R+n$$

$$h_2 = 1$$

$$h_3 = r$$

and for clarity taking h=1+n/R to be the ratio of local (R+n) to reference (R) radius of

curvature so that Rh=R+n, we obtain;

$$div\vec{V} = \frac{1}{Rrh}\left(\frac{\partial}{\partial\theta}(Ur) + \frac{\partial}{\partial n}(VRrh) + \frac{\partial}{\partial\phi}(WRh)\right) = 0$$

$$= \frac{1}{Rrh}\left(r\frac{\partial U}{\partial\theta} + U\frac{\partial r}{\partial\theta} + Rrh\frac{\partial V}{\partial n} + VRh\frac{\partial r}{\partial n} + VRr\frac{\partial h}{\partial n} + Vrh\frac{\partial R}{\partial n} + Rh\frac{\partial W}{\partial\phi} + WR\frac{\partial h}{\partial\phi} + Wh\frac{\partial r}{\partial\phi}\right) = 0$$

Thus, the continuity equation in the s,n,ϕ coordinate system (since R$\partial\theta$=∂s) can be written as;

$$div\vec{V} = \frac{1}{h}\frac{\partial U}{\partial s} + \frac{U}{rh}\frac{\partial r}{\partial s} + \frac{\partial V}{\partial n} + \frac{V}{r}\frac{\partial r}{\partial n} + \frac{V}{h}\frac{\partial h}{\partial n} + \frac{V}{R}\frac{\partial R}{\partial n} + \frac{1}{r}\frac{\partial W}{\partial\phi} + \frac{W}{rh}\frac{\partial h}{\partial\phi} + \frac{W}{Rr}\frac{\partial r}{\partial\phi} = 0 \qquad \text{(Eqn.A.2.12)}$$

As already shown, the momentum equation can be written in invariant vector form as;

$$\frac{\partial\vec{V}}{\partial t} + grad\left(\frac{1}{2}\vec{V}^2\right) - \vec{V}\times\vec{\omega} = -\frac{1}{\rho}grad(p) + \nu\nabla^2\vec{V} \qquad \text{(Eqn.A.2.2)}$$

The s-component momentum equation, for example, can be derived by considering each of the terms in Eqn.A.2.2 separately i.e.;

$$\frac{\partial V_1}{\partial t} = \frac{\partial U}{\partial t} \qquad \text{(Eqn.A.2.13)}$$

next, from Eqn.A.2.10;

$$grad_1\left(\frac{1}{2}V^2\right) = \frac{1}{h_1}\frac{\partial}{\partial x_1}\left(\frac{1}{2}V^2\right)$$

$$= \frac{1}{Rh}\frac{\partial}{\partial\theta}\left(\frac{1}{2}U^2 + \frac{1}{2}V^2 + \frac{1}{2}W^2\right)$$

$$= \frac{U}{h}\frac{\partial U}{\partial s} + \frac{V}{h}\frac{\partial V}{\partial s} + \frac{W}{h}\frac{\partial W}{\partial s} \qquad \text{(Eqn.A.2.14)}$$

The third term on the left hand side of Eqn.A.2.2 is given by;

$$\vec{V} \times \vec{\omega} = (V_2\omega_3) - (V_3\omega_2) = (V_2\omega_3) - (V_3\omega_2) \qquad \text{(Eqn.A.2.15)}$$

where from Eqn.A.2.5;

$$\omega_2 = \frac{1}{Rrh}\left(\frac{\partial}{\partial\phi}(URh) - \frac{\partial}{\partial\theta}(Wr)\right)$$

$$= \frac{1}{Rrh}\left(Rh\frac{\partial U}{\partial\phi} + UR\frac{\partial h}{\partial\phi} + Uh\frac{\partial R}{\partial\phi} - r\frac{\partial W}{\partial\theta} - W\frac{\partial r}{\partial\theta}\right)$$

$$= \frac{1}{r}\frac{\partial U}{\partial\phi} + \frac{U}{rh}\frac{\partial h}{\partial\phi} + \frac{U}{Rr}\frac{\partial R}{\partial\phi} - \frac{1}{h}\frac{\partial W}{\partial s} - \frac{W}{rh}\frac{\partial r}{\partial s} \qquad \text{(Eqn.A.2.16)}$$

and from Eqn.A.2.6;

$$\omega_3 = \frac{1}{Rh}\left(\frac{\partial}{\partial\theta}(V) - \frac{\partial}{\partial n}(URh)\right)$$

$$= \frac{1}{Rh}\left(\frac{\partial V}{\partial\theta} - Rh\frac{\partial U}{\partial n} - UR\frac{\partial h}{\partial n} - Uh\frac{\partial R}{\partial n}\right)$$

$$= \frac{1}{h}\frac{\partial V}{\partial s} - \frac{\partial U}{\partial n} - \frac{U}{h}\frac{\partial h}{\partial n} - \frac{U}{R}\frac{\partial R}{\partial n} \qquad \text{(Eqn.A.2.17)}$$

Thus;

$$\vec{V} \times \vec{\omega} = V\left(\frac{1}{h}\frac{\partial V}{\partial s} - \frac{\partial U}{\partial n} - \frac{U}{h}\frac{\partial h}{\partial n} - \frac{U}{R}\frac{\partial R}{\partial n}\right) - W\left(\frac{1}{r}\frac{\partial U}{\partial\phi} + \frac{U}{rh}\frac{\partial h}{\partial\phi} + \frac{U}{Rr}\frac{\partial R}{\partial\phi} - \frac{1}{h}\frac{\partial W}{\partial s} - \frac{W}{rh}\frac{\partial r}{\partial s}\right)$$

$$= \frac{V}{h}\frac{\partial V}{\partial s} - V\frac{\partial U}{\partial n} - \frac{UV}{h}\frac{\partial h}{\partial n} - \frac{W}{r}\frac{\partial U}{\partial\phi} - \frac{UW}{rh}\frac{\partial h}{\partial\phi} - \frac{UW}{Rr}\frac{\partial R}{\partial\phi} + \frac{W}{h}\frac{\partial W}{\partial s} + \frac{W^2}{rh}\frac{\partial r}{\partial s}$$

(Eqn.A.2.18)

Now, from Eqn.A.2.10, the pressure gradient on the right hand side of Eqn.A.2.2 can be written as;

$$-\frac{1}{\rho}gradp = -\frac{1}{\rho h_1}\frac{\partial p}{\partial x_1} = -\frac{1}{\rho Rh}\frac{\partial p}{\partial \theta} = -\frac{1}{\rho h}\frac{\partial p}{\partial s} \qquad \text{(Eqn.A.2.19)}$$

while the viscous terms are given by;

$$\nu\nabla^2\vec{V} = grad(div\vec{V}) - curl(\vec{\omega}) \qquad \text{(Eqn.A.2.20)}$$

However, the viscous terms are not developed further here since it is assumed in this investigation that the molecular viscosity is small compared with the turbulent viscosity in the regions where experimental data has been obtained. The s-component momentum equation is therefore obtained by substituting Eqns.A.13,14,15,18 and 19 into Eqn.A.2.2 such that;

$$\frac{\partial U}{\partial t} + \frac{U}{h}\frac{\partial U}{\partial s} + V\frac{\partial U}{\partial n} + \frac{UV}{h}\frac{\partial h}{\partial n} + \frac{W}{r}\frac{\partial U}{\partial \phi} + \frac{UW}{rh}\frac{\partial h}{\partial \phi} + \frac{UW}{Rr}\frac{\partial R}{\partial \phi} - \frac{W^2}{rh}\frac{\partial r}{\partial s} = -\frac{1}{\rho h}\frac{\partial p}{\partial s}$$

(Eqn.A.2.21)

Now, if we consider (from Eqn.A.2.21) that;

$$V\frac{\partial U}{\partial n} + \frac{W}{r}\frac{\partial U}{\partial \phi} = \frac{\partial}{\partial n}(UV) - U\frac{\partial V}{\partial n} + \frac{1}{r}\frac{\partial}{\partial \phi}(UW) - \frac{U}{r}\frac{\partial W}{\partial \phi} \qquad \text{(Eqn.A.2.22)}$$

and if we multiply the continuity equation (Eqn.A.2.12) by the streamwise velocity (U) then we obtain;

$$\frac{U}{h}\frac{\partial U}{\partial s} + \frac{U^2}{rh}\frac{\partial r}{\partial s} + U\frac{\partial V}{\partial n} + \frac{UV}{r}\frac{\partial r}{\partial n} + \frac{UV}{h}\frac{\partial h}{\partial n} + \frac{UV}{R}\frac{\partial R}{\partial n} + \frac{U}{r}\frac{\partial W}{\partial \phi} + \frac{UW}{rh}\frac{\partial h}{\partial \phi} + \frac{UW}{Rr}\frac{\partial r}{\partial \phi} = 0$$

(Eqn.A.2.23)

Combining Eqn.A.2.22 and Eqn.A.2.23 gives;

$$V\frac{\partial U}{\partial n} + \frac{W}{r}\frac{\partial U}{\partial \phi} = \frac{\partial}{\partial n}(UV) + \frac{1}{r}\frac{\partial}{\partial \phi}(UW) + \frac{U}{h}\frac{\partial U}{\partial s} + \frac{U^2}{rh}\frac{\partial r}{\partial s} +$$

$$\frac{UV}{r}\frac{\partial r}{\partial n} + \frac{UV}{h}\frac{\partial h}{\partial n} + \frac{UV}{R}\frac{\partial R}{\partial n} + \frac{UW}{rh}\frac{\partial h}{\partial \phi} + \frac{UW}{Rr}\frac{\partial r}{\partial \phi} \qquad \text{(Eqn.A.2.24)}$$

Substitution of Eqn.A.2.24 into Eqn.A.2.21 leads to;

$$\frac{\partial U}{\partial t} + \frac{U}{h}\frac{\partial U}{\partial s} + \frac{UV}{h}\frac{\partial h}{\partial n} + \frac{UW}{rh}\frac{\partial h}{\partial \phi} + \frac{UW}{Rr}\frac{\partial R}{\partial \phi} - \frac{W^2}{rh}\frac{\partial r}{\partial s} + \frac{\partial}{\partial n}(UV) + \frac{1}{r}\frac{\partial}{\partial \phi}(UW)$$

$$+ \frac{U}{h}\frac{\partial U}{\partial s} + \frac{U^2}{rh}\frac{\partial r}{\partial s} + \frac{UV}{r}\frac{\partial r}{\partial n} + \frac{UV}{h}\frac{\partial h}{\partial n} + \frac{UV}{R}\frac{\partial R}{\partial n} + \frac{UW}{rh}\frac{\partial h}{\partial \phi} + \frac{UW}{Rr}\frac{\partial r}{\partial \phi} = -\frac{1}{\rho h}\frac{\partial p}{\partial s}$$

(Eqn.A.2.25)

and assuming;

$$\frac{\partial h}{\partial \phi} = \frac{\partial R}{\partial \phi} = \frac{\partial R}{\partial n} = \frac{\partial r}{\partial \phi} = 0$$

and that;

$$\frac{\partial h}{\partial n} = \frac{\partial}{\partial n}\left(1 + \frac{n}{R}\right) = \frac{1}{R}$$

then Eqn.A.2.25 can be simplified to;

$$\frac{\partial U}{\partial t} + \frac{1}{h}\frac{\partial U^2}{\partial s} + \frac{1}{r}\frac{\partial}{\partial n}(UVr) + \frac{2UV}{Rh} + \frac{1}{r}\frac{\partial}{\partial \phi}(UW) + \frac{1}{rh}\frac{\partial r}{\partial s}(U^2 - W^2) = -\frac{1}{\rho h}\frac{\partial p}{\partial s}$$

(Eqn.A.2.26)

If we now assume the static pressure (p) and the velocity components (U,V,W) to be

described by a mean and fluctuating component such that;

$$U = \overline{U} + u'$$

$$V = \overline{V} + v'$$

$$W = \overline{W} + w'$$

$$p = \overline{p} + p'$$

then Eqn.A.2.26 becomes;

$$\frac{\partial}{\partial t}(\overline{U}+u') + \frac{1}{h}\frac{\partial}{\partial s}(\overline{U}+u')^2 + \frac{1}{r}\frac{\partial}{\partial n}\{(\overline{U}+u')(\overline{V}+v')r\} + \frac{2(\overline{U}+u')(\overline{V}+v')}{Rh}$$

$$+ \frac{1}{r}\frac{\partial}{\partial \phi}\{(\overline{U}+u')(\overline{W}+w')\} + \frac{1}{rh}\frac{\partial r}{\partial s}\{(\overline{U}+u')^2 - (\overline{W}+w')^2\} = -\frac{1}{\rho h}\frac{\partial}{\partial s}(\overline{p}+p')$$

Rearranging further gives;

$$\frac{\partial}{\partial t}(\overline{U}+u') + \frac{1}{h}\frac{\partial}{\partial s}(\overline{U}^2 + 2\overline{U}u' + u'^2) + \frac{1}{r}\frac{\partial}{\partial n}\{(\overline{U}\overline{V} + \overline{U}v' + u'\overline{V} + u'v')r\}$$

$$+ \frac{2(\overline{U}\overline{V} + \overline{U}v' + u'\overline{V} + u'v')}{Rh} + \frac{1}{r}\frac{\partial}{\partial \phi}(\overline{U}\overline{W} + \overline{U}w' + u'\overline{W} + u'w')$$

$$+ \frac{1}{rh}\frac{\partial r}{\partial s}(\overline{U}^2 + 2\overline{U}u' + u'^2 - \overline{W}^2 - 2\overline{W}w' - w'^2) = -\frac{1}{\rho h}\frac{\partial}{\partial s}(\overline{p}+p')$$

(Eqn.A.2.27)

Now, time averaging of Eqn.A.2.27 such that;

$$\frac{\partial}{\partial t}(\overline{\overline{U}+u'}) = 0$$

$$\overline{u'} = \overline{v'} = \overline{w'} = \overline{p'} = 0$$

$$\overline{u'^2}, \overline{v'^2}, \overline{w'^2}, \overline{u'v'}, \overline{v'w'}, \overline{u'w'} \neq 0$$

then the time averaged s-component momentum equation can be written as;

$$\frac{1}{h}\frac{\partial \overline{U}^2}{\partial s} + \frac{1}{r}\frac{\partial}{\partial n}(\overline{U}\overline{V}r) + \frac{2\overline{U}\overline{V}}{Rh} + \frac{1}{r}\frac{\partial}{\partial \phi}(\overline{U}\overline{W}) + \frac{1}{rh}\frac{\partial r}{\partial s}(\overline{U}^2 - \overline{W}^2) =$$

$$-\frac{1}{\rho h}\frac{\partial \overline{p}}{\partial s} - \left(\frac{1}{h}\frac{\partial \overline{u'}^2}{\partial s} + \frac{1}{r}\frac{\partial}{\partial n}(\overline{u'v'}r) + \frac{2\overline{u'v'}}{Rh} + \frac{1}{r}\frac{\partial}{\partial \phi}(\overline{u'w'}) + \frac{1}{rh}\frac{\partial r}{\partial s}(\overline{u'}^2 - \overline{w'}^2)\right)$$

(Eqn.A.2.28)

Although not developed here, by following the same arguments, the time averaged n-component momentum equation can be shown to be;

$$\frac{1}{rh}\frac{\partial}{\partial s}(\overline{U}\overline{V}r) + \frac{\partial \overline{V}^2}{\partial n} + \frac{(\overline{V}^2 - \overline{U}^2)}{Rh} + \frac{1}{r}\frac{\partial}{\partial \phi}(\overline{V}\overline{W}) + \frac{1}{r}\frac{\partial r}{\partial n}(\overline{V}^2 - \overline{W}^2) =$$

$$-\frac{1}{\rho}\frac{\partial \overline{p}}{\partial n} - \left(\frac{1}{rh}\frac{\partial}{\partial s}(\overline{u'v'}r) + \frac{\partial \overline{v'}^2}{\partial n} + \frac{(\overline{v'}^2 - \overline{u'}^2)}{Rh} + \frac{1}{r}\frac{\partial}{\partial \phi}(\overline{v'w'}) + \frac{1}{r}\frac{\partial r}{\partial n}(\overline{v'}^2 - \overline{w'}^2)\right)$$

(Eqn.A.2.29)

while the time averaged ϕ-component momentum equation can be shown to be;

$$\frac{1}{rh}\frac{\partial}{\partial s}(\overline{U}\overline{W}r) + \frac{1}{r}\frac{\partial}{\partial n}(\overline{V}\overline{W}r) + \frac{(\overline{V}\overline{W})}{Rh} + \frac{1}{r}\frac{\partial}{\partial \phi}(\overline{W}^2) + \frac{\overline{U}\overline{W}}{rh}\frac{\partial r}{\partial s} + \frac{\overline{V}\overline{W}}{r}\frac{\partial r}{\partial n} =$$

$$-\frac{1}{\rho r}\frac{\partial \overline{p}}{\partial \phi} - \left(\frac{1}{rh}\frac{\partial}{\partial s}(\overline{u'w'}r) + \frac{1}{r}\frac{\partial}{\partial n}(\overline{v'w'}r) + \frac{(\overline{v'w'})}{Rh} + \frac{1}{r}\frac{\partial}{\partial \phi}(\overline{w'}^2) + \frac{\overline{u'w'}}{rh}\frac{\partial r}{\partial s} + \frac{\overline{v'w'}}{r}\frac{\partial r}{\partial n}\right)$$

(Eqn.A.2.30)

A.2.1 Comparison With Previously Published Work

Bradshaw (1973) developed the equations of motion in a two-dimensional s,n coordinate system. Bradshaw has shown that the two dimensional s-component momentum equation can be written as;

$$\frac{\partial \overline{U}^2}{\partial s} + h\frac{\partial}{\partial n}(\overline{U}\overline{V}) + \frac{2\overline{U}\overline{V}}{R} = -\frac{1}{\rho}\frac{\partial p}{\partial s} - \frac{\partial \overline{u}^2}{\partial s} - h\frac{\partial}{\partial n}(\overline{uv}) - \frac{2\overline{uv}}{R} \qquad \text{(Eqn.A.2.31)}$$

Bradshaw further suggests that the axisymmetric form of the equation can be obtained if all of the velocity products and the pressure gradients are multiplied through by the radius (r) i.e.;

$$\frac{\partial}{\partial s}(\overline{U}^2 r) + h\frac{\partial}{\partial n}(\overline{U}\overline{V}r) + \frac{2\overline{U}\overline{V}r}{R} = -\frac{r}{\rho}\frac{\partial p}{\partial s} - \frac{\partial}{\partial s}(\overline{u}^2 r) - h\frac{\partial}{\partial n}(\overline{uv}r) - \frac{2\overline{uv}r}{R}$$

(Eqn.A.2.32)

Dividing through by rh, leads to;

$$\frac{1}{rh}\frac{\partial}{\partial s}(\overline{U}^2 r) + \frac{1}{r}\frac{\partial}{\partial n}(\overline{U}\overline{V}r) + \frac{2\overline{U}\overline{V}}{Rh} = -\frac{1}{\rho h}\frac{\partial p}{\partial s} - \frac{1}{rh}\frac{\partial}{\partial s}(\overline{u}^2 r) - \frac{1}{r}\frac{\partial}{\partial n}(\overline{uv}r) - \frac{2\overline{uv}}{Rh}$$

(Eqn.A.2.33)

Now if we consider the three dimensional form of the s-component momentum equation derived earlier (Eqn.A.2.28) such that;

$$\frac{1}{h}\frac{\partial \overline{U}^2}{\partial s} + \frac{1}{r}\frac{\partial}{\partial n}(\overline{U}\overline{V}r) + \frac{2\overline{U}\overline{V}}{Rh} + \frac{1}{r}\frac{\partial}{\partial \phi}(\overline{U}\overline{W}) + \frac{1}{rh}\frac{\partial r}{\partial s}(\overline{U}^2 - \overline{W}^2) =$$

$$-\frac{1}{\rho h}\frac{\partial \overline{p}}{\partial s} - \left(\frac{1}{h}\frac{\partial \overline{u'}^2}{\partial s} + \frac{1}{r}\frac{\partial}{\partial n}(\overline{u'v'}r) + \frac{2\overline{u'v'}}{Rh} + \frac{1}{r}\frac{\partial}{\partial \phi}(\overline{u'w'}) + \frac{1}{rh}\frac{\partial r}{\partial s}(\overline{u'}^2 - \overline{w'}^2)\right)$$

(Eqn.A.2.28)

then the two dimensional axisymmetric form ($\partial/\partial\phi=0$, W=0) is given by;

$$\frac{1}{h}\frac{\partial \overline{U}^2}{\partial s} + \frac{1}{r}\frac{\partial}{\partial n}(\overline{U}\overline{V}r) + \frac{2\overline{U}\overline{V}}{Rh} + \frac{\overline{U}^2}{rh}\frac{\partial r}{\partial s} = -\frac{1}{\rho h}\frac{\partial \overline{p}}{\partial s}$$

$$-\frac{1}{h}\frac{\partial \overline{u'}^2}{\partial s} - \frac{1}{r}\frac{\partial}{\partial n}(\overline{u'v'}r) - \frac{2\overline{u'v'}}{Rh} - \frac{\overline{u'}^2}{rh}\frac{\partial r}{\partial s}$$

and since ;

$$\frac{1}{rh}\frac{\partial}{\partial s}(\overline{U}^2 r) = \frac{1}{h}\frac{\partial \overline{U}^2}{\partial s} + \frac{\overline{U}^2}{rh}\frac{\partial r}{\partial s}$$

the equation can be seen to be of the same form as that presented by Bradshaw. Furthermore, a number of authors have used Bradshaws two dimensional form of the equations in published work, including Gibson and Rodi (1981), Rodi and Scheuerer (1983) and Baskaran et. al. (1991).

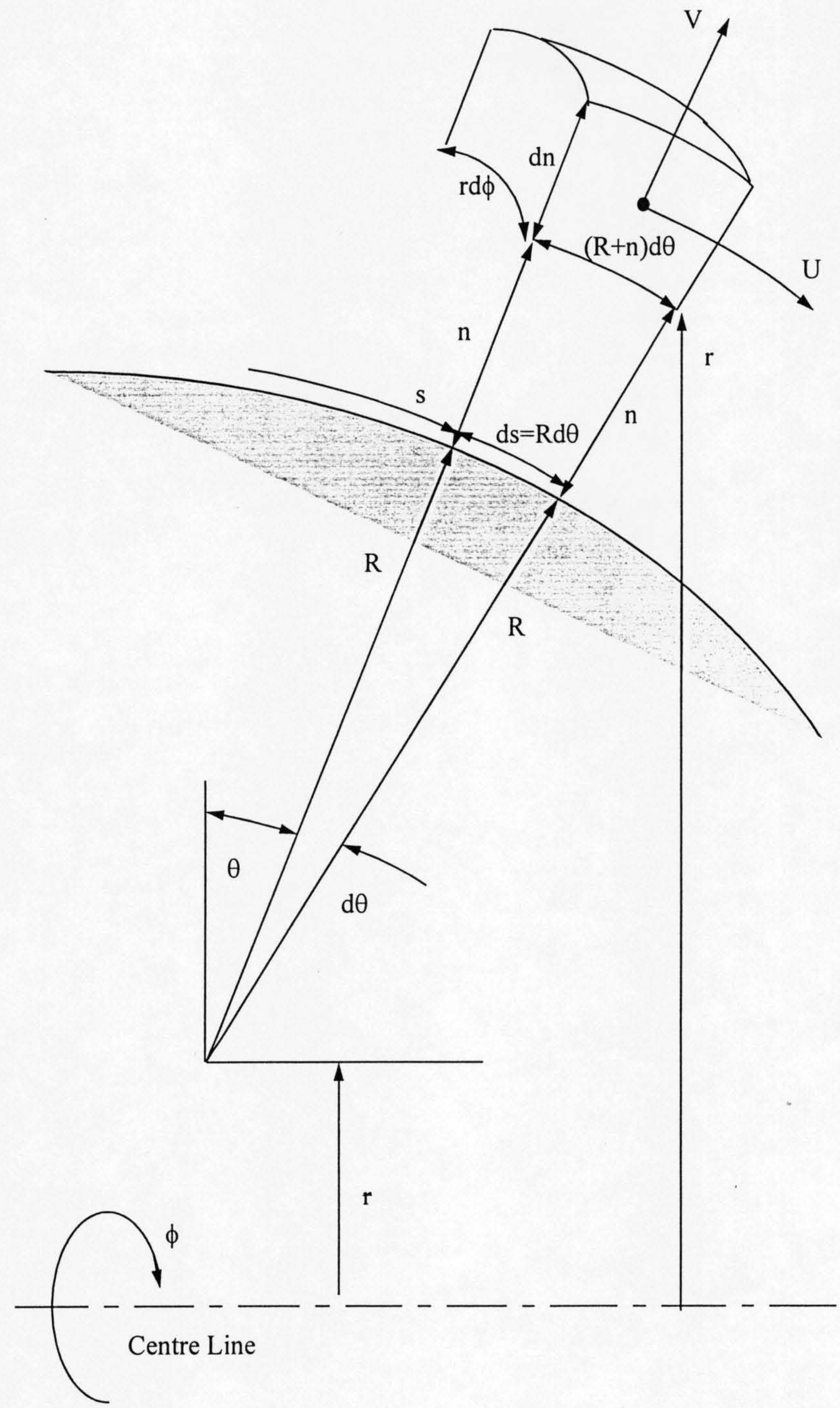

Fig.A.2.1 The s,n,ϕ coordinate system.